Probing New Physics with Spectroscopy of Trapped Ions

by

Joonseok Hur

Bachelor of Science in Physics,
Korea Advanced Institute of Science and Technology (2015)

Submitted to the Department of Physics
in partial fulfillment of the requirements for the degree of

Doctor of Philosophy in Physics

at the

MASSACHUSETTS INSTITUTE OF TECHNOLOGY

May 2022

Author .....
Department of Physics
May 13, 2022

Certified by .....
Vladan Vuletić
Professor of Physics
Thesis Supervisor

Accepted by .....
Deepto Chakrabarty
Associate Department Head of Physics

Probing new physics with spectroscopy of trapped ions

by

Joonseok Hur

Submitted to the Department of Physics
on May 13, 2022, in partial fulfillment of
the requirements for the degree of
Doctor of Philosophy in Physics

Abstract

Dark matter, a missing puzzle piece in our understanding of the Universe, remains dark despite abundant evidence for its existence and concerted experimental searches for candidate particles. In recent decades, experiments with atomic systems, driven by unprecedented developments in precision, have been providing tests for the Standard Model (SM), our current understanding of the Universe, and probing physics beyond the SM, including dark matter. In particular, it has been proposed that a new hypothetical elementary boson, a dark-matter candidate, can violate an SM prediction: linear distributions of measured isotope shifts (ISs) mapped onto graphs called King plots [1, 2, 3]. The prediction can be tested purely experimentally. If the violation is observed, however, possible new-physics contribution has to be distinguished from higher-order SM corrections originating from nuclear physics.

This thesis reports IS spectroscopy experiments with laser-cooled and trapped singly ionized Ytterbium (Yb^+) ions to search for new physics through the proposed novel method. The King-plot nonlinearities thus observed for the optical clock transitions in Yb^+ ions with significance up to 240 standard deviations σ and their implications to the new boson and nuclear physics are presented. In particular, there is a dominant, common source of nonlinearity originating from nuclear charge distributions and yet a small, second source of unknown origin with 4.3σ significance. Pattern analysis of the nonlinearity in the King plots has been developed as a method for identifying or removing the sources of the observed nonlinearity. Atomic and nuclear structure calculations translate the measured nonlinearity patterns into bounds on new-boson interaction between subatomic particles as well as information on nuclear properties. The atomic structure calculations performed for Yb^+ ions are illustrated in detail. Outlook and future works are discussed, including measurements for more transitions and isotopes and improving the experimental precision.

Thesis Supervisor: Vladan Vuletić
Title: Professor of Physics

Acknowledgments

The seven-year journey toward a doctoral degree at MIT has been one of the best periods in my life.

I would like to thank my thesis supervisor, Professor Vladan Vuletić, for his support and teaching throughout my Ph.D. I have learned from him how keeping an optimistic attitude is crucial to a scientist. I hope I have absorbed a tiny piece of his insights on physics and research in general.

I would also like to thank my thesis committee members, Professor Wolfgang Ketterle and Professor Ronald Fernando Garcia Ruiz. I took introductory AMO physics classes given by Prof. Ketterle, so he is the father of all my fundamental knowledge of AMO physics. I am eager to see the results of the isotope-shift experiments with radioactive isotopes that Prof. Garcia Ruiz is planning, which would make the research topic of this thesis much richer.

I cannot thank my lab colleagues, Eugene Kynazev and Diana P. L. Aude Craik, enough. Our synergy has enabled us to reach what we set out to accomplish.

I would like to give a special thanks to Calvin Leung, with whom I started to work on atomic structure calculations. I would not have been able to work as seriously on such a new subject without him.

I acknowledge all the members in Prof. Vuletić's group and in CUA. We have always been the first and best resource to each other for advice, discussions, and emergency needs in the lab.

Lastly, my biggest thanks to my parents and sister for their endless support and encouragement throughout my entire life.

Contents

List of Figures

List of Tables

Part I

Introduction

Chapter 1

The concert of cold ion trapping, precision spectroscopy, and atomic and nuclear calculations to go beyond the Standard Model

1.1 Physics beyond Standard Model and dark matter

The Standard Model (SM) of particle physics describes virtually all measurements of elementary particles exquisitely well. However, there have been various observations that have not been explained by the SM, which implies the necessity of physics beyond the SM (BSM), or simply new physics. Naturally, a vast variety of classes of BSM physics have been proposed aiming to solve at least a part of such anomalies, and experimental efforts to probe them have been made in various fields of physics with their own techniques [34, 35].

One of the significant evidences for BSM physics is dark matter: preponderance of mass with unknown composition in our Universe. The existence of dark matter has been suggested from astronomical observations with several different method-

ologies such as the rotation curves of galaxies [36], the motion of colliding galaxy clusters [37], gravitational lensing [38], and the power spectrum of the cosmic microwave background [39]. Various candidates for dark matter have been proposed including, but far from limited to, weakly interacting massive particles (WIMPs) [34], primordial black holes [40], axion, axionlike particles (ALP), and light force carriers [34, 35] (cf. Fig. 4-7 in Ref. [41]), and numerous laboratory experiments have been conducted to find evidence for the candidates. Despite the extensive efforts, however, there has been no decisive confirmation for any of the candidates and the nature of dark matter is still unknown. In particular, the search for dark matter has been largely focused on theoretically well-motivated WIMPs with mass of $\gtrsim$10 GeV/c^2 [42] until relatively recently, with no significant success. In consequence, relatively light candidates with intermediate mass of $\sim$10 eV/c^2 to $\sim$100 MeV/c^2 or lighter has been gaining increasing attention.

1.1.1 New boson as the carrier of fifth force

In this thesis, one of the classes of light dark matter will be considered as the new physics to probe: a new hypothetical boson ϕ as a force carrier, which can be characterized by its mass m_ϕ, spin s, and interactions. If the new boson interacts with the particles in the SM such as leptons and quarks, it may include a new fundamental force (*fifth force*) in the corresponding BSM physics via exchange of a virtual boson between the particles (see a Feynman diagram in Fig. 1-1). The potential between the particles from the new force is given as Yukawa-like potential:

$$V_{XY}^{\phi}(r) = \hbar c \underbrace{(-1)^{s+1}\frac{y_X y_Y}{4\pi\hbar c}}_{\equiv \upsilon_{XY}} \frac{e^{-r/\lambda\!\!\!^{-}_c^{\phi}}}{r} \tag{1.1}$$

in general, where y_X and y_Y are the coupling constants of the boson to two particles X and Y, respectively (e.g., $X = n$: neutron and $Y = e$: electron), in the unit of rationalized charge (i.e. 4π factor) and the $\lambda\!\!\!^{-}_c^{\phi} = \hbar/(m_\phi c)$ is the reduced Compton wavelength of the boson. The expression is given with an emphasis of the

natural units, and $\upsilon_{XY} \equiv (-1)^{s+1} y_X y_Y/(4\pi\hbar c)$ serves effectively as the *fine-structure constant* of the new force just as the fine-structure constant $\alpha \approx 1/137$ for the electromagnetic interactions. The mass of a boson limits the length scale of the potential to λ_c^ϕ through the exponential decay.

It is noteworthy that the Yukawa potential is not a consequence of *real* bosons (i.e., excited field of bosons with energy of $m_\phi c^2$ per boson) interacting with (SM) particles. As far as there are the dimensions to accommodate the potential existence of such bosons in the Universe, the creation and exchange of *virtual* bosons will always occur to exert the new force. It is comparable to the fact that there are always Coulomb potentials between charged particles regardless of the existence of light (i.e. real photons) around the charges. Therefore, efforts to observe the effect of new Yukawa-like potential can be regarded as searches for the virtual new boson.

1.2 Atomic systems as low-energy probes for the Standard-Model tests and new-physics searches

The traditional approaches to search for new physics can be largely categorized as the following: directly probing new physics via processes under high energy involved via particle colliders (e.g., observation of Higgs boson [43]); detecting rare events by increasing the amount of samples (e.g., neutrino experiments [44, 45]); or obtaining observational evidences from astrophysical phenomena, complementing laboratory experiments (e.g., SN1987A supernova [46] giving bounds on axion [47, 48, 49]; see also Fig. 1-2). In addition to the relatively traditional methods, there has been a concerted effort in the field of atomic, molecular, and optical (AMO) physics to test the SM and probe new physics of various kinds [50]. It is motivated by unprecedented developments in experimental precision in AMO physics since lasers had been invented. The SM tests or new-physics searches are typically established by measuring the deviations from predictions of the SM, which could be originated from the effect of BSM physics of particular types. The deviations may be tiny at the low energy

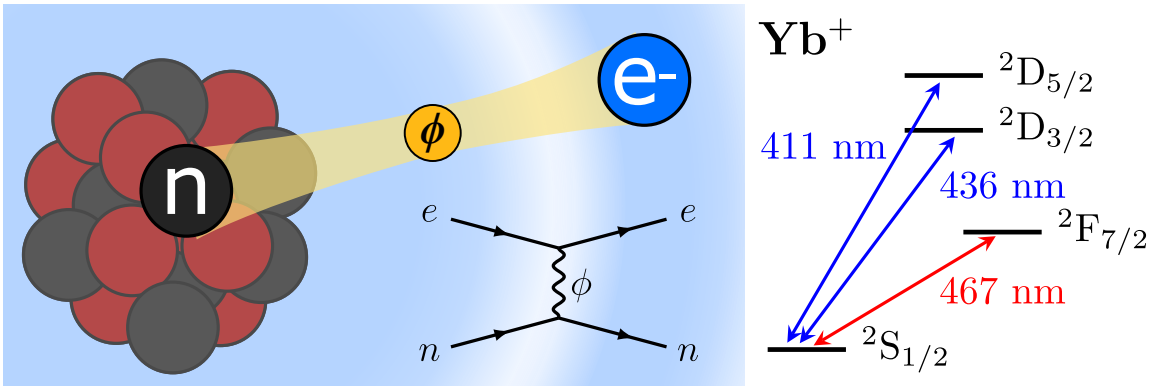

Figure 1-1: New interatomic force arising from the exchange of a hypothetical ϕ boson between neutrons and electrons (left), and simplified Yb^+ level structure (right). In this work, the two electric quadrupole optical transitions at 411 nm and 436 nm (blue arrows) and the highly forbidden octupole transition at 467 nm (red arrow) are measured.

scale of atomic systems, which might be nevertheless measurable taking advantage of the high precision of recent AMO experiments' techniques. The high-precision techniques include atomic clocks [51, 52, 53, 54, 55, 56] as a representative example and also atomic mass spectroscopy [20, 26, 57], optical magnetometry [58, 59], atom-wave interferometry [60], and more [50], and non-exhaustive examples of SM tests and new-physics searches are tests on symmetries [61, 62, 63], variation in physical constants [64, 65], fundamental particles' properties such as $g-2$ and electric dipole moments [66, 67], gravitational wave detection [68, 69, 70], search for dark energy [71, 72] and new elementary particles [2, 3, 28].

1.2.1 Trapped ions as a probe for new boson

This thesis probes the effect of a new, hypothetical boson described in Section 1.1.1. If the Universe has dimensions to accommodate the new bosons, the new Yukawa-like potentials between subatomic particles may overlap with the particles' wave-functions and perturb their states. In particular, if the new boson mediates the new force between electrons and nucleons in an atomic system, the new overlap with the wavefunctions of the electrons shifts the frequencies of transitions between bound states of the electrons in the Coulomb potential well, which have low energy scales

(e.g., few eV for optical transitions), as described in Fig. 1-1. If the $\lambda\!\!\!^{-}_c^{\phi}$ is longer than the size of the nucleus in the atomic system, corresponding to the mass range $\lesssim$100 MeV/c^2 of a new boson, then the overlap will be dominated by the wavefunction of the electrons outside the nucleus. The effect of the new boson, therefore, would not be sensitive to the internal structure of the nucleus which might affect the intranuclear wavefunction. If the coupling of the new boson to the subatomic particles is strong enough and the shifts in the transition frequencies can be resolved with a state-of-art precision experiment for the atomic system, it may provide evidence for the new boson. Therefore, precision spectroscopy for atomic systems may be a suitable probe for the new boson with $\sim$100 MeV/c^2 or lighter mass.

The direct detection of such shifts is challenging, however, because the accuracy of calculations for transition frequencies (unshifted in the case of no new boson) is far worse than the measurement precision of real transition frequencies; state-of-art atomic clocks, which are essentially absolute transition frequency measurements, have fractional uncertainty of $\sim 10^{-18}$ or better [51, 52, 53, 54, 55], while the accuracy of *ab initio* atomic structure calculations is limited to $\sim 10^{-5}$ for the species commonly used in atomic clocks [73, 74] (see Chapter 12 for more discussion). The precision calculation might be feasible for species with very simple structures such as hydrogen [74], but the calculation accuracy has been bound to the proton radius puzzle [75, 76, 77],[1] and trapping or laser cooling to a sufficiently low velocity are technically challenging for the species [78, 79, 80].

There have been proposals to sidestep the difficulty in the direct detection by measuring isotope shifts (ISs) in atomic transitions [2, 3]. Properly normalized ISs in different transitions exhibit a highly linear relationship when they are mapped onto two-dimensional (2D) graphs called King plots [1]. Refs. [2, 3] argue that a deviation from the linearity may indicate the effect of a new force mediator ϕ (see Chapter 8). The (non)linearity in a King plot is an observable which can be tested purely through experiments, making the knowledge of the detailed structure of the

[1] Which might be the effect of new physics.

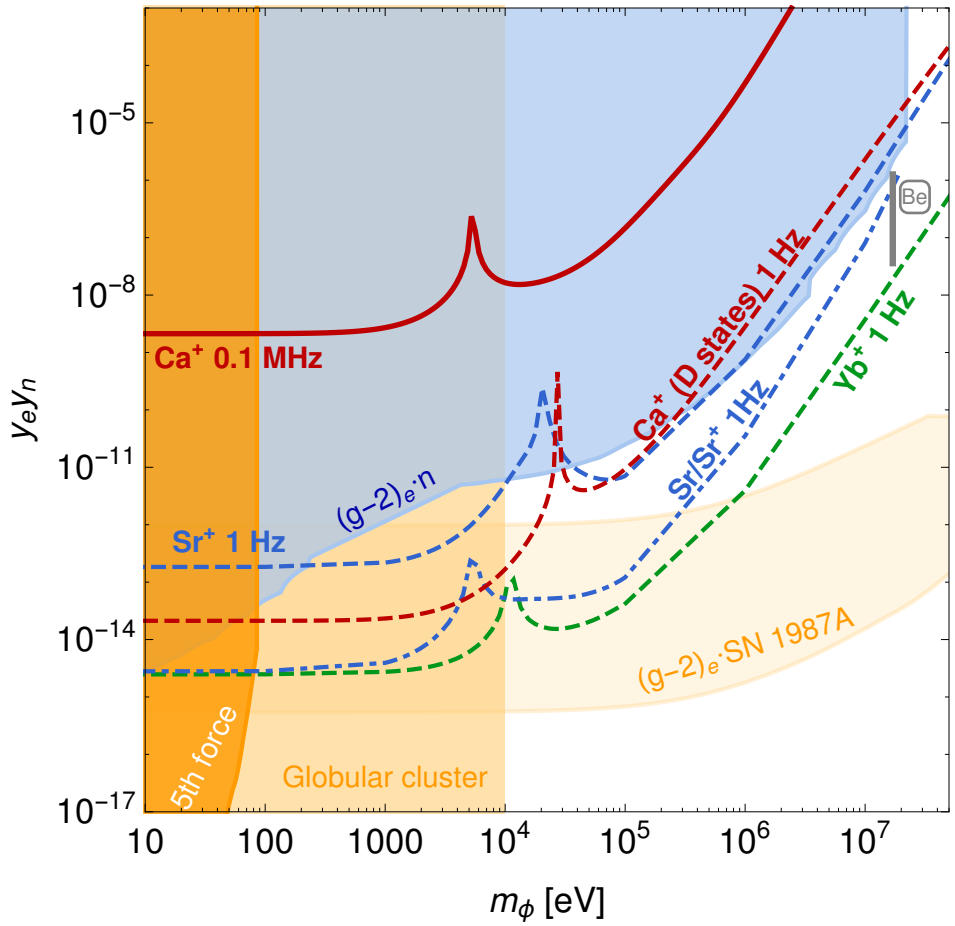

Figure 1-2: Limits on new boson couplings $y_e y_n$ (absolute value; in the unit of $\hbar c$) to electrons and neutrons vs new boson mass m_ϕ for transitions in Ca^+, Sr^+, neutral Sr and Yb^+ in Ref. [3]; bounds from other laboratory experiments or cosmic data are shown as colored areas with the details in the reference therein.

probe (e.g, the wavefunction of electrons) irrelevant for the test.[2] The price paid for the sidestep, however, is higher-order nuclear effects within the SM, which can also result in nonlinearities that might limit the sensitivity to new physics unless the associated atomic and nuclear structures are examined [5, 8, 81, 82, 83, 84, 85, 86]. Therefore, the sources of nonlinearity have to be identified once the nonlinearity is observed experimentally, and a strategy to distinguish the sources is proposed (Section 8.3) and demonstrated (Section 10.2) in this thesis.

Ref. [3] proposed suitable atomic systems for the King linearity test, individual

[2]The shift from comparing absolute frequencies to testing King-plot linearity also illuminates the importance of finding suitable observables for tests in general.

neutral or ionized atoms, based on the calculated sensitivity of the atomic species to the shift induced by the new Yukawa potential. As shown in Fig. 1-2, IS measurements in the species with the precision of 1 Hz, especially for the heavier elements Sr and Yb^+, are expected to give bounds on the new boson's interactions which are comparable to some of the bounds from other experiments or astrophysical observations, and probe a part of the area which has not been explored in $10\,\mathrm{keV} \lesssim m_\phi c^2 < 100\,\mathrm{MHz}$ mass range.[3]

The work in this thesis uses singly-ionized Ytterbium (Yb^+) atoms among atomic species including in Ref. [3] as Yb^+ is one of the preferred choices for several reasons. First, Yb^+ has a wide transition from the ground state for efficient laser cooling and state detection as described in Section 3.1.1. It also has transitions for efficient optical repumping to keep the population in the ground state. All the transitions have the wavelengths for which lasers are technically straightforward to achieve. Second, there are enough numbers of transitions and isotopes in Yb^+ ions to test the King linearity. For the test, at least two narrow transitions for the IS measurement (i.e., two axes in the King plot) and three *independent* isotope pairs (i.e., three points to test the linearity, implying four isotopes; see Section 11.5) are required. In Yb^+, there are three known optical clock transitions that have the linewidths on the order of 10 Hz or narrower, which are suitable for precision spectroscopy (see Section 3.1.2). Yb has also 7 stable isotopes (mass number $A \in \{168, 170, 171, 172, 173, 174, 176\}$), and 5 of them with even A have no nuclear spin to avoid complications from the hyperfine structure.[4] It is important to note that there are one extra transition and isotope than the minimum requirement for the King linearity test, and they provide essential information on the physical origin of the King nonlinearity as described in Section 10.2. Also, Yb is a relatively heavy element among the species of which ISs have been measured (see the last paragraph in this section). The masses of isotopes in Yb measured by atomic mass spectrometry have been reported with

[3]Note that the bounds for the atomic species were obtained from the effect of new boson only; the effect of the higher-order SM corrections are not considered in the figure.

[4]Uses of isotopes with nuclear spins or unstable isotopes are discussed in Chapters 19 and 20, respectively.

better fractional uncertainty than lighter species in general [6, 7], presumably due to their heavier masses. Yb^+ is also sensitive to both new-physics and nuclear-physics contributions by having many electrons in general. As a potential consequence, the measured ISs in a lighter species Ca^+ [87], reported at the same time as the first result of the thesis work was published [5], showed no King nonlinearity despite the 10-fold better precision in the IS measurement.

Lastly, ions are relatively less demanding to perform spectroscopy with than neutral atoms in general. An ion can be trapped in a (pseudo)potential formed by external electromagnetic fields (e.g., Paul or Penning trap) which provide tighter and deeper confinement compared to the trap for neutral atoms (e.g., optical lattice). The tight confinement enables precise and accurate measurements of transition frequencies by letting the ions in the Lamb-Dicke regime with well-resolved carrier and sideband vibronic transitions (see Sections 3.2 and 7.1). The external-field traps also allow to turn off the other beams to avoid light shifts while the clock transitions are interrogated. On the other hand, neutral atoms are subject to light shifts from the optical lattices, and the magic wavelengths for the transitions have to be predicted [88, 89] and measured [90] to suppress the light shifts.[5]

ISs had been measured for various other atomic species including Ca^+ [87, 91, 92], Sr^+ [93], Sr [94], Cd [95], Ba^+ [96], Ba [97], Nd^+ [98], and Dy [99] until the first result of the thesis work was published [5]. However, there was no significant evidence of the King nonlinearity to the best of the thesis author's knowledge, unless isotopes with nuclear spins are involved as in Refs. [94, 99] which might be from the complications in their hyperfine structures (see Chapter 19).[6] The King nonlinearity for spinless isotopes has been confirmed only with Yb^+ ions by this thesis work or with neutral Yb atoms [9, 10] to date.

[5]Note, however, experiments with careful analysis for systematic effects enable spectroscopy with neutral atoms as in Refs. [9, 10]; the precisely measured ISs in Refs. [9, 10] have been essential parts of data to derive conclusions of this thesis work as described in Section 10.2.

[6]There is an old example of King nonlinearity with even-A isotopes of Sm [100], which is due to the mixing of two closely-spaced electronic levels [101]. It is also not relevant to new-physics or nuclear effects.

Chapter 2

Thesis overview

This thesis reports isotope-shift (IS) spectroscopy experiments with laser-cooled and trapped singly ionized Ytterbium (Yb^+) atoms to probe a new hypothetical boson and presents the results. After the brief introduction on background concepts, research goal, and experimental platform, the details on the IS spectroscopy experiments and data analysis with King plots follow. The results including observed violation of King linearity and the source of the nonlinearity are shown. In particular, from the measured ISs with $\lesssim$500 Hz uncertainty, King nonlinearities were observed with the significance up to 240 standard deviations σ. It is shown that there is a dominant, common source of nonlinearity originating from particular shapes of charge distributions inside nuclei and yet a small, second source of unknown origin with 4.3σ significance, which could be from the new boson. Pattern analysis of King nonlinearities has been developed as a method for identifying or removing the sources of the observed nonlinearity. Calculations on atomic structures, rather independent from the other parts of this work, performed to translate the measured nonlinearity patterns into bounds on new-boson interactions or nuclear properties, are illustrated in detail. Finally, future works and outlook are discussed subsequently.

The thesis is structured as follows:

- Part I provides introductions on physics beyond the Standard Model, dark

matter, and search for them (Chapter 1); the outline of this thesis (Chapter 2); and a brief overview of Yb^+ ions in an ion trap for spectroscopy (Chapter 3).

- Part II describes experiments for IS spectroscopy performed in the thesis work. This part starts with the description of the experimental setup in detail, including the upgrades that have been made since the last thesis on this new-physic probing research [4] (Chapter 4). The procedure of the IS spectroscopy experiment for each clock transition follows (Chapter 5). The data obtained from the experiments are presented and analyzed in Chapter 6 to derive the values of ISs. The systematic effects to the measured ISs are carefully analyzed (Chapter 7). The summary of the measured ISs can be found in Appendix A.

- Part III presents the main subject of the thesis. King plots and the associated linearity are introduced, and methods of analyzing the observed King-plot nonlinearities are developed in Chapters 8 and 9. Chapter 10 presents the results: the King plots from the ISs measured in Part II and the observed nonlinear patterns in the plots with high significance. Discussion of the results follows in Chapter 11, including the physical origin of the observed nonlinearities.

- Part IV illustrates calculations of atomic structures and IS electronic factors used in Part III. The atomic structure calculations (ASCs) of different methods (Chapter 12) and a software package GRASP2018 [24] used for this work (Chapter 13) are introduced. The step-by-step procedure of atomic structure calculations for the optical clock transitions in Yb^+ is presented in Chapter 14. Chapter 15 introduces the methods to calculate the electronic factors from the electronic wavefunctions that GRASP2018 outputs, which translate the measured ISs into the new boson or nuclear properties. In particular, an add-on package for GRASP2018 named REDF for extracting Radial Electron Density Function over space has been developed by the thesis author as introduced in Section 13.2. The summary of the calculated electronic factors can be found in Appendix C.

- Part V discusses various future works and research directions to further investigate possible new-physics and nuclear effects: upgrading the experimental setup to improve the precision of IS spectroscopy (Chapter 17), cotrapping ions of different isotopes (Chapter 18), using isotopes with hyperfine structures (Chapter 19) or radioactive isotopes (Chapter 20), and driving transitions that involve Rydberg states (Chapter 21). The general outlook on the search for new physics with IS spectroscopy and King plots is briefly discussed in Chapter 22, the last chapter of this thesis.

This thesis contains the following appendices:

- Appendix A for the summary of the measured ISs and the values with reduced uncertainties (see Section 6.7). The absolute frequencies derived from the measured ISs are also presented.

- Appendix B for the summary of the transitions in Yb^+ ions relevant to this work and the properties of the laser beams addressing the transitions.

- Appendix C for the summary of the calculated IS electronic factors for the transitions in Yb^+ ions and neutral Yb atoms from the atomic structure calculations.

- Appendix D for the theory of electric multipole transitions and, subsequently, the selection rules and relative transition rates for the optical clock transitions in Yb^+ ions.

- Appendices E and F for the reprints of the publications from this work, Refs. [5] and [8], respectively.

Chapter 3

Singly ionized Ytterbium atoms in ion trap

A singly ionized Ytterbium (Yb^+) ion in an ion trap, the most essential part of the whole experimental setup for this thesis work, is introduced in this chapter.

3.1 Transitions

Figure 3-1 shows a partial level diagram of Yb^+ ions (with no nuclear spin) with all the relevant electronic states and the transitions between them for this work. The transitions' uses are divided into two parts: the transitions for cooling and controlling ions; and the optical clock transitions for which the ISs will be measured with high precision.

The details on the transitions are summarized in Table B.1 with the references therein. Tables A.3 and A.2 also list the absolute frequencies and ISs of the transitions, respectively, to address each individual isotope; most of the values have been either the first reports in literature or with reduced uncertainties.

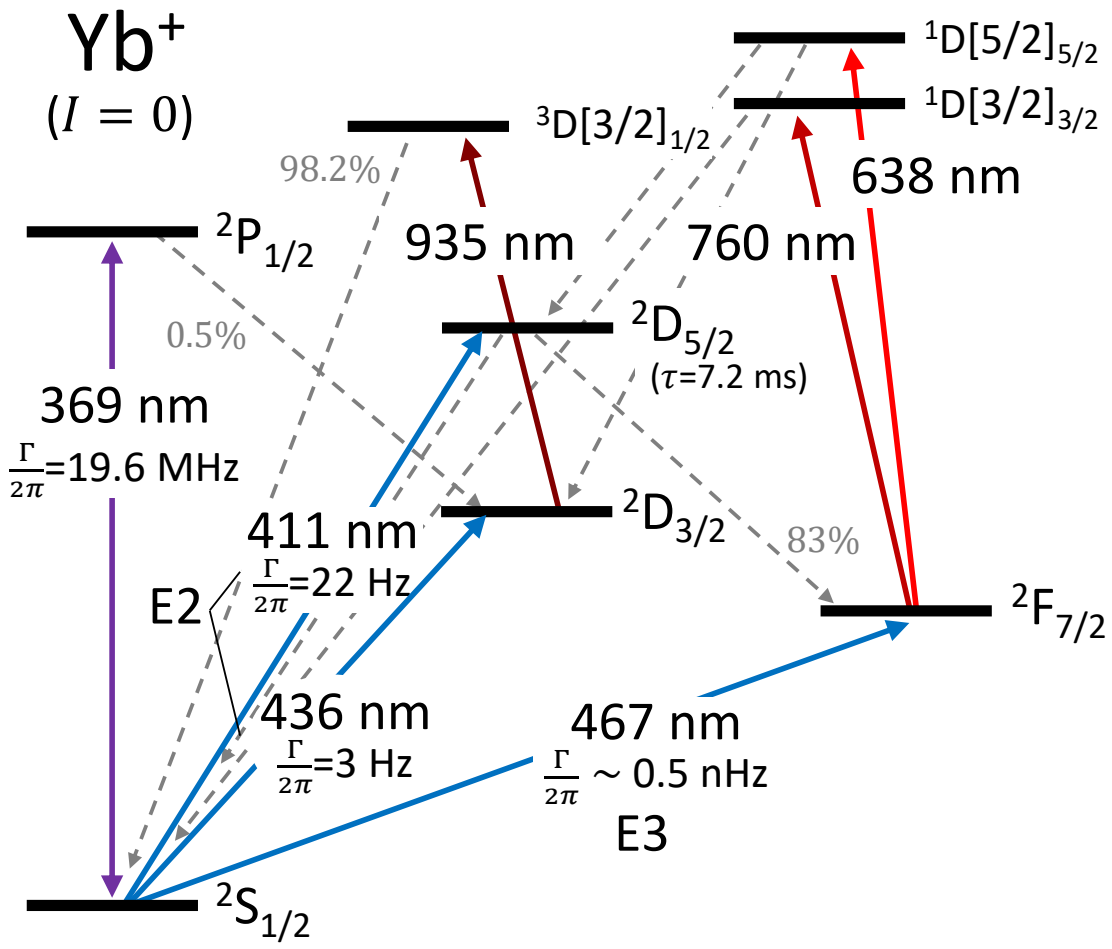

Figure 3-1: Partial level diagram for Yb^+ ions with zero nuclear spin ($I = 0$). Transitions for cooling (369 nm; purple), $^2D_{3/2}$-state repumping (935 nm; brown), and $^2F_{7/2}$-state repumping (760 nm or 638 nm; red) are presented. Blue arrows show the optical clock transitions: two electric quadrupole (E2) transitions α: $^2S_{1/2} \rightarrow {}^2D_{5/2}$ (411 nm) and β: $^2S_{1/2} \rightarrow {}^2D_{3/2}$ (436 nm), and an electric octupole (E3) transition γ: $^2S_{1/2} \rightarrow {}^2F_{7/2}$ (467 nm). Details on the transitions and decay channels (gray dashed arrows) are summarized in Table B.1 with the references therein.

3.1.1 Cooling and control

There is a wide transition from the ground state, $^2S_{1/2} \rightarrow {}^2P_{1/2}$ at 369 nm with 19.6 MHz linewidth. It provides efficient laser cooling, fast optical pumping for initial state preperation (see Section 4.1.4), and state detection (see Section 5.1).

The ion falls into the metastable $^2D_{3/2}$ and $^2F_{7/2}$ states spontaneously or by driving the optical clock transitions (see Fig. 3-1). To bring the population in the metastable states to the ground state, suitable transitions for *optical repumping* are necessary. $^2D_{3/2} \rightarrow {}^2D[3/2]_{1/2}$ transition at 935 nm is the primary choice as a $^2D_{3/2}$-state repumper. To repump the $^2F_{7/2}$ state, $^2F_{7/2} \rightarrow {}^2D[5/2]_{5/2}$ at 638 nm were used in initial works [4], which has been replaced by $^2F_{7/2} \rightarrow {}^2D[3/2]_{3/2}$ at 760 nm for faster repumping (see Section 4.2.6).

The detailed procedure of trapping and cooling is described in Section 4.1.2 for the experimental setup used in the thesis work.

3.1.2 Clock transitions

There are total three optical clock transitions at the blue wavelengths: α: $6s\,^2S_{1/2} \rightarrow 5d\,^2D_{5/2}$ at 411 nm, β: $6s\,^2S_{1/2} \rightarrow 5d\,^2D_{3/2}$ at 435.5 nm (or simply 436 nm), and γ: $4f^{14}6s\,^2S_{1/2} \rightarrow 4f^{13}6s^2\,^2F_{7/2}$ at 467 nm, labeled with the Greek letters for convenience.

The first two transitions α and β are electric quadrupole (E2) transitions and have reasonably narrow linewidths from the ms-level excited-state lifetimes. It is noteworthy that the two transitions have very similar electron configurations. The excited states' energies differ primarily by the spin-orbit coupling, which leaves their radial wavefunctions largely the same (see Section 10.2). The two transitions are also relatively simple in the sense that it excites only a valence electron while maintaining the core electrons.

The remaining γ transition is an electric octupole (E3) transition. This transition is highly forbidden and a lifetime of a few years is expected (see Table B.1). It is known to be the narrowest optical transition found to date and is regarded as one of

the suitable transitions for an atomic clock.[1] The transition takes out an electron in a closed f shell and put it into the valence s shell, resulting in a significant change in the electrons' wavefunction. The γ transition thus provides higher sensitivity to new boson and nuclear effects compared to the α and β transitions, manifested by the increased size of measured nonlinearity in King plots (see Fig 10-1 and Table C.3).

The knowledge of selection rules for transitions is helpful for identifying the substructure of the transition: different peaks from, for instance, Zeeman structure, vibronic transitions due to the trap (see Section 3.2), and the micromotion of ions. The selection rules for the α, β, and γ transitions can be found in Appendix D.

3.2 Spectroscopy of trapped ion

Spectroscopy without strong confinement of resonators (e.g., gas in vapor cells) is subject to huge Doppler broadenings typically on the order of GHz. Propagating beams to flying atomic beams at a perpendicular angle can reduce the broadening, but the linewidth is still typically on the order of 10 MHz, and also subject to the Doppler shift by an imperfect angle. Saturation absorption spectroscopy is not a choice in general for narrow transitions, presumably because the saturation of transitions is fundamentally based on spontaneous emission processes which are slow for the narrow transitions, as well as the high power required to saturate the transitions.

Confining atoms' positions makes the first-order Doppler shift in the center of a transition vanishes due to the zero velocity of atoms on average,[2] and enables continuous cooling of the atoms to the low temperature. Furthermore, a *tight* trap gives two more advantages. First, a trap with motional energy spacing $\hbar\omega$ bigger than photon recoil energy suppresses photon recoils (Lamb-Dicke regime), which is quantum mechanically the source of the Doppler shift [103]. Second, if the trap's energy spacing in frequency ω is bigger than the linewidth Γ of the transition to be measured, the Doppler broadening is *resolved* in the form of carrier and sideband

[1] The transition is a recommended secondary representation of the second in the International System of Units (SI) [51, 102].

[2] Unless the center of the confinement moves.

vibronic transitions. The effect of the confinement and the remaining systematic shifts from the Doppler effect are described in Section 7.1 in detail.

Part II

Isotope Shift Spectroscopy

Chapter 4

Experimental setup

This chapter describes the experimental setup for precision isotope-shift (IS) spectroscopy of trapped Yb^+ ions, the means to probe new physics in this thesis. The setup used here has been designed as a versatile ion trap platform, and it has been used for various research topics [5, 8, 104, 105, 106, 107] with appropriate customization for each project.

This chapter consists of two parts. A rather brief overview of the setup as an ion trapping system and essential customization for IS spectroscopy are presented in Section 4.1. More details on this part, including step-by-step procedures of trapping and cooling ions and associated beam configurations, can be found in Ref. [4], a thesis that covers the earlier works on this new-physics probing research. The following Section 4.2 then describes the upgrades in the setup that have been made, especially after the work of Ref. [4], to adapt the setup more for the precision experiment.

The details on the fundamental parts of the setup and relevant initial works, from the fabrication of the ion trap chip to building vacuum chambers, lasers, and optics setups, are elaborated in the theses of former Ph.D. students [4, 108, 109, 110].

4.1 Overview of setup

The composition and basic controls of the system for trapping, cooling, and imaging ions as a versatile ion trap apparatus are overviewed in the first few subsections. The

subsections with more focus on spectroscopy experiment then follow: state preparation of ions and the generation and frequency control of the probe beam that drives optical clock transitions in Yb^+ ions.

4.1.1 Yb^+ ion trap system

Figure 4-1 illustrates the setup in the experimental chamber. All the experiments with trapped ion samples undergo in an ultrahigh vacuum (UHV) chamber with the internal pressure below 10^{-9} Torr.[1] A surface Paul trap is placed in the vacuum chamber upside-down. The trap chip, fabricated by a former PhD student Marko Cetina [108], generates an axial potential along the chip by outer, segmented electrodes to which DC voltages are applied (see Fig. 4-1). A two-dimensional radial pseudopotential (i.e. cylindrical trap) is formed by RF electric field from a pair of the thin, linear electrodes placed inner than the DC electrodes and driven by $\omega_{\mathrm{RF}}/(2\pi) = 16.16\,\mathrm{MHz}$ signal. The confinements along the axial and radial directions can be tuned by changing the (amplitude of) voltages at the electrodes, up to the secular frequency $\omega_{tr}/(2\pi) = 2.3\,\mathrm{MHz}$ in the radial direction [105]. The radial potential is tilted (i.e. elliptical trap in the radial plane), with the principal axes not parallel to the surface of the chip, by applying DC voltages of opposite polarity to each of the RF linear electrodes, and applying opposite-polarity compensating voltages to the outer DC electrodes [109]. The tilted potential makes trapped ions cooled in both the radial dimensions with a single cooling beam parallel to the surface of the chip (see also Section 4.1.2).

The center of the trap for Yb^+ ions is placed $135\,\mu\mathrm{m}$ *below* the surface of the chip. The secular frequencies of the trap along the radial and axial directions are listed in Table 4.1. A neutral Yb flux is generated from an oven inside the chamber that contains an Yb sample (having all stable isotopes with their natural abundance [111]), heated up by flowing electric current. The Yb atoms fly toward the potential well that the trap chip creates.

The values of parameters regarding the ion trap for the experiments in this thesis

[1] From an ion pump current reading.

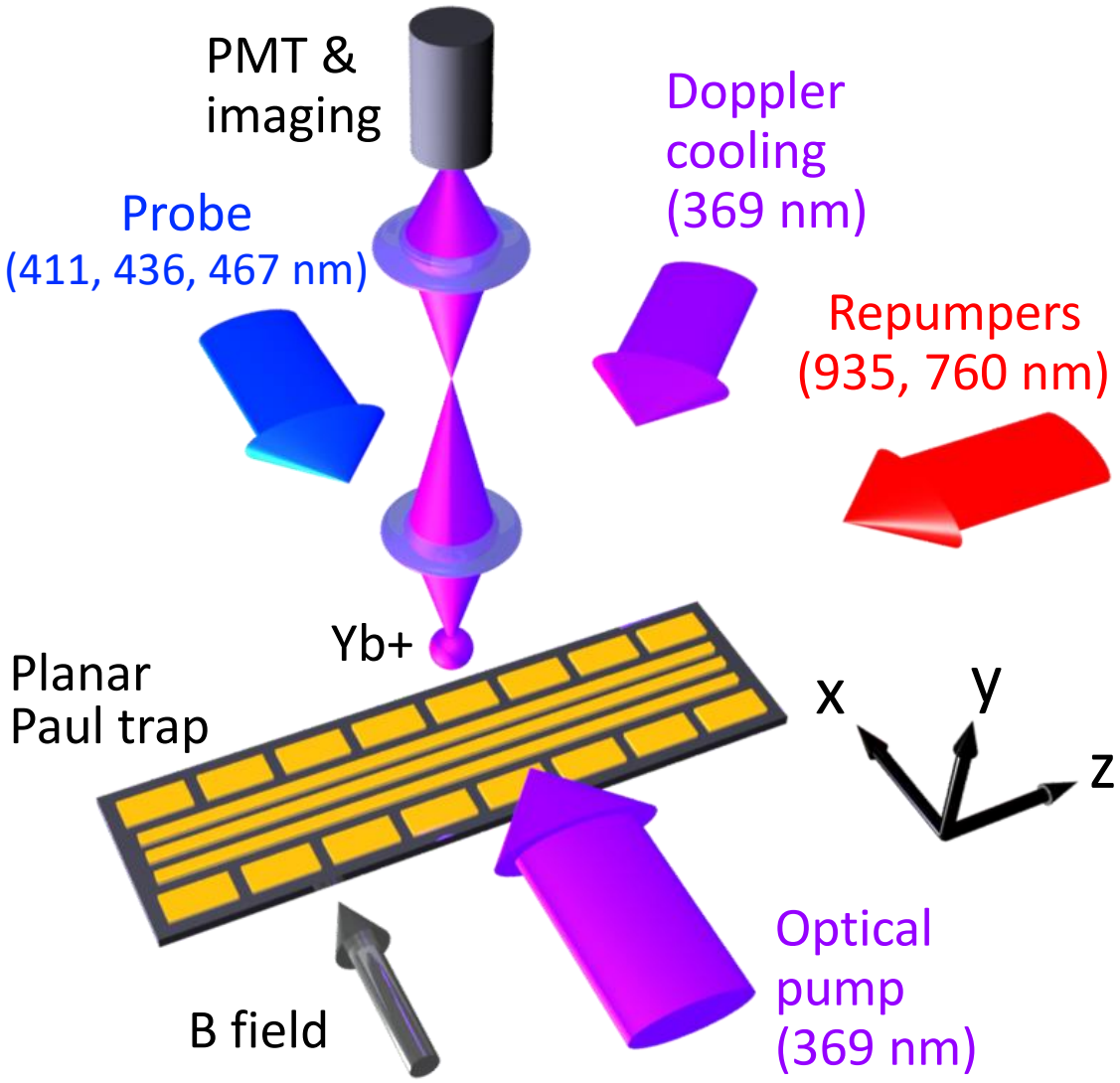

Figure 4-1: Schematic drawing of the experimental setup. A single ytterbium ion is trapped 135 µm away from the surface of a microfabricated planar Paul trap housed in an ultrahigh vacuum chamber. The propagation directions of the laser beams used for cooling, repumping, ground-state optical pumping, and optical clock transition probing (see Fig. 3-1) are indicated by labeled arrows. Fluorescence from trapped ions is collected using either a PMT or an EMCCD camera (see Section 4.1.3). The probe laser beam is linearly polarized along the trap axis (the z direction in this figure).

Table 4.1: Trap parameters for the experiments in this thesis. Each column corresponds to one of $i \in \{tx, tr1, tr2\}$: the trapping potentials along the axial direction (tx) and the principal axes of the radial direction ($tr1, tr2$). If equations are given in a table footnote, all the necessary values are from this table.

Parmeter			tx	$tr1$	$tr2$
RF drive frequency		ω_{RF}		16.16 MHz	
Secular frequencies		$\omega_i/(2\pi)$	364 kHz[a]	1.38 MHz[b]	0.88 MHz[b]
Mathieu parameters	DC	a_i	2.0×10^{-3}[c]	-1.0×10^{-3}[d]	-1.0×10^{-3}[d]
	RF	$\lvert q_i \rvert$	0	0.23[c]	0.14[c]

[a] via *tickle spectroscopy* [109]. [b] From the secular-motional sideband peaks in measured spectra of α: 411 nm transition in Yb^+ ions (see Chapter 5).
[c] Eq. (4.1c) [d] Eq. (4.1a)

are listed in Table 4.1, which will be useful to estimate some of systematic effects in Chapter 7. The relevant relations between the parameters are also listed below [112]:

$$a_{tr1} = a_{tr2} = -\frac{1}{2}a_{tx} \propto \frac{1}{m} \tag{4.1a}$$

$$q_{tr1} = -q_{tr2} \propto \frac{1}{m}, \quad q_{tx} = 0 \tag{4.1b}$$

$$\omega_i \simeq \frac{1}{2}\omega_{\mathrm{RF}}\sqrt{a_i + \frac{1}{2}q_i^2} \tag{4.1c}$$

where m is the mass of a trapped ion.

4.1.2 Trapping, cooling, and repumping

As soon as Yb atoms fly into the trapping area of the Paul-trap chip, they meet two beams to get ionized: a 399 nm beam to drive ${}^1S_0 \rightarrow {}^1P_1$ transition (see Table B.1) and a 369 nm beam to excite the population in the ${}^1P_1$ state to continuum. The 399 nm transition has ISs of $\gtrsim$250 MHz between nearest neighboring isotopes [113] and thus allows isotope-selective Yb^+ ion loading by tuning the 399 nm beam's frequency. At the moment the Yb atoms get ionized, the same 369 nm beam starts to drive ${}^2S_{1/2} \rightarrow {}^2P_{1/2}$ transition (see Fig. 3-1 and Table B.1) and Doppler-cools

the Yb^+ ions.[2] The 369 nm beam is parallel to the trap chip's surface (xz plane) and diagonal to the axis of the chip (z direction; see Fig. 4-1) so that the beam cools the ions' kinetic energy in all directions (the RF trap potential is tilted so that the principal axes are not along y or z direction; see Section 4.1.1). Two beams are placed to repump the population that leaks from the ${}^2S_{1/2}-{}^2P_{1/2}$ subspace to other states back to the two-level subspace. A 935 nm beam repumps the population in ${}^2D_{3/2}$ states, which is leaked from the ${}^2P_{1/2}$ states in every $\sim$50 µs in this setup,[3] through saturated ${}^2D_{3/2} \rightarrow {}^3D[3/2]_{1/2}$ transition and subsequent decay to the ${}^2S_{1/2}$ ground state, with the repumping time well below 5 µs.[4] A 760 (638) nm beam drives ${}^2F_{7/2} \rightarrow {}^1D[3/2]_{3/2}$ (${}^1D[5/2]_{5/2}$) transition and, with following decay to the ${}^2S_{1/2}$ (${}^2D_{3/2}$) state, repumps the population that falls into ${}^2F_{7/2}$ state in every few hours, presumably due to the trapped ion's collision with with background gas [114, 115]. Note that the repumpers pump the ${}^2D_{3/2}$ and ${}^2F_{7/2}$ states populated by driving the optical clock transitions as well.

The beams with shorter wavelengths 369 nm and 399 nm are generated by external cavity diode lasers (DL Pro HP and MDL Pro Yb+, respectively, Toptica) with typical maximum powers of 35 mW and 85 mW before isolators, and operating at $\sim$10 mW and $\sim$20 mW, respectively. The 935 nm and 760 nm repumping beams are obtained from distributed feedback (DFB) lasers (MDL Pro Yb+, Toptica). A homemade 638 nm laser had been used for the earlier measurements for α: 411 nm and β: 436 nm clock transitions [4], which has been replaced by the 760 nm laser for the later measurements for γ: 467 nm clock transition (see Section 4.2.6). The waist and power of each beam can be found in Table B.1.

[2]To Doppler temperature $T_{\mathrm{Doppler}} = \hbar\Gamma_{369\,\mathrm{nm}}/(2k_{\mathrm{B}}) = 470\,\mu\mathrm{K}$ (see Table B.1).

[3]It depends on the rate of the 369 nm transition and thus on the power and detuning of the beam and the the ions' temperature. Minimum decay time is $1/[\Gamma_{369} \times 0.5 \times (0.5\,\%)]) \approx 3.2\,\mu\mathrm{s}$ where Γ_{369} (see Table B.1), 0.5, and 0.5 % are the cooling transition's linewidth, maximum probability in the excited state, and the branching ratio to the ${}^2D_{3/2}$ state, when the transition is highly saturated.

[4]The transition is highly saturated by the 935 nm beam; see Table B.1.

4.1.3 Fluorescence imaging

Collecting scattered 369 nm light from trapped ions is the primary way to achieve information on the ions' states. The scattered beam that propagates below the surface trap is collected by a folding mirror and then a large convex lens with a high numerical aperture (NA). The collected beam is bandpass filtered to block other laser beams (e.g., repumpers) and either measured by a photomultiplier tube (PMT) (H10682-210, Hamamatsu) [109, 110] through a $4f$ system or an electron-multiplying charge-coupled device (EMCCD) camera (Luca$^{\mathrm{EM}}$ R 604, Andor). In the path for the PMT, a pinhole is placed at the focus of the $4f$ system to reduce the effect of the ambient light. The EMCCD camera is slow ($\gtrsim$0.5 s per image) but gives the number and positions of trapped ions. The existence of *dark* ions, ions of different isotopes that do not scatter the cooling beam but stay in the trap via sympathetic cooling, can be discovered through the distribution of bright ions' positions. Once the correct number of ions with no dark ion is confirmed, the scatter beam's path is folded to the PMT by placing a mirror, and the PMT measures the fluorescence with a higher signal-to-noise ratio and broader bandwidth. With the PMT, the count rate of photons is limited by the scattering rate (limited by the linewidth of the 369 nm transition) and the total *yield* of the detection (e.g., the NA of photon collection and quantum efficiency of the PMT).

4.1.4 State preparation

In the presence of an external magnetic field, Zeeman splitting occurs for the states with nonzero total angular momentum J or F. Another 369 nm beam from the same Toptica laser is along the quantization axis of the ions that the magnetic field defines and optically pumps the population in either of the two Zeeman levels ($m_J = \pm\frac{1}{2}$) of the $^2S_{1/2}$ ground state to another, for state preparation. In the thesis work, the external magnetic field of $\sim$1.1 G is applied along the x direction by flowing DC currents in Helmholtz coil pairs in x, y, and z directions around the vacuum chamber. The background fields including the earth's magnetic field are compensated by the

coils. The 369 nm optical pump beam propagates in x direction, parallel to the magnetic field. The beam's polarization is set to be either of circular polarizations $\hat{c}^{\pm}$ (see Section 4.2.5) and thus $\hat{\sigma}^{\pm}$ polarizations with respect to the quantization axis.

The alignment and polarization of the optical pump beam are optimized by measuring the characteristic time of the pumping.[5] The pumping time of $\lesssim$10 µs is typically achieved with about 80 µW power at the focus (see Table B.1).

4.1.5 Probe beam for driving clock transitions

The probe beams to drive α: $^2S_{1/2} \rightarrow {}^2D_{5/2}$ (411 nm), β: $^2S_{1/2} \rightarrow {}^2D_{3/2}$ (436 nm), and γ: $^2S_{1/2} \rightarrow {}^2F_{7/2}$ (467 nm) clock transitions, which are of the main interest in this thesis, are generated by a Ti:sapphire laser (SolsTis 4000 XF, M Squared) followed by either a waveguide frequency doubler (MgO:LN Ridge Waveguide, AdvR) (for the α and β transitions) or a frequency-doubling cavity (ECD-X, M Squared) (for the γ transition). The beam propagates along the $-x$ direction (antiparallel to the external magnetic field) and has linear horizontal polarization along the z direction.[6] The beam is focused on the center of the trap by an achromatic lens (see L1 in Fig. 4-8) to minimize the difference in the deflection angles and focal lengths of the 411, 436, and 467 nm beams. See Table B.1 for the powers and focal waists of the beam at each wavelength.

Ref. [4] contains more details on the beam setup (Fig. 8-7 therein) and the procedure to align and focus the probe beam (Chapter 8.5 therein); note, however, the way to precisely align the probe beam to an ion for IS spectroscopy, after the initial alignment and focusing, has been changed from the way using a 369 nm *align* beam, as described in Section 5.3.3.

[5] Measured through the repeated pulse sequence and time-resolved integration of the PMT counts (see, e.g., Sections 5.3.7, 5.6, and Fig. 6-10).

[6] The propagation direction and the polarization of the beam with respect to the quantization axis determine the selection rules for the clock transitions; see Appendix D.

4.1.5.1 Frequency stabilization and control

The Ti:sapphire laser's frequency is actively stabilized to a 10 cm-long optical two-mirror cavity [1.5 GHz free spectral range (FSR)] with a cylindrical ultralow-thermal-expansion (ULE) spacer, that has the finesse $\mathcal{F} \sim 50,000$ and linewidth $\kappa_c \sim 30\,\text{kHz}$, in a cylindrical vacuum chamber (Stable Laser System), which serves as the frequency reference in the IS spectroscopy experiment. A laser beam before frequency-doubled is picked off from the main beam path and goes through a broadband electro-optic modulator (EOM) (PM-0k5-10-PFA-PFA-850-DC, EOSPACE) to generate sidebands. One of the sidebands (called *branching* sideband here) is stabilized to the reference cavity so to continuously tune the frequency of the carrier by tuning the EOM's modulation frequency. The EOM is driven at few GHz by a signal synthesizer (8672A, HP). The synthesizer has 1 kHz resolution of the set frequency,[7] which gives *coarse* tuning of the probe's frequency before frequency-doubled. The first-order red sideband is stabilized to a cavity mode so that the change in the synthesize set frequency and the change in the probe frequency have the same sign.

To employ Pound-Drever-Hall (PDH) technique [116, 117], the EOM is driven by an additional 4 MHz signal. The two added driving signals with the different frequencies have the same effect to two independent EOMs in series driven by each signal: $\exp[i(\phi_1(t) + \phi_2(t))] = \exp[i\phi_1(t)]\exp[i\phi_2(t)]$. Therefore, each of the GHz branching carrier and sidebands has its own 4 MHz *PDH* carrier and sidebands, generating its own PDH error signal.

A *fine* tuning is given by an acousto-optic modulator (AOM) after the probe beam is frequency-doubled. The AOM is driven by ≈120 MHz signal from frequency-mixing of a ≈25 MHz signal generated by a function generator [DS345, Standard Research Systems (SRS)] and a 95 MHz signal from a direct digital synthesizer (DDS) (AD9959, Analog Devices, mounted on an evaluation board EVAL-AD9958). The exact AOM drive frequency is controlled by the SRS function generator which has the 1 µHz resolution of the frequency control. The blue-detuned first-order deflection beam is delivered to the ions. Therefore, the frequency change in the SRS function

[7] up to 6.2 GHz. It has bigger frequency steps at higher frequencies.

generator is given as the change in the probe frequency at the ions.

It is useful to define some frequencies to describe how the frequency of the probe beam at ions is controlled and how far it is *detuned* from a mode of the reference cavity [i.e. $n \times$FSR of the cavity]. First, two frequencies tuned by the HP synthesizer and SRS function generator are defined:

$$\texttt{CoarseFrequency} = f_{\text{Coarse}} = f_{\text{HP}} \tag{4.2}$$

$$\texttt{FineFrequency} = f_{\text{Fine}} = f_{\text{SRS}}, \tag{4.3}$$

$$\tag{4.4}$$

respectively. The two frequency controls have different effects to the probe beam that ions see. While the `FineFrequency` tunes the probe frequency at ions with the same scale, change in `CoarseFrequency` changes the probe frequency by twice. Taking that into account, another frequency that captures the total effect of f_{HP} and f_{SRS} tuning is defined:

$$\texttt{MasterFrequency} = f_{\text{Master}} = 2f_{\text{Coarse}} + (f_{\text{Fine}} - 25\,\text{MHz}) \tag{4.5}$$

The 25 MHz offset has been placed for a historical reason in the laboratory; it makes the value of $(f_{\text{Fine}} - 25\,\text{MHz})$ the detuning of AOM drive from 120 MHz, the resonant frequency of the AOM. The absolute frequency of the probe beam at an ion is, then, given as:

$$f_{\text{probe}} = \omega_{\text{probe}}/(2\pi) = \underbrace{2n \times \text{FSR}}_{\text{Cavity}} + \underbrace{120\,\text{MHz}}_{\text{AOM resonance}} + \underbrace{f_{\text{Master}}}_{\text{Control}} \tag{4.6}$$

when the branching sideband is stabilized to the n's longitudinal mode of the reference cavity. Note also that the probe beam is picked off before frequency-doubled and goes into a wavemeter (WS/7, HighFinesse/Ångstrom) to measure the beam's frequency, `WMFrequency` or f_{WM}, with 50 MHz uncertainty. The `WMFrequency` and

the probe's frequency at an ion is related as follows:

$$f_{\text{probe}} = 2f_{\text{WM}} + \underbrace{f_{\text{Fine}} + 95\,\text{MHz}}_{\text{AOM}} \approx 2f_{\text{WM}} + 120\,\text{MHz}. \tag{4.7}$$

The last approximation is from the fact that the value of $(f_{\text{Fine}} - 25\,\text{MHz})$ has been controlled within 0 to 8 kHz range, which is much narrower than the wavemeter's precision.

Most importantly, if the frequencies of a transition in different isotopes are measured at the same time with the same cavity mode n, the ISs between the isotopes are simply given by the difference in the measured `MasterFrequency`s at the resonance of the transition.

All the signal generators that are relevant to the probe beam's frequency at ions are synchronized to a 10 MHz signal generated by another SRS DS345 function generator named *master clock*. Its accuracy is ±5 ppm between 20–30 °C according to the manual. By assuming the linear dependence of the signal's frequency on the temperature and considering 1 °C drift in the device temperature, <5 GHz signal from the HP signal synthesizer, and optical frequency doubling, the temperature-dependent long-term contribution to the probe frequency drift is estimated to be $\lesssim$5 Hz. Very recently, after all the IS measurements in this thesis were performed, the master clock has been synchronized to a rubidium frequency standard (FS725, SRS) which provide $<2 \times 10^{-12}$ stability (i.e., 20 µHz stability in probe frequency) over 100 s (cf. $\lesssim$2 hr isotope switching period; see Section 5.3.2).

4.2 Upgrading setup

The experimental setup for IS spectroscopy has been upgraded after the works in Ref. [5]. The goals of the upgrades have been mainly in two parts. One is to improve the stability of the overall setup, primarily for better convenience in running the experiment, which will not be described in detail in this thesis. However, It is important, for instance, to make the frequency stabilization of lasers robust to envi-

ronmental disturbance, to build automated detection of problems, and to properly handle runtime errors in control software, for experiments with long running time; a single continuous run for isotope-shift measurement takes more than 15 hours (see Fig. 6-4). It makes the experiments mentally and physically less demanding for researchers, and thus improves the time efficiency of the experiments and reduces potential human errors.

Another goal of the upgrades is to improve the precision of the experiment, by reducing systematic effects and statistical uncertainties. The works for this goal are elaborated in the following subsections.

4.2.1 Suppressing the effect of residual amplitude modulation on laser frequency stabilization.

During the first-round data was being taken [4], the probe beam's frequency was drifting due to residual amplitude modulation (RAM), dominantly from the EOM used for PDH frequency stabilization [118, 119, 120], by adding DC or AC modulations to the PDH error signal. Long-term drift in the probe's frequency with a time scale comparable to or longer than the time scale of isotope switching is especially harmful to the IS measurement (see Section 5.3.2) as a source of systematic shift and uncertainty. Therefore, the RAM-induced drift in the PDH error signal is actively compensated as elaborated below.

Figure 4-2 describes the setup used for monitoring and compensating the RAM effect in the PDH error signal. It is started by copying the work in Ref. [120]. To monitor the RAM before the beam couples to the reference cavity, a beam splitter is placed right before the cavity. A beam splitter with an appropriate reflection/transmission ratio is chosen so that the RAM monitor photodiode sees higher beam power than the PDH photodiode and thus has a higher signal-to-noise ratio (SNR) for the shot noise. Placing the beam splitter right before the cavity helps the RAM monitor captures RAM from all the optics that the beam goes through before the cavity. The same photodiode modules (PDA10A2, Thorlabs) are used to measure the beams for

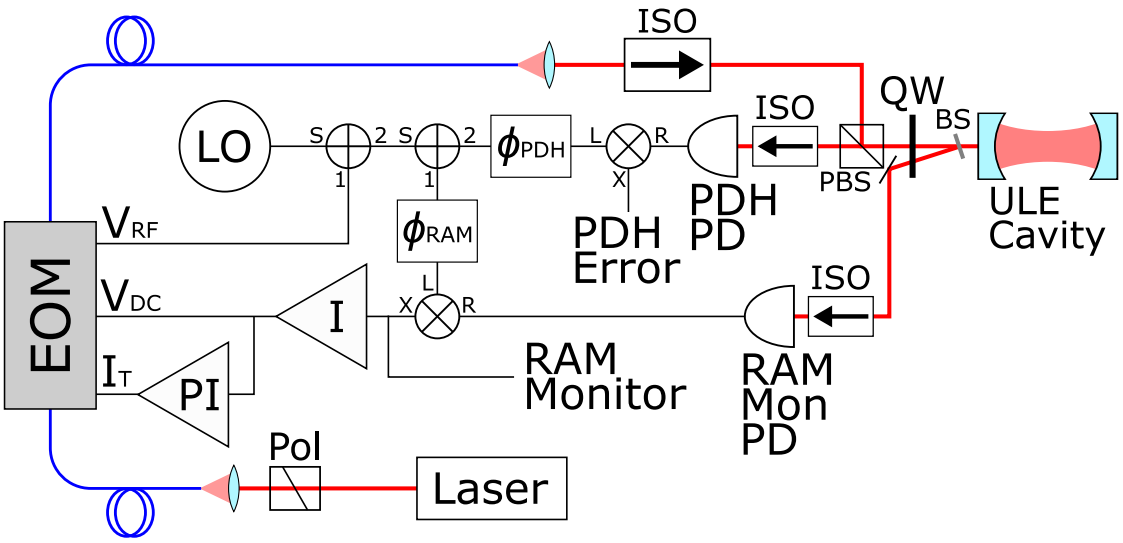

Figure 4-2: Schematic drawing of the configuration of optics and electronic components for the PDH error and RAM monitor signal generation. 4 MHz local oscillator (LO) signal is split by power splitters ($\oplus$ symbols) and drives the RF port (V_{RF}) of EOM and the LO ports (L) of frequency mixers ($\otimes$ symbols) for PDH error and RAM monitor signals. The beams reflected from the cavity or picked off by a beamsplitter (BS) before the cavity go to the photodiode modules for PDH error (PHD PD) or RAM monitor (RAM Mon PD) signals, respectively. The photodiode signals go to the RF port (R) of the corresponding mixers. The output signal from the IF port (X) of each mixer serves as PDH error or RAM monitor signal after lowpass filtered to kill RF components. The phases of local oscillator signals for the two mixers (ϕ_{PDH} and ϕ_{RAM}) are adjusted to make sure that RAM monitor sees the same in-phase component of RAM effect in PDH error signal. Optical isolators (ISO) placed in front of PDs suppress the crosstalk between the PDs. To compensate the effect of RAM in PDH error signal, RAM monitor signal goes into integrator (I) and fed back to the DC voltage (V_{DC}) input of the EOM. V_{DC} is picked off and goes into proportional and integral (PI) transimpedance gains and the current (I_{T}) is fed to the thermoelectric cooler (TEC) module attached to the EOM body, to prevent required V_{DC} from drifting out of the control range. Pol, PBS, and QW stand for polarizer, polarizing beamsplitting cube, and quarter-wave plate, respectively. Labels S, 1, and 2 refer to the input and the two outputs of each power splitter, respectively.

the RAM monitoring and the PDH error signal generation. An optical isolator is placed in front of each photodiode to suppress the crosstalk between the photodiodes. To cover the frequencies of all the probe beams before frequency-doubled, broadband optical isolators (EURYS, Electro-optics Technology) are used; they have over 30 dB (27 dB) isolation and 95 % (80 %) transmission at 822 and 871 nm (at 934 nm). A polarizer (GL10-B, Thorlabs) in a rotation mount is placed before the free-space-to-fiber coupling of the beam for polarization filtering and axis matching to the fiber axis.[8]

A crucial difference in the setups here and in Ref. [120] is the use of the temperature control of the EOM. Reference [120] has two separate feedback loops which measure in-phase and quadrature components of the RAM signal (using IQ mixer) and stabilize them by controlling the EOM's DC input voltage and temperature, respectively, achieving 56 dB suppression of the RAM effect. In such a case, the absolute size of the RAM is fixed as both components of the RAM signal are stabilized. In this work, we use the temperature control as the slow and wider control of the RAM effect. It slowly takes over the DC voltage's role and keeps the DC voltage within the range of the voltage that the EOM's DC input port can take. In this case, not the absolute size but only a component of RAM signal is stabilized. Therefore, it is vital to make the RAM monitor signal sees the same component of the RAM signal in the PDH error signal. The procedure of matching the components is as follows. The frequency of EOM modulation is slightly detuned from the mixers' local oscillator frequency, and then the PDH and RAM monitor signals oscillate at the frequency of the detuning with certain phases. The phases are then matched by adjusting the phases of local oscillator signals ϕ_{PDH} and ϕ_{RAM} to the mixers for the PDH error and RAM monitor signals, respectively. In practice, ϕ_{PDH} is adjusted first to optimize the shape of the PDH error signal (when there is no detuning, of course), and then ϕ_{RAM} is adjusted to match the phases of oscillations in the PDH

[8] Using the Glan-Taylor calcite polarizers with 50 dB extinction ratio might be an overkill for the purpose here. The extinction ratios of polarization-maintaining optical fiber patchcords (OZ Optics) or the axis matching between the fiber and the crystal in the EOM typically do not exceed 30 dB.

error[9] and the RAM monitor signals (with detuning). In this work, the minimum resolution of phase control was ∼0.5° at 4 MHz, made by a pair of male-to-male and female-to-female BNC connectors. The relative phase of the two signals was measured using an oscilloscope[10], but it would be more straightforward and precise (i.e., less systematic shifts) if a phasemeter is used instead. After all, the relative phase of the signals are matched with ∼0.5° = 0.001 rad accuracy, giving ∼30 dB suppression of the RAM effect. It is helpful to deliberately increase the size of the RAM for the procedure above, by disturbing axis matching of free-space-to-fiber coupling before the EOM or adjusting the EOM temperature.

The effects of the EOM's DC voltage and temperature changes are somewhat different [120], and there is a risk that the RAM stabilization fails if the system's condition drifts too much from the starting point. Nevertheless, the stabilization has been sufficiently stable for most of the time in practice.

The temperature stabilization and control were done by following the work of Enrique Mendez, a fellow Ph.D. student in Vuletić Group. As shown in Fig. 4-3, a fiber-coupled waveguide EOM with DC input port (PM-0k5-10-PFA-PFA-850-DC, EOSPACE), used to generate branching and PDH sidebands (see Section 4.1.5.1), was attached on top of a thermoelectric cooler (TEC) module mounted on a metal substrate for heat dissipation. Thermal paste was applied to the contact areas. Then the EOM was sealed by an acrylic enclosure filled with foam sheets to reduce the temperature fluctuation and gradient.

As shown in Fig. 4-2, the current flowing through the TEC module is given by a temperature controller with proportional and integral (PI) transimpedance gain. The temperature response of the EOM is slow (order of minutes). Therefore, the input signal[11] has been integrated digitally for reliable integration over a long time period.

[9] The frequency of the laser should be far from the cavity's resonant frequencies to see the effect of the RAM only.

[10] A long BNC cable assembly is prepared so that it gives 90° phase delay at 4 MHz; the length is adjusted by adding short cables or connectors while measuring the total phase delay using a network analyzer. The cable assembly is added to the cable for one of the signals. The two signals are then mixed and lowpass-filtered using multiplication and averaging functions of the scope.

[11] The EOM's temperature or DC voltage for temperature or RAM stabilization, respectively.

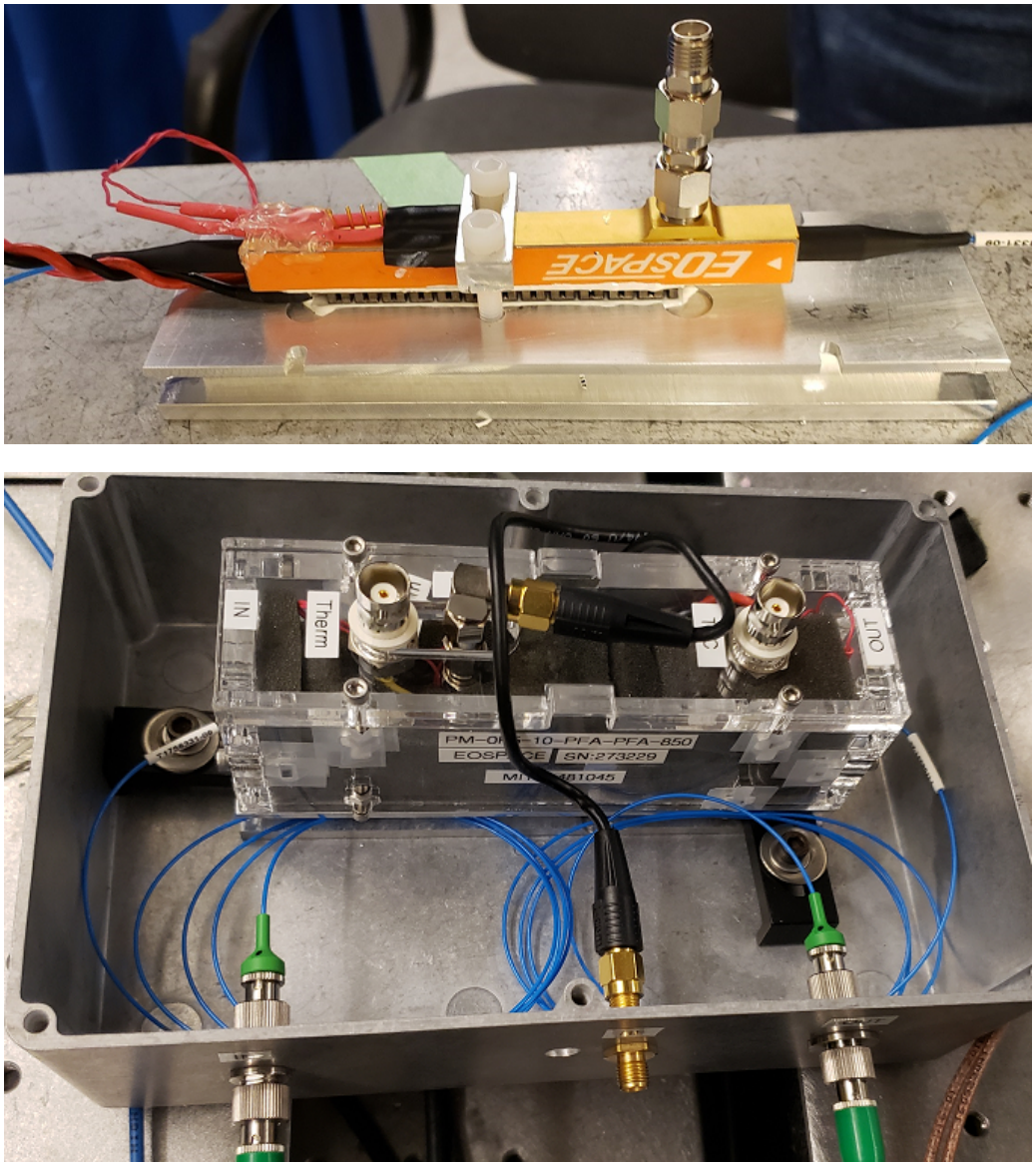

Figure 4-3: Fiber-coupled electro-optic modulator (EOM) for stabilization and continuous tuning of the Ti:sapphire laser frequency. (Top) EOM mounted on thermoelectric cooler (TEC) module over a metal substrate, with negative-temperature-coefficient (NTC) thermistor attached to the opposite side of EOM from the TEC module. (Bottom) complete setup. Acrylic enclosure is filled with foam sheets for thermal isolation. A port for DC input has been added afterward.

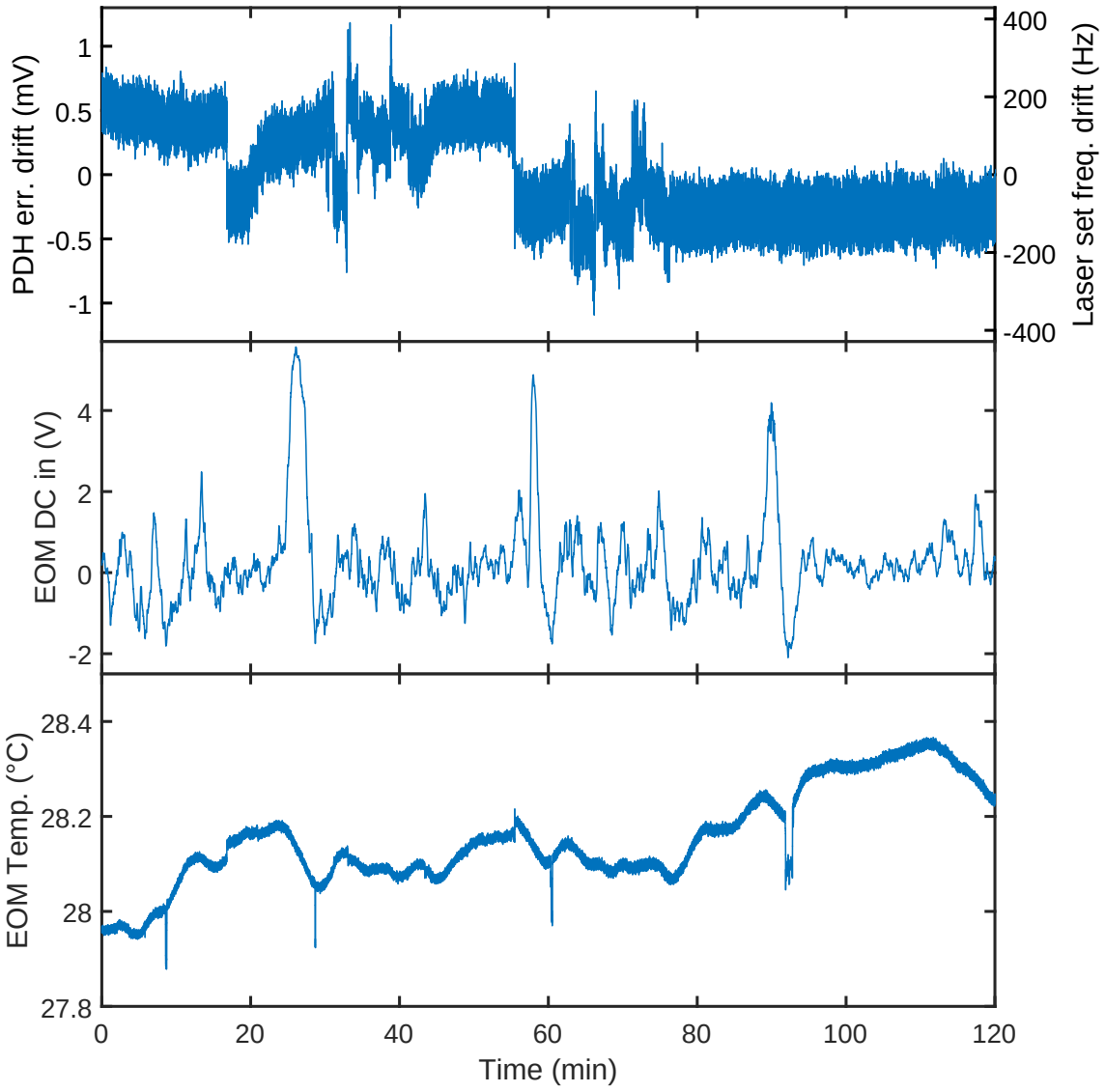

Figure 4-4: Drift in PDH error signal offset and EOM's DC input voltage and temperature over 2 hours, while RAM-induced PDH error signal offset drift was actively stabilized. Data taken by Eugene Knyazev, a research team member and fellow PhD student. The dips in EOM temperature are spurious readings.

The amplitude and phase of the RAM signal depend on various factors (e.g., axis matchings, the EOM's input DC voltage and temperature, mechanical stress on and temperature of optical fibers), and are subject to potential significant drift over time. Stabilizing the RAM signal's in-phase component does not suppress or stabilize the signal's amplitude and rather increases the amplitude fluctuation over time in general,[12] Therefore, it is not straightforward to predict the size of the remaining RAM effect after the RAM signal is suppressed by 30 dB, and the typical size of the effect was estimated empirically by recording the PDH error signal, far from the cavity's resonances, while RAM compensation is engaged.[13]

The result is shown in Fig. 4-4. The PDH signal drifts typically by ± 1 mV, which would shift laser frequency by ± 300 Hz if the PDH lock was engaged, considering the 300 Hz/mV slope of the PDH error signal in this setup. The drift's effect on the measured ISs is expected to be further reduced by the isotope switching several times (see Section 5.3.2). Note that no visible correlation between the PDH signal drift and the measured EOM DC voltage or temperature was observed.

4.2.2 Temperature stabilization of reference cavity

The ULE cavity is the ultimate frequency reference for the isotope shift measurement in this work (see Section 4.1.5.1). Therefore, it is hard to overstate the importance of the cavity's stability, especially over the long time periods for the same reason described in Section 4.2.1. As the temperature drift of the cavity is one of the most obvious sources of the slow drift, the dependence of the cavity's resonant frequencies on the temperature has been examined, and the effort to stabilize the temperature has been made, as follows.

For a single trapped $^{174}Yb^+$ ion, the resonant frequency of α: $^2S_{1/2} \rightarrow {}^2D_{5/2}$ (411 nm) optical clock transition (see Fig. 3-1) offset by a cavity mode is measured

[12]For instance, the in-phase component of the RAM signal can be suppressed at the expense of a bigger increase in the quadrature component by changing the EOM's DC voltage and temperature; in other words, the phase of the RAM signal is shifted to be orthogonal to the local oscillator while the signal's amplitude increases, potentially by a large factor.

[13]The PDH stabilization should be off, of course.

(see Chapter 5) after stabilizing the cavity's temperature to different values. The drift in the cavity mode's frequency is then shown as the drift in the measured frequency from the reference.

Figure 4-5 shows the result of the measurement. It shows a clear quadratic dependence of the the cavity with a ULE spacer near the zero-crossing temperature:

$$\frac{\delta f_c}{f_c} = -\frac{\delta L_c}{L_c} = a(T - T_{\mathrm{ZC}})^2 \tag{4.8}$$

where $f_c = n \times \mathrm{FSR}$ is resonant frequency of nth longitudinal cavity mode for a given free spectral range (FSR), L_c is the length of the cavity, T_{ZC} is the cavity's zero-crossing temperature, and a is the quadratic coefficient of the temperature dependence.

Fitting the measured dependence gives the values $T_{\mathrm{ZC}} = 29.46(1)\,^{\circ}\mathrm{C}$ and $a = -5.32(4) \times 10^{-10}\,\mathrm{K}^{-2}$ ($af_c \sim -20\,\mathrm{kHz/K^2}$ for f_c between $2 \times 411\,\mathrm{nm}$ and $2 \times 467\,\mathrm{nm}$). It gives $\delta f_c = 20\,\mathrm{Hz}$ shift of the cavity's resonant frequency, and thus 40 Hz shift in probe beam's frequency f_{probe} after frequency-doubled, for $0.01\,^{\circ}\mathrm{C}$ temperature change from T_{zc}, which corresponds to the uncertainty in the measurd T_{zc} and the resolution of the temperature reading of the temperature controller (LFI-3751, Wavelength Electronics) used to stabilize the temperature inside the vacuum chamber.

To reduce the effect of the temperature further,[14] the volume around the vacuum chamber and the relevant optics has been enclosed by an acrylic box that sits on the optical breadboard. The temperature inside the box has been actively stabilized using a thermistor hanging from the ceiling and wide planar heat sheets (5692T49, McMaster-Carr) attached to the inner sides of the box. The half-inch-thick foam sheets cover the whole outer side of the box to decrease heat conductivity (by a factor of 4 to 8; 2–4 W/K after the sheets are attached) and reduce the acoustic noise that the enclosure picks up from the environment.

Figure 6-4 shows the measured temperature inside the box while the main exper-

[14] e.g., residual fluctuation of the cavity spacer's temperature after being stabilized by the temperature controller and change in temperature gradient and subsequent mechanical stress in the supporting structure such as vacuum chamber.

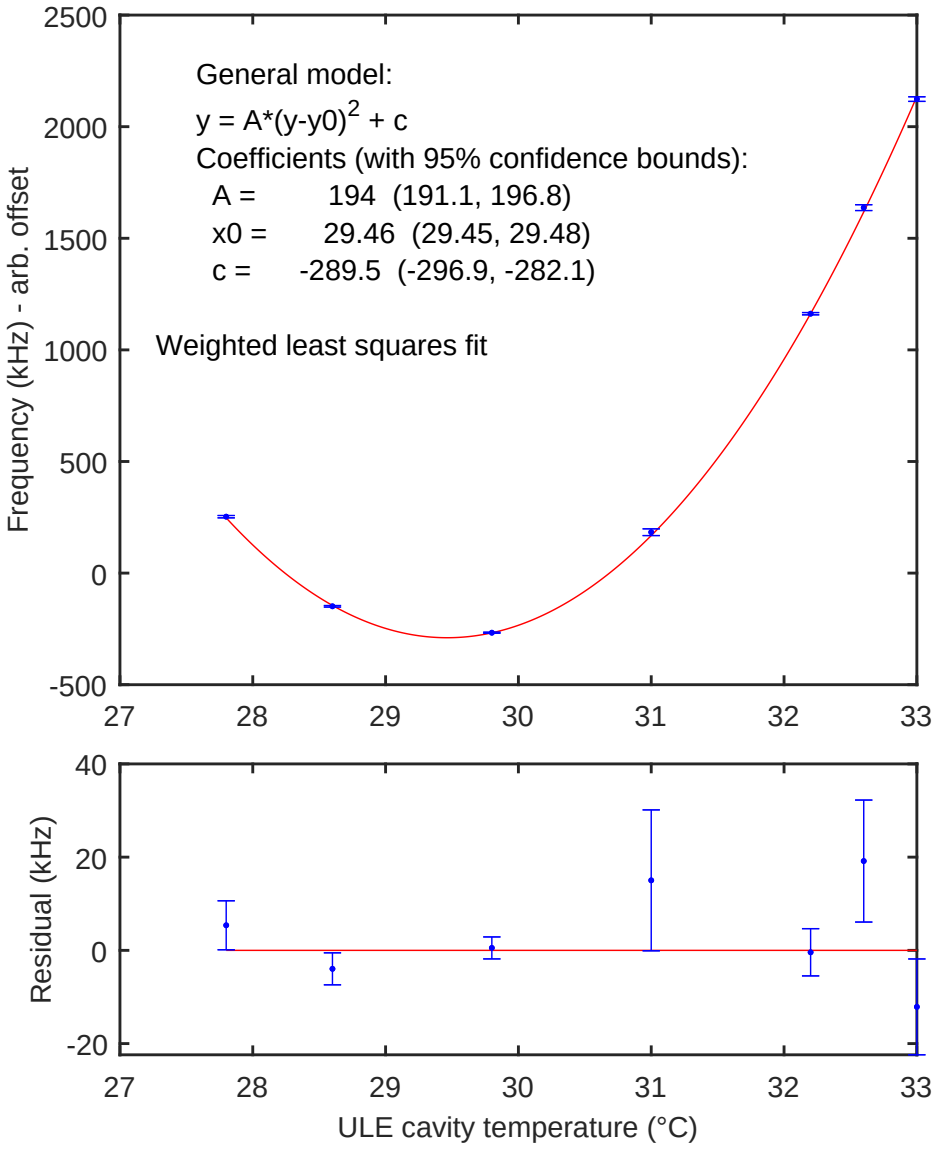

Figure 4-5: Measured drift in a longitudinal mode's frequency vs. temperature of the ULE cavity, using α: 411 nm clock transition in Yb^+ ions (see Fig. 3-1). The y-axis shows the detuning of the Ti:sapphire laser (before frequency-doubled) from the cavity mode. The cavity mode frequency is $f_c = 365\,\mathrm{THz}$ as the beam after frequency-doubled probes the clock transition (see Section 4.1.5.1). The laser frequency is referenced to the transition, and therefore the direction of the change in the cavity mode's frequency is the opposite of the frequency change in the y-axis. Fitting the results gives the cavity's zero-crossing temperature $T_{\mathrm{ZC}} = 29.46(1)\,^{\circ}\mathrm{C}$ and quadratic coefficient $A = -af_c = +194.0(15)\,\mathrm{kHz/K^2}$.

iment was running. Periodic oscillation in the temperature was inevitable with the PI feedback due to the slow response time of the temperature inside the enclosure. Nevertheless, it should keep the temperature stable on average and thus prevent systematic shifts in measured ISs. Furthermore, the temperature oscillation has a much shorter period ($\lesssim$10 min) than the typical period of the isotope switching ($\lesssim$2 hr; see Section 5.3.2) and barely leads to the systematic shifts. Note that Figure 6-4 also shows that the measured transition frequency has no noticeable correlation with the temperature oscillation.

4.2.3 Stabilizing probe beam intensity

The probe beam has high intensities to drive the narrow clock transitions. The strong field can, however, off-resonantly drive other transitions and shift the energies of associated states. If one of those states is involved in a clock transition as well, it will result in a systematic shift in the frequency measurement for the clock transition (i.e. probe-induced AC Stark shift; see Section 7.2.1). The light shift has been especially an issue for the extremely narrow γ: 467 nm transition which requires a high intensity of the probe beam [121, 122, 123] (see Table B.1). While the absolute size of the shifts is largely in common across the different isotopes, the fluctuation of the probe beam's intensity during the $\lesssim$2 hr isotope switching period (see Section 5.3.2) will introduce a differential systematic shift. The long-term drift in the measured frequency indeed has been measured in the previous measurement for the γ: 467 nm transition [4] [see Fig. 4-6(a)], and the intensity instability of the probe was suspected as the primary contribution.

The stability of the probe beam intensity has been improved in three different methods: actively stabilizing the power of the probe beam, precisely aligning the center of the beam to an ion, and increasing the beam waist. The details are described in the following subsections.

After the upgrades, the long-term drift in the measured frequency over time has been indeed reduced in new experiments as shown in Fig. 4-6.

In the future, narrowing the probe beam's linewidth will reduce the required

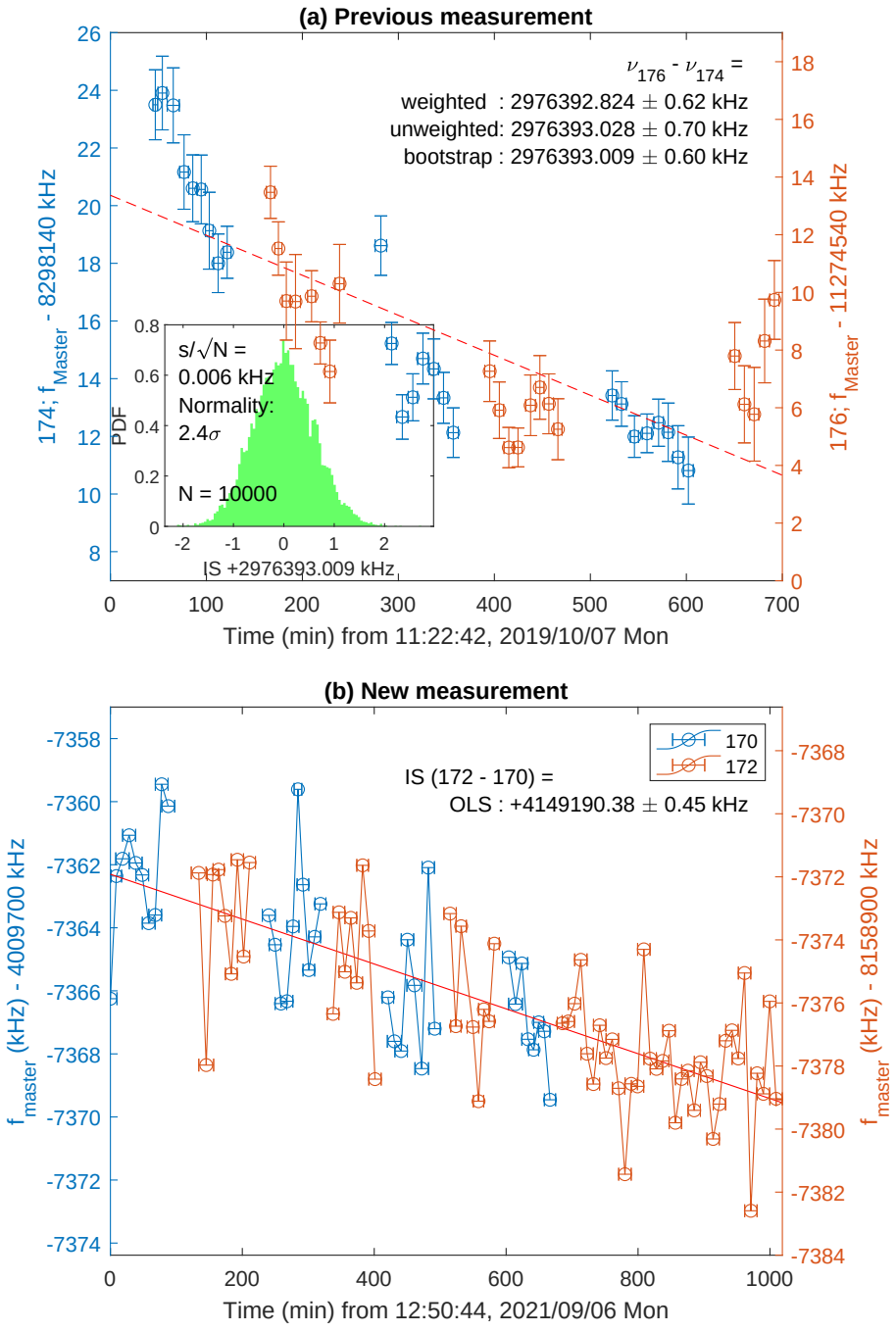

Figure 4-6: Zero-field `MasterFrequency` of γ: 467 nm transition over time (see Section 4.1.5.1 and Chapter 5; cf. Fig. 6-4) measured in (a) previous [4] and (b) new measurements in this thesis.

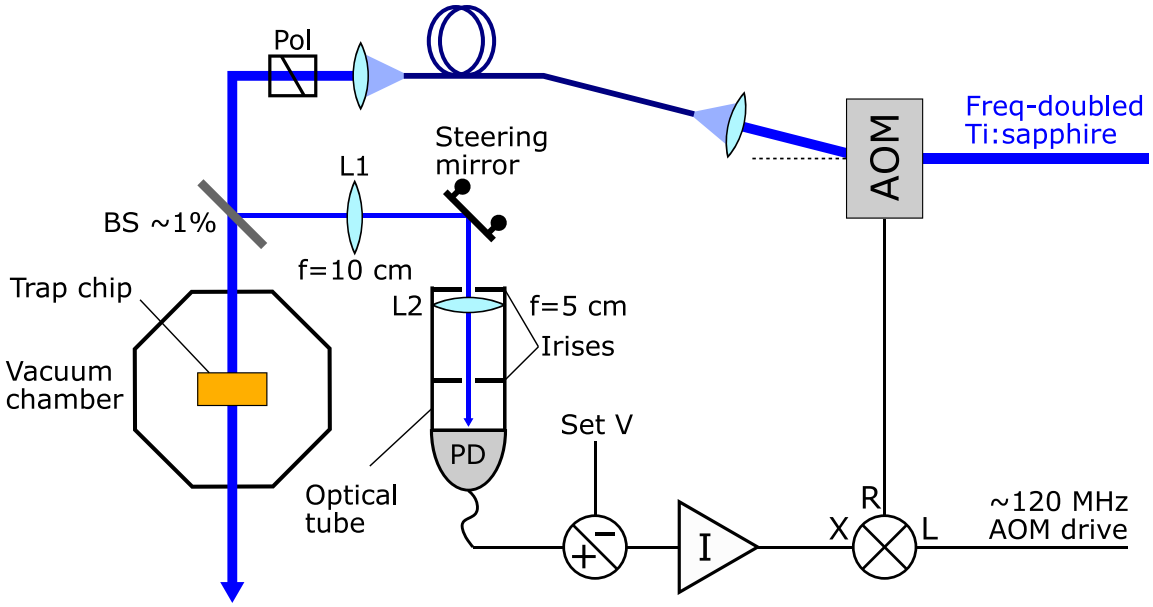

Figure 4-7: Setup for active stabilization of probe beam power. BS refers to beam sampler, AOM to acousto-optic modulator, Set V to set voltage, and L1 and L2 for focusing lenses. See the caption in Fig. 4-2 for other notations and symbols. The set voltage is subtracted from the photodiode signal. Amplifiers used in the circuit are omitted.

beam power to drive the transition (see Section 17.1) and thus the absolute size of the light shift (Section 7.2.1).

4.2.3.1 Active stabilization of probe beam power

The probe beam power is actively stabilized as shown in Fig. 4-7 as the first step of the intensity stabilization. An AOM is used to control the beam power; the amplitude of the AOM drive signal (see Section 4.1.5.1) determines the power of the deflected beams. A beam sampler picks off ∼1 % of the probe beam (BSF10-A, Thorlabs; p-polarization at 45° incident angle) after the AOM and before passing through the chamber. The power of the sampled beam is measured by a photodiode module (PDA100A2, Thorlabs). A *set* voltage is subtracted from the photodiode signal to set the beam power during the stabilization. The *error* signal goes through the integrator gain and subsequently to the IF port of a mixer (ZFM-2-S+, Mini-Circuits). It controls the amplitude of the AOM drive output from the RF port of the mixer, for a given input drive to the LO port. The range of the voltages to the

IF port is limited to 0–2 V so that it linearly controls the drive amplitude and also maintains the polarity of the control.

The drift in the probe beam's polarization at the beam sampler from p-polarization would cause the increase in the pick-off ratio from ∼1 %. The polarization drift is prevented by placing a polarizer (GL10-A, Thorlabs).

Optical tubes (1 in diameter and total 2 in length) and two irises, one at the end of the tubes and another in the middle, are attached to the photodiode module to block the ambient light. A lens with $f = 5$ cm focal length is also placed at the beginning of the optical tubes which focuses the beam at the iris in the middle, so that the iris hole can be as small as possible. This configuration has provided $\gtrsim$50 dB suppression of the ambient light.

Considering, e.g., drifts in or temperature dependence of the pick-off ratio, the photodiode reading, and operational amplifiers (op amps) for the set voltage subtraction and the integration gain, the drift in the probe beam power is conservatively bound to 0.1 %.

4.2.3.2 Probe beam alignment monitor

Precise alignment of the probe beam's center to an ion is also crucial. If the ion is placed at the side of the beam, the intensity that the ion sees would be sensitive to a small displacement of the beam or drift in the ion trap's center (see Section 4.2.3.4). Furthermore, the misalignment would not allow driving the transition with the peak intensity of the beam.

Due to the limited accuracy of the earlier alignment method [4] (see Section 5.3.3), a direct method to align the beam has been developed: scanning transition probabilities through a clock transition over different beam alignments. However, precise and *reproducible* control of the beam angle better than 0.1 µrad is required for the alignment scan,[15] which would be difficult to achieve by the mechanical precision of tilting mirrors. In this work, to realize such alignment control, the position of the beam on the other side of the vacuum chamber has been directly measured using a

[15]Focal waist O(10) um over O(10) cm-long beam path from tilting mirrors to an ion.

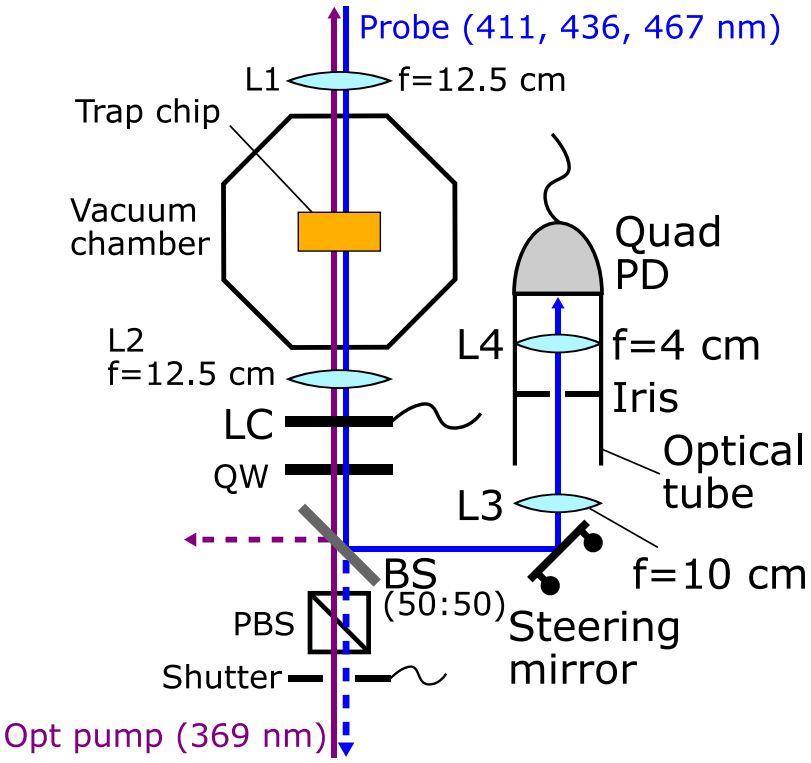

Figure 4-8: Probe beam alignment monitor and 369 nm optical pump beam polarization control setup. L1–4 refer to focusing lenses, LC to liquid crystal, QW to quarter-wave plate, (P)BS to (polarizing) beam splitter, and Quad PD to quadrant photodiode module. The separation of optical pump and probe beams is exaggerated; the beams are almost overlapped in practice. A shutter before PBS closes to protect the tip of fiber for the optical pump beam while strong probe beam is on.

quadrant photodiode as follows.

Figure 4-8 shows the setup for the probe beam alignment monitoring. A 50:50 beam splitter (BSW26, Thorlabs) picks off the probe beam after the beam passes through the vacuum chamber. The polarization of the beam changes by a liquid crystal and quarter-wave plate (see Section 4.2.5) and change the exact beam splitting ratio which, however, does not affect the position measurement of the beam.

A quadrant photodiode module (PDQ80A, Thorlabs) measures the power of the probe beam split by the quadrant areas of the photodiode. The module provides three signals: the sum of all quadrants' readings (SUM), the difference in the sum of the two left quadrants and the sum of the right quadrants (X), and the difference in top and bottom readings (Y). The position in the x and y directions of the photodiode[16] can be obtained by normalizing X and Y signal by SUM. The beam waist at the photodiode was measured to be 360 µm for 467 nm probe beam.

A steering mirror in Fig. 4-8 initially aligns the beam to the origin of the quadrants for the maximum beam position sensitivity. The optical tubes (1 in diameter and total 2 in length) with an iris in the middle are attached to the quadrant photodiode to block the ambient light.

The procedure of aligning the probe beam to an ion is described in Section 5.3.3. The position of the probe beam is also recorded while the main experiments of IS measurement are running, to check if there is any correlation between the measured transition frequency and the beam position (see Fig. 6-4 and Section 7.2.1.2).

4.2.3.3 Increased beam waist

Thanks to the precise alignment (see Section 4.2.3.2) and longer pulse time (due to faster $^2F_{7/2}$-state repumping; see Sections 4.2.6 and 5.4) of the probe beam, γ: 467 nm transition could be driven by a 4-fold weak probe beam compared to the previous experiments [4] (see Section 5.3.3). It enabled increasing the focal waist of the beam by twice instead of reducing the beam power, from 15 µm [4] to 30 µm.[17]. Due to the

[16] Aligned to $\pm x$ and $\pm z$ in the lab frame defined in Fig. 4-1.

[17] Increasing the waist further might start to bring issues from the excessive scattering of the probe beam from the surface of the trap chip (the trapping site is 135 µm away from the surface

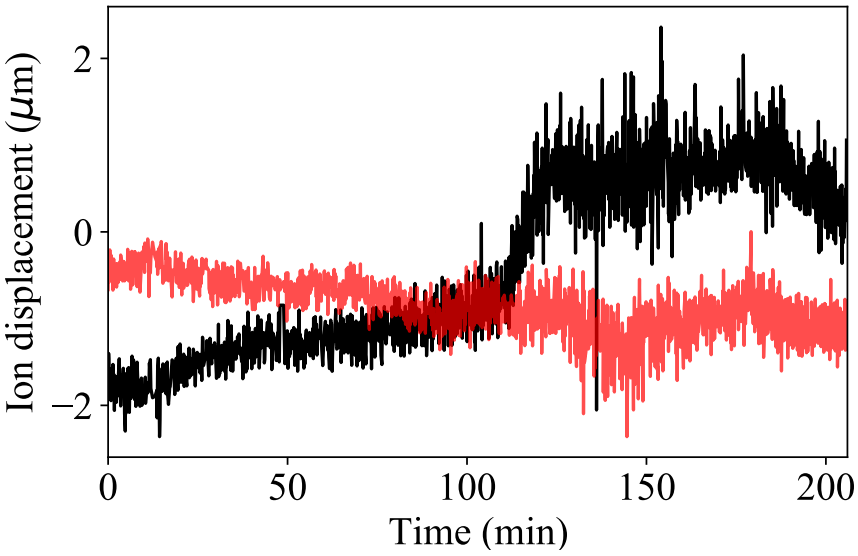

Figure 4-9: Position of a single ion in the plane of the trap as a function of time: along the trap axis (black; z direction), and perpendicular to the trap axis and parallel to the plane of the trap (red; x direction) (see Fig. 4-1 for the direction assignments). The ion was interrogated with the same laser pulse sequence used during the IS spectroscopy experiment for γ: 467 nm clock transition [see Fig. 5-3(c)], but the probe laser was far-detuned from the resonance.

increased waist, the probe beam intensity became less sensitive to the drift in the relative position of the beam and an ion (see 4.2.3.4).

4.2.3.4 Ion trap center drift

While the probe's power and alignment have been improved, reducing the ion's motion due to the drifts of the trap's center is not straightforward. The drift was measured directly via the EMCCD camera image (see Section 4.1.3) to, e.g., estimate the resulting change in the probe beam intensity.

Figure 4.2.3.4 shows the measured drift of an ion in the trap. The pulse sequence for the IS spectroscopy experiments for γ: 467 nm clock transition [see Fig. 5-3(c)] was running during the measurement to reproduce the environment for the ion (e.g., trap surface charging from laser beam scattering), except that the probe beam was far-detuned not to drive the clock transitions. The displacement of the trap center

; see Section 4.1.1), such as systematic shifts from the surface charge (Chapter 7) and potential damages on the chip.

was shown to be $\lesssim$2 µm in the measurement. The decreased ion displacement along the radial direction of the trap (red line) presumably reflected the tighter confinement along the direction (see Table 4.1).

The measurement has been also useful to estimate other systematic shifts as in 7.1.3 and 7.5. Note, however, that the camera could not measure the ion's motion along the direction perpendicular to the trap chip, leaving uncertainty in the systematic shift estimation based on the trap center displacement.

4.2.4 Active stabilization of transmission power through reference cavity

Another setup in the research group has experienced transmission power-dependent frequency shifts in cavity modes, presumably due to the thermalization of the mirror coatings by a high-power beam built inside the cavity. The effect was measured to be ∼50 Hz per 1 µW of the transmitted power (out of the cavity) for the cavity with the finesse of $\mathcal{F} = O(10,000)$. It could be a significant source of systematic shift if it is valid for the setup in this thesis as well, as the cavity finesse is $\mathcal{F} = O(50,000)$ for the clock transitions, and the transmission power had been typically ∼100 µW, which would result in ∼5 kHz absolute shift. As the cavity input beam power was not stabilized, if the power drifted by 5 % between the measurements for different isotopes (see Section 5.3.2), ∼250 Hz differential shift could occur.

To investigate the effect on the cavity in this work, the transition frequencies of clock transitions from a cavity mode have been measured for different cavity transmission powers, as shown in Fig. 4-10. The measurement procedure was essentially the same for the IS measurement for each clock transition in Chapter 5, except that the cavity transmission power was switched during the measurement, instead of the isotope.

Slightly nonzero transmission power-dependent shifts in cavity mode frequencies were measured as results. However, the rate of the shift per transmission power was much lower than the previously reported ∼50 Hz/µW for another cavity. Further-

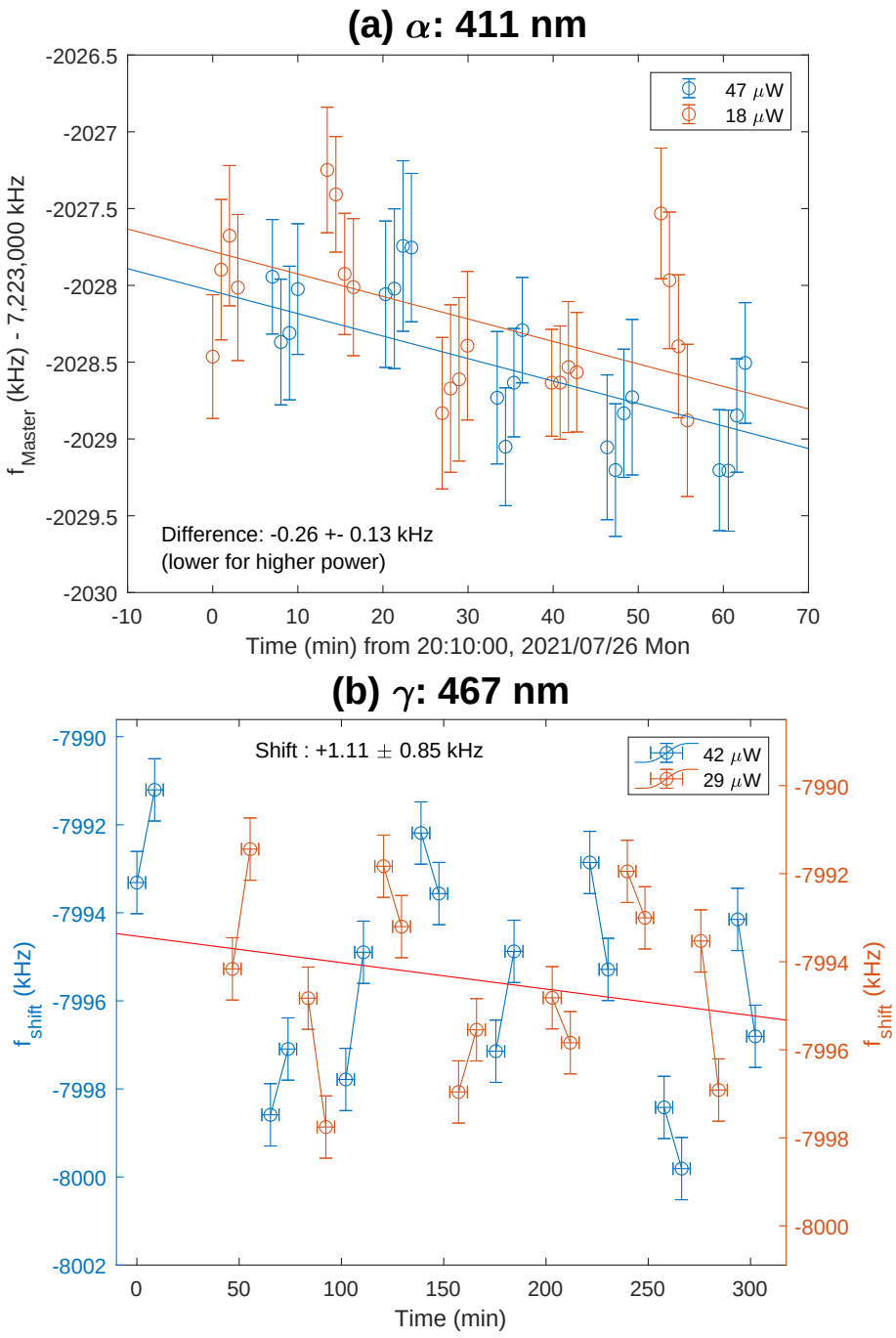

Figure 4-10: Measured transition frequency offset by a cavity mode (Section 4.1.5.1) vs time for (a) α: 411 nm and (b) γ: 467 nm clock transitions. The transmission power-dependent shifts are obtained in essentially the same way described in Section 6.4.

Table 4.2: Measured shifts in (frequency-doubled) probe beams' frequencies from different reference cavity transmission powers. Bound on the shift rates is determined from 95 % confidence intervals measured for α: 411 nm clock transition (see Section 4.2.4).

		α: 411 nm		γ: 467 nm	
		Low	High	Low	High
Power	[µW]	18	47	29	42
Shift	[kHz]	-0.26(13)		+1.11(85)	
Rate	[Hz/µW]	-9.0(4.5)		85(65)	
Bound	[Hz/µW]	-18 to 0			

more, the measured values were consistent with zero within their 2σ uncertainties, and the shift rate had opposite signs for the different transitions, which is in fact unlikely. Therefore, it has been concluded that the shifts in cavity modes due to the beam power were too small to be measured with the precision of the experiments, and thus an upper bound on the rate from 95 % confidence interval for more accurately measured α: 411 nm transition has been used to calculate the associated systematic shifts (see Section 7.9.3.2). It has also been assumed that there is no much wavelength dependence between 822–934 nm (the wavelengths of probe beams for α: 411 nm, β: 436 nm, and γ: 467 nm transitions before frequency-doubled; see Section 4.1.5.1).

To suppress the effect of the beam power, the transmitted beam power through the reference cavity has been stabilized in a very similar way to the active stabilization of the probe beam power described in Section 4.2.3.1: using an AOM[18] and frequency mixer to control the beam power, measuring the transmitted beam power with a sensitive photodiode module (C10439-02, Hamamatsu), and engaging an integration gain to stabilize the power. The residual long-term drift in the actively stabilized transmission power is conservatively bound to 0.1 % as in Section 4.2.3.1.

[18]The zeroth-order (i.e., not deflected) beam from the AOM has been used in this case, as a frequency control is not desired.

4.2.5 Electrical control of 369 nm optical pump polarization

The initial state of an Yb^+ ion should be prepared in the different Zeeman levels $m_J = \pm\frac{1}{2}$ of the $^2S_{1/2}$ ground state to drive two different symmetric Zeeman transitions in each optical clock transition (see Section 5.3.4). The choice of the Zeeman levels is done by choosing the polarization of the 369 nm optical pump beam between $\hat{\sigma}^+$ (for $m_J = +\frac{1}{2}$) and $\hat{\sigma}^-$ (for $m_J = -\frac{1}{2}$). In the earlier works [4], the control of the polarization was done by manually rotating a quarter-wave plate (QWP) that the optical pump beam passes through before the ion. Obviously, the human control provides a limited number, speed, and consistency of the control. Therefore, electrical control of the polarization has been introduced for this thesis work by using a liquid crystal (LC) variable retarder.

It is basically a thin layer of birefringent material (LC), just like a wave plate, that, however, provides variable differences in the refractive indices along the ordinary and extraordinary axes (i.e., retardation). The LC retarder is controlled by a square-wave AC voltage of which amplitude controls the size of the retardation.

Figure 4-8 illustrates the setup for the polarization control. The LC retarder used (LCC1413-A, Thorlabs) provides a moderately fast control ($\lesssim$40 ms)[19] and the retardance of nearly -0.05 to 1.2 wavelengths λ. The circular polarizations $\hat{c}^{\pm}$ could be achieved by setting the LC retarder to have $\frac{1}{4}\lambda$ or $\frac{3}{4}\lambda$ retardances for the input beam with linear polarization. However, to avoid the steep dependence of retardance to the control voltage at large retardances, another quarter-wave plate has been placed to provide $-\frac{1}{4}\lambda$ retardance. The total retardance, then, has been controlled between $\pm\frac{1}{4}\lambda$ retardances by letting the LC retarder has zero or $+\frac{1}{2}\lambda$ retardances.

The electrical control allows automated, fast, and frequent switching of the polarization between $\hat{\sigma}^+$ and $\hat{\sigma}^-$. It not only enables fully automated experiments for a clock transition and isotope (see Chapter 5) but also provides a qualitative improvement in the transition frequency measurement: simultaneous scanning of different Zeeman transitions described in Section 5.3.4.

[19] 40 ms rise time and 0.3 ms fall time at 25 °C and faster responses at higher temperature, according to the data sheet.

There are drawbacks of using LC retarders: their performance is temperature-dependent and also subject to long-term drift due to a residual DC component in the AC drive. An alternative way to control the polarization is to divide the beam into two different paths, place a QWP and an optical shutter in each path, recombine the beams to a common path toward the ion, and choose one of the beams by the optical shutters at each time. Zero-order waveplates typically have much better temperature stability and no long-term drift in their performances. Faster polarization controls can also be achieved by using fast optical shutters (below few ms [124]).

4.2.6 760 nm $^2F_{7/2}$ state repumper

In earlier works [4], $^2F_{7/2} \rightarrow {}^1D[5/2]_{5/2}$ transition at 638 nm had been used to repump $^2F_{7/2}$ state in Yb^+ ions (see Fig. 3-1). The repumping through this transition is slow; the characteristic time is around 100 ms.[20] It brought a significant overhead in the pulse sequence for α: 411 nm transition (see Section 5.5) of which excited state decays to the $^2F_{7/2}$ state with 83 % chances (see Fig. 3-1). The pulse time for the 638 nm repumper was also comparable to the probe beam's pulse time in the pulse sequence for γ: 467 nm transition (Section 5.4).

On the other hand, $^2F_{7/2} \rightarrow {}^1D[3/2]_{3/2}$ transition at 760 nm provides at least 10 times faster repumping than the 638 nm transition [122, 125, 126, 127, 128, 129]. The $^1D[3/2]_{3/2}$ excited state has 28.6 ns lifetime [130] and directly decays to the ground state (see Fig. 3-1 and Table B.1). The time that takes for the repumping has been measured to be $\lesssim$10 ms in this experiment, with $\sim$7 mW power of a focused beam with 100 µm waist, which is consistent with Refs. [122, 125] (see Section 6.6 for the measurement procedure).

By replacing the $^2F_{7/2}$-state repumper from the 638 nm to the 760 nm beam, at least 4-fold fast experiments (i.e., 4 times many data from the experiments during a

[20] Note that the $^1D[5/2]_{5/2}$ state does not decay directly to the ground state but decays to the $^2D_{3/2}$ state which needs to be repumped again by the 935 nm repumper (see Fig. 3-1 and Table B.1). The excited state could also decay into $^2D_{5/2}$ state which likely decays back to the $^2F_{7/2}$ state. The latter decay takes 7.2 ms, and then it has to be repumped again.

given period) for α: 411 nm transition[21] and a nearly twice longer probe pulse time for γ: 467 nm transition have been achieved.

Table A.4 lists the measured frequencies and ISs for the 760 nm transition for all the stable even-A isotopes. The values are either the first reports in literature [8] or with the highest precision known so far. The procedure of the measurement is described in Section 6.6.

4.2.7 Monitoring experimental parameters

During the later experiments for γ: 467 nm clock transition, various experimental parameters, conceivably affect the measurement precision, have been monitored as shown in Fig. 6-4. The correlation of each parameter with the measured transition frequencies has been investigated, and no significant correlation has been so far observed with the current precision of the experiments.

[21] 4 times faster pulse sequence and higher probability of successful repumping (i.e., higher *quantum opportunity* QO; see Section 5.4).

Chapter 5

Isotope-shift measurement protocol

The scheme and procedure of IS measurements will be described in this chapter. As the preliminary works and the detailed experimental procedure have been elaborated in Ref. [4] in a step-by-step manner, this thesis will present them rather briefly, and focus on the changes that have been made after the work in Ref. [4] was established. In short, one ion of an isotope was loaded in the ion trap at a time, and the ion's state was prepared in a Zeeman sublevel of the ion's ground state. An optical clock transition was driven repeatedly while scanning a probe beam's frequency to achieve a spectrum, from which the resonant frequency can be obtained. The resonant frequencies of two symmetrically red and blue-detuned Zeeman transitions were measured and averaged as the measure of the zero-magnetic-field resonant frequency of the clock transition. Finally, the frequencies for two different isotopes were alternately measured by replacing the trapped ion with an ion of another isotope, and the difference in the measured transition frequencies was taken as the IS between the isotopes.

5.1 Electron-shelving state readout

The first thing to consider is what is *measured* for spectroscopy. Due to slow responses of the narrow transitions, measuring fluorescence or absorption is inefficient or practically impossible. In this work, the states of atoms after driving transitions of

interest are measured. In particular, by driving the fast 369 nm cooling transition (see Fig. 3-1) and measuring whether the ion scatters the light or not (see Section 4.1.3), it can be quickly determined whether an ion is in the ground state $^2S_{1/2}$ or not. As all the optical clock transitions in Yb^+ start from the ground state, reading for the $^2S_{1/2}$ state is sufficient to check if the transitions were made. This readout scheme is valid also because of the long lifetimes of the excited states of the transitions. Once the electronic state is excited to a metastable state, the population is *shelved* in the state while the fast $^2S_{1/2}$-state readout is performed (i.e., electron-shelving scheme [131]).

5.2 Types of spectroscopy

There are two types of spectroscopy used in this work.

Ramsey interferometry [132, 133] has been used for α: 411 nm and β: 436 nm transitions as the transitions could be driven coherently; the total interrogation time has been $\sim$30 µs while the decoherence time has been $\sim$100 µs (see Fig. 6-5).

For γ: 467 nm transition, transition rate has scanned over probe frequency instead, as the Rabi period was much longer (>10 ms at the probe intensity used in this work [121]) than the decoherence time.

In retrospect, there was not much benefit to using Ramsey interferometry compared to Rabi spectroscopy [133, 134]. Using Rabi spectroscopy might be preferred for future measurements as it does not introduce excessive phase chirp, has less sensitivity to laser frequency noise [135], and provides more suppression to recoil shift (see Section 7.1.1).

5.3 General procedure

5.3.1 Setup initialization

Before starting each cycle of IS measurement experiments for a pair of isotopes, all the necessary devices are powered up and the lasers are turned on for at least 24

hours to achieve the temperature stabilization and test the stability of the system.

It is also checked whether the sufficient power and the desired frequencies for both the isotopes can be achieved for each laser.[1] In particular, external cavity diode lasers (ECDLs) are subject to drift in their frequency modes. The angle of the grating that serves as the external cavity is adjusted when the desired laser frequency can not be achieved (or is unstable) by adjusting the diode current or the voltage applied to a piezoelectric module for adjusting the cavity length.

Micromotion compensation of ions is also achieved at this stage [4].

5.3.2 Isotope-selective ion loading

The IS measurements are performed on individual cold trapped $^{A}\mathrm{Yb}^{+}$ ions with zero nuclear spin ($A \in \{168, 170, 172, 174, 176\}$). One ion is loaded, isotope-selectively (see Section 4.1.2), at a time (i.e., single-ion spectroscopy). The beams for cooling and repumping are always on while the main experiments are not running to keep the ion in the trap; the ion never escapes from the trap in practice.

During the course of the measurement for one isotope pair, one isotope is interrogated for 1–2 hr and replaced by another isotope for the same measurement (see Figs. 6-4, 6-8, 6-12). The isotope switching is repeated so that each isotope is measured 3–4 times.

5.3.3 Aligning probe beam to an ion

When the system and an ion are ready for an experiment, the probe beam is aligned to the trapped ion, only at the beginning of the experiment (i.e., before measuring spectra of the first isotope). In the earlier measurements, it is done by using 369 nm *align* beam, co-aligned with the probe beam [4]: the 369 nm align beam is aligned to the ion by measuring the ion's fluorescence and steering common mirrors for the two beams, and by checking if the probe beam can drive the clock transitions (see the following sections for measuring the clock transitions). It has been an efficient

[1] The frequency is measured by a wavemeter (HighFinesse/Ångstrom WS/7) (see Section 4.2.6).

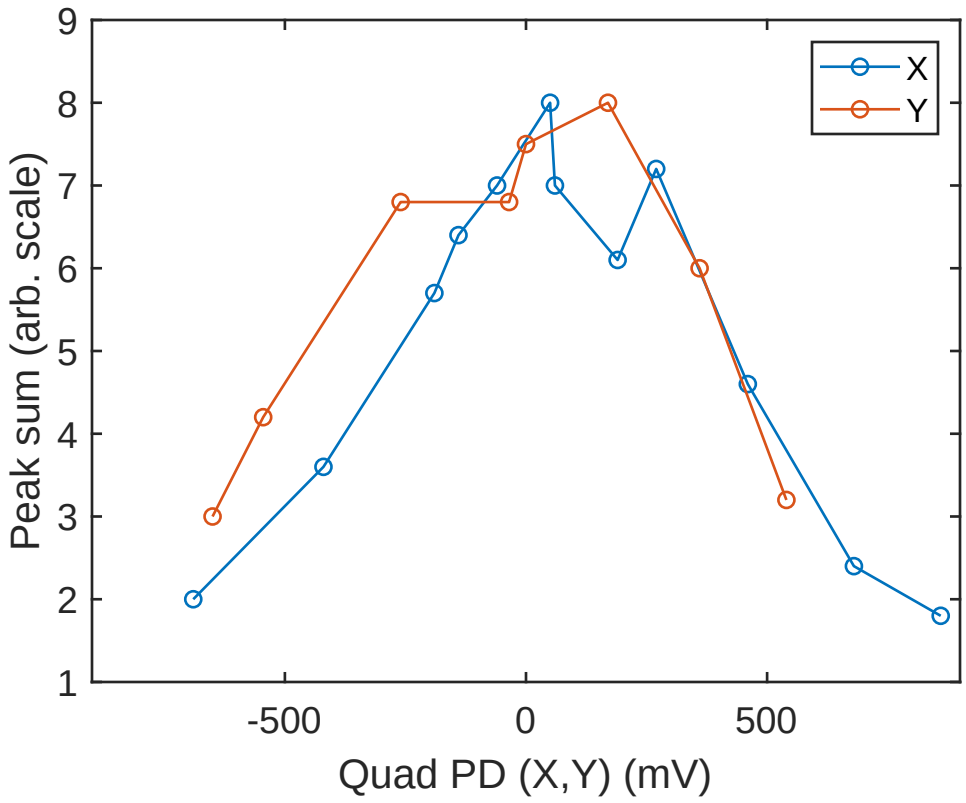

Figure 5-1: Area of a γ: 467 nm transition peak (see Fig. 6-3) vs quadrant photodiode (Quad PD) reading in the x and y directions of the Quad PD (corresponding to horizontal and vertical alignments of the probe beam).

method for the initial alignment of the probe beam. However, despite the time-consuming procedure of co-aligning, the accuracy of the overlap of two beams at their focuses has been questioned. Therefore, a direct approach for the alignment has been developed for later experiments for γ: 467 nm transition: scanning the probe beam's alignment and measuring the rate of the clock transition.

Figure 5-1 shows the transition rate vs probe beam's horizontal and vertical alignments. The beam is tilted by a steering mirror placed before the vacuum chamber, and a quadrant photodiode measures the change in the beam's position at the opposite side of the chamber (see Section 4.2.3.2). It enables precise and, more importantly, *reproducible* scan of the beam alignment. After the scans in each direction, the beam can be aligned to the quadrant photodiode readings that gave the maximum transition rate. This process has taken about an hour to achieve a reliable

alignment.

Indeed, the transition rate for a given optical power of the probe beam has been enhanced by at least factor of 4 after the direct and precise alignment.[2]

5.3.4 Selection of Zeeman transitions

Out of numerous possible transitions between Zeeman sublevels in Fig. 5-2, two transitions that are symmetrically detuned from the zero-field transition, labeled as R and B transitions, are chosen for the frequency measurements. Magnetic field of $\sim$1.1 G is applied which gives 0.6–2.5 MHz separation between the Zeeman transitions depending on the clock transitions [see, Figs. 6-4(b), 6-8(b), and 6-12(b)]. The zero-field transition frequencies are then determined by taking the mean of the measured frequencies of the two R and B Zeeman transitions.

The R and B transitions necessarily start from the different Zeeman levels of the ${}^2S_{1/2}$ ground state $m_J = \pm\frac{1}{2}$. Therefore, the initial state is prepared to be the corresponding ground-state Zeeman level via a 369 nm optical pump beam (see Section 4.1.4 and Fig. 5-3).

In the earlier works, the α: 411 nm and β: 436 nm clock transitions had been scanned for one of R and B transitions and then for another [4], in every $\sim$5 min (see Figs. 6-7, 6-8, and 6-12). The drift in the magnetic field[3] between the measurement for the R and B transitions can induce a systematic shift in the zero-field transition frequency obtained above. In the later measurement for γ: 467 nm transition in this thesis work, the corresponding R and B transitions have been measured nearly simultaneously, with the help of the electrical control of the optical pump beam's polarization (see Section 4.2.5). The procedure is as follows: for each frequency step in a scan, one of the R and B transitions is first measured. The optical pump polarization is switched after the measurement, and the probe beam's frequency is detuned by a fixed amount $\Delta f_{\mathrm{Master}}$ (as close to the separation of the two transitions

[2]Similar probe beam powers $P = 150 \to 160$ mW, twice wide focal waist $w = 15 \to 30$ µm, and nearly twice long pulse time $\tau = 200 \to 390$ ms (see Ref. [4], Tables B.1, and 5.1) gave more than twice of the excitation probability $P_e \sim 0.1 \to \gtrsim 0.2$ (see Fig. 6-3) through the γ transition.

[3]Due to, for instance, a local subway station and elevator.

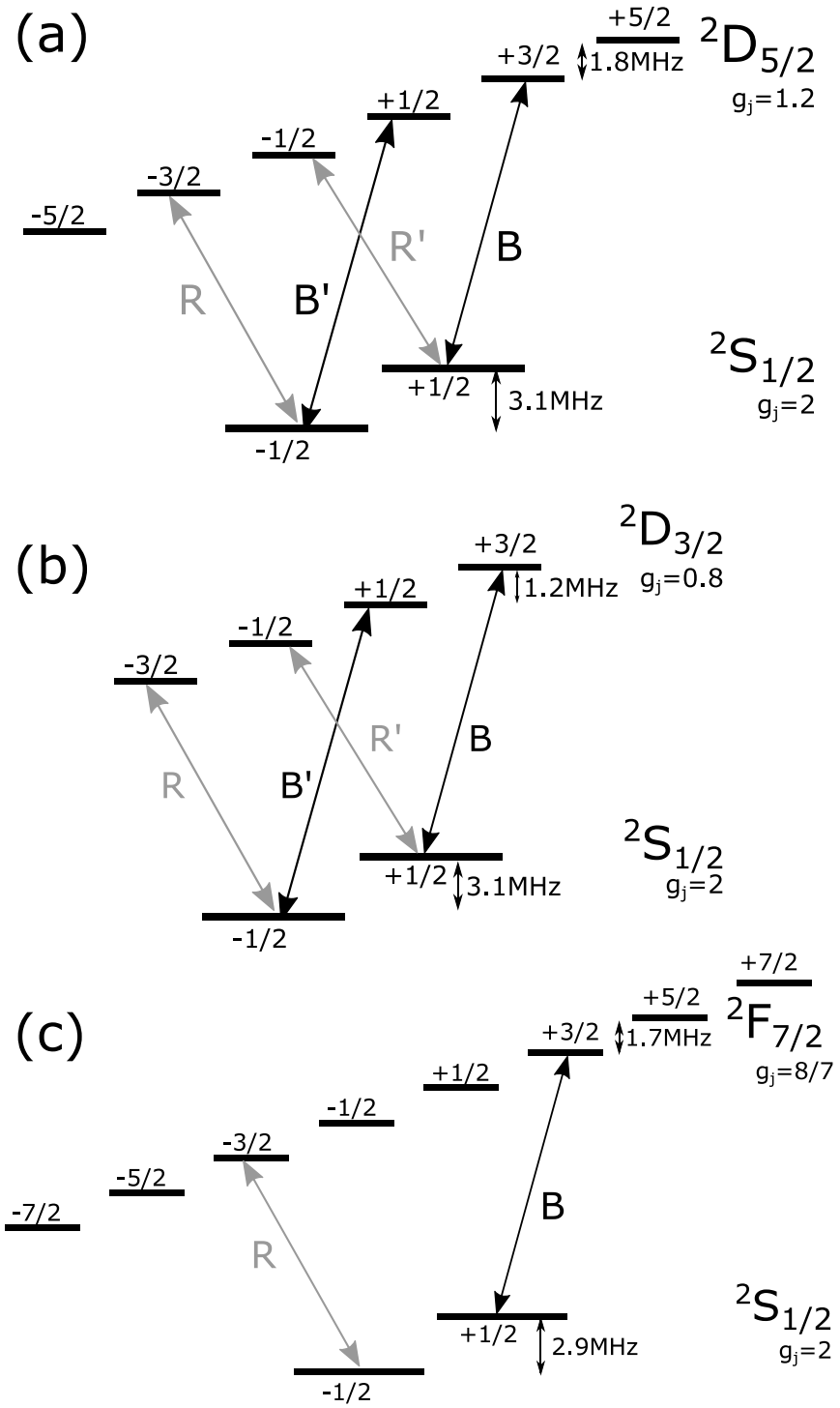

Figure 5-2: Zeeman structures of (a) α: 411 nm, (b) β: 436 nm, and (c) γ: 467 nm clock transitions. A pair of transitions that are red (R) and blue (B)-detuned from the center transition frequency (i.e., the frequency for zero magnetic field) by the same amount are measured and averaged for each clock transition. The R and B transitions are chosen to be measured, while R' and B' transitions are off-resonantly driven and induce light shifts (see Section 7.2.1.1).

as possible) by switching the AOM drive frequency (i.e., `FineFrequency`; see Section 4.1.5.1) at the same time to address to another transition. After a short pulse time (500 ms) for the polarization and probe frequency to settle down, the second transition is measured at the switched probe frequency. After the measurement, the polarization and probe frequency are switched back to the first values, and then the scan moves on to the next frequency scan step. Through this process, the two Zeeman transitions in different frequency ranges can be scanned nearly at the same time, and the temporal separation between the two transitions (i.e., the time that a scan step for each Zeeman transition takes) has been reduced to $\sim$5 s for the γ: 467 nm transition.

5.3.5 Finding transitions and testing scans

The exact locations of the symmetric Zeeman transitions (i.e. the values of `MasterFrequency` in the system here; see Section 4.1.5.1) are pinpointed by initial scans (see Section 5.3.6 for the scan procedure). The ranges of the initial scans are determined from the previously found `MasterFrequency`s for the transitions [4]. The performance of the 369 nm optical pump beam is also tested by measuring the increased or suppressed peak heights (i.e., excitation probabilities; see Sections 5.3.7, 6.1.1, and 6.3) for the Zeeman transitions depending on the polarization of the pump beam [see Fig. 5-4(b)].

For α: 411 nm and β: 436 nm transitions with the Ramsey interferometry (see Section 5.2), the $\frac{\pi}{2}$-pulse time $\tau_{\pi/2}$ for the probe beam is determined by scanning the excitation probability P_e over different pulse times τ, as shown in Fig. 6-5. The measured Rabi oscillation is fitted by Eqs. (6.4) and (6.5) to obtain the value of $\tau_{\pi/2}$. The exact determination of the Rabi frequency ω_R (and thus $\tau_{\pi/2}$) is not required as it is one of the fit parameters in Eq. (6.5).

5.3.6 Scanning spectrum over probe frequency

At this point, the measurement for a Zeeman transition is ready. The excitation probability P_e of the transition (measured as in Section 5.3.7) is scanned over the probe frequency to obtain the Ramsey fringe, for α: 411 nm and β: 436 nm transitions (see Figs. 6-6 and 6-11), or the transition peak for γ: 467 nm transition 6-3. The scanned P_e vs f_{Master} are either fitted or statistically averaged to obtain the center of the spectrum (i.e., resonant `MasterFrequency` of the Zeeman transition), as described in Eqs. (6.2), (6.7), and (6.8).

5.3.7 Measuring transition probability and pulse sequence

This part is the heart of the experiment: driving the optical clock transitions and measuring the excitation probabilities P_e through the transitions. All the beams in the system follow programmed pulse sequences to be turned on and off at the desired timings, which consist of three different parts: to prepare and check the initial state of the ion, to drive a clock transition in a way to perform a desired type of spectroscopy, and to measure the state of the ion after the transition is driven.

The beams are controlled mainly by AOMs through signals generated by a field programmable gate arrays (FPGA) module, with the aid of optical shutters in some cases (see Section 5.4).

The 369 nm fluorescence scattering from the ion is measured through a photomultiplier tube (PMT) (see Fig. 4-1). The same FPGA module used for the pulse generation also counts the number of pulse signals arrived from the PMT in a time-resolved manner [4, 109]. It divides a period of pulse sequence into 100 different *time bins* and counts the number of PMT pulses that arrived within each bin separately. The expectation value of the PMT counts per bin is less than one in general (the duration of the bins are 5 µs to 5 ms depending on the clock transitions; see Table 5.1). Nonetheless, the FPGA module accumulates the PMT counts in the same order of bins over many different cycles until a computer for experimental control reads the total counts in the bins, providing a time-resolved *integration* of fluorescence read-

Table 5.1: Durations of segments in pulse sequences in Fig. 5-3.

		α: 411 nm [µs]	β: 436 nm[c] [µs]	γ: 467 nm [ms]
Repumping & cooling	①	∼35 195[a]	100	50
Pause	②	5		1
Optical pumping	③	10		1
Pause	④	5		7
Probe pulse time	τ	∼10[a]	5[a]	390
Pulse separation	T	10	10	
Pause	⑤	5		1
Readout	⑥	14 759	100	50
Total		50 000[b]	500[b d]	500

[a] exact value adjusted to achieve $\frac{\pi}{2}$ probe pulses (see Section 5.3.5).
[b] Note that there are two probe pulses.
[c] Approximated values used in Ref. [4]'s work.
[d] Consecutive sequences with the same total duration, for calibration and data acquisition.

ing over many consecutive cycles. It enables the *averaged* spectroscopy described in Section 5.6.

The cycle of the preparation, drive, and state readout is repeated many times to obtain the statistics of the ion's excitation through the clock transitions. In particular, the excitation probability P_e is given by the ratio of the number of times that the ion is read to be in the excited state (i.e., being in the dark state for the 369 nm transition; see Section 5.1) to the number of total (successful) attempts.

The particular pulse sequence and the associated method of state readout and P_e calculation for each clock transition are introduced in Sections 5.4, 5.5, and 5.6, and summarized in Fig. 5-3 and Table 5.1.

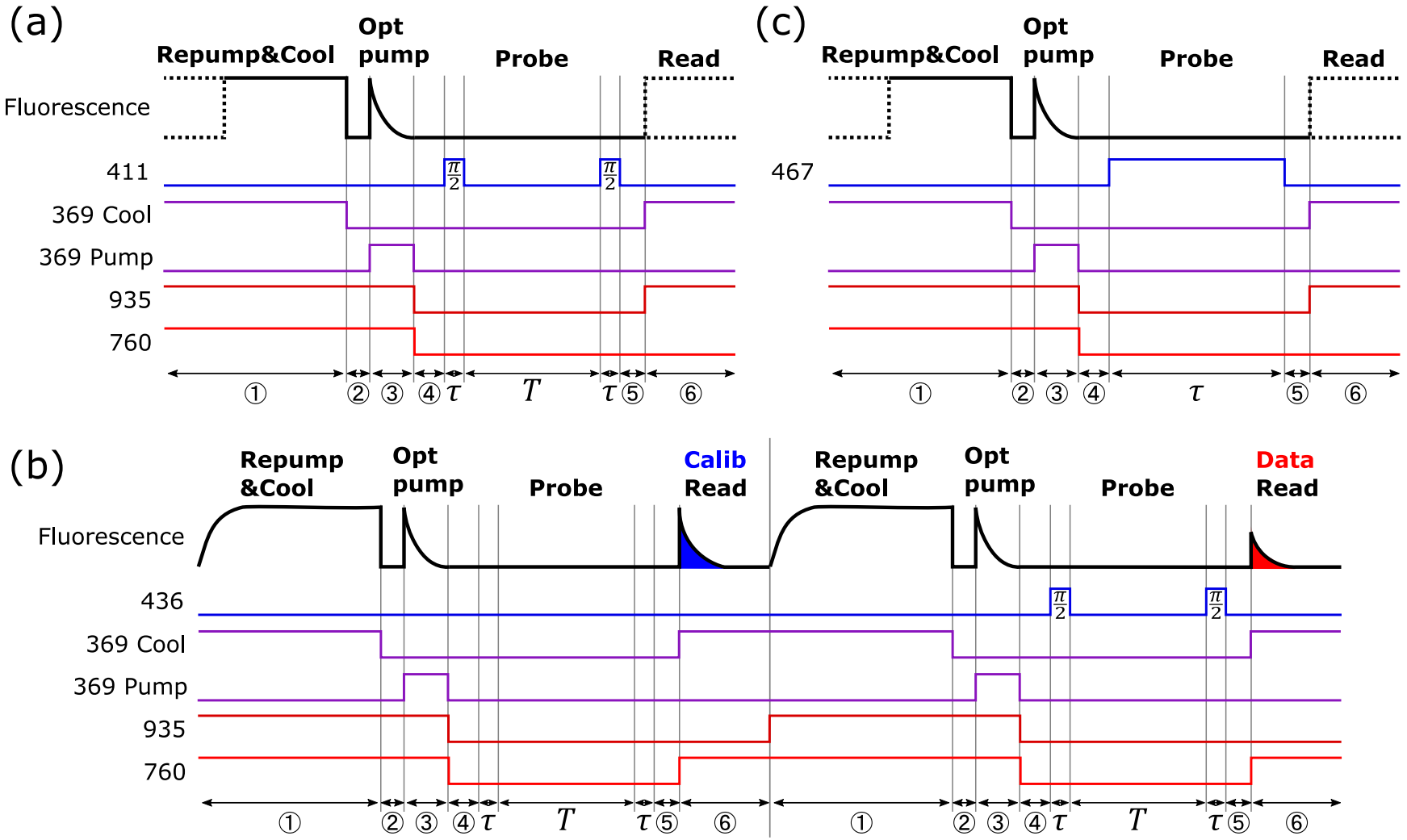

Figure 5-3: Pulse sequences for (a) α: 411 nm, (b) β: 436 nm, and (c) γ: 467 nm spectroscopy. The sequences in (a) and (b) are for Ramsey interferometry, while (c) is for transition-rate spectroscopy. The sequences in (a) and (c) describe single-shot measurements (see Sections 5.4 and 6.1.1), while (b) describes integrated measurement (see Section 5.6 and 6.3). The durations ① – ⑥, τ, and T can be found in Table 5.1.

5.3.8 Repeated procedures for isotope-shift measurement

A pulse sequence is repeated to measure the excitation probability P_e of ion through a clock transition for a given `MasterFrequency` (see Section 4.1.5.1) as in Section 5.3.7. Such measurement is repeated for different `MasterFrequency` steps to obtain a desired P_e vs f_{Master} spectrum (Section 5.3.6) and thus the resonant `MasterFrequency` for a Zeeman transition. The P_e for the different symmetric Zeeman transitions are alternately measured in a single scan or in different scans (Section 5.3.4). The resonant `MasterFrequency`s of the two Zeeman transitions are properly averaged to obtain the center, zero-field `MasterFrequency` of the clock transition for an isotope (Sections 6.1.2 and 6.2). The clock transition's zero-field `MasterFrequency` is repeatedly measured for one isotope at a time for $\lesssim$2 hr, and then for another by trapping an ion of another isotope (Section 5.3.2). Finally, the measurements for the different isotopes are alternately repeated over 8–16 hr or longer (see Figs. 6-4,6-8, and 6-12), depending on the clock transitions, and the overall difference in the measured zero-field `MasterFrequency`s for the two isotopes is given as the IS of the isotope pair.

5.4 γ: $^2S_{1/2} \rightarrow {}^2F_{7/2}$ (467 nm) transition

Figure 5-3(c) shows the pulse sequence and the possible patterns of the time-resolved 369 nm fluorescence reading through the PMT for the γ transition, with the duration of each time segment listed in Table 5.1. The sequence starts with the cooling and repumping beams in segment ① to repump and cool the ion that might be driven to the $^2F_{7/2}$ state or heated up during the remaining duration of the sequence in the last cycle. The 369 nm cooling beam is replaced by the optical pump beam during segment ③ (1 ms), after a 1 ms pause time during segment ② (both beam are off). After another 1 ms pause time (segment ④), the probe is on for $T = 390$ ms to drive the clock transition. All the other beams are properly blocked (see below paragraphs) during the probe beam is on to avoid light shifts from the beams (see Section 7.2.2). After the last 1 ms pause time (segment ⑤), all the non-probe beams except the

760 nm $^2F_{7/2}$-state repumper are turned on to read the ion's state during segment ⑥.

The γ clock transition excites the ion to the extremely long-lived $^2F_{7/2}$ state (see Fig. 3-1 and Table B.1). Due to the extremely narrow linewidth, a long probe pulse time (chosen to be 390 ms here) is necessary to excite the ion with a visible probability P_e. The total period of the pulse sequence, 500 ms, was long enough that the ion's state after each cycle can be measured (i.e., *single-shot* spectroscopy) without losing the efficiency of the measurement cycle; reading out the ion state with high fidelity by collecting enough number of scattered photons takes $\gtrsim$10 ms in the experimental setup used here (see Section 6-2). In each pulse sequence period, the 369 nm fluorescence is measured during segment ① and ⑥ to read *quantum opportunity* (`QO`) and *quantum jump* (`QJ`), respectively. `QO` is the flag for successful repumping of the ion from the $^2F_{7/2}$ state; `QO` is true (or there is `QO`) if the ion is in the $^2S_{1/2}$ state, and false (or no `QO`) if it is not. It can be read by measuring if there is fluorescence from the ion; true `QO` if the ion is bright and false `QO` if the ion is in a dark state. The definition and reading of `QJ` are similar. If the ion is dark after the optical transition is driven, it implies the ion is excited and thus `QJ` is true (i.e., a quantum jump is made). `QJ` is false if the ion is bright after the clock transition is driven. Among many cycles of the sequence for the same Zeeman transition and `MasterFrequency` value, the cycle with false `QO` is dropped from the data set for an obvious reason. The total number $N_{\texttt{QJ}}$ of cycles with true `QJ` out of the $N_{\texttt{QO}}$ remaining cycles, all with true `QO`, are counted and divided by $N_{\texttt{QO}}$ to obtain $P_e(f_{\text{Master}})$:

$$P_e(f_{\text{Master}}) = \frac{N_{\texttt{QJ}}}{N_{\texttt{QO}}}. \tag{5.1}$$

In the relatively later experiments for the γ: 467 nm transition in this work, the sequence ran until a fixed number of $N_{\texttt{QO}}$ were obtained before moving onto the next `MasterFrequency` step (see Section 5.3.6).

During the long probe pulse time, any leakage beams through the AOMs or stray lights can compromise the measurements. In particular, 369 nm light has high

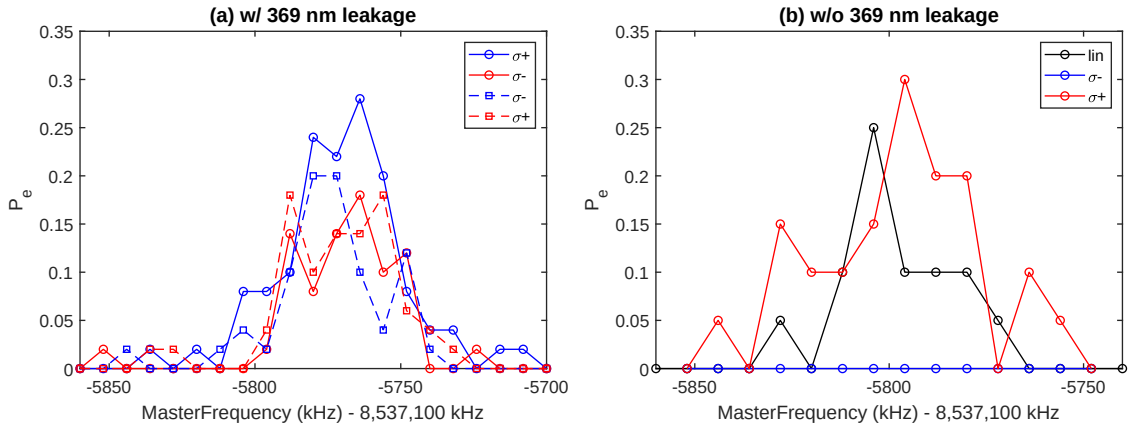

Figure 5-4: Scanned transition peak for B Zeeman transition of γ: 467 nm clock transition [see Fig. 5-2(c)] (a) before and (b) after 369 nm beams leaked through AOMs were blocked by shutters (see Section 5.4). In (a), the same peak was scanned twice for each of σ^+ (red) or σ^- (blue) circular polarizations of 369 nm optical pump beam (see Section 5.3.4), shown by different symbols and line styles. In (b), the peak is scanned for $\hat{\sigma}^+$, $\hat{\sigma}^-$, and linear (black) [$= (\hat{\sigma}^+ + e^{i\phi}\hat{\sigma}^-)/\sqrt{2}$ with an arbitrary relative phase ϕ] polarizations.

efficiency for pumping the $^2S_{1/2}$ Zeeman states back to have 50:50 % population, only by the 369 nm cooling beam leaked through the AOM while the AOM is not driven. To block the AOM leakage beams, optical shutters have been placed for 369 nm cooling and optical pump beams and controlled together with the beams.[4] The timings of the shutter controls have been adjusted carefully to ensure the full use or block of the beams, which is one of the main purposes of the pauses in segments ②, ④, and ⑥. Laser safety black fabric has been also placed to block the stray beams from the 369 nm laser system to the experimental chamber. Figures 5-4(a) and (b) show the scans for a Zeeman transition before and after the optical shutters and the fabric were placed, respectively. In this figure, B Zeeman transition was scanned [see Fig. 5-2(c)] which requires $m_J = +\frac{1}{2}$ for the ion's initial state and thus $\hat{\sigma}^+$ polarization of the optical pump beam. Fig. (b) indeed shows clear contrasts between the scanned excitation probabilities P_e with linear, $\hat{\sigma}^-$, and $\hat{\sigma}^+$ polarizations, while Fig. (a) does not.

There have been several upgrades for the later experiments for the γ transi-

[4]The shutter for the optical pump beam also prevents the fiber tip damage from the counter-propagating probe beam (see Fig. 4-8).

tions since the preliminary results were obtained in Ref. [4], described in Section 4.2 and earlier in this chapter. In summary, the probe beam power has been actively stabilized (Section 4.2.3.1), the beam has been aligned precisely using a quadrant photodiode (Section 5.3.3), the beam focal size has increased (Section 4.2.3.3) to suppress the systematic effect from the drift in probe beam intensity that an ion sees (Section 7.2.1), and the drift in the beam alignment has been recorded during the experiments by the quadrant photodiode to check if there has been any excessive drift or the correlation of the drift with the measured transition frequencies over time [see Figs. 6-4(a,c)]. The new introduced 760 nm repumping beam, that replaces the previous 638 nm repumper [4], has pumped the $^2F_{7/2}$ state at least 10 times faster ($\gtrsim 100\,\text{ms} \rightarrow \lesssim 10\,\text{ms}$ characteristic time) (Section 4.2.6). It has enabled the twice longer probe beam (200 $\rightarrow$ 390 ms) in the pulse sequence cycles of the same total duration, increasing the efficiency of the measurements effectively twice.

5.5 α: $^2S_{1/2} \rightarrow {}^2D_{5/2}$ (411 nm) transition

Figure 5-3(a) shows the pulse sequence for the α transition. This transition excites the ion to $^2D_{5/2}$ states, which decays more likely to the extremely long-lived $^2F_{7/2}$ state (83 % branching ratio) than back to the $^2S_{1/2}$ ground state, in 7.2 ms (see Fig. 3-1 and Table B.1). Therefore, the duration of a pulse sequence cycle is limited by the 7.2 ms decay time and $\lesssim$10 ms $^2F_{7/2}$-state repumping by the 760 nm beam (see Section 4.2.6). The total period of the pulse sequence 50 ms is long enough to perform single-shot spectroscopy as in Section 5.4.

Naturally, the pulse sequence and state readout scheme are similar to the γ transition, except for the overall durations of the segments and, more importantly, the two $\tau \sim 10\,\mu\text{s}$ (near-)$\frac{\pi}{2}$ probe pulses separated by $T = 10\,\text{ms}$ to perform the Ramsey interferometry. The pulse time τ is found in the initial stage of the experiment (see Section 5.3.5).

Replacing the 638 nm $^2F_{7/2}$-state repumping beam to the 760 nm repumper (see Section 4.2.6) has more significant effect for the α transition than the γ transition

described in Section 5.4. The $\gtrsim$100 ms characteristic repumping time of 638 nm dominated the total period of the corresponding pulse sequence cycle for the α transition [4]. By achieving $\lesssim$10 ms of repumping time with the 760 nm repumper, 4 times faster cycle has been achieved (200 ms $\rightarrow$ 50 ms). Together with the active stabilization of RAM (in Section 4.2.1), the new measurements have demonstrated $\sim$100 Hz precision of the IS measurement over 1 hr [see Fig. 4-10; it is not for measuring ISs but essentially identical in terms of the form and analysis of the data]. Given the suppressed long-term systematic drift in the system since the earlier experiments, a naïve projection would give $\lesssim$30 Hz for the measurement over $\geq$9 hr, which would be an order-of-magnitude improvement in the precision from the first-round measurements (see Table A.1).

Due to the short duration of driving the clock transition (total $\sim$30 µs), no optical shutter has been placed to date. However, it would be worth sparing a few ms[5] for the shutters to block the 369 nm beams while the clock transition is being driven, to prevent the 1.3 kHz absolute light shift from the leakage beams through the AOMs (see Section 7.2.2).

Note that, however, no IS measurement has been made with such upgrades yet, and the values of the measure ISs in Table A.1 are from the first-round experiments [4, 5] performed before any upgrades in Section 4.2 were established or simultaneous measurements of Zeeman transitions in Section 5.3.4 was employed.

5.6 β: $^2S_{1/2} \rightarrow {}^2D_{3/2}$ (436 nm) transition

The pulse sequence for the β transition is shown in Fig. 5-3(b). It is somewhat different from the sequences for the α and γ transitions, due to the difference in the state readout methods.

The β transition excites the ion to the $^2D_{3/2}$ states. However, when the ion is in the $^2S_{1/2}$ state and the 369 nm cooling transition is driven to read the ion's state, the ion decays from $^2P_{1/2}$ (the excited state of 369 nm transition) to the $^2D_{3/2}$ states

[5] Considering the typical response time of optical shutters.

in $\sim$50 µs (see Section 4.1.2). It is not enough time to collect enough number of photons, which takes $\gtrsim$10 ms as mentioned in Section 5.4, before the ion falls in the $^2D_{3/2}$ and the previous state[6] right after the clock state is driven becomes indistinguishable. Thanks to the time-resolved integration of the PMT counts over cycles (see Section 5.3.7), the averaged ratio of the ion's state after the transition is driven (i.e., the excitation probability P_e) over many cycles (i.e., *averaged* spectroscopy) can be measured as below.

One cycle of the pulse sequence consists of two subsequences, of the same period, that are almost similar. The only difference is the existence of a probe pulse. In the first subsequence, the probe is off and the transition is not driven, assuring that the ion is in the $^2S_{1/2}$ ground state when the state readout begins in segment ⑥. By averaging many cycles, the averaged peak showing the scattered 369 nm photons decaying in the $\sim$50 µs can be observed. On the other hand, when the probe drives the ion to the excited state in the fraction of the cycles with the ratio of P_e, those cycles do not add scattered photons in the peak, and the peak area is reduced in the second state readout by a factor of P_e. Therefore, the first peak serves as a calibration peak, of which area normalizes the second peak's area to obtain the value of P_e.[7]

As the repumping of $^2D_{3/2}$ state with the 935 nm beam is very quick ($<$5 µs; see Section 4.1.2), and there is no $\gtrsim$10 ms overhead for the single-shot state readout in Sections 5.4 and 5.5, the period of the pulse sequence can be as short as 500 µs (250 µs per subsequence). This constitutes another reason for preferring the average spectroscopy to the single-shot spectroscopy.

Just as in Section 5.5 for the α: 411 nm transition, a new experiment for IS

[6] An alternative view of this limitation is from the fact that the number of 369 nm photons that the ion can scatter before decayed to the $^2D_{3/2}$ state (200 photons) is determined by the branching ratio of the 935 nm decaying channel to the $^2D_{3/2}$ state, regardless of the scattering or decay rates given by the rate of 369 nm transitions (i.e., the 369 nm beam's intensity and detuning). Given the limited numerical aperture (NA) of the imaging system in the experimental setup and quantum efficiency of the PMT, the expectation value of the scattered photons detected by the system would be less than one.

[7] See Footnote 6 for the reason why the peak area is a more appropriate measure than peak height.

spectroscopy after the upgrades have not been performed for the β transition yet, and the values reported in Table A.1 are from the earlier measurements published in Ref. [5] carried out by Ian Counts, a former research team member and fellow PhD student [4].

Chapter 6

Results

In this chapter, the results of the isotope-shift (IS) spectroscopy experiments introduced in Chapter 5 are presented, and the obtained data are analyzed to obtain the experimental values of ISs.

The measured values of the ISs between different pairs of isotopes for α: 411 nm, β: 436 nm, and γ: 467 nm optical clock transitions in Yb^+ ions (see Fig. 3-1) are summarized in Appendix A (see Table A.1). The updated values with reduced uncertainties from the measured ISs between redundant isotope pairs (see Section 6.7) were presented in the appendix as well (see Table A.2). The appendix also lists the absolute frequencies of all the 5 stable even-A isotopes ($A \in \{168, 170, 172, 174, 176\}$), in Table A.3, obtained from the absolute transitions frequency of a reference isotope for each clock transition (see Section 6.5). The absolute frequencies and ISs for the 369 nm cooling, 935 nm $^2D_{3/2}$-state repumping, and 760 nm $^2F_{7/2}$-state repumping transitions (see Fig. 3-1), of which measurements are described in Section 6.6, has been also listed in Table A.4 in the appendix.

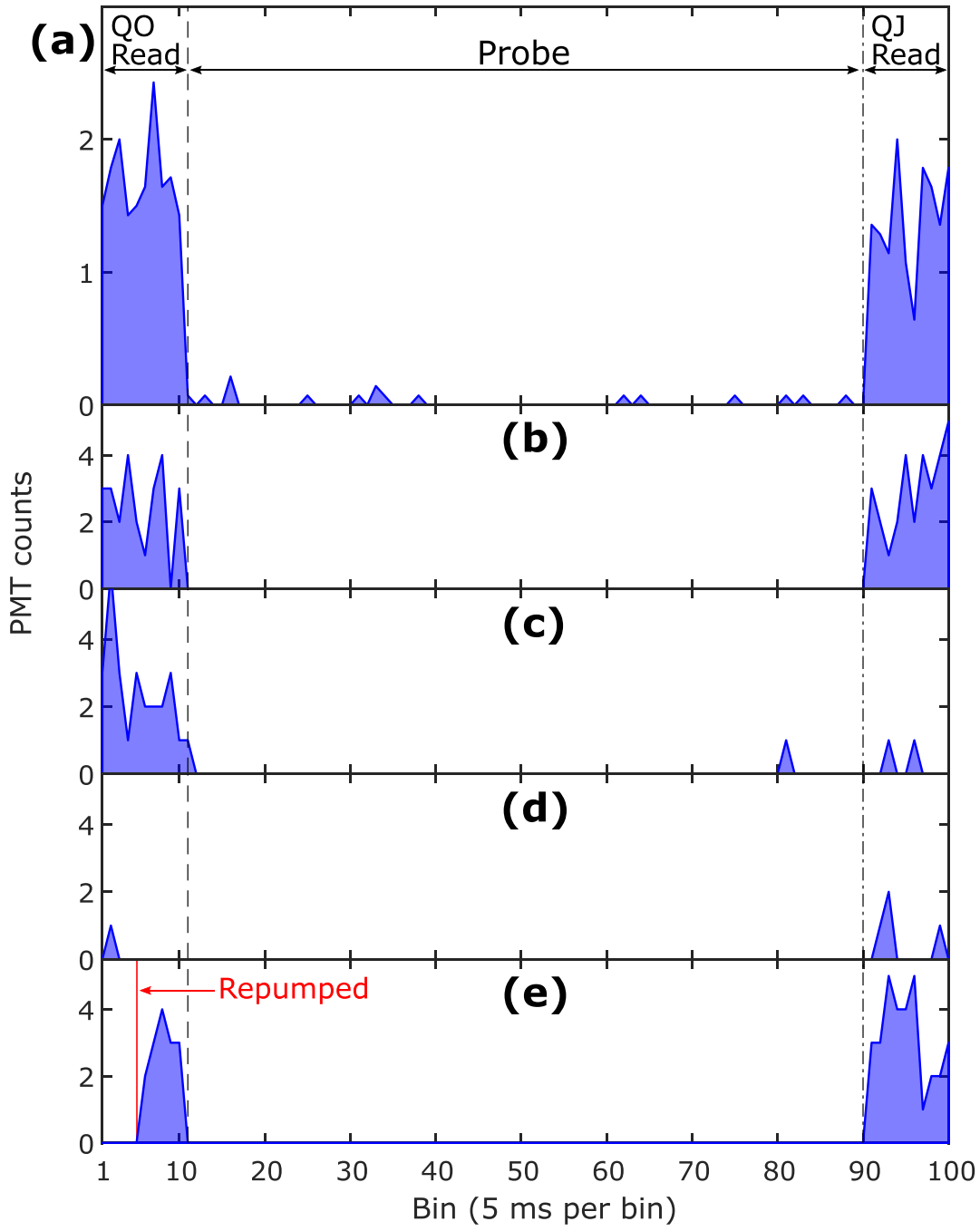

Figure 6-1: Time-resolved PMT counts (see Section 5.3.7) in each of 100 time bins during a pulse sequence cycle for γ: 467 nm transition [see Fig. 5-3(c)]. (a) The averaged PMT counts over 10 cycles for each `MasterFrequency` step (see Section 6.1.2). Other figures shows the example PMT counts for $[\texttt{QO}, \texttt{QJ}] =$ (b) $[\texttt{true}, \texttt{false}]$, (c) $[\texttt{true}, \texttt{true}]$, and (d) $[\texttt{false}, -]$ (see Section 5.4). Figure (e) shows a cycle in which ion is repumped from $^2F_{7/2}$ state in the middle of repumping and cooling segment (red vertical line). This kind of cycles might be determined to have false `QO`and discarded from the data, depending on the total PMT counts collected after the ion is repumped (i.e., $[\texttt{QO}, \texttt{QJ}] = [\,?\,, \texttt{false}]$).

6.1 γ: $^2S_{1/2} \rightarrow {}^2F_{7/2}$ (467 nm) transition

6.1.1 Single-shot spectroscopy

Figure 6-1 shows selected PMT counts over different pulse sequence cycles in Fig. 5-3(c), to describe the determination of `QO` and `QJ` in each cycle (see Section 5.4). If the ion scatters the 369 nm cooling beam in the state readout segments ① or ⑥, measured by the PMT, it implies that the ion was in the $^2S_{1/2}$ ground state before the readout (see Section 5.1). The ion is, then, ready for the experiment (segment ①; true `QO`) or was not excited through the clock state (segment ⑥; false `QJ`). On the other hand, if no scattering is measured, the ion is not in the ground state, implying the ion's state is not properly prepared and the cycle is to be ignored (segment ①; false `QO`), or the ion made a transition to the excited state (segment ⑥; true `QJ`) given that the ion's state was properly prepared (i.e., true `QO`) at the beginning of the cycle.

Figure 6-1(b–e) shows different possible results of the readouts during a cycle. Fig. (d) shows the case that there is no (sufficient) 369 nm scattering during the first readout, and thus no `QO`, and this cycle is ignored. Fig. (b) and (c) show enough PMT counts during the first segment and the control software determines that those cycles have true `QO`. The two cycles have different results for the next readout: enough counts (i.e, false `QJ`) for cycle (b) and not enough counts (i.e., true `QJ`) for cycle (c). The case in Fig. (e) shows a tricky situation. The ion was in the excited state of the clock transition at the beginning of the cycle, due to the true `QJ` in the last cycle (or even before and failure of repumping until the last cycle). The ion is repumped, then, in the middle of the segment ① for readout and repumping at the same time. Then, depending on the timing that the repumping happened, the total PMT counts after the repumping might not exceed the threshold counts for assigning true `QO` to the cycle, and the cycle is dropped from the data set. It is obvious that this does not harm the data quality (i.e., systematic shifts). The repumping and the `QO` readout can be separated to avoid such a case, in principle, but doing so brings only a worse time efficiency of the measurement. Note also that the second readout for `QJ` could

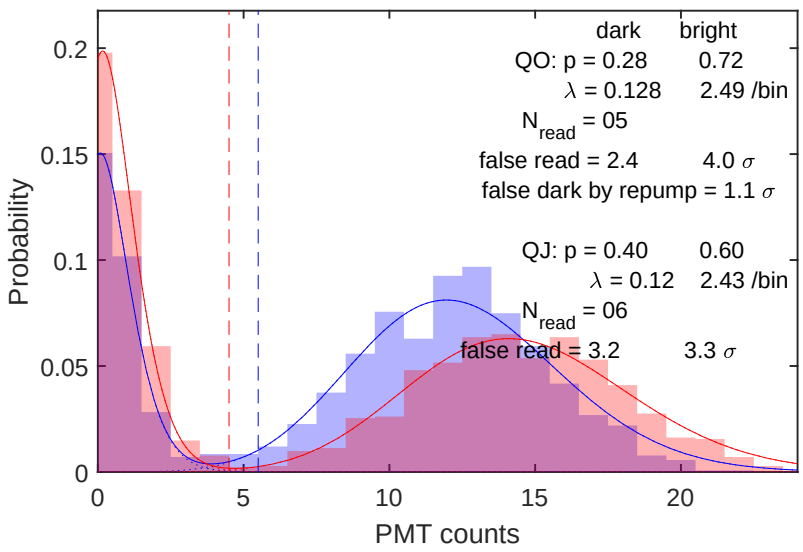

Figure 6-2: Typical histograms of PMT counts during `QO` (blue) and `QJ` (read) (see Section 5.4) readouts [segments ① and ⑥; see Fig. 5-3(c)] per cycle, over a scan for γ: 467 nm transition. The vertical dashed lines show the threshold PMT counts for determination of `QO` and `QJ` flags' states.

be either true or false for the cycle with the indefinite `QO`, and only the latter case is shown in Fig. (e).

As implied in the earlier paragraphs, a threshold number of PMT counts have to be set to determine the `QO` and `QJ` flags' states. A proper choice of the number is important when there is *a dark signal*: low, but nonzero PMT counts when the ion is not scattering the 369 nm beam, which was observed consistently as in Fig. 6-1. To determine the threshold, the distribution of the PMT counts per cycle across each transition scan (see Section 6.1.2) was analyzed as shown in Fig. 6-2. The histograms of PMT counts per cycle were obtained separately for the `QO` and `QJ` readouts, and each histogram was fitted with the bimodal Poisson distribution:

$$P(\text{PMT counts} = k) = P_{\text{d}} \frac{e^{-\lambda_{\text{d}}} \lambda_{\text{d}}^{k}}{k!} + \underbrace{P_{\text{b}}}_{=1-P_{\text{d}}} \frac{e^{-\lambda_{\text{b}}} \lambda_{\text{b}}^{k}}{k!} \tag{6.1}$$

where the subscript d and b denote *dark* and *bright* states of the ion (i.e., ion does not or does scatter the 369 nm beam, respectively), $P_{d,b}$ are the overall fractions of the cases, across the scan, that the ion is in the dark or bright states during a readout,

and λ is the parameter for the Poisson distribution for each of dark and bright ion's states. The values of P_d (or P_b) and $\lambda_{d,b}$ are fit parameters in Eq. (6.1), and the fitted $\lambda_{d,b}$ are used to determine the threshold counts for `QO` and `QJ` determination as below.

For `QO`, a false negative reading [i.e., `QO` is determined to be false when it should be true as the ion is in fact bright] is safe; the cycle is just dropped from the data set. However, false positive reading is troublesome, as the following invalid `QJ` reading will be included in the data set to calculate P_e [Eq. (5.1)]. Therefore, relatively higher PMT counts were chosen as the threshold to suppress the false positive reading with over 4σ significance as shown in Fig. 6-2. In contrast, the false positive and false negative readings are equally undesirable for `QJ`, and the threshold counts that equally minimize both the false readings were chosen (with $\approx 3.2\sigma$ significance in the figure).

6.1.2 Scanning Zeeman transitions

The R and B Zeeman transitions in Fig. 5-2(c) were simultaneously measured during each scan as described in Section 5.3.4. Figure 6-3 shows the typical results from the simultaneous scan. The probe frequency was bridged by $f^B_{\text{Master}} - f^R_{\text{Master}} = +2,105\,\text{kHz}$ (very close to the separation of the transition frequencies), and the two frequencies were scanned with the same `MasterFrequency` (see Section 4.1.5.1) step size.

After each scan, the resonant frequency of each Zeeman transition was obtained by calculating the statistical mean of `MasterFrequency` steps weighted by the measured excitation probabilities P_e:

$$f^{R,B}_{\text{Master}} = \frac{\sum_f f \times P_e^{R,B}(f)}{\sum_f P_e^{R,B}(f)}. \tag{6.2}$$

From these values, the center, zero-field `MasterFrequency` of the clock transition

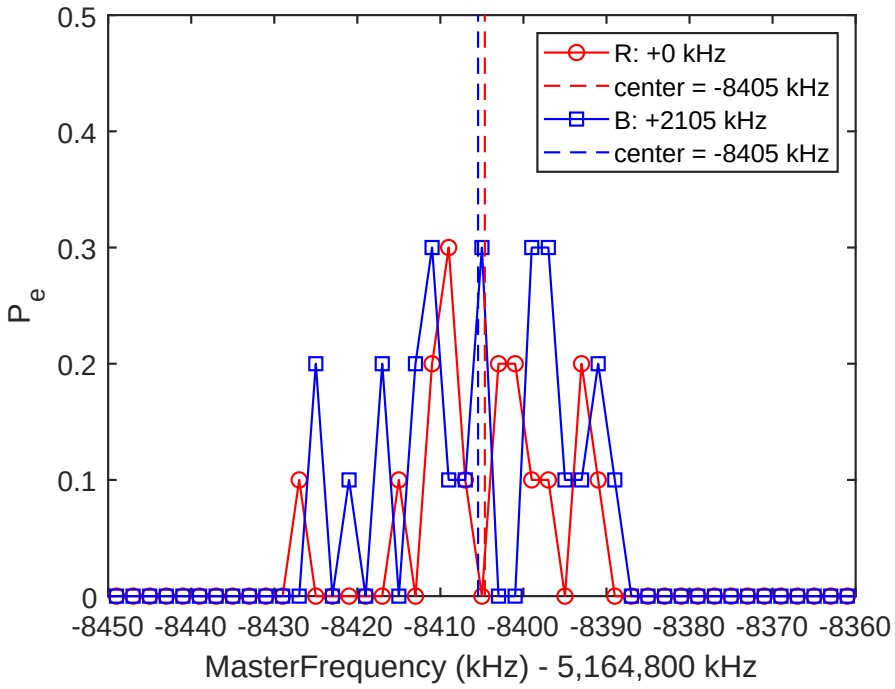

Figure 6-3: Scanned R (red) and B (blue) Zeeman transitions of γ: 467 nm clock transition [see Fig. 5-2(c)] at the same time (see Section 5.3.4). A fixed amount of frequency jumps $\Delta f_{\text{Master}} = 2,105\,\text{kHz}$ were made between measurements for the two transitions. The vertical dashed lines show the resonant `MasterFrequency` (see Section 4.1.5.1) of the two transitions obtained from the statistical means of the `MasterFrequency` steps weighted by the measured P_e's [see Eq. (6.2)].

and the separation of the two Zeeman transitions were obtained for each scan:

$$f^{\mathrm{Comm}}_{\mathrm{Master}} = \frac{f^{R}_{\mathrm{Master}} + f^{B}_{\mathrm{Master}}}{2} \tag{6.3a}$$

$$f^{\mathrm{Diff}}_{\mathrm{Master}} = f^{B}_{\mathrm{Master}} - f^{R}_{\mathrm{Master}} \tag{6.3b}$$

For γ: 467 nm transition, the pulse sequence cycles were repeated until 10 cycles with true `QO` were accumulated and the excitation probability P_e was obtained (see Section 5.4), for each `MasterFrequency` step in a scan. As a cycle had 500 ms period (see Table 5.1), P_e for one `MasterFrequency` scan took $\sim$5 s. It could have been slightly longer due to the unsuccessful repumping (i.e., no `QO`) dropped in the data set. A 0.5 s pause time was given between Zeeman transitions to settle down the 369 nm optical pump polarization and probe frequency (see Section 5.3.4). Therefore, the measurement for one `MasterFrequency` step took total $\sim$11 s. The size of the scan step was 2 kHz. Considering $\lesssim$50 MHz linewidth, P_e was scanned over 100 kHz range (i.e., 50 `MasterFrequency` steps). Therefore, $\sim$10 min was taken per scan.

At the resonance of each Zeeman transition, $P \sim 160$ mW probe power at the focus with $w = 30$ µs waist has been necessary to obtain sufficient excitation probability $P_e \gtrsim 0.2$ (see Table B.1).

6.1.3 Measurements for isotope pair

Figure 6-4 shows the data taken across the IS measurement for a pair of isotopes. The trapped ion of one isotope was switched to another in every $\sim$1.5 hr (i.e., 9–10 consecutive transition scans per isotope segment). Fig. (a) and (b) show the measured $f^{\mathrm{Comm}}_{\mathrm{Master}}$ and $f^{\mathrm{Diff}}_{\mathrm{Master}}$, respectively, over time. Fig. (a) shows the linear drift in $f^{\mathrm{Comm}}_{\mathrm{Master}}$ as expected (see Section 6.4). Various parameters were monitored and recorded (Section 4.2.7) as shown in Fig. (c). The correlations between the nonlinear components of each parameter value and $f^{\mathrm{Comm}}_{\mathrm{Master}}$ over time were calculated, as shown in the figure, but no significant correlation was observed.

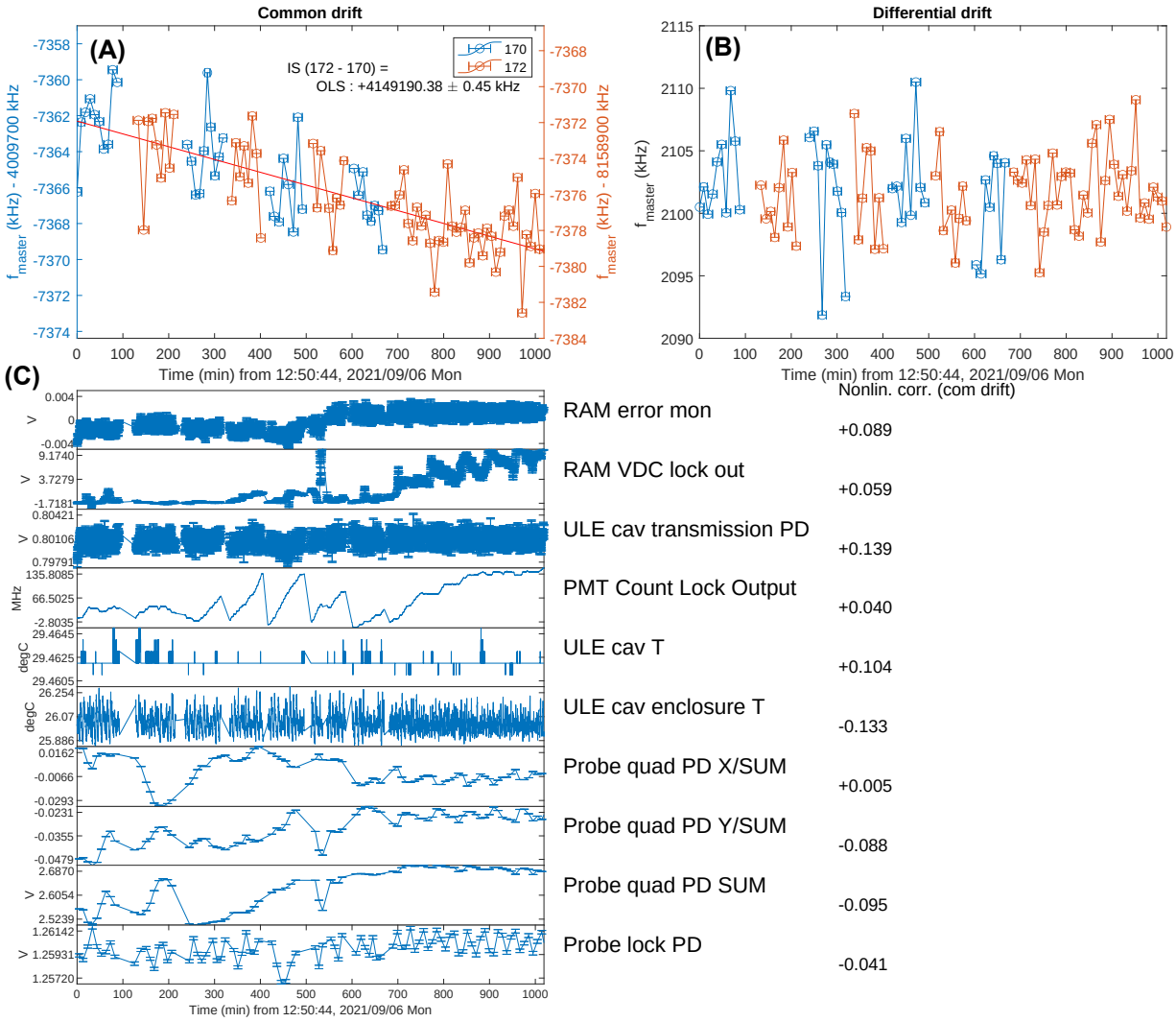

Figure 6-4: Example of data taken over the course of an IS spectroscopy experiment for γ: 467 nm transition and for a pair of isotopes [$^{170}Yb^{+}$ (blue) and $^{172}Yb^{+}$ (red) for this data]. The drift in (a) measured zero-field `MasterFrequency` (see Section 4.1.5.1) (*Common drift*; $f^{\mathrm{Comm}}_{\mathrm{Master}}$) and (b) the frequency separation of R and B Zeeman transitions [see Fig. 5-2(c) and Section 5.3.4] (*Differential drift*; $f^{\mathrm{Diff}}_{\mathrm{Master}}$) are presented. Figure (c) shows the values of various experimental parameters recorded during the experiment (see Section 4.2.7). Each of the values at the right shows the correlation between the nonlinear components of zero-field `MasterFrequency` and the corresponding recorded value.

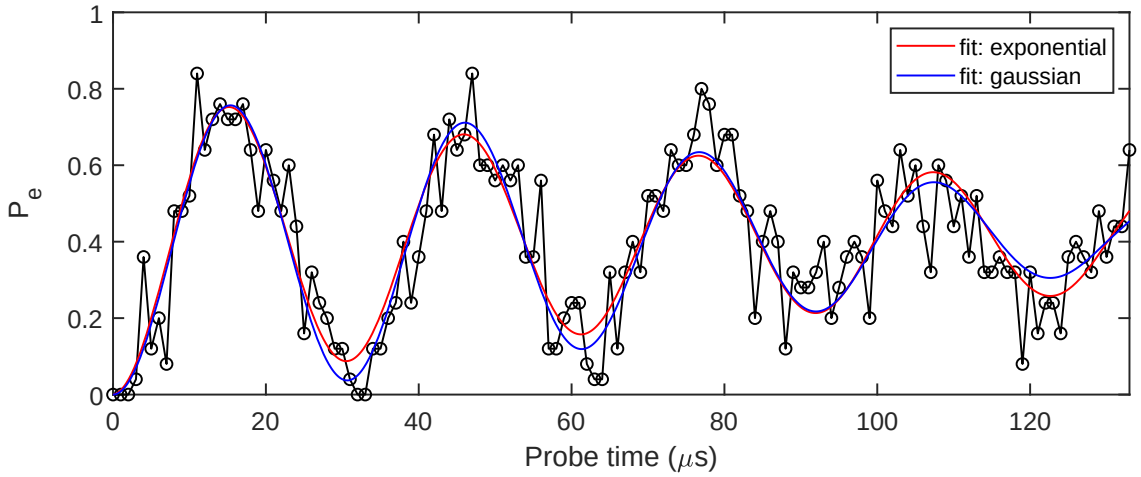

Figure 6-5: Typical Rabi oscillation of excitation probabilities P_e through α: 411 nm transition for different probe pulse times τ (see Fig. 5-3). The data are fitted using Eq. (6.5), assuming exponential [red; Eq. (6.4d)] or Gaussian [blue; Eq. (6.6)] decay of the Rabi oscillation's contrast. $\frac{\pi}{2}$-pulse time is fitted to be $\tau_{\pi/2} = 7.7\,\mu\text{s}$ at typical probe power $P \sim 1\,\text{mW}$ at the focus with $w = 60\,\mu\text{m}$ waist (see Table B.1).

6.2 α: $^2S_{1/2} \to {}^2D_{5/2}$ (411 nm) transition

α: 411 nm transition's PMT counts per cycle and the determination of `QO` and `QJ` for single-shot spectroscopy were essentially the same to the γ: 467 nm transition (see Section 6-1), except for the timings and durations of the readouts (see Table 5.1).

The $\frac{\pi}{2}$ probe pulse time $\tau_{\pi/2}$ was obtained from the Rabi oscillation scan shown in Fig. 6-5; the excitation probabilities P_e were measured for different pulse times τ. The results were fitted with the expression:

$$\delta = 2\pi(f - f_0) \tag{6.4a}$$

$$\Omega = \sqrt{\omega_R^2 + \delta^2} \tag{6.4b}$$

$$P_e^0 = \frac{\omega_R^2}{\Omega^2} \sin^2 \frac{\Omega\tau}{2} \tag{6.4c}$$

$$P_e = \frac{\omega_R^2}{\Omega^2} \frac{1}{2} \left(1 - e^{-\tau/\tau_{\text{dec}}} \cos \Omega\tau\right) \tag{6.4d}$$

where f is the probe frequency, f_0 is the resonant frequency of the transition to be measured, $\delta/(2\pi)$ is the detuning of the probe beam from the resonance, $\Omega/(2\pi)$ is

the generalized Rabi frequency,[1] P_e^0 is the ideal Rabi oscillation of the excited-state population when there is no decoherence in the system (e.g., from the excited state's lifetime or probe beam's phase noise) [133, 134]. P_e describes the exponentially decaying contrast of the Rabi oscillation with the characteristic time constant $\tau_{\rm dec}$, and the convergence of P_e to 1/2. Finally, the following expression was used:

$$P_e^{\rm fit} = aP_e(\omega_R, \tau, \tau_{\rm dec}, f_0, f) \tag{6.5}$$

with an additional fit parameter a for the overall scale to take account of imperfect 369 nm optical pumping (i.e., the ion's initial state is not prepared purely in the desired ground-state Zeeman level) due to, e.g., impurity of the circular polarization of the beam or the imperfect alignment of the beam along the magnetic field. The a, ω_R, $\tau_{\rm dec}$, and f_0 were fitting parameters while τ and f were input parameters. The decoherence in Gaussian form was also tried:

$$P_e = \frac{\omega_R^2}{\Omega^2}\frac{1}{2}\left(1 - e^{-(\tau/\tau_{\rm dec})^2}\cos\Omega\tau\right). \tag{6.6}$$

However, the Gaussian decay could not be distinguished from the exponential decay, at least during the $\frac{\pi}{2}$ time, as shown in Fig. 6-5. $\tau_{\pi/2} \lesssim 10\,\mu$s was typically measured as the $\frac{\pi}{2}$-pulse time, as shown in Fig. 6-5, at typical probe power $P \sim 1$ mW and $w = 60$ um focal waist (see Table B.1).

After $\tau_{\pi/2}$ was obtained for a given probe beam power and alignment, the Ramsey fringe of each Zeeman transition was measured, as demonstrated in Fig 6-6 for different $\tau_{\pi/2}$ pulse times and separation T between the pulses. For the IS measurement, the Ramsey scanning was tested by scanning 3 peaks as in Fig. (e), and then the center peak was scanned repeatedly over time, as shown in Fig. (f).

[1] The frequency of Rabi oscillation of the excited-state probability for a transition driven by a nonresonant light (i.e., $\delta \neq 0$).

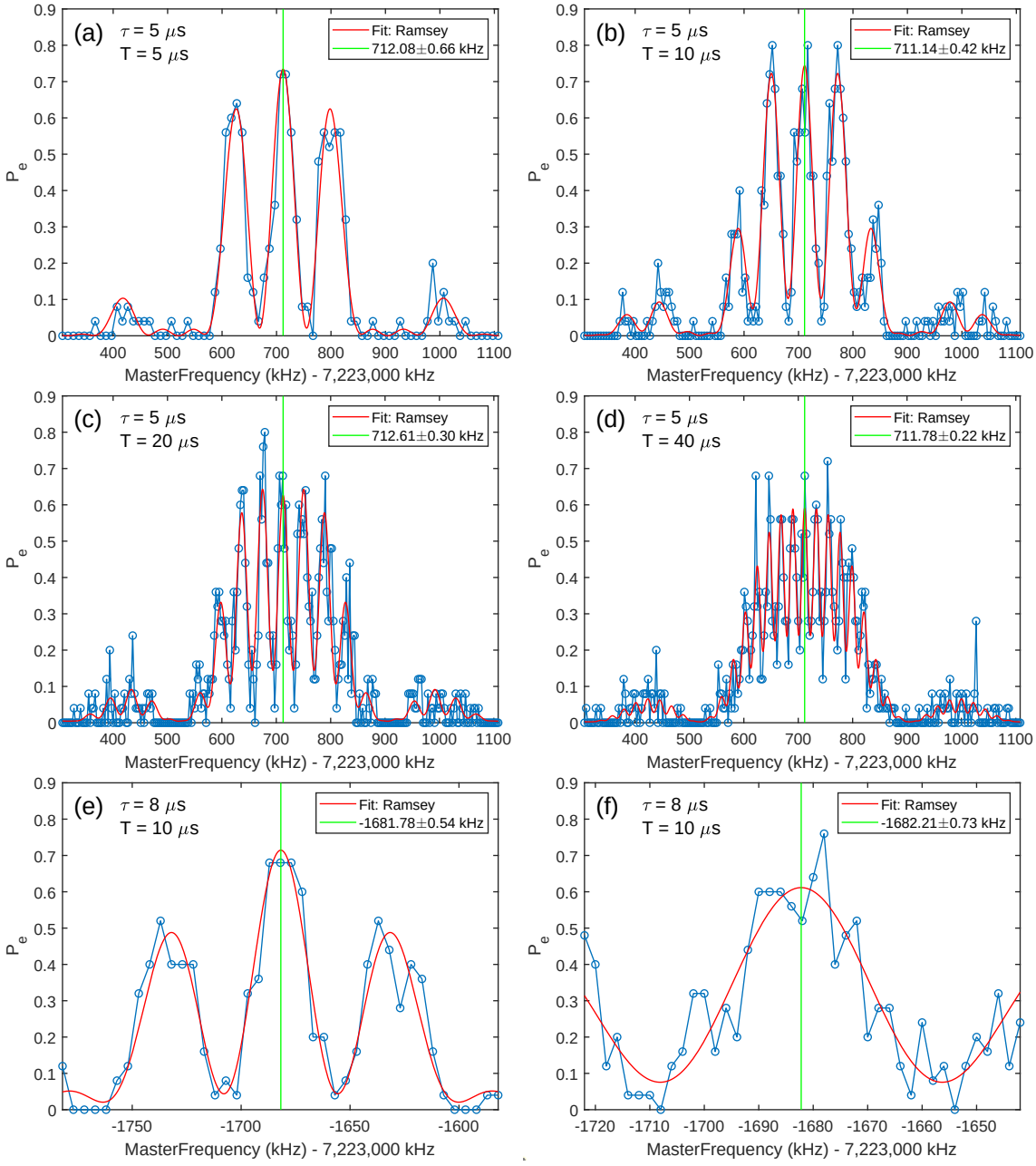

Figure 6-6: Ramsey fringes (excitation probability P_e vs `MasterFrequency`) measured for α: 411 nm transition with different $\frac{\pi}{2}$ pulse times $\tau_{\pi/2}$ and two pulses' separations T of the probe beam: $(\tau_{\pi/2}, T) =$ (a) $(5, 5)$ µs, (b) $(5, 10)$ µs, (c) $(5, 20)$ µs, (d) $(5, 40)$ µs, and (e,f) $(8, 10)$ µs. Figs. (e) and (f) differ only by the scan ranges and step sizes. The data are fitted using Eqs. (6.8) and (6.7). Green vertical lines show the fitted resonant `MasterFrequency` values.

The expression for Ramsey fringes under decoherence in the system is given as:

$$\begin{aligned} P_e^0 &= 4\frac{\omega_R^2}{\Omega^2}\sin^2\frac{\Omega\tau}{2}\left(\cos\frac{\Omega\tau}{2}\cos\frac{\delta T-\phi}{2}-\frac{\delta}{\Omega}\sin\frac{\Omega\tau}{2}\sin\frac{\delta T-\phi}{2}\right)^2 \\ &= A_p\cos^2\left[\frac{\delta T-\phi}{2}+\tan^{-1}\left(\frac{\delta}{\Omega}\tan\frac{\Omega\tau}{2}\right)\right] \qquad (6.7a) \\ A_p &= 4\frac{\omega_R^2}{\Omega^2}\sin^2\frac{\Omega\tau}{2}\left(1-\frac{\omega_R^2}{\Omega^2}\sin^2\frac{\Omega\tau}{2}\right) \qquad (6.7b) \\ P_e &= \frac{A_p}{2}+\left(P_e^0-\frac{A_p}{2}\right)e^{-T/\tau_{\rm dec}} \\ &= P_e^0 e^{-T/\tau_{\rm dec}}+\frac{A_p}{2}\left(1-e^{-T/\tau_{\rm dec}}\right) \qquad (6.7c) \end{aligned}$$

where ϕ is the additional phase between the two pulses,[2] P_e^0 is the expression for the ideal Ramsey oscillation of the excited-state probability over T with the amplitude A_p when there is no decoherence [132, 133], and P_e is the probability when the decoherence is introduced in the system. The following expression was used for the fitting:

$$P_e^{\rm fit} = aP_e(\omega_R, \tau, T, \phi, \tau_{\rm dec}, f_0, f) \qquad (6.8)$$

with fit parameters a, ω_R, $\tau_{\rm dec}$, and f_0, and input parameters τ, T, ϕ, and f.

In the earlier measurements for α: 411 nm transitions [5], The two R and B Zeeman transitions in Fig. 5-2(a) were scanned one at a time, alternately: $(f^R_{\rm Master})_1$, $(f^B_{\rm Master})_2$, $(f^R_{\rm Master})_3$, $\cdots$, measured at t_1, t_2, t_3, $\cdots$, as shown in Fig. 6-7. Then, the zero-field frequency $f^{\rm Comm}_{\rm Master}$ and the separation of the transitions $f^{\rm Diff}_{\rm Master}$ were obtained through the following way: if the R transition was measured at time t_k, the $(f^B_{\rm Master})_k$ was obtained from the linear interpolation of the nearest-neighboring measurements:

$$(f^B_{\rm Master})_k \approx \frac{(t_{k+1}-t_k)(f^B_{\rm Master})_{k-1}+(t_k-t_{k-1})(f^B_{\rm Master})_{k+1}}{t_{k+1}-t_{k-1}} \qquad (6.9)$$

and vise versa if the B transition was measured at another time $t_{k'}$. $f^{\rm Comm}_{\rm Master}$ and $f^{\rm Diff}_{\rm Master}$ were then obtained using Eq. (6.3) for each k. In this way, total $N-2$ data

[2] If the first pulse is of the field $\propto \cos(\omega t)$ during $t=0$ to τ, then the second pulse is of the field $\propto \cos(\omega t+\phi)$ during $t=\tau+T$ to $\tau+T+\tau$. $\phi = 90^\circ$ gives the maximum slope at the resonance (i.e., $\delta = 0$). However, $\phi = 0$ was used for the most of the scans to ensure the symmetry of the Ramsey fringes.

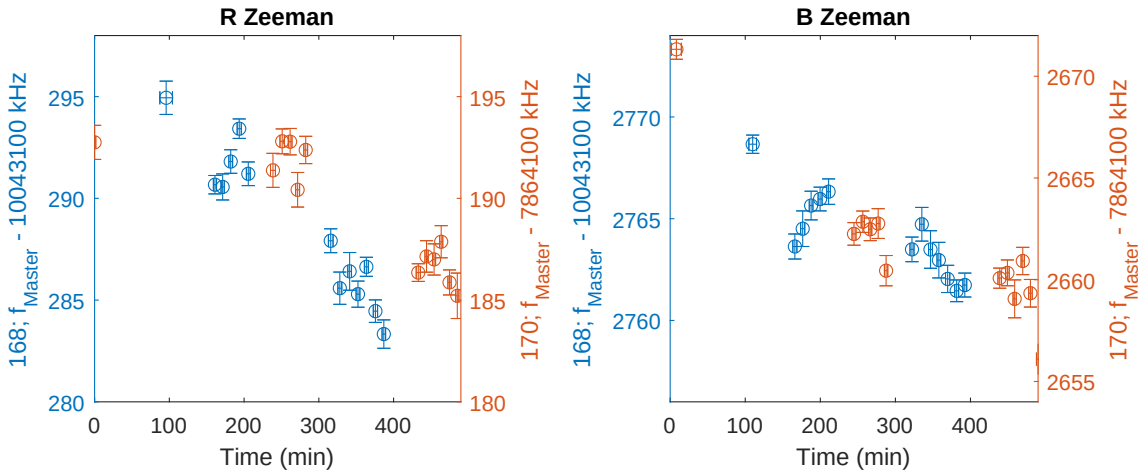

Figure 6-7: Example of data taken over the course of an IS spectroscopy experiment for α: 411 nm transition and for a pair of isotopes [^{168}Yb$^+$ (blue) and ^{170}Yb$^+$ (red) for this data]. The drift in the resonant `MasterFrequency`'s (see Section 4.1.5.1) of (left) R and (right) B Zeeman transitions [see Fig. 5-2(a)] over time.

points could be obtained for $k = 2, \cdots, N-1$.

$\sim$40 cycles were taken to measure P_e for each `MasterFrequency` step, which took $\sim$8 s (the period of a cycle was 200 ms in the earlier measurements for α: 411 nm). The size of `MasterFrequency` step was 2 kHz, and the typically 80 kHz range was scanned over, taking total $\sim$5 min per scan.

Figure 6-8 shows the measured (a) $f^{\mathrm{Comm}}_{\mathrm{Master}}$ and (b) $f^{\mathrm{Diff}}_{\mathrm{Master}}$ for a pair of isotopes over time. The trapped ion of one isotope was switched to another in every $\sim$2 hr ($\sim$10 consecutive scans per isotope segment).

After the experimental setup was upgraded as described in Section 4.2, more linear and much faster measurements of $f^{\mathrm{Comm}}_{\mathrm{Master}}$ have been demonstrated, as shown in Fig. 6-9. The pulse sequence in Table 5.1 has been used for the new measurement. It is expected that the ISs for α: 411 nm transition can be measured with lower uncertainties in the future (see also Section 5.5).

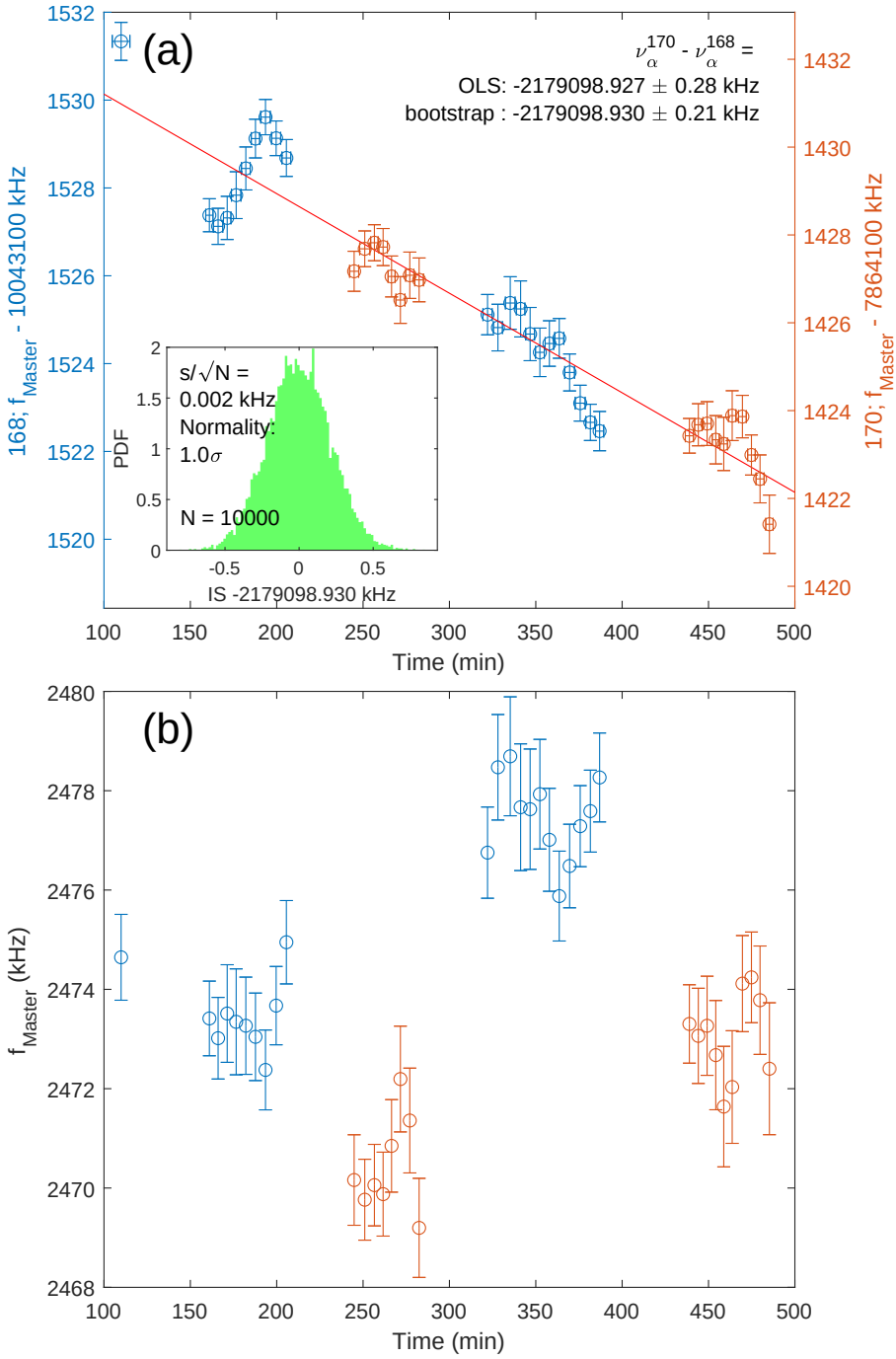

Figure 6-8: Example of data taken over the course of an IS spectroscopy experiment for α: 411 nm transition and for a pair of isotopes [$^{168}Yb^+$ (blue) and $^{170}Yb^+$ (red) for this data]. The drift in (a) measured zero-field `MasterFrequency` (see Section 4.1.5.1) (Common drift) and (b) the frequency separation of R and B Zeeman transitions [see Fig. 5-2(a) and Section 5.3.4] (Differential drift) are presented.

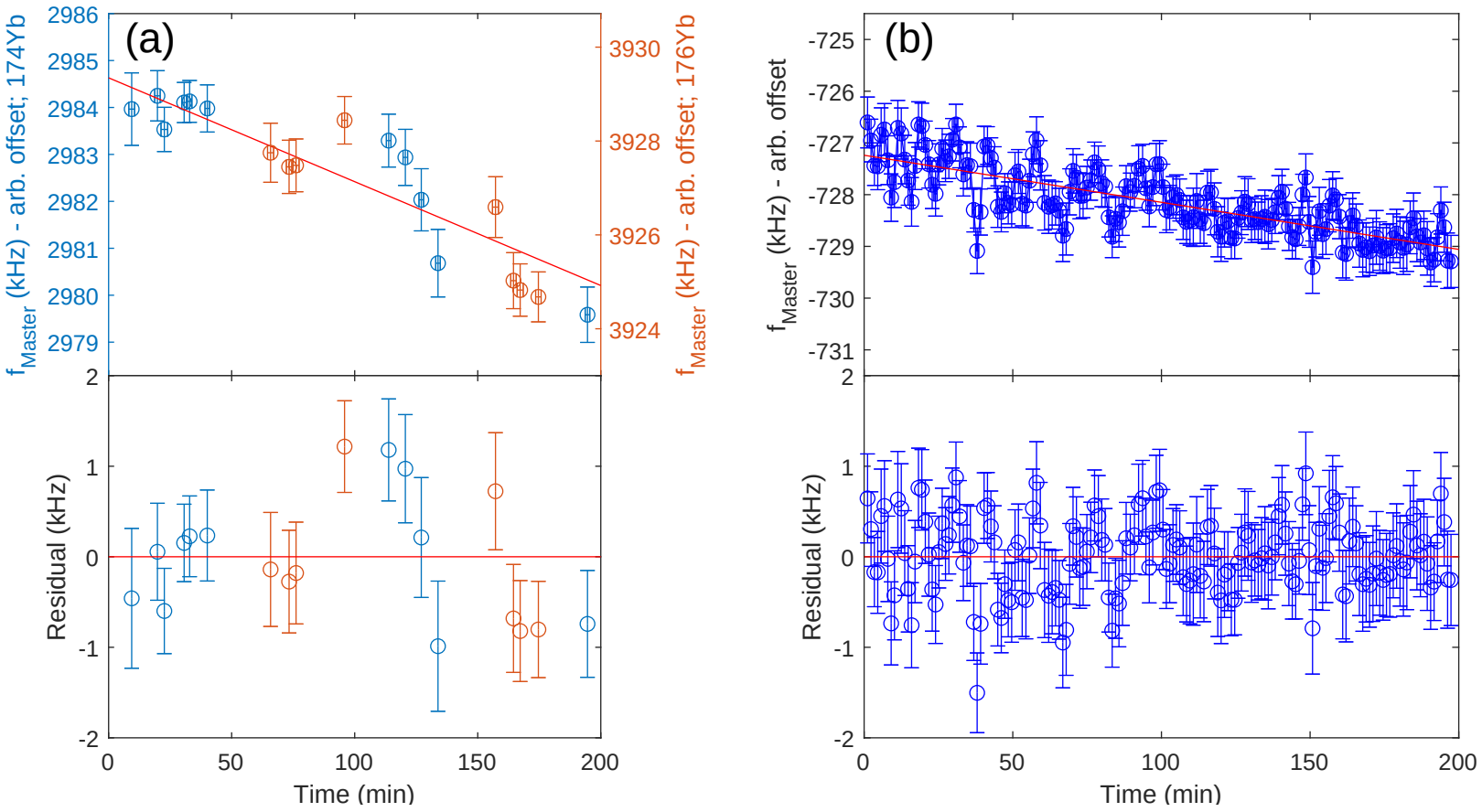

Figure 6-9: Measured zero-field `MasterFrequency` of α: 411 nm transition (a) before and (b) after the experimental setup was upgraded (see Section 4.2).

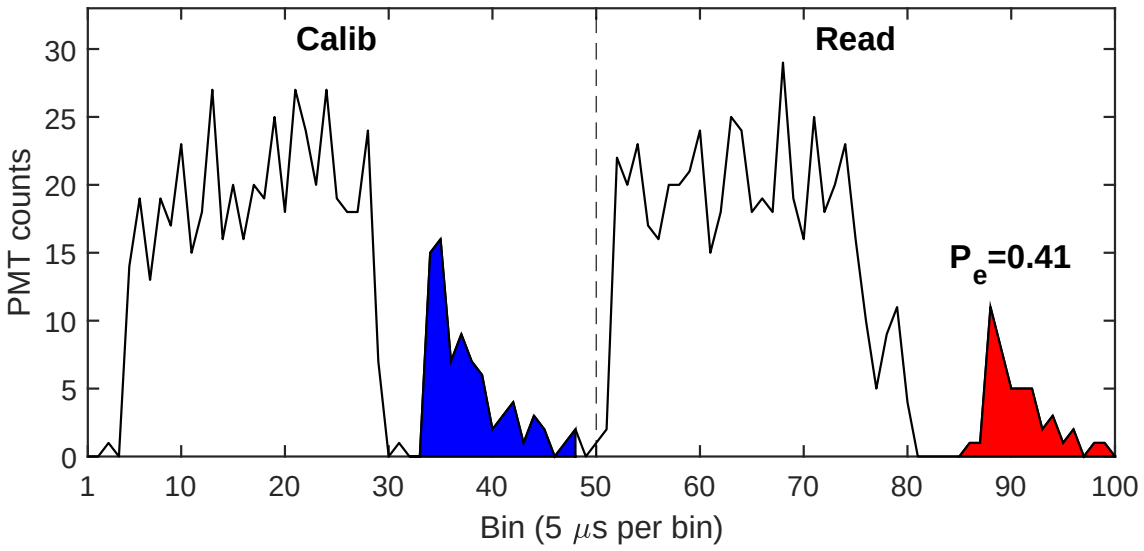

Figure 6-10: Typical time-resolved PMT counts (see Section 5.3.7) in each of 100 time bins averaged over 20 pulse sequence cycles for β: 436 nm transition [see Fig. 5-3(b) and Section 5.6]. The ratio of the averaged PMT counts during readouts (segment ⑥) in calibration (blue area) and measurement (red area) subsequences is given as the excitation probability P_e of the ion through the clock transition.

6.3 β: $^2S_{1/2} \rightarrow {}^2D_{3/2}$ (436 nm) transition

As described in Section 5.6, the PMT counts in each time bin were averaged over many cycles. Figure 6-10 shows the typical results for the averaged PMT counts over 20 cycles. The average number $\langle N_{\text{read}} \rangle$ of PMT counts during the readout (segment ⑥; see Fig. 5-3) in the read subsequence (red area) was divided by the average number $\langle N_{\text{calib}} \rangle$ during the same segment in the calibration subsequence (blue area), to obtain the excitation probability P_e:

$$P_e(f_{\text{Master}}) = 1 - \frac{\langle N_{\text{read}} \rangle}{\langle N_{\text{calib}} \rangle} \tag{6.10}$$

The remaining procedures to measure $\frac{\pi}{2}$ probe pulse time, scan Ramsey fringes (see Fig. 6-11), and measure zero-field `MasterFrequency` $f^{\text{Comm}}_{\text{Master}}$ over time for a pair of isotopes (see Fig. 6-12) were essentially the same to the corresponding procedures for α: 411 nm transition in Section 6.2. $\tau_{\pi/2} \lesssim 5\,\mu\text{s}$ was typically measured as the $\frac{\pi}{2}$-pulse time at typical probe power $P \sim 0.2\,\text{mW}$ and $w = 15\,\text{um}$ focal waist (see

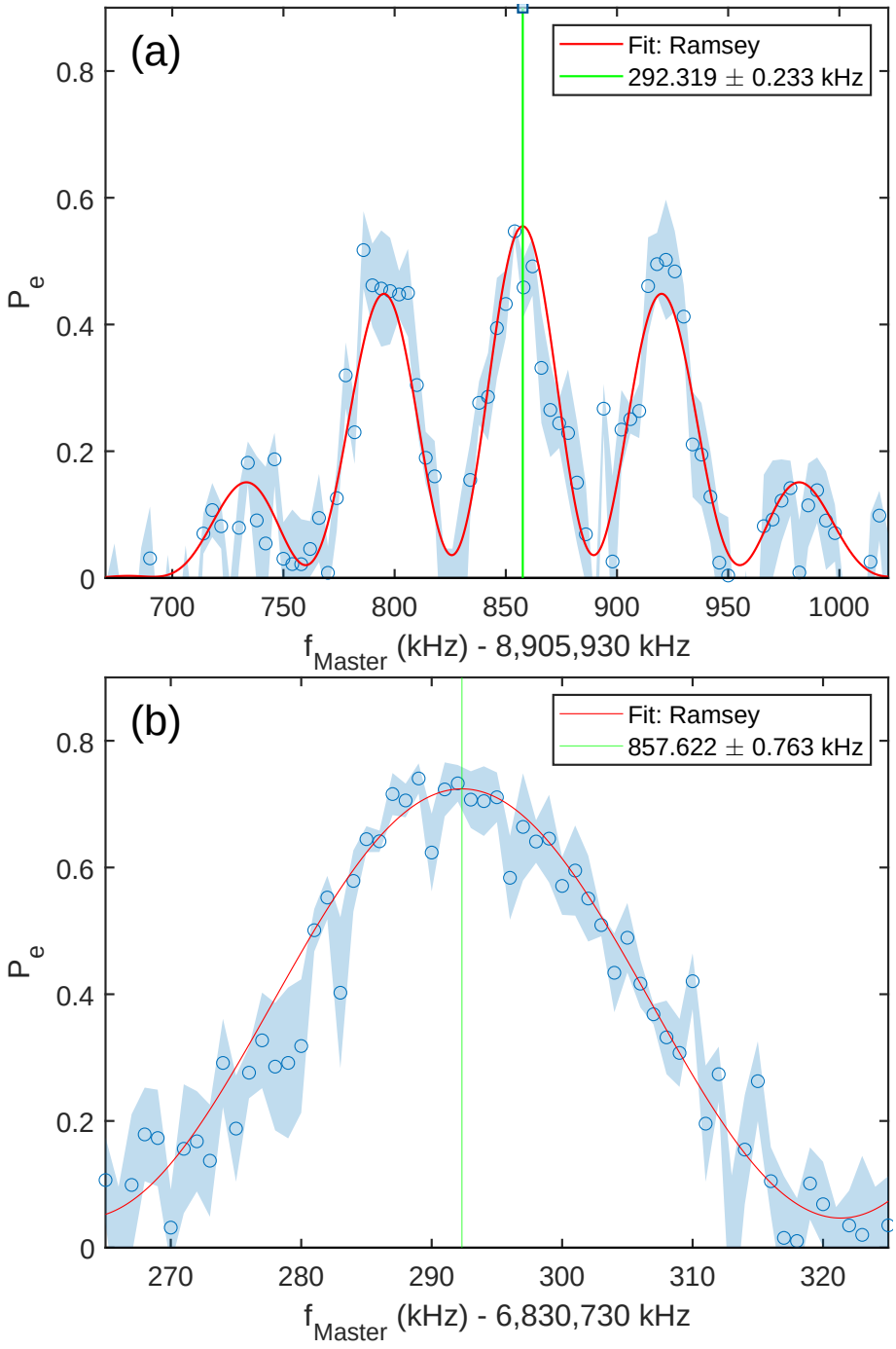

Figure 6-11: Ramsey fringes (excitation probability P_e vs `MasterFrequency`) measured for β: 436 nm transition with $(\tau_{\pi/2}, T) = (5, 10)$ µs (see the caption of Fig. 6-6) over frequency ranges for (a) 5 peaks and (b) center peak. The data are fitted using Eqs. (6.8) and (6.7). Green vertical lines show the fitted resonant `MasterFrequency` values.

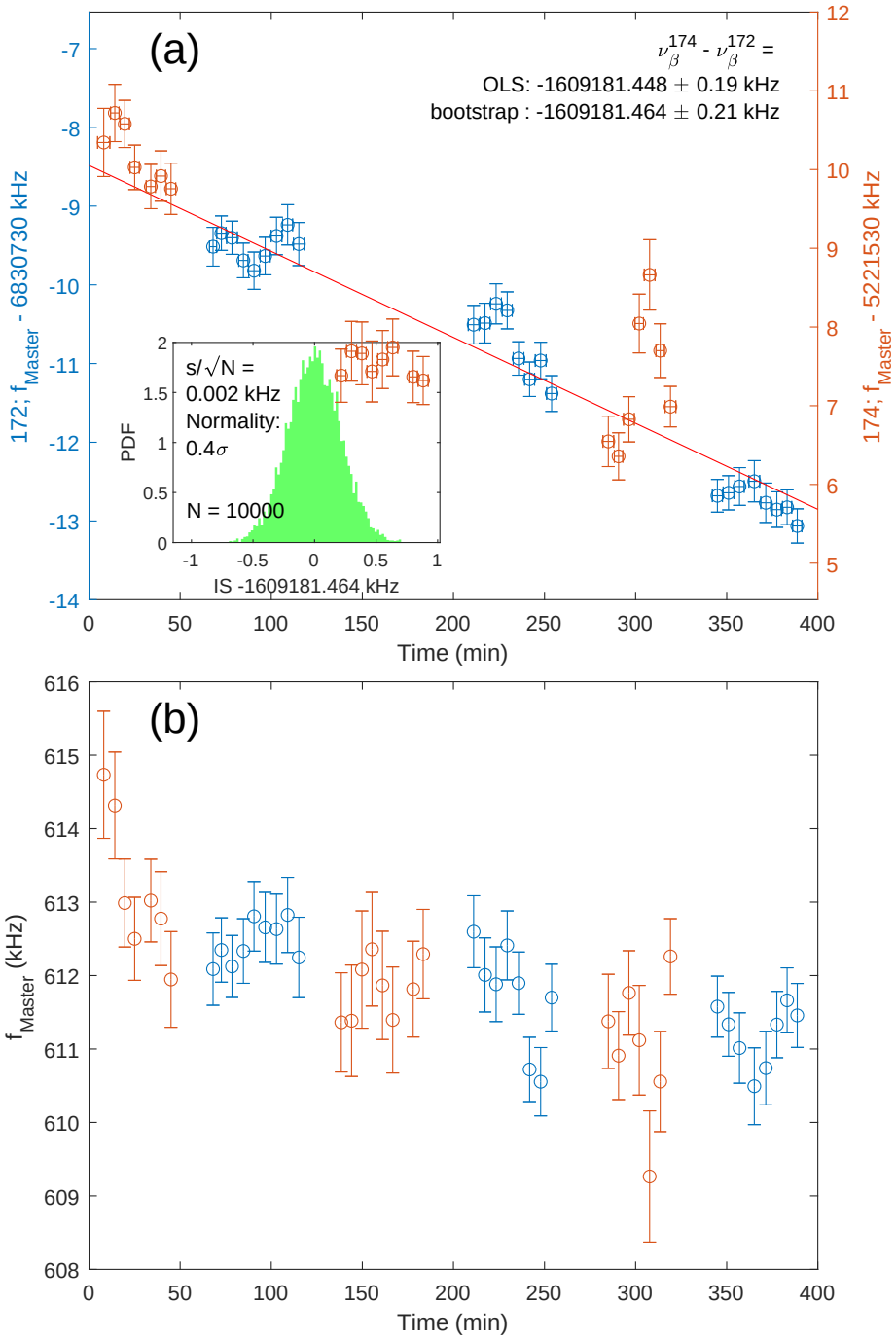

Figure 6-12: Example data taken over the course of an experiment for β: 436 nm transition and for a pair of isotopes [$^{172}Yb^+$ (blue) and $^{174}Yb^+$ (red) for this data]. The drift in (a) measured zero-field `MasterFrequency` (see Section 4.1.5.1) (Common drift) and (b) the frequency separation of R and B transitions [see Fig. 5-2(b) and Section 5.3.4] (Differential drift) are presented.

Table B.1). The excitation probability P_e was measured for 5 s (i.e., PMT counts were averaged over 100 pulse sequence cycles; see Table 5.1 for the period of a cycle) per `MasterFrequency` step. `MasterFrequency` was stepped by 1 kHz over ∼60 kHz range as shown in Fig. 6-11(b), taking ∼5 min per scan. The isotopes were switched in every ∼1 hr as shown in Fig. 6-12.

Note that this section describes the earlier experiments for β: 436 nm transition in Ref. [5]. A new IS measurement after the system upgrade (Section 4.2) has not been performed for this clock transition yet.

6.4 Determination of isotope shift

Figures 6-4(a), 6-8(a), and 6-12(a) present the linear drifts measured in the clock transition frequency offset by a cavity mode (i.e., `MasterFrequency`; see Section 4.1.5.1), manifesting the well-known fact that the cavity is subject to highly linear drift [136] (see also Section 7.9.3.3). The drifting $f^{\mathrm{Comm}}_{\mathrm{Master}}$ for the two isotopes were fitted with a function:

$$(f^{\mathrm{Comm}}_{\mathrm{Master}})_k = a + bt_k + cz_k \tag{6.11}$$

where a, b, and c are fit parameters, k is the index for each $f^{\mathrm{Comm}}_{\mathrm{Master}}$ measured, and t_k is the time that $(f^{\mathrm{Comm}}_{\mathrm{Master}})_k$ is measured, and z_k is the label for different isotopes: 1 for A and 0 for A'. Then, a is given as the $(f^{\mathrm{Comm}}_{\mathrm{Master}})^{A'}$ of the isotope A' at $t = 0$, b is the (average) rate of the drift $\mathrm{d}f^{\mathrm{Comm}}_{\mathrm{Master}}/\mathrm{d}t$, and, most importantly, c is given as the IS $\nu_\chi^{AA'}$ between the isotopes.

Two different methods of the fitting have been considered for the linear fit: ordinary least squares (OLS)[3] and bootstrapping (see Chapter 9 in Ref. [137]). To perform the bootstrapping, a new set of data points is formed by randomly re-sampling points from the set of measured data points, allowing for multiple instances of each point, until the number of elements in the re-sampled set is the same as the original

[3] A special case of the standard GLS method with an identity matrix as the VCM (see Section 9.2.1).

set. The OLS fit is applied to the re-sampled set to find a value for the IS. Repeating the procedure N times (with sufficiently large N) gives the histogram of ISs from the different re-sampled sets. The mean and standard deviation of the distribution are taken as the measured IS and its uncertainty, respectively. The inset in Figs. 6-8(a) and 6-12(a) show the bootstrapping statistics. The results from the two methods are in good agreement within their uncertainties. Given that, only the OLS fit was used for γ: 467 nm transition.

6.5 Absolute frequencies of optical clock transitions in Yb^+

Ref. [121] has reported very precise values of α: 411 nm and γ: 467 nm optical clock transitions' absolute frequencies for $^{172}Yb^+$ isotope, with only few-Hz uncertainties. Using these values, the absolute frequencies for all the five isotopes $A \in \{168, 170, 172, 174, 176\}$ can be obtained by adding the ISs measured in this work. The results are listed in Table A.3.

For β: 436 nm transition, the absolute transition frequency has not been measured for any of those even-A isotopes to date, to the best of the thesis author's knowledge, while the absolute frequency of a transition between the ground and excited states' hyperfine levels $\nu_\beta^{171}(0 \to 2)$ in $^{171}Yb^+$ isotope has been measured precisely [138, 139]. Therefore, the difference in $\nu_\beta^{171}(0 \to 2)$ from the frequency ν_β^{172} for $^{172}Yb^+$ isotope is estimated from other transitions in Yb^+ ions or Yb atoms by inter/extrapolating the King plots, as elaborated in Section A.1.

6.6 Absolute frequencies of 370 nm cooling, 935 nm $^2D_{3/2}$-state and 760 nm $^2F_{7/2}$-state repumping transitions in Yb^+

For the experiments in this work, the frequencies of the transitions for trapping, cooling, and repumping (e.g., 399 nm, 369 nm, 935 nm, and 760 nm transitions; see Fig. 3-1 and Table B.1) should be known for all the five isotopes $A \in \{168, 170, 172, 174, 176\}$. While the frequencies for the 399 nm $^1S_0 \rightarrow {}^1P_1$ transition in neutral Yb atoms have been measured with high precision [113], the accurate measurements for the transitions in Yb^+ ions were largely missing. Furthermore, the values for less abundant $^{168}Yb^+$ isotope [111] were not available in literature. The resonant frequencies for the 760 nm $^2F_{7/2}$-state repumping transition (see Section 4.2.6) had been also reported only for the most abundant $^{172}Yb^+$ and $^{174}Yb^+$ isotopes with limited precision [125, 126, 127].

In this work, all the transition frequencies were found and measured with a Fizeau wavemeter (WS/7, HighFinesse/Ångstrom) that has been periodically calibrated to an atomic reference (Rb). To maximize the accuracy for ISs between the isotopes, all the isotopes were trapped and measured in a few hours. The measured transition frequencies and ISs are shown in Table A.4. The uncertainties in the absolute frequencies are specified by the manufacturer of the wavemeter, while observed daily drifts in the wavemeter readings give upper bounds on the ISs' uncertainties. See Ref. [4] for the resonant frequencies for 638 nm $^2F_{7/2}$-state repumping transition for all the 5 isotopes.

The resonant frequency of the 760 nm transition for each isotope was measured as follows. The beam's frequency was measured through and actively stabilized to the wavemeter reading, with the resolution of 5 MHz (half of the last digit of the wavemeter reading). At each frequency step, the pulse sequence in 5-3(a) was repeatedly driven for α: 411 nm transition to prepare the ion into the $^2F_{7/2}$ state (see Fig. 3-1 for the decay channel), and the PMT counts were averaged over many

cycles (see Section 5.3.7). In consequence, the exponential repumping of the ion from the $^2F_{7/2}$ state was observed in segment ①. Finally, the 760 nm beam's frequency was scanned (i.e., the set point of the frequency stabilization to the wavemeter was stepped by 5 MHz) until the shortest characteristic time constant of the exponential repumping curve was obtained.

The procedures of the measurements for the 369 nm and 935 nm transitions were similar, except that the frequencies that produce maximum ion fluorescence were measured for the 935 nm transition, while, for the 369 nm transition, the frequencies at which the ion suddenly stops scattering the beam were measured while increasing the 369 nm beam frequency, due to the change in the effect of the 369 nm beam's scattering from cooling to heating the ion.

6.7 Consistency check and reduced uncertainty from redundant isotope pair

To check for systematic errors and improve the uncertainties, redundant measurements of the IS were performed by measuring ISs between next-nearest-neighboring even-A (NNNE) isotopes pairs: $(168, 172)$, $(170, 174)$, and $(172, 176)$, in addition to the nearest-neighboring even-A (NNE) isotopes pairs: $(A, A+2)$ with $A \in \{168, 170, 172, 174\}$.

Redundant pairs, in addition to *independent* pairs (see Section 11.5), provide are useful in two different ways. First, they provide consistency check with other measured isotope pairs. For instance, if the ISs between the two NNE pairs (A, A'), (A', A''), and a NNNE pair (A, A'') are measured for three isotopes $A < A' < A''$ (see, e.g., a triangle in Fig. 6-13), the consistency between the ISs can be confirmed by checking if the two values $\nu^{AA'} + \nu^{A'A''}$ and $\nu^{AA''}$ agree within their uncertainties, $\sqrt{(\Delta\nu^{AA'})^2 + (\Delta\nu^{A'A''})^2}$ and $\Delta\nu^{AA''}$,[4] respectively, or, equivalently, by checking how much $\nu^{AA'} + \nu^{A'A''} - \nu^{AA''}$ deviates from zero in its uncertainty

[4] Assuming the ISs $\nu^{AA'}$, $\nu^{A'A''}$, and $\nu^{AA'}$ are independently measured.

$\sqrt{(\Delta\nu^{AA'})^2 + (\Delta\nu^{A'A''})^2 + (\Delta\nu^{AA''})^2}$ (i.e., the *σ-significance* of disagreement).

Another power of the redundant pairs is to improve the precision of each measured value. For the example above, there are two independent measurements for each quantity: e.g., measured $\nu^{AA'}$ and $\nu^{AA''} - \nu^{A'A''}$ as $\nu^{AA'}$. Then, a new estimate $(\nu^{AA'})'$ with a better uncertainty $(\Delta\nu^{AA'})'$ can be obtained as follows:

$$\begin{aligned} \frac{1}{[(\Delta\nu^{AA'})']^2} &= \frac{1}{(\Delta\nu^{AA'})^2} + \frac{1}{(\Delta\nu^{A'A''})^2 + (\Delta\nu^{AA''})^2} \\ (\nu^{AA'})' &= [(\Delta\nu^{AA'})']^2 \left[\frac{\nu^{AA'}}{(\Delta\nu^{AA'})^2} + \frac{\nu^{AA''} - \nu^{A'A''}}{(\Delta\nu^{AA''})^2 + (\Delta\nu^{A'A''})^2} \right], \end{aligned} \tag{6.12}$$

and so for other pairs $(\nu^{A'A''})'$ and $(\nu^{AA''})'$.

A general approach for more complicated relations between the pairs is as follows. First, determine the minimum number of isotope pairs p and a particular such set that can determine the values of all the N pairs of which the ISs were measured. For instance, for the NNE and NNNE pairs instroduced above, knowing the ISs for all the NNE pairs, but not less, are sufficient to determine all the pairs' values. As the next step, express the relation between all the measured set and the *reduced* set in the following form:

$$\underbrace{\begin{bmatrix} \nu_\alpha^{168,170} \\ \nu_\alpha^{170,172} \\ \nu_\alpha^{172,174} \\ \nu_\alpha^{174,176} \\ \nu_\alpha^{168,172} \\ \nu_\alpha^{170,174} \\ \nu_\alpha^{172,176} \end{bmatrix}}_{\mathbf{y}_N} = \underbrace{\begin{bmatrix} 1 & 0 & 0 & 0 \\ 0 & 1 & 0 & 0 \\ 0 & 0 & 1 & 0 \\ 0 & 0 & 0 & 1 \\ 1 & 1 & 0 & 0 \\ 0 & 1 & 1 & 0 \\ 0 & 0 & 1 & 1 \end{bmatrix}}_{X_{N\times p}} \underbrace{\begin{bmatrix} \nu_\alpha^{168,170} \\ \nu_\alpha^{170,172} \\ \nu_\alpha^{172,174} \\ \nu_\alpha^{174,176} \end{bmatrix}}_{\boldsymbol{\beta}_p} \tag{6.13}$$

Then, finding the best estimates of the $p = 4$ ISs $\hat{\boldsymbol{\beta}}$ from the N observations $\mathbf{y}$ becomes a typical least square problem $\mathbf{y} = X\boldsymbol{\beta}$ (see, e.g., Section 9.2.1). The improved IS values $\hat{\boldsymbol{\beta}}$ are obtained via a weighted least squares (WLS) fit with

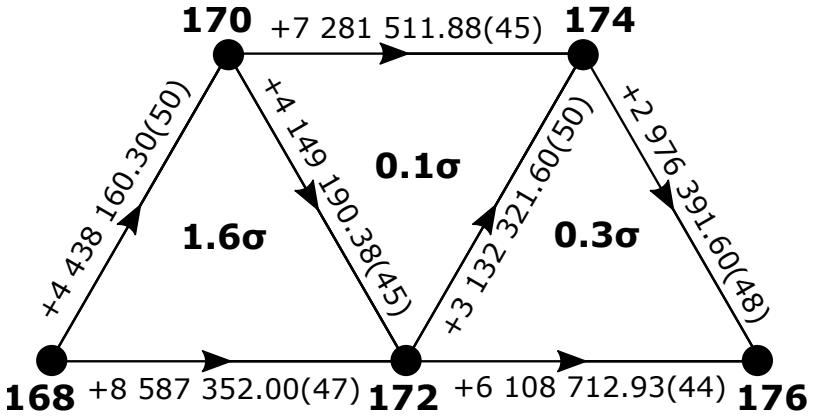

Figure 6-13: Measured values of ISs (values along edges in kHz) for different pairs of Yb^+ isotopes (vertices labeled with the mass numbers A of isotopes $^AYb^+$) and consistency of values forming shortest loops (σ-significance in the center of each triangle). The IS value $\nu^{AA'} = \nu^A - \nu^{A'}$ is shown for an edge directed from vertex A to vertex A'. The measured values agree overall with 0.86σ significance.

the weights given by inverse-squared measurement uncertainties.[5] It can be also confirmed, at this stage, whether the choice of the reduced pairs is really minimal by checking if X has full (column) rank (i.e., the column vectors in X are linearity independent). The overall σ-significance of the measured ISs' disagreement can be obtained from the $\hat{\chi}^2$ value of the fit [see Eq. (9.18c)]. The significance of the fit tests the consistency of samples with the model, and the model (i.e., the relation between the ISs) has to be true by the ISs' construction. Therefore, the significance of the fit serves as a quantity showing if the measured ISs were compromised by some systematic effects. It can also be checked, in this step, whether the choice of $\boldsymbol{\beta}$ is sufficient for all the measured pairs. The fit would give an excessive $\hat{\chi}^2$ value if the pairs in $\boldsymbol{\beta}$ are not enough and thus cannot approximate all the measured IS values.

The graphical representation of the values and relations of measured ISs are shown in Fig. 6-13. In particular, the significance of each three-isotope triangular pair is shown in the corresponding triangles. The values, uncertainties, and correlations of the reduced ISs $\hat{\boldsymbol{\beta}}$ using the method developed above are listed in Table A.2. The overall significance of the measured ISs is given to be 0.86σ from the $\hat{\chi}^2$ of the fit.

[5] A special case of GLS with $\Sigma_{\mathbf{y}} = \mathrm{diag}(\sigma_{y_1}^2, \cdots, \sigma_{y_N}^2)$ in Section 9.2.1 when the measured ISs are independent. The GLS fit can be used instead if the measured ISs are already correlated for some reasons.

It is straightforward to generalize this method for any other pairings for measurement $\mathbf{y}$ or reduced pairs $\boldsymbol{\beta}$.[6] The method can be also applied to converting a pairing to another ($N = p$ in this case), always yielding a perfect fit.

[6]Or any arbitrary variables that parameterize the measured ISs, if needed.

Chapter 7

Analysis of systematic effects

Investigating systematic effects is one of the essential parts of precision measurements. In the experiments for IS spectroscopy in this thesis, most of the systematic effects pertaining in the measurements of absolute transition frequencies in atoms are common-mode between the isotopes, with only small differential components that affect the measured ISs. Drifts in experimental parameters can lead to uncertainties in these differential shifts, however, and these are the main source of the statistical uncertainties in the measured ISs (see Table A.1).

In this chapter, the sources of the systematic shifts and their estimated sizes and long-term drifts are investigated. The results are summarized in Table 7.1 for the absolute and differential sizes of the systematic shifts and drifts, for each of the optical clock transitions $\alpha : {}^2S_{1/2} \rightarrow {}^2D_{5/2}$ (411 nm), $\beta : {}^2S_{1/2} \rightarrow {}^2D_{3/2}$ (436 nm), and $\gamma : {}^2S_{1/2} \rightarrow {}^2F_{7/2}$ (467 nm) in Yb^+ ions. While most of the long-term differential drifts are estimated to be smaller than the statistical uncertainties in the measured ISs ($\sim$300 Hz for α and β transitions and $\sim$500 Hz for γ transition; see Table A.1), some of the effects give drifts that are potentially comparable to the uncertainties. Note, however, that such drifts show up as the drift in the measured zero-field transition frequencies and averaged over 8 to 16 hr or longer (see Figs. 6-4, 6-8, and 6-12), and their effects on the measured ISs are reduced by switching isotopes several times over the course of the measurements (see Section 5.3.2).

A significant portion of the analysis has been done by Diana P. L. Audo Craik,

a research team member and postdoctoral researcher, and also partially contributed by Luke Caldwell, a research collaborator [8].

Table 7.1: Estimated systematic shifts and long-term drifts in the IS spectroscopy experiments for α: 411 nm, β: 436 nm, and γ: 467 nm transitions. Absolute shifts in each isotope and differential shifts between different isotopes are listed. The values followed by square parentheses show the center value while the values inside the square parentheses are the magnitude of long-term drifts, with the following notation: $x[y] \times 10^b$ for the center value of $x \times 10^b$ and long-term drift of $y \times 10^b$.

	Absolute shift (Hz)			Differential shift (Hz)		
Effect	α: 411 nm	β: 436 nm	γ: 467 nm	α: 411 nm	β: 436 nm	γ: 467 nm
Doppler						
0st-order (recoil)	$\pm 1.3^{a}[.25^{a}] \times 10^{0}$	$\pm 1.1^{a}[.22^{a}] \times 10^{0}$	$\pm 2.3^{a} \times 10^{-1}$	$1.5^{a}[25.^{a}] \times 10^{-2}$	$1.4^{a}[22.^{a}] \times 10^{-2}$	$5.5^{a} \times 10^{-3}$
1st-order		$+\mathrm{O}(1)^{ab}[\mathrm{O}(1)^{ab}] \times 10^{-3}$			$0[\mathrm{O}(1)^{a}] \times 10^{-3}$	
2nd-order		$-1.^{a}[1.^{a}] \times 10^{1}$			$2^{a}[100.^{a}] \times 10^{-1}$	
AC Stark						
Laser-induced	$+1.5[.2^{a}] \times 10^{3}$	$+2.5^{a}[.3^{a}] \times 10^{3}$	$+1.^{a}[\mathrm{O}(0.01)^{a}] \times 10^{4}$	$0.[2.^{a}] \times 10^{2}$	$0.[3.^{a}] \times 10^{2}$	$0.[\mathrm{O}(1)^{a}] \times 10^{2}$
BBR		$-4.[0.15] \times 10^{-1}$	$-6.[0.25] \times 10^{-2}$		$0.[1.5] \times 10^{-2}$	$0.[2.5] \times 10^{-3}$
Micromotional	$-7.^{a}[7.^{a}] \times 10^{1}$	$\pm 1.^{a}[1.^{a}] \times 10^{2}$	$-1.^{a}[1.^{a}] \times 10^{1}$	$0.[7.^{a}] \times 10^{1}$	$0.[1.^{a}] \times 10^{2}$	$0.[1.^{a}] \times 10^{1}$
Off-resonant excitation		$\pm 2.^{a}[1.^{a}] \times 10^{1}$	$\pm 1.^{a}[0.02^{a}] \times 10^{0}$		$0.^{a}[1.^{a}] \times 10^{1}$	$0.^{a}[2.^{a}] \times 10^{-2}$
Zeeman						
1st-order		$0.^{a}[5.^{a}] \times 10^{2}$	$0.^{a}[1.^{a}] \times 10^{1}$		$0.^{a}[5.^{a}] \times 10^{2}$	$0.^{a}[1.^{a}] \times 10^{1}$
2nd-order[c]	$+4.2^{a}[0.042^{a}] \times 10^{3}$	$+6.3^{a}[0.063^{a}] \times 10^{2}$	$-2.5^{a}[0.025^{a}] \times 10^{1}$	$0.[4.2^{a}] \times 10^{1}$	$0[6.3^{a}] \times 10^{0}$	$0.[2.5^{a}] \times 10^{-1}$
Electric quadrupole		$\pm \mathrm{O}(1)^{a}[\mathrm{O}(1)^{a}] \times 10^{0}$	$\pm \mathrm{O}(1)^{a}[\mathrm{O}(1)^{a}] \times 10^{-2}$		$0[\mathrm{O}(1)^{a}] \times 10^{0}$	$0[\mathrm{O}(1)^{a}] \times 10^{-2}$
Gravitational redshift		$0.[8.^{a}] \times 10^{-5}$			$0.[8.^{a}] \times 10^{-5}$	
Probe freq. stability						
Master clock		$0.[5.^{a}] \times 10^{0}$			$0.[5.^{a}] \times 10^{0}$	
RAM		$0.[1.] \times 10^{3}$	$0.[3.^{a}] \times 10^{2}$		$0.[1.] \times 10^{3}$	$0.[3.^{a}] \times 10^{2}$
Reference cavity						
Temp. drift		$0.[4.^{a}] \times 10^{1}$			$0.[4.^{a}] \times 10^{1}$	
Beam power		$0.[8.^{a}] \times 10^{1}$	$0.[5.^{a}] \times 10^{-1}$		$0.[8.^{a}] \times 10^{1}$	$0.[5.^{a}] \times 10^{-1}$
Nonlinear drift		$0.[[\mathrm{O}(1).^{a}] \times 10^{-1}$			$0.[[\mathrm{O}(1).^{a}] \times 10^{-1}$	
AOM phase chirp		$\pm \mathrm{O}(1)^{a}[\mathrm{O}(1)^{a}] \times 10^{0}$			$0[\mathrm{O}(1)^{a}] \times 10^{0}$	

[a] Upper bound on the magnitude.
[b] Omitted potential absolute shift due to the ion trap's motion correlated to the laser pulses.
[c] Potentially much smaller; see Section 7.6.2.

7.1 Doppler Shifts

The Doppler shift in an atomic transition is the result of the interaction between light and atom's motional state (i.e. photon recoil) [103]. The fractional Doppler shift to the atomic transition, $\Delta\nu_D/\nu_0$, caused by the motion of the ion in the classical limit[1] is given by:

$$\frac{\Delta\nu_D}{\nu_0} = \frac{h}{2m\lambda^2} + \hat{k}\cdot\frac{\mathbf{v}}{c} - \frac{v^2}{2c^2} + \mathcal{O}\left(\left(\frac{\mathbf{v}}{c}\right)^3\right) \tag{7.1}$$

where $\mathbf{v}$ is the velocity of the ion relative to the lab frame, λ and $\hat{k}$ are the wavelength and the direction of a photon's momentum in the lab frame, respectively, m is the atom's mass, and ν_0 is the frequency of the atomic transition in the rest frame of the ion. The first two terms can be obtained by the semiclassical description of a free atom's absorption[2] of a photon's momentum in the nonrelativistic limit:

$$\Delta T = \frac{1}{2}m(\mathbf{v}+\Delta\mathbf{v})^2 - \frac{1}{2}mv^2 = \frac{\hbar^2k^2}{2m} + \hbar\mathbf{k}\cdot\mathbf{v} \tag{7.2}$$

where ΔT and $\Delta\mathbf{v} = \hbar\mathbf{k}/m$ is the change in the atom's kinetic energy and velocity, respectively. The photon's energy has to compensate the change in the kinetic energy in addition to the transition energy: $hf_{\text{photon}} = hf_{\text{transition}} + \Delta T$. The first term, the zeroth-order Doppler shift, or *recoil shift*, originates from the quantumness of photons; it vanishes in the limit $h \to 0$. The second term is the first-order Doppler shift which is proportional to the atom's velocity and also depends on the relative direction of the atom's and photon's motions. The third term in Eq. (7.1), the second-order Doppler shift, is due to a relativistic effect, the time dilation in the moving frame, which can be obtained from the same approach through the corresponding relativistic description [140].

Tight confinement of an atom in a trap with well-resolved motional eigenstates of the atom suppresses the zeroth and first-order shifts due to the Mössabauer effect as described in the following subsections, while the second-order Doppler shift is

[1] i.e., no quantum effect. It does not exclude the relativistic effect that causes the second-order Doppler shift as follows.

[2] Considering the case of the photon emission doesn't change the result.

essentially not affected by the confinement.

7.1.1 Zeroth-order Doppler Shift

In a tight trap, the minimum change in the atom's motional energy is given by the spacing $\hbar\omega_t$ between quantized motional eigenstates. Therefore, when the recoil energy $(\hbar k)^2/2m$ in Eq. (7.2) is smaller than the spacing, the effect of the photon recoil is suppressed (the Mössbauer effect; see, e.g., Chapter 6 in Ref. [141]). The factor of the suppression is given by the ratio of the two energies which is defined as the squared Lamb-Dicke parameter:

$$\eta^2 = \frac{(\hbar\mathbf{k}\cdot\hat{u}_t)^2/(2m)}{\hbar\omega_t} \leq \frac{\delta_{\text{recoil}}}{\omega_t} \tag{7.3}$$

where $\omega_t/(2\pi)$ is the vibration frequency of an atom in a trap along the direction $\hat{u}_t$ and $\delta_{\text{recoil}}/(2\pi) = (\hbar k)^2/(2mh)$ is the *recoil shift*. In particular, the atom is said to be in the Lamb-Dicke regime when the motional sideband transitions (the transition that changes the motional state of the atom as well as its electronic state) is suppressed: $\eta^2(2n+1) \ll 1$. In the system for this work, $\omega_t/(2\pi) = 364\,\text{kHz}$ along the axis of the RF potential and higher along the other directions (see Table 4.1), which gives $\eta^2 \leq 0.0193$, 0.0172, and 0.0150 for α: 411 nm, β: 436 nm, and γ: 467 nm transitions, respectively (maximum values given for $\mathbf{k} \parallel \pm\hat{u}_t$ and $m \approx 168\,\text{u}$ for the lightest Yb^+ isotope used). Then, $\langle n\rangle \lesssim 14.3$ from an ion's temperature $\approx$500 μK[3] [4] gives $\eta^2(2\langle n\rangle + 1) \lesssim 0.6$, a moderate Lamb-Dicke regime.

7.1.1.1 Transition-rate spectroscopy

γ: 467 nm transition in Yb^+ ions has been driven in the regime of Fermi's golden rule[5] by a long single pulse (see Section 5.2). In this case, the shift results from the difference between the transition rates of the red sideband ($\propto \eta^2 n$; $n \to n-1$)

[3] $\frac{1}{2}k_{\text{B}}T = \hbar\omega_t\langle n\rangle$ in each principal direction of the three-dimensional trap.

[4] See Footnote 2 in Section 4.1.1 for the temperature.

[5] the transition probability is linear over time as the transition is driven much longer than the decoherence time of the system (see Section 5.2).

and blue sideband ($\propto \eta^2(n+1)$; $n \to n+1$). The tails of the sidebands reach the carrier transition peak ($n \to n$) and shift the frequency at the maximum of the peak. The lineshape of the transition is dominated by the probe beam's frequency noise as the natural linewidth is very small for the clock transitions. Therefore, giving a Voigt profile is given as the peak's shape, depending on the noise profile of the laser frequency. In particular, the tails of the peaks will follow the Lorentzian curve, while the center of the peak is likely dominated by the Gaussian profile in the presence of the white noise or Lorentizan shape otherwise [142, 143]. The Lorentzian distribution of tails is assumed to have the full width at half maximum (FWHM) of the measured peak to obtain an upper bound on the carrier peak frequency's shift,[6] because the FWHM of the underlying Gaussian and Lorentzian distributions do not exceed the FWHM of the Voigt profile.

In case the center of the peak is given by the Lorentzian distribution:

$$A(\delta) = A_0 \frac{(\Gamma/2)^2}{(\Gamma/2)^2 + \delta^2} \tag{7.4}$$

where A is the transition rate as a function of the detuning of the beam from the resonant frequency of the transition, and the Γ is the FWHM of the peak. For the detuning δ of the beam from the carrier transitions frequency, the maximum of the peak is shifted to the point where the slopes of the carrier and sidebands are net zero:

$$\begin{aligned} 0 &= \underbrace{-\frac{2\delta(\Gamma/2)^2}{\left[(\Gamma/2)^2 + (\delta)^2\right]^2}}_{\text{carrier}} \underbrace{-\eta^2 n \frac{2(\delta+\omega_t)(\Gamma/2)^2}{\left[(\Gamma/2)^2 + (\delta+\omega_t)^2\right]^2}}_{\text{red sideband}} \underbrace{-\eta^2(n+1)\frac{2(\delta-\omega_t)(\Gamma/2)^2}{\left[(\Gamma/2)^2 + (\delta-\omega_t)^2\right]^2}}_{\text{blue sideband}} \\ &\approx -\frac{2\delta}{(\Gamma/2)^2} + \eta^2 \frac{2(\Gamma/2)^2}{\omega_t^3} \end{aligned} \tag{7.5}$$

when $\delta \ll \Gamma/2 \ll \omega_t$, which gives the shift

$$\delta \approx \omega_t \eta^2 \left[\frac{\Gamma/2}{\omega_t}\right]^4 = \delta_{\text{recoil}} \left[\frac{\Gamma/2}{\omega_t}\right]^4 \tag{7.6}$$

[6]The shift will be smaller, of course, if the underlying Lorentizan distribution of the tails is narrower.

which is given by the recoil shift $\delta_{\mathrm{recoil}} = 2\pi \times h/(2m\lambda^2)$ that is suppressed by the fourth power of the resolution of carrier and sidebands $(\Gamma/2)/\omega_t$. Note that the frequency *pulling* of the blue sideband does not depend on the atom's motion n as the difference in blue and red-sideband transition rates is constant over n. Therefore, the shift is expressed purely by the suppressed zeroth-order shift, and the higher-order Doppler shifts which depend on the motional energy vanish (see also Section 7.1.2). The shift is also independent of the transition rate (i.e., independent of oscillator strength or beam intensity) unless the transition is saturated and changes the shape of the peaks.

When the center of the peak is Gaussian instead:

$$A(\delta) = A_0 \exp\left[-\ln(2)\left(\frac{\delta}{\Gamma/2}\right)^2\right], \tag{7.7}$$

the shift is given by

$$0 \approx -2\ln(2)\frac{\delta}{(\Gamma/2)^2} + \eta^2\frac{2(\Gamma/2)^2}{\omega_t^3} \tag{7.8}$$

and thus

$$\delta \approx \frac{1}{\ln(2)}\eta^2\omega_t\left[\frac{\Gamma/2}{\omega_t}\right]^4 = \frac{1}{\ln(2)}\delta_{\mathrm{recoil}}\left[\frac{\Gamma/2}{\omega_t}\right]^4 \tag{7.9}$$

that is bigger than the shift for the Lorentzian center by factor of $1/\ln(2) \approx 1.44$. Therefore, the Gaussian peak center serves as the case for the upper bound on the shift. $\Gamma/(2\pi)$ is not bigger than 50 kHz in the experiments done here (see, e.g., Fig. 6-3). Using the values $\delta_{\mathrm{recoil}}/(2\pi) = 5.32\,\mathrm{kHz}$ and $\omega_t/(2\pi) = 364\,\mathrm{kHz}$, $\delta/(2\pi) = 0.23\,\mathrm{Hz}$ is obtained for the γ: 467 nm transition.

The differential shift between different isotopes comes from the different values of δ_{recoil} and ω_{tx} for the different atomic masses m^A and $m^{A'}$. From $\omega_{tx} \propto \sqrt{a} \propto m^{-1/2}$ (see Section 7.1.3), $\delta \propto m$ is given, and the biggest differential shift is 5.5 mHz from the maximum 2.4 % mass difference for $^{168}\mathrm{Yb}^+$ and $^{172}\mathrm{Yb}^+$ pair (see Table A.3).

7.1.1.2 Ramsey interferometry

The motion-independent shift for the Ramsey spectroscopy used for α: 411 nm and β: 436 nm transitions (see Section 5.2) is examined in Ref. [144]. The size of the shift is given by:

$$\delta = \underbrace{\frac{2\omega_R\eta^2}{2+\omega_R T}\left(\frac{\omega_R}{\omega_t}\right)^2}_{\delta_0} \cos\frac{\omega_t(T+2\tau_{\pi/2})}{2}\sin\frac{\omega_t T}{2} \tag{7.10}$$

where $\delta/(2\pi)$ and $\delta_0/(2\pi)$ are the shift in the transition frequency and the upper bound of its magnitude oscillating over the changes in $\frac{\pi}{2}$-pulse time $\tau_{\pi/2}$ and separation T between the two $\frac{\pi}{2}$-pulses, respectively, and $\omega_R/(2\pi)$ is the Rabi frequency for given transition and beam intensity. Roughly speaking, the maximum size of the shift $\delta_0 = 2\delta_{\text{recoil}}(\omega_R/\omega_t)^3/(2+\omega_R T)$ is given by the recoil frequency δ_{recoil} suppressed by the ratio of pulse and separation times $\tau_{\pi/2}/T = \pi/(2\omega_R T)$ (only when $\tau_{\pi/2}/T \gg 1$) and the ratio of the Rabi and trap frequencies cubed: $(\omega_R/\omega_t)^3$. The parameter values for the system, $\omega_t \geq 364$ kHz (see Table 4.1) and pulse sequence $\tau_{\pi/2} = T = 10\,\mu$s [i.e., $\omega_R/(2\pi) \sim 1/(4\tau_{\pi/2}) = 25$ kHz] (see Fig. 5-3 and Table 5.1), give the suppression from $(\omega_R/\omega_t)^3 \leq 3.24\times10^{-4}$ but not from $\tau_{\pi/2}/T = 1$, giving $\delta_0/(2\pi) \leq 1.24$ Hz which is smaller than the statistical uncertainty in the measured ISs by 2 orders of magnitude.

A generous, 10 % bound on the drift in ω_R (i.e., 20 % in the probe beam intensity) and durations T and $\tau_{\pi/2}$ from the ideal case $\omega_R\tau_{\pi/2} = \pi/2$ (i.e., $\delta = -\delta_0/2$) gives ~ 20 % of the drift in δ over time, which corresponds to $\lesssim$0.25 Hz. The slow drift between the measurement periods of different isotopes could result in a systematic shift at this level.

Besides the drift, the differential systematic shift between the isotopes comes from the slightly different masses m^A and $m^{A'}$ for different isotopes: $\delta_0 \propto \sqrt{m}$ from $\omega_{tx} \propto \sqrt{a} \propto m^{-1/2}$ [see Eq. 4.1]. The maximum 2.4 % mass difference for $^{168}\text{Yb}^+$ and $^{172}\text{Yb}^+$ pair (see Table A.3) gives $\lesssim$15 mHz difference in the carrier-transition Doppler shift between the isotopes.

While the differential effect is negligible compared to the statistical uncertainty

in the measured ISs in this work, the future experiment with ∼10 mHz uncertainty might resolve the effect (see Chapter 18). It can be solved by improving the decoherence time of the system, which is also one of the future works described in Section 17.1. Once it is accomplished, one can either make T longer and reduce $\tau_{\pi/2}/T$, or, more preferably, perform Rabi spectroscopy and have long π-pulse time τ_π and thus small ω_R as the shift δ_0 is proportional to ω_R^4 for the Rabi spectroscopy [144].

A difference in overall values in Table 7.1 for α: 411 nm and β: 436 nm transitions are due to the difference in the values of $\delta_{\mathrm{recoil}}/(2\pi)$: 6.87 kHz and 6.12 kHz, respectively.

7.1.2 First-order Doppler Shift

The first-order Doppler shift vanishes in the frame of a trap as $\langle v \rangle = 0$, especially for the thermal states. The motion of the trap center will result in the linear Doppler shift in the lab frame. In particular, the slow drift of the center due to the change in charge distribution over the trap surface (see Section 4.2.3.4) may give a nonzero contribution. The observed few-µm drift over the course of few hours (see Fig. 4-9) gives $O(10^{-18})$ fractional shift, which corresponds to $O(1\,\mathrm{mHz})$ shift in optical transition frequencies. Such a small shift is completely dominated by the zeroth-order Doppler shift within the trap center's frame, as estimated in Section 7.1.1. No differential shift is expected except from the slow drift occurring between the measurement for different isotopes.

The micromotion of an ion due to the RF electric field that exerts a force on the ion can be understood as the oscillation in the position of the trap center. The effect is purely classical, and thus adds symmetric pairs of sidebands, resulting in zero shift at the carrier peak's center.

The trap center's motion is possibly correlated to the laser pulses due to various factors such as stray charges built up on the trap surface due to the pulsed lasers, thermal transients, or optical shutters [65]. The fractional shift was small in Ref. [65], $< 10^{-17}$. More importantly, the shifts are common across different isotopes [92].

Taking those into account, those contributions are omitted here.

7.1.3 Second-order Doppler Shift

The third term in Eq. (7.1), the second-order Doppler shift, shifts the atomic transition frequency due to relativistic time dilation. The contributions from the micromotion and secular motion of an ion in the trap are calculated here:

$$\frac{\Delta\nu_D}{\nu_0} = -\frac{\langle v_s^2\rangle}{2c^2} + \left(\frac{\Delta\nu}{\nu_0}\right)^{\mu\text{motion}} \tag{7.11}$$

where $\langle v_s^2\rangle$ is the mean-square velocity of the secular motion due to a finite temperature of the ion, and $\left(\frac{\Delta\nu}{\nu_0}\right)^{\mu\text{motion}}$ is the micromotion-induced fractional Doppler shift.

The Doppler limit on the 369 nm cooling transition (≈500 µK; see Section 4.1.1) gives $\frac{\langle v_s^2\rangle}{2c^2} \approx 4\times10^{-19}$.[7]

Stray DC electric field around ions in the trap, from, for instance, light-induced stray charges on the surface of the trap chip, shifts the ions' positions from the RF null of the trap and makes the ion under excess micromotion [112]. The micromotion contributes to the second-order Doppler shift of which expression can be found in Ref. [112] [see Eq. (30) therein] with the definition of variables therein:

$$\left(\frac{\Delta\nu}{\nu_0}\right)_i^{\mu\text{motion}} \approx -\frac{4}{m^2c^2}\left(\frac{Qq_i\mathbf{E}_{\text{DC}}\cdot\hat{u}_i}{(2a_i+q_i^2)\omega_{\text{RF}}}\right)^2 - \frac{(q_xR\alpha\phi_{\text{AC}}\omega_{\text{RF}})^2}{64c^2}\delta_{i,x} \tag{7.12}$$

for the two radial directions $i = x, y$ of the cylindrical RF trap,[8] which can be calculated from the trap parameters [see Table 4.1 and Eq. (4.1)] and an Yb^+ ion's mass m^A (see Table A.3) and charge $Q = +e$. The second term is ignored here as the phase difference ϕ_{AC} between different RF electrodes has been minimized [108].

[7] $\langle v_s^2\rangle = (27\,\text{cm/s})^2$ from $\frac{3}{2}k_{\text{B}}T = \frac{1}{2}m\langle v_s^2\rangle$.

[8] There is no RF field along the axial direction z of the RF confinement (i.e., $q_z = 0$).

Together with $a_i \ll q_i$, it reduces the Eq. (7.12) further:

$$\left(\frac{\Delta\nu}{\nu_0}\right)_i^{\mu\text{motion}} \lesssim -\frac{4}{m^2c^2}\left(\frac{e|\mathbf{E}_{\text{DC}}|}{q_i\omega_{\text{RF}}}\right)^2 \tag{7.13}$$

The size of the DC electric field $\mathbf{E}_{\text{DC}}$ that the ion experiences is estimated from the observed $\pm 2\,\mu\text{m}$ drift in an ion's position (i.e., trap center) (see Fig. 4-9). The field shifts the center of the trap by

$$u_{0t} = \frac{Q\mathbf{E}_{\text{DC}} \cdot \hat{u}_t}{m\omega_t^2} \tag{7.14}$$

where $\hat{u}_t$ is the direction of a principal axis of the trap and ω_t^2 is the associated secular frequency [see Eq. (16) in [112]].

Using the maximum $\omega_t = 1.4\,\text{MHz}$ in a radial direction (see Table 4.1), the maximum E_{DC} is estimated to be $280\,\text{V/m}$. Considering the known typical values of E_{DC} and potential displacement of ion perpendicular to the trap chip which could not be measured in Section 4.2.3.4, $E_{\text{DC}} \lesssim 500\,\text{V/m}$ has been taken as a conservative bound. The bound gives $-(\Delta\nu/\nu_0)^{\mu\text{motion}} \lesssim 10^{-14}$, dominating over the secular-motion shift and giving the absolute shift $-\Delta\nu \lesssim 7.3\,\text{Hz}$.

The differential second-order Doppler shift of 200 mHz is estimated arising from the maximum 2.4 % mass difference for $^{168}\text{Yb}^+$ and $^{172}\text{Yb}^+$ pair (see Table A.3) and $(\Delta\nu/\nu_0)_{i,\max}^{\mu\text{motion}} \propto 1/m$ as $q_i \propto 1/m$ [Eq. (4.1b)]. The main source of the uncertainty in this differential shift is expected to be temporal drifts in the micromotion. As E_{DC} is expected to drift between zero (at the RF null) to $\lesssim$500 V/m (at the maximum deviation from the RF null), the magnitude of the estimated absolute shift is taken also as the long-term drift in the differential shift.

7.2 Laser-induced AC Stark shift

The energies of the two states in a transition to be driven can be shifted through other transitions that involve those states, resonantly or off-resonantly driven by the laser beams in the setup.

The amount of the AC Stark shift through a transition is given by (see, e.g., Chapter 7.2 in Ref. [141] and Section 7.7 in Ref. [145]):

$$\Delta\nu^{(g)} = +\frac{1}{8\pi}\frac{\delta}{\delta^2 + (\Gamma/2)^2}\omega_R^2 = \begin{cases} +\frac{1}{8\pi}\frac{\omega_R^2}{\delta} & \delta \gg \Gamma/2 \\ \pm\frac{1}{8\pi}\frac{\omega_R^2}{\Gamma} & \delta = \pm\Gamma/2 \\ +\frac{1}{8\pi}\frac{\delta}{(\Gamma/2)^2}\omega_R^2 & \delta \ll \Gamma/2 \end{cases} \tag{7.15}$$

$$\Delta\nu^{(e)} = -\Delta\nu^{(g)}$$

in the weak field limit $\omega_R \ll \delta, \Gamma$, where $\Delta\nu^{(g)}$ and $\Delta\nu^{(e)}$ are the shifts in the ground and excited states,[9] respectively,

$$\omega_R = \Gamma\sqrt{\frac{I}{2I_{\text{sat}}}} \tag{7.16}$$

is the (angular) Rabi frequency for the intensity of light I and the transition's linewidth Γ and saturation intensity I_{sat} [see also Eq. (B.3)], and $\delta/(2\pi)$ is the light's detuning from the atomic resonance, with the maximum magnitude of the shift at $\delta = \pm\Gamma/2$. The ground and excited states pull each other towards them (i.e., $\Delta\nu^{(g)} > 0$ and $\Delta\nu^{(e)} < 0$) for blue-detuned light ($\delta > 0$), and push each other away (i.e., $\Delta\nu^{(g)} < 0$ and $\Delta\nu^{(e)} > 0$) for red detuning ($\delta < 0$).

There are mainly two kinds of beams that cause the light shift in this experiment: the probe beam that drives the optical clock transitions and other beams for cooling and repumping that are supposed to be turned off but leaked through the AOMs that control the beams (see Fig. 5-3). The analysis of each case is presented in the following subsections, and the estimated shifts and long-term drifts are summarized in Table 7.2.

[9] In the form of (energy)/h (i.e., they are not *angular* frequencies, while the Rabi frequency ω_R and the detuning of light δ are).

Table 7.2: Estimated laser-induced AC Stark shifts and long-term drifts due to the probe and leakage beams. See the caption in Table 7.1 for the notation of the values.

		Shift [Hz]		
		α: 411 nm	β: 436 nm	γ: 467 nm
Probe	Zeeman	0[40[a]]		0[0.6] pHz
	Other	+120[O(1)]	+240[O(1)]	+7,000[O(100)]
Leakage	369 nm	+1,300[130[a]]		+1,300[1[a]]
	935 nm	+0.4[0.04[a]]	$\pm 1,000$[a][100[a]]	
	760 nm			$\pm 3,300$[a][330[a]]
402 nm		+30[10[a]]		
Total		+1,500[180[a]]	+2,500[a][280[a]]	+10,300[a][O(100)]

[a] upper bound on magnitude.

7.2.1 Probe beam-induced shift

The contribution of the probe beam is again divided into two parts: the shifts due to the relatively close-detuned other Zeeman transitions while a Zeeman transition is resonantly driven (Fig. 5-2) and far-detuned transitions in Yb^+ ions other than the clock transitions (see Fig. 3-1)

The shifts in α: 411 nm and β: 436 nm transitions are mainly from the Zeeman transitions (before two symmetric transition frequencies are averaged; see Section 7.2.1.1) due to their smaller detunings, while γ: 467 nm transition is dominated by the shift from the far-detuned other transitions due to the high power of probe beam (see Table B.1) and yet much smaller Rabi frequency for the clock transition compared to the α: 411 nm and β: 436 nm transitions (see Section 5.2).

The power of the probe beam was also actively stabilized only in the later experiments for the γ: 467 nm transition in this thesis work (see Section 4.2.3.1), while it was not the case for the earlier measurements for the α: 411 nm and β: 436 nm transitions in Ref. [4], causing bigger long-term drifts for the two transitions.

The effect of each case is analyzed in the following subsections.

7.2.1.1 From other Zeeman components

While a Zeeman transition is driven, other closely detuned Zeeman transitions (see Fig. 5-2) may be driven off-resonantly if the polarization and propagation direction of the probe beam meets the selection rules for the transitions (see R' and B' transitions in Fig. 5-2 and Appendix D). Ref. [4] elaborates the procedures and provides the estimated absolute shifts for α: 411 nm and β: 436 nm transitions: -1 kHz (-1.16 kHz) for R transition and $+1$ kHz ($+1.16$ kHz) for B transition, for the α: 411 nm (β: 436 nm) clock transition. In the reference, it is not clear whether the selection rules, the Zeeman transitions with the same ground Zeeman levels, and the relative Rabi frequencies of the transitions for given probe beams' polarization and propagation directions were considered for the estimation. This thesis confirms that it was indeed the case, considering the selection rules and relative peak heights described in Appendix D. The drift in the probe's polarization, which would change the relative Rabi frequencies of the different Zeeman transitions, has been suppressed by 50 dB by a Glan-Tayler calcite polarizer (see Section 4.2.3.1).

The average of the two Zeeman transitions' frequencies as our measure of zero-field transition frequency (see Section 5.3.4) will be highly close to zero. However, the drift in the probe power or magnetic field between the measurements for different Zeeman transitions reveals the underlying close-detuned AC Stark shift. This can be regarded as the *absolute* systematic uncertainty for each isotope, which is also the differential systematic uncertainty between different isotopes. While the magnetic field drift is measured to be <0.5 % (see Section. 7.6.1), probe powers were not actively stabilized for the α: 411 nm and β: 436 nm transitions, and thus the conservative 3 % bound on the drift over $\sim$5 min between scans for different Zeeman transitions (see Section 5.3.4), yielding <40 Hz drifts for the both transitions.

The Rabi frequency for γ: 467 nm transition was much smaller than α: 411 nm and β: 436 nm, and only 0.6 nHz shift for each Zeeman transition was estimated in Ref. [4]. Furthermore, the two Zeeman transitions were scanned in the same scans at only 5 s period of the Zeeman transition switching (see Section 5.3.4). By

conservatively bounding the drift of the probe beam power or magnetic field within every 5 s to 0.1 %, 0.6 pHz of the absolute and differential drifts are estimated.

7.2.1.2 From other Yb^+ transitions

γ: 467 nm transition has extremely narrow linewidth (see Table B.1) and thus requires a high optical power to be driven [51, 122, 138].[10] It results in the significant shifts by far-off-resonantly driving other transitions in Yb^+ ions (e.g., 369 nm cooling transition; see Fig. 3-1). The shift was measured to be 59(8) mHz/(mW/mm^2) [121], yielding 7 kHz absolute shift for the probe intensity used in this experiment (see Table B.1). While the power of the probe beam has been actively stabilized during γ: 467 nm transition measurements (with the drift bound to 0.1 %; see Section 4.2.3.1), the trapped ion's motion (see Section 4.2.3.4) results in the drift in the probe intensity that the ion sees. Considering the ion's few-µm long-term displacement and the probe beam size (see Table B.1), a few % of beam intensity drift is estimated, yielding $O(100)$ Hz.

For the α: 411 nm and β: 436 nm transitions, much lower probe powers were used (see Table B.1), and thus total shifts of +120 Hz for α: 411 nm and +240 Hz for β: 436 nm transitions are estimated in Ref. [4] (with corrected signs). From the few % bound for probe beam intensity drift, $O(1)$ Hz differential drifts are expected.

7.2.2 Non-probe light leakage

The AOM leakage of 369 nm cooling beam while a clock transition is interrogated by the probe beam can shift the $^2S_{1/2}$ ground state and thus the clock transition's frequency (see Fig 3-1). The leakage is estimated to be $\lesssim$5 nW (from a <100 µW, $\gtrsim$20 MHz red-detuned beam focused to a beam waist of 75 µm; see Table B.1), which leads to a shift of +1.3 kHz (in Ref. [4] with corrected sign).

Similarly, the 100 nW leakage of the 935 nm beam shifts the excited $^2D_{3/2}$ state of the β: 436 nm transition by maximum ±1 kHz [see Eq. (7.15) for the maximum

[10] Unless the probe beam has very narrow linewidth so that the transition can be coherently driven [121].

shift] through the rempumping transition (see Fig. 3-1). A less significant light shift arises for α: 411 nm transitions, through the 1070 nm transition connecting the $^2D_{5/2}$ state to the $^3D[3/2]_{1/2}$ state. This shift is estimated to be +0.4 Hz, contributing to the drift by only ≈40 mHz.

The 760 nm or 638 nm repumping transitions are not relevant to the α: 411 nm and β: 436 nm transitions. It can, however, shift the $^2F_{7/2}$ state the in γ: 467 nm transition.

The shifts from other transitions or beams are negligible compared to the contributions considered above. All the shifts above, total +1.3 kHz for α: 411 nm, <2.3 kHz for β: 436 nm, and <4.6 kHz for γ: 467 nm, are common-mode between isotopes

The differential drifts are estimated from the drifts in the leakage beams' intensities. For the 369 nm beam's shift in the γ: 467 nm transition measurement, the beam was blocked further by an optical shutter during the long probe pulse time (see Section 6.1), and the shift from 369 nm stray beams at the ion is conservatively bound to 0.1 % of the shift estimated above: <1 Hz. For all other cases, the intensity drifts are bound to 10 % during $\lesssim$2 hr of isotope switching time (see Section 5.3.2). The optical power drift would, then, contribute to the long-term drifts by $\lesssim$130 Hz, $\lesssim$230 Hz, and $\lesssim$330 Hz, for α: 411 nm, β: 436 nm, and γ: 467 nm, respectively.

Finally, a 402 nm laser beam was also used during the experiments for the α: 411 nm and β: 436 nm transitions, to transfer-lock an optical cavity used for increasing the ionization power during ion loading [105]. The associated long-term drift is estimated to be <10 Hz, assuming a maximum intensity drift of 30 %. The 402 nm beam was blocked during the experiments for the γ: 467 nm transition.

7.3 Shift in spectrum center by off-resonant excitation

For α: 411 nm and β: 436 nm transitions, the measured Ramsey fringe from a Zeeman transition of interest is perturbed by other Zeeman transitions that are being driven off-resonantly at the same time [see Eq. (6.7)]. The observed signal can be either a sum of different Ramsey fringes, or there may be quantum interference if the off-resonant transitions share a state with the transition to be probed. Here the magnitude of the frequency pulling is numerically estimated by fitting a sum of different Ramsey fringes from off-resonantly driven Zeeman transitions (see R' and B' transitions and the g factors in Fig. 5-2) with the associated detunings obtained from the measured magnetic field $\sim$1.1 G (see Section 7.6.1).

The maximum size of the pulling is $\sim$20 Hz for a detuning $\sim$1 MHz. The frequency pullings have opposite signs for the symmetric R and B Zeeman transitions, and the effect will cancel out after the measured frequencies of the Zeeman transitions are averaged. The drift in the pulling due to magnetic field fluctuation can be significant and $O(10)$ Hz is taken as the upper bound of the effect.

For γ: 467 nm transition, the effect of the off-resonant transition is estimated in a similar way used in Section 7.1.1.1 [e.g., Eq. (7.6) with the $\sim$1 MHz detuning of other Zeeman transitions as ω_t and $\eta^2 = O(1)$ for the same order of peak heights), yielding $<$1 Hz shift. The measured 0.5 % drift in the magnetic field (see Section 7.6.2) leads 2 % of drift in the shift (i.e., $<$20 mHz).

7.4 Blackbody-radiation Shift

The blackbody-radiation (BBR) shifts on the transitions probed here are well approximated by [146, 147]:

$$h\Delta\nu_{\mathrm{BBR}} = -\frac{1}{2}\alpha_0^{(eg)}(831.9\ \mathrm{V/m})^2\left(\frac{T}{300\ \mathrm{K}}\right)^4(1+\eta) \tag{7.17}$$

where h is the Plank constant, $\alpha_0^{(eg)} \equiv \alpha_0^{(e)} - \alpha_0^{(g)}$ is the difference in scalar polarizability between the atomic states in the transition of interest, and η is dynamic correction factor which is typically less than few percent [148].

The values of $\alpha_0^{(eg)}$ are calculated to be $7.8(5) \times 10^{-40}\,\mathrm{Jm^2V^{-2}}$ [149] and measured to be $6.9(1.4) \times 10^{-40}\,\mathrm{Jm^2V^{-2}}$ [150] for β: 436 nm transition. A similar value is expected for α: 411 nm transition since the difference in orbital wavefunctions of the $^2D_{3/2}$ and $^2D_{5/2}$ states is relativistically small (see Section 10.2). $1.3(6) \times 10^{-40}\,\mathrm{Jm^2V^{-2}}$ is the measured value for γ: 467 nm transition [122], which is consistent with a calculated value $1.93 \times 10^{-40}\,\mathrm{Jm^2V^{-2}}$ [151].

Using the typical temperature $T \approx 293\,\mathrm{K}$ in the laboratory, the BBR shifts are estimated: $\Delta\nu_{\mathrm{BBR}} \approx -0.4\,\mathrm{Hz}$ for the α and the β transitions and $\approx -0.06\,\mathrm{Hz}$ for the γ transition. The main source of a differential BBR shift in our experiment will be temperature drifts. The temperature drift is conservatively bound to 3 K over the course of the IS measurement in this work, which yields a drift in $\Delta\nu_{\mathrm{BBR}}$ of $\approx 15\,\mathrm{mHz}$ for the α and β transitions and $\approx 2.5\,\mathrm{mHz}$ for the γ transition.

7.5 Micromotional Stark shift

If an ion is shifted off the RF null of the Paul trap by stray DC fields, the RF field will induce Stark shift to the transitions to be probed. This shift is given by [152]:

$$h\Delta\nu = -\frac{\langle E^2 \rangle}{2}\left(\Delta\alpha_0 + \frac{1}{2}\alpha_2(3\cos^2\beta - 1)\left[\frac{3m_J^2 - J(J+1)}{J(2J-1)}\right]\right) \tag{7.18}$$

where h is the Plank constant, $\langle E^2 \rangle$ is the mean-squared value of the electric field experienced by the ion, β is the angle between the electric field and the quantization axis of the ion, and $\alpha_0^{(eg)} = \alpha_0^{(e)} - \alpha_0^{(g)}$ is the difference in the scalar polarizabilities between the ground and excited states of the transition. $\alpha_2^{(e)}$ is the tensor polarizability of the excited level (the $^2S_{1/2}$ ground state has zero tensor polarizability), and J and m_j are the angular-momentum quantum numbers for the excited state.

Eq. (32) in Ref. [112] gives an expression for the $\langle E^2 \rangle$ of the RF field that an ion

displaced from the RF null due to the stray DC electric field $\mathbf{E}_{\mathrm{DC}}$ experiences:

$$\langle E_i^2 \rangle \simeq 8 \left(\frac{q_i \mathbf{E}_{\mathrm{DC}} \cdot \hat{u}_i}{2a_i + q_i^2} \right)^2 \simeq 8 \left(\frac{\mathbf{E}_{\mathrm{DC}} \cdot \hat{u}_i}{q_i} \right)^2 \tag{7.19}$$

The bound on the E_{DC}, $\lesssim$500 V/m used in Section 7.1.3, gives bound on $\langle E^2 \rangle \lesssim (10,000\,\mathrm{V/m})^2$.

The values of the scalar and tensor polarizabilities are $[\alpha_0^{(eg)}, \alpha_2^{(e)}] = [6.9(1.4), -13.6(2.2)] \times 10^{-40}\,\mathrm{J\,m^2\,V^{-2}}$ (measured) [150] and $[7.8(5), -12.3(3)] \times 10^{-40}\,\mathrm{J\,m^2\,V^{-2}}$ (calculated) [149] for β: 436 nm transition, and similar values are expected for α: 411 nm transition (see Section 7.4). For γ: 467 nm transition, $[1.3(6), -0.18(8)] \times 10^{-40}\,\mathrm{J\,m^2\,V^{-2}}$ were measured [122], which are consistent with calculated values $[1.93, -0.2] \times 10^{-40}\,\mathrm{J\,m^2\,V^{-2}}$ [151].

From all the above values for the polarizabilities and $\langle E^2 \rangle \approx (10,000\,\mathrm{V/m})^2$, the micromotional Stark shifts are estimated to be $-72\,\mathrm{Hz} \lesssim \Delta\nu \lesssim -42\,\mathrm{Hz}$ for the α: 411 nm, $-100\,\mathrm{Hz} \lesssim \Delta\nu \lesssim 51\,\mathrm{Hz}$ for the β: 436 nm, and $-10\,\mathrm{Hz} \lesssim \Delta\nu \lesssim -9.5\,\mathrm{Hz}$ for the γ: 467 nm transitions, between $\cos^2\beta = 0$ to 1 ($m_J = \frac{3}{2}$ for the excited state of each clock transition; see Fig. 5-2). The values of the largest magnitude are taken as the bounds on the shifts. As $\langle E^2 \rangle$ is expected to drift between zero (at the RF null) to $\lesssim (10,000\,\mathrm{V/m})^2$ (at the maximum deviation from the RF null), the bounds on the absolute shifts are also taken as the bounds on the differential drifts between different isotopes.

7.6 Zeeman shift

7.6.1 First-order Zeeman shift

The drift in the separation of two Zeeman transitions' frequencies (i.e., Zeeman splitting) was measured to be $\lesssim$0.5 % during all the experiments with $\sim$1.1 G magnetic field (see Figs. 6-4, 6-8, and 6-12 for the splittings and drifts, and Fig. 5-2 for the R and B Zeeman transitions used and the associated g factors). It implies that there are typically <5 mG magnetic field drift, which is expected from local subways or eleva-

tors in the building. The effect of the linear Zeeman shift is, however, suppressed by the alternating or simultaneous measurements of two symmetric Zeeman transitions and subsequent averaging of the transitions' frequencies (see Section 5.3.4).

The time scale of the magnetic field drift was slow: $\gtrsim$30 min (i.e., $\lesssim 0.5\,\%/30$ min drift rate). Given that, for α: 411 nm and β: 436 nm transitions, of which the R and B symmetric Zeeman transitions were alternatively measured in every $\sim$5 min (see Section 5.3.4), <500 Hz of the long-term drift is expected. For γ: 467 nm transitions, the Zeeman transitions were measured in the same scan with switching between the transitions in every 5 s (see Section 5.3.4), and therefore the size of the drift was <10 Hz.

7.6.2 Second-order Zeeman shift

The second-order Zeeman shifts are calculated from the measured values of the coefficients in literature, 350(1) mHz/μT^2 [153] for α: 411 nm, 52.13(9) mHz/μT^2 [138] for β: 436 nm, and $-2.08(1)$ mHz/μT^2 [138] for γ: 467 nm transitions, yielding +4.2 kHz, +630 Hz, and -25 Hz shifts, respectively, from the measured $\sim$1.1 G magnetic field (see Section 7.6.1). The <5 mG long-term drift used in Section 7.6.1 gives the differential shifts of 42 Hz, 6.3 Hz, and 0.25 Hz. It is important to note, however, that the coefficients above were measured for $^{171}Yb^+$ isotope with the hyperfine structure. The quadratic Zeeman shift for spinless isotopes could be much smaller, possibly by 3 orders of magnitude or more, due to the difference in the energy scales of the fine structure (few tens of THz) and hyperfine structure (few to few tens of GHz). Indeed, the coefficients on the order of a few tens of μHz/μT^2 or smaller have been reported for $^{40}Ca^+$ [154] and $^{88}Sr^+$ [155] ions. Therefore, the estimated absolute and differential shifts above should be regarded as very generous upper bounds on their magnitudes.

7.7 Electric quadrupole shift

A frequency shift results from the interaction of the quadrupole moment of the electronic state with electric field gradients from the trap [156, 157]:

$$h\Delta\nu_{\text{quad}} \sim \Theta \cdot \nabla E \tag{7.20}$$

where h is the Plank constant, Θ is the quadrupole moments of a state in Yb^+ ion, and ∇E is the electric field gradient. The quadrupole moments for the $^2D_{5/2}$ and $^2D_{3/2}$ states in α: 411 nm and β: 436 nm transitions have been calculated to be $3.116(15)ea_0^2$ and $2.068(12)ea_0^2$ (consistent with the measured value $2.08(11)ea_0^2$ [150]), respectively [158], and measured to be $-0.041(5)ea_0^2$ for $^2F_{7/2}$ state in γ: 467 nm transition [122]. The $^2S_{1/2}$ ground state for all the clock transitions has zero quadrupole moment.

Time-varying electric field gradients due to patch potentials on the chip trap can lead to a differential shift between isotopes. The typical size and variation of the electric field gradient ∇E is $O(1)\,\text{V/mm}^2$ (see, e.g., Refs. [92, 154, 159] and Section 7.4.2 in Ref. [160]), which would lead to a differential quadrupole shift of $O(1)$ Hz for the α and β transitions and of order $O(10)$ mHz for γ transition.

7.8 Gravitational redshift

The gravitational redshift shifts the light's frequency travelling across the points with gravitational potential difference [161, 162]:

$$\frac{\nu(R+h)}{\nu_\infty} = \left(1 - \frac{2GM}{c^2(R+h)}\right)^{-1/2} = \alpha - \alpha^3 \frac{gh}{c^2}\left[1 + O\left(\frac{h}{R}\right)\right] \tag{7.21}$$

and thus

$$\frac{\Delta\nu}{\nu} \approx -\frac{g\Delta h}{c^2} \tag{7.22}$$

where $g = GM/R^2 = 9.807\,\text{m/s}^2$ is the earth's gravitational acceleration, c is the speed of the light, and Δh is the height between the two points from the earth

ground. G is the gravitational constant, M and R are the mass and radius of the earth, and $\alpha \equiv (1 - 2gR/c^2)^{-1/2} \approx 1$.

While the absolute size of the shift is arbitrary depending on the gravitational potential difference between the atom and the observer (and thus zero value is assigned for the absolute shift), the drift in positions of different parts in the apparatus, including atoms, probe lasers, and the reference cavity, can cause drift in the measured transition frequency. Considering the thermal expansion of the setup, a generous bound of 1 mm is given to such relative height changes, which would lead to a bound on differential shift uncertainty: < 0.08 mHz.

7.9 Absolute frequency stability of probe beam

The frequency of the probe beam at an ion is affected by the stability of the signal sources that drive, e.g., EOMs and AOMs, offset in the laser frequency stabilization, and the reference cavity modes to which the laser frequency is stabilized. Each effect will be described in the following subsections.

7.9.1 Reference clock stability

The long-term drift in the probe frequency due to the finite stability of the master clock that synchronizes all the relevant signal sources is estimated to be $\lesssim$5 Hz as described in Section 4.1.5.1.

7.9.2 Residual-amplitude-modulation-induced drift in stabilized probe frequency

Residual amplitude modulation (RAM) induces the drift in the Pound-Drever-Hall (PDH) stabilized laser frequency as introduced in Section 4.2.1. The residual long-term shift after the RAM is actively stabilized is bound to be $\pm$300 Hz from the measurement introduced in Section 4.2.1. The RAM was stabilized during only γ: 467 nm transition measurements, however, and the RAM drift for α: 411 nm and

β: 436 nm transitions could be estimated only from the nonlinear drift in the measured zero-field frequencies over time: $\sim\pm1$ kHz (see Figs. 6-8 and 6-12).

7.9.3 Reference cavity mode stability

7.9.3.1 Temperature dependence

The temperature of the inner side of the vacuum chamber for the ULE reference cavity was actively stabilized (see Section 4.2.2) and monitored while IS spectroscopy experiments were running (Fig. 6-4). The monitored temperature occasionally shifted by 0.002 °C, possibly due to the noise in the reading. Considering the temperature gradient across the cavity from the measurement point and the uncertainty in the measured zero-crossing temperature T_{zc}, the long-term drift in the probe beams' frequencies is bound to 40 Hz as described in Section 4.2.2.

7.9.3.2 Transmission power dependence

The dependence of the reference cavity mode frequencies on the optical powers of transmitted beams for PDH frequency stabilization (see Section 4.1.5.1) is investigated in Section 4.2.4. For earlier measurements for α: 411 nm and β: 436 nm transitions, the transmission power was not actively stabilized, and thus the drift in the powers is conservatively bound to 10 % of the total power $\sim$40 µW. For γ: 467 nm transition, the power was actively stabilized at 24.9 µW, and the residual drift in the stabilized power is conservatively bound to 0.1 % (see Section 4.2.4). Using the bound on the (doubled) cavity modes' resonant frequency shift rate in Table 4.2, $\lesssim$80 Hz for the α: 411 nm and the β: 436 nm transitions, and $\lesssim$0.5 Hz for the γ: 467 nm transition are obtained as the bounds on the long-term drift.

7.9.3.3 Nonlinear temporal drift of cavity mode frequency

A smooth, but nonlinear drift in a cavity mode's resonant frequency over time was reported in a system for measuring the absolute frequency of γ: 467 nm transition, in Ref. [123] (see Fig. 5 therein). A 934 nm beam was frequency-stabilized to a 10 mm-

long ULE cavity in the reference work, which is a very similar configuration to the system in this thesis work (see Section 4.1.5.1). The drift rate was also measured to be 0.50 Hz/s in the reference, which is of the same order as the rate measured for the reference cavity in this work: 0.13 Hz/s (see Fig. 6-4).

In Ref. [123], the deviation of the drift from the linear tendency by 3.5 Hz over 35,000 s, which implies 2.3×10^{-9} Hz/s^2 rate if the deviation is dominated by the quadratic drift. It gives deviation from the linear drift by 0.14 Hz during $\lesssim$2 hr of isotope switching time (see 5.3.2), which would contribute to the differential shift. The deviation would be even smaller if there are contributions from higher-order drifts. Therefore, the differential shift from the nonlinear drift in the cavity modes is estimated to be $O(0.1)$ Hz.

7.10 AOM switching-induced phase chirp

Phase shifts in $\frac{\pi}{2}$-pulses induced when an AOM switches the light are known to cause systematic errors in transition frequencies measured via Ramsey spectroscopy [163, 164] used for α: 411 nm and β: 436 nm transitions. Ref. [163] reported the shift in transition frequency by 1.6 Hz when the pulse time $\tau = 1.5$ µs and the pulse separation time $T = 21.6$ µs were used for 657 nm transition in neutral Ca atoms. As the pulse time in our experiment is longer (which makes the effect smaller), the interrogation time is of the same order of magnitude, and the wavelengths of the probe beams are similar, the shift is expected to be $O(1)$ Hz or smaller.

The phase instability is not relevant for γ: 467 nm transition for which the incoherent transition rate has been measured instead (See Section 5.4).

Part III

Search for New Physics

Chapter 8

Search for new physics via King-plot nonlinearity pattern

As introduced in Section 1.2.1, new physics has been probed by testing the linearity of the measured ISs in Part II, mapped onto *King plots*. In this chapter, King plots and the predicted linearity in the plots are introduced, and the idea of probing new physics from the violation of the linearity due to new-physics effects is developed. Refer to Chapter 2 for an entire overview of this part.

8.1 King plot and linearity

Isotope shifts (ISs), small differences in transition frequencies between different isotopes of an atomic species, have been an active research topic since at least the 1930s, as a sensitive probe for atomic and nuclear structure [100, 165, 166, 167, 168, 169, 170, 171]. In particular, in 1963, W. H. King proposed a way to present measured ISs in two-dimensional (2D) graphs called *King plots*, with an interesting general property of the ISs mapped onto the graphs: all the points in a King plot lie on a straight line [1, 172].

The way to construct a King plot is the following. It is required that the ISs between different pairs of isotopes for two different transitions are available. A King plot has two axes, one for the ISs for each transition. One pair of isotopes is then

mapped as a point in the plot. As adding the two transitions' ISs of more isotope pairs, the King plot reveals a linear distribution in the plot.

In short, the reason behind the linearity is that there are two primary sources of ISs in general, and each source is factorized into transition-dependent and independent parts.

8.1.1 Field shift

One of the two contributions originates from the difference in the charge distributions $\rho_N(\mathbf{r})$ in the nuclei between different isotopes, which is called *field shift* (FS). Given that an atomic system's (nonrelativistic) Hamiltonian is given as:[1]

$$H = \frac{\mathbf{P}_N^2}{2m_N} + \sum_{i=1}^{Z-I} \left[\frac{\mathbf{P}_{e,i}^2}{2m_e} + V(\mathbf{r}_i) \right] \tag{8.1}$$

for an isotope, where $\mathbf{P}_{N(e,i)}$ and $m_{N(e)}$ are the momentum and mass of the nucleus (ith electron), $\mathbf{r}_i = \mathbf{r}_{e,i} - \mathbf{r}_N$ is the relative position of ith electron to the nucleus, and $Z - I$ is the number of electrons in an I-ionized atom with atomic number Z, the interacting Hamiltonian that describes the difference in $\rho_N(\mathbf{r})$ between two isotopes (A, A'), labeled by their atomic mass numbers, is given as the following:[2]

$$H_{\mathrm{FS}}^{AA'} = \sum_{i=1}^{Z-I} V^{AA'}(\mathbf{r}_i) = \sum_{i=1}^{Z-I} \int_0^\infty \mathrm{d}\mathbf{r}' \frac{(-e)\rho_N^{AA'}(\mathbf{r}')}{4\pi \left| \mathbf{r}_i - \mathbf{r}' \right|} \tag{8.2}$$

where the subscrips AA' refers to the difference in the variables between the two isotopes.[3] The *Seltzer expansion* expresses the shift (in frequency) due to the interaction Hamiltonian in the first-order perturbation theory as a series of radial moment differences $\langle r^k \rangle^{AA'}$ of the $\rho_N(\mathbf{r})$ [168]:

$$\frac{\langle H_{\mathrm{FS}}^{AA'} \rangle_\Psi}{h} = \sum_{k=0}^{\infty} F_\Psi^{(k)} \langle r^{k+2} \rangle^{AA'} \tag{8.3}$$

[1] The relativistic description of FS and MS can be found in, e.g., Refs. [169, 173].
[2] in Lorentz-Heaviside units with rationalized charges (i.e., the 4π factor).
[3] The convention of sign is as follows: $X^{AA'} = X^A - X^{A'}$.

for an electrons' state Ψ, where h is the Plank constant,

$$\begin{aligned}\langle r^k\rangle^{AA'} &= \langle r^k\rangle^{A} - \langle r^k\rangle^{A'} \\ &= \int \mathrm{d}\mathbf{r}\, r^k \rho_N^A(\mathbf{r}) - \int \mathrm{d}\mathbf{r}\, r^k \rho_N^{A'}(\mathbf{r}) = \int \mathrm{d}\mathbf{r}\, r^k \rho_N^{AA'}(\mathbf{r}),\end{aligned} \tag{8.4}$$

and $F_\Psi^{(k)}$ with the lowest odd order appears at $k = 7$ or higher due to the relativistic effects [169].[4] Naturally, the FS for a transition χ from the state $\Psi_\chi^{(i)}$ to $\Psi_\chi^{(f)}$ is given by

$$(\nu_{\mathrm{FS}})_\chi^{AA'} = \frac{\langle H_{\mathrm{FS}}^{AA'}\rangle_{\Psi_\chi^{(f)}} - \langle H_{\mathrm{FS}}^{AA'}\rangle_{\Psi_\chi^{(i)}}}{h} = \sum_{k=0}^{\infty} F_\chi^{(k)} \langle r^{k+2}\rangle^{AA'} \tag{8.5}$$

where subscript χ indicates the difference in the quantities for $\Psi_\chi^{(f)}$ and $\Psi_\chi^{(i)}$ electronic states, and thus $F_\chi^{(k)}$ are field-shift electronic factors for the χ transition. As the contribution gets smaller for higher-order terms, the FS is given by $F_\chi \langle r^2\rangle^{AA'}$ with the omitted (0) superscript, coupled to the difference in the mean-squared charge radius of the nuclei.

8.1.2 Mass shift

Another significant source of ISs is the difference in the nuclear masses between isotopes, resulting in *mass shift* (MS). The (total) mass shift can be, again, divided into two parts, normal mass shift (NMS), due to the difference in the reduced masses of electrons in the frames of nuclei, and specific mass shift (SMS) originating from the kinetic correlations between electrons [1].[5] The distinction is not relevant for King linearity, however, as both effects are proportional to the same nuclear factors as below:[6]

$$H_{\mathrm{MS}}^{AA'} = \frac{\mathbf{P}_N^2}{2}\mu^{AA'} = \underbrace{\left(\sum_{i=0}^{Z-I} \frac{\mathbf{P}_{e,i}^2}{2}\right)\mu^{AA'}}_{\mathrm{NMS}} + \underbrace{\left(\sum_{i\neq j} \frac{\mathbf{P}_{e,i}\cdot\mathbf{P}_{e,j}}{2}\right)\mu^{AA'}}_{\mathrm{SMS}} \tag{8.6}$$

[4] $F^{(0)}$ and $F^{(2)}$ are defined as F and $G^{(4)}$, respectively, throughout this thesis for convenience.
[5] The division was first introduced in Ref. [165] according to Ref. [174]
[6] See Footnote 1.

where $\mathbf{P}_N + \sum_{i=0}^{Z-I} \mathbf{P}_{e,i} = 0$ in the frame of the atom and $\mu^{AA'} = 1/m_N^A - 1/m_N^{A'}$ is the inverse-mass difference of the nuclei.

As in Section 8.1.1, the MS of a transition χ, in the first-order perturbation theory, is given by

$$(\nu_{\mathrm{MS}})_\chi^{AA'} = K_\chi \mu^{AA'} \tag{8.7}$$

where K_χ is the difference in $\langle(\sum_{i=0}^{Z-I} \mathbf{P}_{e,i})^2\rangle/(2h)$ between the initial and final states of the transition.

In general, the MSs dominate over the FSs for light atomic species, and the FSs take over the MSs as the atomic number increases; the FSs are at least 7 times bigger than MSs for Yb, in the transitions of interest in this work.

8.1.3 Electronic and nuclear factorization

It is important to notice that each term in the expression for ISs is factorized into the corresponding *electronic* and *nuclear factors*. F_χ and K_χ depend only on the electronic properties, related to the electrons' wavefunction at the origin [see Eq. (15.1)] and momenta, respectively, and thus carry only the subscript χ which is the label for electronic transitions. On the other hand, $\langle r^2\rangle^{AA'}$ and $\mu^{AA'}$ are solely determined by nuclei, and carry only the superscript AA' for the isotope pair, which is a sufficient label for nuclear differences. This factorization turns out to be true for any contributions to ISs that will be introduced later in this thesis. For instance, each term in the higher-order FS in Eq. (8.5) is a product of the derivatives of electronic wavefunctions at the origin and the corresponding order of radial charge moment [see Eq. (15.1)].

A general perspective on the expansion of ISs and the factorization is presented in Section 11.6.

8.1.4 Linearity from shared nuclear factor

Due to the factorization, an important consequence appears while the IS measurements are extended in one direction: increasing the number of transitions χ, κ, η,

and so on of which the ISs are to be measured. For two transitions χ and κ, the total isotope shifts $\nu_{\chi,\kappa}^{AA'}$ are given by

$$\begin{aligned}\nu_{\chi}^{AA'} &= F_{\chi}\langle r^2\rangle^{AA'} + K_{\chi}\mu^{AA'} \\ \nu_{\kappa}^{AA'} &= F_{\kappa}\langle r^2\rangle^{AA'} + K_{\kappa}\mu^{AA'}.\end{aligned} \tag{8.8}$$

While the electronic factors $F_{\chi,\kappa}$ and $K_{\chi,\kappa}$ depend on the transitions, the nuclear factors $\langle r^2\rangle^{AA'}$ and $\mu^{AA'}$ are in common. It is natural, then, to solve the system of equations to remove the *shared* variables in the equations. In this case, in particular, $\mu^{AA'}$ are generally known with high precision thanks to the atomic mass spectrometry [20, 26, 57], and therefore, the two equations are solved to remove relatively poorly measured $\langle r^2\rangle^{AA'}$ in the expression:

$$\nu_{\kappa}^{AA'} = f_{\kappa\chi}\nu_{\chi}^{AA'} + K_{\kappa\chi}\mu^{AA'} \tag{8.9}$$

where $f_{\kappa\chi} = F_{\kappa}/F_{\chi}$ and $K_{\kappa\chi} = K_{\kappa} - f_{\kappa\chi}K_{\chi}$ are *two-transition* electronic factors. Finally, to reduce the geometric dimension of the expression, the equation is divided by one of the known parameters. The standard choice of normalization parameter is $\mu^{AA'}$ and the expression is reduced to

$$\overline{\overline{\nu}}_{\kappa}^{AA'} = f_{\kappa\chi}\overline{\overline{\nu}}_{\chi}^{AA'} + K_{\kappa\chi} \tag{8.10}$$

where the double overlines show that the variables are normalized by $\mu^{AA'}$.

The last equation immediately shows the linearity in (inverse-mass-normalized) King plots. If the normalized ISs in two transitions are taken as two axes, and the ISs for different pairs of isotopes,[7] the points should show linear distribution with $f_{\kappa\chi}$ as the slope and $K_{\kappa\chi}$ as the y-intercept [see, e.g., the inset in Fig. 8-1(a)].

This thesis work has alternatively proposed King plots that are normalization by $\nu_{\chi}^{AA'}$:

$$\overline{\nu}_{\kappa}^{AA'} = f_{\kappa\chi} + K_{\kappa\chi}\overline{\mu}^{AA'} \tag{8.11}$$

[7] e.g., (A, A'), (A', A''), (A'', A''') and so on for nearest-neighbor pairing

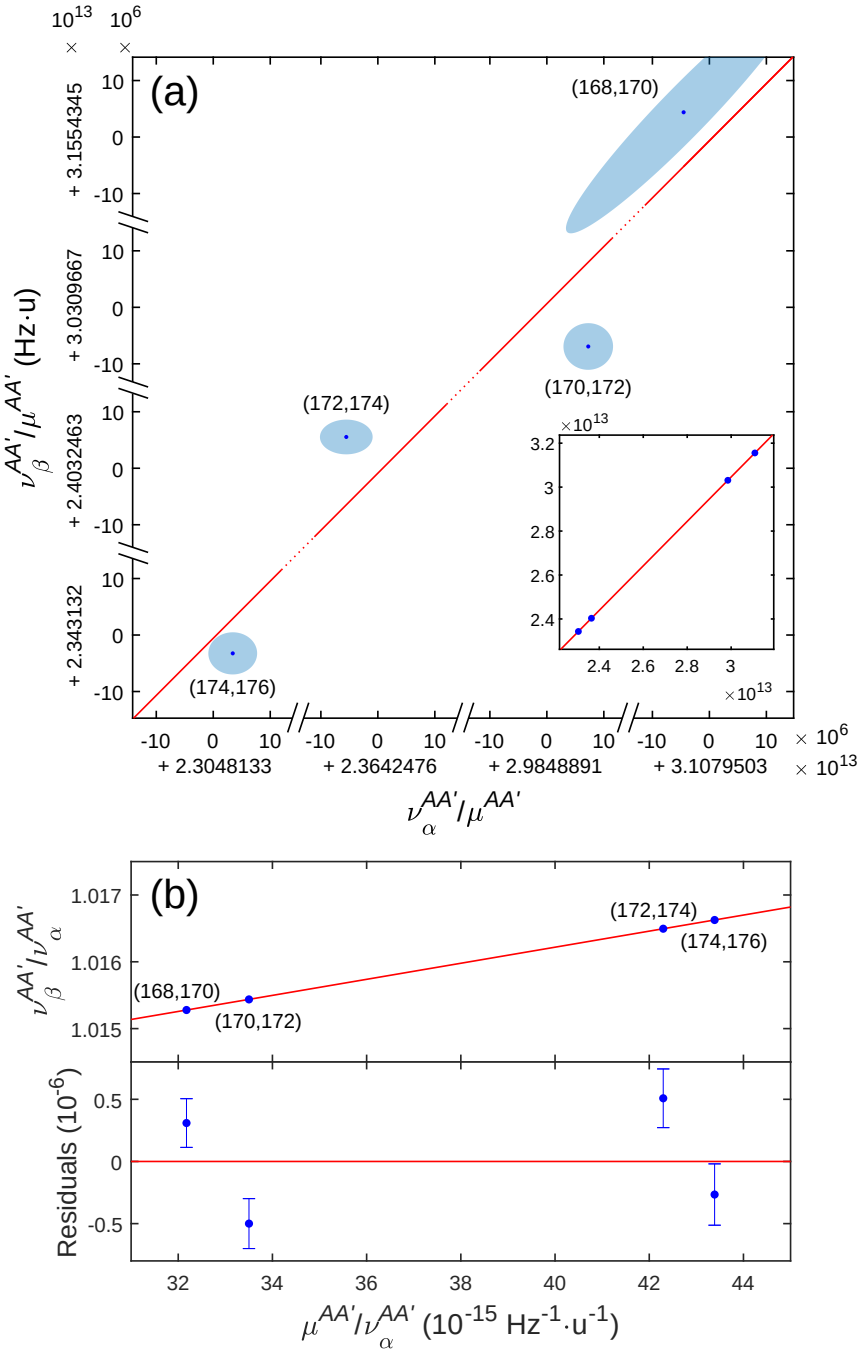

Figure 8-1: (a) Standard King plot [Eq. (8.10)] for the α: 411 nm and β: 436 nm transitions for pairs of neighboring even Yb^+ isotopes in Ref. [5]. The inset shows the full King plot. The main figure is zoomed into the data points by a factor of 10^6. A deviation from linearity (red line) by 3 standard deviations σ is observed. The larger diagonal uncertainty for the (168, 170) pair is due to the larger mass uncertainty for the $^{168}Yb^+$ isotope by the time that the result was published [5, 6, 7]. (b) Frequency-normalized King plot [Eq. (8.11)] and residuals. The error bars and error ellipses indicate 1σ measurement uncertainties.

where the overlines show the normalization with $\nu_\chi^{AA'}$. The *frequency-normalized* King plots have been used throughout this thesis, as discussed in Section 11.3 [see, e.g., Fig. 8-1(b)].

8.2 Violation of King-plot linearity

If there is more than two contributions in ISs with an additional source $X_\chi x^{AA'}$:

$$\nu_\chi^{AA'} = F_\chi \langle r^2 \rangle^{AA'} + K_\chi \mu^{AA'} + X_\chi x^{AA'}, \tag{8.12}$$

the linear relation between two transitions does not hold anymore:

$$\overline{\nu}_\kappa^{AA'} = f_{\kappa\chi} + K_{\kappa\chi} \overline{\mu}^{AA'} + X_{\kappa\chi} \overline{x}^{AA'} \tag{8.13}$$

where $X_{\kappa\chi} = X_\kappa - f_{\kappa\chi} X_\chi$, unless the $X_{\kappa\chi}$ vanishes or the $x^{AA'}$ is a linear combination of $\langle r^2 \rangle^{AA'}$ and $\mu^{AA'}$ for arbitrary isotope pairs AA' (i.e., $\mathbf{x}$ can be decomposed with $\langle \mathbf{r^2} \rangle$ and $\boldsymbol{\mu}$; see Section 8.3.1).

Adding all the contributions described in the following subsections, the total ISs are given by:

$$\begin{aligned} \nu_\chi^{AA'} =& F_\chi \delta \langle r^2 \rangle^{AA'} + K_\chi \mu^{AA'} \\ &+ G_\chi^{(4)} \langle r^4 \rangle^{AA'} + G_\chi^{(2)} [\langle r^2 \rangle^2]^{AA'} + \cdots \\ &+ \upsilon_{ne} D_\chi a^{AA'} \end{aligned} \tag{8.14}$$

with the terms in the order of the expected sizes of the contributions. The corresponding frequency-normalized King-plot relation is:

$$\begin{aligned} \overline{\nu}_\kappa^{AA'} =& f_{\kappa\chi} + K_{\kappa\chi} \overline{\mu}^{AA'} \\ &+ G_{\kappa\chi}^{(4)} \overline{\langle r^4 \rangle}^{AA'} + G_{\kappa\chi}^{(2)} \overline{[\langle r^2 \rangle^2]}^{AA'} + \cdots \\ &+ \upsilon_{ne} D_{\kappa\chi} \overline{a}^{AA'}. \end{aligned} \tag{8.15}$$

8.2.1 New boson ϕ

The most important possible contribution for the purpose of this work is the shift due to the new-boson coupling between neutrons in nuclei and electrons in atoms:

$$V_{ne}^{\phi}(r) = \hbar c \underbrace{(-1)^{s+1} \frac{y_e y_n}{4\pi\hbar c}}_{\equiv \upsilon_{ne}} \frac{e^{-r/\lambda\!\!\!^{-}_c^{\phi}}}{r} \tag{8.16}$$

from Eq. (1.1). The new field from a nucleus overlaps with the extranuclear wavefunction of electrons and shifts ISs by $(\nu_\phi)_\chi^{AA'} = \upsilon_{ne} D_\chi a^{AA'}$ where $a^{AA'} = A - A'$ is the difference in the number of neutrons [(see Eqs. (15.2) and (15.3)].

As the mass of a boson m_ϕ increases (i.e., the corresponding reduced Compton wavelength $\lambda\!\!\!^{-}_c^{\phi}$ decreases), the overlap of the Yukawa-like potential and electronic wavefunction reduces, which results in the decreasing sensitivity D_χ of an atom as a probe for the new boson (for given coupling constants y_n and y_e) (see Figs. 1-2 and 11-1). If m_ϕ is bigger than $100\,\mathrm{MeV/c^2}$ and $\lambda\!\!\!^{-}_c^{\phi}$ becomes comparable to (or shorter than) nuclear sizes ($O(10)\,\mathrm{fm}$), the most of the overlap happens inside the nuclei where the new field depend on the neutrons' distributions in the nucleus, which are not precisely known in general (e.g., neutron skin [175]).

It is also noteworthy that $D_{\kappa\chi} = D_\chi(d_{\kappa\chi} - f_{\kappa\chi})$ occasionally vanishes (i.e., the ratio $d_{\kappa\chi} \equiv D_\kappa/D_\chi$ becomes the same to the field-shift factors' ratio $f_{\kappa\chi}$) at certain boson masses m_ϕ, shown up as *dips* in the atom's sensitivity (i.e., peaks in, e.g., Figs. 1-2 and 11-1). The intuition behind such cases is that the new-boson shifts occasionally move the points along the *King line* [i.e., $(\nu_\phi)_\kappa^{AA'}/(\nu_\phi)_\chi^{AA'} = d_{\kappa\chi} = f_{\kappa\chi}$: the slope of the line], which do not cause the violation of King linearity.

8.2.2 Higher-order Standard-Model isotope shifts

Unfortunately, hypothetical effects of physics beyond the Standard Model (SM) is not the only additional contributions to ISs. An example is already described in Eq. (8.5): higher-order FSs ($k > 0$) that capture particular shapes of the nuclear charge distributions, including fourth-moment FS (FFS) $G_\chi^{(4)}\langle r^4\rangle^{AA'}$, in the first-order pertur-

bation theory. The higher-order perturbation theory, which takes account of the change in wavefunctions due to the interaction Hamiltonian, brings the higher-order SM corrections of another kind: e.g., quadratic FS (QFS) $G_\chi^{(2)}[\langle r^2\rangle^2]^{AA'}$, quadratic MS $L_\chi[\mu^2]^{AA'}$, and field-mass shift $C_\chi[\langle r^2\rangle\mu]^{AA'}$, where $[x]^{AA'} \equiv x^{AA_0} - x^{A'A_0}$ with irrelevant choice of a *reference* isotope A_0 [5] from which the perturbation occurs (see Section 11.6).

Considering the results from atomic and nuclear calculations (see Sections 11.1.1 and 11.1.2) and the fact that FSs are bigger than MSs for Yb, the sizes of the contributions are expected to be ordered as in Eq. (8.15) except for the hypothetical contribution from new boson $\upsilon_{ne} D_\chi a^{AA'}$.

8.3 Pattern analysis: revealing the origin of King nonlinearity

Figure 8-1 shows the first experimental evidence of King nonlinearity for new-physics search [5]. As the evidence started to be obtained, the physical origin of the violation had to be identified. This thesis work has proposed that extending IS measurements in another direction, increasing the number of isotope pairs (A, A'), in addition to the number of transitions (see Section 8.3.4), can provide crucial information on the sources of the nonlinearity.

At least three points (i.e., three isotope pairs) in a King plot are required to test the (non)linearity of the points' distribution. On the other hand, at least $n+1$ isotope should be available for the IS measurement to obtain n *independent* isotope pairs (see Section 11.5). Therefore, at least 4 isotopes are required for the linearity test.

However, the test with three points can show only if King nonlinearity exists or not. Once the nonlinearity is observed, it would not be possible to determine whether it is from new physics, unless the sizes of all the higher-order SM corrections are exhaustively and accurately investigated, which requires precise information on both

atomic and nuclear structures of the atom.

A solution for the problem starts from the observation that there are infinitely many different possible *shapes* of the residuals when the least-squares ($\hat{\chi}^2$) fit is performed for more than 4 points in a 2D plane. For instance, Yb has 5 observationally stable isotopes (i.e., 4 King-plot points) with zero nuclear spins (to avoid hyperfine structures; see Section 19.2.2), and Fig. 8-1(a) shows a zigzag shape ($-\ +\ -+$) of the observed residuals, but it could be instead a curved, bowline shape ($-\ +\ +-$) of the same overall scale.[8]

The most essential idea here is that not only the size but also the shape of the pattern should be predictable for a particular source of nonlinearity. By comparing observed nonlinearities with the predicted pattern shapes from different possible sources, the dominant contribution might be pointed out even in the case that the size of the contribution is unknown (e.g., new physics). Moreover, they are the isotope pairs that determine the relative positions of the points in the King plot. Therefore, the shape of the pattern is determined only by isotope-dependent nuclear terms (e.g., $a^{AA'}$ and $\langle r^4 \rangle^{AA'}$) while the electronic factors such as $\upsilon_{ne} D_{\kappa\chi}$ and $G^{(4)}_{\kappa\chi}$ affect the overall signs and magnitudes of the contributions [see Eq. (8.15)]. This point is essential for new-physics search as the associated nuclear parameter (e.g., neutron number difference $a^{AA'}$ for the new-boson contribution) is independent of the new physics' properties (e.g., υ_{ne}) which would be unknown by its definition.

8.3.1 Vector representation of King plot and nonlinearity

To develop the methodology of the pattern analysis, an alternative approach for investigating the King nonlinearity has been developed: vector analysis.

The following vector notation for isotope-pair-dependent parameters is defined:

$$\mathbf{x} = (x^{A_1 A_1'}, x^{A_2 A_2'}, x^{A_3 A_3'}, x^{A_4 A_4'}) \equiv (x_1, x_2, x_3, x_4) \tag{8.17}$$

[8]Note that this is not the case if there are only three points in a King plot; regardless of the overall scale, the ratio of the points' deviations from the $\hat{\chi}^2$-fit line is invariant under small changes in their position, once the positions of the points are largely determined by the ISs $\nu_\chi^{AA'}$ and $\nu_\kappa^{AA'}$ and the inverse-mass-difference factor $\mu^{AA'}$.

where $A_k A'_k$ are the isotopes in the k-th pair. This notation provides an alternative view of King plot: if the King plot is linear, then the vector with components $\overline{\nu}_\kappa^{AA'} = \nu_\kappa^{AA'}/\nu_\tau^{AA'}$ resides in the plane that two *King vectors* $\mathbf{1}$ and $\overline{\boldsymbol{\mu}}$ define, with $f_{\kappa\tau}$ and $K_{\kappa\tau}$ as the coefficient of the vectors, respectively [see Eq. (8.15)]:

$$\overline{\boldsymbol{\nu}}_\kappa = f_{\kappa\tau}\mathbf{1} + K_{\kappa\tau}\overline{\boldsymbol{\mu}}. \tag{8.18}$$

Since the vectors are four-dimensional (4D) for the 5 stable, even-A Yb isotopes, one can define two vectors $\hat{\boldsymbol{\Lambda}}_+$ and $\hat{\boldsymbol{\Lambda}}_-$ (named *nonlinearity vectors*) that span the space orthogonal to the *King plane*. When measured ISs $\overline{\nu}_\kappa^{AA'}$ do not exactly lie in the King plane, the out-of-plane component can be decomposed along the nonlinearity vectors with components λ_+ and λ_-. In other words, the King plane and nonlinearity plane corresponds to the best fit and the remaining residuals of the ordinary-least-square (OLS) fit in the King plot, respectively:

$$\overline{\boldsymbol{\nu}}_\kappa = f_{\kappa\tau}\mathbf{1} + K_{\kappa\tau}\overline{\boldsymbol{\mu}} + \lambda_+\hat{\boldsymbol{\Lambda}}_+ + \lambda_-\hat{\boldsymbol{\Lambda}}_-. \tag{8.19}$$

Furthermore, the nonlinearity vectors $\hat{\boldsymbol{\Lambda}}_\pm$ decompose the observed nonlinearity to $\boldsymbol{\lambda} = (\lambda_+, \lambda_-)$ components, reducing the geometric dimension of the nonlinearity from 4D to 2D.

There is an infinite number of ways to define nonlinearity vectors, and this thesis suggests the following unit vectors:

$$\begin{aligned}
\hat{\boldsymbol{\Lambda}}_+ &\propto (\overline{\mu}_3 - \overline{\mu}_2, \overline{\mu}_1 - \overline{\mu}_4, \overline{\mu}_4 - \overline{\mu}_1, \overline{\mu}_2 - \overline{\mu}_3) \\
\hat{\boldsymbol{\Lambda}}_- &\propto (\overline{\mu}_4 - \overline{\mu}_2, \overline{\mu}_1 - \overline{\mu}_3, \overline{\mu}_2 - \overline{\mu}_4, \overline{\mu}_3 - \overline{\mu}_1)
\end{aligned} \tag{8.20}$$

where $\overline{\mu}_k \equiv \overline{\mu}^{A_k A'_k}$. The proposed nonlinearity vectors have several advantages: They have fairly simple, linear forms while being orthogonal to the King vectors, which simplify the error propagation in the measured quantities $\mu^{AA'}$, $\nu_\tau^{AA'}$, and $\nu_\kappa^{AA'}$ to $\boldsymbol{\Lambda}_\pm$ and $\lambda_\pm$. Furthermore, the $\hat{\boldsymbol{\Lambda}}_+$ and $\hat{\boldsymbol{\Lambda}}_-$ vectors represent zigzag ($+-+-$) and curved ($+--+$) patterns of nonlinearity if $\overline{\mu}_1$ to $\overline{\mu}_4$ are in increasing order (i.e., $\overline{\mu}_k < \overline{\mu}_{k+1}$),

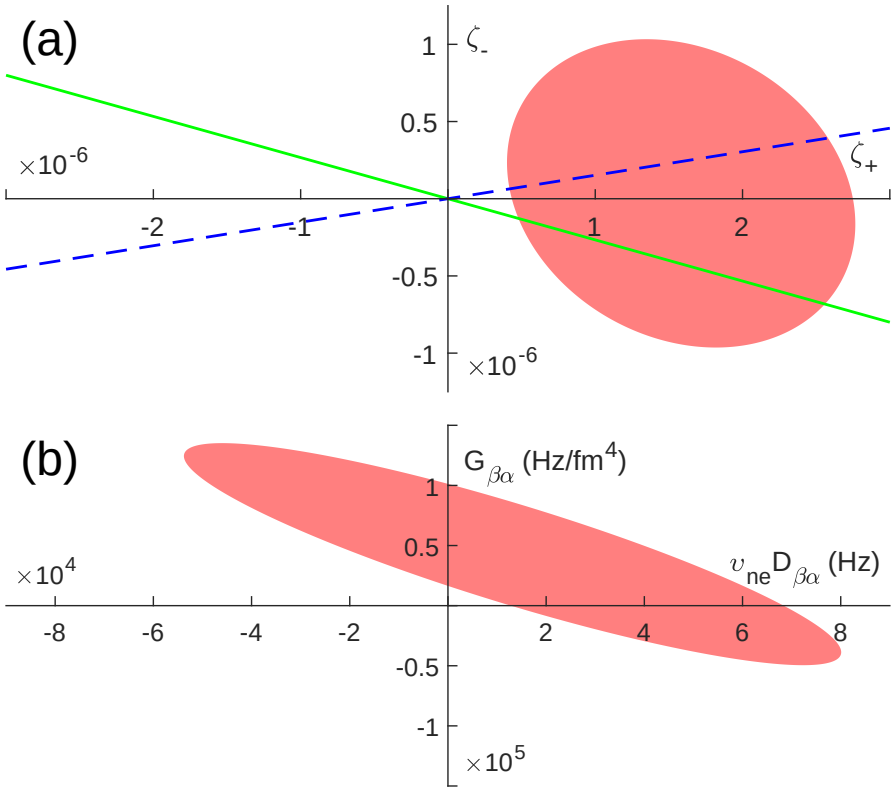

Figure 8-2: (a) Nonlinearity measure (ζ_+, ζ_-) for next-neighbor isotope pairs (see Section 11.7) in Ref. [5]. The red shaded region indicates the 95% confidence interval from our data. The green solid line and the blue dashed line indicate the required ratio ζ_-/ζ_+ if the nonlinearity is purely due to a new boson ϕ and the QFS, respectively. (b) Nonlinearity measure along the axes of a new boson (x-axis) and the QFS (y-axis).

replacing the role of $\boldsymbol{\zeta}_\pm = (1, -1, \pm 1, \mp 1)$ in the earlier work of the thesis [5] (the choice of $\boldsymbol{\zeta}_\pm$ vs $\boldsymbol{\Lambda}_\pm$ is discussed in Section 11.7).

8.3.2 Nonlinearity map

As the nonlinearity vectors provide 2D representation $\lambda_\pm$ of 4-point nonlinearities, the values (λ_+, λ_-) can be mapped onto a 2D graph, named *nonlinearity map*, as (x, y) coordinates. Figure 8-2(a) shows the graphical representation in the earlier thesis work [5]. The observed nonlinearity in the King plot for α: 411 nm and β: 436 nm transitions is mapped as an ellipse rather than a point, representing the uncertainties in the measured ISs.

8.3.3 Pattern shape prediction for particular sources

An important feature of the nonlinearity map is that the shape of a pattern is shown as a straight line in the nonlinearity map that crosses the origin,[9], with a slope given by the ratio λ_-/λ_+ of the two basis patterns. The direction is given by decomposing the associated nuclear factor of a nonlinearity source (e.g., $[\langle \mathbf{r^2} \rangle^2]$ for QFS) with $\hat{\mathbf{\Lambda}}_\pm$, and it also set the *scale* or *unit* along the line; when the associated electronic factor (e.g. $G^{(2)}_{\kappa\tau}$) is multiplied to $[\langle \mathbf{r^2} \rangle^2]$, then the resulting nonlinearity coefficient will have the unit of normalized ISs $\overline{\boldsymbol{\nu}}_\kappa$.[10] [11] Given that, each source's line can serve as an *axis* with the unit of the associated electronic factor (e.g., kHz/fm^4 for $G^{(2)}_{\kappa\tau}$). As an application of the idea, the measured IS nonlinearity is decomposed with the two axes for the QFS and the new boson ϕ in Fig. 8-2(b).

8.3.4 Pattern shape comparison as a probe for next-order sources

Extending the idea of having more transitions in Section 8.1.4 further, another interesting test has been proposed in this thesis work [8]. If the ISs are measured for n transitions τ, κ, η, and so on, then the transitions τ can be taken as a *reference* transition, and all the other transitions can be paired with the reference transition: (τ, κ), (τ, η), and so on. Subsequently, the King nonlinearity pattern for each of the $n-1$ transition pairs can be obtained and compared.

In particular, if there is only one underlying source for the nonlinearities, namely $X\mathbf{x}$, while the overall magnitudes and signs of the patterns may differ by the difference in $X_{\kappa\tau}$, $X_{\eta\tau}$, and so on, the shapes of the patterns should be the same as they are determined by the nuclear factor $\mathbf{x}$. It implies that the patterns mapped onto the nonlinearity map $\lambda_\pm$ should lie on the same line that crosses the origin. If it is not the case, however, there is the only possible explanation: there is at least one another nonlinearity source, $Y\mathbf{y}$ ($\mathbf{y} \nparallel \mathbf{x}$), and different ratios Y/X of the two elec-

[9] when there are no other nonlinearity sources

[10] Dimensionless for frequency-normalized King plots.

[11] Recall that $\hat{\mathbf{\Lambda}}_\pm$ are dimensionless unit vectors.

tronic factors between different transitions pairs make total nonlinearities $X\mathbf{x} + Y\mathbf{y}$ have different directions from the origin in the nonlinearity map.

It shows that comparing the shapes of the patterns from different transition pairs serves as a test for the minimum numbers of the nonlinearity sources in an atomic system. The test can be done by fitting the points $\boldsymbol{\lambda}_\kappa^{(\tau)} = \left((\lambda_+)_\kappa^{(\tau)}, (\lambda_-)_\kappa^{(\tau)}\right)$, $\boldsymbol{\lambda}_\eta^{(\tau)}$, and so on[12] in the nonlinearity map with a line that crosses the origin (see, e.g., Fig. 10-3).

This new test is interesting in two different ways. First, the test is again for linearity in a useful graph, just as the King-plot linearity test in the beginning. More importantly, the test is purely experimental; it is not necessary to know the physical origin or λ_-/λ_+ ratios associated with the sources $X\mathbf{x}$ or $Y\mathbf{y}$, and all that needs to be done is to compare patterns from measured ISs.

It can be shown that testing whether there are at most n sources or more can be done with $n+2$ transitions and $n+3$ isotope pairs (i.e. $n+4$ isotopes) in general, which is, in fact, straightforward to understand in the context of Section 8.4. Yb^+ alone has 3 transitions and 5 stable isotopes, so it just meets the requirements for the test at the minimum level: testing if there is only one nonlinearity source or more.

8.4 n-dimensional King plot

An alternative way to accommodate more than two transitions is to generalize King plots for higher-dimension [82, 176]. For three transitions χ, κ, η, for instance, with two nonlinearity sources $X_\alpha x^{AA'} \gg Y_\alpha y^{AA'}$:

$$\nu_{\chi,\kappa,\eta}^{AA'} = F_{\chi,\kappa,\eta}\langle r^2\rangle^{AA'} + K_{\chi,\kappa,\eta}\mu^{AA'} + X_{\chi,\kappa,\eta}x^{AA'} + Y_{\chi,\kappa,\eta}y^{AA'} \tag{8.21}$$

[12] $\lambda_\pm$ for nonlinearity in King plot for transition κ (in y axis) paired with reference transition τ (in x axis). $\boldsymbol{\lambda}_{\kappa\tau} \equiv \boldsymbol{\lambda}_\kappa^{(\tau)}$ might be a useful alternative notation.

can be expressed as

$$\begin{bmatrix} \nu_\chi^{AA'} \\ \nu_\kappa^{AA'} \\ \nu_\eta^{AA'} \end{bmatrix} - \begin{bmatrix} Y_\chi \\ Y_\kappa \\ Y_\eta \end{bmatrix} y^{AA'} = \underbrace{\begin{bmatrix} K_\chi & F_\chi & X_\chi \\ K_\kappa & F_\kappa & X_\kappa \\ K_\eta & F_\eta & X_\eta \end{bmatrix}}_{T} \begin{bmatrix} \mu^{AA'} \\ \langle r^2 \rangle^{AA'} \\ x^{AA'} \end{bmatrix} \tag{8.22}$$

and the solution for $\mu^{AA'}$ is expressed as:

$$\mu^{AA'} = \sum_{\iota=\chi,\kappa,\eta} \left(T^{-1}\right)_{1\iota} \left(\nu_\iota^{AA'} - Y_\iota y^{AA'}\right). \tag{8.23}$$

By rearranging Eq. (8.23), the expression for inverse-mass-normalized three-dimensional (3D) King plots is obtained as follows:

$$\overline{\overline{\nu}}_\eta^{AA'} = K_{\eta\kappa\chi} + f_{\eta\kappa\chi}\overline{\overline{\nu}}_\chi^{AA'} + f_{\eta\chi\kappa}\overline{\overline{\nu}}_\kappa^{AA'} + Y_{\eta\kappa\chi}\overline{\overline{y}}^{AA'} \tag{8.24}$$

where $\overline{\overline{z}}^{AA'} \equiv z^{AA'}/\mu^{AA'}$ ($z \in \{\nu_\chi, \nu_\kappa, \nu_\eta, y\}$) are inverse-mass-normalized quantities (see Section 8.1.4),

$$f_{\eta\kappa\chi} = \frac{\frac{F_\eta}{F_\kappa} - \frac{X_\eta}{X_\kappa}}{\frac{F_\chi}{F_\kappa} - \frac{X_\chi}{X_\kappa}} = \frac{X_{\eta\kappa}}{X_{\chi\kappa}} \text{ and} \tag{8.25}$$

$$f_{\eta\chi\kappa} = \frac{\frac{F_\eta}{F_\chi} - \frac{X_\eta}{X_\chi}}{\frac{F_\kappa}{F_\chi} - \frac{X_\kappa}{X_\chi}} = \frac{X_{\eta\chi}}{X_{\kappa\chi}} \tag{8.26}$$

are the slopes of the plane in 3D the King plot along the axes corresponding to the transitions χ and κ, respectively,

$$\begin{aligned} Z_{\eta\kappa\chi} &= Z_\eta - f_{\eta\kappa\chi}Z_\chi - f_{\eta\chi\kappa}Z_\kappa \\ &= Z_{\eta\chi} - \frac{X_{\eta\chi}}{X_{\kappa\chi}}Z_{\kappa\chi} \\ &= Z_{\kappa\chi}(z_{\eta\chi\kappa} - f_{\eta\chi\kappa}) \end{aligned} \tag{8.27}$$

where $Z = K, Y$ are the z-intercept of the plane and the electronic factor associated with the nonlinearity source $y^{AA'}$, respectively, and $z_{\eta\chi\kappa} \equiv z_{\eta\chi}/z_{\kappa\chi}$.

The 3D King plot has two related effects. The leading-order nonlinearity nuclear source $x^{AA'}$ disappears in Eq. (8.24). It is because the three equations in Eq. (8.22 are solved to remove two shared unknowns $\langle r^2\rangle^{AA'}$ and $x^{AA'}$, just as a 2D King plot is obtained by solving two equations for one unknown $\langle r^2\rangle^{AA'}$. As result, there is only one source of nonlinearity in the 2D King plots (namely $X_\chi x^{AA'}$) if all the points in the 3D King plot lie in a *plane*, barring the case that $\mathbf{y}$ can be decomposed to $\langle\mathbf{r^2}\rangle$, $\boldsymbol{\mu}$, and $\mathbf{x}$ (see Section 8.3.1 for the vector notation) or Y_χ, Y_κ, and Y_η cancel out in $Y_{\eta\kappa\chi}$. Therefore, fitting the points in the 3D King plot with a linear plane serves as a test if there are only one or more contributions to the ISs besides the FS and the MS (see, e.g., Fig. 10-6). At least 4 points in the 3D King plot (i.e., 5 isotopes) are required to test their King *planarity*. It is straightforward to generalize the results for n transition, with which an n-dimensional (nD) King plot can be formed, $(n-1)$D hyperplanarity can be tested with n points (i.e. $n+1$ isotopes), and it can be tested whether there are at most $n-2$ nonlinearity sources or more.

It can be noticed that the capabilities and requirements of the pattern shape comparison and nD King plot are very similar. It indeed turns out that the nD-King-plot hyperplanarity test is equivalent to the comparison of corresponding $n-1$ different nonlinearity patterns developed in Section 8.3, as proved in Section 11.4. Given that, the pattern comparison may be more preferred for its lower geometric dimension and capability of the test with a limited number of available isotopes, as discussed in Section 11.4 (see, e.g., Fig. 10-3).

Chapter 9

Uncertainty propagation and King-plot fitting

To obtain uncertainties of the variables for King plots and the correlations between them from measured values,[1] the uncertainties and correlations need to be properly propagated during arithmetic operations. In particular, the uncertainty propagation becomes somewhat complicated for vector analysis in Section 8.3.1.[2] The basics of the method will be covered in Section 9.1 with some complicated examples used in the thesis work.

The uncertainty propagation in an analysis can be achieved in an alternative way based on the Monte Carlo approach: generating numerous random *sample* sets of values of all necessary variables, which have the distribution that the measured values have (i.e., mean values, uncertainties, and correlations), and observing the distribution of analysis results from each sample set. The Monte Carlo analysis has been established by Diana P. L. Aude Craik, a research team member and a postdoctoral researcher (results not presented here), and the results agreed well with the analytic analysis of the uncertainty propagation described here.

On the other hand, it is straightforward to fit data in 2D graphs with uncer-

[1] e.g., $\overline{\overline{\nu}}^{AA'}_{\alpha,\beta} = \nu^{AA'}_{\alpha,\beta}/\mu^{AA'}$ from measured $\nu^{AA'}_{\alpha}$, $\nu^{AA'}_{\beta}$, and $\mu^{AA'}$ (see Section 8.1.4); see, e.g., the ellipse for $(168, 170)$ isotope pair in Fig. 8-1(a)

[2] e.g., propagating uncertainties in vectors $\mathbf{x}$, $\mathbf{\Lambda}_+$, and $\mathbf{\Lambda}_-$ to the coefficients $\lambda_\pm$ under the two-vector decomposition of $\mathbf{x}$ with $\mathbf{\Lambda}_\pm$.

tainties along the y direction, possibly with the correlations between them, through the standard generalized-least-square (GLS) regression. However, fitting points in King plots in correct way may not be as straightforward. It is because there is uncertainty in the x coordinates of the points as well ($\overline{\overline{\nu}}_\chi^{AA'}$ or $\overline{\mu}^{AA'}$; see Section 11.3), and there can be correlations between the x and y-coordinates of each point (e.g., from the uncertainties in parameters normalizing King relation; see Section 8.1.4) or between the points (e.g., from improving precisions of ISs using redundant ISs; see Section 6.7). The procedure for the proper Errors-in-Variables GLS (EiVGLS) fit that accommodates the uncertainties in both the x and y directions and all the possible correlations will be presented in Section 9.2. In particular, obtaining the significance of nonlinearity is important as it is the significance of the signal potentially from new physics under test.

9.1 Uncertainty propagation

Suppose there are two (set of) random variables $\mathbf{x} = (x_1, x_2, \cdots, x_M)$ and $\mathbf{y} = (y_1, y_2, \cdots, y_N)$ as column vectors,[3] with associated variance-covariance matrices (VCMs) $\Sigma_\mathbf{x}$ and $\Sigma_\mathbf{y}$, respectively;[4] the diagonal elements $(\Sigma_\mathbf{x})_{ii} = \sigma_{x_i}^2$ are the variances of the random variables x_i, while the off-diagonal elements $(\Sigma_\mathbf{x})_{ij} = \sigma_{x_i x_j}$ are the covariances between x_i and x_j (and as well for $\Sigma_\mathbf{y}$).

The most fundamental relation in this chapter is the following: if the random variables $\mathbf{x}$ and $\mathbf{y}$ are related by a linear transformation

$$\mathbf{y}_N = T_{N\times M}\mathbf{x}_M + \mathbf{b}, \tag{9.1}$$

with T named *propagation matrix*, then the VCMs are related as

$$(\Sigma_\mathbf{y})_{N\times N} = T_{N\times M}(\Sigma_\mathbf{x})_{M\times M}(T^\intercal)_{M\times N}. \tag{9.2}$$

[3] Inline arrays with round brackets are assumed to represent column vectors: $(a_1, \cdots, a_N) \equiv [a_1, \cdots, a_N]^\intercal$.

[4] $\Sigma_\mathbf{x} \equiv \langle(\mathbf{x} - \langle\mathbf{x}\rangle)(\mathbf{x} - \langle\mathbf{x}\rangle)^\intercal\rangle$.

If $\mathbf{x}$ and $\mathbf{y}$ have multivariate normal distributions, the mean values:

$$\langle \mathbf{y} \rangle = T \langle \mathbf{x} \rangle + \mathbf{b} \tag{9.3}$$

and the VCM is sufficient to identify the distributions of the variables $\mathbf{x}$ and $\mathbf{y}$, as it is one of the most important properties of the normal distributions in general. Note that the normal distribution is defined as

$$\mathbf{x}_M = (A_{\mathbf{x}})_{M \times L} \, \mathbf{z}_L \tag{9.4}$$

where $\mathbf{z} = (z_1, \cdots, z_L)$ is the set of independent standard normal variables and $A_{\mathbf{x}}$ is a matrix such that $\Sigma_{\mathbf{x}} = A_{\mathbf{x}} A_{\mathbf{x}}^{\intercal}$, and the probability density function is given as

$$f_{\mathbf{x}}(\mathbf{x}) = \frac{1}{\sqrt{(2\pi)^M |\Sigma_{\mathbf{x}}|}} \exp\left[-\frac{1}{2} \left(\mathbf{x} - \langle \mathbf{x} \rangle \right)^{\intercal} \Sigma_{\mathbf{x}}^{-1} \left(\mathbf{x} - \langle \mathbf{x} \rangle \right) \right] \tag{9.5}$$

(and so for $\mathbf{y}$).[5]

If the relation between $\mathbf{x}$ and $\mathbf{y}$ is not linear:

$$\mathbf{y} = \mathbf{f}(\mathbf{x}), \tag{9.6}$$

the instantaneous rate of change in $\mathbf{y}$ with respect to change in $\mathbf{x}$ replaces the role of T in Eq. (9.2):

$$\mathrm{d}\mathbf{y} = \frac{\partial \mathbf{y}}{\partial \mathbf{x}} \mathrm{d}\mathbf{x} = \begin{bmatrix} \frac{\partial y_1}{\partial x_1} & \cdot & \frac{\partial y_1}{\partial x_M} \\ \vdots & & \vdots \\ \frac{\partial y_N}{\partial x_1} & \cdot & \frac{\partial y_N}{\partial x_M} \end{bmatrix} (\mathbf{x}) \mathrm{d}\mathbf{x} \equiv T(\mathbf{x}) \mathrm{d}\mathbf{x} \approx T\left(\langle \mathbf{x} \rangle \right) \mathrm{d}\mathbf{x} \tag{9.7}$$

and Eq. (9.2) is approximately true as far as the variances of $\mathbf{x}$ are small enough that the slopes $\partial \mathbf{y} / \partial \mathbf{x}$ barely change within the variances.[6] Note that the propagation

[5] For the case of degenerate normal distributions (i.e., $M > L$), $|\Sigma_{\mathbf{x}}|$ and $\Sigma_{\mathbf{x}}^{-1}$ are replaced by the pseudodeterminant and pseudoinverse $\Sigma_{\mathbf{x}}^{+}$ of the VCM, respectively, in Eq. (9.5).

[6] This quasilinearity condition also guarantees that the distribution of $\mathbf{y}$ is approximately normal for normally distributed $\mathbf{x}$.

matrices $T(\langle \mathbf{x} \rangle)$ depend on the center values of measured $\mathbf{x}$ for the nonlinear cases.

From the relations in Eqs. (9.1), (9.2) and (9.7), one can propagate any uncertainties from one set of variables to another. A simple example is a linear combination of two normal random variables:

$$y = ax_1 + bx_2 = \begin{bmatrix} a & b \end{bmatrix} \begin{bmatrix} x_1 \\ x_2 \end{bmatrix} \tag{9.8}$$

gives

$$\sigma_y = \begin{bmatrix} a & b \end{bmatrix} \begin{bmatrix} \sigma_{x_1}^2 & \sigma_{x_1 x_2} \\ \sigma_{x_1 x_2} & \sigma_{x_2}^2 \end{bmatrix} \begin{bmatrix} a \\ b \end{bmatrix} = a^2\sigma_{x_1}^2 + b^2\sigma_{x_2}^2 + 2ab\sigma_{x_1 x_2} \tag{9.9}$$

as well known. For a nonlinear case, the division of two variables:

$$y = x_1/x_2 \tag{9.10a}$$

$$\mathrm{d}y = \begin{bmatrix} \frac{\partial y}{\partial x_1} & \frac{\partial y}{\partial x_2} \end{bmatrix} \begin{bmatrix} \mathrm{d}x_1 & \mathrm{d}x_2 \end{bmatrix} = \underbrace{\begin{bmatrix} \frac{1}{x_2} & -\frac{x_1}{x_2^2} \end{bmatrix}}_{=T(\mathbf{x})} \mathrm{d}\mathbf{x} \tag{9.10b}$$

$$\sigma_y^2 \approx T(\langle \mathbf{x} \rangle) \begin{bmatrix} \sigma_{x_1}^2 & \sigma_{x_1 x_2} \\ \sigma_{x_1 x_2} & \sigma_{x_2}^2 \end{bmatrix} T^{\intercal}(\langle \mathbf{x} \rangle) \tag{9.10c}$$

$$= \frac{1}{\langle x_2 \rangle^2}\sigma_{x_1}^2 + \frac{\langle x_1 \rangle^2}{\langle x_2 \rangle^4}\sigma_{x_1} - \frac{2x_1}{\langle x_2 \rangle^3}\sigma_{x_1 x_2} \tag{9.10d}$$

$$\approx \langle y \rangle^2 \left[\left(\frac{\sigma_{x_1}}{\langle x_1 \rangle} \right)^2 + \left(\frac{\sigma_{x_2}}{\langle x_2 \rangle} \right)^2 - 2\frac{\sigma_{x_1 x_2}}{\langle x_1 \rangle \langle x_2 \rangle} \right] \tag{9.10e}$$

is achieved as expected. In this manner, the uncertainty propagation through various vector operations have been achieved including addition $\mathbf{x}+\mathbf{y}$ and subtraction $\mathbf{x}-\mathbf{y}$; elementwise multiplication $x_i y_i$, division x_i/y_i, and inversion x_i^{-1}; magnitude of a vector $|\mathbf{x}|$; scalar multiplication $c\mathbf{x}$; a vector $\mathbf{x}$ to the unit vector $\mathbf{x}/|\mathbf{x}|$; and inner product $\mathbf{x} \cdot \mathbf{y}$.

Lastly, the uncertainty propagation via two complicated but important operations will be presented, as they are used in the King-plot nonlinearity analysis in Section 8.3.1:

Vector component of x along a

$$\mathbf{y} = \frac{(\mathbf{x}\cdot\mathbf{a})\mathbf{a}}{|\mathbf{a}|^2} \tag{9.11a}$$

$$\mathrm{d}\mathbf{y} = T\begin{bmatrix}\mathrm{d}\mathbf{x}\\ \mathrm{d}\mathbf{a}\end{bmatrix} \tag{9.11b}$$

$$T = \begin{bmatrix}\frac{\partial \mathbf{y}}{\partial \mathbf{x}} & \frac{\partial \mathbf{y}}{\partial \mathbf{a}}\end{bmatrix} = \begin{bmatrix}\frac{1}{|\mathbf{a}|^2}\mathbf{a}\mathbf{a}^\intercal & \frac{1}{|\mathbf{a}|^2}\mathbf{a}\mathbf{x}^\intercal - \frac{2(\mathbf{x}\cdot\mathbf{a})}{|\mathbf{a}|^4}\mathbf{a}\mathbf{a}^\intercal + \frac{(\mathbf{x}\cdot\mathbf{a})}{|\mathbf{a}|^2}I\end{bmatrix} \tag{9.11c}$$

$$\Sigma_{\mathbf{y}} = T\Sigma_{(\mathbf{x},\mathbf{a})}T^\intercal = T\begin{bmatrix}\Sigma_{\mathbf{x}} & \Sigma_{\mathbf{xa}}\\ \Sigma_{\mathbf{ax}} & \Sigma_{\mathbf{a}}\end{bmatrix}T^\intercal \tag{9.11d}$$

where I is an identity matrix and $\Sigma_{\mathbf{xa}} = \Sigma_{\mathbf{ax}}^\intercal$ is the cross-covariance matrix (CCM) between $\mathbf{x}$ and $\mathbf{a}$,[7] which is a zero matrix if $\mathbf{x}$ and $\mathbf{a}$ are independent.

[7] $\Sigma_{\mathbf{xy}} \equiv \langle(\mathbf{x} - \langle\mathbf{x}\rangle)(\mathbf{y} - \langle\mathbf{y}\rangle)^\intercal\rangle$.

Two-vector decomposition of x with a and b

$$\mathbf{x} = \alpha\mathbf{a} + \beta\mathbf{b} \tag{9.12a}$$

$$M \equiv \begin{bmatrix} |\mathbf{a}|^2 & \mathbf{a}\cdot\mathbf{b} \\ \mathbf{a}\cdot\mathbf{b} & |\mathbf{b}|^2 \end{bmatrix}, \quad |M| = |\mathbf{a}|^2|\mathbf{b}|^2 - (\mathbf{a}\cdot\mathbf{b})^2 \tag{9.12b}$$

$$\begin{bmatrix} \alpha \\ \beta \end{bmatrix} = M^{-1} \begin{bmatrix} \mathbf{x}\cdot\mathbf{a} \\ \mathbf{x}\cdot\mathbf{b} \end{bmatrix} = \frac{1}{|M|} \begin{bmatrix} |\mathbf{b}|^2(\mathbf{x}\cdot\mathbf{a}) - (\mathbf{x}\cdot\mathbf{b})(\mathbf{a}\cdot\mathbf{b}) \\ |\mathbf{a}|^2(\mathbf{x}\cdot\mathbf{b}) - (\mathbf{x}\cdot\mathbf{a})(\mathbf{a}\cdot\mathbf{b}) \end{bmatrix} \tag{9.12c}$$

$$\alpha \xleftrightarrow{\mathbf{a}\leftrightarrow\mathbf{b}} \beta \tag{9.12d}$$

$$\begin{bmatrix} \mathrm{d}\alpha \\ \mathrm{d}\beta \end{bmatrix} = \begin{bmatrix} \frac{\partial\alpha}{\partial\mathbf{x}} & \frac{\partial\alpha}{\partial\mathbf{a}} & \frac{\partial\alpha}{\partial\mathbf{b}} \\ \frac{\partial\beta}{\partial\mathbf{x}} & \frac{\partial\beta}{\partial\mathbf{a}} & \frac{\partial\beta}{\partial\mathbf{b}} \end{bmatrix} \begin{bmatrix} \mathrm{d}\mathbf{x} \\ \mathrm{d}\mathbf{a} \\ \mathrm{d}\mathbf{b} \end{bmatrix} = T \begin{bmatrix} \mathrm{d}\mathbf{x} \\ \mathrm{d}\mathbf{a} \\ \mathrm{d}\mathbf{b} \end{bmatrix} \tag{9.12e}$$

$$\frac{\partial\alpha}{\partial\mathbf{x}} = \frac{|\mathbf{b}|^2\mathbf{a} - (\mathbf{a}\cdot\mathbf{b})\mathbf{b}}{|M|} \tag{9.12f}$$

$$\frac{\partial\alpha}{\partial\mathbf{a}} = \frac{|\mathbf{b}|^2\mathbf{x} + (\mathbf{x}\cdot\mathbf{b})\mathbf{b}}{|M|} \tag{9.12g}$$

$$+ \frac{2|\mathbf{b}|^2}{|M|^2}\left[\left\{\left((\mathbf{x}\cdot\mathbf{b})(\mathbf{a}\cdot\mathbf{b}) - |\mathbf{b}|^2(\mathbf{x}\cdot\mathbf{a})\right)\mathbf{a}\right\} + \{\mathbf{a}\leftrightarrow\mathbf{b}\}\right] \tag{9.12h}$$

$$\frac{\partial\alpha}{\partial\mathbf{b}} = \frac{-(\mathbf{a}\cdot\mathbf{b})\mathbf{x} + (\mathbf{x}\cdot\mathbf{b})\mathbf{a}}{|M|} \tag{9.12i}$$

$$+ \frac{2\left[(\mathbf{x}\cdot\mathbf{a})(\mathbf{a}\cdot\mathbf{b}) - |\mathbf{a}|^2(\mathbf{x}\cdot\mathbf{b})\right]}{|M|^2}\left[|\mathbf{b}|^2\mathbf{a} - (\mathbf{a}\cdot\mathbf{b})\mathbf{b}\right] \tag{9.12j}$$

$$\frac{\partial\alpha}{\partial\mathbf{x}} \xleftrightarrow{\mathbf{a}\leftrightarrow\mathbf{b}} \frac{\partial\beta}{\partial\mathbf{x}}, \quad \frac{\partial\alpha}{\partial\mathbf{a}} \xleftrightarrow{\mathbf{a}\leftrightarrow\mathbf{b}} \frac{\partial\beta}{\partial\mathbf{b}}, \quad \frac{\partial\alpha}{\partial\mathbf{b}} \xleftrightarrow{\mathbf{a}\leftrightarrow\mathbf{b}} \frac{\partial\beta}{\partial\mathbf{a}} \tag{9.12k}$$

$$\Sigma_{(\alpha,\beta)} = \begin{bmatrix} \sigma_\alpha^2 & \sigma_{\alpha\beta} \\ \sigma_{\alpha\beta} & \sigma_\beta^2 \end{bmatrix} = T\Sigma_{(\mathbf{x},\mathbf{a},\mathbf{b})}T^\intercal = T \begin{bmatrix} \Sigma_{\mathbf{x}} & \Sigma_{\mathbf{xa}} & \Sigma_{\mathbf{xb}} \\ \Sigma_{\mathbf{ax}} & \Sigma_{\mathbf{a}} & \Sigma_{\mathbf{ab}} \\ \Sigma_{\mathbf{bx}} & \Sigma_{\mathbf{ba}} & \Sigma_{\mathbf{b}} \end{bmatrix} T^\intercal \tag{9.12l}$$

9.2 Errors-in-Variables generalized-least-square fitting

9.2.1 Standard generalized least squares

Suppose that N different observations are made for different values of p independent variables:

$$\mathbf{y} = \begin{bmatrix} y_1 \\ \vdots \\ y_N \end{bmatrix}, \quad X = \begin{bmatrix} \mathbf{x}_1^\intercal \\ \vdots \\ \mathbf{x}_N^\intercal \end{bmatrix} = \begin{bmatrix} x_{11} & \cdots & x_{1p} \\ \vdots & & \vdots \\ x_{N1} & \cdots & x_{Np} \end{bmatrix} \tag{9.13}$$

In the case where the points' positions have uncertainties only in y direction (i.e., dependent variable), finding statistically the most likely solution of a linear function

$$\mathbf{y}_N = X_{N\times p}\,\boldsymbol{\beta}_p \tag{9.14}$$

where $\boldsymbol{\beta} = (\beta_1, \cdots, \beta_p)$, for given uncertainties in the points' positions and the correlations between them (i.e., $\Sigma_{\mathbf{y}}$) is straightforward via the (standard) generalized-least-square (GLS) method; the best fit parameter values $\hat{\boldsymbol{\beta}}$ are given in Eq. (9.18a), with the uncertainties and correlations of the fit parameters $\Sigma_{\hat{\boldsymbol{\beta}}}$ in Eq. (9.18b), and the significance of the fit can be derived from $\hat{\chi}^2$ value from the residuals [Eq. (9.18c)] for the chi-squared distributions with $n - p$ degrees of freedom.

The reasoning behind the GLS is the following. The distribution of the positions of points is the representation of underlying independent standard normal distributions under transformation $A_{\mathbf{y}}$ [see Eq.(9.4)]: $\mathbf{y} = A_{\mathbf{y}}\,\mathbf{z} + \langle\mathbf{y}\rangle$ such that $\Sigma_{\mathbf{y}} = A_{\mathbf{y}} A_{\mathbf{y}}^\intercal$. Therefore, the transformation $X' = A_{\mathbf{y}}^{-1} X$ and $\mathbf{y}' = A_{\mathbf{y}}^{-1}\mathbf{y} = \langle\mathbf{y}'\rangle + \mathbf{z}$ turns the GLS fit

$$\mathbf{y} = X\boldsymbol{\beta} \tag{9.15}$$

into an OLS fit (i.e., $\Sigma_{\mathbf{y}'} = \Sigma_{\mathbf{z}} = I$):

$$\langle\mathbf{y}'\rangle + \mathbf{z} = X'\boldsymbol{\beta} \tag{9.16}$$

of which the solution $\hat{\boldsymbol{\beta}}$ for the minimum χ^2 defined as:[8] [9]

$$\chi^2(\boldsymbol{\beta}) \equiv \mathbf{r}^\intercal(\boldsymbol{\beta})\Sigma_{\mathbf{y}}^{-1}\mathbf{r}(\boldsymbol{\beta}) \tag{9.17}$$

and the significance of the model is known:

$$\hat{\boldsymbol{\beta}} = (X')^{+}\mathbf{y'} = [(X')^\intercal X']^{-1}(X')^\intercal \mathbf{y'} = (X^\intercal \Sigma_{\mathbf{y}}^{-1} X)^{-1} X^\intercal \Sigma_{\mathbf{y}}^{-1}\mathbf{y} \tag{9.18a}$$

$$\Sigma_{\hat{\boldsymbol{\beta}}} = [(X')^\intercal X']^{-1} = (X^\intercal \Sigma_{\mathbf{y}}^{-1} X)^{-1} \tag{9.18b}$$

$$\hat{\chi}^2 = \hat{\mathbf{r}}'^\intercal \hat{\mathbf{r}}' = \hat{\mathbf{r}}^\intercal \Sigma_{\mathbf{y}}^{-1}\hat{\mathbf{r}} \sim \chi^2_\nu \tag{9.18c}$$

where $\hat{\mathbf{r}}$ and $\hat{\mathbf{r}}' = A_{\mathbf{y}}^{-1}\hat{\mathbf{r}}$ are the residuals of points (in y direction) after the best fit $\hat{\boldsymbol{\beta}}$ is achieved in the original coordinate and the coordinate transformed by $A_{\mathbf{y}}^{-1}$, respectively, and χ^2_ν is the chi-squared distribution with $\nu = N - p$ degrees of freedom for N points and p fit parameters.[10]

9.2.2 Propagating x-uncertainties to y-residuals

When the positions of the points have uncertainties along the x direction as well, the (y-)residuals of the points $\mathbf{r}$, defined as the deviations of the points from a given model with parameters $\boldsymbol{\beta}$ along y direction, are not only from the points' distribution along y but also contributed by the distributions of the independent variables x_j

[8] The variable is named chi-squared value because it has the chi-squared distribution; it is somewhat confusing.

[9] The condition of minimum χ^2 gives the model with maximum likelihood with no prior knowledge on the likelihood, in the context of the Bayesian probability.

[10] The degrees of freedom of the fit $\nu = N - p$ reflects that the dimension of distribution in the residuals $\hat{\mathbf{r}}'$ for the best fit $\hat{\boldsymbol{\beta}}$ is reduced by p fitting parameters from the original N-dimensional distribution in the y'-coordinate of the points: $\mathbf{z} = (z_1, \cdots, z_N)$. The best fit's residuals still have normal distribution as $\hat{\mathbf{r}'} = \mathbf{y'} - X'\hat{\boldsymbol{\beta}} = [I - X'[(X')^\intercal X']^{-1}(X')^\intercal]\mathbf{y'} = Q\mathbf{z} + (\text{constant})$ [see Eq. (9.4)], and it can be proved that the sum-squared of the residuals $\hat{\chi}^2 \equiv \hat{\mathbf{r}'}^\intercal \hat{\mathbf{r}'}$ has the chi-squared distribution with the reduced $N - p$ degrees of freedom from $Q^2 = Q$ and $\mathrm{Tr}(Q) = n - p$ (cf. Cochran's theorem).

propagated by the *slopes* β_j:

$$\mathrm{d}\mathbf{r}_N(\boldsymbol{\beta}) = \begin{bmatrix} dr_1 \\ \vdots \\ dr_N \end{bmatrix} = \begin{bmatrix} -\sum_{j=1}^{p} x_{1j}\beta_j + dy_1 \\ \vdots \\ -\sum_{j=1}^{p} x_{Nj}\beta_j + dy_N \end{bmatrix} = -(\mathrm{d}X)_{N\times p}\,\boldsymbol{\beta}_p + \mathrm{d}\mathbf{y}_N \tag{9.19}$$

To describe the VCM of all variables it is convenient to define a column vector for all variables in X and $\mathbf{y}$:

$$(\mathbf{c}_\mathrm{p})_{N(p+1)} \equiv \begin{bmatrix} \mathbf{c}_{\mathrm{p}1}^\intercal & \cdots & \mathbf{c}_{\mathrm{p}N}^\intercal \end{bmatrix}^\intercal \tag{9.20a}$$

$$(\mathbf{c}_{\mathrm{p}\,i})_{p+1} \equiv \begin{bmatrix} \mathbf{x}_i^\intercal & y_i \end{bmatrix}^\intercal = \begin{bmatrix} x_{i1} & \cdots & x_{ip} & y_i \end{bmatrix}^\intercal \tag{9.20b}$$

Then, Eq. (9.19) becomes:

$$\mathrm{d}\mathbf{r}_N(\boldsymbol{\beta}) = \underbrace{\left[\begin{array}{c|c|c} -\boldsymbol{\beta}^\intercal \quad 1 & & \\ \hline & \ddots & \\ \hline & & -\boldsymbol{\beta}^\intercal \quad 1 \end{array}\right]}_{\equiv (B_\mathrm{p})_{N\times N(p+1)} = I_{N\times N}\otimes[-\boldsymbol{\beta}^\intercal\ 1]} \begin{bmatrix} \mathrm{d}\mathbf{c}_{\mathrm{p}1} \\ \vdots \\ \mathrm{d}\mathbf{c}_{\mathrm{p}N} \end{bmatrix} = B_\mathrm{p}(\boldsymbol{\beta})\,\mathrm{d}\mathbf{c}_\mathrm{p} \tag{9.21}$$

If variances of the x and y variables and the correlations between them are known and expressed in the proper order in $\Sigma_{\mathbf{c}_\mathrm{p}}$, propagating them into the residuals $\mathbf{r}$ is straightforward [see Eqs. 9.1 and 9.2]:

$$[\Sigma_\mathbf{r}(\boldsymbol{\beta})]_{N\times N} = [B_\mathrm{p}(\boldsymbol{\beta})]_{N\times N(p+1)}(\Sigma_{\mathbf{c}_\mathrm{p}})_{N(p+1)\times N(p+1)}[B_\mathrm{p}(\boldsymbol{\beta})]^\intercal_{N(p+1)\times N} \tag{9.22}$$

Once the VCM of the residuals $\Sigma_\mathbf{r}$ is obtained, it can be treated in a similar

manner to the standard GLS:

$$\mathbf{r}(\boldsymbol{\beta}) = \mathbf{y} - X\boldsymbol{\beta} \tag{9.23a}$$

$$\hat{\boldsymbol{\beta}} = \underset{\boldsymbol{\beta}}{\operatorname{argmin}}\, \chi^2(\boldsymbol{\beta}) = \underset{\boldsymbol{\beta}}{\operatorname{argmin}}\, [\mathbf{r}^\intercal(\boldsymbol{\beta})\Sigma_{\mathbf{r}}(\boldsymbol{\beta})\mathbf{r}(\boldsymbol{\beta})] \tag{9.23b}$$

$$\hat{\mathbf{r}} = \mathbf{r}(\hat{\boldsymbol{\beta}}) \tag{9.23c}$$

$$\Sigma_{\hat{\boldsymbol{\beta}}} = (X^\intercal \Sigma_{\mathbf{r}}^{-1}(\hat{\boldsymbol{\beta}})X)^{-1} \tag{9.23d}$$

$$\hat{\chi}^2 = \hat{\mathbf{r}}^\intercal \Sigma_{\hat{\boldsymbol{\beta}}} \hat{\mathbf{r}} \sim \chi^2_\nu \tag{9.23e}$$

with $\nu = N - p$. One crucial difference in solving the EiVGLS is that the analytic solutions are not given in general, unlike in Eq. (9.18) for the standard GLS fit, due to the parameter-dependent VCM of residuals $\Sigma_{\mathbf{r}}(\boldsymbol{\beta})$. Therefore the minimum-$\chi^2$ solution in Eq. (9.23b) has to be found numerically in general. Nonetheless, if the uncertainties in points' positions are so small that the slopes $\boldsymbol{\beta}$ barely changes within the uncertainties,[11] which has been exactly the case for King plots, then the analytic expression in Eq. (9.18) works well for EiVGLS as well, with an initial value of $\hat{\boldsymbol{\beta}}_0$ obtained by, e.g., simple ordinary-least-squares (OLS) fit. For better accuracy and consistency check, the $\hat{\boldsymbol{\beta}}_1$ obtained from the analytic solution can be fed back into $\Sigma_{\mathbf{r}}(\hat{\boldsymbol{\beta}}_1)$ and obtain a new analytic solution $\hat{\boldsymbol{\beta}}_2$, and so on (i.e., *iterative* EiVGLS).

9.2.2.1 Variable groupings and conversions

Eqs. (9.20) and (9.21) show the grouping variables for each points i, $\mathbf{x}_i$ and y_i, and then concatenating them into a column vector $\mathbf{c}_{\mathrm{p}}$ (i.e., the subscript p for *pointwise* grouping). An alternative grouping might be preferred in some cases (e.g., correlations between ISs with reduced uncertainties; see Section 6.7), which groups the

[11] e.g., cases that the separations between points are much larger than the uncertainties.

different observations i of the same variables first (i.e., *variablewise* grouping):

$$(\mathbf{c}_\mathrm{v})_{N(p+1)} \equiv \begin{bmatrix} \mathbf{c}_{\mathrm{v}1}^\intercal & \cdots & \mathbf{c}_{\mathrm{v}(p+1)}^\intercal \end{bmatrix}^\intercal \tag{9.24a}$$

$$(\mathbf{c}_{\mathrm{v}\,j})_N \equiv \begin{cases} [x_{1j} & \cdots & x_{Nj}]^\intercal & 1 \le j \le p \\ [y_1 & \cdots & y_N]^\intercal = \mathbf{y} & j = p+1 \end{cases} \tag{9.24b}$$

Then, Eq. (9.19) becomes

$$\begin{aligned} \mathrm{d}\mathbf{r}_N(\boldsymbol{\beta}) &= \underbrace{\left[\begin{array}{ccc|c|ccc|ccc} -\beta_1 & & & & -\beta_p & & & 1 & & \\ & \ddots & & \cdots & & \ddots & & & \ddots & \\ & & -\beta_1 & & & & -\beta_p & & & 1 \end{array}\right]}_{\equiv (B_\mathrm{v})_{N\times N(p+1)} = [-\boldsymbol{\beta}^\intercal \;\; 1] \otimes I_{N\times N}} \begin{bmatrix} \mathrm{d}\mathbf{c}_{\mathrm{v}1} \\ \vdots \\ \mathrm{d}\mathbf{c}_{\mathrm{v}p} \\ \mathrm{d}\mathbf{c}_{\mathrm{v}(p+1)} \end{bmatrix} \\ &= B_\mathrm{v}(\boldsymbol{\beta})\,\mathrm{d}\mathbf{c}_\mathrm{v} \end{aligned} \tag{9.25}$$

and consequently:

$$[\Sigma_\mathbf{r}(\boldsymbol{\beta})]_{N\times N} = [B_\mathrm{v}(\boldsymbol{\beta})]_{N\times N(p+1)} (\Sigma_{\mathbf{c}_\mathrm{v}})_{N(p+1)\times N(p+1)} [B_\mathrm{v}(\boldsymbol{\beta})]^\intercal_{N(p+1)\times N} \tag{9.26}$$

[cf. Eq. (9.22)].

The conversion between the two groupings can be done using *perfect shuffle matrices* $S_{p,q}$, defined as [177, 178]:

$$(S_{p,q})_{pq\times pq} \equiv \begin{bmatrix} I_{pq}(1:q:pq,:) \\ I_{pq}(2:q:pq,:) \\ \vdots \\ I_{pq}(q:q:pq,:) \end{bmatrix} \tag{9.27}$$

where I_{pq} is the identity matrix of size $(pq) \times (pq)$ and $(m:n:l)$ is the well-known colon notation used in MATLAB [each block matrix has the size of $p \times (pq)$]. Then,

the conversions between the groupings are given as:

$$C_\mathrm{v} = T_\mathrm{vp} C_\mathrm{p}, \quad B_\mathrm{v} = B_\mathrm{p} T_\mathrm{pv} \tag{9.28a}$$

$$C_\mathrm{p} = T_\mathrm{pv} C_\mathrm{v}, \quad B_\mathrm{p} = B_\mathrm{v} T_\mathrm{vp} \tag{9.28b}$$

$$T_\mathrm{vp} = S_{N,p+1}, \quad T_\mathrm{pv} = S_{p+1,N} \tag{9.28c}$$

$$T_\mathrm{vp} = T_\mathrm{pv}^\intercal = T_\mathrm{pv}^{-1} \tag{9.28d}$$

as $B \otimes A = S_{k,m}(A_{k\times l} \otimes B_{m\times n})S_{l,n}$ [see Eq. (9.21) and (9.25)].

9.3 Fitting King plot

From Eq. (8.11),

$$\mathbf{y} = \overline{\boldsymbol{\nu}}_\kappa = \begin{bmatrix} \overline{\nu}_\kappa^{168,170} \\ \overline{\nu}_\kappa^{170,172} \\ \overline{\nu}_\kappa^{172,174} \\ \overline{\nu}_\kappa^{174,176} \end{bmatrix}, \quad X = \begin{bmatrix} \mathbf{1} & \overline{\boldsymbol{\mu}} \end{bmatrix} = \begin{bmatrix} 1 & \overline{\mu}^{168,170} \\ 1 & \overline{\mu}^{170,172} \\ 1 & \overline{\mu}^{172,174} \\ 1 & \overline{\mu}^{174,176} \end{bmatrix}, \quad \boldsymbol{\beta} = \begin{bmatrix} f_{\kappa\chi} \\ K_{\kappa\chi} \end{bmatrix} \tag{9.29}$$

with $N = 4$ and $p = 2$ [see Eq. (8.17) for the vector notation of isotope-dependent quantities]. The first step for the EiVGLS fit is to configure the VCM of all variables for the fit, $\boldsymbol{\nu}_\kappa = \boldsymbol{\nu}_\kappa ./ \boldsymbol{\nu}_\chi$ and $\boldsymbol{\mu} = \boldsymbol{\mu} ./ \boldsymbol{\nu}_\chi$ (./ denotes the elementwise division). Here, the relevant measured variables are $\boldsymbol{\nu}_\chi$, $\boldsymbol{\nu}_\kappa$ for the 4 isotopes and $\mathbf{m} = (m^{168}, m^{170}, m^{172}, m^{174}, m^{176})$ for 5 isotopes (see Tables A.1 and A.3). The values and VCM of $\boldsymbol{\mu}$ are obtained by applying elementwise inversion to the masses

($\mathbf{m}^{ei}$) and transform the inverted masses via the propagation matrix (see Section 9.1):

$$\boldsymbol{\mu} = \begin{bmatrix} \mu^{168,170} \\ \mu^{170,172} \\ \mu^{172,174} \\ \mu^{174,176} \end{bmatrix} = \underbrace{\begin{bmatrix} 1 & -1 & 0 & 0 & 0 \\ 0 & 1 & -1 & 0 & 0 \\ 0 & 0 & 1 & -1 & 0 \\ 0 & 0 & 0 & 1 & -1 \end{bmatrix}}_{=T} \begin{bmatrix} 1/m^{168} \\ 1/m^{170} \\ 1/m^{172} \\ 1/m^{174} \\ 1/m^{176} \end{bmatrix} \tag{9.30}$$

$$\Sigma_{\boldsymbol{\mu}} = T\Sigma_{\mathbf{m}^{ei}}T^{\intercal}, \tag{9.31}$$

The values and VCM of each of $\boldsymbol{\nu}_{\chi}$ and $\boldsymbol{\nu}_{\kappa}$ are obtained by improving the ISs's uncertainties from all measured ISs including redundant isotope pairs (see Section 6.7). The propagation matrix from $(\boldsymbol{\mu}, \boldsymbol{\nu}_{\chi}, \boldsymbol{\nu}_{\kappa})$ to $(\overline{\boldsymbol{\mu}}, \overline{\boldsymbol{\nu}}_{\kappa})$ is, then, formed:

$$\mathrm{d}\begin{bmatrix} \overline{\boldsymbol{\mu}} \\ \\ bvec\overline{\nu}_{\kappa} \end{bmatrix}_{8} = \underbrace{\left[\begin{array}{c|c} [T_{./}(\boldsymbol{\mu}, \boldsymbol{\nu}_{\chi})]_{4\times 8} & O_4 \\ \hline O_4 & [T_{./}(\boldsymbol{\nu}_{\kappa}, \boldsymbol{\nu}_{\chi})]_{4\times 8} \end{array}\right]}_{=T_{8\times 12}} \mathrm{d}\begin{bmatrix} \boldsymbol{\mu} \\ \boldsymbol{\nu}_{\chi} \\ \boldsymbol{\nu}_{\kappa} \end{bmatrix}_{12} \tag{9.32}$$

where $T_{./}$ are the propagation matrix for the elementwise divisions (with proper orderings of the matrix elements) (see Section 9.1) and O_4 is the zero matrix of the size 4×4, and the VCM of $(\overline{\boldsymbol{\mu}}, \overline{\boldsymbol{\nu}}_{\kappa})$ is obtained from the the VCMs obtained above:

$$(\Sigma_{(\overline{\boldsymbol{\mu}}, \overline{\boldsymbol{\nu}}_{\kappa})})_{8\times 8} = T\Sigma_{(\boldsymbol{\mu}, \boldsymbol{\nu}_{\chi}, \boldsymbol{\nu}_{\kappa})}T^{\intercal} = T_{8\times 12}\begin{bmatrix} (\Sigma_{\boldsymbol{\mu}})_{4\times 4} & & \\ & (\Sigma_{\boldsymbol{\nu}_{\chi}})_{4\times 4} & \\ & & (\Sigma_{\boldsymbol{\nu}_{\kappa}})_{4\times 4} \end{bmatrix} T_{12\times 8}^{\intercal} \tag{9.33}$$

($\Sigma_{(\boldsymbol{\mu}, \boldsymbol{\nu}_{\chi}, \boldsymbol{\nu}_{\kappa})}$ is block-diagonal as the measured $\boldsymbol{\mu}$, $\boldsymbol{\nu}_{\chi}$, and $\boldsymbol{\nu}_{\kappa}$ would be measured independently in general). The first independent variable in X (i.e., the first column) is constant which cannot have uncertainty or correlation with other variables. There-

fore, the VCM of all variables for the fit is given by:

$$(\Sigma_{\mathbf{c}_v})_{12\times 12} = \begin{bmatrix} O_4 & \\ & [\Sigma_{(\overline{\boldsymbol{\mu}},\overline{\boldsymbol{\nu}}_\kappa)}]_{8\times 8} \end{bmatrix} \tag{9.34}$$

for $\mathbf{c}_v = [\mathbf{1}^\intercal \;\; \overline{\boldsymbol{\mu}}^\intercal \;\; \overline{\boldsymbol{\nu}}_\kappa^\intercal]^\intercal$. The remaining step is performing EiVGLS using Eqs. (9.26) and (9.23).

The best-fit electronic factors $f_{\kappa\chi}$ and $K_{\kappa\chi}$ and the significance of the model (i.e., King linearity) are of the special interest in this thesis. The former is obtained using Eq. (9.23b). The significance is obtained by calculating the $\hat{\chi}^2$ value in Eq. (9.23e) and obtain corresponding p-value for chi-squared distribution χ^2_ν with $\nu = N - p = 2$ degrees of freedom. Standard deviation (σ)-significance is given by the amount of deviation from the center of the standard normal distribution with the corresponding (two-sided) p-value.

9.4 Fitting three-dimensional King plot

For 3D King plots in Eq. (8.24), the fit variables are set to be

$$\mathbf{y} = \overline{\overline{\boldsymbol{\nu}}}_\eta = \begin{bmatrix} \overline{\overline{\nu}}_\eta^{168,170} \\ \overline{\overline{\nu}}_\eta^{170,172} \\ \overline{\overline{\nu}}_\eta^{172,174} \\ \overline{\overline{\nu}}_\eta^{174,176} \end{bmatrix}, \quad X = \begin{bmatrix} \mathbf{1} & \overline{\overline{\boldsymbol{\nu}}}_\chi & \overline{\overline{\boldsymbol{\nu}}}_\kappa \end{bmatrix} = \begin{bmatrix} 1 & \overline{\overline{\nu}}_\chi^{168,170} & \overline{\overline{\nu}}_\kappa^{168,170} \\ 1 & \overline{\overline{\nu}}_\chi^{170,172} & \overline{\overline{\nu}}_\kappa^{170,172} \\ 1 & \overline{\overline{\nu}}_\chi^{172,174} & \overline{\overline{\nu}}_\kappa^{172,174} \\ 1 & \overline{\overline{\nu}}_\chi^{174,176} & \overline{\overline{\nu}}_\kappa^{174,176} \end{bmatrix}, \quad \boldsymbol{\beta} = \begin{bmatrix} K_{\eta\kappa\chi} \\ f_{\eta\kappa\chi} \\ f_{\eta\chi\kappa} \end{bmatrix} \tag{9.35}$$

with $N = 4$ and $p = 3$. The procedure of fitting is straightforward as the extension of the procedure for (2D) King plots in Section 9.3, with an additional measured values $\boldsymbol{\nu}_\eta$ and change in the variable for the normalization from $\boldsymbol{\nu}_\chi$ to $\boldsymbol{\mu}$.

9.5 Drawing and Fitting nonlinearity map

Nonlinearity maps $\boldsymbol{\lambda} = (\lambda_+, \lambda_-)$ introduced in Sections 8.3.1 and 8.3.2 can be fitted with a line that crosses origin $y = (\lambda_-/\lambda_+)\, x$ to test the number of nonlinearity sources as shown in Section 8.3.4. The fit variables are given by, then,

$$\mathbf{y} = \begin{bmatrix} (\lambda_-)_\kappa^{(\tau)} \\ (\lambda_-)_\eta^{(\tau)} \\ \vdots \end{bmatrix}, \quad X = \begin{bmatrix} (\lambda_+)_\kappa^{(\tau)} \\ (\lambda_+)_\eta^{(\tau)} \\ \vdots \end{bmatrix}, \quad \boldsymbol{\beta} = \frac{(\lambda_-)^{(\tau)}}{(\lambda_+)^{(\tau)}}. \tag{9.36}$$

From measured $\boldsymbol{\mu}$, $\boldsymbol{\nu}_\chi$, $\boldsymbol{\nu}_\kappa$, $\boldsymbol{\nu}_\eta$, $\cdots$ with the associated VCMs, $\overline{\boldsymbol{\mu}}$, $\overline{\boldsymbol{\nu}}_\kappa$, $\overline{\boldsymbol{\nu}}_\eta$, $\cdots$ are obtained by propagating uncertainties through elementwise divisions, as in Section 9.3. To obtain the nonlinearity component each of $\overline{\boldsymbol{\nu}}_\kappa$, $\overline{\boldsymbol{\nu}}_\eta$, $\cdots$ (i.e., the vector component that is orthogonal to King plan formed by $\mathbf{1}$ and $\overline{\boldsymbol{\mu}}$; see Section 8.3.1), the vector component along $\mathbf{1}$ is first obtained using Eq. (9.11) and subtracted from the original vector ($\overline{\boldsymbol{\nu}}' = \overline{\boldsymbol{\nu}} - (\overline{\boldsymbol{\nu}} \cdot \mathbf{1})\mathbf{1}/|\mathbf{1}|^2$), and then the vector component along $\overline{\boldsymbol{\mu}}$ is subtracted from $\overline{\boldsymbol{\nu}}'$ in the same manner ($\overline{\boldsymbol{\nu}}_\perp = \overline{\boldsymbol{\nu}}' - (\overline{\boldsymbol{\nu}}' \cdot \overline{\boldsymbol{\mu}})\overline{\boldsymbol{\mu}}/|\overline{\boldsymbol{\mu}}|^2$).[12] It is important to note that the normalization and subtraction procedures have to be done for all $\overline{\boldsymbol{\nu}}$ vectors ($\overline{\boldsymbol{\nu}}_\kappa$, $\overline{\boldsymbol{\mu}}_\eta$, $\cdots$) together to achieve the correlation between the vectors. On the other hand, the nonlinearity vectors $\hat{\boldsymbol{\Lambda}}_\pm^{(\tau)}$ in Eq. (8.20) are constructed from $\overline{\boldsymbol{\mu}}$ through the propagation matrix:

$$\begin{bmatrix} (\boldsymbol{\Lambda}_+)_4 \\ (\boldsymbol{\Lambda}_-)_4 \end{bmatrix} = \left[\begin{array}{cccc} 0 & -1 & 1 & 0 \\ 1 & 0 & 0 & -1 \\ -1 & 0 & 0 & 1 \\ 0 & 1 & -1 & 0 \\ \hline 0 & -1 & 0 & 1 \\ 1 & 0 & -1 & 0 \\ 0 & 1 & 0 & -1 \\ -1 & 0 & 1 & 0 \end{array}\right] (\overline{\boldsymbol{\mu}})_4 \tag{9.37}$$

and then propagate the uncertainties and correlations through the normalization of

[12] The order of the vector-component subtractions is irrelevant.

the vectors $\hat{\mathbf{\Lambda}}_\pm = \mathbf{\Lambda}_\pm/|\mathbf{\Lambda}_\pm|$. Finally, the nonlinear components $\boldsymbol{\lambda}_\kappa^{(\chi)}$, $\boldsymbol{\lambda}_\eta^{(\chi)}$, $\cdots$ are obtained by decomposing $\overline{\boldsymbol{\nu}}_\perp$ obtained above with the $\hat{\mathbf{\Lambda}}_\pm$ using Eq. (9.12).

The rest of work is to perform the EiVGLS fitting using Eqs. (9.26) and (9.23) with the $\boldsymbol{\lambda}$ and their overall VCMs[13] calculated above, and to obtain the common slope $\beta = \lambda_-/\lambda_+$ and the significance of the test (i.e., second source of nonlinearities).

9.5.1 Pattern prediction for nonlinearity source

The predicted pattern of a particular (possible) source of nonlinearity $X_\chi x^{AA'}$ and the corresponding direction $(\lambda_-/\lambda_+)_{\mathbf{x}}$ in the nonlinearity map can be obtained in the same manner, from the associated nuclear factor $\mathbf{x}$: decomposing $\mathbf{x}$ into $\boldsymbol{\lambda}_{\mathbf{x}}^{(\tau)}$ by $\mathbf{\Lambda}_\pm^{(\tau)}$. The *angular* uncertainty in the direction can be obtained from by propagating the VCM of (λ_+, λ_-) to the ratio $\beta = \lambda_-/\lambda_+$ using Eq. (9.10), and then propagate the β's uncertainty through the inverse tangent function, which turns out to be:

$$\theta = \tan^{-1}\beta = \tan^{-1}\frac{\lambda_-}{\lambda_+} \tag{9.38a}$$

$$\mathrm{d}\theta = \frac{1}{1+\beta^2}\mathrm{d}\beta = \frac{[-\lambda_- \quad \lambda_+]}{(\lambda_+)^2+(\lambda_-)^2}\mathrm{d}\begin{bmatrix} x \\ y \end{bmatrix} \tag{9.38b}$$

$$\sigma_\theta^2 \approx \frac{\sigma_\beta^2}{(1+\langle\beta\rangle^2)^2} \approx \frac{\langle\lambda_-\rangle^2\sigma_{\lambda_+}^2 + \langle\lambda_+\rangle\sigma_{\lambda_+}^2 - 2\langle\lambda_+\rangle\langle\lambda_-\rangle\sigma_{\lambda_+\lambda_-}}{|\boldsymbol{\lambda}|^4}. \tag{9.38c}$$

[13] i.e., the VCM of each of $\boldsymbol{\lambda}_\kappa^{(\tau)}$, $\boldsymbol{\lambda}_\eta^{(\tau)}$, $\cdots$ and the CCM between them.

Chapter 10

Results

In this chapter, the results of the King-plot analyses introduced in Chapters 8 and 9 for the isotope shifts (ISs) measured in Part II are presented. In short, King nonlinearities have been observed with very high significance (240σ), and 4.3σ evidence that there are at least two sources of the King nonlinearities (A dominant source and small additional contributions) in Yb^+/Yb transitions has been obtained. The various discussions including the possible physical origin of the sources follow in Chapter 11.

10.1 King plots and nonlinearities

Following Section 9.3, the values and variance-covariance matrix (VCM) for all relevant variables are obtained from the measured quantities to draw King plots. The inverse-mass differences $\mu^{AA'}$ are obtained from the known atomic masses m^A of Yb^+ isotopes from atomic mass spectroscopy [6, 7, 20, 26], listed in Tables A.2 and A.3. The values of $\nu_\chi^{AA'}$ for different transitions χ with improved precisions in Table A.2 are obtained from the isotope shifts (ISs) measured in Part II, listed in Table A.1, including redundant isotope pairs (see Section 6.7). Frequency-normalized King plots $(\overline{\mu}, \overline{\nu}_\kappa^{AA'})$ normalized by $\nu_\tau^{AA'}$ for a reference transition τ (see Eq. 8.15, Sections 8.3.4 and 11.3) are obtained subsequently, and the points in each King plot are fitted with the EiVGLS method described in Section 9.2.

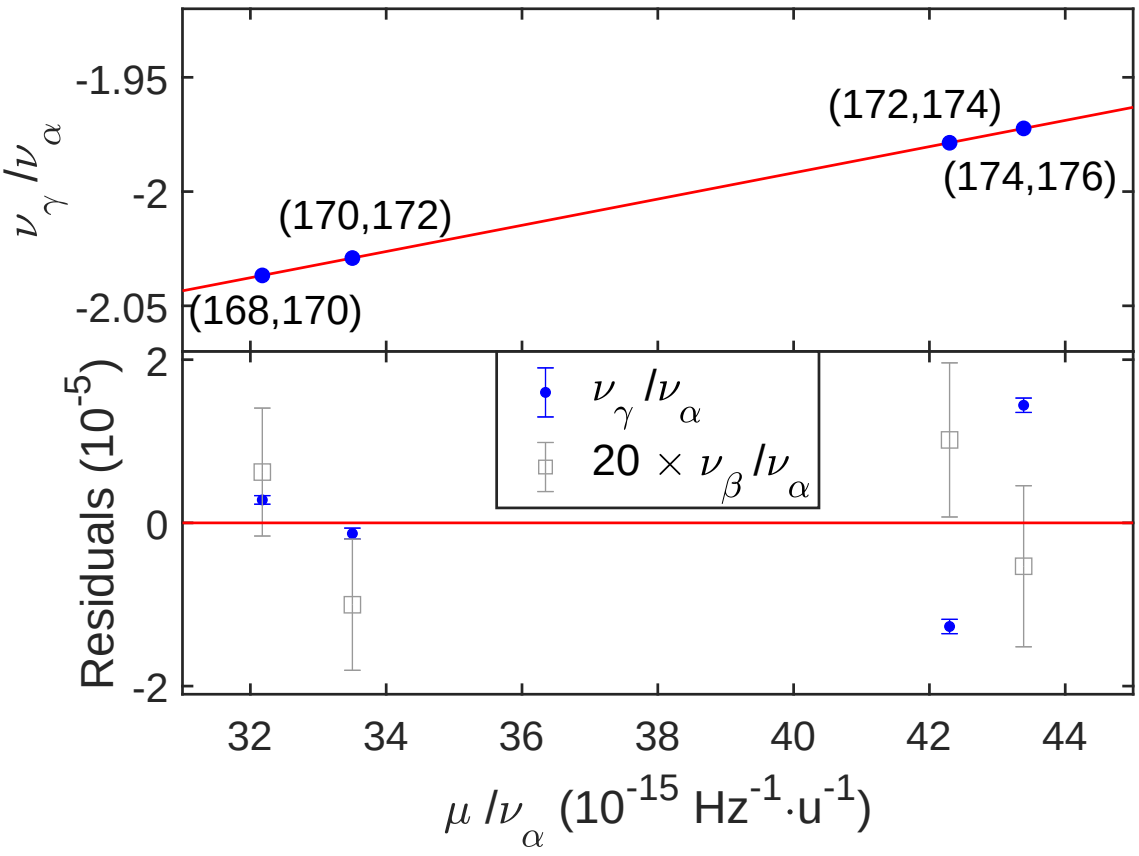

Figure 10-1: Frequency-normalized King plot [top; see Eq. (8.15)] and residuals (bottom, blue) for the γ: $^2S_{1/2} \to {}^2F_{7/2}$ (467 nm) transition and reference transition α: $^2S_{1/2} \to {}^2D_{5/2}$ (411 nm) for nearest-neighboring even-A pairs ($A' = A+2$) of Yb^+ isotopes from the measured ISs values in Table A.2, fitted using EiVGLS method (see Section 9.2), in Ref. [8]. A deviation from linearity (red line) by 41 standard deviations σ is observed. For reference, residuals for the β : $^2S_{1/2} \to {}^2D_{3/2}$ (436 nm) transition, magnified 20-fold, are also plotted in gray, which has 3σ nonlinearity [see Fig. 8-1(b)]. The error bars indicate 2σ uncertainties; for correlations between the errors, see Table A.2. The results of the fits (slopes, y-intercepts, and significance) for all different pairs of transitions (see Fig. 10-2) can be found in Table C.4.

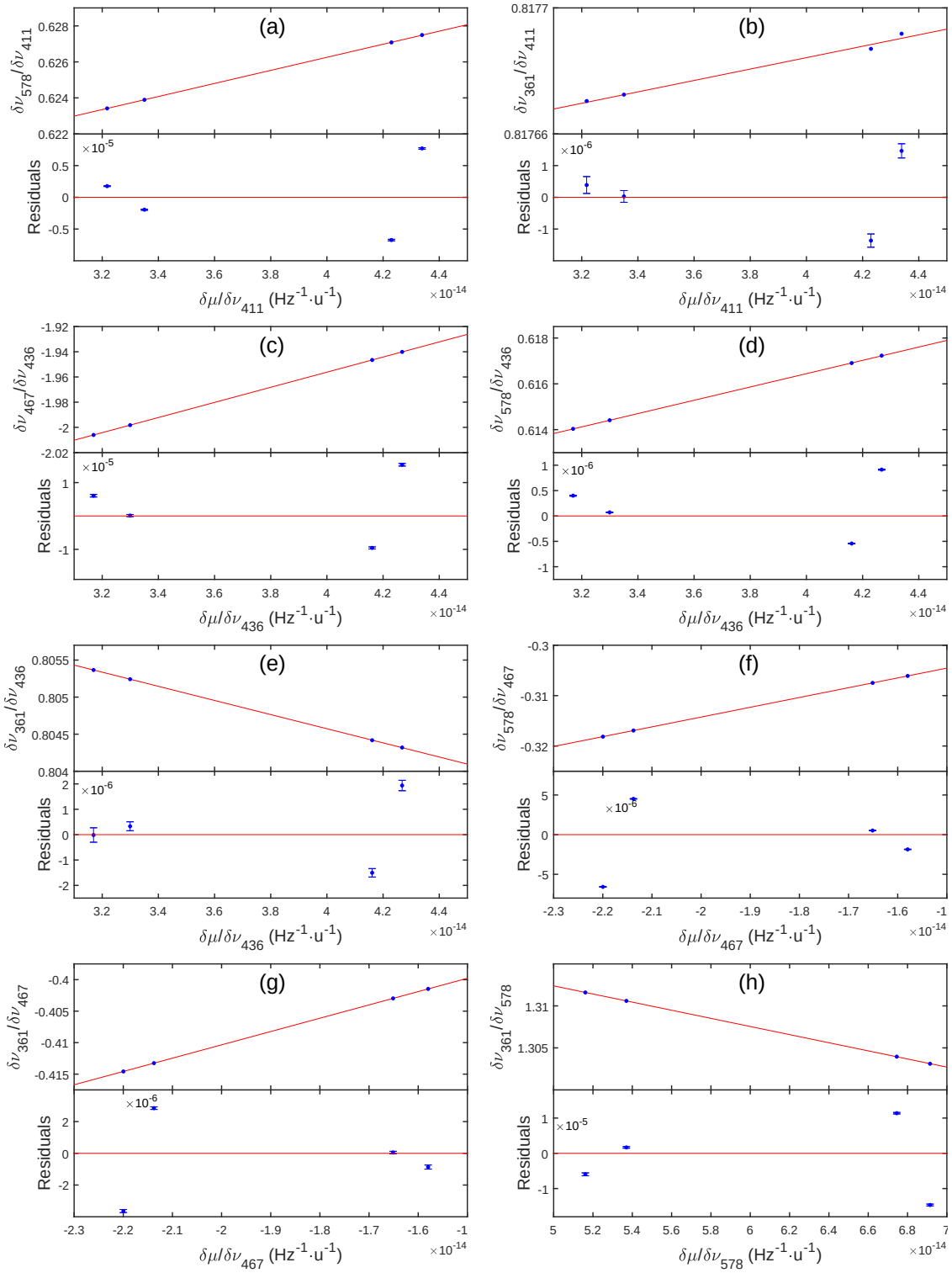

Figure 10-2: King plots for transition pairs not shown in Fig. 10-1: (a) (α, δ), (b) (α, ϵ), (c) (β, γ), (d) (β, δ), (e) (β, ϵ), (f) (γ, δ), (g) (γ, ϵ), and (h) (δ, ϵ) transition pairs. δ: $^1S_0 \rightarrow {}^3P_0$ (578 nm) and ϵ: $^1S_0 \rightarrow {}^1D_2$ (361 nm) are the optical transitions in neutral Yb atoms. See the caption in Fig. 10-1 for other details. All relevant data can be found in Table A.2.

Figure 10-1 shows a frequency-normalized King plot for the recently measured γ: 467 nm ($^2S_{1/2} \rightarrow {}^2F_{7/2}$) optical clock transition in Yb^+ ions, with α: 411 nm ($^2S_{1/2} \rightarrow {}^2D_{5/2}$) transition measured in earlier thesis work [5] as the reference transition τ. The residuals from the linear fit reveal a nonlinearity at the 10^{-5} level, corresponding to the significance of 41 standard deviations σ, confirming the *observation* of King-plot nonlinearity.

For comparison, the residuals in the King plot for β: 436 nm ($^2S_{1/2} \rightarrow {}^2D_{3/2}$) transition measured earlier in this work [4, 5] are also presented in Fig. 10-1 [see also Fig. 8-1(b)], which show only 3σ *evidence* of the nonlinearity. The nonlinearity for γ transitions is observed to be bigger, as expected from the bigger sensitivity of γ to nonlinearity sources compared to the very similar (α, β) transition pairs (see Sections 3.1.2, 10.2, and Table C.4), by a factor of 20. Furthermore, the two β and γ transitions (referenced with the third α transition) show different shapes of the nonlinearity patterns: a zigzag pattern for the β transition while a curved shape for the γ transition. The pattern shapes are further investigated in the following Section 10.2. The results of the linear fits (slopes, y-intercepts, and significance) are listed in Table C.4.

Very recently, measured ISs for optical transitions in neutral Yb atoms have been also reported: δ: 578 nm ($^1S_0 \rightarrow {}^3P_0$) [10] and ϵ: 361 nm ($^1S_0 \rightarrow {}^1D_2$) [9]. Accordingly, the King plots and their significance of nonlinearity for all different possible pairs between the α, β, and γ transitions in Yb^+ ions measured in this work; and the δ and ϵ transitions in Yb atoms have been investigated as shown in Fig. 10-2.[1] In particular, the pair of the γ transition in Yb^+, the latest work in this thesis, and the δ transition in Yb with the highest precision reported for Yb^+/Yb ($\lesssim$3 Hz; see Table A.2) shows the King nonlinearity with the highest significant, 240σ, among all the transition pairs (see Table C.4).

[1]The transitions in the ions and neutral atoms can be paired for the King plots as they share the same nuclei; recall the factorization of ISs to electronic and nuclear factors as described in Section 8.1.4

10.2 Pattern analysis with nonlinearity maps

The nonlinear components $\boldsymbol{\lambda}_{\kappa}^{(\tau)} = \left((\lambda_{+})_{\kappa}^{(\tau)}, (\lambda_{-})_{\kappa}^{(\tau)}\right)$ in the ISs $\overline{\boldsymbol{\nu}}_{\kappa}$ in the different transitions κ referenced to a transition τ are calculated and mapped onto nonlinearity maps as described in Sections 8.3.1, 8.3.2, and 9.5.

Figure 10-3 shows the nonlinearity map $\boldsymbol{\lambda}_{\kappa}^{(\delta)}$ for all the available transitions, $\kappa = \alpha$, β, γ (in Yb^{+}), and ϵ (in Yb), referenced to δ transition (in Yb). δ transition is chosen in this figure as the reference because the measured ISs for the transition have much smaller uncertainties than the ISs for other transitions (see Table A.2), letting the points in the map are barely correlated with each other.

The γ transition paired with the δ transition indeed shows the furthest deviation from the origin relative to the point's uncertainty (the size of the ellipse), reflecting the highest significance of the King nonlinearity (see Section 10.1). It also shows the good agreement of the lasted measurements in this thesis work to the preliminary measurements in Ref. [4] (red filled ellipse vs dotted ellipse).

One of the crucial results derived from this nonlinearity map is from the observation that all of the points from the different transitions have almost parallel directions from the origin. It implies that there is a dominant, common source of the nonlinearity, of which the associated nuclear factor determines the direction (see Section 8.3.3). Note also that the choice of ionized or neutral species is relevant only to the scale of the nonlinearity (i.e., the distance of the points from the origin) but not to the direction, allowing the comparison of Yb^{+} and Yb under the same basis.

The observed common direction is compared with the directions predicted by several possible contributions as described in Section 8.3.3. In particular, the pattern shapes of the two of such sources can be accurately calculated. The new boson, introduced in Section 1.1.1 as the new physics to probe, has the neutron number difference $a^{AA'} = A - A'$ between the nuclei of the ^{A}Yb and ${}^{A'}$Yb isotopes (see Section 8.2.1), as the associated nuclear factor. Therefore, the directions from the origin in nonlinearity maps are calculated from $a^{AA'}$, following the method in Section 9.5.1. The uncertainty in the predicted direction is from the accurately measured $\boldsymbol{\nu}_{\delta}$ for

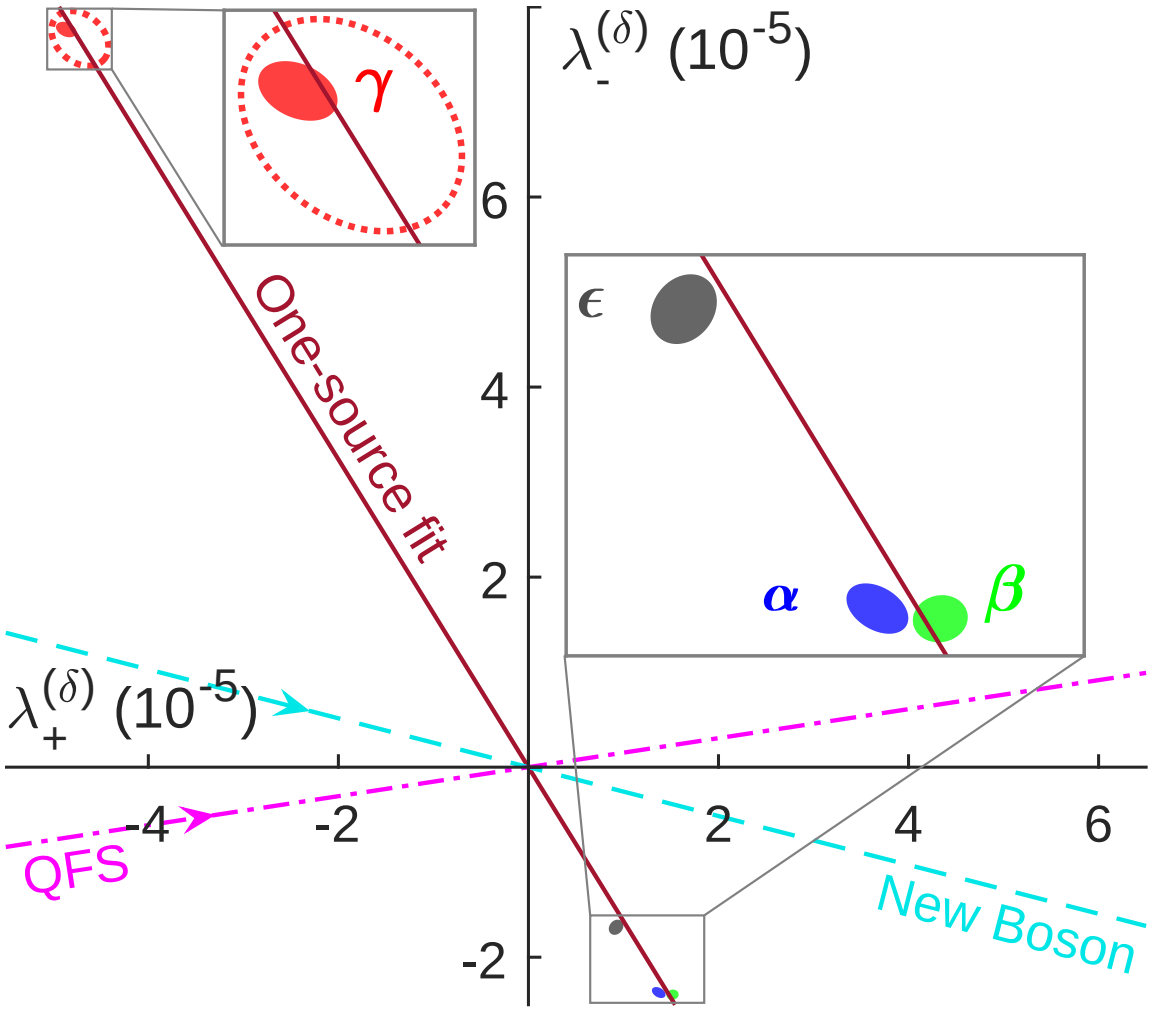

Figure 10-3: Decomposition of the measured nonlinearity onto the (λ_+, λ_-) basis (solid ellipses, 95 % confidence interval; see Section 8.3.1) for the transitions α : $^2S_{1/2} \rightarrow {}^2D_{5/2}$ (blue), β : $^2S_{1/2} \rightarrow {}^2D_{3/2}$ (green), and γ : $^2S_{1/2} \rightarrow {}^2F_{7/2}$ (red) in Yb^+ ions (see Fig. 3-1); and ϵ : $^1S_0 \rightarrow {}^1D_2$ (dark gray) in Yb atoms [9], in Ref. [8]. The corresponding frequency-normalized King plot [Eq. (8.15)] is generated with the reference transition δ : $^1S_0 \rightarrow {}^3P_0$ in Yb atoms [10] ($\lambda_\pm^{(\delta)}$), for which the isotope shifts have been measured with the highest precision (see Table A.2). The dotted ellipse indicates a preliminary measurement for the γ transition [4]. The dashed lines indicate the ratio λ_+/λ_- that would arise solely from a new boson (light blue dashed) or the QFS (pink dash-dotted) (see Section 8.3.3). The arrows indicate the direction in which a given nonlinearity changes with increasing value of its associated electronic factor (i.e. $D_{\kappa\delta}$ or $G^{(2)}_{\kappa\delta}$). The brown solid line is a single-source fit to all four transitions α, β, γ, and ϵ, yielding evidence for a second nonlinearity source with 4.3σ significance ($\hat{\chi}^2 = 25.4$). The nonlinearity maps for other choices of reference transition can be found in Figs. 10-4 and 10-5.

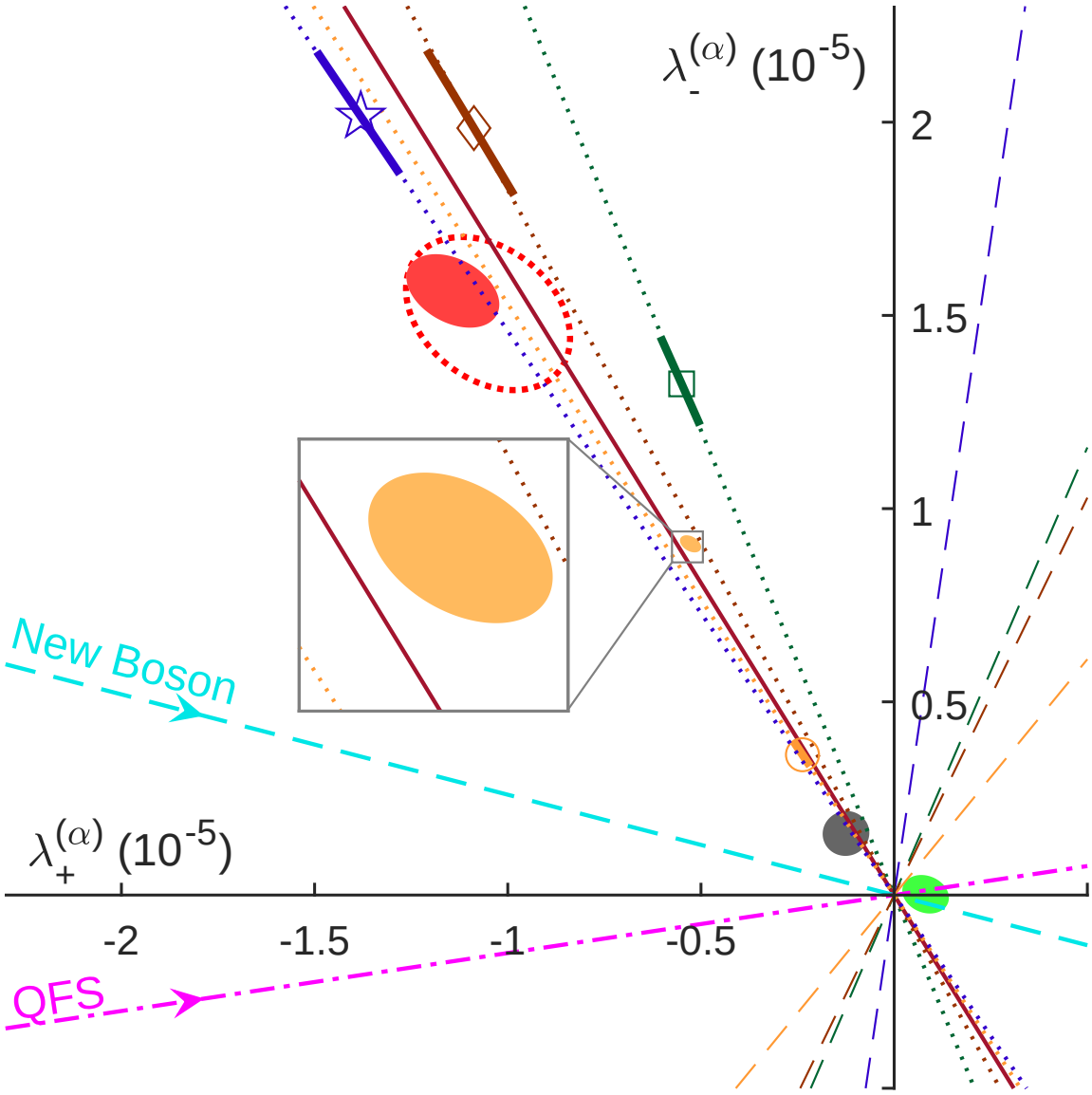

Figure 10-4: Nonlinearity maps $(\lambda_+^{(\alpha)}, \lambda_-^{(\alpha)})$ with the reference transition α. Open symbols indicate the nonlinearity due to $\langle r^4 \rangle^{AA'}$ from nuclear DFT calculations with SV-min (square), RD-min (diamond), UNEDF1 (circle), and Fy(Δr) (star) energy density functionals (see Section 11.1.1). Thick solid lines across the open symbols indicate the uncertainty in atomic structure calculations (see Section 11.1.1.1). The thin dashed lines with the colors matched to the open symbols show the corresponding predicted directions of $\boldsymbol{\lambda}^{(\alpha)}$ when the calculated $\langle r^4 \rangle^{AA'}$ are normalized by the measured isotope shifts $\nu_\alpha^{AA'}$ (see Section 11.1.1.1). The yellow solid ellipse indicates the 95 % confidence interval for $\delta : {}^1S_0 \rightarrow {}^3P_0$ transition in Yb atoms [10]. The correlations between the ellipses are not displayed. See the caption in Fig. 10-3 for other details.

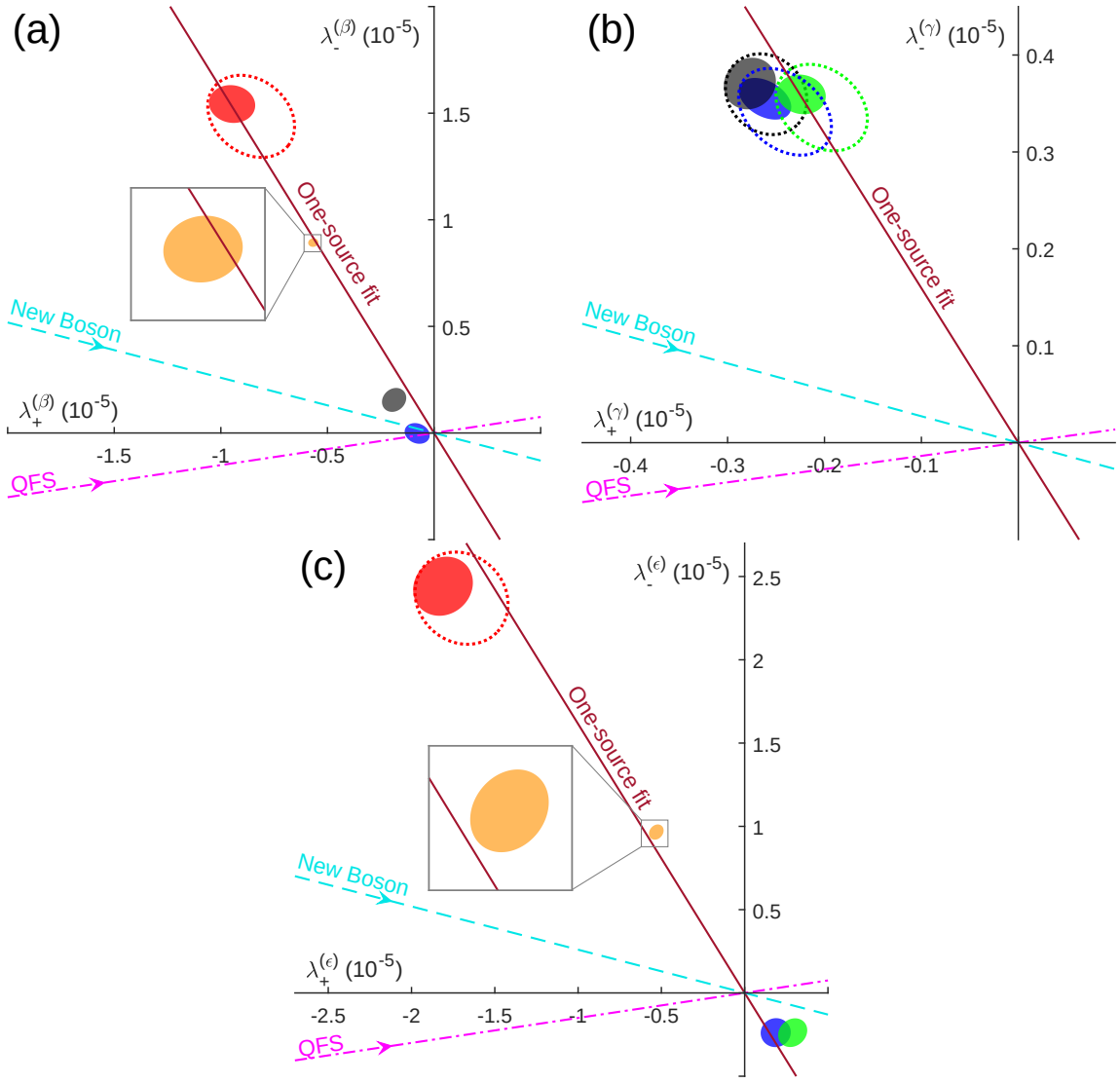

Figure 10-5: Nonlinearity maps $(\lambda_+^{(\tau)}, \lambda_-^{(\tau)})$ with reference transitions τ not shown in Figs 10-3 or 10-4: (a) $\tau = \beta$, (b) γ, and (c) ϵ. The yellow solid ellipse indicates the 95 % confidence interval for $\delta : {}^1S_0 \rightarrow {}^3P_0$ transition in Yb atoms [10]. The correlations between the ellipses are not displayed. See the caption in Fig. 10-3 for other details.

the normalization, as **a** are a vector of integers, giving negligible angular uncertainty ($10^{-4}\,^\circ$). The resulting direction is shown as a light blue dashed line in Fig. 10-3.

The same calculation is carried out for the quadratic field shift (QFS) from the associated nuclear factor $[\langle r^2\rangle^2]^{AA'}$ (see Section 8.2.2), of which the shape of the nonlinearity pattern (i.e., the ratio of the values between different isotope) is accurately given [see Section 11.2.1 and Fig. 11-2(b)] and the result is shown as a pink dash-dotted line in Fig. 10-3. The angular uncertainty is negligible again: $\sim 10^{-5}\,^\circ$.

However, the common direction across all the transitions does not agree with either of the predicted directions for the new boson or QFS. The combination of significant sizable nonlinearity from both contributions would reach the measured nonlinearities in principle, but such sizes of the effects are not consistent with the calculated values of $G^{(2)}$ (in Table C.4) or bounds on new-boson couplings $y_e y_n$ from other experiments (see Figs. 11-1 and 1-2).

The origin of the common nonlinearity source has recently been suggested to be the fourth-order field shift (FFS) with the associated nuclear factor $\langle r^4\rangle^{AA'}$, which essentially captures the details in the shapes of charge distributions inside nuclei. To investigate the contribution of the effect to the King nonlinearities, nuclear density functional theory (DFT) calculations were performed by research collaborators Witold Nazarewicz and Paul-Gerhard Reinhard [8], as elaborated in Section 11.1.1.

On the other hand, the existence of second nonlinearity source is tested by fitting the points with a line that crosses the origin in the nonlinearity map (see Sections 8.3.4 and 9.5). In Fig. 10-3, the points from different transitions are noticeably deviated from the brown solid fit line, giving 4.3σ evidence of a small, second source of the nonlinearities. Note that the different choices of the reference transition (shown in Figs. 10-4 and 10-5) are irrelevant to the calculated significance, showing that the uncertainties along the x and y directions and the correlations between coordinates and points are well taken into account by the EiVGLS fit developed in Section 9.2.

Although the significance has not been reached to the criterion for observation, 5σ with corresponding p-value of 3×10^{-7}, it is of high significance with $p = 1.7 \times 10^{-5}$. In contrast, the two-source significant is only 3σ ($p = 0.003$) for only α, β, and

γ transitions in Yb^+ measured in this work, shown in Fig. 10-4. As proved in Section 11.4, it is equivalent to the significance of the plane fit in the corresponding 3D King plot (see Section 8.4 and 9.4) for the three transitions, shown in Fig. 10-6. Furthermore, none of the possible groups of three transitions out of the α to ϵ transitions gives the two-source significances above 4σ (see Table C.5). The 4.3σ significance is indeed a joint effect of all the 5 transitions' ISs that have been timely measured.

The possible physical origin of the dominant common component and the small second source of the observed nonlinearities is discussed in Section 11.1.

As the last remark, Figure 10-4 highlights the higher sensitivity of the γ transition (red solid ellipse) to the King nonlinearity compared to the β transition (green solid ellipse) when the transitions are referenced to the α transition. The size of the nonlinearity $\boldsymbol{\lambda}_{\beta}^{(\alpha)}$, from the earlier IS measurements in this work, was comparable to the uncertainty in the $\boldsymbol{\lambda}_{\beta}^{(\alpha)}$ (i.e., the deviation of the green ellipse from the origin in Fig. 10-4 are comparable to the size of the ellipse; see also Fig. 8-2), limiting the angular resolution to resolve the predicted lines for different nonlinearity sources. While improving the precision of the IS spectroscopy is one way to improve the resolution, measuring King nonlinearities with bigger sizes is another way for a given level of precision. In this work, the uncertainties in the measured ISs for γ transition ($\sim$500 Hz) were similar to, or slightly worse than, the uncertainties for α and β transitions ($\sim$300 Hz). Nevertheless, the recently measured γ transition has provided much better angular resolution due to the bigger size of the nonlinearity observed. The higher sensitivity of γ transition is partly due to the bigger change in the electronic wavefunction during the transitions, as pointed out in Section 3.1.2. Another, possibly more significant reason is the high similarity in α and β transitions' wavefunctions. The transitions start from the same ground state $^2S_{1/2}$, and thus all the difference in the wavefunctions comes from the excited states $^2D_{5/2}$ and $^2D_{3/2}$, respectively, which have the same electron configuration $5d$. Therefore, the radial wavefunctions of the two excited states are identical in the nonrelativistic limit,[2] and

[2]The significant energy difference of the two excited states (i.e., different wavelengths of the

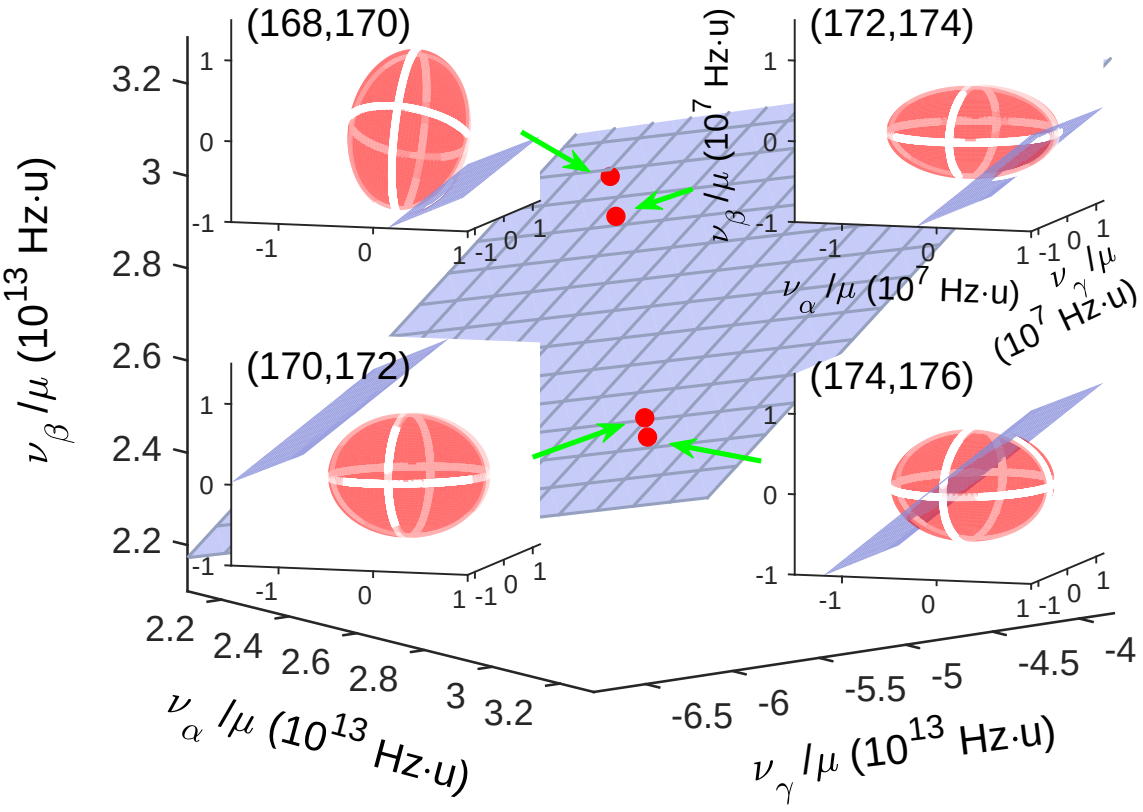

Figure 10-6: Plane fitted to a 3D inverse-mass-normalized King plot constructed from isotope shifts measured for the $\alpha : {}^2S_{1/2} \rightarrow {}^2D_{5/2}$ (411 nm), $\beta : {}^2S_{1/2} \rightarrow {}^2D_{3/2}$ (436 nm), and $\gamma : {}^2S_{1/2} \rightarrow {}^2F_{7/2}$ (467 nm) transitions for nearest-neighboring pairs of even-A Yb^+ isotopes, as described by Eq. (8.24). Insets display a magnified view of each point to show deviation from the fitted plane. The origin of the inset axes has been set to the center of each point. The red ellipsoids depict 1σ confidence intervals of the data. The fit to the plane gives 3.2σ significance of nonlinearity (see Table C.5). Each point in the King plot is correlated with other points (see Table A.2).

the small difference in the wavefunctions are solely from the relativistic effect (i.e., the difference in Dirac wavefunctions for different J's). As a consequence, comparing the two very similar transitions in the King plot has low sensitivity to any effects that are to be probed through the coupling to the electronic wavefunctions.

transitions 411 nm vs 436 nm) comes from the different alignments of the angular momenta (i.e., spin-orbit coupling) to form different total angular momenta $J = \frac{5}{2}$ vs $\frac{3}{2}$.

Chapter 11

Discussion

11.1 Possible Sources of observed nonlinearities

This section discusses the possible sources of the observed nonlinearities in Chapter 10. In short, the fourth-order field shift (FFS) $G^{(4)}\langle r^4\rangle^{AA'}$ is suggested as the common, dominant nonlinearity source, the quadratic field shift (QFS) $G^{(2)}[\langle r^2\rangle^2]^{AA'}$ is rejected as the small, second source, and the bound on the new-boson coupling $y_e y_n$ is obtained by assuming the new boson as the second source, using new-boson electronic factor D calculated in Part IV (see Section 8.2 for the definitions of the shifts and the associated electronic and nuclear factors), as described in the following subsections in detail.

11.1.1 Fourth-moment field shift $G^{(4)}\langle r^4\rangle$

To investigate the possibility of other SM contributions as the sources of the King nonlinearity, calculations on the nuclear structures have been performed by research collaborators Witold Nazarewicz and Paul-Gerhard Reinhard [8]. In particular, the difference in fourth-order nuclear charge distribution $\langle r^4\rangle^{AA'}$ had been once believed to be highly correlated with $[\langle r^2\rangle^2]^{AA'}$ and thus be a part of QFS [5], assuming the *shape* of nuclear charge distribution does not change while more neutrons are added in a nucleus. However, Ref. [179] pointed out that the FFS might have dominated

the observed nonlinearity by then (the zigzag-pattern nonlinearity in Fig. 8-1) due to the deformation in the nuclear charge distribution, which would have served as another degree of freedom for the charge distributions' shapes.

To investigate the effect of $\langle r^4 \rangle^{AA'}$, quantified nuclear calculations for each isotope were performed by the collaborators using nuclear density functional theory (DFT) with realistic energy density functionals (EDFs). While the details of the calculations performed for this work can be found in Ref. [8], the crucial feature of the calculations was that the nuclear charge radial moments including $\langle r^2 \rangle^A$ and $\langle r^4 \rangle^A$ were obtained directly from the calculated nuclear charge densities $\rho_N(\mathbf{r})$ [180, 181]. Using the values of $\langle r^2 \rangle^A$ and $\langle r^4 \rangle^A$ (which can be found in the Supplemental Material of Ref. [8]), the nonlinearity component in $\langle r^4 \rangle^A$ was calculated carefully as described in Section 11.1.1.1.

On the other hand, the associated two-transition electronic factor $G^{(4)}_{\kappa\chi} = G^{(4)}_{\kappa} - f_{\kappa\chi} G^{(4)}_{\chi}$ (see Section 8.2) was calculated by the thesis author, by performing atomic structure calculations (ASCs) as described in Part IV. α: 411 nm and γ: 467 nm transition pair in Yb^+ ions were chosen for the reliable calculation of two-transition electronic factors (see Section 16.3). The calculated $G^{(4)}_{\gamma\alpha}$ value was multiplied by the calculated $\langle r^4 \rangle^{AA'}$ to obtain the the predicted nonlinearity for the FFS $G^{(4)}_{\gamma\alpha} \langle r^4 \rangle^{AA'}$.

Figure 10-4 shows the predicted nonlinearity patterns mapped onto the corresponding α transition-referenced nonlinearity map $\boldsymbol{\lambda}^{(\alpha)}$. To explore a possible span of predictions, four different EDFs were used in the nuclear DFT calculations: Skyrme functionals SV-min and UNEDF1, extended Skyrme functional RD-min, and the Fayans functional Fy(Δr). While all the predicted directions from the calculations (dotted lines) are consistent with the direction of the points from measured ISs (solid ellipses), the Fy(Δr) functional's prediction supports the FFS particularly well as the dominant nonlinearity source; it is the only functional of which predicted direction agrees to the measured $\boldsymbol{\lambda}^{(\alpha)}_{\gamma}$ (red solid ellipse) within the 95 % confidence interval. It also predicts the size of $\boldsymbol{\lambda}^{(\alpha)}_{\gamma}$ reasonably well, and the less accuracy on the magnitude could be from the limited accuracy of the ASC for the γ transition performed in this work (see Section 14.5). The better reliability of Fy(Δr) functional is also supported

by comparisons with other types of experimental data including nuclear deformation from the measured nuclear transitions probabilities [182] (see Fig. S13 in the Supplementary Material of Ref. [8]) and the ratio of nuclear charge radius differences $\langle r^2\rangle^{AA'}$ obtained from the measured ISs in this work (see Section 11.2.1).

The predicted values of $\langle r^2\rangle^A$ and $\langle r^4\rangle^A$ are impacted by several effects [180, 181, 183, 184], including the neutron skin thickness; intrinsic nucleon form factors; and nuclear deformation and pairing effects, spin-orbit contributions, all of which could be taken into account in the collaborators' DFT calculations. In this respect, the nonlinearity from FFS may be rooted in several different nuclear structure effects impacting nuclear charge moments $\langle r^n\rangle^A$, not just one as discussed in Ref. [179].

11.1.1.1 Predicting nonlinearity pattern shape from calculated nuclear charge distributions $\rho_N(r)$

Caution is necessary when deriving nonlinearity patterns associated to higher-order charge moments $\langle r^n\rangle^{AA'}$ ($n > 2$) from nuclear calculations. As $\langle r^n\rangle^{AA'}$ of different n are obtained from the same nuclear charge distribution difference $\rho_N^{AA'}(\mathbf{r})$ from the nuclear calculations, and thus the $\langle r^n\rangle^{AA'}$ are highly correlated with each other. Since the (linear) field shifts (FSs), which are proportional to $\langle r^2\rangle^{AA'}$, are the dominant sources of total ISs for Yb^+/Yb, *calculated* ISs using $\langle r^2\rangle^{AA'}$ the from nuclear calculations should be used to ensure self-consistency in the derivation of King nonlinearities from $\langle r^n\rangle^{AA'}$. It is especially important when the calculated $\langle r^2\rangle^{AA'}$ do not reflect the actual, experimentally determined pattern of ISs [see Fig. 11-2(a)], because the positions of the points in the King plot will be different, which changes the nonlinearity pattern significantly.

$G_{\gamma\alpha}^{(4)}\overline{\langle r^4\rangle}_{\perp}^{AA'}$, the nonlinearity from $\langle r^4\rangle^{AA'}$, is given as the component of the vector

$$\begin{aligned} G_{\gamma\alpha}^{(4)}\overline{\langle r^4\rangle}^{AA'} &= G_{\gamma\alpha}^{(4)}\frac{\langle r^4\rangle^{AA'}}{\nu_\alpha^{AA'}} \\ &= \frac{G_{\gamma\alpha}^{(4)}}{F_\alpha}\frac{\langle r^4\rangle^{AA'}}{\langle r^2\rangle^{AA'} + \frac{K_\alpha}{F_\alpha}\mu^{AA'} + \frac{G_\alpha^{(4)}}{F_\alpha}\langle r^4\rangle^{AA'}} \end{aligned} \tag{11.1}$$

which is orthogonal to **1** and

$$\overline{\mu}^{AA'} \propto \frac{\mu^{AA'}}{\langle r^2 \rangle^{AA'} + \frac{K_\alpha}{F_\alpha}\mu^{AA'} + \frac{G_\alpha^{(4)}}{F_\alpha}\langle r^4 \rangle^{AA'}} \tag{11.2}$$

(see Section 8.3.1 for the vector notation). One can see that the nonlinearity arises mainly from the difference in $\langle r^2 \rangle^{AA'}$ and $\langle r^4 \rangle^{AA'}$'s patterns, and it is thus important to use not only $\langle r^4 \rangle^{AA'}$ from nuclear calculations, but also $\langle r^2 \rangle^{AA'}$ from the same nuclear calculations for self-consistency.

Figure 10-4 clearly confirms the above argument. The predicted nonlinearities from the normalization with the calculated IS $\nu_\alpha^{AA'}$ using Eqs. (11.1) and (11.2) (dotted lines) agree well with the measured nonlinearity, despite the significant difference in the measured and calculated $\langle r^2 \rangle$'s distribution as shown in Fig. 11-2. In contrary, the normalization with the measured $\nu_\alpha^{AA'}$ in Table A.2 (thin dashed lines) results in a significantly different $\lambda_-^{(\alpha)}/\lambda_+^{(\alpha)}$ ratio from the observed nonlinearity.

While $\langle r^2 \rangle^{AA'}$ and $\langle r^4 \rangle^{AA'}$ largely determine the shape of nonlinearity pattern, the change in the ratio K_α/F_α and $G_\alpha^{(4)}/F_\alpha$ in Eqs. (11.1) and (11.2) can affect the predicted shape. In Fig. 10-4, the thick solid lines across the open symbols show the change in $\lambda_\pm^{(\alpha)}$ when $G_\alpha^{(4)}/F_\alpha$ ratio changes by $\pm 50\%$ of the calculated value. Changing K_α in between -2604.4 GHz·u and +174.2 GHz·u, which covers three times the difference in K_α values for the different atomic structure calculations (ASCs), GRASP2018 and AMBiT (see Table C.3), moves $\lambda_\pm^{(\alpha)}$ points along the solid lines by smaller amounts. Interestingly, it is observed in Fig. 10-4 that the change in the K_α/F_α or $G_\alpha^{(4)}/F_\alpha$ ratios in Eq. (11.1) merely scales the size of the nonlinearities $\boldsymbol{\lambda}^{(\alpha)}$ along the λ_-/λ_+ ratio lines [i.e., the thick solid lines are almost parallel to the corresponding dotted lines], just as the change in $G_{\gamma\alpha}^{(4)}/F_\alpha$ ratio does. This suggests that the calculated λ_-/λ_+ ratios (i.e., the direction of the dotted lines) are robust with respect to the uncertainty in the calculated electronic factors F_α, K_α, $G_\alpha^{(4)}$, and $G_{\gamma\alpha}^{(4)}$.

11.1.2 Quadratic field shift $G^{(2)}[\langle r^2\rangle^2]$

As the dominant source of the nonlinearities observed in the 2D King plots is expected to be from the FFS $G^{(4)}\langle r^4\rangle^{AA'}$, it can be eliminated by drawing a 3D King plot (see Section 8.4). Assuming that the nonlinearity remaining in the 3D King plot originates from the QFS, the value of $G^{(4)}_{\eta\kappa\chi}$ can be obtained by fitting the 3D King plot using the relation:

$$\overline{\overline{\nu}}^{AA'}_{\eta} = K_{\eta\kappa\chi} + f_{\eta\kappa\chi}\overline{\overline{\nu}}^{AA'}_{\chi} + f_{\eta\chi\kappa}\overline{\overline{\nu}}^{AA'}_{\kappa} + G^{(2)}_{\eta\kappa\chi}\overline{\overline{[\delta\langle r^2\rangle^2]}}^{AA'} \tag{11.3}$$

As there is no degree of freedom of the fit (i.e., the number of fitting parameters and points are the same), all the points are always fitted perfectly, effectively attributing the observed 3D King-plot nonlinearity in Fig. 10-6 solely to the QFS.

The fitted value of $G^{(2)}_{\beta\gamma\alpha}$ in Table C.5 has bigger magnitude than the two-transition factor $G^{(2)}_{\beta\alpha}$ in Tables C.4. However, the three-transition factor $G^{(2)}_{\beta\gamma\alpha}$ is expected to be significantly smaller than the two-transition factor $G^{(2)}_{\beta\alpha}$ (see Section 16.3). This implies that the observed nonlinearity might not be mainly from the QFS, and the fitting overestimates $G^{(2)}_{\beta\gamma\alpha}$ as a consequence. Note, however, future measurements for the α and β transitions with the better precision might result in smaller fitted $G^{(2)}_{\beta\gamma\alpha}$ (i.e., the green ellipse in Fig 10-4 shrinks towards the origin).

11.1.3 New boson

As the QFS is rejected as the second source of nonlinearity, there is no significant candidate for the observed second source to date. Given the situation, the bound on a new boson's coupling $y_e y_n$ to a neutron and electron is obtained from the unexplained component in the nonlinearity. As in Section 11.1.2, the values of the associated electronic factor $\upsilon_{ne}D_{\eta\kappa\chi}$ can be obtained by fitting the King plots using the relation

$$\overline{\overline{\nu}}^{AA'}_{\eta} = K_{\eta\kappa\chi} + f_{\eta\kappa\chi}\overline{\overline{\nu}}^{AA'}_{\chi} + f_{\eta\chi\kappa}\overline{\overline{\nu}}^{AA'}_{\kappa} + \upsilon_{ne}D_{\eta\kappa\chi}\overline{\overline{a}}^{AA'}, \tag{11.4}$$

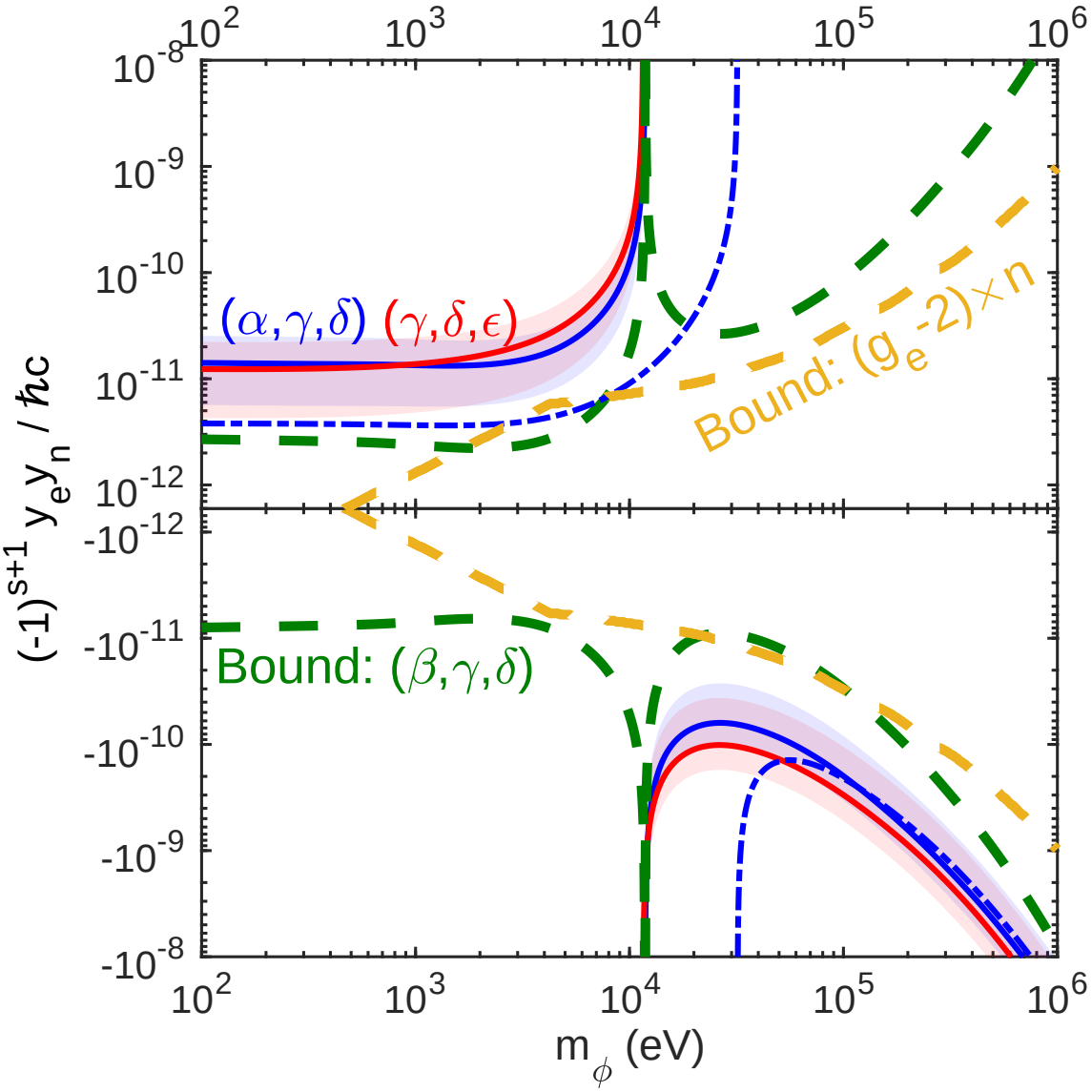

Figure 11-1: Product of coupling constants $y_e y_n$ of a new boson with spin s versus boson mass m_ϕ [Eq. (8.16)], derived from 3D King plots [Eq. (8.24)] for three transitions (α, γ, δ) (blue), $(\gamma, \delta, \epsilon)$ (red), and (β, γ, δ) (green), assuming that the observed second nonlinearity is dominated by a new boson [Eq. (11.4)]. Dashed lines indicate the upper bounds on $y_e y_n$'s magnitude. Solid lines show the center values of $y_e y_n$ obtained using the configuration-interaction calculations' (see Section 12.2) results with AMBiT [8] [see Fig. C-3(d,j,g)]. Shaded area along the solid lines show the $\approx 95\%$ confidence interval that arises from the statistical uncertainty in the measured isotope shifts. The systematic uncertainty in the atomic structure calculations is larger; the dash-dotted line shows the center value of $y_e y_n$ for the (α, γ, δ) transitions using GRASP2018 calculation results in Part IV, for comparison. The yellow line indicates the bound derived from electron $g_e - 2$ measurements [11, 12, 13, 14] in combination with with neutron scattering measurements [15, 16, 17, 18], from Ref. [3].

attributing the 3D King-plot nonlinearity solely to the new boson. The fitted values for different transition groups are listed in Table C.5.

On the other hand, the three-transition new-boson sensitivity of the atom $D_{\eta\kappa\chi}(m_\phi)$ can be calculated as a function of a new boson's mass m_ϕ through ASCs (see Sections 15.1.2 and 15.2). Therefore, the value of new-boson-coupling product $y_e y_n$ can be obtained by dividing the fitted $\upsilon_{ne} D_{\eta\kappa\chi}$ by the calculated $D_{\eta\kappa\chi}(m_\phi)$:

$$y_e y_n = (-1)^{s+1} 4\pi\hbar c \frac{[\upsilon_{ne} D_{\eta\kappa\chi}]_{\rm fit}}{[D_{\eta\kappa\chi}(m_\phi)]_{\rm cal}} \tag{11.5}$$

as $\upsilon_{ne} = (-1)^{s+1} y_e y_n/(4\pi\hbar c)$ (see Section 8.2.1).

Figure 11-1 shows the $y_e y_n$ vs m_ϕ for some of possible three-transition groups of transitions: (α, γ, δ) (blue solid line), $(\gamma, \delta, \epsilon)$ (red solid), and (β, γ, δ) (green dashed line). The transition groups are chosen as they have relatively small uncertainty in the $D_{\eta\kappa\chi}$ across the different m_ϕ [see Figs. C-3(d,j,g), respectively]; the calculated $D_{\eta\kappa\chi}$ has statistical uncertainty from the fitted value of $f_{\eta\chi\kappa}$ (see Section 15.2). To obtain the statistical uncertainties in $y_e y_n$ in Eq. (11.5) from the measured ISs, a simple way to treat uncertainties in the numerator and the denominator is used: a certain range of each value is considered [e.g., 95 % confidence intervals: $(\langle x\rangle - 2\sigma_x, \langle x\rangle + 2\sigma_x)$ and $(\langle y\rangle - 2\sigma_y, \langle y\rangle + 2\sigma_y)$], and the minimum and maximum value of x/y in the ranges of x and y is taken as the confidence interval of x/y. From the 95% confidence interval of each value, the range of $y_e y_n$ is conservatively obtained here. For the transitions groups considered in Fig. 11-1, the fractional uncertainty in the fitted $\upsilon_{ne} D_{\eta\kappa\chi}$ is much larger than the calculated $D_{\eta\kappa\chi}$'s uncertainties, except for the boson mass m_ϕ at which the sensitivity $D_{\eta\kappa\chi}$ vanishes. Therefore, the uncertainty in the ratio $(\upsilon_{ne} D_{\eta\kappa\chi})_{\rm fit}/(D_{\eta\kappa\chi})_{\rm cal}$ is given by the numerator in the above simple approach, and so does the fractional uncertainty in the resulting $y_e y_n$, except for the m_ϕ at which the $y_e y_n$ diverges.

All the bounds from the different transition groups are consistent within the accuracy of the ASCs, which is estimated by the difference in the bounds from the different ASCs (blue solid line vs blue dash-dotted line). Although the nonzero ranges

of finite $y_e y_n$ values are obtained from (α, γ, δ) and $(\gamma, \delta, \epsilon)$ groups, they still serve as *bounds* on $y_e y_n$, just as the remaining group (β, γ, δ), as the values are obtained upon the assumption that the new boson is the sole contribution to the second nonlinearity source.

The green dashed line for (β, γ, δ) transition group provides the best bound in this work. The bound is improved nearly by two orders of magnitude from the previous bound obtained in this work (see Fig. 4 in Ref. [5]). It is now comparable to another bound from other types of experiments: measurements on electron $g-2$ [11, 12, 13, 14] and neutron scattering[15, 16, 17, 18]; the bound from this work is even slightly better in a narrow range of the boson mass $m_\phi = 2$ to $7\,\mathrm{keV/c^2}$. The bound is expected to be further improved, or the value of $y_e y_n$ vs m_ϕ is found if the new boson exists, as ISs are measured for more transitions and isotopes in the future (see Sections 8.3.4, 8.4, 21, and 20).

11.2 Contribution of isotope-shift spectroscopy to atomic and nuclear structure calculations

While the atomic structure calculations (ASCs) and nuclear density functional theory (DFT) calculations provide the information for interpreting the measured King nonlinearity as in Section 11.1, the measured ISs can also provide valuable data for improving the calculations by, e.g., the testing the validity of a certain model for the calculations, comparing accuracies of different models, and tuning or developing calculation models further to better adapt the predictions to the experimental observations.

Comparing the predicted nonlinearity from the calculated $G^{(4)}\langle r^4\rangle^{AA'}$ to the measured nonlinearities is already one such example; it is determined that Fayans functional Fy(Δr) explains better than the other energy density functionals used (see Section 11.1.1). This section will introduce two other examples that the measured ISs in this thesis contribute to nuclear and atomic structure calculations in the fol-

lowing subsections 11.2.1 and 11.2.2, respectively.

11.2.1 Nuclear charge radius pattern data

From the measured ISs $\nu_\alpha^{AA'}$ for the α: 411 nm transition in Yb^+ ions (see Fig. 3-1), the difference in mean-square nuclear charge radii $\langle r^2\rangle^{AA'}$ between different isotope can be derived using the calculated values of single-transition electronic factors F_χ and K_χ (in Table C.3) as follows:

$$\langle r^2\rangle^{AA'} = \frac{\nu_\chi^{AA'} - K_\chi \mu^{AA'}}{F_\chi}. \tag{11.6}$$

While the overall scale of $\langle r^2\rangle^{AA'}$ depends strongly on the calculated value of F_χ which might not be reliable due to the limited accuracy of ASCs, the ratios of $\langle r^2\rangle^{AA'}$ between different isotope pairs do not rely on F_χ and largely determined by the ratio of ISs $\nu_\chi^{AA'}/\nu_\chi^{A'A''}$ as follows:

$$\begin{aligned}\frac{\langle r^2\rangle^{AA'}}{\langle r^2\rangle^{A'A''}} &= \frac{\nu_\chi^{AA'} - K_\chi \mu^{AA'}}{\nu_\chi^{A'A''} - K_\chi \mu^{A'A''}} \\ &= \frac{\nu_\chi^{AA'}}{\nu_\chi^{A'A''}}\left[1 - \left(\left(\tfrac{K\mu}{\nu}\right)_\chi^{AA'} - \left(\tfrac{K\mu}{\nu}\right)_\chi^{A'A''}\right)\left(1 + \left(\tfrac{K\mu}{\nu}\right)_\chi^{A'A''}\right) + \cdots\right].\end{aligned} \tag{11.7}$$

with the omitted terms of third order or higher. The ratio is not sensitive to the value of calculated K_χ for heavy atomic species for two reasons : the contribution of mass shifts (MS) to the total ISs is small [1] (see Section 8.1.2); $\left(\frac{K\mu}{\nu}\right)_\chi^{A'A''} < 10\,\%$ for the α: 411 nm transition in Yb^+ ions. The similar MS-to-IS ratios $(K\mu/\nu)_\chi^{AA'}$ between different isotope pairs further suppress the effect of K_χ [i.e., $\left(\frac{K\mu}{\nu}\right)_\chi^{AA'} - \left(\frac{K\mu}{\nu}\right)_\chi^{A'A''} \ll 1$].

Figure 11-2(b) shows the $\langle r^2\rangle^{A,A+2}/\langle r^2\rangle^{A-2,A}$ for the nearest-neighboring pairs of nearest-neighboring even-A isotope pairs from Eq. (11.7) and the ISs for α: 411 nm transition measured in this work (red filled square), over a range of K_α values that covers the uncertainty in the ASCs. The ratios of all the pairs of isotope pairs are insensitive to the value of K_α and thus precisely obtained, as expected.

Figure 11-2(a) then compares the trend of the measured $\nu_\chi^{A,A+2}/\nu_\chi^{A-2,A}$ values for

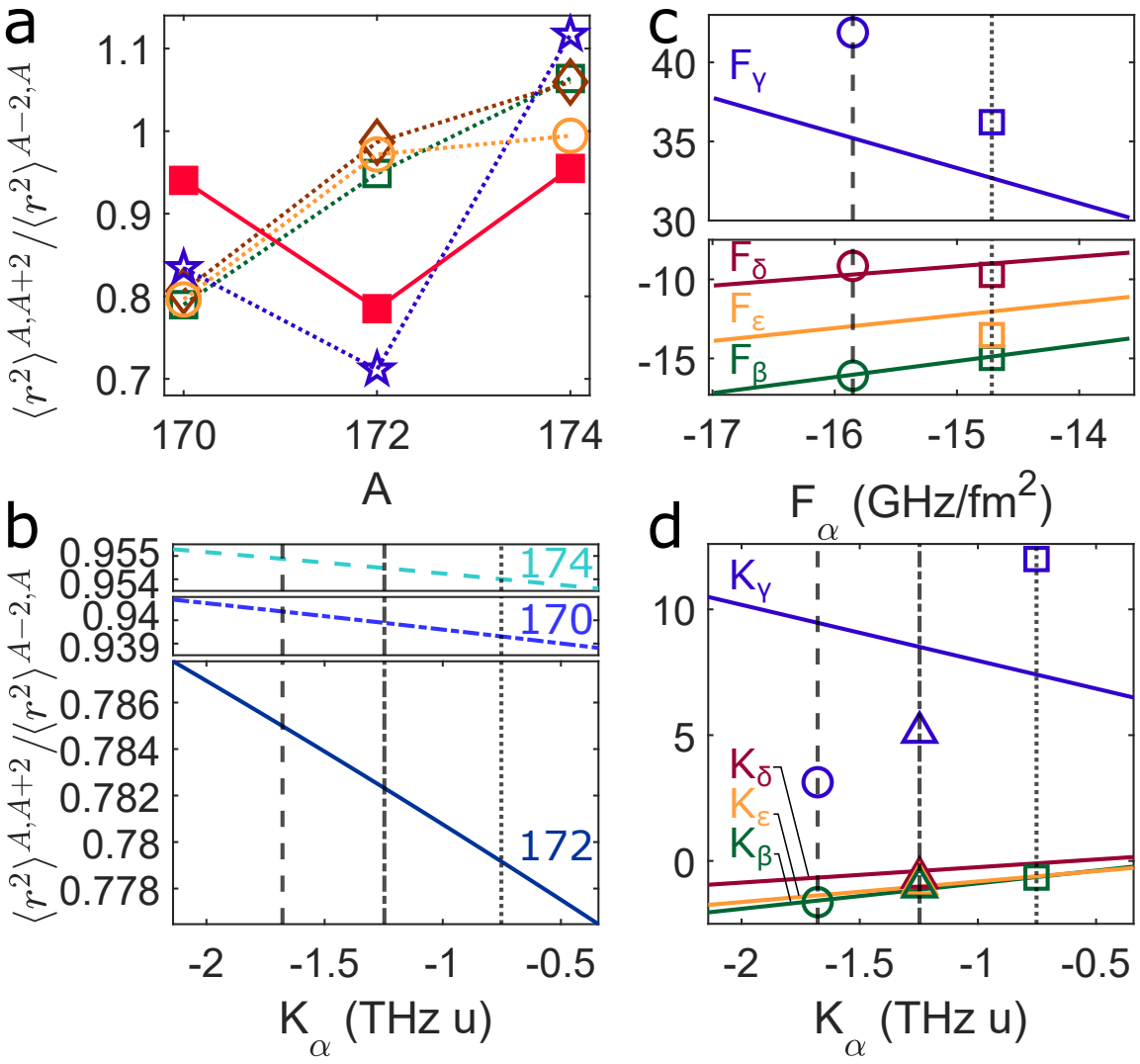

Figure 11-2: (a) Comparison plot of derived values for the ratio of the mean-square nuclear charge radius differences $\langle r^2\rangle^{A,A+2}/\langle r^2\rangle^{A-2,A}$ between nearest-neighboring even-A isotope pairs in Ref. [8] (drawn by Diana P. L. Aude Craik). Open symbols mark the values derived from nuclear density functional theory (DFT) calculations using SV-min, RD-min, UNEDF1, and Fy(Δr) energy density functionals (see Fig. 10-4 for symbol assignments). The red filled square symbols are values derived from measured isotope shifts for the α: $^2S_{1/2} \rightarrow {}^2D_{5/2}$ (411 nm) transition in Yb^+ ions measured in Part II in combination with mass shifts from configuration-interaction (CI) calculations (see Section 12.2). (b) Plot of derived values for the ratios of the mean-square nuclear radius differences between sequential isotope pairs as a function of K_α, showing very weak dependence on K_α. (c, d) Derived values of $F_\beta, F_\gamma, F_\delta, F_\epsilon$ ($K_\beta, K_\gamma, K_\delta, K_\epsilon$) as a function of F_α (K_α), using the experimentally-determined quantities $f_{\kappa\alpha}$ ($K_{\kappa\alpha}$) for $\kappa = \beta, \gamma, \delta, \epsilon$ in Table C.4. In (b), (c), and (d), dashed (dotted) vertical lines and round (square) markers indicate values from CI calculations using GRASP2018 (AMBiT [8]). Dash-dotted lines and open triangle markers correspond to CI and many-body perturbation theory (CI+MBPT) calculations (see Section 12.2) using AMBiT.

increasing A with the predictions from the nuclear DFT calculations (open symbols). The ratios obtained from nuclear theory show monotonically increasing trends for the three EDFs SV-min, RD-min, and UNEDF1. Only Fy(Δr) produces a trend that complies with the experimentally determined trend, highlighting the better reliability of the calculations with the Fayans functional.

11.2.2 Relating electronic factors

The fitted values of two-transition electronic factors $f_{\kappa\chi} = F_\kappa/F_\chi$ and $K_{\kappa\chi} = K_\kappa - f_{\kappa\chi}K_\chi$ in the corresponding (2D) King plots relate the value of the single-transition electronic factors calculated for different transitions. Therefore, if at least 3 ISs are measured for different transitions in the same atomic species, the values of F_χ and K_χ for one transition determine the values for all other transitions, providing strong tests on the consistency of predicted values from ASCs. In particular, if calculations of F_χ and K_χ for a particular transition χ are reliable, then the derived electronic factors F_κ and K_κ for other transitions κ that are challenging for ASCs will be useful as themselves, or for testing the validity of ASCs for the other transitions κ.

Figures 11-2(c) and (d) shows such test for β: 436 nm and γ: 467 nm transitions in Yb^+ ions, and δ: 578 nm and ϵ: 361 nm transitions in neutral Yb atoms, referenced to α: 411 nm transition in Yb^+ (see Fig. 3-1). It is known to be challenging tasks to calculate mass-shift coefficients K_χ for heavy atoms precisely [185, 186]. This turns out to be especially the case for the γ transition; values from calculations with GRASP2018 and AMBiT don't agree on the sign, and neither of them predicts $K_{\gamma\alpha}$ close enough to the experimental value from the King plot [see Tables C.3, C.4, and Fig. 11-2(d)]. On the other hand, the $K_{\beta\alpha}$ for the α and β transition are relatively reliable; values from GRASP2018 and AMBiT agree in about a factor of two, and the experimental value of $K_{\beta\alpha}$ agrees relatively well with the values from GRASP2018 and AMBiT. This is presumably because of the similar electronic structures of α and β transitions and, in contrast, the significant disturbance during the γ transition, which are discussed in Sections 3.1.2 and 10.2. Given that, the one-electron factors calculated for all different transitions are presented with respect to the α transitions,

and their accuracy (or at least their consistency with the α transition) are tested in Figs. 11-2(c) and (d).

11.3 Normalization of King plot

Two different ways to normalize ISs to obtain 2D King plots are introduced in Section 8.1.4: normalization with inverse-mass differences $\mu^{AA'}$ as the standard choice or with ISs $\nu_\tau^{AA'}$ for a reference transition τ (frequency-normalized King plot) used in this work.

In this thesis work, two motivations to use the frequency-normalized King plot instead of the more conventional choice have been found. First, It makes the y-axis of King plots $\nu_\kappa^{AA'}/\nu_\tau^{AA'}$ dimensionless, and so thus the nonlinearity components from the y-residuals in King plots. Equivalently, the King and nonlinearity vectors in Section 8.3.1 become dimensionless.

The frequency-normalized King plots also allow avoiding the complex fit with errors and correlations in the x-direction developed in Section 9.2. It can be observed from Eq. (8.11) that the uncertainties in the x coordinate $\overline{\mu}^{AA'}$ are propagated through the slope given by the mass-shift electronic factor K_χ which is small for heavy atomic species [1] (see Section 8.1.2). In particular, as long as the fractional uncertainty in the measured mass difference $\mu^{AA'}$ is smaller than the fractional precision of the IS measurements (i.e., x and y uncertainties are dominated by the measured ISs' uncertainties), the ratio of the propagated x uncertainty to the native y uncertainty can be written as:

$$\begin{aligned}\frac{K_{\kappa\chi}\sigma_{\overline{\mu}}}{\sigma_{\overline{\nu}_\kappa}} &= \frac{K_{\kappa\chi}\frac{\mu}{\nu_\chi}\sqrt{\left(\frac{\sigma_\mu}{\mu}\right)^2+\left(\frac{\sigma_{\nu_\chi}}{\nu_\chi}\right)^2}}{\frac{\nu_\kappa}{\nu_\chi}\sqrt{\left(\frac{\sigma_{\nu_\kappa}}{\nu_\kappa}\right)^2+\left(\frac{\sigma_{\nu_\chi}}{\nu_\chi}\right)^2}} \\ &\sim \frac{K_{\kappa\chi}\mu}{\nu_\kappa} \lesssim \frac{K_\kappa \mu}{\nu_\kappa} \\ &= \frac{(\mathrm{MS})_\kappa}{(\mathrm{FS})_\kappa + (\mathrm{MS})_\kappa} \ll 1,\end{aligned} \tag{11.8}$$

(with omitted AA' superscripts) where it is assumed that the fractional uncertainties in the measured isotope shifts $\nu_\chi^{AA'}$ and $\nu_\kappa^{AA'}$ are similar.

Table C.4 compares the results of the fits with and without x-errors and correlations, which are in good agreement. Therefore, the standard GLS fit with simple analytic solutions (see Section 9.2.1) would be enough to obtain a sufficiently reliable preliminary significance of the King nonlinearity, before performing the more complicated EiVGLS fit in Section 9.2.

11.4 Equivalence of n-dimensional King plot and nonlinearity pattern comparison

This section provides a geometric proof of the equivalence of a 3D King plot (Section 8.4) and 2-pattern comparison in a nonlinearity map $\lambda_\pm$ (Section 8.3.4), which is readily generalized for higher dimensions.

Consider a frequency-normalized 3D King plot for (α, β, γ) transitions [equivalent to Eq. (8.24); see Section 8.1.4]:

$$\overline{\boldsymbol{\nu}}_\gamma = K_{\gamma\beta\alpha}\overline{\boldsymbol{\mu}} + f_{\gamma\beta\alpha}\mathbf{1} + f_{\gamma\alpha\beta}\overline{\boldsymbol{\nu}}_\beta + Y_{\gamma\beta\alpha}\overline{\mathbf{y}} \tag{11.9}$$

[see Eq. (8.17) for the vector notation] with $Xx^{AA'} \gg Yy^{AA'}$ as in Section 8.4. From Fig. 11-3, one can easily see that the linear fit in 3D King plot corresponds to finding the values of $f_{\gamma\alpha\beta} = X_{\gamma\alpha}/X_{\beta\alpha}$ and $Y_{\gamma\beta\alpha} = Y_{\gamma\alpha} - f_{\gamma\alpha\beta}Y_{\beta\alpha}$ to form a triangle along nonlinearity patterns for $\nu_\beta^{AA'}$, $\nu_\gamma^{AA'}$, and $y^{AA'}$. Therefore, if the 3D King plot is linear, the area of the corresponding triangle vanishes, (i.e., $\overline{\boldsymbol{\nu}}_\beta$ and $\overline{\boldsymbol{\nu}}_\gamma$ are parallel to each other). Thus a test of whether two nonlinearity points have the same direction from the origin can be used to probe for the existence of a second nonlinearity source $y^{AA'}$ (see Fig. 2 in the main text).

It is straightforward to see that the λ_-/λ_+ ratio for $y^{AA'}$ (dotted lines' direction in Fig. 11-3) determines the ratio $f_{\eta\chi\kappa} = X_{\eta\chi}/X_{\kappa\chi}$ (ratio of red arrows' lengths) and vice versa, independent of the λ_-/λ_+ ratio of the dominant source of nonlinearity

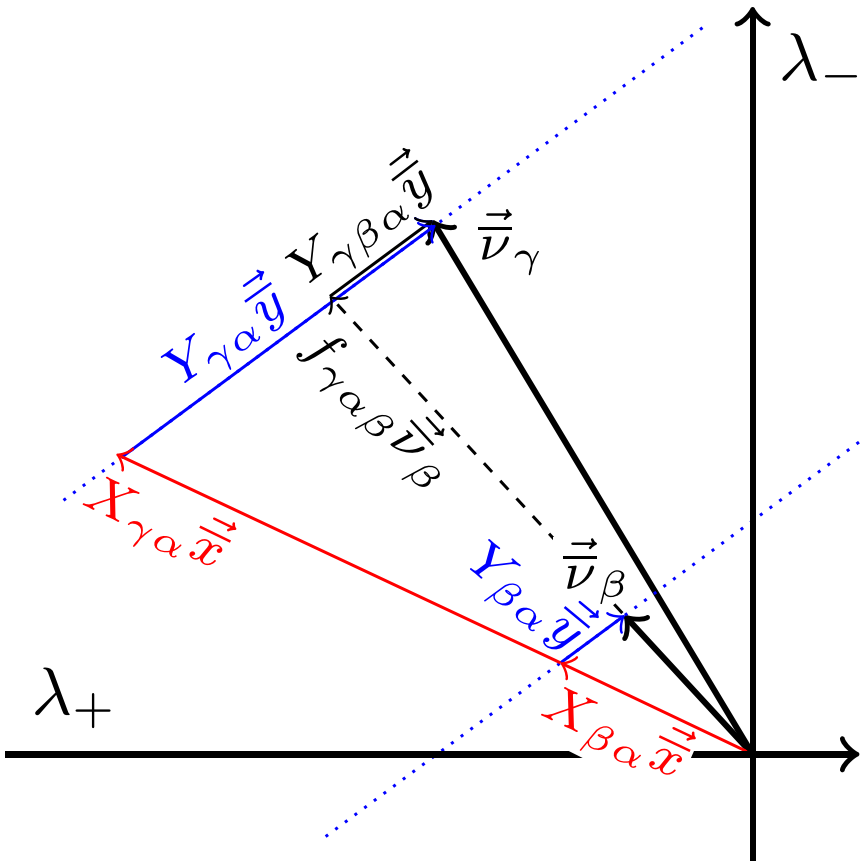

Figure 11-3: Two-source-nonlinearity analysis in a nonlinearity map $\lambda_\pm^{(\alpha)}$ with reference transition α. Thick black arrows indicate the measured ν_β and ν_γ. The nonlinearity from $x^{AA'}$ ($y^{AA'}$) is coded with red (blue) color. The blue dotted line shows the direction of $\lambda_\pm$ due to $y^{AA'}$. The 3D King plot corresponds to stretching the nonlinearity from ν_β (dashed black arrow; $f_{\gamma\beta\alpha}\vec{\nu}_\beta$) and moving along $y^{AA'}$'s direction (thin black arrow; $Y_{\gamma\beta\alpha}\vec{y}$) to form a triangle with nonlinearity for ν_γ.

$x^{AA'}$ (i.e., the direction of the red arrow). The former is equivalent to fitting the 3D King plot with a known nonlinearity pattern from nuclear parameters $y^{AA'}$ (see Eqs. 11.3 and 11.4). The latter suggests that if $f_{\eta\chi\kappa}$ can be calculated precisely in the future, the pattern shape of second nonlinearity source $y_\perp^{AA'}$ can be deduced and compared with the predicted shapes from the QFS, new boson, or any other proposed sources.

Pattern comparison performed in Section 10.2 (see Fig. 10-3) demonstrates the advantage of pattern comparison tests (with the aid of nonlinearity maps) compared to n-dimensional King plots which can not provide tests without having $n+2$ available

isotopes (see Section 8.4).

11.5 Independent isotope pairs

It might be argued that three different isotopes A, A', and A'' are enough to form three different isotope pairs. However, if the ISs for (A, A') and (A', A'') are mapped in a King plot, for instance, the point for a remaining pair (A, A'') is mathematically guaranteed to be linear with the other two points as it does not introduce new information on the three isotopes (e.g., IS $\nu^{AA''}$ is simply $\nu^{AA'} + \nu^{A'A''}$). Therefore, each isotope pair should be *independent* of other pairs in a way that the pair introduces a new isotope that does not belong to any other pairs. In general, at least $n + 1$ isotopes are required to form n independent isotope pairs. One of such constructions used in the thesis work is forming nearest-neighboring pairs of isotopes ordered in their mass numbers A. Measuring next-neighboring pairs (A, A'') for $A < A' < A''$, for instance, is still useful to test the consistency of the measured ISs for (A, A') and (A', A'') pairs. It has not been used by adding more points in King plots, however, but rather in a way to improve the precision of the measured ISs for the nearest pairs (A, A') and (A', A'') as discussed in Sections 6.7 in detail, to enable simple and consistent pattern analysis.

Proving the linearity of the third point (A, A'') is simple. First, the values $\nu_\chi^{AA'}$, $\nu_\kappa^{AA'}$, $\mu^{AA'}$ and $\nu_\chi^{AA'}$, $\nu_\kappa^{A'A''}$, $\mu^{A'A''}$ are given. The third set of values, then, must be given as $\nu_{\chi,\kappa}^{AA''} = \nu_{\chi,\kappa}^{AA'} + \nu_{\chi,\kappa}^{A'A''}$ and $\mu^{AA''} = \mu^{AA'} + \mu^{A'A''}$. If the two values F and K exist (as they should) such that

$$\begin{aligned} \nu_\kappa^{AA'} &= F\nu_\chi^{AA'} + K\mu^{AA'} \\ \nu_\kappa^{A'A''} &= F\nu_\chi^{A'A''} + K\mu^{A'A''} \end{aligned} \tag{11.10}$$

Then

$$\nu_\kappa^{AA''} = F\nu_\chi^{AA''} + K\mu^{AA''} \tag{11.11}$$

must be true. King plot is then about normalizing each equation with one of

the isotope-dependent parameters; e.g., for frequency-normalized King plot [see Eq. (8.15)], each equation is normalized by the associated $\nu_\chi^{AA'}$, giving

$$\begin{aligned} \overline{\nu}_\kappa^{AA'} &= F + K\overline{\mu}^{AA'} \\ \overline{\nu}_\kappa^{A'A''} &= F + K\overline{\mu}^{A'A''} \\ \overline{\nu}_\kappa^{AA''} &= F + K\overline{\mu}^{AA''} \end{aligned} \tag{11.12}$$

which guarantees the linearity of the three points.

It is straightforward to generalize the proof for more isotope pairs with underlying (deterministic) correlations between them (i.e., *redundant* isotope pairs; more pairs than the internal degrees of freedom).

11.6 Expansion of isotope shifts

In Sections 8.1 and 8.2, the contributions to ISs are introduced in the context of the Seltzer expansion of nuclear charge distribution and the first and second-order perturbation theory. While these concepts provide constructive ways to understand, e.g., the electronic-nuclear factorization (Section 8.1.3) and the properties of electronic states that determine the electronic factors (Sections 8.1 and 15.1), there is a simple abstract view of how each term in the expression of ISs (should) occurs: the Taylor series. If an isotope A is taken as a reference system and the IS of another isotope A' from the isotope A is to be described as the change in the transition frequency due to the change in the system from A to A', then IS should be described as a function of all parameters that determine the system's change. The *external* change that is made by hand is of the nucleus, and thus the nuclear parameters are given as the independent variables (or arguments) of the function. Parameters such as $\langle r^2 \rangle^{AA'}$ and $a^{AA'}$ are merely particular examples of them. On the other hand, the change in the electronic structure is the result of the external change in the nucleus, and the electronic structure as well as all the quantities derived from the electronic structures are dependent variables (or images); transition frequency is just

one example in this view. Therefore, the IS can be expressed in the following form:

$$\nu^{AA'} = \nu\left(\mu^{AA'}, \langle r^2\rangle^{AA'}, \langle r^4\rangle^{AA'}, \langle r^6\rangle^{AA'}, \cdots, a^{AA'}, x^{AA'}, \cdots\right) \tag{11.13}$$

with $\nu(0, 0, \cdots) = 0$, where $x^{AA'}$ represents nuclear properties that have not been considered.

Then, the function can be expanded in the form of the Taylor expansion, assuming that the change of the system from one isotope to another is not too big for the function to be analytic. The first-order terms will give the terms with the nuclear parameters of first order, including MS $K\langle r^2\rangle^{AA'}$, FS $F\langle r^2\rangle^{AA'}$, FFS $G^{(4)}\langle r^4\rangle^{AA'}$, $F^{(4)}\langle r^6\rangle$, boson shift $Da^{AA'}$, and $Xx^{AA'}$. The second-order expansion gives the terms with the nuclear parameters of the second order, e.g., QMS $L(\mu^2)^{AA'}$ and QFS $G^{(2)}(\langle r^2\rangle^2)^{AA'}$ as well as the terms with mixed nuclear parameters of total second order, e.g., mass-field shift $C(\mu\langle r^2\rangle)^{AA'}$. There are, obviously, third or higher-order terms in the expansion, in principle.

As a side insight, the expression for QFS between two arbitrary isotopes A' and A'' given in Section 8.2.2 is natural in this view:

$$(\nu_{\text{QFS}})^{A'A''} = (\nu_{\text{QFS}})^{AA''} - (\nu_{\text{QFS}})^{AA'} = G^{(2)}\left[(\langle r^2\rangle^2)^{AA''} - (\langle r^2\rangle^2)^{AA'}\right] \equiv G^{(2)}[\langle r^2\rangle^2]^{A'A''} \tag{11.14}$$

as the shifts for any isotopes should be described from a fixed reference isotope A for the consistency of the description, especially for the nonlinear terms (i.e., nth order with $n > 1$).

11.7 Basis for nonlinear pattern decomposition

There are two sets of basis vectors suggested in this thesis: $\boldsymbol{\zeta}_\pm = (1, -1, \pm 1, \mp 1)$ in the earlier thesis works [5] and $\hat{\boldsymbol{\Lambda}}_\pm$ [Eq. 8.20] in the later work [8]. Both bases, or any other choices are mathematically valid to describe the nonlinearity components $\mathbf{x}_\perp$ of a given vector $\mathbf{x}$ (i.e., the component of $\mathbf{x}$ that are orthogonal to the King plane), as far as the basis vectors are not parallel to the King plane that $\mathbf{1}$ and $\overline{\boldsymbol{\mu}}$ form, as

such basis can uniquely determine an arbitrary orthogonal component $\mathbf{x}_\perp$.

The advantage of $\boldsymbol{\zeta}_\pm$ is their maximum conceptual simplicity; it is two orthogonal vectors, and two vectors clearly represent two qualitatively different pattern shapes: zigzag ($\boldsymbol{\zeta}_+$) and bowline ($\boldsymbol{\zeta}_-$). Generalizing the nonlinearity vectors for higher dimensions by having more isotopes would also be relatively easier: finding orthogonal vectors that consist of some simple forms of numbers (e.g., integers or square-root of integers) with zero sum, possibly with associated qualitatively meaningful shapes. The downside of the $\boldsymbol{\zeta}_\pm$ is that they are not orthogonal to $\overline{\boldsymbol{\mu}}$ or thus the King plane in general. Therefore, to describe the nonlinearity component in $\mathbf{x}$, the orthogonal component with respect to the King plane $\mathbf{x}_\perp$ is first obtained, and it is projected to the plane that $\boldsymbol{\zeta}_\pm$ form, and the projected vector is decomposed with the two vectors. Given that, the nonlinearity map $\zeta_\pm(\mathbf{x})$ cannot be regarded as the coordinate of $\mathbf{x}$ in a frame with $(\mathbf{1}, \overline{\boldsymbol{\mu}}, \boldsymbol{\zeta}_+, \boldsymbol{\zeta}_-)$ as the axes.

The disadvantage of the $\boldsymbol{\zeta}_\pm$ basis can be resolved if the nonlinearity vectors are orthogonal to the King vectors, which is one of the motivations for using $\hat{\boldsymbol{\Lambda}}_\pm$. They are constructed to be orthogonal to both $\mathbf{1}$ and $\overline{\boldsymbol{\mu}}$. There are still infinite numbers of different possible choices that satisfy the condition, and $\hat{\boldsymbol{\Lambda}}_\pm$ are chosen to retain $\boldsymbol{\zeta}_\pm$'s representation of different shapes and the linear constructions for straightforward error propagation, as introduced in Section 8.3.1.

A drawback of the above basis is that $\hat{\boldsymbol{\Lambda}}_+$ and $\hat{\boldsymbol{\Lambda}}_-$ are not orthogonal to each other in general. One can alternatively, for instance, keep $\hat{\boldsymbol{\Lambda}}_+$ and define $\hat{\boldsymbol{\Lambda}}_-$ as the vector that is orthogonal to the two King vectors and $\hat{\boldsymbol{\Lambda}}_+$. With choices of this kind, however, the propagation of the uncertainty is less straightforward (see Section 9.5). Interestingly, the values of $\overline{\mu}^{AA'}$ for Yb are given that the nonlinearity vectors in Eq. (8.20) are very close to be perpendicular to each other ($\hat{\boldsymbol{\Lambda}}_+ \cdot \hat{\boldsymbol{\Lambda}}_- = 0.0014$). The vectors $\hat{\boldsymbol{\Lambda}}_+$ are also less straightforward to generalize for higher dimensions.

Note also that the orthogonality of nonlinearity basis vectors is not significant because the metric (i.e., defining the distances between points) hardly has its physical meaning in a nonlinearity map, or in the whole space (e.g, 4D space for 4 points in a King plot). It fundamentally stems from the fact that comparing the (somehow

defined) sizes of two patterns of different shapes is not so much useful as they are different just by their underlying sources. The comparison of the size is meaningful only when the comparison is for the same effect along the certain associated direction in the nonlinearity map, which does not require a metric defined.

Part IV

Atomic Structure Calculation

Chapter 12

Atomic Structure Calculation: translating measured isotope shift into new boson and nuclear physics

Once measurements for King nonlinearity are established as in Chapter 8, the result should be interpreted in terms of the new boson or nuclear physics. If the points in King plots are linear within the measurement uncertainty, the uncertainty is to be used to set a bound on the strength of new-boson-mediated electron-neutron coupling. If the King nonlinearity is observed, and especially when the contribution of each source of the nonlinearity is distinguished from others, the measured size of the contribution should be translated into the source's properties (e.g., the new-boson coupling or nuclear properties). Given that the change in atoms' spectra is ultimately due to the electrons' coupling to those sources, obtaining the electronic wavefunctions in the atoms is the key for such translations.

There is virtually no way to determine an atom's electronic wavefunction purely by experiments, however. Wavefunctions are values over continuously-infinite dimensions while the measurable quantities for the atomic system are not so many.[1]

[1] In practice, it is common to reduce the effective dimensions of a quantum system by focusing on the states of interest (e.g., using a $^{171}Yb^{+}$ ion's ground state as a two-level hyperfine qubit). However, in this particular case, we are interested in the wavefunction over space with sufficient resolution in general. Therefore, the required number of dimensions is still massive even after, for

Therefore, the determination of wavefunction is fundamentally a *modeling* problem. It is inevitable to start with some models built upon our prior knowledge about the system (i.e., quantum theory), calculate the values of the measurable quantities that the models predict, and compare the predicted values with the measured values to test the validity of the models or even refine the models[2], which constitute the field of atomic structure calculation (ASC).

Because of the nature of underdetermined problems, the accuracy of the results is not straightforward to examine and not comparable to the precision of present-day state-of-art atomic, molecular, and optical (AMO) physics experiments. The *translation* from the King nonliterary to the sources' properties, however, does not often require such high precision; the bounds on the new physics are typically presented in log scale, for instance (see Figs. 11-1 and 1-2).

Note that this point reveals one important distinction between the test using King plots and the direct comparison of measured and calculated absolute transition frequencies described in Section 1.2.1. The uncertainty in the calculation propagates directly to the observable under the test (the difference in measured and calculated frequencies here) in the latter approach, making the test limited by the calculation accuracy. Contrarily, the linearity in King plots can be tested purely by experiments, letting the test takes full advantage of the high experimental precision, and the uncertainty in calculations is taken into account only while interpreting the result for the details of the system.

Here in Part IV, different methods of ASCs, including ones that are used by the thesis author the research collaborators, are briefly introduced in the first two sections 12.1 and 12.2. A package used by the thesis author, GRASP2018 [24], is introduced in Chapter 13. In particular, the add-on packages REDF, which has been

instance, (real) space of interest is limited to a finite range (e.g., some factor times the atomic sizes) and divided by a grid. In other words, on the other hand, if wavefunction's properties relevant to some particular observables have the associated subspace of which the number dimensions is manageable, then wavefunction in the particular subspace might be able to be determined by experiments; an example is in Section 19.4: obtaining wavefunction at the origin from measured hyperfine splittings.

[2]For instance, one can decide to add more terms in the model for better compliance in the measured value, or tune some free parameters to make the prediction closer to the measurement.

developed by the thesis author, and RIS4 [173] are introduced in Sections 13.2 and 13.1, respectively. The procedures of ASCs for an Yb^+ ion and a neutral Yb atom using GRASP2018 are described in Chapter 14, and, finally, obtaining electronic factors in ISs, which are the electron's coupling strengths (i.e., the atoms' sensitivity) to King nonlinearity sources, from the ASC results is detailed in Chapter 15. The part ends with several discussions in Chapter 16.

12.1 Methods of atomic structure calculation

There are largely two branches of ASCs for many-electron atomic systems: density functional theory (DFT) and wavefunction-based approach, e.g., Hartree-Fock (HF) method and its descendants. For the purpose of this research, the latter has been regarded as the better choice for several reasons. HF-based methods provide *ab initio* calculations on the electronic structures in a given atomic system, while DFT involves rather an arbitrary choice of energy functional [187]. Presumably due to this fact, HF-based methods have traditionally been regarded to provide more reliable calculation results compared to DFT-based approaches. HF-based calculations also provide the total wavefunctions of all the electrons in an atomic system, while DFT calculates the density of the electrons. The wavefunctions are obviously more useful for further analyses of the system following after ASCs, e.g., through the perturbation theory to calculate the effect of a small perturbation to the system (Section 15 shows nice examples), although knowing the electrons' density is sufficient in some of the cases. A limitation of the HF-based methods is that the calculation becomes too complicated for relatively complex atomic systems, e.g., molecules, letting DFT has an advantage in the field of quantum chemistry for its relative simplicity of the calculation [188]. However, it has been not an issue in this research, as individual atoms have been atomic systems in consideration.

12.2 Hartree-Fock-based methods

Elaborating on the derivation of the HF method and its descendants, e.g, post-HF methods introduced later in this section is beyond the scope of this thesis. Therefore, comprehensive references [27, 189] are suggested instead, and only a very brief introduction to the subjects is presented here.

The HF method itself treats each electron in an atomic system to be independent (i.e., neglecting the correlation between electrons) and solves the approximated, separable Hamiltonian of the system:

$$H \approx \sum_{i=1}^{N} H_i = \sum_{i=1}^{N} \left[-\frac{\hbar^2}{2m} \left(\frac{\partial}{\partial \mathbf{r}_i} \right)^2 + V_{N-e}(\mathbf{r}_i) + V_{e-e}(\mathbf{r}_i) \right] \tag{12.1}$$

from the central-field approximation, where N is the total number of the electrons in the system, H_i and $\mathbf{r}_i$ are the Hamiltonian and position of ith electron, respectively, $V_{N-e}(\mathbf{r}_i)$ is the Coulomb potential between the electron and nuclei (e.g., for a single atom, $V_{N-e}(\mathbf{r}_i) \approx \frac{1}{4\pi\epsilon_0}\frac{Ze^2}{r_i}$ with the proton number Z in the nucleus[3]), and $V_{e-e}(\mathbf{r}_i)$ is the *effective* potential that describes effect of the Coulomb repulsion of all other electrons to the ith electron. As the Hamiltonian is separable for each electron, the solution state Ψ can be given as the product of each electron's state $\phi_i(\mathbf{r}_i)$, which is constrained by the Pauli exclusion principle [i.e., no multiple occupancies of the electrons in the same state and antisymmetrized wavefunction in the form of (linear combination of) Slater determinant(s)]. Considering the effective potential $V_{e-e}(\mathbf{r}_i)$ and also the antisymmetry, the effective Hamiltonian of each *one-electron* wavefunction is given as the Fock operator F which depends on the state of the electron.[4] The one-electron wavefunction and the associated energy should be an eigenstate and the eigenvalue the Fock operator F which is the function of its own solutions (i.e., *self-dependent*). One way to solve this kind of problem is what is called the *self-consistent-field* (SCF) procedure: to start from an initial solution,

[3] which is *not* exact due to the finite size of the nucleus.

[4] The dependence is especially obvious for the effective potential $V_{e-e}(\mathbf{r})$; the state of other electrons will determine their effects on a single electron.

obtain the F for the solution, solve the F for its eigenstates and values, compare the new solution to the previous one, and repeat the procedure until the solution converges sufficiently.

The solution of the HF method provides an approximated solution for one-electron wavefunctions $\phi(\mathbf{r})$ for the orbitals involved in the system, and the total wavefunction for the dominant electron configuration γ of the system (e.g., [Xe $4f^{14}\,6s$ for the ground state of Yb^+ ions) or, rigorously, the configuration state function (CSF) Φ which further specify the property of the state such as the couplings of angular momenta of the one-electron states (see Section 14.2.2). The real state of the electrons, called atomic state function (ASF) Ψ, does not consist of only one CSFs which omits the electron-electron correlations. Various post-HF methods have been introduced, therefore, to take the correlations into account, and let ASFs be given to be linear combinations of CSFs corresponding to different electron configurations γ. Taking the correlations into account would be especially important for states with open electron subshells (e.g., $^2F_{7/2}$ state in Yb^+ ions or the excited states in neutral Yb atoms considered in this work), of which ASFs are not dominated by single CSFs.

One of such methods is the configuration interaction (CI) method [190, 191, 192, 193]. The idea starts from the fact that all possible different electron configurations and the associated CSFs Φ_i will span the physical Hilbert space for the (bound) states of the atomic system. Therefore, if the full Hamiltonian H of the system is expressed as the matrix elements $\langle\Phi_i|\,H\,|\Phi_j\rangle$ with respect to the CSFs $\{\Phi_i\}$ as a basis, a better solution for the states and energy levels of the system can be obtained by diagonalizing the matrix:

$$H\Psi = E\Psi \tag{12.2}$$

where the ASF $\Psi = (c_1, \cdots, c_{N_{\rm CSF}})$ is given as a linear combination of the basis CSFs:

$$\Psi = \sum_{i=1}^{N_{\rm CSF}} c_i \Phi_i \tag{12.3}$$

with *mixing coefficients* c_i (see also Section 14.2.2). In practice, having all the possi-

ble CSFs in the basis set $\{\Phi_i\}$ (*Full CI*) would not be feasible except for very simple atomic systems, and the CSFs that are expected to be sufficiently relevant to the states of interest are considered in general. The active set approach is a popular method of preparing the set of the CSFs: exciting electrons in the dominant configuration γ of the state. For instance, for $[\mathrm{Xe}]4f^{14}\,6s\;{}^2S_{1/2}$ state in Yb^+ ions, the CSFs from the configurations including $7s$, $8s$, $4f^{13}\,6s\,5f$, and $4f^{13}\,7s\,5f$ can be derived. The excitation of the electrons and the new CSF are constrained to have the same properties as the ASF, e.g., total angular momentum J or parity P of the state. One another advantage of the CI procedure is that more contributions to the full Hamiltonian of an atomic system that has not been considered in the HF calculation [e.g., relativistic or quantum electrodynamic (QED) corrections] can be included in the Hamiltonian for the diagonalization, as described in Section 14.3.

There are other post-HF methods including CI combined with many-body perturbation theory (CI+MBTP) [3, 88, 194] (used in this work by a collaborator Prof. Julian C. Berengut at the University of New South Wales, Sydney) and CI+All order method [146, 195], both for efficiently describing valence-core electron correlations in the CI calculations, and coupling-cluster (CC) method which excites CSFs from the HF method in the exponential form $e^T\Phi$ with the *cluster* operator T, rather than in the linear manner as in the CI method.

Furthermore, more than one CFSs can be considered when the solution for the one-electron wavefunctions $\phi(\mathbf{r})$ are calculated through the iterative SCF procedure, which is called multiconfigurational HF (MCHF) method (Chapter 4 in Ref. [189]).

On the other hand, the relativistic effect should be considered for relatively heavy species, including Yb (see Section 16.1), as the velocities of orbital motions of some of the electrons in the system reach the speed of light.[5] While one approach is to consider the leading-order relativistic corrections in the frame of Schrödinger equation (i.e., HF method) (Chapter 7 in Ref. [189]), the HF method can be reformulated for the Dirac equation, yielding Dirac-Hartree-Fock (DHF) method [27, 196, 197] used

[5]The lighter species with $Z\alpha \ll 1$ are free from the relativistic correction in general (see Section 16.1).

in this thesis work.

Chapter 13

GRASP2018: package for multiconfigurational-Dirac-Hartree-Fock and configurational-interaction calculations

In this work, the multiconfigurational Dirac-Hartree-Fock (MCDHF) method followed by the configuration interaction (CI) method, introduced in Section 12.1, has been used with a software package called GRASP2018. GRASP (an acronym of a General-purpose Relativistic Atomic Structure Program) is a popular package that has been developed at least since 1989 [24, 197, 198, 199, 200], and GRASP2018 [24] is the last version of the package. GRASP2018 can be downloaded at Ref. [201] or from the official GitHub repository [202].

A selection of features of GRASP2018 will be introduced here. First, it solves the Dirac equation for the system (and thus DHF) and derives a four-component Dirac wavefunction for each electron $\phi(\mathbf{r})$ in Eq. (14.3) as detailed in Section 14.2. Second, the basis of describing the radial parts $P(r)$ and $Q(r)$ of wavefunctions $\phi(\mathbf{r})$ [see Eq. (14.3)] is given to be a discretized real space. In other word, $P(r)$ and $Q(r)$ are approximately expressed by arrays of the values $P_i = P(r_i)$ and $Q_i = Q(r_i)$

over a properly-spaced radial grid $\{r_i\}$ over the real space. The real-space grids are not the only choice in general, but there are other common basis sets to describe wavefunctions including Slater $\propto r^l e^{-\alpha r}$ and Gaussian $\propto r^l e^{-\alpha r^2}$ orbital bases. The real-space representation of wavefunctions in GRASP2018 would be particularly more suitable for this thesis' work, as it will naturally provide a more versatile description of the wavefunctions near nuclei, which probe the leading-order King-plot nonlinearity sources within the Standard Model and new boson with relatively heavy mass (see Chapter 15, Sections 8.2, and 16.3). In this regards, GRASP2018 also uses logarithmic grids (see Chapter 9 in Ref. [203]):

$$r_i = \texttt{RNT}\left(e^{\texttt{H}(i-1)} - 1\right) a_0 \tag{13.1}$$

where a_0 is the Bohr radius, which can provide a fine discretization inside and near the nucleus.

Third, the active set approach described in Section 12.1 is taken in GRASP2018 to generate a configuration set for MCDHF and CI calculations (Section 5.3 in Ref. [203]). Furthermore, a concept called multireference (MR) is introduced in the package: when the CSFs are generated through the active set method, more than one *reference* configuration can be set, from which new CSFs are generated by the electron excitations (see Sections 5.2 in Ref. [203] and 14.3 in this thesis). The generation of CSF sets from MR configurations would cover the significant CSFs for given states more efficiently, as discussed at the beginning of Section 14.3.

Lastly, parallel computing with more than one processor has been supported in the lasted GRASP2018 version, which allows the use of high power computing clusters for calculations with significant numbers of CSFs, as demonstrated in Section 14.3.

The full details on the GRASP2018 package can be found in the manual of the package [201, 202] (`GRASP2018-manual.pdf`; titled *A practical guide to GRASP2018 – A collection of Fortran 95 programs with parallel computing using MPI*), which includes installation (Chapter 2), available features and how-to-use (Section 3.2 and

Chapter 8), the flow of calculations (Section 3.3), ample examples (Chapters 6 – 12), and troubleshooting and general tips for calculation (Part IV).

The preferred operating system is Linux. The package has been running well with 18.04 LTS and 20.04 LTS versions of Ubuntu Desktop [204].

The procedure of setting and performing ACSs using GRASP2018 will be elaborated in Chapter 14 for Yb^+ ions as an example atomic system.

13.1 RIS4 add-on subroutine package

There is an add-on package called RIS4 [173] which can load the results of ACSs from GRASP2018 and calculate the electronic factors F_χ and K_χ of the two major contributions, field shifts (FSs) and mass shifts (MSs), respectively (see Section 8.1).

For the MSs, RIS4 constructs the interaction Hamiltonians for normal MSs (NMSs) and specific MSs (SMSs) (see Section 8.1.2) and calculates the expectation values of each Hamiltonian for the calculated ASFs (i.e., the first-order perturbation theory). The sum of the two effects is, then, given as the total MSs.

For the FSs, the radial electron density function $\rho_\Psi(r)$ over space inside and near the nucleus is derived from an ASF Ψ, and the density is fitted to obtain the field-shifts electronic factors, as described in Section 15.1.1.

The results are saved in a generated file with the extension `.i` (if the electronic factors are derived from the results of DHF calculations) or `.ci` (for CI calculations); Listing 14.17 shows an example output in the file.

In this thesis work, the RIS4 has been used to obtain only the mass-shift coefficients K_χ as described in Section 14.4.

13.2 REDF: add-on GRASP2018 subroutine for extracting radial electron density function

GRASP2018 does not have a built-in subroutine for extracting the density functions $\rho_\Psi(r)$ of the electrons from wavefunctions Ψ calculated by GRASP2018. Therefore,

an add-on package name REDF (an acronym for Radial Electron Density Function) has been developed by the thesis author for this research, by modifying and merging the source codes of the RIS4 routine [173] introduced in Section 13.1.[1] In particular, RIS4 extract the wavefunction only near the nucleus, and the codes have been modified to expand the extraction to the full range of the radial grid used for calculating Ψ.

The routine is available in Ref. [205]. Just as RIS4, it can be installed together with GRASP2018 or after GRASP2018 is installed. The installation procedure and how-to-use can be found in the `README` file in the root folder. A very simple example with the ground state of the hydrogen is included in the `test` folder with the way to run the example code in the `README` file in the folder. Similar to RIS4, the extracted density functions are stored in a generated file with the extension `.ed` (for the results of DHF calculations) or `.ced` (for CI calculations); Listing 14.15 shows an example output in the file. The package REDF is MIT-licensed.

Refer to Section 14.4 also to see how the electron density functions $\rho_\Psi(r)$ were obtained using REDF for Yb^+ ions.

[1] Note that RIS4 [173] is MIT-licensed.

Chapter 14

Calculations of Yb^+ and Yb structures

In this chapter, the procedures of DHF and CI calculations with GRASP2018 are elaborated in step-by-step manner. In short, the parameters for ^{172}Yb nucleus were setup (Section 14.1), DHF calculations were performed to build up the basis wavefunctions of core, valence, and correlation orbitals (Section 14.2), and the CI calculations for the $^2S_{1/2}$, $^2D_{5/2}$, $^2D_{3/2}$, and $^2F_{7/2}$ states involved in α: 411 nm, β: 436 nm, or γ: 467 nm optical clock transitions in Yb^+ ions (see Fig. 3-1) were followed. The calculations for δ: 578 nm and ϵ: 361 nm optical transitions in neutral Yb atoms, performed by Calvin Leung, a research collaborator and a PhD student in MIT, through almost the same procedure to Yb^+ states, are also briefly introduced in Section 14.6.

Although the procedure described here is implemented for GRASP2018, the strategy of the calculations could be used for any other packages using the same methods, (D)HF and CI.

14.1 Yb Nucleus

The calculation starts from identifying the nucleus using `rnucleus` command:

```
>>rnucleus
 Enter the atomic number:
>>70
 Enter the atomic number:
```

```
>>172
 Enter the mass number (0 if the nucleus is to be modelled as a
    point source:
 The default root mean squared radius is    5.2192449328117521
     fm;
  the default nuclear skin thickness is    2.2999999999999998
    fm;
 Revise these values?
>>y
 Enter the root mean squared radius of the nucleus (in fm):
>>5.294
 Enter the skin thickness of the nucleus (in fm):
>>2.18
 Enter the mass of the neutral atom (in amu) (0 if the nucleus is to
     be static):
>>0
 Enter the nuclear spin quantum number (I) (in units of h / 2 pi):
>>0
 Enter the nuclear dipole moment (in nuclear magnetons):
>>0
 Enter the nuclear quadrupole moment (in barns):
>>0
```

The default charge distribution factors are overridden to the experimental values for ^{172}Yb: $r_{\mathrm{rms}}^{172} = \sqrt{\langle r^2 \rangle^{172}} = 5.294\,\mathrm{fm}$ (line 12) and $t^{172} = 2.18\,\mathrm{fm}$ (line 14) [19].[1] The values of parameters in the last four queries are set to zero (lines 15–22) as they are not used in the calculation here. The command outputs a text file `isodata` that contains the below contents, which will be used as an input file for some of the following commands in the calculations.[2]

Listing 14.1: Nuclear parameters in `isodata` file.

```
Atomic number:
   70.000000000000000
Mass number (integer) :
   172.00000000000000
Fermi distribution parameter a:
  0.52338755531043146
Fermi distribution parameter c:
   6.2523918780155956
Mass of nucleus (in amu):
   171.96159940678999
Nuclear spin (I) (in units of h / 2 pi):
   0.0000000000000000
Nuclear dipole moment (in nuclear magnetons):
   0.0000000000000000
Nuclear quadrupole moment (in barns):
   0.0000000000000000
```

[1] $c^{172} = 6.227\,\mathrm{fm}$ and $t^{172} = 2.18\,\mathrm{fm}$ in Ref. [19] give $r_{\mathrm{rms}}^{172} = 5.294\,\mathrm{fm}$.

[2] It is possible to create `isodata` file and set the parameter values directly without using `rnucleus` command.

14.2 Yb^+: Dirac-Hartree-Fock calculation

Next steps are for DHF calculations of the target atomic states: $[\mathrm{Xe}]\,4f^{14}\,6s\ {}^2S_{1/2}$, $[\mathrm{Xe}]\,4f^{14}\,5d\ {}^2D_{5/2}$ and ${}^2D_{3/2}$, and $[\mathrm{Xe}]\,4f^{13}\,6s^2\ {}^2F_{7/2}$. For a given states with the configuration γ, parity P, and total angular momentum J, CSF-configurations[3] γ_i ($i = 1, \cdots, N_{\mathrm{MR}}$ for the MR; N_{MR} is the number of the chosen MR configurations) are chosen and, from them, all other configurations γ_i ($i = n_{\mathrm{MR}}+1, \cdots, N_{\mathrm{CSF}}$; N_{CSF} is the total number of the CSFs) involving excitation of electrons in the MR and associated CSFs $\Phi(\gamma_i PJ)$ with the given states' P and J are generated via active set approach (see Section 12.2 and Chapter 13). For such atomic states, the radial parts $P_{nk}(r)$ and $Q_{nk}(r)$ of one-electron four-component Dirac wavefunctions $\phi_{nk}(\mathbf{r})$:[4]

$$\phi_{nk}(\mathbf{r}) = \frac{1}{\sqrt{4\pi}}\frac{1}{r}\begin{pmatrix} P_{nk}(r)\chi^m_{+k}(\theta,\phi) \\ Q_{nk}(r)\chi^m_{-k}(\theta,\phi) \end{pmatrix} \tag{14.3}$$

where

$$k = \mp(j+\frac{1}{2}) \text{ for } j = l \pm \frac{1}{2} = -[\mathrm{sgn}(j-l)](j+\frac{1}{2}) = \begin{cases} +l, & j = l - \frac{1}{2} \\ -(l+1), & j = l + \frac{1}{2} \end{cases}, \tag{14.4}$$

j, and l are the relativistic, total, and orbital angular quantum numbers, respectively,

$$\chi^m_k = \frac{1}{\sqrt{2k+1}}\begin{pmatrix} \sqrt{k+\frac{1}{2}-m}\,Y_k^{m-\frac{1}{2}}(\theta,\phi) \\ -\mathrm{sgn}\,k\sqrt{k+\frac{1}{2}-m}\,Y_k^{m+\frac{1}{2}}(\theta,\phi) \end{pmatrix}, \tag{14.5}$$

and $Y_l^m(\theta,\phi)$ is spherical harmonics, are self-consistently obtained through MCDHF calculation (see Section 12.2). The self-consistent-field (SCF) procedures start with

[3] Configurations with the angular coupling trees, (see Section 5.1 in Ref. [203]).

[4] The wavefunction is normalized as:

$$1 = \int \mathrm{d}\mathbf{r}\,\phi^\dagger(\mathbf{r})\phi(\mathbf{r}) = \int_0^\infty \mathrm{d}r\ \left[|P(r)|^2 + |Q(r)|^2\right] = \int_0^\infty 4\pi r^2 \mathrm{d}r\,\rho(r) \tag{14.1}$$

where

$$\rho(r) = \left[|P(r)|^2 + |Q(r)|^2\right]/(4\pi r^2) \tag{14.2}$$

is the radial electron density (see also Section 14.4).

appropriate seed functions (i.e., initial wavefunctions). The usual choice of the seed functions has been approximate wavefunctions from Thomas-Fermi potential (see, e.g., line 18 in Listing 14.2). Finally the ASFs were given as the superposition of the calculated CSFs: $\Psi(\gamma PJ) \approx \sum_{i=1}^{N_{\mathrm{CSF}}} c_i \Phi(\gamma_i PJ)$ and the mixing coefficients c_i.

Before starting the DHF calculation procedure with GRASP2018, a customized ordering of different subshells was prepared in a text file named `clist.ref`, as follows:

```
1s
2s
2p
3s
3p
3d
4s
4p
4d
5s
5p
4f
5d
6s
6p
5f
6d
7p
8s
```

Unfortunately, the GRASP2018 manual does not specify the exact role of the ordering in the calculations or for what the preset orderings (default, reverse, and symmetry) are (see Section 6.9 in the manual). An example in the section, however, suggests that the ordering should follow the increasing order of energy levels of the orbitals. Given the observation, a customized ordering is set as above so that the spectroscopic orbitals (see Section 4.4 in Ref. [203]) follow the order of energy levels from DHF calculations (see Table C.1) and correlation orbitals follow the Madelung rule.[5] Customizing the order stopped at $8s$ as the higher orbitals are far from the spectroscopic orbitals and thus have a tiny occupation,[6] but it might be worth adding more orbitals ordered by the Madelung rule. In a practical sense, the customized ordering was one of the essential parts of reliably achieving the convergence of the DHF calculations in this work (see Section 14.2.2); it was increasingly difficult to

[5] There has been an error in the order of $6s$ and $5d$, in retrospect.

[6] The number of electrons in an orbital.

achieve the convergence with the typical strategies (see Part IV in the GRASP2018 manual) as higher correlation orbitals were added, with the default ordering.

14.2.1 Core electrons: [Xe] f^{14}

The state of a Yb's core electrons were calculated first: $\gamma = [\mathrm{Xe}]\, 4f^{14}$.[7] Note that the calculation of core electrons does not have to be accurate, as the resulting one-electron wavefunctions will serve as seed wavefunctions in the following calculations of the states of interest in Yb^+ (see Section 14.2.2). Therefore, only a single CSF for the configuration consisting of spectroscopic orbitals was allowed for DHF calculation.[8] In other words, the configuration γ above was the only reference and there were only one CSF that approximated the ASF (i.e., $N_{\mathrm{MR}} = N_{\mathrm{CSF}} = 1$), and the excitation from γ was not allowed for the active set approach, reducing the calculation to the simplest form of DHF method: $\Psi(\gamma PJ) = \Phi(\gamma_1 PJ)$.

14.2.1.1 $1s$, $2sp$, $3spd$, and $4sp$ shells

As the calculation with all the shells in the γ failed to converge (see Listing 14.4 for an example GRASP2018 output in the case of such failure), the calculation ran for $1s$ to $4p$ shells[9] at once as the start. First, the list of CSFs for the calculation was generated using `rcsfgenerate` command:

```
>>rcsfgenerate

 RCSFGENERATE
 This program generates a list of CSFs

 Configurations should be entered in spectroscopic notation
 with occupation numbers and indications if orbitals are
 closed (c), inactive (i), active (*) or has a minimal
 occupation e.g. 1s(2,1)2s(2,*)
 Outputfiles: rcsf.out, rcsfgenerate.log

 Default, reverse, symmetry or user specified ordering? (*/r/s/u)
>>*

 Select core
        0: No core
        1: He (       1s(2)                    =  2 electrons)
```

[7] The full configuration is $\phi_r = 1s^2\, 2s^2\, 2p^6\, 3s^2\, 3p^6\, 3d^{10}\, 4s^2\, 4p^6\, 4d^{10}\, 5s^2\, 5p^6\, 4f^{14}$.
[8] The configuration γ has only one associated CSF-configuration γ_1 as γ contains no open shell.
[9] $1s^2\, 2s^2\, 2p^6\, 3s^2\, 3p^6\, 3d^{10}\, 4s^2\, 4p^6$

```
18          2: Ne ([He] + 2s(2)2p(6)              = 10 electrons)
19          3: Ar ([Ne] + 3s(2)3p(6)              = 18 electrons)
20          4: Kr ([Ar] + 3d(10)4s(2)4p(6)        = 36 electrons)
21          5: Xe ([Kr] + 4d(10)5s(2)5p(6)        = 54 electrons)
22          6: Rn ([Xe] + 4f(14)5d(10)6s(2)6p(6)  = 86 electrons)
23 >>0
24
25  Enter list of (maximum 100) configurations. End list with a blank
      line or an asterisk (*)
26
27  Give configuration           1
28 >>1s(2,c)2s(2,c)2p(6,c)3s(2,c)3p(6,c)3d(10,c)4s(2,i)4p(6,i)
29  Give configuration           2
30 >>
31  Give set of active orbitals, as defined by the highest principal
      quantum number
32  per l-symmetry, in a comma delimited list in s,p,d etc order, e.g.
      5s,4p,3d
33 >>4s,4p,3d
34  Resulting 2*J-number? lower, higher (J=1 -> 2*J=2 etc.)
35 >>0,0
36  Number of excitations (if negative number e.g. -2, correlation
37  orbitals will always be doubly occupied)
38 >>0
39  Generate more lists ? (y/n)
40 >>n
41   Excitationdata file opened
42
43 ...(skipped)...
44
45  Group CSFs into symmetry blocks
46
47  1 blocks were created
48
49        block   J/P             NCSF
50            1     0+               1
```

The ordering of orbitals in line 13 was set to default for now, but changed for correlations orbitals lying on higher levels, as described in Section 14.2.2.1. Lines 15–30 set the reference configuration for the calculation. No pre-selected core is used to manually set up the core configuration. The shells up to $3d$ were set to closed shells in the calculation (e.g., `c` in `3d(10,c)`) as the electrons in those shells would never be excited to higher shells to generate CSFs in this work. On the other hand, $4s$ and $4p$ shells were set to inactive shells (`i`'s in `4s(2,i)4p(6,i)`) so that their electrons could be excited for the future calculations to capture the effect of core-core and core-valence electrons' correlation (see Section 14.3.2). The maximum and minimum values of $2J$ were set to 0 as any closed shells have zero total angular momenta.No correlation orbital (i.e., non-spectroscopic orbitals) was involved by setting active

orbital of highest level to be the highest spectroscopic orbital in each orbital angular momentum state l: $4s$, $4p$, and $3d$ in line 33. It made the input reference configuration the only configuration for the calculation. It was printed out that $N_{\mathrm{CSF}} = 1$ in line 50indeed. The list of the generated CSF-configuration γ_1 could be found in an output file from `rcsfgenerate` command, `rcsf.out`.

```
Core subshells:
  3d-  3d   3p-  3p   3s   2p-  2p   2s   1s
Peel subshells:
  4p-  4p   4s
CSF(s):
  4p-( 2)  4p ( 4)  4s ( 2)

                             0+
```

The CSF-configuration was too simple and had no angular coupling tree in this case. More complicated examples can be found in, e.g., Listing 14.12.

Spin-angular integration, which takes care of the angular part of the calculations (e.g., angular part of an operator's matrix element for a given CSFs as bases) [173, 206, 207, 208], followed using `rangular` command.

```
>>cp rcsf.out rcsf.inp
>>rangular

 RANGULAR
 This program performs angular integration
 Input file:  rcsf.inp
 Outputfiles: mcp.30, mcp.31, ....
 rangular.log

 Full interaction?  (y/n)
>>y
 Block             1 ,  ncf =            1
 Loading CSF file ... Header only
 There are/is           12  relativistic subshells;

...(skipped)...

 RANGULAR: Execution complete.
```

Before running the `rangular` command, the CSF-configuration list file `rcsf.out` was copied as `rcsf.inp` to be an input of `rangular`, as in line 1:

Next, the seed one-electron wavefunctions were generated using `rwfnestimate` command.

Listing 14.2: `rwfnestimate` input and output to generate initial wavefunctions with which `rmcdhf` routine starts.

```
 >>rwfnestimate
```

```
 RWFNESTIMATE
 This program estimates radial wave functions
 for orbitals
 Input files: isodata, rcsf.inp, optional rwfn file
 Output file: rwfn.inp
 Default settings ?
>>y
 Loading CSF file ... Header only
 There are/is           12  relativistic subshells;
 The following subshell radial wavefunctions remain to be estimated:
 1s 2s 2p- 2p 3s 3p- 3p 3d- 3d 4s 4p- 4p

 Read subshell radial wavefunctions. Choose one below
     1 -- GRASP92 File
     2 -- Thomas-Fermi
     3 -- Screened Hydrogenic
>>2
 Enter the list of relativistic subshells:
>>*
 All required subshell radial wavefunctions  have been estimated:
Shell      e           p0        gamma        P(2)       Q(2)
   MTP  SRC

  1s   0.2471D+04  0.2339D+04  0.1000D+01  0.3427D-05 -0.1525D-10
    328  T-F
  2s   0.5459D+03  0.9090D+03  0.1000D+01  0.1332D-05 -0.5940D-11
    345  T-F
  2p-  0.5394D+03  0.5514D+02  0.1000D+01  0.1474D-11  0.3163D-06
    344  T-F
...(skipped)...
  4p-  0.9077D+02  0.1913D+02  0.1000D+01  0.5117D-12  0.1097D-06
    365  T-F
  4p   0.8643D+02  0.4499D+04  0.2000D+01  0.9655D-14 -0.4310D-19
    366  T-F
 RWFNESTIMATE: Execution complete.
Note: The following floating-point exceptions are signalling:
   IEEE_UNDERFLOW_FLAG IEEE_DENORMAL
```

By the second input (2) in the line 18, the radial wavefunction $(P_{nk}(r), Q_{nk}(r))^{\mathrm{T}}$ of an electron in each shell (n, k) was solved for the Thomas-Fermi model.[10] The third input (*) in the line 20 set all the orbitals to be relativistic. The *standard output* (stdout) from the command has rich information. The notation for each shell consists of the principal quantum number n followed by the symbol for orbital angular momentum l and, optionally, minus sign if the total angular momentum j is lower possible value (i.e., $j = l - \frac{1}{2}$); for instance, `3p-` and `3p` refer $p_{1/2}$ and $p_{3/2}$ with $n = 3$, respectively. For each shell, several parameters are shown. `e` is the calculated orbital energy eigenvalue in Hartree energy $E_h = \hbar c\alpha/a_0$. `p0` and `gamma`

[10]The model treats the effect of all other electrons to an electron as a screening potential of a particular form in addition to the Coulomb potential between the electron and nucleus.

are dimensionless parameters $p_{nk}^{(0)}$ and γ in

$$u_{nk}(r) = \tilde{r}^{\gamma}\left(u_{nk}^{(0)} + u_{nk}^{(1)}\tilde{r} + u_{nk}^{(2)}\tilde{r}^2 + \cdots\right), \quad u_{nk}^{(m)} = \begin{pmatrix} p_{nk}^{(m)} \\ q_{nk}^{(m)} \end{pmatrix}. \tag{14.6}$$

where $\tilde{r} = r/a_0$ is the r normalized by the Bohr radius a_0. `P(2)` and `Q(2)` is the value of $P_{nk}(r)$ and $Q_{nk}(r)$, in the unit of $a_0^{-1/2}$, at the grid point that is closest to (but not at) the origin.

Then it was ready to run MCDHF calculation using `rmcdhf` command.

```
>>rmcdhf

 RMCDHF
 This program determines the radial orbitals
 and the expansion coefficients of the CSFs
 in a self-onsistent field proceedure
 Input file:  isodata, rcsf.inp, rwfn.inp, mcp.30, ...
 Outputfiles: rwfn.out, rmix.out, rmcdhf.sum, rmcdhf.log

Default settings?  (y/n)
>>y
 Loading CSF file ... Header only
 There are/is           12  relativistic subshells;
 Loading CSF File for ALL blocks
 There are            1  relativistic CSFs... load complete;
 Loading Radial WaveFunction File ...
 There are            1  blocks  (block   J/Parity   NCF):
  1    0+       1

 Enter ASF serial numbers for each block
 Block            1    ncf =            1  id =    0+
1
 Radial functions
 1s 2s 2p- 2p 3s 3p- 3p 3d- 3d 4s 4p- 4p
 Enter orbitals to be varied (Updating order)
>>*
 Which of these are spectroscopic orbitals?
>>*
 Enter the maximum number of SCF cycles:
>>1000

 Average energy =  -1.3283229562D+04 Hartrees

Optimise on the following level(s):

Level  1    Energy = -1.328322956181D+04    Weight =  1.00000D+00

Weights of major contributors to ASF:

Block Level J Parity      CSF contributions

  1     1     0 +       1.0000
                              1

```

```
Generalised occupation numbers:

   2.0000D+00  2.0000D+00  2.0000D+00  4.0000D+00  2.0000D+00
   2.0000D+00
   4.0000D+00  4.0000D+00  6.0000D+00  2.0000D+00  2.0000D+00
   4.0000D+00

 Iteration number   1
 --------------------

Lagrange multipliers are not required
                                          Self-            Damping
Subshell    Energy    Method   P0    consistency  Norm-1  factor  JP
    MTP INV NNP

  1s    2.2870480D+03  1  2.327D+03  1.05D-01  1.24D-02 0.000   276
      355  0  0
...(skipped)...
  4s    6.1356652D+01  1  2.269D+02  1.47D-01  1.26D-02 0.100   338
      371  0  3

 Average energy =  -1.3415109114D+04 Hartrees

Optimise on the following level(s):

Level  1    Energy = -1.341510911444D+04    Weight =  1.00000D+00

Weights of major contributors to ASF:

Block Level J Parity      CSF contributions

  1     1     0 +       1.0000
                              1

Generalised occupation numbers:

   2.0000D+00  2.0000D+00  2.0000D+00  4.0000D+00  2.0000D+00
   2.0000D+00
   4.0000D+00  4.0000D+00  6.0000D+00  2.0000D+00  2.0000D+00
   4.0000D+00

 Iteration number   2
 --------------------
...(skipped)...
 Iteration number   3
 --------------------
...(skipped)...
 Iteration number   5
 --------------------
...(skipped)...
Generalised occupation numbers:

   2.0000D+00  2.0000D+00  2.0000D+00  4.0000D+00  2.0000D+00
   2.0000D+00
   4.0000D+00  4.0000D+00  6.0000D+00  2.0000D+00  2.0000D+00
   4.0000D+00

 Wall time:
       28 seconds

```

```
 Finish Date and Time:
   Date (Yr/Mon/Day): 2022/03/14
   Time (Hr/Min/Sec): 16/15/15.915
   Zone: -0400

 RMCDHF: Execution complete.
Note: The following floating-point exceptions are signalling:
   IEEE_UNDERFLOW_FLAG IEEE_DENORMAL
```

The second input (`*`) in the line 24 set all orbitals to be solved for their one-electron radial wavefunctions. The third input (`*`) set all orbitals to be *spectroscopic orbitals* so that the number of nodes in each radial wavefunction was forced to be $n - l - 1$ (see Sections 4.4 and 3.3 in the GRASP2018 manual and Ref. [189], respectively). An output file `rmcdhf.sum`, rather than the long stdout, contains useful data in a better form, including information about nucleus; parameters for radial grid; `e`, `p0`, `gamma`, `P(2)`, and `Q(2)` as in the stdout of the `rwfnestimate` command; the radial moments of the distribution of electrons; and the energy of the state.

```
 There are 36 electrons in the cloud
  in 1 relativistic CSFs
  based on 12 relativistic subshells.

The atomic number is  70.0000000000;
 the mass of the nucleus is  3.133508267869D+05 electron masses;
  Fermi nucleus:
  c = 1.210654914042D-04 Bohr radii,
  a = 9.374560516004D-06 Bohr radii;
  there are 169 tabulation points in the nucleus.

Speed of light =  137.0359991390D+00 atomic units.

Radial grid: R(I) = RNT*(exp((I-1)*H)-1), I = 1, ..., N;

 RNT  =  2.857142857143D-08 Bohr radii;
 H    =  5.000000000000D-02 Bohr radii;
 N    =  590;
 R(1) =  0.000000000000D+00 Bohr radii;
 R(2) =  1.464888467886D-09 Bohr radii;
 R(N) =  1.761588423842D+05 Bohr radii.

 OL calculation.
 Level 1 will be optimised.

Radial wavefunction summary:


   Self
Subshell      e              p0      gamma      P(2)        Q(2)
   Consistency MTP

  1s   2.3189453392D+03  2.328D+03  1.00  3.411D-06 -1.517D-11
   5.749D-06  359
...(skipped)...
```

```
  4p    5.5776736585D+01   3.270D+03   2.00   7.017D-15 -3.130D-20
    6.360D-06   372

                   -3              -1                                  2
                4      Generalised
Subshell     <  r  >         <  r  >         <  r  >         <  r  >
       <  r  >       occupation

  1s       0.00000D+00     8.06082D+01     1.96608D-02     5.29929D-04
     7.56510D-07     2.00000D+00
...(skipped)...
  4p       9.20523D+02     3.06249D+00     4.58798D-01     2.37563D-01
     7.91511D-02     4.00000D+00

Eigenenergies:

Level   J Parity        Hartrees               Kaysers
    eV

  1        0 +     -1.342679356171D+04   -2.946840567440D+09
    -3.653616625917D+05

Weights of major contributors to ASF:

Block Level J Parity      CSF contributions

  1     1     0 +        1.0000
                              1
```

`rmcdhf` also outputs `rwfn.out`, a binary file that stores the calculated radial wavefunctions.

The one cycle of DHF calculation typically ends here or by running `rsave` command for the following CI calculations, which rename all the output files from the last procedure to the input argument of the command; for instance, `rcsf.inp`, `rmcdhf.sum`, and `rwfn.out` are renamed as `Yb_core.c`, `Yb_core.sum`, and `Yb_core.w`, respectively, by the following line:

```
rsave Yb_core
```

14.2.1.2 $4d$ shell

The orbitals higher than $4p$ is to be added next in the reference configuration.[11] To achieve convergence of the calculation, no more than two orbitals were added at one cycle of DHF calculation. It is not necessary to start from `rnucleus` again. Rather, `rcsfgenerate` was run to add shells in the configuration. Adding orbitals started

[11] $\gamma = 1s^2\,2s^2\,2p^6\,3s^2\,3p^6\,3d^{10}\,4s^2\,4p^6\,4d^{10}$

from $4d$.

```
>>rcsfgenerate

 RCSFGENERATE
...(skipped)...
 Default, reverse, symmetry or user specified ordering? (*/r/s/u)
>>*

 Select core
...(skipped)...
>>0
...(skipped)...
 Give configuration            1
>>1s(2,c)2s(2,c)2p(6,c)3s(2,c)3p(6,c)3d(10,c)4s(2,i)4p(6,i)4d(10,i)
...(skipped)...
 Give set of active orbitals, as defined by the highest principal
    quantum number
 per l-symmetry, in a comma delimited list in s,p,d etc order, e.g.
    5s,4p,3d
>>4s,4p,4d
 Resulting 2*J-number? lower, higher (J=1 -> 2*J=2 etc.)
>>0,0
 Number of excitations (if negative number e.g. -2, correlation
 orbitals will always be doubly occupied)
>>0
 Generate more lists ? (y/n)
>>n
...(skipped)...
       block   J/P             NCSF
           1     0+               1
```

The excitation of electrons in the reference configuration to higher orbitals was not allowed again, as well as all the following DHF calculations, resulting in $N_{\mathrm{CSF}} = 1$ for the configuration with the closed shells.

The angular integration with `rangular` and generating seed wavefunctions using `rwfnestimate` followed.

```
>>cp rcsf.out rcsf.inp
>>rangular < rangular_input
 RANGULAR
...(skipped)...
 RANGULAR: Execution complete.
```

```
>>rwfnestimate
 RWFNESTIMATE
 This program estimates radial wave functions
 for orbitals
 Input files: isodata, rcsf.inp, optional rwfn file
 Output file: rwfn.inp
 Default settings ?
>>y
 Loading CSF file ... Header only
 There are/is           14  relativistic subshells;
 The following subshell radial wavefunctions remain to be estimated:
 1s 2s 2p- 2p 3s 3p- 3p 3d- 3d 4s 4p- 4p 4d- 4d
```

```
13
14  Read subshell radial wavefunctions. Choose one below
15      1 -- GRASP92 File
16      2 -- Thomas-Fermi
17      3 -- Screened Hydrogenic
18 >>1
19  Enter the file name (Null then "rwfn.out")
20 >>
21  Enter the list of relativistic subshells:
22 >>*
23  The following subshell radial wavefunctions remain to be estimated:
24  4d- 4d
25
26  Read subshell radial wavefunctions. Choose one below
27      1 -- GRASP92 File
28      2 -- Thomas-Fermi
29      3 -- Screened Hydrogenic
30 >>2
31  Enter the list of relativistic subshells:
32 >>*
33  All required subshell radial wavefunctions  have been estimated:
34 Shell      e           p0        gamma        P(2)        Q(2)
     MTP  SRC
35
36   1s   0.2319D+04  0.2334D+04  0.1000D+01  0.3419D-05 -0.1549D-10
      359  rwf
37 ...(skipped)...
38   4d   0.5935D+02  0.1859D+05  0.3000D+01  0.5843D-22 -0.2656D-27
      369  T-F
39  RWFNESTIMATE: Execution complete.
40 Note: The following floating-point exceptions are signalling:
     IEEE_UNDERFLOW_FLAG IEEE_DENORMAL
```

The calculated wavefunctions in `rwfn.out` file from the previous calculation for $\gamma' = 1s^2 \cdots 4p^6$ was used as the seed wavefunctions for all the previous orbitals, by choosing `1` as the first input in the line 18. The only new orbital is $4d$,[12] and the wavefunction from Thomas-Fermi model was chosen for the seed wavefunction by the input in the line 30. All the orbitals were set to be relativistic again here (the lines 22 and 32) and for all the following DHF calculations.

Finally, `rmcdhf` command was executed for the DHF calculation.

```
1 >>rmcdhf
2
3  RMCDHF
4 ...(skipped)...
5 Default settings?  (y/n)
6 >>y
7 ...(skipped)...
8  Enter ASF serial numbers for each block
9  Block            1    ncf =            1  id =    0+
10 >>1
11  Radial functions
```

[12] `4d-` and `4d` (i.e., $4d_{3/2}$ and $4d_{5/2}$), relativistically.

```
 1s 2s 2p- 2p 3s 3p- 3p 3d- 3d 4s 4p- 4p 4d- 4d
 Enter orbitals to be varied (Updating order)
>>*
 Which of these are spectroscopic orbitals?
>>*
 Enter the maximum number of SCF cycles:
>>1000

 Average energy =  -1.3753595143D+04 Hartrees
...(skipped)...
 Iteration number   1
 --------------------
...(skipped)...
 Iteration number   5
 --------------------
...(skipped)...
Wall time:
...(skipped)...
 RMCDHF: Execution complete.
Note: The following floating-point exceptions are signalling:
   IEEE_UNDERFLOW_FLAG IEEE_DENORMAL
```

An input to be emphasized here is for the second query at the line 13. The previously calculated one-electron wavefunctions for $1s$ to $4p$ shell are loaded when `rwfnestimate` was run, but the orbitals participated in the DHF calculation again when $4d$ shell was included in the configuration, by setting all orbitals to be varied. Therefore, the interaction between electrons in $4d$ and all other shells was taken into account, resulting in the perturbation in $1s$–$4p$ orbital wavefunctions from the previous solution with no electron in $4d$ shell. The same technique will be used whenever possible (i.e., the convergence can be achieved), especially for the valence and low-lying correlation orbitals described in Section. 14.2.2 in addition to the core orbitals.

The convergence is obtained again with the small number of iterations. (see line 25)

14.2.1.3 $4f$ shell

$4f$ orbital was added next. The convergence of DHF calculation could not be achieved via the procedure described above, and a technique to handle such a case introduced in Section 4.4 in the GRASP2018 manual was used: increasing the nuclear charge number from Z to Z', performing DHF calculation, and using the resulting wavefunction as seed wavefunctions for DHF calculation for the original charge Z. Here

Z was increased by one at a time until the convergence was achieved at $Z = 72$. The atomic number in the `isodata` file was directly modified to 72:

```
Atomic number:
   72.000000000000000
Mass number (integer) :
...(skipped)...
```

and the solutions for all the orbitals that had been included by then were updated for $Z = 72$:

```
>>cp rcsf.out rcsf.inp
>>rangular

 RANGULAR
...(skipped)...
 Full interaction?  (y/n)
>>y
...(skipped)...
 RANGULAR: Execution complete.
```

```
>>rwfnestimate
 RWFNESTIMATE
...(skipped)...
 Default settings ?
>>y
 Read subshell radial wavefunctions. Choose one below
     1 -- GRASP92 File
     2 -- Thomas-Fermi
     3 -- Screened Hydrogenic
>>1
 Enter the file name (Null then "rwfn.out")
>>
 Enter the list of relativistic subshells:
*
 All required subshell radial wavefunctions  have been estimated:
...(skipped)...
 RWFNESTIMATE: Execution complete. ...(skipped)
```

[here, seed wavefunctions for all orbitals were set to be the solutions of the previous DHF calculations for $Z = 70$ (the input in the line 10)]

```
>>rmcdhf

 RMCDHF
...(skipped)...
Default settings?  (y/n)
>>y
...(skipped)...
 Enter ASF serial numbers for each block
 Block            1    ncf =            1  id =    0+
>>1
 Radial functions
 1s 2s 2p- 2p 3s 3p- 3p 3d- 3d 4s 4p- 4p 4d- 4d
 Enter orbitals to be varied (Updating order)
>>*
 Which of these are spectroscopic orbitals?
```

```
>>*
 Enter the maximum number of SCF cycles:
>>1000
...(skipped)...
 Iteration number   5
 --------------------
...(skipped)...
 Wall time:
...(skipped)...
 RMCDHF: Execution complete. ...(skipped)
```

Then, $4f$ shell was added in the configuration,[13]

```
>>rcsfgenerate

 RCSFGENERATE
...(skipped)...
 Default, reverse, symmetry or user specified ordering? (*/r/s/u)
>>*

 Select core
...(skipped)...
>>0
...(skipped)...
 Give configuration           1
>>1s(2,c)2s(2,c)2p(6,c)3s(2,c)3p(6,c)3d(10,c)4s(2,i)4p(6,i)4d(10,i)4
   f(14,i)
 Give configuration           2
>>
 Give set of active orbitals, ...(skipped)...
>>4s,4p,4d,4f
 Resulting 2*J-number? lower, higher (J=1 -> 2*J=2 etc.)
>>0,0
 Number of excitations ...(skipped)...
>>0
 Generate more lists ? (y/n)
>>n
...(skipped)...
       block  J/P            NCSF
           1    0+               1
```

a seed wavefunctions for the new $4f_{5/2}$ and $4f_{7/2}$ orbitals were given from the Thomas-Fermi model,

```
>>rwfnestimate
...(skipped)...
 Read subshell radial wavefunctions. Choose one below
...(skipped)...
>>1
 Enter the file name (Null then "rwfn.out")
>>
 Enter the list of relativistic subshells:
>>*
 The following subshell radial wavefunctions remain to be estimated:
 4f- 4f

 Read subshell radial wavefunctions. Choose one below
```

[13] $\gamma = 1s^2\,2s^2\,2p^6\,3s^2\,3p^6\,3d^{10}\,4s^2\,4p^6\,4d^{10}\,4f^{14}$

```
...(skipped)...
>>2
 Enter the list of relativistic subshells:
>>2
...(skipped)...
 RWFNESTIMATE: Execution complete. ...(skipped)
```

and the DHF calculation was run.

```
>>rmcdhf
...(skipped)...
>>y
...(skipped)...
>>1
...(skipped)...
>>*
 Which of these are spectroscopic orbitals?
>>*
 Enter the maximum number of SCF cycles:
>>1000
...(skipped)...
 Iteration number   8
 --------------------
...(skipped)...
 RMCDHF: Execution complete. ...(skipped)
```

Since the DHF calculation with the $4f$ shell converged, all the orbitals were solved again for $Z = 70$. The `isodata` file were edited again for $Z = 70$, and `rcsfgenerate`, `rangular` (after copying `rcsf.out` to `rcsf.inp`), `rwfnestimate` (setting all the seed wavefunctions to be the DHF solution for $Z = 72$), and `rmcdhf` were executed in the listed order.

14.2.1.4 $5sp$ shells

As the last step for the core electrons in Yb^+, $5s$ and $5p$ shells were added at the same time[14] by running `rcsfgenerate`,

```
>>rcsfgenerate
...(skipped)...
>>*
...(skipped)...
>>0
...(skipped)...
 Give configuration           1
>>1s(2,c)2s(2,c)2p(6,c)3s(2,c)3p(6,c)3d(10,c)4s(2,c)4p(6,c)4d(10,c)4
   f(14,c)5s(2,i)5p(6,i)
 Give configuration           2
>>
 Give set of active orbitals, ...(skipped)...
>>5s,5p,4d,4f
```

[14] $\gamma = 1s^2\,2s^2\,2p^6\,3s^2\,3p^6\,3d^{10}\,4s^2\,4p^6\,4d^{10}\,5s^2\,5p^6\,4f^{14} = [\mathrm{Xe}]\,4f^{14}$

```
 Resulting 2*J-number? lower, higher (J=1 -> 2*J=2 etc.)
>>0,0
 Number of excitations ...(skipped)...
>>0
 Generate more lists ? (y/n)
>>n
...(skipped)...
       block   J/P             NCSF
           1     0+               1
```

`rangular`, `rwfnestimate` (previous DHF solutions and Thomas-Fermi solutions as seed functions for all the previously counted orbitals and the new orbitals, respectively), and `rmcdhf`.

The resulting energy eigenvalues of all the orbitals are compared with Ref. [27] in Table C.1.

14.2.2 Valence and correlation electrons up to $8spdf$

The calculations for valence and correlation electrons were somewhat different from the calculations for core electrons in several aspects: custom orbital ordering, radial grid, way to add orbitals, simultaneous calculations of different configurations, manual choice of integration method, and comparison for energy orders. Also, as the energies of orbitals got closer to the continuum (i.e., the energy of unbound electrons), the convergence and the convergence with the right order of energies of different orbitals were increasingly difficult to achieve. To endure the right results, several new strategies were employed as described below, and the relations between orbital energies were checked after each step:

$$E_{nj} < E_{(n+1)j} \tag{14.7a}$$

$$E_{n,l+1/2} < E_{n,l-1/2} \tag{14.7b}$$

where E_{nj} is the energy of the relativistic orbital with the principal number n and total angular momentum number $j = l \pm \frac{1}{2}$.[15] [16].

[15] For instance, $E(\texttt{6p}) < E(\texttt{7p})$ and $E(\texttt{6p}) < E(\texttt{6p-})$.

[16] $E_{nj} < 0$ as it is the energy of a bound state. Lower energy means state bound more tightly.

14.2.2.1 $6sp$ and $5d$ shells

First, the valence shells $6s$ and $5d$ in $^2S_{1/2}$, $^2D_{3/2}$, or $^2D_{5/2}$ states, and a correlation shell $6p$ were added,[17] which are the lowest shells over the core orbitals. Here, calculating different configurations at the same time was introduced. The ASFs of different states with configurations $\gamma^{(m)}$ were approximated with the form $\Psi(\gamma^{(m)}P^{(m)}J^{(m)}) \approx \sum_{i=1}^{N_{\mathrm{CSF}}^{(m)}} c_i^{(m)}\Phi(\gamma_i^{(m)}P^{(m)}J^{(m)})$, while all the CSFs for the different states were constructed over the same set of one-electron orbital wavefunctions $\phi_{nk}(\mathbf{r})$. In other words, MCDHF calculations found the solutions to $c_i^{(m)}$ of each state and *shared* $\phi_{nk}(\mathbf{r})$ to approximate all the states, for the list of CFS-configurations given for each of the states.

```
>>rcsfgenerate

 RCSFGENERATE
...(skipped)...
 Default, reverse, symmetry or user specified ordering? (*/r/s/u)
>>u

 Select core
...(skipped)...
        4: Kr ([Ar] + 3d(10)4s(2)4p(6)       = 36 electrons)
...(skipped)...
>>4

 Enter list of (maximum 100) configurations. End list with a blank
    line or an asterisk (*)

 Give configuration           1
>>4d(10,c)5s(2,i)5p(6,i)4f(14,i)6s(1,i)
 Give configuration           2

 Give set of active orbitals, ...(skipped)...
>>6s,5p,4d,4f
 Resulting 2*J-number? lower, higher (J=1 -> 2*J=2 etc.)
>>1,1
 Number of excitations ...(skipped)...
>>0
 Generate more lists ? (y/n)
>>y
 Enter list of (maximum 100) configurations. End list with a blank
    line or an asterisk (*)

 Give configuration           1
>>4d(10,c)5s(2,i)5p(6,i)4f(14,i)6p(1,i)
 Give configuration           2
>>
 Give set of active orbitals, ...(skipped)...
```

[17] $6p$ shell could be a valence shell if, for instance, [Xe] $4f^{14}\,6p\ ^2P_{1/2}$ state was of interest, which is the excited state of the cooling transition $^2S_{1/2} \leftrightarrow {}^2P_{1/2}$.

```
35 >>5s,6p,4d,4f
36  Resulting 2*J-number? lower, higher (J=1 -> 2*J=2 etc.)
37 >>1,3
38  Number of excitations ...(skipped)...
39 >>0
40  Generate more lists ? (y/n)
41 >>y
42  Enter list of (maximum 100) configurations. End list with a blank
      line or an asterisk (*)
43
44  Give configuration            1
45 >>4d(10,c)5s(2,i)5p(6,i)4f(14,i)5d(1,i)
46  Give configuration            2
47 >>
48  Give set of active orbitals, ...(skipped)...
49 >>5s,5p,5d,4f
50  Resulting 2*J-number? lower, higher (J=1 -> 2*J=2 etc.)
51 >>3,5
52  Number of excitations ...(skipped)...
53 >>0
54  Generate more lists ? (y/n)
55 >>n
56   Excitationdata file opened
57 ...(skipped)...
58        block   J/P             NCSF
59            1   1/2+               1
60            2   1/2-               1
61            3   3/2+               1
62            4   3/2-               1
63            5   5/2+               1
```

The first input (`u`) at the line 6 chose to use the customized orbital ordering introduced in the beginning of Section 14.2, which will be used for all the DHF calculations here and below. A preset core configuration `4:  Kr`[18] was chosen at the line 12 to simplify the configuration inputs. The first set of inputs for state configurations (lines 16–25) set the configuration $\gamma^S \equiv \gamma^{(1)} = [\mathrm{Xe}]\, 4f^{14}\, 6s$ with $2J = 1$.[19] The inputs (`y`) in lines 27 and 41 were to add more states by repeating the same set of queries. The second (lines 30–39) and third (lines 44–53) sets of inputs set $\gamma^P \equiv \gamma^{(2)} = \gamma^{(3)} = [\mathrm{Xe}]\, 4f^{14}\, 6p$ with $2J = 1, 3$ and $\gamma^D \equiv \gamma^{(4)} = \gamma^{(5)} = [\mathrm{Xe}]\, 4f^{14}\, 5d$ with $2J = 3, 5$. Therefore, there are total five ASFs to be calculated: $\left(\gamma^{(m)}, P^{(m)}, J^{(m)}\right) = (\gamma^S, +, \frac{1}{2})$, $(\gamma^P, -, \frac{1}{2})$, $(\gamma^P, -, \frac{3}{2})$, $(\gamma^D, +, \frac{3}{2})$, and $(\gamma^D, +, \frac{5}{2})$,[20] which correspond to the block 1, 2, 4, 3, and 5 in the output lines 58–63, respectively. For each configuration, all

[18] $1s^2\, 2s^2\, 2p^6\, 3s^2\, 3p^6\, 3d^{10}\, 4s^2\, 4p^6$

[19] The superscript is omitted if the occupation of an orbital is one (e.g., $6s = 6s^1$).

[20] The corresponding term symbols are $^2S_{1/2}$, $^2P_{1/2}$, $^2P_{3/2}$, $^2D_{3/2}$, and $^2D_{5/2}$, respectively, considering the configurations. The terms symbol of ASFs in a calculation can be obtained using `jj2lsj` command, see Section 9.2 in the GRASP2018 manual.

possible values of J were listed (e.g., $2J = 1, 3$ for γ^P) as it helped achieve convergence. The `rangular` command was run as usual. `rwfnestimate` had new inputs to manually set the grid parameters:

Listing 14.3: `rwfnestimate` for $6sp5d$ configuration.

```
rwfnestimate
 RWFNESTIMATE
...(skipped)...
 Default settings ?
>>n
 Generate debug printout?
>>n
 File  erwf.sum  will be created as the ERWF SUMmary File;
 enter another file name if this is not acceptable; null otherwise:
>>
 Loading CSF file ... Header only
 There are/is           26  relativistic subshells;
 Change the default speed of light or radial grid parameters?
>>y
 The physical speed of light in atomic units is   137.03599913900001
          ;
 revise this value?
>>n
 The default radial grid parameters for this case are:
  RNT =    2.8571428571428569E-008 ;
  H =    5.0000000000000003E-002 ;
  HP =    0.0000000000000000      ;
  N =          590 ;
 revise these values?
>>y
 Enter RNT:
>>2.857142857143D-08
 Enter H:
>>5.000000000000D-02
 Enter HP:
>>0
 Enter N:
>>590
 The following subshell radial wavefunctions remain to be estimated:
 1s 2s 2p- 2p 3s 3p- 3p 3d- 3d 4s 4p- 4p 4d- 4d 5s 5p- 5p 4f- 4f 5d-
    5d 6s 6p-
 6p 5f- 5f

 Read subshell radial wavefunctions. Choose one below
...(skipped)...
>>1
 Enter the file name (Null then "rwfn.out")
>>
 Enter the list of relativistic subshells:
>>*
 The following subshell radial wavefunctions remain to be estimated:
 5d- 5d 6s 6p- 6p

 Read subshell radial wavefunctions. Choose one below
...(skipped)...
>>2
 Enter the list of relativistic subshells:
>>*
```

```
 All required subshell radial wavefunctions  have been estimated:
Shell       e            p0         gamma         P(2)        Q(2)
    MTP  SRC

  1s   0.2268D+04  0.2334D+04  0.1000D+01  0.3419D-05 -0.1549D-10
    379  rwf
...(skipped)...
  6p   0.6182D+00  0.5087D+03  0.2000D+01  0.1092D-14 -0.4872D-20
    412  T-F
 Revise any of these estimates?
>>n
 RWFNESTIMATE: Execution complete. ...(skipped)
```

The lines 23–32 sets the parameters for the radial grid `R(I) = RNT*(exp((I-1)*H)-1), I = 1, ..., N`, where `RNT` has a_0 as its unit, `H` is dimensionless, and `N` is the total number of the grid points (see Section 9.1 in the GRASP2018 manual).[21] The grid parameters were manually set for future calculations while varying nuclear parameters, as described in Section 15.1.3. The seed wavefunctions for the core orbitals were loaded from the calculations in Section 14.2.1 while the Thomas-Fermi model's solutions were assigned for the new, valence and correlation shells, as usual.

```
>>rmcdhf
...(skipped)...
Default settings?  (y/n)
>>n
Generate debug output?  (y/n)
>>n
 Loading CSF file ... Header only
 There are/is           24  relativistic subshells;
 Loading CSF File for ALL blocks
 There are             5  relativistic CSFs... load complete;
Change the default speed of
 light or radial grid parameters?  (y/n) y
 Speed of light =    137.03599913900001      ; revise ?
>>n
 The default radial grid parameters for this case are:
  RNT =    2.8571428571428569E-008
  H =    5.0000000000000003E-002
  HP =    0.0000000000000000
  N =          590
  revise these values?
>>y
 Enter RNT:
>>2.857142857143D-08
 Enter H:
>>5.000000000000D-02
 Enter HP:
>>0
 Enter N:
>>590
 Revised RNT =    2.8571428571430001E-008
```

[21] GRASP2018 uses *logarithmic grids* in which the spacing between neighboring grid points is exponentially increasing.

```
 Revised H    =     5.00000000000000003E-002
 Revised HP   =     0.0000000000000000
 Revised N    =           590
 Revise the default ACCY =    1.56250000000000006E-008
>>n
 Loading Radial WaveFunction File ...
 There are            5  blocks  (block   J/Parity   NCF):
  1  1/2+       1       2  1/2-       1       3  3/2+       1
    4  3/2-       1
  5  5/2+       1

 Enter ASF serial numbers for each block
 Block            1    ncf =            1  id =  1/2+
>>1
 Block            2    ncf =            1  id =  1/2-
>>1
 Block            3    ncf =            1  id =  3/2+
>>1
 Block            4    ncf =            1  id =  3/2-
>>1
 Block            5    ncf =            1  id =  5/2+
>>1
 level weights (1 equal;  5 standard;  9 user)
>>1
 Radial functions
 1s 2s 2p- 2p 3s 3p- 3p 3d- 3d 4s 4p- 4p 4d- 4d 5s 5p- 5p 4f- 4f 5d-
    5d 6s 6p-
 6p
 Enter orbitals to be varied (Updating order)
>>*
 Which of these are spectroscopic orbitals?
>>*
 Enter the maximum number of SCF cycles:
>>1000
Modify other defaults?  (y/n)
>>y
 An oscillation in the large-component of the radial wavefunction is
    diregarded
 for the purposes of node counting if its amplitude is less than
    1/20 the
 maximum amplitude.   Revise this?
>>n
 Method            1  is used for integrating the radial
    differential equation for subshells
  1s 2s 2p- 2p 3s 3p- 3p 3d- 3d 4s 4p- 4p 4d- 4d 5s 5p- 5p 4f- 4f 5d
    - 5d 6s 6p-
  6p
 Select a different integration method for any subshell radial
    wavefunction?
>>y
 Method            1 :
>>*
 Method            2 :
>>
 Method            3 :
>>
 Method            4 :
>>
 The first oscillation of the large component
 of all radial wavefunctions will be required to be positive.
```

```
   Revise this?
>>n
 Set accelerating parameters for subshell radial wavefunctions?
>>n
 Set accelerating parameters for the eigenvectors?
>>n
 Following the improvement of each of the subshell radial
   wavefunctions in turn,
 the            6  least self-consistent functions will be improved
   at the
 end of the first SCF cycle. Revise this setting?
>>n
 The maximum number of cycles in attempting to solve each radial
   equation is
          3  times the principal quantum number of the radial
 wave-function to be estimated.   Revise this setting?
>>n
 Subshell radial wavefunctions will be Schmidt orthogonalised
   immediately
 following their estimation to all functions with poorer self-
   consistency.
  Revise this?
>>n
 Orthonomalization order?
      1 -- Update order
      2 -- Self consistency connected
>>1

 Average energy =  -1.4067080329D+04 Hartrees
...(skipped)...
 Iteration number   1
 --------------------
...(skipped)...
 Iteration number   7
 --------------------
...(skipped)...
 RMCDHF: Execution complete. ...(skipped)
```

Choosing not to use default settings (line 6) showed a long list of additional queries. The same grid parameters used for `rwfnestimate` were input in lines 23–29. Another new step was to compare the results of the different integration methods specified in the lines 72–81; one of the four methods can be chosen for each of the relativistic orbitals. Here, all the orbitals in the calculation (an asterisk symbol `*`)[22] chose Method 1. Although the GRASP2018 manual does not specify what the methods are about, they sometimes give significant differences in DHF calculation results. For this run, for instance, Method 1 gave convergence, the right order of energies [Eq. (14.7)], and consistent energy levels with the results previously obtained for core

[22]The asterisk `*` is not merely a mark for choosing a method. It refers to any orbitals in the calculation.

electrons only (Section 14.2.1 and Table C.1). On the other hand, Method 2 did not converge the calculation for $6p_{3/2}$ orbital as shown in the stdout:

Listing 14.4: `rmcdhf` run that failed to achieve a convergence.

```
(skipped including inputs)...
 Method 2 unable to solve for  6p  orbital
 Iteration number: 18, limit: 18
 Present estimate of P0;  0.57921939441735D+03
 Present estimate of E(J):  0.81812498927639D+02, DELEPS:
   -0.18572643659401D+02
 Lower bound on energy:  0.81189740939245D+02, upper bound:
   0.82435256916032D+02
 Join point:  324, Maximum tabulation point: 434
 Number of nodes counted:  6, Correct number:  4
 Sign of P at first oscillation:  1.

 Failure; equation for orbital  6p  could not be solved using method
    2


 ****** Error in SUBROUTINE IMPROV ******
 Convergence not obtained
...(skipped)
```

Method 3 converged but gave inconsistent energies with the core-electron calculation. Method 4 failed to make some states to be bound states:[23]

```
(skipped including inputs)...
 IN: maximum tabulation point exceeds
  dimensional limit (currently 590);
  radial wavefunction may indicate a
  continuum state.
Note: The following floating-point exceptions are signalling:
   IEEE_UNDERFLOW_FLAG IEEE_DENORMAL
```

Obviously, the choice was Method 1.

There was a new query in between the typical queries: `level weights` in line 53. It appears when there are more than one states to be calculated, and asks the relative weight of each state for calculating the shared orbital wavefunctions $\phi_{nk}(\mathbf{r})$. The usual choice is the standard weights (`5`) which weights each state with the value of $2J + 1$ (i.e., the number of internal states). For this run, however, the standard weights failed to converge the calculation, so equal weights (`1`) were chosen instead.

14.2.2.2 $5f$ shell

$5f$ was added by adding a reference configuration $\gamma^F \equiv \gamma^{(6)} = \gamma^{(7)} = [\mathrm{Xe}]\, 4f^{14}\, 5f$:

[23] i.e., the radial wavefunctions do not decay out at some positions away from the origin by many a_0.

```
>>rcsfgenerate
...(skipped)...
>>u
...(skipped)...
>>4
...(skipped for the previous state configurations)...
 Generate more lists ? (y/n)
>>y
...(skipped)...
 Give configuration            1
>>4d(10,c)5s(2,i)5p(6,i)4f(14,i)5f(1,i)
 Give configuration            2
>>
 Give set of active orbitals, ...(skipped)...
>>5s,5p,5d,5f
 Resulting 2*J-number? lower, higher (J=1 -> 2*J=2 etc.)
>>5,7
 Number of excitations ...(skipped)...
>>0
 Generate more lists ? (y/n)
>>n
...(skipped)...
       block   J/P             NCSF
           1   1/2+               1
           2   1/2-               1
           3   3/2+               1
           4   3/2-               1
           5   5/2+               1
           6   5/2-               1
           7   7/2-               1
```

There were then two more ASFs added: $\left(\gamma^{(m)}, P^{(m)}, J^{(m)}\right) = (\gamma^F, -, \frac{5}{2})$ and $(\gamma^F, -, \frac{7}{2})$ in block 6 and 7 in the output lines 23–30, respectively.

`rangular`, `rwfnestimate` were run just as for the last time. `rmcdhf` were mostly the same as the last time except for several inputs:

```
>>rmcdhf
...(skipped)...
Default settings?  (y/n)
>>n
...(skipped including inputs)...
 Enter RNT:
>>2.857142857143D-08
 Enter H:
>>5.000000000000D-02
 Enter HP:
>>0
 Enter N:
>>590
...(skipped including inputs)...
 level weights (1 equal;  5 standard;  9 user)
>>1
...(skipped)...
 Enter orbitals to be varied (Updating order)
>>5f*
...(skipped including inputs)...
 Select a different integration method for any subshell radial
```

```
   wavefunction?
>>y
 Method             1 :
>>
 Method             2 :
>>
 Method             3 :
>>
 Method             4 :
>>*
...(skipped including inputs)...
 Iteration number    1
 --------------------
...(skipped)...
 Iteration number    6
 --------------------
...(skipped)...
 RMCDHF: Execution complete. ...(skipped)
```

From here, the previous orbitals were not varied when the new orbitals were added. In other words, all orbitals calculated in a calculation were *fixed* in the following calculations. To do so, the query at line 18 was answered with the input `5f*`, meaning `5f` and `5f-` (i.e., all possible relativistic $5f$ orbitals). Method 1 and 3 gave no convergence and continuum state, respectively. Method 2 gave an example violating Eq. (14.7b):

```
(skipped)...
Subshell       e            ...(skipped)...
...(skipped)...
  5f-   7.1630736498D-02   ...(skipped)...
  5f    1.2509928741D-01   ...(skipped)...
...(skipped)
```

in the `rmcdhf.sum` file. Method 4 gave the right values:

```
  5f-   5.5631754199D-02
  5f    5.5625231837D-02
```

Therefore, Method 4 was the choice.

14.2.2.3 $6df$ shells

The correlation orbitals higher than $6sp$ or $5df$ were added not by adding them in the reference configurations $\gamma^{(m)}$ but by setting higher maximum active orbitals:

```
>>rcsfgenerate
...(skipped)...
>>u
...(skipped)...
>>4
...(skipped)...
```

```
...(skipped for the previous state configurations for γ^S and γ^P)...
 Give configuration            1
>>4d(10,c)5s(2,i)5p(6,i)4f(14,i)5d(1,*)
 Give configuration            2

 Give set of active orbitals, ...(skipped)...
>>5s,5p,6d,4f
 Resulting 2*J-number? lower, higher (J=1 -> 2*J=2 etc.)
>>3,5
 Number of excitations ...(skipped)...
>>1
...(skipped including inputs)...
 Give configuration            1
>>4d(10,c)5s(2,i)5p(6,i)4f(14,i)5f(1,*)
 Give configuration            2
>>
 Give set of active orbitals, ...(skipped)...
>>5s,5p,5d,6f
 Resulting 2*J-number? lower, higher (J=1 -> 2*J=2 etc.)
>>5,7
 Number of excitations ...(skipped)...
>>1
...(skipped including inputs)...
       block   J/P             NCSF
           1   1/2+               1
           2   1/2-               1
           3   3/2+               2
           4   3/2-               1
           5   5/2+               2
           6   5/2-               2
           7   7/2-               2
```

The $5d$ orbital's configuration in γ^D had an asterisk (`*`) in line 9 instead of `i` for being inactive, which allowed single or double-electron excitations from the orbital.[24]. The highest active d orbital was increased from $5d$ to $6d$ in line 13, so to allow the electron's excitation from $5d$ to $6d$. In this way, $6d$ orbital was involved in the calculation, and DHF found the solution for $\phi_{6,2\pm1/2}(\mathbf{r})$. The maximum total number of excitation needed to be also set (line 27); it was one in this calculation. Similarly, The $5f$ orbital's configuration in γ^F was allowed for excitations (line 20), and the highest active f orbital was set to be $6f$ (line 24).

A states with γ^D (γ^F) configurations had two CSFs, as shown in lines 30–37, as the configurations obtained by exciting the electron in $5d$ ($5f$) to $6d$ ($6f$) is additionally included in the list of CSFs for the states. `rcsf.out` file showed the generated list of CFSs for, e.g., $^2D_{3/2}$ and $^2D_{5/2}$ states (see Section 14.2.1):

```
(skipped)...
```

[24]Maximum one electron could be excited here as there is only one electron in the shell.

```
  5s ( 2)   5p-( 2)   5p ( 4)   4f-( 6)   4f ( 8)   5d-( 1)
                                                        3/2
                                                         3/2+
  5s ( 2)   5p-( 2)   5p ( 4)   4f-( 6)   4f ( 8)   6d-( 1)
                                                        3/2
                                                         3/2+
 *
...(skipped)...
  5s ( 2)   5p-( 2)   5p ( 4)   4f-( 6)   4f ( 8)   5d ( 1)
                                                        5/2
                                                         5/2+
  5s ( 2)   5p-( 2)   5p ( 4)   4f-( 6)   4f ( 8)   6d ( 1)
                                                        5/2
                                                         5/2+
 *
 ...(skipped)
```

`rangular`, `rwfnestimate` were run like the last time. The MCDHF calculations for $6d$ and $6f$ shells were run separately as the convergence of calculations for both shells at the same time could not be achieved.

```
>>rmcdhf
...(skipped including inputs)...
 level weights (1 equal;  5 standard;  9 user)
>>5
...(skipped)...
 Enter orbitals to be varied (Updating order)
>>6d*
...(skipped including inputs)...
 Method             1 :
>>6d*
...(skipped including inputs)...
 Iteration number   2
 --------------------
...(skipped)...
 RMCDHF: Execution complete. ...(skipped)
```

Only $6d_{3/2}$ and $6d_{5/2}$ orbitals (i.e., `6d*`) were solved while all other, previously solved orbitals were fixed as before. Method 1 was chosen for `6d*` orbitals to achieve convergence and the correct energy orders [Eq. (14.7)]. A similar calculation was followed for `6f*` orbitals, except that Method 4 was chosen in the calculation.

14.2.2.4 $7spdf$ shells

The correlation *layer* of $n = 7$ is configured by allowing excitation of an electron in the last orbitals in $\gamma^{S,P,D,F}$ to $7spdf$ shells:

```
>>rcsfgenerate
...(skipped for the previous state configurations for γ^S and γ^P)...
 Give configuration            1
>>4d(10,c)5s(2,i)5p(6,i)4f(14,i)6s(1,*)
```

```
...(skipped)...
 Give set of active orbitals, ...(skipped)...
>>7s,5p,4d,4f
...(skipped including inputs)...
 Give configuration            1
>>4d(10,c)5s(2,i)5p(6,i)4f(14,i)6p(1,*)
...(skipped)...
 Give set of active orbitals, ...(skipped)...
>>5s,7p,4d,4f
...(skipped including inputs)...
 Give configuration            1
>>4d(10,c)5s(2,i)5p(6,i)4f(14,i)5d(1,*)
...(skipped)...
 Give set of active orbitals, ...(skipped)...
>>5s,5p,7d,4f
...(skipped including inputs)...
 Give configuration            1
>>4d(10,c)5s(2,i)5p(6,i)4f(14,i)5d(1,*)
...(skipped)...
 Give set of active orbitals, ...(skipped)...
>>5s,5p,5d,7f
...(skipped including inputs)...
       block   J/P             NCSF
           1   1/2+               2
           2   1/2-               2
           3   3/2+               3
           4   3/2-               2
           5   5/2+               3
           6   5/2-               3
           7   7/2-               3
```

In particular, `6s*` and `6p*` shells in γ^S and γ^P were also allowed for the excitation in lines 4 and 10, respectively. Maximum active orbitals were set to be $7s$, $7p$, $7d$, and $7f$ for γ^S, γ^P, γ^D, and γ^F in lines 7, 13, 19, and 25, respectively.

As for $6df$ shells, The DHF calculations were executed for each of $7spdf$ shells separately. For $7s$, all the method failed; Method 1, 3, or 4 gave $E(6s)$ (i.e., $E_{6,1/2}$) reasonably close to but slightly bigger than $E(6s)$, violating Eq. (14.7a). To fix the issue, new approach was introduced: calculating `6s*` and `7s*` shells at the same time (line 7):

```
>>rmcdhf
...(skipped including inputs)...
 level weights (1 equal;  5 standard;  9 user)
>>5
...(skipped)...
 Enter orbitals to be varied (Updating order)
>>6s*, 7s*
...(skipped including inputs)...
 Method             1 :
>>*
...(skipped including inputs)...
 Iteration number   2
 --------------------
```

```
...(skipped)...
 RMCDHF: Execution complete. ...(skipped)
```

which gave the correct energy relations [Eq. (14.7)] including for $6s$ and $7s$ orbitals:

```
(skipped)...
Subshell       e           ...(skipped)...
...(skipped)...
  6s    4.1606928904D-01   ...(skipped)...
...(skipped)...
  7s    4.1481811979D-01   ...(skipped)...
...(skipped)
```

in `rmcdhf.sum`. The same approach was used for $7p$ shell as well; 6p* and 7p* were calculated at the same time using Method 1 and the standard level weights, giving convergence in 2 iterations. $7d$ shell could be calculated alone with Method 3 and the standard level weights, converged in 2 iterations. For $7f$ shell, another, slightly different method was introduced: `7d*` and `7f*` shells were calculated together for the correct energy orders:

```
>>rmcdhf
...(skipped including inputs)...
 level weights (1 equal;  5 standard;  9 user)
>>5
...(skipped)...
 Enter orbitals to be varied (Updating order)
7d*, 7f*
...(skipped including inputs)...
 Method             1 :
>>7f*
 Method             2 :
>>
 Method             3 :
>>7d*
 Method             4 :
>>
...(skipped including inputs)...
 Iteration number   2
 --------------------
...(skipped)...
 RMCDHF: Execution complete. ...(skipped)
```

Method 1 and 3 were chosen for $7f$ and $7d$ shells as shown in lines 10 and 14, respectively.

14.2.2.5 $8spdf$ shells

The last correlation layer $8spdf$ was calculated in a similar fashion:

```
>>rcsfgenerate
...(skipped for the previous state configurations for γ^S and γ^P)...
 Give configuration            1
>>4d(10,c)5s(2,i)5p(6,i)4f(14,i)6s(1,*)
...(skipped)...
 Give set of active orbitals, ...(skipped)...
>>8s,5p,4d,4f
...(skipped including inputs)...
 Give configuration            1
>>4d(10,c)5s(2,i)5p(6,i)4f(14,i)6p(1,*)
...(skipped)...
 Give set of active orbitals, ...(skipped)...
>>5s,8p,4d,4f
...(skipped including inputs)...
 Give configuration            1
>>4d(10,c)5s(2,i)5p(6,i)4f(14,i)5d(1,*)
...(skipped)...
 Give set of active orbitals, ...(skipped)...
>>5s,5p,8d,4f
...(skipped including inputs)...
 Give configuration            1
>>4d(10,c)5s(2,i)5p(6,i)4f(14,i)5f(1,*)
...(skipped)...
 Give set of active orbitals, ...(skipped)...
>>5s,5p,5d,8f
...(skipped including inputs)...
       block  J/P             NCSF
           1  1/2+               3
           2  1/2-               3
           3  3/2+               4
           4  3/2-               3
           5  5/2+               4
           6  5/2-               4
           7  7/2-               4
```

For this layer, the standard level weights were used in all the `rmcdhf` calculations. 8s shell was calculated together with 6s and 7s shells using Method 1 for all the orbitals, giving convergence in 2 iterations. 8p and 7p shells were calculated together, with Method 4 and 1, respectively. The stdout of `rmcdhf` showed an error message for 8p orbital, *this fails the accuracy criterion* in the stdout, after total 2 iterations:

```
(skipped including inputs)...
Subshell    Energy    Method   P0    consistency  Norm-1  factor  JP
    MTP INV NNP

  7p-   3.0210023D-01  1  9.799D+04  4.99D-09 -3.54D-03 0.000   387
     450  0  5
  7p    2.8910585D-01  1  4.709D+06  6.12D-08 -1.66D-02 0.000   388
     451  0  5
  8p-   2.8677497D-01  4  1.188D+05  1.47D-08  0.00D+00 0.000   388
     454  0  6
START:  8p  subshell: accuracy  5.5D-01
 attained after 36 iterations; this fails the
 accuracy criterion  1.6D-08.
  8p    2.4289008D-01  4  8.918D+06  7.16D-07  3.74D+01 0.000   391
     468  0  5
```

```
 E( 8p ) = -8.0010D-02; adjusted to EPSMIN
START:  8p  subshell: accuracy  5.5D-01
 attained after 36 iterations; this fails the
 accuracy criterion  1.6D-08.
  8p    2.7681947D-02  4  9.702D+05  1.13D-07  1.24D+01 0.100   435
     462  0 10
...(skipped)
```

However, it gave correct energy relations in `rmcdhf.sum`:

```
(skipped)...
Subshell      e           ...(skipped)...
...(skipped)...
  8p-  2.8677497255D-01   ...(skipped)...
  8p   2.7681946544D-02   ...(skipped)...
...(skipped)...
...(skipped)...              Generalised
Subshell  ...(skipped)...  occupation
...(skipped)...
  8p-     ...(skipped)...  2.23634D-15
  8p      ...(skipped)...  1.87034D-15
...(skipped)
```

so the result was accepted. In general, the accuracy of correlation layers is less important as its n increases because the occupations of electrons in the orbitals become smaller (see Table C.1). The occupation was only 10^{-15} level for `8p*` orbitals as shown in the file.

$8d$ shell was calculated alone with Method 3, and took only 1 iteration.

$8f$ was calculated alone. As no integration methods gave convergence with the correct orders of energies, The requirement for the $8f$ shell to be spectroscopic (see Section 14.2.1) was lifted by input nothing in line 6, and Method 3 was chosen:

```
>>rmcdhf
...(skipped including inputs)...
 Enter orbitals to be varied (Updating order)
>>8f*
 Which of these are spectroscopic orbitals?
>>
...(skipped including inputs)...
 Iteration number   8
 --------------------
...(skipped)...
 RMCDHF: Execution complete. ...(skipped)
```

Adding correlation layers was stopped at $n = 8$ as achieving reliable calculation results (i.e., convergence and the correct energy orders) failed. The full list of the energies and occupations of the orbitals can be found in Table C.1.

14.3 Yb^+: configuration interaction calculation

After the *basis* one-electron orbital wavefunction set $\{\phi_{nk}(r)\}$ was prepared for core, valence, and correlation orbitals via the the DHF calculations, configuration-interaction (CI) calculations (see Section 12.2) were carried out for $^2S_{1/2}$, $^2D_{3/2}$, $^2D_{5/2}$, and $^2F_{7/2}$ states in the Yb^+'s optical clock transitions (see Fig. 3-1).

The first step was to configure an appropriate CSF list for each state. The active set approach generated configurations by exciting the reference configurations. It was worth having more than one such reference configurations called *multireference* (MR) (see Chapter 13). A practical way to choose MR configurations is to run some reasonable calculations for a target state (e.g., MCDHF caculations or CI calculations with a relatively simple CSF set), and choose CSFs with significant mixing coefficients as MRs. By doing so, one can efficiently capture most of the significant configurations, the MRs themselves and the configurations excited from the MRs; too many configurations may be generated if the active approach is used with only one reference configuration instead to generate all the configurations generated from the reference. The calculated values of the mixing coefficients c_i can be extracted by executing `rmixextract` command which save the results in `[Name of state].(c)ed` file.[25]. Finding a good MR set is not straightforwards but rather an iterative procedure in general: carrying out calculations using a MR and active set approach and checking if the resulting c_i agrees to MR that had been selected. The converged MR may depends also on the detail of the active set approach (e.g., the number of correlation layers and the maximum allowed excitations total and from each orbital). The MR sets used in the following CI calculations were not from such exhaustive searches and will be left as suggested, working MR sets.

As the numbers of CSFs for the following calculations were significant (see Table C.2), a high-power computing cluster was used: MIT Satori [209], a POWER9 [210] cluster system from IBM with Red Hat Enterprise Linux 8 [211] as the operating system (OS).

[25] `.ed` for DHF calculations and `.ced` for CI calculations.

The following inputs and outputs shows the procedure for a CI calculation for all the four $^2S_{1/2}$, $^2D_{5/2}$, $^2D_{3/2}$, and $^2F_{7/2}$ states. First of all, the following set of configurations was chosen as the MR configurations used for all the states of interest:

$$\{6s, 6p, 5d, 4f^{13}6s^2, 4f^{13}\,6s\,5d, 4f^{13}\,6p^2, 4f^{13}\,5d^2\} \tag{14.8}$$

From the MR configurations, a list of CSFs $\{\gamma_i\}$ was generated using `rcsfgenerate` command and the active set approach. For $^2S_{1/2}$ state:

Listing 14.5: `rcsfgenerate` inputs and ouputs to generate the list of CSFs for $^2S_{1/2}$-state calculations

```
>>rcsfgenerate

 RCSFGENERATE
...(skipped)...
 Default, reverse, symmetry or user specified ordering? (*/r/s/u)
>>u

 Select core
...(skipped)...
         3: Ar ([Ne] + 3s(2)3p(6)              = 18 electrons)
...(skipped)...
>>3
...(skipped)...
 Give configuration            1
>>3d(10,c)4s(2,i)4p(6,i)4d(10,i)5s(2,i)5p(6,i)4f(14,13)6s(1,*)
 Give configuration            2
>>3d(10,c)4s(2,i)4p(6,i)4d(10,i)5s(2,i)5p(6,i)4f(14,13)6p(1,*)
 Give configuration            3
>>3d(10,c)4s(2,i)4p(6,i)4d(10,i)5s(2,i)5p(6,i)4f(14,13)5d(1,*)
 Give configuration            4
>>3d(10,c)4s(2,i)4p(6,i)4d(10,i)5s(2,i)5p(6,i)4f(13,12)6s(2,*)
 Give configuration            5
>>3d(10,c)4s(2,i)4p(6,i)4d(10,i)5s(2,i)5p(6,i)4f(13,12)6s(1,*)5d
   (1,*)
 Give configuration            6
>>3d(10,c)4s(2,i)4p(6,i)4d(10,i)5s(2,i)5p(6,i)4f(13,12)6p(2,*)
 Give configuration            7
>>3d(10,c)4s(2,i)4p(6,i)4d(10,i)5s(2,i)5p(6,i)4f(13,12)6p(2,*)
 Give configuration            8
>>
 Give set of active orbitals, ...(skipped)...
>>8s,8p,8d,8f
 Resulting 2*J-number? lower, higher (J=1 -> 2*J=2 etc.)
>>1,1
 Number of excitations ...(skipped)...
>>2
 Generate more lists ? (y/n)
>>n
  Excitationdata file opened
...(skipped)...
       block  J/P            NCSF
           1  1/2+            472
```

```
42            2   1/2-           27682
43 >>cp rcsf.out rcsf.inp
```

The output `rcsf.out` file that contained the generated CSFs was copied as `rcsf.inp` (line 43) for later use. The active approach was set up in a way that single or double-electron excitations were allowed from $6s$, $6p$, or $5d$ (asterisk symbols `*`), only single excitation was allowed from $4f$ shell [`4f(14,13)` or `4f(13,12)`], and maximum total two electrons were allowed for the excitation (line 35). The stdout showed that 472 CSFs were generated for the state with $(P, J) = (+, \frac{1}{2})$ (line 41) which corresponds to the $^2S_{1/2}$ state, while there were also 27,682 CSFs with $(P, J) = (-, \frac{1}{2})$ (line 42) which were not relevant to the state of interest. The `rscf.inp` file indeed contained those 27,682 CSFs (lines 14–20):

Listing 14.6: List of CSFs $\{\gamma_i\}$ for $^2S_{1/2}$-state calculations in `rscf.inp` before removing lines 13–20.

```
1  Core subshells:
2    1s    2s    2p-   2p    3s    3p-   3p    3d-   3d
3  Peel subshells:
4    4s    4p-   4p    4d-   4d    5s    5p-   5p    4f-   4f    5d-   5d    6s    6
     p-   6p
5  CSF(s):
6    4s ( 2)  4p-( 2)  4p ( 4)  4d-( 4)  4d ( 6)  5s ( 2)  5p-( 2)  5p
     ( 4)  4f-( 6)  4f ( 8)  6s ( 1)
7
                                    1/2
8
                                     1/2+
9  ...(skipped)...
10   4s ( 2)  4p-( 2)  4p ( 4)  4d-( 4)  4d ( 6)  5s ( 2)  5p-( 2)  5p
     ( 4)  4f-( 6)  4f ( 7)  8d-( 1)  8f-( 1)
11
                          7/2       3/2       5/2
12
                                         3    1/2+
13 *
14   4s ( 2)  4p-( 2)  4p ( 4)  4d-( 4)  4d ( 6)  5s ( 2)  5p-( 2)  5p
     ( 4)  4f-( 6)  4f ( 8)  6p-( 1)
15
                                    1/2
16
                                     1/2-
17 ...(skipped)...
18   4s ( 2)  4p-( 2)  4p ( 4)  4d-( 4)  4d ( 6)  5s ( 2)  5p-( 2)  5p
     ( 4)  4f-( 6)  4f ( 6)  6p-( 1)  8f-( 2)
19
                             4       1/2         4
20
                                        9/2     1/2-
```

Therefore, the undesired CSFs were manually deleted in the file, leaving only lines 1–

12 as the CSF list for the $^2S_{1/2}$ state. The MR CSFs $\{(\gamma_{\rm MR})_i\}$ relevant to the $^2S_{1/2}$ state out of the MR configurations in Eq. (14.8) were also generated by changing only the input configurations (lines 14–27 in Listing 14.5), the active orbitals with highest n (line 31 in Listing 14.5), and the maximum total number of excited electrons (line 35 in Listing 14.5), as in lines 4–16, 20, and 22 in Listing 14.7, respectively:

Listing 14.7: `rcsfgenerate` inputs and ouputs to generate MR set for $^2S_{1/2}$ state.

```
1 >>rcsfgenerate
2 ...(skipped)...
3  Give configuration            1
4 >>3d(10,c)4s(2,i)4p(6,i)4d(10,i)5s(2,i)5p(6,i)4f(14,i)6s(1,i)
5  Give configuration            2
6 >>3d(10,c)4s(2,i)4p(6,i)4d(10,i)5s(2,i)5p(6,i)4f(14,i)6p(1,i)
7  Give configuration            3
8 >>3d(10,c)4s(2,i)4p(6,i)4d(10,i)5s(2,i)5p(6,i)4f(14,i)5d(1,i)
9  Give configuration            4
10 >>3d(10,c)4s(2,i)4p(6,i)4d(10,i)5s(2,i)5p(6,i)4f(13,i)6s(2,i)
11  Give configuration            5
12 >>3d(10,c)4s(2,i)4p(6,i)4d(10,i)5s(2,i)5p(6,i)4f(13,i)6s(1,i)5d(1,i)
13  Give configuration            6
14 >>3d(10,c)4s(2,i)4p(6,i)4d(10,i)5s(2,i)5p(6,i)4f(13,i)6p(2,i)
15  Give configuration            7
16 >>3d(10,c)4s(2,i)4p(6,i)4d(10,i)5s(2,i)5p(6,i)4f(13,i)5d(2,i)
17  Give configuration            8
18 >>
19  Give set of active orbitals, ...(skipped)...
20 >>6s,6p,5d,4f
21  Resulting 2*J-number? lower, higher (J=1 -> 2*J=2 etc.)
22 >>1,1
23  Number of excitations ...(skipped)...
24 >>0
25 ...(skipped)...
26        block   J/P             NCSF
27            1   1/2+               1
28            2   1/2-              14
29 >>cp rcsf.out rcsfmr.inp
```

The resulting CSFs in the `rcsf.out` file was copied in `rcsfmr.inp` (line 29 above), as follows, to use `rcsfinteract` command as described in a later paragraph. Again, the 14 CSFs with $(P, J) = (-, \frac{1}{2})$ (line 28) should be manually deleted in the `rscfmr.inp` file, leaving a CSF for the $^2S_{1/2}$ state (line 27):

Listing 14.8: MR set $\{(\gamma_{\rm MR})_i\}$ for $^2S_{1/2}$-state calculations in `rcsfmr.inp`.

```
1 Core subshells:
2   1s   2s   2p-  2p   3s   3p-  3p   3d-  3d
3 Peel subshells:
4   4s   4p-  4p   4d-  4d   5s   5p-  5p   4f-  4f   5d-  5d   6s   6
    p-  6p
5 CSF(s):
6   4s ( 2)  4p-( 2)  4p ( 4)  4d-( 4)  4d ( 6)  5s ( 2)  5p-( 2)  5p
    ( 4)  4f-( 6)  4f ( 8)  6s ( 1)
```

```
                                  1/2

                                   1/2+
```

Similarly, by changing only the range of $2J$ values (e.g., line 33 in Listing 14.5) and deleting the irrelevant CFSs in the `rscf.inp` and `rscfmr.inp` files, lists of CSFs and MR sets were prepared for the other states of interest. For the $^2D_{5/2}$ and $^2D_{3/2}$ states, lists of CSFs were generated from the MR configurations in Eq. (14.8):

```
>>rcsfgenerate
...(skipped)...
 Give configuration            1
>>3d(10,c)4s(2,i)4p(6,i)4d(10,i)5s(2,i)5p(6,i)4f(14,13)6s(1,*)
...(skipped)...
 Resulting 2*J-number? lower, higher (J=1 -> 2*J=2 etc.)
>>3,5
...(skipped)...
       block   J/P             NCSF
           1   3/2+             844
           2   3/2-           51030
           3   5/2+            1047
           4   5/2-           66729
>>cp rcsf.out rcsf.inp
```

The 1047 and 844 CSFs for $^2D_{5/2}$ and $^2D_{3/2}$ states, respectively, were remained in the `rcsf.inp`:

Listing 14.9: Lists of CSFs $\{\gamma_i\}$ for $^2D_{5/2}$ and $^2D_{3/2}$-state calculations in `rscf.inp`, separated by a asterisk symbol `*`.

```
(skipped)...
  4s ( 2)  4p-( 2)  4p ( 4)  4d-( 4)  4d ( 6)  5s ( 2)  5p-( 2)  5p
   ( 4)  4f-( 6)  4f ( 8)  5d ( 1)

                                  5/2

                                   5/2+
...(skipped)...
  4s ( 2)  4p-( 2)  4p ( 4)  4d-( 4)  4d ( 6)  5s ( 2)  5p-( 2)  5p
   ( 4)  4f-( 6)  4f ( 7)  8d-( 1)  8f-( 1)

                       7/2       3/2       5/2

                                      5     5/2+
*
  4s ( 2)  4p-( 2)  4p ( 4)  4d-( 4)  4d ( 6)  5s ( 2)  5p-( 2)  5p
   ( 4)  4f-( 6)  4f ( 8)  5d-( 1)

                                  3/2

                                   3/2+
...(skipped)...
  4s ( 2)  4p-( 2)  4p ( 4)  4d-( 4)  4d ( 6)  5s ( 2)  5p-( 2)  5p
   ( 4)  4f-( 6)  4f ( 7)  8d-( 1)  8f-( 1)
```

```
                        7/2       3/2       5/2

                                        4     3/2+
```

MR sets were generated by:

```
>>rcsfgenerate
...(skipped)...
 Give configuration            1
>>3d(10,c)4s(2,i)4p(6,i)4d(10,i)5s(2,i)5p(6,i)4f(14,i)6s(1,i)
...(skipped)...
 Resulting 2*J-number? lower, higher (J=1 -> 2*J=2 etc.)
>>3,5
...(skipped)...
       block  J/P             NCSF
           1  3/2+               1
           2  3/2-              26
           3  5/2+               1
           4  5/2-              33
>>cp rcsf.out rcsfmr.inp
```

and CSFs with $(P, J) = (+, \frac{5}{2})$ and $(+, \frac{3}{2})$ were remained in the `rcsfmr.inp` as MR sets:

Listing 14.10: MR sets $\{(\gamma_{\mathrm{MR}})_i\}$ for $^2D_{5/2}$ and $^2D_{3/2}$-state calculations in `rscfmr.inp`.

```
(skipped)...
CSF(s):
  4s ( 2)  4p-( 2)  4p ( 4)  4d-( 4)  4d ( 6)  5s ( 2)  5p-( 2)  5p
    ( 4)  4f-( 6)  4f ( 8)  5d ( 1)

                                  5/2

                                   5/2+
 *
  4s ( 2)  4p-( 2)  4p ( 4)  4d-( 4)  4d ( 6)  5s ( 2)  5p-( 2)  5p
    ( 4)  4f-( 6)  4f ( 8)  5d-( 1)

                                  3/2

                                   3/2+
```

For the $^2F_{7/2}$ state, a list of CSFs was generated:

```
>>rcsfgenerate
...(skipped)...
 Give configuration            1
>>3d(10,c)4s(2,i)4p(6,i)4d(10,i)5s(2,i)5p(6,i)4f(14,13)6s(1,*)
...(skipped)...
 Resulting 2*J-number? lower, higher (J=1 -> 2*J=2 etc.)
>>7,7
...(skipped)...
       block  J/P             NCSF
           1  7/2+            1059
           2  7/2-           73286
>>cp rcsf.out rcsf.inp
```

and the 1059 CSFs for the $^2F_{7/2}$ were remained in the `rcsf.inp`:

Listing 14.11: List of CSFs $\{\gamma_i\}$ for $^2F_{7/2}$-state calculations in `rscf.inp`.

```
(skipped)...
  4s ( 2)  4p-( 2)  4p ( 4)  4d-( 4)  4d ( 6)  5s ( 2)  5p-( 2)  5p
   ( 4)  4f-( 6)  4f ( 8)  5f ( 1)

                                  7/2

                                   7/2-
...(skipped)...
  4s ( 2)  4p-( 2)  4p ( 4)  4d-( 4)  4d ( 6)  5s ( 2)  5p-( 2)  5p
   ( 4)  4f-( 6)  4f ( 6)  6p-( 1)  8f-( 2)

                          6       1/2         4

                                    13/2    7/2-
```

An MR set was generated by:

```
>>rcsfgenerate
...(skipped)...
 Give configuration            1
>>3d(10,c)4s(2,i)4p(6,i)4d(10,i)5s(2,i)5p(6,i)4f(14,i)6s(1,i)
...(skipped)...
 Resulting 2*J-number? lower, higher (J=1 -> 2*J=2 etc.)
>>7,7
...(skipped)...
       block  J/P             NCSF
           1  7/2-              33
>>cp rcsf.out rcsfmr.inp
```

in the `rcsfmr.inp`:

Listing 14.12: MR set $\{(\gamma_{\rm MR})_i\}$ for $^2F_{7/2}$-state calculations in `rscfmr.inp`.

```
(skipped)...
CSF(s):
  4s ( 2)  4p-( 2)  4p ( 4)  4d-( 4)  4d ( 6)  5s ( 2)  5p-( 2)  5p
   ( 4)  4f-( 5)  4f ( 8)  5d ( 2)

             5/2                  2

                                  7/2-
...(skipped)...
  4s ( 2)  4p-( 2)  4p ( 4)  4d-( 4)  4d ( 6)  5s ( 2)  5p-( 2)  5p
   ( 4)  4f-( 6)  4f ( 7)  6p-( 2)

                        7/2

                                  7/2-
```

Finally, for the following CI calculation, the lists of the CSFs in Listings 14.6, 14.9, and 14.11, and the MR sets in Listings 14.8, 14.10, and 14.12, for all the $^2S_{1/2}$, $^2D_{5/2}$, $^2D_{3/2}$, and $^2F_{7/2}$ states, were placed in a single `rscf.inp` and `rscfmr.inp`

files, respectively, separated by asterisk symbols between the lists for different states (see line 9 in Listing 14.9).

The last step of preparing a CSF list for each state was to reduce the number of the CSFs using `rcsfinteract` command which takes existing `rcsf.inp` and `rcsfmr.inp` as input files and copies CSFs in the `rcsf.inp` file that interacts with CSFs in the `rcsfmr.inp` file into `rcsf.out` file generated by the command (see Section 5.6 in Ref. [203]):

```
1  >>rcsfinteract
2
3   RCSFinteract: Determines all the CSFs (rcsf.inp) that interact
4                 with the CSFs in the multireference (rcsfmr.inp)
5                 (C)  Copyright by G. Gaigalas and Ch. F. Fischer
6                 (Fortran 95 version)               NIST  (2017).
7                 Input files: rcsfmr.inp, rcsf.inp
8                 Output file: rcsf.out
9
10  Reduction based on Dirac-Coulomb (1) or
11  Dirac-Coulomb-Breit (2) Hamiltonian?
12 >>1
13  Loading Configuration Symmetry List File ...
14  There are 44 relativistic subshells;
15   Block     MR NCSF    Before NCSF    After NCSF
16     1             1           472           463
17     2             1          1047          1047
18     3             1           844           832
19     4            33         73286         72775
20
21  Wall time:
22         5 seconds
23
24  Finish Date and Time:
25    Date (Yr/Mon/Day): 2022/04/30
26    Time (Hr/Min/Sec): 20/33/00.420
27    Zone: -0400
28
29  RCSFinteract: Execution complete.
```

The reduction of the number of CSFs was shown in lines 16, 17, 18, and 19 for the $^2S_{1/2}$, $^2D_{5/2}$, $^2D_{3/2}$, and $^2F_{7/2}$ states, respectively.

It would have been the time to run `rangular` command. However, a similar command, `rangular_mpi` was used instead:

```
1 >>cp rcsf.out rcsf.inp
2 >>mpirun -np (number of processors to assign) rangular_mpi
3  ====================================================
4         RANGULAR_MPI: Execution Begins ...
5  ====================================================
6  Participating nodes:
7 ...(skipped)...
8  Date and Time:
```

```
...(skipped)...
 Start Dir:
...(skipped)...
 Serial I/O Dir (node-0 only):
...(skipped)...
 Work Dir (Parallel I/O):
...(skipped)...
 Full interaction?  (y/n)
>>y
 Block            1 ,  ncf =          472
 Block            2 ,  ncf =         1047
 Block            3 ,  ncf =          844
 Block            4 ,  ncf =        73286
 Loading CSF file ... Header only
 There are/is           44  relativistic subshells;

 Block            1 ,  ncf =          472
 Loading CSF File for block            1
 There are          472  relativistic CSFs... load complete;
...(skipped)...
 ====================================================
        RANGULAR_MPI: Execution Finished ...
 ====================================================
 Wall time:
...(skipped)...
 Finish Date and Time:
...(skipped)...
 mpi stopped by node-           0  from RANGULAR_MPI: Execution
    complete.
...(skipped)
```

The two commands perform the same calculation, and the difference is that `rangular_mpi` enables parallel computing with more than one processor by utilizing the OpenMPI library [212], as described in Sections 1.2, 4.11, and 7.4 in Ref. [203]. The number of processors to be used, which has to be the power of 2 (e.g. `128`), is assigned with the command as in line 1 above. Most of the time-consuming commands in GRASP2018 have their MPI version with the suffix `_mpi` in the command names, and some of them were used as in the following paragraphs. The runtime of the calculation here was investigated and showed a proportional increase in the calculation speed with the number of processors at least up to 128, in the high-power computing cluster introduced at the beginning of this section.

The `rmcdhf_mpi` command followed as the next step:

```
>>mpirun -np (number of processors to assign) rmcdhf_mpi
 ====================================================
        RMCDHF_MPI: Execution Begins ...
 ====================================================
...(skipped)...
Default settings?  (y/n)
>>y
```

```
 Loading CSF file ... Header only
 There are/is           44  relativistic subshells;
 Loading CSF File for ALL blocks
 There are        75649  relativistic CSFs... load complete;
 There are            4  blocks  (block   J/Parity   NCF):
  1  1/2+     472       2  5/2+    1047       3  3/2+     844
    4  7/2-   73286

 Enter ASF serial numbers for each block
 Block            1    ncf =          472  id =  1/2+
>>1
 Block            2    ncf =         1047  id =  5/2+
>>1
 Block            3    ncf =          844  id =  3/2+
>>1
 Block            4    ncf =        73286  id =  7/2-
>>1
 level weights (1 equal;  5 standard;  9 user)
>>5
 Radial functions
 1s 2s 2p- 2p 3s 3p- 3p 3d- 3d 4s 4p- 4p 4d- 4d 5s 5p- 5p 4f- 4f 5d-
    5d 6s 6p-
 6p 5f- 5f 6d- 6d 7p- 7p 8s 6f- 6f 7s 7d- 7d 7f- 7f 8p- 8p 8d- 8d 8f
   - 8f
 Enter orbitals to be varied (Updating order)
>>
 All subshell radial wavefunctions are fixed; performing CI
   calculations with RCI.
 Which of these are spectroscopic orbitals?
>>*
 Enter the maximum number of SCF cycles:
>>1000

 Average energy =  -1.4066261013D+04 Hartrees
 Average energy =  -1.4066267588D+04 Hartrees
 Average energy =  -1.4066263216D+04 Hartrees
 Average energy =  -1.4065001056D+04 Hartrees
  Calling dvdson!!!         200           1
DVDSON:  34 loops;  35 matrix-vector multiplies.

Optimise on the following level(s):

Level  1    Energy = -1.406745810602D+04    Weight =  1.00000D-01
Level  1    Energy = -1.406733995433D+04    Weight =  3.00000D-01
Level  1    Energy = -1.406734414678D+04    Weight =  2.00000D-01
Level  1    Energy = -1.406733751686D+04    Weight =  4.00000D-01

Weights of major contributors to ASF:

Block Level J Parity      CSF contributions

  1     1   1/2 +       0.9902     0.0624    -0.0529     0.0459
    0.0376
                            1        256        258         36
       263
  2     1   5/2 +       0.9967     0.0443     0.0295     0.0247
    0.0177
                            1        548         75        565
        89
  3     1   3/2 +       0.9953     0.0516     0.0329     0.0267
```

```
    -0.0226
                                1         463          65         476
       623
  4      1   7/2 -        0.9169      0.1919     -0.1754     -0.1255
    -0.1113
                               28         747         746          15
        22

Weighted average energy of these levels =  -1.4067351633D+04
Weighted average energy:  -1.4067351633D+04

Generalised occupation numbers:

   2.0000D+00  2.0000D+00  2.0000D+00  4.0000D+00  2.0000D+00
   2.0000D+00
   4.0000D+00  4.0000D+00  6.0000D+00  2.0000D+00  2.0000D+00
   4.0000D+00
   4.0000D+00  6.0000D+00  2.0000D+00  2.0000D+00  4.0000D+00
   5.9885D+00
   7.5942D+00  2.1160D-01  3.1630D-01  8.1707D-01  1.0128D-02
   1.3011D-02
   1.6318D-04  2.3614D-04  1.3982D-03  2.1978D-03  2.7123D-03
   4.6362D-03
   2.9972D-04  1.1798D-03  4.5704D-04  2.7836D-02  1.8448D-04
   3.0504D-04
   6.7334D-03  3.2703D-05  7.7298D-05  2.0551D-04  1.4854D-06
   1.5523D-06
   5.0100D-04  1.4222D-05

 Iteration number   1
 --------------------
...(skipped)...
 ======================================================
        RMCDHF_MPI: Execution Finished ...
 ======================================================
 ...(skipped)
```

The `rmcdhf` command here did not (re-)calculate any basis orbital wavefunctions (line 30), but only prepared the basis wavefunctions obtained in Section 14.2 in the generated output files (see Fig. 3.2 in Ref. [203]) for the following CI calculations, as implied in line 31.

Before running CI calculations, `rsave` command should have been also run to save the results obtained so far to files with a file name assigned in line 1 below (see Sections 3.2, 3.3, and Fig. 3.2 in Ref. [203]):

Listing 14.13: Execution of `rsave` command to assign the *name* of a calculation.

```
1 >>rsave (name of state to assign)
2 Created (the assigned name).w, (the assigned name).c, (the assigned
    name).m, (the assigned name).sum (the assigned name).alog and (the
    assigned name).log
```

As the final step, `rci_mpi` command was run for the CI calculation for all the

$^2S_{1/2}$, $^2D_{5/2}$, $^2D_{3/2}$, and $^2F_{7/2}$ states at once:

```
>>mpirun -np (number of processors to assign) rci_mpi
Invalid MIT-MAGIC-COOKIE-1 key
    ====================================================
         RCI_MPI: Execution Begins ...
 ====================================================
 Participating nodes:
...(skipped)...
 Date and Time:
...(skipped)...
 Start Dir:
...(skipped)...
 Serial I/O Dir (node-0 only):
...(skipped)...
 Work Dir (Parallel I/O):
...(skipped)...
 Default settings?
>>y
 Name of state:
>>(the name of state assigned in Listing 14.13)
 Block            1 ,  ncf =          463
 Block            2 ,  ncf =         1047
 Block            3 ,  ncf =          832
 Block            4 ,  ncf =        72775
 Loading CSF file ... Header only
 There are/is           44  relativistic subshells;
 Calling SETISO ...
...(skipped)...
 Calling SETISO ...
 Include contribution of H (Transverse)?
>>y
 Modify all transverse photon frequencies?
>>y
 Enter the scale factor:
>>1.d-6
 Include H (Vacuum Polarisation)?
>>y
 Include H (Normal Mass Shift)?
>>n
 Include H (Specific Mass Shift)?
>>n
 Estimate self-energy?
>>y
 Largest n quantum number for including self-energy for orbital
 n should be less or equal 8
>>8
 There are            4  blocks  (block   J/Parity   NCF):
  1  1/2+     463       2  5/2+    1047       3  3/2+     832
    4  7/2-   72775

 Enter ASF serial numbers for each block
 Block            1    ncf =          463  id =  1/2+
>>1
 Block            2    ncf =         1047  id =  5/2+
>>1
 Block            3    ncf =          832  id =  3/2+
>>1
 Block            4    ncf =        72775  id =  7/2-
>>1
```

```
 Allocating space for       354711  Rk integrals
...(skipped)...
 RCI90 MIXing coefficients File generated.
 ====================================================
        RCI_MPI: Execution Finished ...
 ====================================================
 Wall time:
...(skipped)...
 Finish Date and Time:
...(skipped)...
 mpi stopped by node-           0  from RCI_MPI: Execution complete.
...(skipped)
```

The correction to the atom's Hamiltonian including the contributions from the transverse photon (Breit) interaction [213], the vacuum polarization, and the self-energy correction,[26] were included as shown in lines 28–33, 35, and 41, respectively, while the mass shifts were not considered during the CI calculation (lines 37 and 39) as they were to be calculated using the RIS4 subroutine (Section 13.1) as described in Section 14.4.

The one set of ASCs for the $^2S_{1/2}$, $^2D_{5/2}$, $^2D_{3/2}$, and $^2F_{7/2}$ states were over at this point, and the desired quantities (e.g., electrons' density over space) were extracted from the output files generated through the ASCs for future use, as described in Sections 14.4 and Chapter 15.

14.3.1 Calculations with correlation layers up to $n = 6$–8

The CI calculations introduced so far involved all the correlation orbital layers with $n = 6$ to 8 prepared in Section 14.2.2 via the DHF calculations, as shown in, e.g., line 31 in Listing 14.5. To observe the convergence of the calculation results as the layer with higher n was introduced, and thus determine whether the layers up to $n = 8$ were enough, the CI calculations with the correlation layers up to $n = 7$ and $n = 6$, respectively, were performed through the same procedure in Section 14.3 except that the highest n values for correlation orbitals were set to be:

```
>>rcsfgenerate
...(skipped including inputs)...
```

[26] The Breit interaction is the leading relativistic correction to the electron-electron Coulomb interaction beyond Dirac-Coulomb approximation, while the vacuum polarization and self-energy effects are known to be the leading quantum electrodynamic (QED) corrections (see Section 4.7 in Ref. [203]).

```
 Give set of active orbitals, ...(skipped)...
>>7s,7p,7d,7f
...(skipped including inputs)
```

or

```
>>6s,6p,6d,6f
```

instead of inputting `8s,8p,8d,8f` as in Listing 14.5, when the CSFs for each state were generated by `rcsfgenerate` command. As shown in Table C.2, most of the IS electronic factors derived from the ASC results show a good convergence of the values, which will be further discussed in Section 14.5.

14.3.2 Calculations with excited core electrons

In the calculations described so far, only the valence electrons in the orbitals listed in Eq. (14.8) were allowed to be excited to the orbitals with higher n, while all the core electrons, especially in the closed s or p orbitals, were not. It implies that only the correlations between the valence electrons were taken into account during the CI calculation, while the core electrons' states remain the same across the $^2S_{1/2}$, $^2D_{5/2}$, $^2D_{3/2}$, and $^2F_{7/2}$ states in the results of the ASCs above. First of all, it is wrong results, as the change in the valence electrons' state perturbs the core electrons' state as well, regardless of how small the effect would be. Furthermore, taking account of the small changes in the $s_{1/2}$ and $p_{1/2}$ core electrons' states during the transitions were in fact crucial for IS electronic factors including F_χ, $G^{(4)}_\chi$ and $G^{(2)}_\chi$,[27] as discussed in Section 16.3.

Indeed, most of the electronic factors in Table C.2 showed big changes as the $5sp$ electrons were excited, while further excitation of $4sp$ electrons demonstrated good convergence of the calculations, implying the valence-core interactions[28] are dominated by the interaction with $5sp$ electrons.

In this work, the electrons in the core s and p orbitals were allowed to be excited, and the following different configurations of the active set approach were considered. First, the electrons in $5s$ and $5p$ shells were allowed to be excited, with the maxi-

[27] which are especially important in this thesis work (see Section 11.1).
[28] cf. Section 6.2 and 6.3 in Ref. [203].

mum number of excited electrons limited to one per shell (i.e., single excitation); the configuration is labeled as 5spS (S for single excitation). In another configuration, named 4sp5spS, the $4sp$ shells were additionally involved in the core excitation configuration, with the maximum number from each shell still limited to one. In the last configuration, labeled as 5spSD, only $5sp$ shells were considered, but at most two electrons were allowed to be excited from each shell (i.e., SD for single or double excitations). The previous calculations without core excitation were labeled as *None*. Finally, in all the configurations, the core excitations were allowed only from the most representative configuration γ of each state [i.e., γ in the state's ASF $\Psi(\gamma PJ)$] out of the 7 MRs in Eq. (14.8) used to generate the list of CSFs; for instance, $\gamma = 4f^{13}\,6s^2$ for the $^2F_{7/2}$ state.

The new configurations for the active set method were implemented by changing inputs for `rcsfgenerate` command in, e.g., Listing 14.5. For $^2S_{1/2}$ state, the first input configuration for $6s$ in line 15 was replaced by

```
 Give configuration            1
>>3d(10,c)4s(2,i)4p(6,i)4d(10,i)5s(2,1)5p(6,5)4f(14,13)6s(1,*)
```

for $^2D_{5/2}$ and $^2D_{3/2}$ states, the third input configuration for $5d$ in line 19 was replaced by

```
 Give configuration            3
>>3d(10,c)4s(2,i)4p(6,i)4d(10,i)5s(2,1)5p(6,5)4f(14,13)5d(1,*)
```

and for $^2F_{7/2}$ state, the fourth input configuration for $4f^{13}\,6s^2$ in line 21 was replaced by

```
 Give configuration            4
>>3d(10,c)4s(2,i)4p(6,i)4d(10,i)5s(2,1)5p(6,5)4f(13,12)6s(2,*)
```

for the 5spS core excitation configuration. Similarly, the input configurations were replaced by

```
 Give configuration            1
>>3d(10,c)4s(2,1)4p(6,1)4d(10,i)5s(2,1)5p(6,5)4f(14,13)6s(1,*)
```

```
 Give configuration            3
>>3d(10,c)4s(2,1)4p(6,1)4d(10,i)5s(2,1)5p(6,5)4f(14,13)5d(1,*)
```

or

```
 Give configuration            4
>>3d(10,c)4s(2,1)4p(6,1)4d(10,i)5s(2,1)5p(6,5)4f(13,12)6s(2,*)
```

for the 4sp5spS configuration, and

```
 Give configuration            1
>>3d(10,c)4s(2,i)4p(6,i)4d(10,i)5s(2,*)5p(6,*)4f(14,13)6s(1,*)
```

```
 Give configuration            3
>>3d(10,c)4s(2,i)4p(6,i)4d(10,i)5s(2,*)5p(6,*)4f(14,13)5d(1,*)
```

or

```
 Give configuration            4
>>3d(10,c)4s(2,i)4p(6,i)4d(10,i)5s(2,*)5p(6,*)4f(13,12)6s(2,*)
```

for the 5sdSD configuration, respectively, depending on the states.

The increased numbers of total CSFs by allowing the core excitation are presented in Table C.2. The 4sp5spSD configuration could not be tried as it introduces too many CSFs for the computing resources that were available for this work. Therefore, the ASC results with 4sp5spS with verified convergence were taken as the final results (see Section 14.5).

14.4 Yb^+: extracting radial electron density $\rho_\Psi(r)$ and mass-shift electronic factor K_Ψ

As introduced in Section 13.2, the radial number density of electrons $\rho_\Psi(r)$ for each state Φ can be extracted using REDF package [205] developed for this work. It is very straightforward to use:

Listing 14.14: `redf` input and output to extract electron density functions.

```
>>redf

 REDF1
 This is the radial electron density function program
 Input files:  isodata, name.c, name.(c)m, name.w
 Output files: name.(c)ed

 Default settings?
>>y

 Name of state
>>(the name of state assigned in Listing 14.13)

 Mixing coefficients from a CI calc.?
>>y
 Loading Configuration Symmetry List File ...
 There are 44 relativistic subshells;
 There are 75117 relativistic CSFs;
```

```
 ... load complete;
Loading Radial WaveFunction File ...
   nelec  =           69
   ncftot =        75117
   nw     =           44
   nblock =            4

  block     ncf     nev    2j+1  parity
      1     463       1       2       1
      2    1047       1       6       1
      3     832       1       4       1
      4   72775       1       8      -1
--------------------------------
REDF_CAL: Execution Begins ...
--------------------------------
Column 100 complete;
Column 200 complete;
...(skipped)...
Column 75100 complete;
NELEC =  69
No  Pos   J Parity  Total population from ED
 1   1      1/2 +     69.000000000001
 2   1      5/2 +     69.000000000001
 3   1      3/2 +     69.000000000022
 4   1      7/2 -     69.000000000095
--------------------------------
REDF_CAL: Execution Finished ...
--------------------------------

REDF: Execution complete.
```

generating a `[the name of state assigned in Listing 14.13].ced` file which contains the electron density `n(r)` [$\rho_\Psi(r)$ in this thesis] over different radial grid points `r` in the unit of a_0^{-3} and a_0, respectively, where a_0 is the Bohr radius.

Listing 14.15: Result of REDF in `.ced` file.

```
REDF1: Radial (volume) electron density function over r
NNNP =  590
No  Pos   J Parity  Total population from ED
 1   1      1/2 +     69.000000000001
       r (a_0)           n(r) (a_0^(-3))
  0.000000000000D+00   0.000000000000D+00
  0.146488846789D-08   0.102398896636D+07
  0.300488337359D-08   0.102398896609D+07
...(skipped)...
  0.167567474262D+06   0.000000000000D+00
  0.176158842384D+06   0.000000000000D+00

No  Pos   J Parity  Total population from ED
 2   1      5/2 +     69.000000000001
       r (a_0)           n(r) (a_0^(-3))
  0.000000000000D+00   0.000000000000D+00
  0.146488846789D-08   0.102395150198D+07
...(skipped)...
  0.176158842384D+06   0.000000000000D+00

No  Pos   J Parity  Total population from ED
```

```
 3    1       3/2 +      69.000000000022
        r (a_0)             n(r) (a_0^(-3))
   0.000000000000D+00   0.000000000000D+00
   0.146488846789D-08   0.102395154180D+07
...(skipped)...
   0.176158842384D+06   0.000000000000D+00

 No   Pos    J Parity   Total population from ED
  4    1       7/2 -      69.000000000095
        r (a_0)             n(r) (a_0^(-3))
   0.000000000000D+00   0.000000000000D+00
   0.146488846789D-08   0.102408443284D+07
...(skipped)...
   0.176158842384D+06   0.000000000000D+00

 REDF1: End of file
```

The above outputs were for 8spdf None configurations (see Sections 14.3.1 and 14.3.2). The normalization of radial electron *number* density $\rho_\Psi(r)$ is given as:

$$\int_0^\infty 4\pi r^2 \mathrm{d}r\, \rho_\Psi(r) = Z - I \tag{14.9}$$

where $Z - I$, for the proton number Z and ionization number I, is the total number of electrons in the atomic system. The stdout in lines 40–43 in Listing 14.14 and the population values in lines 4, 14, 22, and 30 in Listing 14.15 show if the normalization was properly obtained for each state (e.g., 69 electrons in an Yb^+ ion).

While all the other IS electronic factors were derived from the electron density obtained above (see Section 15), the density is not enough to calculate the mass-shift factor K_χ [173]. The values of K_χ were obtained using RIS4 instead as introduced in Section 13.1. The usage of RIS4 is also simple:

Listing 14.16: `ris4` input and output to extract mass-shift electronic factors K_Ψ.

```
>>ris4

 RIS: Execution begins ...
 ================================================
        RIS: Execution Begins ...
 ================================================

 Default settings?
>>y

 Name of state
>>(the name of state assigned in Listing 14.13)

 Mixing coefficients from a CI calc.?
>>y

```

```
 Loading Configuration Symmetry List File ...
 There are 44 relativistic subshells;
 There are 75117 relativistic CSFs;
  ... load complete;
 Loading Radial WaveFunction File ...
    nelec  =           69
    ncftot =        75117
    nw     =           44
    nblock =            4

   block      ncf      nev    2j+1  parity
       1      463        1       2       1
       2     1047        1       6       1
       3      832        1       4       1
       4    72775        1       8      -1
 -------------------------------
 RIS_CAL: Execution Begins ...
 -------------------------------
  Compute higher order field shift electronic factors?
>>y
  One-body angular file not available
  Two-body angular file not available
  Save ang. coefficients of one- and two-body op.?
>>n

 Columns 100 complete;
 Columns 200 complete;
...(skipped)...
 Column 75100 complete;
 -------------------------------
 RIS_CAL: Execution Finished ...
 -------------------------------

 ====================================================
        RIS: Execution Finished ...
 ====================================================
 Wall time:
...(skipped)...
 Finish Date and Time:
...(skipped)...
 RIS: Execution complete.
```

generating a `[the name of state assigned in Listing 14.13].ci` file which contains normal mass shift (NMS) and specific mass shift (SMS) factors (`<K^1 + K^2 + K^3>`; see Ref. [173] for the notations), as in lines 11–27 and 30–46 in Listing 14.17, respectively. The total mass-shift (MS) factors K_Ψ for each *state* Ψ can be obtained by adding the values for NMS and SMS. Then, the MS factors K_χ for *transitions* χ can be obtained by taking difference in the K_Ψ for the ground and excited states of the transition:

$$K_\chi = K_{\Psi_\chi^{(e)}} - K_{\Psi_\chi^{(g)}}. \tag{14.10}$$

The calculated values of K_χ for $\chi = \alpha$: 411 nm, β: 436 nm, and γ: 467 nm optical clock transitions in Yb^+ ions (see Fig. 3-1) and for different active set method configurations (see Sections 14.3.1 and 14.3.2) are listed in Table C.2.

Listing 14.17: Result of RIS4 in `.ci` file.

```
Number of eigenvalues:   4


Level  J Parity  Energy
  1      1/2 +         -0.1404395345D+05  (a.u.)
  1      5/2 +         -0.1404383577D+05  (a.u.)
  1      3/2 +         -0.1404383987D+05  (a.u.)
  1      7/2 -         -0.1404383514D+05  (a.u.)


Level  J Parity  Normal mass shift parameter

                            <K^1>             <K^2+K^3>          <K^1+K^2+K^3>
  1      1/2 +          0.1909439412D+05   -0.5651931010D+04    0.1344246311D+05  (a.u.)
                        0.6892087971D+08   -0.2040054556D+08    0.4852033415D+08  (GHz u)

                            <K^1>             <K^2+K^3>          <K^1+K^2+K^3>
  1      5/2 +          0.1909468546D+05   -0.5651709216D+04    0.1344297625D+05  (a.u.)
                        0.6892193130D+08   -0.2039974500D+08    0.4852218630D+08  (GHz u)

                            <K^1>             <K^2+K^3>          <K^1+K^2+K^3>
  1      3/2 +          0.1909455081D+05   -0.5651727760D+04    0.1344282305D+05  (a.u.)
                        0.6892144527D+08   -0.2039981193D+08    0.4852163334D+08  (GHz u)

                            <K^1>             <K^2+K^3>          <K^1+K^2+K^3>
  1      7/2 -          0.1907929325D+05   -0.5652476677D+04    0.1342681657D+05  (a.u.)
                        0.6886637336D+08   -0.2040251514D+08    0.4846385823D+08  (GHz u)


Level  J Parity  Specific mass shift parameter

                            <K^1>             <K^2+K^3>          <K^1+K^2+K^3>
  1      1/2 +         -0.5239182548D+04    0.9363466851D+03   -0.4302835863D+04  (a.u.)
                       -0.1891073725D+08    0.3379726889D+07   -0.1553101036D+08  (GHz u)

                            <K^1>             <K^2+K^3>          <K^1+K^2+K^3>
  1      5/2 +         -0.5239794800D+04    0.9363873152D+03   -0.4303407485D+04  (a.u.)
                       -0.1891294716D+08    0.3379873543D+07   -0.1553307362D+08  (GHz u)

                            <K^1>             <K^2+K^3>          <K^1+K^2+K^3>
  1      3/2 +         -0.5239657256D+04    0.9364098069D+03   -0.4303247449D+04  (a.u.)
                       -0.1891245070D+08    0.3379954726D+07   -0.1553249597D+08  (GHz u)
```

```
                              <K^1>             <K^2+K^3>         <K^1+K^2+K^3>
  1      7/2 -         -0.5224887787D+04    0.9362233442D+03   -0.4288664443D+04  (a.u.)
                       -0.1885914056D+08    0.3379281692D+07   -0.1547985887D+08  (GHz u)


Level  J Parity  Electron density in atomic units

                        Dens. (a.u.)
  1      1/2 +         0.1023988966D+07
  1      5/2 +         0.1023951502D+07
  1      3/2 +         0.1023951542D+07
  1      7/2 -         0.1024084433D+07


Level  J Parity  Field shift electronic factors and average point discrepancy in fit

                        F0 (GHz/fm^2)       F2 (GHz/fm^4)       F4 (GHz/fm^6)       F6 (GHz/fm^8)
   Disc. (per mille)
  1      1/2 +         0.3527399882D+06   -0.3306780853D+03    0.9383553890D+00   -0.1623716858D-02
   0.0018
  1      5/2 +         0.3527270826D+06   -0.3306659286D+03    0.9383209201D+00   -0.1623657185D-02
   0.0018
  1      3/2 +         0.3527270963D+06   -0.3306659410D+03    0.9383209555D+00   -0.1623657246D-02
   0.0018
  1      7/2 -         0.3527728741D+06   -0.3307090677D+03    0.9384432737D+00   -0.1623869142D-02
   0.0018


Level  J Parity  Field shift electronic factors (corrected for varying density inside nucleus)

                        F0VED0 (GHz/fm^2)   F0VED1 (GHz/fm^4)
  1      1/2 +         0.3334181222D+06   -0.2832708734D+03
  1      5/2 +         0.3334059270D+06   -0.2832604560D+03
  1      3/2 +         0.3334059400D+06   -0.2832604665D+03
  1      7/2 -         0.3334491976D+06   -0.2832974206D+03
```

14.5 Yb^+: Results and convergence

Figure 14-1 shows the extracted radial electron density functions $\rho_\Psi(r)$ obtained in Section 14.4 for $^2S_{1/2}$, $^2D_{5/2}$, $^2D_{3/2}$, and $^2F_{7/2}$ states in Yb^+ ions. In Fig. 14-1(a), the density function is dominated by the core electrons with a relatively shorter extent over space ($r \leq a_0$), and the densities for different states, which differ by only one electron's configurations, look almost identical.

Once the $\rho_\Psi(r)$ were obtained for the states Ψ involved in the transitions of interest, the change in the radial electron density function $\rho_\chi(r) = \rho_{\Psi_\chi^{(e)}}(r) - \rho_{\Psi_\chi^{(g)}}(r)$ during a transition χ with the ground and excited states denoted as $\Psi_\chi^{(g)}$ and $\Psi_\chi^{(e)}$, respectively, can be also obtained. Figures 14-2 and 14-3 show the $\rho_\chi(r)$ for $\chi = \alpha$: 411 nm, β: 436 nm, and γ: 467 nm transitions in Yb^+ ions for different numbers of correlations orbital layers and core electron excitation configurations, respectively. The $\rho_\Psi(r)$ for each transition indeed converged as the *spdf* layers with higher n were introduced in the CI calculations; in Fig. 14-2, the calculation with up to 7*spdf* (dashed line) and 8*spdf* (solid line) almost agree to each other. In particular, the α and β transitions showed better convergence, presumably due to the simpler configurations, $6s \rightarrow 5d$, compared to the γ transition ($4f^{14}\,6s \rightarrow 4f^{13}\,6s^2$). Similarly, in Fig, 14-3, single excitation of electrons in $5sp$ (5spS; dashed line) and additional $4sp$ (4sp5spS; solid line) demonstrate a good convergence of the results, implying the valence-core correlations are dominantly from the electrons in $5sp$ shells while core-core correlations between $4sp$ and $5sp$ are not significant. Allowing double excitation from the $5sp$ shells (5spSD; dash-dotted line) shows slightly different $\rho_\chi(r)$, of which convergence might be worth being investigated in the future. It has not been done to date due to the limited available computing resources (see Section 14.3.2).

As a consequence of the converging wavefunctions, the same trends appeared in the isotope-shift (IS) electronic factors (see Chapter 15) derived from the electron densities $\rho_\chi(r)$ as well, as shown in Table C.2, while the rates of the convergence were different for different factors and transitions χ. In particular, while the factors for $\chi = \alpha$ and β transitions showed great convergences due to the associated $6s\ ^2S_{1/2}$

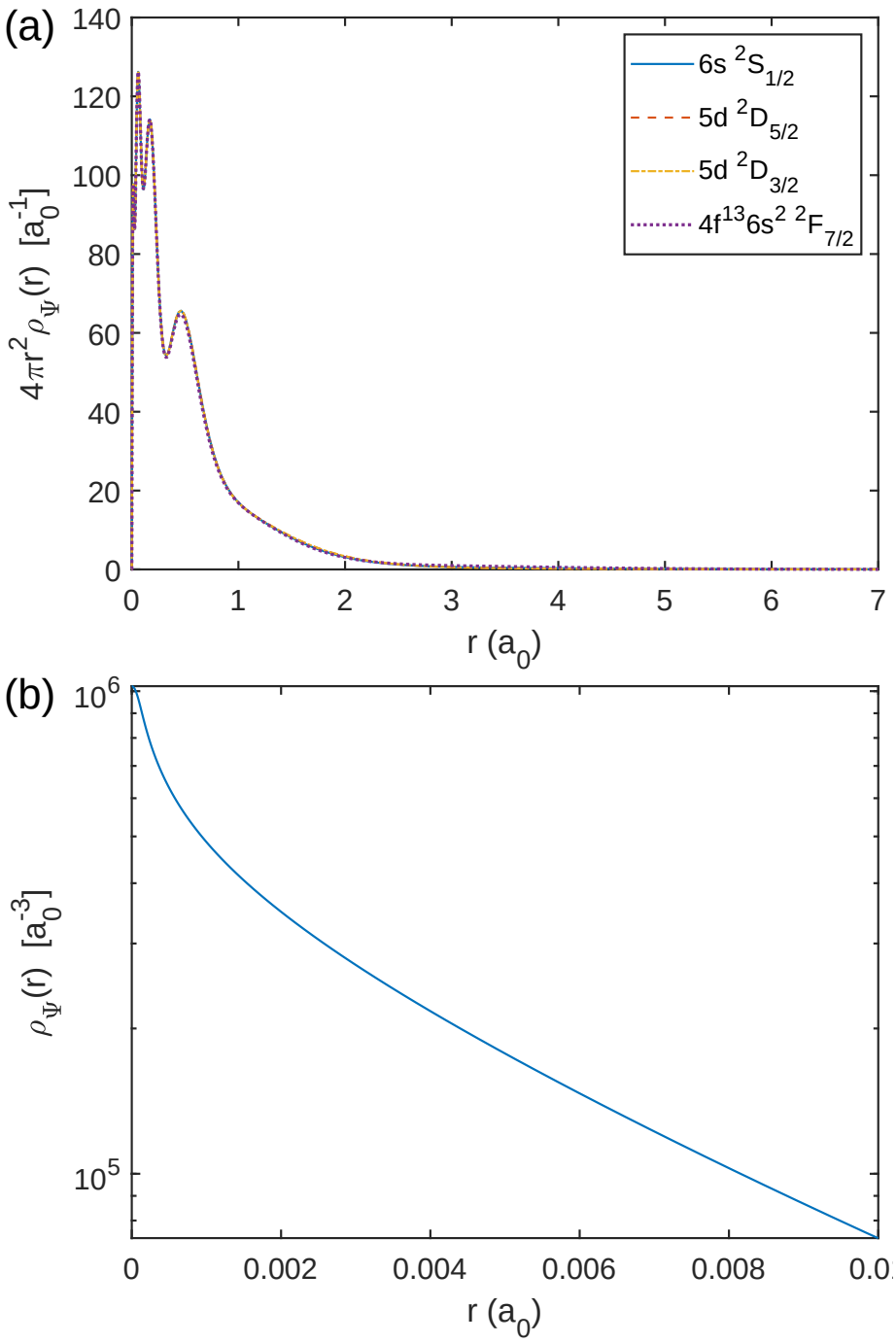

Figure 14-1: (a) Radial electron densities $4\pi r^2 \rho_\Psi(r)$ over r in the unit of the Bohr radius $a_0 \approx 52.9\,\text{pm}$ for $^2S_{1/2}$ (blue), $^2D_{5/2}$ (orange), $^2D_{3/2}$ (yellow), and $^2F_{7/2}$ (purple) states in Yb^+ ions (see Fig. 3-1) from atomic structure calculations (ASCs). The difference in the densities between different states are much smaller than the total density of 69 electrons (see also Figs. 14-2 and 14-3). (b) Magnified $\rho_\Psi(r)$ near the origin, shown in logarithmic scale. The density is exponential $\propto e^{-\alpha r}$ to r (i.e., linear in the graph) down to $r \approx 0.002 a_0$ and starts to show relativistic divergence below the distance (see Section 16.1).

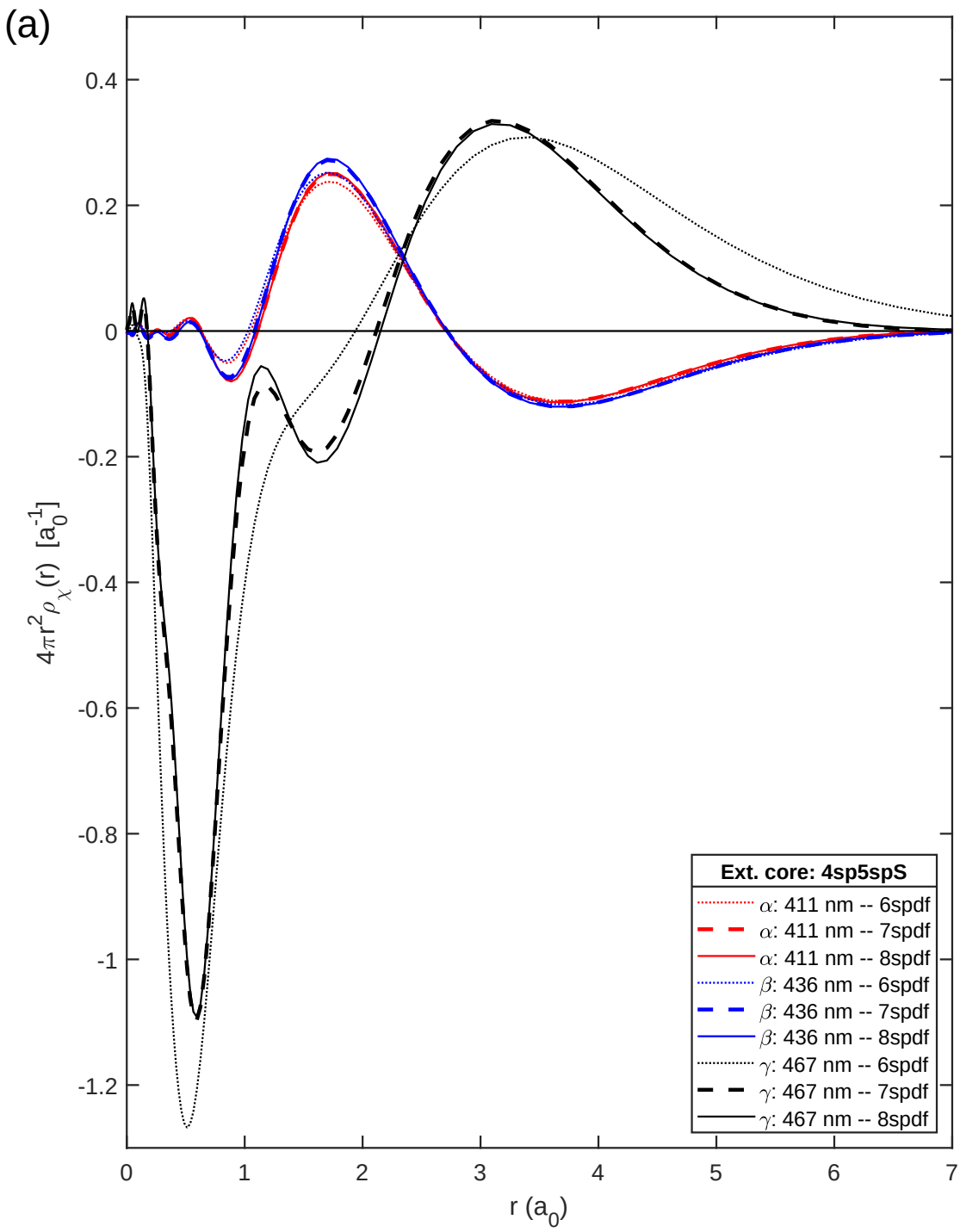

Figure 14-2: Changes in radial electron densities (a) $4\pi r^2 \rho_\chi(r)$ and (b) $\rho_\chi(r) = \rho_{\Psi_\chi^{(e)}}(r) - \rho_{\Psi_\chi^{(g)}}(r)$ over r in the unit of the Bohr radius $a_0 \approx 52.9\,\text{pm}$ for α: 411 nm (red), β: 436 nm (blue), and γ: 467 nm (black) optical clock transitions in Yb^+ ions (see Fig. 3-1) from atomic structure calculations (ASCs). The densities converge as *spdf* orbital correlation layers with higher n are added in the ASCs to take account of the correlations between electrons (see Section 14.3.1). (Figures and caption continue on the next page.)

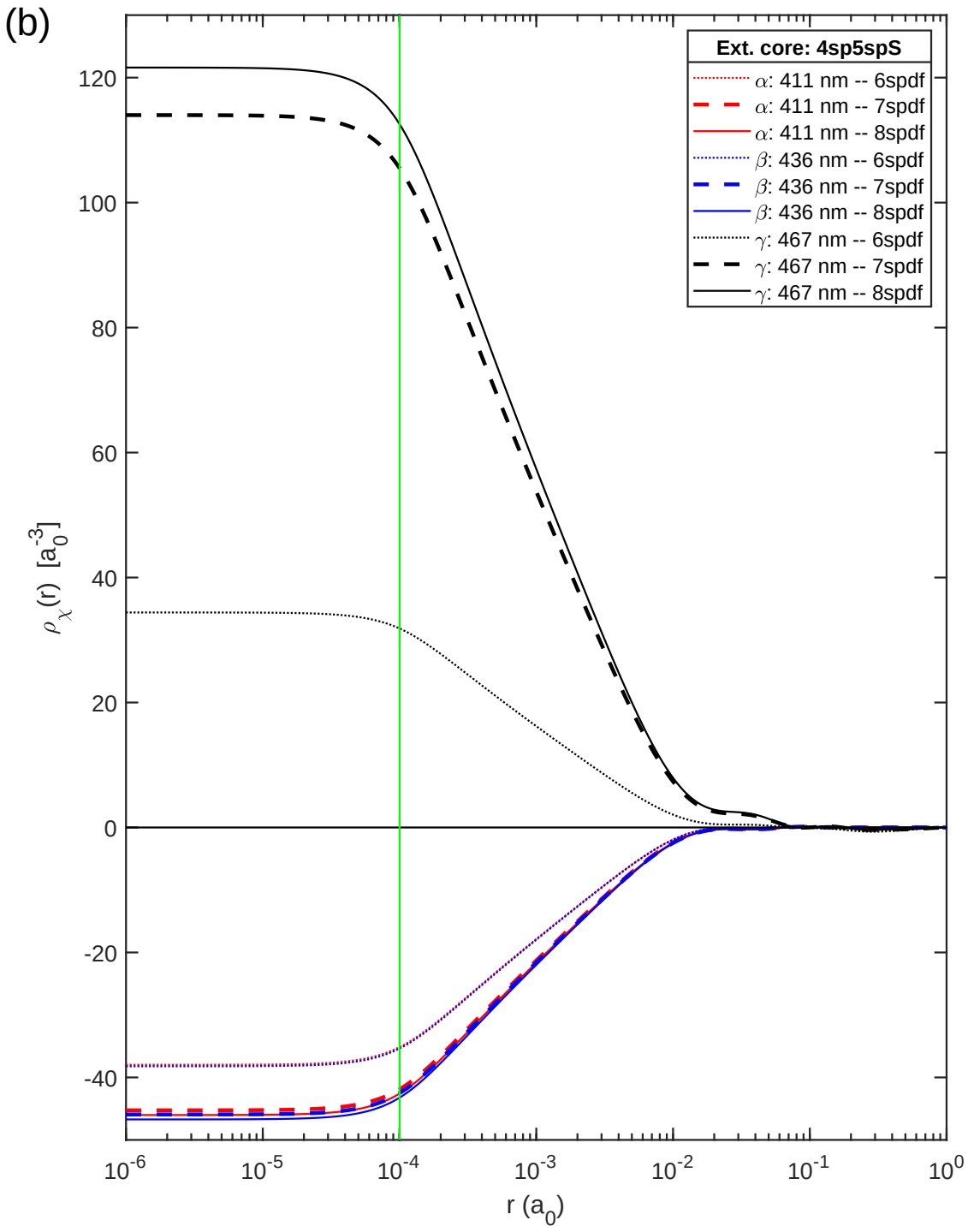

Figure 14-2: (Continued) The results for 4sp5spS core excitation configuration for valence-core or core-core correlations (see Section 14.3.2 and Fig. 14-3) are presented. Green vertical line in (b) shows the RMS nuclear charge radius $\sqrt{\langle r^2 \rangle} = 5.294\,\text{fm}$ of ^{172}Yb [19].

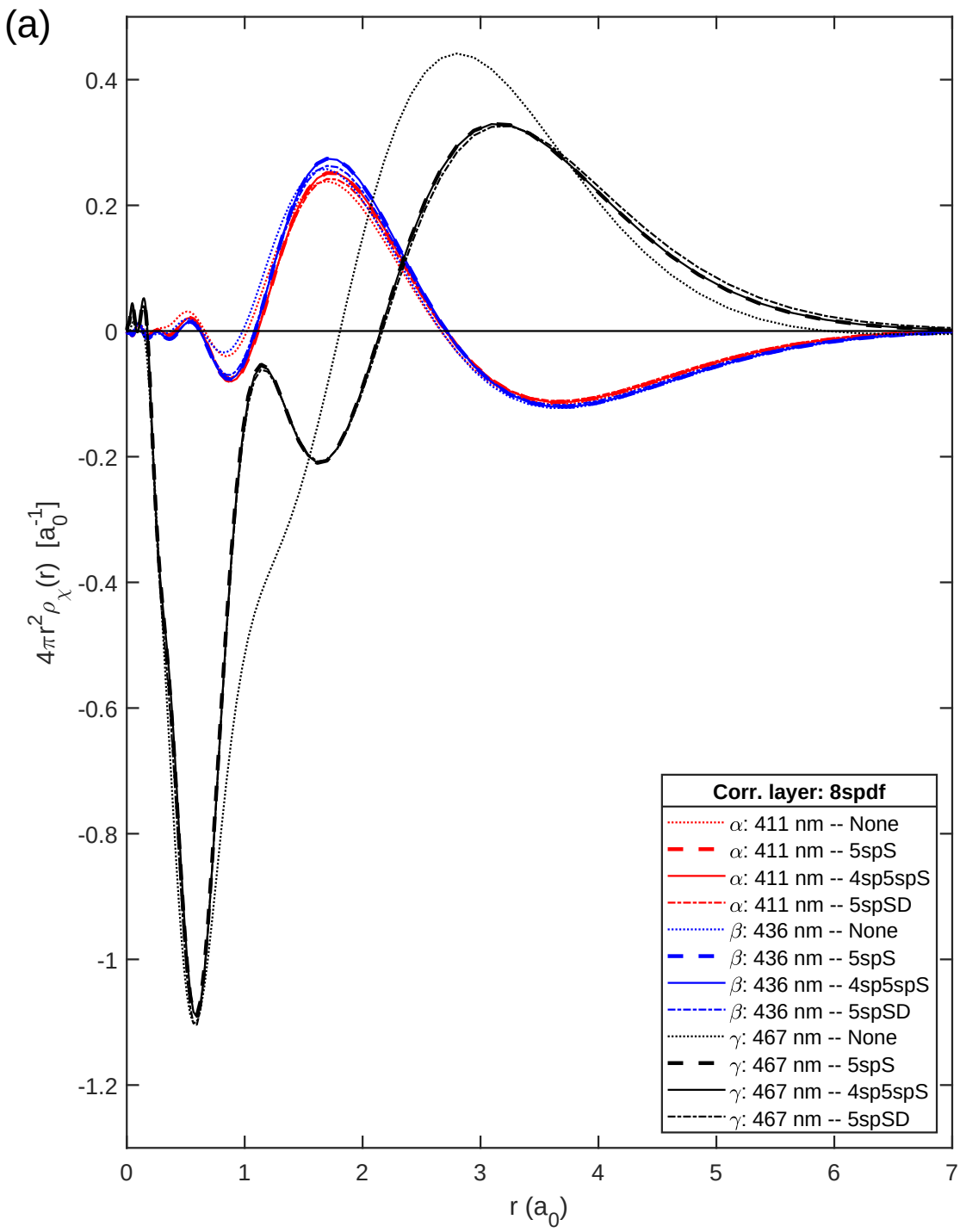

Figure 14-3: Changes in radial electron densities (a) $4\pi r^2 \rho_\chi(r)$ and (b) $\rho_\chi(r) = \rho_{\Psi_\chi^{(e)}}(r) - \rho_{\Psi_\chi^{(g)}}(r)$ over r in the unit of the Bohr radius $a_0 \approx 52.9\,\text{pm}$ for α: 411 nm (red), β: 436 nm (blue), and γ: 467 nm (black) optical clock transitions in Yb^+ ions (see Fig. 3-1) from atomic structure calculations (ASCs). Valence-core or core-core electron correlations are taken into account in CI calculations via different configurations of active set method (see Section 14.3.2): (Figures and caption continue on the next page.)

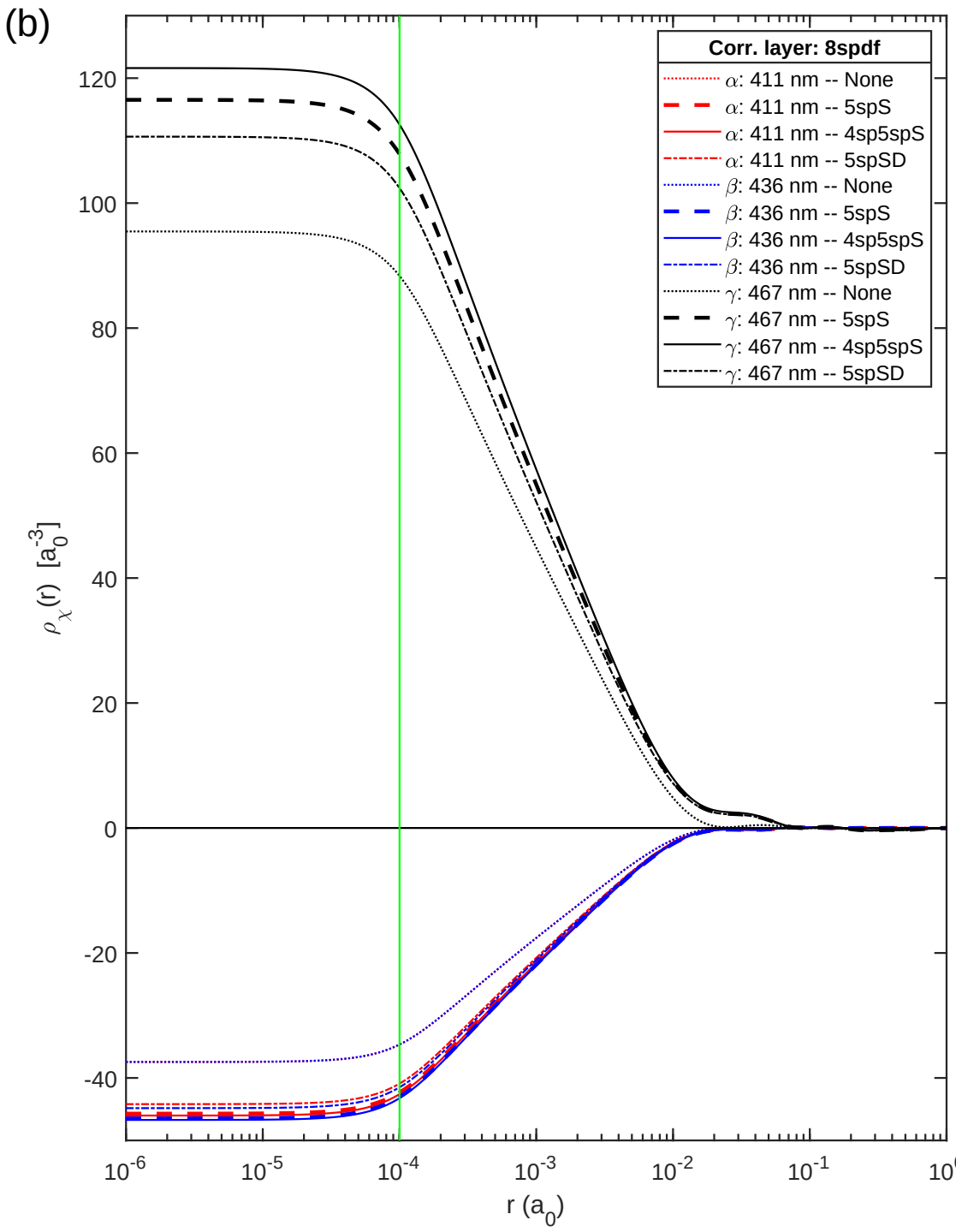

Figure 14-3: (Continued) no core electron excitation (None; dotted), single excitation from each orbital in $5sp$ (5spS; dashed) or $4sp5sp$ (4sp5spS; solid), and single or double excitations from each of $5s$ and $5p$ orbitals (5spSD; dash-dotted) (see also the caption in Table C.2 for the notations). *spdf* orbital correlation layers up to $n = 8$ is added in the ASCs (see Section 14.3.1 and Fig. 14-2). Green vertical line in (b) shows the RMS nuclear charge radius $\sqrt{\langle r^2 \rangle} = 5.294\,\text{fm}$ of ^{172}Yb [19].

and $5d\ ^2D_{5/2,3/2}$ states' simple electron configurations, the convergences for the γ transition were slower due to the complex excited-state configuration: $4f^{13}\,6s^2\ ^2F_{7/2}$. Indeed, the ASCs for the states with open f shells have been known to be challenging because of the strong valence electron correlations and nearly generate configurations, which require higher correlation layers and larger numbers of the CSFs [214] (i.e., slower convergence). Also, the convergence of mass-shift factors K_χ is noticeably slower than other electronic factors, demonstrating that the calculation of K_χ is challenging for heavy atomic species [185, 186] (see also Section 11.2.2).

Considering the verified convergences in the correlation layers and core excitations, the results [the radial density function change $\rho_\chi(r)$ and the IS electronic factors] from *spdf* correlation layers up to $n = 8$ with single excitation from each of $4sp5sp$ core shells (i.e., 8spdf 4sp5spS) has been taken as the final quantities to be used in the King-plot analysis in Part III. The values of the electronic factors can be found in Tables C.3, C.4, and C.5, and Figs. C-1, C-2 and C-3.

14.6 Neutral Yb: Dirac-Hartree-Fock and configuration-interaction calculations

The ASCs were performed for δ: 578 nm and ϵ: 361 nm optical transitions in neutral Yb atoms (see Section 10.1) as well; full credit to Calvin Leung, a research collaborator and a PhD student at MIT.

The general strategy and procedure of the ASCs were the same to the Yb^+ ions: constructing one-electron basis wavefunctions (Section 14.2), performing CI calculations with the lists of CFSs generated from a selected MR set:

$$\{4f^{14}\,6s^2, 4f^{14}\,6s\,6p, 4f^{13}\,6s^2\,5d, 4f^{14}\,6s5d\} \tag{14.11}$$

like in Section 14.3, and extracting the electron densities $\rho_\Psi(r)$ and the mass-shift electronic factors K_Ψ (Section 14.4). There were several differences between the ASCs for Yb atoms and Yb^+ ion, however, which are potentially significant.

First, while the core and valence orbital wavefunctions were constructed through DHF calculations as in Section 14.2, wavefunctions obtained from the Thomas-Fermi approximation of the effective screening potential[29] were used for the correlation orbitals, to avoid DHF calculations for them. Preparing correlation layers in this way is much easier as it can avoid the convergence issues in the DHF calculations which are increasingly tricky to deal with as n increases (see Section 14.2.2). A question is how well the approximated correlation basis can describe the effect of the electron correlations in ASFs within or near nuclei, which would be important to calculate the IS electronic factors of interest in this work (see Section 16.3). This aspect will be investigated in the future. In GRASP2018, the Thomas-Fermi wavefunctions can be obtained by simply running `rwfnestimate` command with the relevant choices of inputs (see, e.g., line 18 in Listing 14.2). *spdfg* correlation orbitals up to $n = 10$ could be obtained in this way for the neutral Yb calculations.

Another difference was that only one electron was allowed to be excited from any of the orbitals (e.g.,

```
1 Number of excitations ...(skipped)...
2 >>1
```

in line 35 in Listing 14.5), while maximum two total electrons were allowed in the calculations for Yb^+ ions.

Finally, the core electrons in $4spd$ and $5sp$ shells were allowed to be excited (i.e., additional $4d$ core orbital from the case of Yb^+ calculations; see Section 14.3).

The values of IS electronic factors derived from the ASCs for δ: 578 nm and ϵ: 361 nm optical transitions in neutral Yb atoms can be found in Tables C.3, C.4, and C.5, and Figs. C-1, C-2 and C-3.

[29]The effective potential that each electron feels from all the other electrons due to the Coulomb interaction.

Chapter 15

Calculation of isotope-shift electronic factors

The procedures for calculating isotope-shift (IS) electronic factors used in this thesis are introduced in this chapter. The results are presented in Appendix C; see Tables C.3, C.4, and C.5, and Figs. C-1, C-2 and C-3.

15.1 Calculation for one-transition electronic factors

The IS electronic factors including F_χ, $G_\chi^{(4)}$, $G_\chi^{(2)}$, and D_χ, introduced in Sections 8.1 and 8.2, can be derived from the calculated electron density change $\rho_\chi(r)$ during transition χ (see Section 14.5), as described in the following subsections. The only exception in this work is the mass-shift factors K_χ, which are calculated directly from the results of ASCs using the software package RIS4 introduced in Section 13.1 (see Section 14.4).

15.1.1 F_χ and $G_\chi^{(4)}$ for linear and fourth-moment field shifts

The Seltzer moment expansion relates field shifts and the expansion of $\rho_\chi(r)$ at the origin [82, 168, 169]:

$$\rho_\chi(r) = \frac{1}{4\pi}\left[\xi_\chi^{(0)} + \xi_\chi^{(2)} r^2 + \cdots\right] \tag{15.1a}$$

$$(\nu_{\mathrm{FS}})_\chi^{AA'} = \sum_{k=0}^{\infty} \underbrace{\frac{c\alpha Z}{2\pi}\frac{\xi_\chi^{(k)}}{(k+2)(k+3)}}_{F_\chi^{(k)}} \langle r^{k+2}\rangle^{AA'} \tag{15.1b}$$

where $\alpha \approx 1/137$ in Eq. (15.1b) is the fine-structure constant and Z is the proton number. $F_\chi \equiv F_\chi^{(0)}$ and $G_\chi^{(4)} \equiv F_\chi^{(2)}$ in this thesis. Therefore, $\xi_\chi^{(0)}$ and $\xi_\chi^{(2)}$ obtained by fitting $\rho_\chi(r)$ with a power series at the origin can be converted into F_χ and $G_\chi^{(4)}$, respectively.

15.1.2 D_χ for new-boson shift

The shift in transition frequency due to a new boson:

$$(\nu_\phi)_\chi^{AA'} = \left\langle a^{AA'} V_{ne}(r)\right\rangle_\chi / h = \upsilon_{ne} D_\chi a^{AA'} \tag{15.2}$$

[all quantities are defined for Eq. (8.16)] gives an expression for D_χ:

$$D_\chi(m_\phi) = \frac{c}{2\pi}\int_0^\infty 4\pi r^2 \mathrm{d}r \rho_\chi(r) \frac{e^{-m_\phi r c/\hbar}}{r}. \tag{15.3}$$

The numerical calculation of D_χ for a given $\rho_\chi(r)$ and m_ϕ is straightforward.

15.1.3 $G_\chi^{(2)}$ for quadratic field shift

The quadratic FS (QFS) $G_\chi^{(2)}[\langle r^2\rangle^2]^{AA'}$ captures the change in wavefunction itself due to the change in nuclear size, which is illustrated in the expression for the electronic

factor $G_\chi^{(2)}$:

$$\begin{aligned} G_\chi^{(2)} &= \frac{1}{2}\left.\frac{\partial^2 \nu_\chi}{(\partial\langle r^2\rangle)^2}\right|_{\langle r^2\rangle^{A_0}} = \frac{1}{2}\left.\frac{\partial F_\chi}{\partial\langle r^2\rangle}\right|_{\langle r^2\rangle^{A_0}} \\ &= \frac{c\alpha Z}{24\pi}\left.\frac{\partial \xi_\chi^{(0)}}{\partial\langle r^2\rangle}\right|_{\langle r^2\rangle^{A_0}} = \frac{c\alpha Z}{6}\left.\frac{\partial \rho_\chi(0;\langle r^2\rangle)}{\partial\langle r^2\rangle}\right|_{\langle r^2\rangle^{A_0}} \end{aligned} \tag{15.4}$$

where the last two equation are obtained from Eq. (15.1), c is the speed of light, $\alpha \approx 1/137$ is the fine structure constant, $Z = 70$ is the proton number of Yb, A_0 is a reference isotope ($A_0 = 172$ here; see Sections 8.2.2 and 11.6), and $\rho_\chi(0;\langle r^2\rangle)$ is the electron number density change during the transition χ at the origin ($r = 0$) for a nucleus with the second charge moment $\langle r^2\rangle$. Therefore, $G_\chi^{(2)}$ is given as the rate of change in electron density change at the origin as the nuclear size changes, and evaluating such change requires repeated atomic structure calculations while gradually varying the nuclear size, in principle.

The repeated calculations were performed while varying the nuclear size (line 8 in Listing 14.1), but the calculated values of wavefunctions at origin showed significant numerical noises, presumably due to the nature of the iterative self-consistent-field procedure (see Section 16.2). Such noise did not allow to obtain reliable values of two-transition factors $G_{\kappa\chi}^{(2)}$. The numerical noises were also pointed out in Ref. [179], and the reference developed a method to suppress the noise in the repeated calculations. Furthermore, the DHF calculation procedures described in Section 14.2 did not give the convergence for some of the nuclear sizes $\langle r^2\rangle$, shown as the nonuniform data in Fig. 14-1(b) along x-axis. GRASP2018 adapts the default grid parameters in, e.g., lines 19–22 in Listing 14.3 to input nuclear parameters in `isodata` file (Listing 14.1), and the fraction of the cases with no convergence and the size of the numerical noise could be reduced by disabling the adaptation and fixing the grid parameters for all the repeated ASCs, as described in Section 14.2.2.1. Nevertheless, a visible size of the numerical noise was observed, as shown in Fig. 14-1(b).

In this work, the strategy to calculate $G_\chi^{(2)}$ without the repeated ASCs has been developed instead (i.e., determination of $G_\chi^{(2)}$ from a single ASC result). It is assumed that the finite size of the nucleus *caps* the electronic wavefunction which

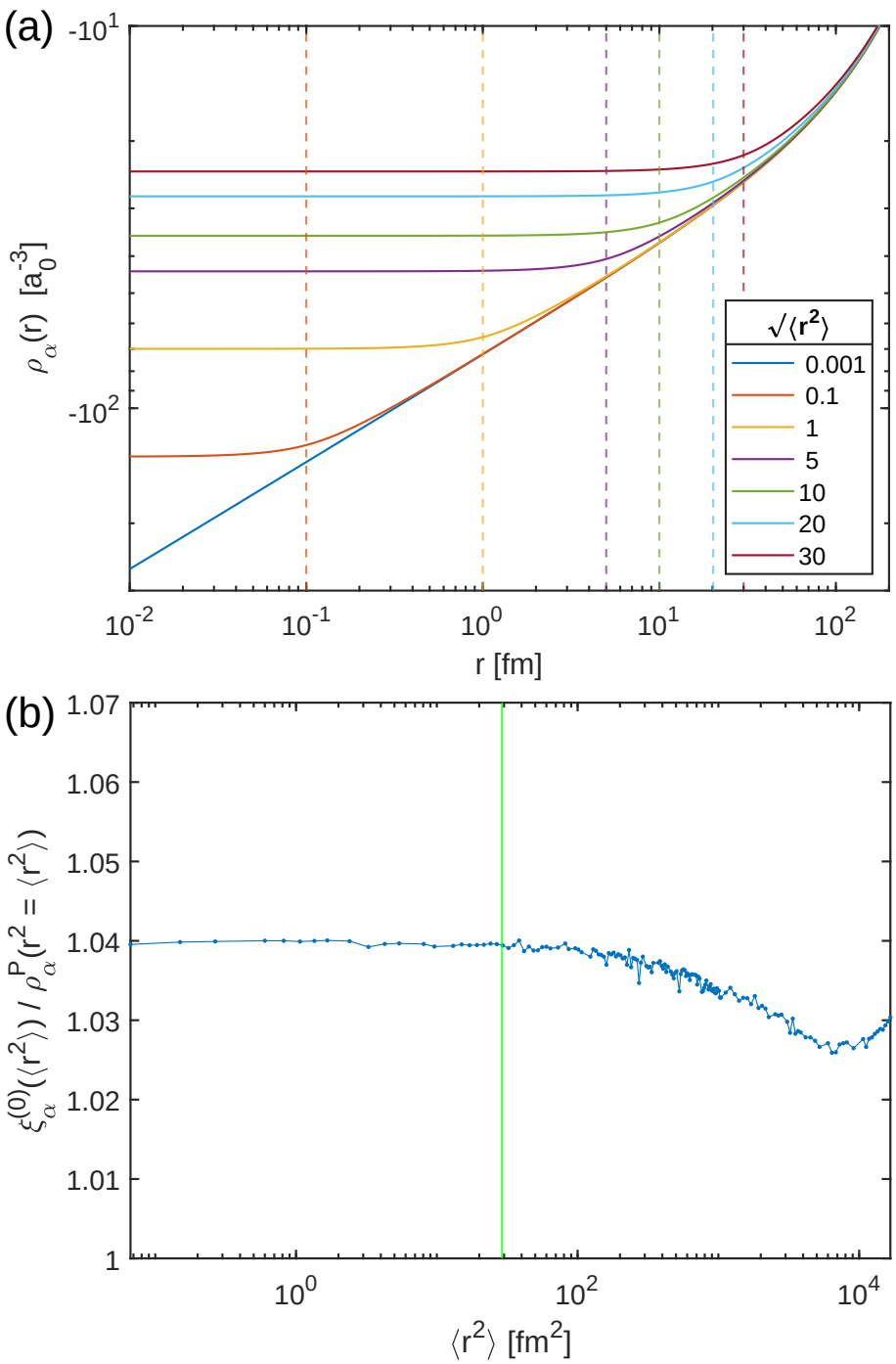

Figure 15-1: (a) Electron density change $\rho_\alpha(r)$ during α: 411 nm transition in Yb^+ ions, for different RMS nuclear charge radii $\sqrt{\langle r^2\rangle}$ [see Eq. (8.4)]. The finite size of nuclear charge caps the increase in the magnitude of the density as getting closer to the origin. (b) Comparison of the electron density $\rho_\alpha(0;\langle r^2\rangle)$ at the origin for the nucleus with second radial nuclear moment $\langle r^2\rangle$ to the electron density $\rho_\alpha^P(r)$ for point-charge nucleus at $r = \sqrt{\langle r^2\rangle}$. The two quantities are essentially the same, with a constant 4 % difference, if the charge radius is not too big: $\langle r^2\rangle \gtrsim (10\,\mathrm{fm})^2$.

would diverge at the origin if the nucleus were a point charge. The assumption is demonstrated in Fig. 15-1(a) for α: 411 nm transition in Yb^+ ions. The radial electron number density change $\rho_\alpha(r)$ calculated for the nuclear size of 0.001 fm (blue line) serves effectively as the density change $\rho_\alpha^P(r)$ for point-charge nucleus, which diverges as it approaches the origin. For all other $\rho_\alpha(r)$ for the finite sizes of nuclei, they follow the line for $\rho_\alpha^P(r)$ as approaching the origin and then stop growing at around the RMS charge radii of the nuclei.

From this observation, a further assumption that the electron density change $\rho_\chi(0;\langle r^2\rangle)$ at the origin ($r = 0$) for a nucleus with the second charge moment $\langle r^2\rangle$ is given by the value of $\rho_\chi^P(\langle r^2\rangle)$ for a point-charge nucleus at the RMS size of the nucleus ($r^2 = \langle r^2\rangle$):

$$\rho_\chi(0;\langle r^2\rangle) = C\rho_\chi^P(\langle r^2\rangle) \tag{15.5}$$

with a constant C close to the unity has been made. This assumption is demonstrated for the α transition as shown in Fig. 15-1(b). The ratio of $\rho_\alpha(0;\langle r^2\rangle)$ and $\rho_\alpha^P(\langle r^2\rangle)$ (i.e., C) is indeed constant and only 4 % deviated from the unity, until the charge radius become too big [$\langle r^2\rangle > (10\,\text{fm})^2$], within the numerical noise from the repeated ASCs to obtain $\rho_\alpha(0;\langle r^2\rangle)$ values. Within $\langle r^2\rangle = 0$ to $(10\,\text{fm})^2$, the variation of the C ratio is largely linear with the slope of only $\lesssim 2\times10^{-6}/\text{fm}^2$.

The relation in Eq. 15.5 allows the determination of $G_\chi^{(2)}$ from a $\rho_\chi^P(r)$ as follows:

$$G_\chi^{(2)} = \frac{c\alpha Z}{6}\left.\frac{\partial\rho_\chi(0;\langle r^2\rangle)}{\partial\langle r^2\rangle}\right|_{\langle r^2\rangle^{A_0}} = C\,\frac{c\alpha Z}{6}\left.\frac{\partial\rho_\chi^P}{\partial(r^2)}\right|_{\langle r^2\rangle^{A_0}} \tag{15.6}$$

Therefore, a single atomic structure calculation with a point-charge nucleus is sufficient to obtain $G_\chi^{(2)}$. In particular, this method provided reliable suppression factors of the two-electron factors $G_{\kappa\chi}^{(2)} = G_\chi^{(2)}(g_{\kappa\chi}^{(2)} - f_{\kappa\chi})$ (see Section 15.2):

$$g_{\kappa\chi}^{(2)} - f_{\kappa\chi} = \frac{G_\kappa^{(2)}}{G_\chi^{(2)}} - \frac{F_\kappa}{F_\chi} = \left.\frac{\partial\rho_\kappa^P/\partial\langle r^2\rangle}{\partial\rho_\chi^P/\partial\langle r^2\rangle}\right|_{\langle r^2\rangle^{A_0}} - \frac{\rho_\kappa(0;\langle r^2\rangle^{A_0})}{\rho_\chi(0;\langle r^2\rangle^{A_0})} \tag{15.7}$$

as shown in Tables C.2 and C.4.

It turned out that a similar idea on relating the finite-nuclear-size electron density

and the point-nucleus density as in Eq. (15.5) appeared in Ref. [81] for the analytic estimation of the King plot nonlinearity as well.

15.2 Calculation for two and three-transition electronic factors

Two-transition electronic factors $f_{\kappa\chi} = F_\kappa/F_\chi$, $z_{\kappa\chi} = Z_\kappa/Z_\chi$, and $Z_{\kappa\chi} = Z_\kappa - f_{\kappa\chi}Z_\chi = (z_{\kappa\chi} - f_{\kappa\chi})Z_\chi$ where $Z \in \{K, G^{(4)}, G^{(2)}, D\}$, defined for (2D) King plots (see Sections 8.1 and 8.2), are calculated from the single-transition factors in Section 15.1. In particular, the factors $z_{\kappa\chi} - f_{\kappa\chi}$ serve as the *suppression* factors for the two-transition factors $Z_{\kappa\chi}$ from single-transition factors Z_χ.

Similarly, three-transition electronic factors $f_{\eta\chi\kappa} = G^{(4)}_{\eta\chi}/G^{(4)}_{\kappa\chi}$, $z_{\eta\chi\kappa} = z_{\eta\chi}/z_{\kappa\chi}$, and $Z_{\eta\kappa\chi} = Z_{\eta\chi} - f_{\eta\chi\kappa}Z_{\kappa\chi} = (z_{\eta\chi\kappa} - f_{\eta\chi\kappa})Z_{\kappa\chi}$ where $Z \in \{K, G^{(2)}, D\}$ are defined for the 3D King plot (see Section 8.4), assuming that the fourth-moment field shifts $G^{(4)}_{\chi,\kappa,\eta}\langle r^4\rangle^{AA'}$ are the dominant source of the nonlinearity in 2D King plot (see Section 11.1.1), and calculated from the two-transition factors. As in the two-transition case, the factors $z_{\eta\chi\kappa} - f_{\eta\chi\kappa}$ are given as the suppression factors for the three-transition factors $Z_{\eta\kappa\chi}$ from two-transition factors $Z_{\kappa\chi}$.

There are two choices of using either the calculated values or the fitted values of $f_{\kappa\chi}$ or $f_{\eta\chi\kappa}$ in 2D [see Eq. (8.15) and Table C.4] or 3D King plots [see Eq. (8.24) and Table C.5] to obtain $Z_{\kappa\chi} = (z_{\kappa\chi} - f_{\kappa\chi})Z_\chi$ or $Z_{\eta\kappa\chi} = (z_{\eta\chi\kappa} - f_{\eta\chi\kappa})Z_{\kappa\chi}$, respectively. It has been determined that using calculated values for the two-transition factors $f_{\kappa\chi}$ and experimental, fitted values for the three-transition factors $f_{\eta\chi\kappa}$ are the better choices, as argued in Supplemental Material of Ref. [8].

Chapter 16

Discussion

16.1 Relativistic effect in Yb^+

Fig. 14-1(b) highlights a crucial aspect of the wavefunctions of Yb^+ states. One of the significant differences of Dirac wavefunctions from the corresponding Schrödinger wavefunctions is the divergence of $s_{1/2}$ and $p_{1/2}$ orbitals' wavefunctions at the origin (see Section 1.2.5 in Ref. [27]): $P(r), Q(r) \sim r^{\gamma}$ and thus $\rho(r) \sim r^{2(\gamma-1)}$ [see Eqs. (14.3) and (14.2)] where $\gamma < 1$ for Dirac wavefunctions [e.g., for hydrogen-like atoms, $\gamma = \sqrt{k^2 - \alpha^2 Z^2}$ where $k = \pm 1$ for $s_{1/2}$ and $p_{1/2}$ orbitals as in Eq. (14.4), α is the fine structure constant, and Z is the proton number; $\gamma = 0.86$ for Yb^{69+}].

The $\rho_\Psi(r)$ in Fig. 14-1(b) increases exponentially as getting closer to the origin (i.e., linear increase in the graph with the logarithmic y axis), just as the Schrödinger wavefunction for $1s$ orbital, and then, at the distances r below $\sim 0.001 a_0$, it manifests the Dirac wavefunctions' divergence.

Such divergence is especially important for the King-plot analysis. Considering the nuclear charge radius $\sqrt{\langle r^2 \rangle} \sim 6\,\text{fm}$ (i.e. $\sim 10^{-4} a_0$) which determines the value of the wavefunction at the origin (see Section 15.1.3), the values of IS electronic factors that are derived from the wavefunctions near the origin, including F_χ, $G_\chi^{(4)}$, $G_\chi^{(2)}$, and D_χ for heavy new bosons (see Section 16.3), are dominated by the Dirac wavefunctions' divergence.

Note that not only at the origin but also the overall distributions of the Schrödinger

and Dirac wavefunctions in Yb ($Z = 70$) are likely different as well, as demonstrated in Figs. 1.1–3 in Ref. [27] for Hg ($Z = 80$).

16.2 Advantage of electronic-factor calculation from wavefunction

Two approaches of calculating IS electronic factors can be found in literature. One of the methods is to observe the shifts in calculated transition energy while varying associated nuclear parameters, which seemingly is a more popular approach, at least in the works for King-plot analysis including Refs. [3, 9, 84, 176, 215]. If a source of isotope shift (IS) is given by $X_\chi x^{AA_0}$ (see Sections 8.1, 8.2 and 11.6):

$$\nu_\chi^{AA_0} = \cdots + X_\chi x^{AA_0} + \cdots ; \tag{16.1}$$

where A_0 denotes a reference isotope, then the electronic factor X_χ is given by the rate of the change in the calculated value of ν_χ^A while the essentially the same calculations with varied values of x^A from x^{A_0} are repeated.[1] [2] In other words, X_χ is given by a *partial* derivative:[3]

$$X_\chi = \left.\frac{\partial \nu_\chi^A}{\partial x^A}\right|_{A_0} . \tag{16.2}$$

The advantage of this approach is that one does not need to extract wavefunctions from the results of ASCs; it is not straightforward to deal with the wavefunctions of a

[1] An insignificant exception, in concept, is new-boson contribution $(-1)^{s+1} y_e y_n/(4\pi\hbar c) D_\chi a^A =$ [Eqs. 15.2,15.3, and 8.16]. The new-boson effect is *turned on* by increasing coupling strength $y_e y_n$: $D_\chi = (-1)^{s+1} 4\pi\hbar c/a^A [\partial \nu_\chi^A/\partial(y_e y_n)]$.

[2] Another type of exceptions is when two parameters are intrinsically correlated. For instance, $\langle r^2\rangle^A$ and $(\langle r^2\rangle^A)^2$ are of the same variable with different powers, so one can fit the change in the transition frequency with the power series up to the second order, $\nu_\chi^{AA_0} = c + F_\chi \langle r^2\rangle^{AA_0} + G_\chi^{(2)} (\langle r^2\rangle^2)^{AA_0}$, while varying $\langle r^2\rangle^A$, and obtain $F_\chi = (\partial \nu_\chi^A)/(\partial \langle r^2\rangle^2)|_{A_0}$ and $G_\chi^{(2)} = \frac{1}{2}(\partial^2 \nu_\chi^A)/(\partial\langle r^2\rangle)^2|_{A_0}$. Similarly, the mass-field shift $C_\chi (\mu\langle r^2\rangle)^{AA_0}$ can be investigated by varying μ^A and $\langle r^2\rangle^A$, fitting with the relation $\nu_\chi^{AA_0} = c + F_\chi \langle r^2\rangle^{AA_0} + G_\chi^{(2)} (\langle r^2\rangle^2)^{AA_0} + K_\chi \mu^{AA_0} + C_\chi (\mu\langle r^2\rangle)^{AA_0}$, and obtaining $C_\chi = (\partial^2 \nu_\chi^A)/(\partial\mu\partial\langle r^2\rangle)|_{A_0}$.

[3] ν_χ^A and x^A are the (absolute) transition χ's frequency and nuclear parameters for an isotope A, respectively. $\nu_\chi^{AA_0} = \nu_\chi^A - \nu_\chi^{A_0}$ is then the IS between a pair of isotopes (A, A_0), and the difference in the isotopes' nuclear parameter values $x^{AA_0} = x^A - x^{A_0}$ is the IS's associated nuclear parameter.

few tens of electrons, and the large set of values to describe the wavefunctions might be a significant overhead for a few scalar values X_χ. Moreover, the basis for the representation of wavefunctions is often not the real space, and retrieving electron densities $\rho_\Psi(\mathbf{r})$ over real space $\mathbf{r}$ might not be straightforward in such a case.

There are two potential disadvantages of the method above, however. The keyword *partial* is highlighted above to point out that all other parameters relevant to ISs should remain the same while a parameter of interest x^A varies, which involves careful examination for some parameters. For example, the nuclear charge distribution moments $\langle r^n \rangle$ [Eq. (8.4)] of different orders n are easily correlated via the change in the charge distribution $\rho^A(r)$. To get the partial derivative, the *shape* of charge distribution[4] should be tuned so to change the value of a moment, e.g., $\langle r^4 \rangle$, while maintaining the moments of all other orders. Unfortunately, GRASP2018 does not support an arbitrary shaping of the nuclear charge distribution and thus provides limited investigation in this approach; GRASP2018 takes Fermi distribution:

$$\rho^A(r) \propto 1/\left[1 + \exp[(r - c^A)/a^A]\right], \tag{16.3}$$

a popular choice as a model for nuclear densities [19, 216]. By tuning the two parameters, 50 %-density radius c^A and 90 %-to-10 % tail thickness $t^A = (4 \ln 3) a^A$, $\langle r^2 \rangle$ and $\langle r^4 \rangle$ can be tuned independently, with possible effects from the correlated changes in higher moments ($\langle r^n \rangle$ with $n > 4$).

Another drawback is that the repeated ASCs with different initial conditions are subject to numerical noise. It is partly from the nature of iterative processes seeking for convergence (the self-consistent-field approach here; see Section 12.2); setting too small tolerance of the process (i.e., the maximum difference in neighboring steps' results to stop the process) results in high computational costs. The effect of the noise is significant especially for the electronic factors for more than one transition with small suppression factors (e.g., a two-transition electronic factor $X_{\kappa\chi}$ with $x_{\kappa\chi} - f_{\kappa\chi} \ll 1$) (see Section 16.3). It is because the value of n-transition

[4] Beyond mere scaling: $\rho_1^A(r) \propto \rho_2^A(cr)$ with a constant c.

factor is, then, very sensitive to the noises in the values of the $(n-1)$-transition factors involved. Due to this effect, $G^{(2)}_{\beta\alpha}$ could be calculated with the uncertainty comparable to the center value in Ref. [5]. New-boson factor D_χ for high boson mass m_ϕ is another such example (i.e., $d_{\kappa\chi} - f_{\kappa\chi} \ll 1$).

As already introduced in Section 15.1, another approach is to use the wavefunctions from ASCs to calculate the electronic factors. This approach was taken also in, for instance, Ref. [82].[5] This method does not require the repeated ASCs for the most of the electronic factors considered in this work,[6] and thus gives no place for the numerical noise or the difficulty in varying only one nuclear parameter.

16.3 Calculation strategy for electronic factors with high correlations with wavefunction near the origin

When electronic factors Z_χ are highly correlated with the field-shift factors F_χ across the different transitions χ, the ratios of the electronic factors $z_{\kappa\chi} = Z_\kappa/Z_\chi$ and $f_{\kappa\chi} = F_\kappa/F_\chi$ are very similar. In other words, the corresponding two-transition electronic factors $Z_{\kappa\chi} = (z_{\kappa\chi} - f_{\kappa\chi})Z_\chi$ are highly reduced from the single-transition factors Z_χ (i.e., the suppression factor's magnitude $|z_{\kappa\chi} - f_{\kappa\chi}| \ll 1$). Such strong correlations can be observed in Table C.2 for FFS $G^{(4)}$, QFS $G^{(2)}$, and new-boson shift factors $D(m_\phi)$ for the heavy boson mass ($m_\phi = 17\,\mathrm{MeV/c^2}$).

The correlations originate from the fact that all those electronic factors are determined by the wavefunctions near the origin. For instance, the F_χ and $G^{(4)}_\chi$ are determined by the electron density differences $\rho_\chi(r)$ and their curvatures at the origin, respectively, as shown in the Seltzer moment expansion [Eq. (15.1)]. The $G^{(2)}$

[5]The Ref. [82] took the wavefunctions of only a valence electron in an Yb^+ ion.

[6]It is true for the terms from the first-order perturbation theory (i.e., the terms that are linearly proportional to the nuclear parameters such as $G^{(4)}_\chi\langle r^4\rangle^{AA'}$ and $\upsilon_{ne}D_\chi a^{AA'}$). The terms that arise from the higher-order perturbation theory capture the change in wavefunctions, and thus repeating ASCs is unavoidable to calculate such changes. QFS is an example that arises from the second-order perturbation theory, and a reasonable assumption on the change in the wavefunction had to be imposed to avoid the repeated ASCs; see Section 15.1.3.

are given by the slopes of the density differences $\rho_\chi^P(r)$ (for the point-charge nuclei) at the sizes of the nuclei [see Eq. (15.6)]. The new-boson-induced Yukawa-like potential [Eq. (8.16)] has short interaction range given by the reduced Compton wavelength of the boson $\lambda\!\!\!^{-}_c^\phi = \hbar/(m_\phi c)$ and couples to the electrons' wavefunction only near the origin [Eq. (15.2)] for heavy bosons (e.g., $\lambda\!\!\!^{-}_c^\phi \sim 10\,\mathrm{fm}$ for $m_\phi = 17\,\mathrm{MeV/c^2}$ while the size of Yb nuclei is $\sim$6 fm [19]). Naturally, the properties of a wavefunction near the origin are highly correlated in terms of their ratios, and thus the suppression factors $z_{\kappa\chi} - f_{\kappa\chi}$ which capture the differences in the ratios are tiny. Note, on other hand, the mass-shift factors K and new-boson factors D for massless bosons (i.e., the Yukawa-like potential is reduced to a Coulomb-like $1/r$ potential), the small suppression factor is not expected in general nor observed in Table C.4, as they encode the global properties of the wavefunctions (see Sections 8.1.2 and 15.1.2).

Furthermore, the change in the wavefunctions during the α and β transitions are intrinsically very similar (see Section 3.1.2), giving further suppression of the two-transition factors. Indeed, the calculated suppression factors $z_{\beta\alpha} - f_{\beta\alpha}$ for the two transitions were consistently smaller by an order of magnitude than the corresponding suppression factors $z_{\gamma\alpha} - f_{\gamma\alpha}$ for the (α, γ) transition pair, as shown in Table C.2.

To capture such strong correlations and yet calculate the tiny differences between the ratios accurately, self-consistency across the calculations for different atomic states is required. In this work, the *shared* basis orbital wavefunctions (see Section 12.2) for all the relevant states ($^2S_{1/2}$, $^2D_{5/2,3/2}$, and $^2F_{7/2}$) were constructed through one stream of DHF calculations (Section 14.2) and used in the following CI calculation (Section 14.3). By doing so, the numerical noise from different DHF calculations[7] due to the nature of the SCF procedures (Section 16.2) could be avoided, and the differences in the states' wavefunctions (i.e., ASFs) were described by the corresponding mixing coefficients (see Section 12.2) using the same basis wavefunctions, maximizing the self-consistency in the comparison for different states.

Note that a new set of basis wavefunctions was built for neutral Yb atoms (see

[7]MCDHF calculations (see Sections 12.2 and 13) could have been performed for each state separately (they were tried in fact), which might be argued as a better estimation of each atomic state.

Section 14.6). Therefore, the thesis author regards the two-(and three-)transition factors and the associated suppression factors that involve the neutral Yb atoms' transitions, in Tables C.4 and C.5, less reliable than the factors for only the α, β, and γ transitions in Yb^+ ions.

One side remark is that the wavefunctions at the origin are dominated by $s_{1/2}$ or $p_{1/2}$ Dirac wavefunctions with $k = \pm 1$ [Eq. (14.3)] as argued in Section 16.1; the wavefunctions for $|k| > 1$ vanishes at the origin. Therefore, the contributions in the electronic factors above are mainly from the electrons in $s_{1/2}$ and $p_{1/2}$ orbitals. Furthermore, the α: 411 nm, β: 436 nm, and γ: 467 nm clock transitions share the same $^2S_{1/2}$ ground state, and thus the one valence s electron in the ground state does not contribute to the sensitivity to the King nonlinearity sources: FFS $G^{(4)}$, QFS $G^{(2)}$, or D for heavy bosons. As no excited state of the clock transitions has a valence electron in a s shell, the sensitivity to those sources originates dominantly from the perturbation of the valence-electron state's change to the $s_{1/2}$ and $p_{1/2}$ core electrons. Therefore, the valence-core correlations involving $s_{1/2}$ and $p_{1/2}$ core shells have been taken into account in the ASCs performed in this work (see Section 14.3.2).

Part V

Outlook

Chapter 17

Improving experimental setup: more precise isotope-shift measurement

Various plans or ongoing works to improve the precision of IS spectroscopy are introduced in the following sections.

17.1 Reducing noise and drift in the probe beam

To date, the coherence time of the experimental setup used for the IS spectroscopy has been demonstrated only ∼100 µs coherence time (see Fig. 6-5), limiting the resolution of Ramsey interferometry for the α: 411 nm and β: 436 nm transitions due to the short pulse and phase evolution times (see Table 5.1). It has also prevented coherent excitation of ions' states through the γ: 467 nm transition (see Section 5.2). Therefore, the linewidth of the probe beam at an ion will be narrowed by improving the active stabilization of probe laser frequency to the reference cavity and mechanical stability of the reference cavity, and potentially compensating fiber-induced phase noises, as introduced in the following subsections.

17.1.1 Acousto-optic-modulator laser frequency feedback

The probe beam used in this experiment is generated by a Ti:sapphire laser system (see Section 4.1.5). The frequency of the Ti:sapphire laser is controlled through a round-trip optical length of the optical cavity in which a Ti:sapphire crystal resides. The length is typically adjusted by piezoelectric modules (piezos) which move a cavity mirror. Such a mechanical control provides limited bandwidth, determined by the lowest resonant frequency of the mechanical oscillator that the piezos and mirror form, due to the phase delay that the oscillator introduces to a feedback loop that stabilizes the laser frequency; roughly speaking, the additional phase delay near the resonant frequency makes the loop forms positive feedback, which is set to provide negative feedback at lower frequencies without the phase delay.

To widen the bandwidth of the laser frequency control over the piezo's resonant frequency, an AOM is placed for the Ti:sapphire laser beam. The double-pass AOM scheme is used to suppress the change in the deflection angle of the beam [217], which would result in the optical power modulation, correlated to the frequency feedback through the AOM, due to the change in free-space-to-fiber coupling efficiency. The bandwidth of an AOM is ultimately given by the time that the acoustic wave takes to pass through the beam spot and deliver the change in the acoustic wave's frequency to the beam frequency. For instance, the acoustic wave's velocity in the AOM crystal is $v = 4.26\,\mathrm{mm/\mu s}$ for an AOM selected for this work (ATM-802DA1, IntraAction Corp.). Assuming the beam size is $\leq$1 mm, the bandwidth of the control will be $\geq$4.26 MHz. The response time of the resonator in the AOM would not be a problem, as far as the bandwidth of the resonator is wider than $\geq$4.26 MHz. As the piezo in the Ti:sapphire laser used has the first resonance at $\approx$100 kHz, an order-of-magnitude increase in the laser frequency control bandwidth is expected as explained below.

The bandwidth of the control does not only limit the feedback at the frequencies higher than the band, but also the size of the open-loop gain G at lower frequencies,[1] which suppress the amplitude of noises in the system by a factor of $G_{\mathrm{cl}} = 1/(1-G)$ (closed-loop gain). It is because the gain G should be smaller than 0 dB at the

[1] $G \equiv -|G|e^{i\phi}$, implying negative feedback ($G < 0$) when there is no phase ϕ, for convenience.

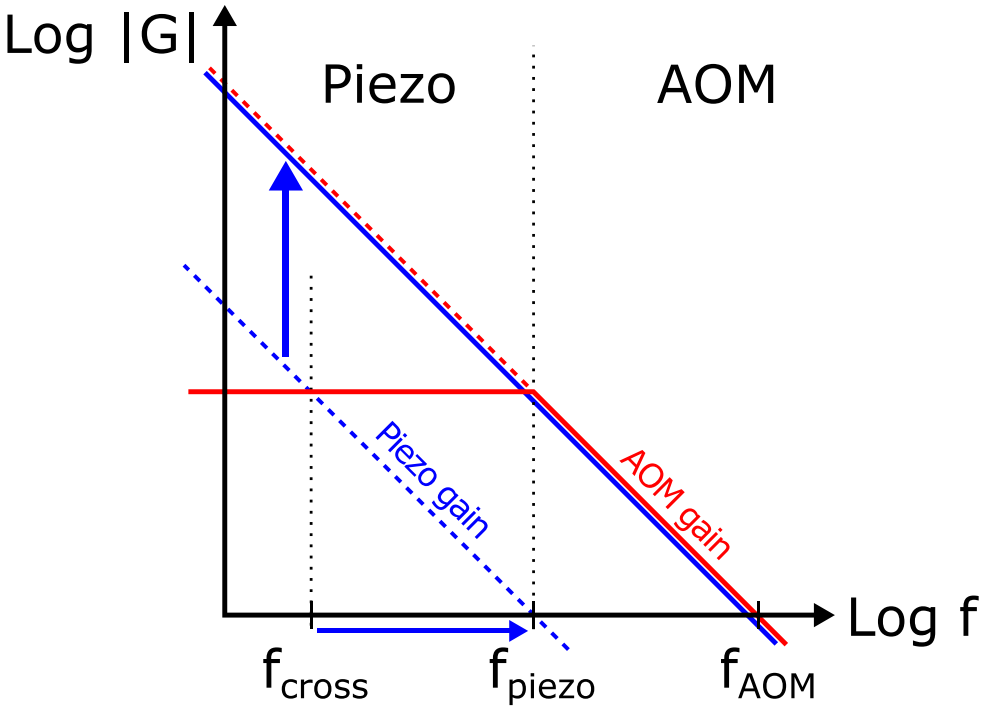

Figure 17-1: Illustration of Ti:sapphire laser frequency active stabilization via dual feedback loops with piezoelectric control of Ti:sapphire cavity optical length and acousto-optic modulator (AOM) drive frequency. f_{piezo} and f_{AOM} refer to the first resonant frequency of the piezoelectric control and the bandwidth of the beam frequency control using the AOM, respectively, which are the upper limits of the corresponding feedback loops' bandwidths and thus determine the maximum magnitudes of gains G_{piezo} (blue) and G_{AOM} (red) of the loops. By capping G_{AOM} by a proportional gain below f_{piezo}, the frequency range that each loop mainly works in is divided by the gain-crossing frequency f_{cross}. Consequently, the G_{piezo} can be increased from the maximum values with piezoelectric loop alone (dashed blue) to the level that makes $f_{\text{cross}} \lesssim f_{\text{piezo}}$ (solid blue). The gross gain $G = G_{\text{piezo}} + G_{\text{AOM}}$ then resembles a continuous integration gain, of which magnitude is limited by f_{AOM}.

frequency at which the gain has 180° phase (i.e., $0 < G < 1$) to prevent the noise at the frequency is amplified through the positive feedback [i.e., G_{cl} diverges]. In other words, the 180°-phase frequency determines the maximum overall level (i.e., total gain) of a gain profile (G vs f) given by, e.g, integration (I) gain, as described in Fig. 17-1.[2] Therefore, increasing the bandwidth of the feedback loop not only stabilizes higher-frequency noises but also suppresses the noise at low frequencies further.

[2]There is, in fact, a double integrator in the feedback loop for the Ti:sapphire laser to achieve higher gain $|G|$ at lower frequencies (i.e., higher suppression of G_{cl}).

The latter effect is the real benefit that is expected in the Ti:sapphire laser system used here. There are several relatively low-frequency sources of the laser frequency noise, including etalon dither, acoustic noise from the optical table that the laser is mounted on, and especially the vibration propagated from a chiller to the Ti:sapphire cavity module through the liquid coolant. On the other hand, the high-frequency noises have been measured to be small and decay as the frequency increases, presumably due to the quieter nature of optically pumped lasers compared to electrically driven lasers (e.g., diode lasers). The remaining noise after engaging the feedback with the piezo has been indeed measured to be significant compared to the high-frequency noise.

AOMs have no lower bandwidth of the frequency control in general. However, the limited range of the control (only a few-MHz width for the AOM used here) and possible remaining change in the beam deflection angle in the double-pass AOM setup, after counteracting to the relatively bigger amplitude of the noises at low frequencies, make the laser frequency stabilization with an AOM alone not feasible. Therefore, it is desired to engage the two feedback loops, each for either the piezo or AOM. As illustrated in Fig. 17-1, the maximum gain magnitude $|G|_{\mathrm{AOM}}$ of the AOM feedback loop, given by the AOM's bandwidth f_{AOM}, is *capped* by a proportional (P) gain applied in parallel with an I gain below the piezo feedback loop's bandwidth (f_{piezo}), and thus the gains of the two loops G_{piezo} and G_{AOM} cross at f_{cross}. In this configuration, the feedback loop with higher gain mainly compensates for the noise at each frequency while the effect of another loop is suppressed. Therefore, at the frequency lower than f_{cross} is taken care by the piezo loop, while the AOM loop works for the higher frequencies $f_{\mathrm{cross}} \lesssim f < f_{\mathrm{AOM}}$. Furthermore, the total gain of the piezo loop can be increased as far as $f_{\mathrm{cross}} \lesssim f_{\mathrm{piezo}}$ to prevent positive feedback by the piezo, and then the *gross* gain of two loops $G = G_{\mathrm{piezo}} + G_{\mathrm{AOM}}$ looks like a continuous gain profile from a single integrator.[3] Due to the unity slope of a single I gain in log-log Bode plots, the increase in the piezo-loop gain G_{piezo} is proportional to the increase in the bandwidth of the gross feedback loop: $G/G_{\mathrm{piezo}} = f_{\mathrm{AOM}}/f_{\mathrm{piezo}}$.

[3]Plus multiple integrators if exist; see Footnote 2.

The implementation of the double-pass AOM feedback at high frequencies is recently achieved by Eugene Knyazev, a research team member, starting from the idea and design by the thesis author and an initial setup built by Diana P. L. Aude Craik another team member, and indeed demonstrated the strong suppression of the noises at frequencies lower than the bandwidth of the feedback loop with the piezo, at least by 20 dB in power (i.e., 10 dB in amplitude) as expected above ($f_{\mathrm{AOM}}/f_{\mathrm{piezo}} > 10$).

The stabilized beam after the AOM is fed to one of waveguide frequency doublers for α: 411 nm and β: 436 nm probe beams (see Section 4.1.5), taking full benefit of the increased bandwidth of the gross feedback. For γ: 467 nm probe beam, however, $\sim$3 W of 934 nm beam out of the Ti:sapphire cavity module goes directly to a frequency-doubling cavity (see Section 4.1.5), in which the frequency noise is not compensated by the AOM. Nevertheless, given that the low-frequency noises ($f < f_{\mathrm{piezo}}$) dominate over high-frequency noises, the γ: 467 nm probe beam would get almost the same benefit from the increased G_{piezo} thanks to the AOM loop, which is somewhat counterintuitive in a sense. If high-frequency noises turn out to be an issue in the future, additional feedforwarding of the high-frequency components in PDH error signal to the AOM frequency control can be considered, with careful consideration of offset drift in the feedforward signal.

In the experiment for the α: 411 nm and β: 436 nm transitions, the >10 times suppressed noise might increase the coherence time in the measurements and allow longer probe pulse time for Rabi and Ramsey spectroscopy [see Section 5.2 and Fig. 5-3(a,b)]. It results in narrower spectra of the transitions in frequency [see Eqs. (6.4]) and (6.7)], which are directly translated into the reduced statistical uncertainties in the measured resonant transition frequencies. It will improve the precision further from already demonstrated $\sim$100 Hz/$\sqrt{\mathrm{hr}}$ uncertainty in ISs for the α: 411 nm transition [see Section 5.5 and Fig. 4-10(a)]. Furthermore, the required probe beam powers will be reduced significantly if the Rabi spectroscopy is performed with a longer pulse time.

For γ: 467 nm transition, if a long enough coherence time (>10 ms) can be

achieved, it lets the transition driven at a moderate, few mW power of the probe beam[4] with a Rabi frequency ω_R of the time scale comparable to the coherence time [121]. Alternatively, if the coherent transition is not feasible even after the upgrade, it will still reduce the amount of the probe power by increasing the power density at the peak frequency, as the transition is driven in broadband excitation limit (i.e., laser linewidth $\gg$ the γ transition's natural linewidth). In either case, reducing the probe beam intensity also reduces the absolute size of probe-induced AC Stark shift (see Section 7.2.1), one of the significant systematic effects for the γ: 467 nm transition in this work.

17.1.2 Vibration isolation platform for reference cavity

Despite the mechanical design of the reference cavity suspension to minimize the transmission of mechanical vibration, the remaining amplitude of the vibration might cause low-frequency noises in cavity modes' resonant frequencies, which will propagate to the probe frequency through the active stabilization to a cavity mode. If the observed low-frequency noise is contributed significantly by the vibration in fact, the upgrade implemented in Section 17.1.1 has not much effect to improve the coherence in the measurement, or even propagate the cavity mode frequency noise slightly further. This effect may be significant for the reference cavity system used here, as the optical breadboard on which the cavity chamber is mounted is placed on an optical table *without* air-compressed table supports; there is only a $\frac{1}{4}$-inch-thick urethane polymer layer between the breadboard and the table.

To reduce the possible low-frequency noise, a passive benchtop vibration isolation platform (150BM-1, Minus K Technology) has been planned to be placed between the breadboard and the table, which provides the suppression of vibration transmission starting from 1 Hz and up to nearly 50 dB (in power) near 50 Hz, according to the datasheet. It is expected to provide information on the effect of the vibration from the support to the cavity system and maximize the mechanical stability of the reference cavity for better precision of the probe beam frequency.

[4]With the typical waist of focused beams (few tens of µm).

17.1.3 Active stabilization of fiber-induced phase noise

Phase noise in the beam transmitted through an optical fiber can be subject to a phase noise induced by the instability in the fiber's optical length (e.g., due to the acoustic vibration), which can be actively compensated using AOMs [218]. Note, however, that the fibers in the current setup have relatively short lengths $\leq$3 m, and Eugene Knyazev, a research team member, demonstrated recently that the noise level is under 1 Hz, so it is not likely an issue in the near future.

17.2 Faster and more sensitive transition frequency measurement scheme

In the experiment performed so far, the entire structure of a peak in each spectrum has been scanned, and then the resonant frequency of the transition is obtained by fitting the peak (see Sections 5.3.6 and Figs. 6-3, 6-6, and 6-11). This measurement is slow; it has taken $\sim$5 min in this work (see Sections 6.1.2, 6.2, and 6.3). Moreover, these full scans of peaks compromise the efficiency of the measurements, as P_e measured at the nodes or antinodes of the spectra have no sensitivity to the center positions of the peaks, while the P_e at the steepest slopes of the peaks have maximal information on the resonant frequencies. Both issues can be resolved by measuring only the two points at the symmetric slopes instead. After one initial full scan, P_e are alternately measured while the probe frequency jumps between the two frequencies at the slopes, and take the difference between P_e at the two frequencies as the *error signal* for an active stabilization, which can be fed back to the center of the two frequencies after a proper gain (e.g., integration) is applied to the error signal. This measurement scheme would provide much improved time resolution ($\lesssim$15 s for two P_e measurements; see Sections 6.1.2, 6.2, and 6.3) and maximized sensitivity of the measured P_e to the resonant frequency. The statistics of the measured resonant transition frequency can then be obtained from the distribution of the center frequency of the two P_e measurements used for each trial over time.

Chapter 18

Cotrapping isotopes: quantum jump of the precision

In this work, the optical clock transitions' frequencies (offset by cavity modes; see Section 4.1.5.1) have been measured for one isotope at a time, and the IS of an isotope pair has been measured by switching a trapped ion of one isotope to another (see Section 5.3.2). A better idea would be to trap ions of different isotopes in the same trap, which would be separated by the Coulomb repulsion between them as illustrated in Fig. 18-1, and measure their transition frequencies simultaneously. Just by doing so, the drift of cavity modes does not need to be considered when ISs are derived from the measured frequencies (see Sections 6.4 and 7.9.3.3), and many of the contributions to the systematic shift in Section 7 would be in common for the trapped ions and canceled out in the measured ISs.

There is a qualitatively advanced use of the cotrapped ions of different isotopes, which has been already demonstrated for $^{86}Sr^{+}$ and $^{88}Sr^{+}$ ions [93]. Consider two cotrapped ions of different isotopes A and A' as the simplest case of the cotrapping. Then, the ions' state that entangles a clock transition χ's ground state of one ion

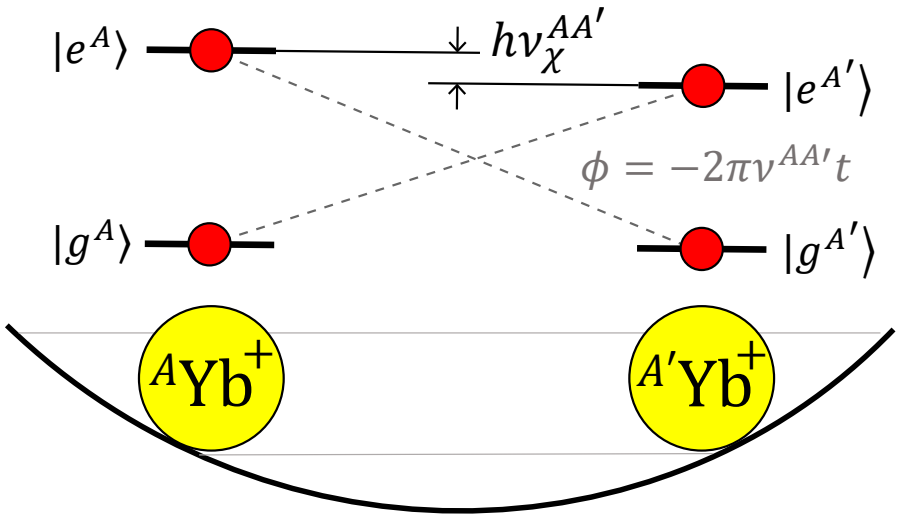

Figure 18-1: Illustration of cotrapped two ions of different isotopes $^A\mathrm{Yb}^+$ and $^{A'}\mathrm{Yb}^+$ in an ion trap of which states are entangled as described by Eq. (18.1). For a transition χ, the ground state for an isotope A is entangled with the excited state of another isotope A' ($|g^A\rangle\,|e^{A'}\rangle$) and vise versa ($|e^A\rangle\,|g^{A'}\rangle$) with equal amplitudes. The energy difference between the two states is given as the isotope shifts between the isotopes times the Plank constant $h\nu_x^{AA'}$, which is encoded in the relative phase evolution $\phi(t) = -2\pi\nu_x^{AA'}t$ between the two states.

and excited state of another ion:

$$\begin{aligned}|\psi(t)\rangle &= \frac{1}{\sqrt{2}}\left[e^{-i(2\pi)\nu_\chi^{A'}}|g^A\rangle|e^{A'}\rangle + e^{-i(2\pi)\nu_\chi^{A}}|e^A\rangle|g^{A'}\rangle\right] \\ &= \frac{e^{-i(2\pi)\nu_\chi^{A'}}}{\sqrt{2}}\left[|g^A\rangle|e^{A'}\rangle + |e^A\rangle|g^{A'}\rangle\exp\left(-i(2\pi)\nu_\chi^{AA'}t\right)\right]\end{aligned} \tag{18.1}$$

can be prepared using a vibrational normal mode of the two ions in the ion trap; the procedure of the preparation is described well in, e.g., Refs. [93, 219]. The energy different between the two terms $|g^A\rangle|e^{A'}\rangle$ and $|e^A\rangle|g^{A'}\rangle$ in Eq. (18.1) is given by the IS $h\nu_\chi^{AA'}$, which will be manifested by their relative phase evolution rate $\mathrm{d}\phi/\mathrm{d}t = -2\pi\nu_\chi^{AA'}$ over time.

The ISs is then measured via parity measurement [93, 220, 221]. The two ions' of isotopes A and A' are driven with the beams with the probe frequencies f^A and $f^{A'}$, respectively, with a common phase noise ϕ_n. The relative phase of the state of

each ion and the beam is then given as:

$$\phi^A(t) = 2\pi(\nu_\chi^A - f^A)t - \phi_n(t) \tag{18.2}$$

and the same for isotope A', and the difference in such relative phases between the ions,

$$\phi^{AA'}(t) = \phi^A - \phi^{A'} = 2\pi(\nu_\chi^{AA'} - f^{AA'})t \tag{18.3}$$

where $f^{AA'} = f^A - f^{A'}$ is the difference in the beams' frequencies, is measured through the *Ramsey* sequence with a $\frac{\pi}{2}$-pulse applied to each ion as follows, after time T since the entangled state in Eq (18.1) is formed. The ions' state in the rotating frame of the two beams' electric fields:

$$\begin{aligned} R(t) &= \left(e^{-i\pi[f^A t+\phi_n(t)]}|g^A\rangle\langle g^A| + e^{+i\pi[f^A t+\phi_n(t)]}|e^A\rangle\langle e^A|\right) \\ &\quad \otimes \left(e^{-i\pi[f^{A'} t+\phi_n(t)]}|g^{A'}\rangle\langle g^{A'}| + e^{+i\pi[f^{A'} t+\phi_n(t)]}|e^{A'}\rangle\langle e^{A'}|\right) \\ &\propto \left(|g^A\rangle\langle g^A| + e^{+i(2\pi)[f^A t+\phi_n(t)]}|e^A\rangle\langle e^A|\right) \\ &\quad \otimes \left(|g^{A'}\rangle\langle g^{A'}| + e^{+i(2\pi)[f^{A'} t+\phi_n(t)]}|e^{A'}\rangle\langle e^{A'}|\right) \end{aligned} \tag{18.4}$$

is given to be

$$\begin{aligned} |\psi(t)\rangle &\xrightarrow{R(T)} \frac{1}{\sqrt{2}}\left[e^{-i\phi^{A'}(T)}|g^A\rangle|e^{A'}\rangle + e^{-i\phi^A(T)}|e^A\rangle|g^{A'}\rangle\right] \\ &\propto \frac{1}{\sqrt{2}}\left[|g^A\rangle|e^{A'}\rangle + e^{-i\phi^{AA'}(T)}|e^A\rangle|g^{A'}\rangle\right] \\ &\xrightarrow[\text{pulses}]{\pi/2} \frac{1}{2^{3/2}}\left[(|g^A\rangle + |e^A\rangle)(|e^{A'}\rangle - |g^{A'}\rangle) + e^{-i\phi^{AA'}(T)}(|e^A\rangle - |g^A\rangle)(|g^{A'}\rangle + |e^{A'}\rangle)\right] \\ &= \frac{1 + e^{-i\phi^{AA'}(T)}}{2^{3/2}}\left(-|g^A g^{A'}\rangle + |e^A e^{A'}\rangle\right) + \frac{1 - e^{-i\phi^{AA'}(T)}}{2^{3/2}}\left(|g^A e^{A'}\rangle - |e^A g^{A'}\rangle\right) \end{aligned} \tag{18.5}$$

which yields

$$\begin{aligned} P_p(T) \equiv \underbrace{(P_{ee} + P_{gg})}_{\equiv P_+} - \underbrace{(P_{eg} + P_{ge})}_{\equiv P_-} &= \frac{1}{2}\cos\phi^{AA'}(T) \\ &= \frac{1}{2}\cos\left[2\pi(\nu_\chi^{AA'} - f^{AA'})T\right] \end{aligned} \tag{18.6}$$

where P_{gg}, P_{ge}, P_{eg}, and P_{ee} denote the probabilities of the ions' state measured to be $|g^A g^{A'}\rangle$, $|g^A e^{A'}\rangle$, $|e^A g^{A'}\rangle$, and $|e^A e^{A'}\rangle$, respectively.

One of the great advantages of such an entangled state is that it alone forms a decoherence-free subspace. The change in the energy of the two terms due to the common-mode magnetic field noise and systematic shifts are the same, not affecting the relative phase evolution which encodes the value of $\nu_\chi^{AA'}$. The common-mode laser noise ϕ_n in Eq. (18.2) also disappears in Eq. (18.6) while the state interferes with the beams. Furthermore, using the long coherence time of the state, an unentangled, separable state:

$$\begin{aligned} |\psi'(0)\rangle &= \frac{1}{\sqrt{2}}(|g^A\rangle + |e^A\rangle) \otimes \frac{1}{\sqrt{2}}(|g^{A'}\rangle + |e^{A'}\rangle) \\ &= \frac{1}{2}|g^A g^{A'}\rangle + \frac{1}{2}|e^A e^{A'}\rangle + \frac{1}{\sqrt{2}}\,|\psi(0)\rangle \end{aligned} \tag{18.7}$$

which can be obtained simply by driving the clock transition by a resonant $\frac{\pi}{2}$ pulse for each ion. Then, as the state evolves, the first two terms in Eq. (18.7) are sensitive to such noises and shifts and quickly decohere to yield the following mixed state:

$$\rho'(t) = \frac{1}{4}\left(|g^A g^{A'}\rangle\langle g^A g^{A'}| + |e^A e^{A'}\rangle\langle e^A e^{A'}|\right) + \frac{1}{2}\,|\psi(t)\rangle\,\langle\psi(t)| \tag{18.8}$$

for $t \gg \tau_{\mathrm{dec}}$ where τ_{dec} is the decoherence time. The effect of the state $\rho'(t)$ is merely the halved contrast in the parity measurement $P_p(T)$, compared to the pure, entangled state $|\psi(t)\rangle$, which would be a fair price for skipping the entangling procedure.

18.1 Plans for experimental realization

18.1.1 Two-frequency beams for different isotopes

Two frequency components in each laser beam, separated by the IS between the isotopes for the corresponding transition, would be a more convenient and reliable way to address both ions almost simultaneously, compared to the fast switching of laser frequencies over GHz distances. Considering the >30 % difference between ISs for dif-

ferent nearest-neighboring even-A (NNE) pairs of isotopes, a resonant EOM or AOM might not be the first choice. If more than one laser is available for the same wavelength, bridging the laser frequencies by beating the two beams and stabilizing the beat frequency (i.e., optical power modulation frequency measured by a photodiode module) using a phase-locked loop (PLL) would be an ideal method, which is planned for the 369 nm lasers. With only one source of laser beams, fiber-coupled broadband EOMs are also a popular choice, especially for relatively longer wavelengths for sufficient power handling. Therefore, fiber-coupled, 6 GHz 3 dB bandwidth EOMs for 935 nm and 760 nm beams that can handle 500 mW and 200 mW input powers, respectively, with the insertion loss of $\leq$6 dB have been purchased for this purpose (WPM-K0935-P85P85AL0 and WPM-K0760-P63P63AL0, AdvR).

Generating probe beams of different frequencies is not as straightforward as the beams for cooling and repumping, unless there is more than one Ti:sapphire laser system or high-power laser system for each of α: 411 nm, β: 436 nm, and γ: 467 nm beams, which would be costly options. High-power (see Table B.1 for the power of the beams used) and broadband EOMs at those blue wavelengths are technically challenging to obtain, but free-space waveguide EOMs potentially handle $\sim$10 mW and $\sim$100 mW for α: 411 nm and γ: 467 nm beams with $\leq$5 dB and $\leq$4 dB insertion losses, respectively, might be available.[1] Considering maximum 34 % of the power in each first-order sideband out of the total output power, it would be able to obtain $\sim$1 mW for α: 411 nm and β: 436 nm beams, which would be enough,[2] [3] and $\sim$13 mW for γ: 467 nm beam, which might be enough [121] after narrowing the linewidth of the probe beam as described in Section 17.1.1.

Modulating the probe beams with broadband EOMs before frequency-doubled may be also an option. It is not possible for γ: 467 nm beam, as an optical cavity used for the frequency doubling would filter the sidebands out. Considering the conversion efficiency of the waveguide frequency doublers (see Section 4.1.5.1), 69 mW

[1] According to a private conversation with AdvR.

[2] The power handling of EOMs for β: 436 nm beam is assumed to have the same power handling, which likely has higher value in fact.

[3] See also Section 17.1.1 for the possible reduction in the required power for the Rabi spectroscopy.

and 5.1 mW second-harmonics power out of 300 mW and 360 mW input power for α: 411 nm and β: 436 nm, respectively, sufficient powers should be possible to obtain from the $\max_\beta 4J_0^2(\beta)J_1^2(\beta) = 46\,\%$ (with $\beta = 0.344\pi$) maximum power of each sideband after frequency-doubled as follows:

$$\begin{aligned} |E_{\rm out}(t)|^2 &\approx |E_{\rm in}(t) + \eta_{\rm SH} E_{\rm in}^2(t) + \cdots|^2 \\ &= \underbrace{|E_{\rm in}(t)|^2}_{\text{fundamental power}} + \underbrace{\eta_{\rm SH}^2 |E_{\rm in}^2(t)|^2}_{=P_{\rm SH}} + \cdots \end{aligned} \tag{18.9}$$

where $E_{\rm in}(t)$ and $E_{\rm out}(t)$ are the electric fields of input and output beams of the frequency doubler, respectively, and $P_{\rm SH}$ is the total power of second-harmonics beams with the frequencies $\approx 2\omega/(2\pi)$, and

$$\begin{aligned} P_{\rm SH} &\approx \eta_{\rm SH}^2 \left| \left[E_0 [J_0(\beta) + J_1(\beta)(e^{i\omega_m t} - e^{-i\omega_m t}) + \cdots] e^{i\omega t} \right]^2 \right|^2 \\ &= \eta_{\rm SH}^2 \left| E_0^2 [J_0^2(\beta) - J_1^2(\beta) + 2J_0(\beta)J_1(\beta)(e^{i\omega_m t} - e^{-i\omega_m t}) + \cdots] e^{i(2\omega)t} \right|^2 \\ &= \eta_{\rm SH}^2 \left(J_0^2(\beta) - J_1^2(\beta) \right) |E_0^2 e^{i(2\omega)t}|^2 \quad \text{(carrier)} \\ &\quad + \eta_{\rm SH}^2 4 J_0^2(\beta) J_1^2(\beta) |E_0^2 e^{i(2\omega + \omega_m)t}|^2 \quad \text{(blue sideband)} \\ &\quad + \eta_{\rm SH}^2 4 J_0^2(\beta) J_1^2(\beta) |E_0^2 e^{i(2\omega - \omega_m)t}|^2 \quad \text{(red sideband)} \\ &\quad + \cdots \end{aligned} \tag{18.10}$$

where $E_{\rm in}(t) = E_0 \left[J_0(\beta) + J_1(\beta)(e^{i\omega_m t} - e^{-i\omega_m t}) + \cdots \right] e^{i\omega t}$ is the EOM-modulated input beam to the frequency doubler driven with the modulation freuqency $\omega_m/(2\pi)$. Broadband EOMs for 200 mW input powers with $\leq$6 dB insertion loss should be available for 2×411 nm to 2×436 nm beams considering the EOMs for 935 nm and 760 nm introduced above.

One another, less preferred way is using two pairs of resonant EOMs of which resonant frequency can be slightly tuned, as the ISs $\nu_\chi^{168,170}$ and $\nu_\chi^{170,172}$ are differ only by $\sim$6 % and $\nu_\chi^{168,170}$ and $\nu_\chi^{170,172}$ are different by $\sim$4 % (see Tables A.2 and A.4). Therefore, $<$10 % tunability is sufficient (e.g., EOMs from Qubig). The two EOMs per beam can be placed in the beam path in series, and then the next-nearest-neighboring even-A isotope pairs can be addressed by driving both the EOMs.

However, only the pairs of the stable even-A isotopes can be addressed in this way, which is not desirable for future experiments with odd-A isotopes (Chapter 19) or radioactive isotopes (Chapter 20).

18.1.2 Beam alignments

Unfortunately, the setup used for this work has a two-mirror optical cavity along the axial direction of the trap chip, along which a chain of ions is arranged, and transmitting a strong probe beam through the cavity mirrors might cause undesirable effects such as the accumulation of charge on the trap chip's surface due to the scattered blue beams (see Section 4.2.3.4) or excessive difference in the probe beam intensities that the two ions see and the intensities' position sensitivity, due to the optical lattice formed inside the cavity. Therefore, the probe beam has to be applied to the ion chain from its side. A major concern is then the differential light shift between the two ions due to the different intensities at the different ions' positions. One method to address each ion with a center of the beam is to split the beam using an acousto-optic deflector (AOD), in case the two ions are separated further than the focal diameter of each beam. If it is not the case, then the two beam spots can be merged in a way that the two maxima of the overlapped (Guassian) beams are distant by the distance between the ions. The latter is the case for the ion trap used in this work; the two trapped ions are separated by $\sim$6.8 µm.[4]

The 935 nm and 760 nm repumping beams (see Fig. 3-1) are free from the issues described above. Therefore, it would be enough to align the beams with few-mW power to the axis of the trap, through the cavity that does not couple to the wavelengths, and to generate sidebands using broadband EOMs.

For the 369 nm beams, the two ions can be addressed with the beams with typical focal waists of $\geq$30 µm (see Table B.1) as the distance between the ions is closer than the beam sizes, and the slight difference in the intensities at the different ions would not be an issue for cooling, optical pumping (Section 5.3.4), and state readout (Section 5.1).

[4]Calculated from the axial trap frequency 364 kHz (see Table 4.1)

Chapter 19

Odd-A isotopes: their own anomaly

The differences in the transition frequencies between isotopes that includes odd-A isotopes with hyperfine (HF) structures can be measured through essentially the same procedure introduced in Part II. However, those frequency differences are not isotope shifts (ISs) in the usual sense, as the transitions in the odd isotopes are between the HF states of which energies are shifted by the HF interactions. Therefore, the transition frequencies before the HF structures are introduced (i.e., *HF-free* frequencies) should be obtained to map the *isotope shifts* onto King plots for the King nonlinearity test. The usual way of experimentally estimating the HF-free transition frequencies, the centroid frequency, has been used for such tests with Sr [94] and Dy [99], reporting the deviation of odd-A-isotope-involved pairs by few MHz from the lines in the King plots formed by even-A isotope pairs without HF structure.

On the other hand, there are other interesting research topics on the HF structures such as HF anomaly, extracting electrons' wavefunctions at the origin, and probing electric hexadecapole nuclear moments.

In this chapter, the theory of HF structure is summarized, possible contributions of HF structures to the MHz-level King nonlinearity are investigated, and the other research subjects are introduced. Finally, The experimental realization of IS and HF splitting measurements with $^{171}Yb^{+}$ and, more interestingly, $^{173}Yb^{+}$ ions to study all the topics above is discussed.

19.1 Hyperfine structure

If the nucleus inside an atom has spin I, the energy levels of the atom for an electronic state with nonzero total angular momentum J are split by the interaction between the magnetic dipole moments of the electrons and nucleus. In fact, the dipole interaction is not the only source of the energy splitting. In general, HF structure in an atom is about all the couplings between electric or magnetic 2^k-poles of the electrons and the nucleus for $k \geq 1$.[1]

The expression for the HF interactions is as follows [222, 223]:

$$H_{\rm HF} = \sum_{k=1}^{\infty} (H_{\rm HF})_k = \sum_{k=1}^{\infty} \sum_{m=-k}^{k} (-1)^m (T_e)_k^m (T_N)_k^{-m} \tag{19.1}$$

where $(H_{\rm HF})_k$ is the HF structure for 2^k-pole, and $(T_e)_k^m$ and $(T_N)_k^m$ are the spherical tensors of rank k acting on the electronic and nuclear spaces. Due to the symmetry of the nuclear structure, nuclear 2^k-poles are electric for even $k = 2q$ $[(T_N)_{2q}^m = (\mathcal{Q}_N)_{2q}^m]$ and magnetic for odd $k = 2q+1$ $[(T_N)_{2q+1}^m = (\mathcal{M}_N)_{2q+1}^m]$. The highest order of nuclear poles (i.e., the maximum value of k for nucleus) is determined by the nuclear spin: $k_N^{\rm max} = 2I$. Similarly, the highest pole for electrons is given by the their angular momentum: $k_e^{\rm max} = 2J$. Therefore, the HF structure is given by

$$\begin{aligned} H_{\rm HF} &= \sum_{k=1}^{k_{\rm max}} (H_{\rm HF})_k \\ &= \sum_{m=-1}^{1} (\mathcal{M}_e)_1^m (\mathcal{M}_N)_1^{-m} + \sum_{m=-2}^{2} (\mathcal{Q}_e)_2^m (\mathcal{Q}_N)_2^{-m} \\ &\quad + \cdots + \sum_{m=-k_{\rm max}}^{k_{\rm max}} (T_e)_{k_{\rm max}}^m (T_N)_{k_{\rm max}}^{-m} \\ k_{\rm max} &= \min(k_e^{\rm max}, k_N^{\rm max}) = \min(2J, 2I) \end{aligned} \tag{19.2}$$

where $k_{\rm max}$ refers to the maximum 2^k-pole interaction in the HF structure. In short, a nucleus with spin I can have up to 2^{2I}-pole, while the electronic state with angular

[1] $k = 0$ corresponds to the coupling of the electric and nuclear electric monopoles (i.e., charges), which is the Coulomb interaction that gives the gross structure of the atom.

momentum J can *probe* up to 2^{2J}-pole of the nucleus.

The matrix elements of $(H_{\rm HF})_k$ for total angular momentum $\mathbf{F} = \mathbf{J} + \mathbf{I}$ basis $|\gamma JIFm_F\rangle$ are:

$$\begin{aligned}
&\langle \gamma' J' I F' m'_F | \, (H_{\rm HF})_k \, | \gamma J I F m_F \rangle \\
&\quad = \delta_{F'F} \delta_{m'_F m_F} (-1)^{I+J+F} \begin{Bmatrix} F & J & I \\ k & I & J' \end{Bmatrix} \langle \gamma' J' || (T_e)_k || \gamma J \rangle \langle I || (T_N)_k || I \rangle
\end{aligned} \tag{19.3}$$

where $\{\cdot\}$ is the Wigner's 6-j symbol and γ contains more quantum numbers to describe the electronic state. Using this relation, the energy shifts W from the gross-structure energy due to the 2^k-pole interactions can be obtained from the perturbation theory. The shifts from the first-order perturbation theory are given by the diagonal elements of Eq. (19.3) [222]:

$$\begin{aligned}
W^{(1)}(F) &= \sum_{k=1}^{k_{\rm max}} \underbrace{\langle (T_e)_k \rangle_{\gamma J} \langle (T_N)_k \rangle_I}_{\equiv h V_k} X_k(JIF) \\
&= hA \underbrace{\frac{F(F+1) - J(J+1) - I(I+1)}{2}}_{= \langle \mathbf{J} \cdot \mathbf{I} \rangle \equiv K(JIF)} \\
&\quad + hB \frac{8I(2I-1)J(2J-1)}{3(K(K+1) - 4I(I+1)J(J+1)} \\
&\quad + \cdots
\end{aligned} \tag{19.4}$$

for different HF states F with the same remaining quantum numbers γJI, where h is the plank constant,

$$\langle (T_e)_k \rangle_{\gamma J} = \begin{pmatrix} J & k & J \\ -J & 0 & J \end{pmatrix} \langle \gamma J || (T_e)_k || \gamma J \rangle \tag{19.5}$$

and

$$\langle (T_N)_k \rangle_I = \begin{pmatrix} I & k & I \\ -I & 0 & I \end{pmatrix} \langle I || (T_N)_k || I \rangle \tag{19.6}$$

are stretched matrix elements,

$$X_k(JIF) \equiv (-1)^{J+I+F} \begin{Bmatrix} F & J & I \\ k & I & J \end{Bmatrix} \left[\begin{pmatrix} J & k & J \\ -J & 0 & J \end{pmatrix} \begin{pmatrix} I & k & I \\ -I & 0 & I \end{pmatrix} \right]^{-1} \tag{19.7}$$

and $K(JIF) \equiv \langle \mathbf{I} \cdot \mathbf{J} \rangle = [F(F+1) - J(J+1) - I(I+1)]/2$ are F-dependent angular-momentum factors, $(\cdot)$ is the Wigner's 3-j symbol, and V_k are the HF coefficients assosiated to the 2^k-pole shifts with the relations to the conventional coefficients: $A \equiv V_1/(JI)$ (magnetic dipole) and $B \equiv 4V_2$ (electric quadrupole). Note also that the nuclear moments are conventionally expressed as: $\mu \equiv \langle (T_N)_1 \rangle_I$ (magnetic dipole), $Q \equiv 2\langle (T_N)_2 \rangle_I$ (electric quadrupole), $\Omega \equiv -\langle (T_N)_3 \rangle_I$ (magnetic octupole), and $\Pi \equiv \langle (T_N)_4 \rangle_I$ (electric hexadecapole). Furthermore, the second-order perturbation theory gives [222]:

$$\begin{aligned} W^{(2)}(F) &= \sum_{\gamma' J' \neq \gamma J} \frac{|\langle \gamma' J' I F m_F | H_{\rm HF} | \gamma J I F m_F \rangle|}{E_{\gamma J} - E_{\gamma' J'}} \\ &= \left| \begin{Bmatrix} F & J & I \\ 1 & I & J-1 \end{Bmatrix} \right|^2 \eta + \begin{Bmatrix} F & J & I \\ 1 & I & J-1 \end{Bmatrix} \begin{Bmatrix} F & J & I \\ 2 & I & J-1 \end{Bmatrix} \zeta \end{aligned} \tag{19.8}$$

where the state-dependent parameters η and ζ are the constants over F.

Out of the full HF structure, the first-order magnetic dipole interaction is of particular interest and is described in the following subsection.

19.1.1 Magnetic dipole interaction

A physical intuition behind the dipole interaction between electrons and nucleus is the magnetic moment of the nucleus $\boldsymbol{\mu}_I = g_I \mu_N \mathbf{I}$ interacting with the magnetic field $\mathbf{B}_e$ that the electrons generate (see, e.g., Section 6.1 in Ref. [145] and Section 9.1 in Ref. [224] for more details):

$$(H_{\rm HF})_1 = -\boldsymbol{\mu}_I \cdot \mathbf{B}_e(\mathbf{0}) \tag{19.9}$$

where g_I is the isotope-dependent nuclear g factor and $\mu_N = \mu_B(m_e/m_p)$ is the nucleon magneton, given by the Bohr magneton $\mu_B = e\hbar/(2m_e) \approx h \times 1.4\,\mathrm{MHz/G}$ that is suppressed by electron-proton mass ratio $m_e/m_p \approx 1/1836$. The magnetic field generated by the electrons is divided into the contributions from the electrons' orbital motions and spins. The magnetic field from the (total) spin $\mathbf{S}$ is again divided into the field from a dipole $-\frac{\mu_0}{4\pi} g_s \mu_B \frac{1}{r^3}[3(\mathbf{S}\cdot\hat{\mathbf{r}})\hat{\mathbf{r}} - \mathbf{S}]$ at a distance $\mathbf{r}$ and the Fermi contact term $-\frac{\mu_0}{4\pi} g_s \mu_B \frac{8\pi}{3}\delta^3(\mathbf{r})\,\mathbf{S}$, where $g_s \approx 2$ is the electron's g factor and μ_0 is the vacuum permeability.

For s orbitals, there is no magnetic field from the orbital angular momentum and the finite-range magnetic field of spins also averages out, and only the contact interaction term is left, giving:

$$W^{(1)}(F) = \underbrace{\frac{\mu_0}{4\pi} g_I \mu_I g_s \mu_B \frac{8\pi}{3}\rho_e(\mathbf{0})}_{=hA}\langle \mathbf{I}\cdot\mathbf{J}\rangle = hAK(JIF) \tag{19.10}$$

where $\rho_e(\mathbf{0})$ is the *number* density of the electrons that form the $\mathbf{S}$ total spin, at the nucleus, and $\mathbf{J} = \mathbf{L} + \mathbf{S} = \mathbf{S}$.[2]

For states with a nonzero angular momenta $L > 0$, the electrons' density vanishes at the origin and the magnetic field at the nucleus is from the electrons' orbital motion and spin outside the nucleus, which can be well approximated to be [224]:

$$W^{(1)}(F) = \underbrace{\frac{\mu_0}{4\pi} g_I \mu_I g_s \mu_B \left\langle \frac{1}{r^3} \right\rangle \frac{L(L+1)}{J(J+1)}}_{=hA}\langle \mathbf{I}\cdot\mathbf{J}\rangle = hAK(JIF) \tag{19.11}$$

Therefore, the first-order HF shifts are of the form $hA\langle \mathbf{I}\cdot\mathbf{J}\rangle$ in either cases. Note that, however, the shifts for s orbitals probe electron density at the origin, while the shifts depend on the global shape of the electronic wavefunctions over space (through $\langle 1/r^3\rangle$) for the $l > 0$ orbitals, complementing each other.

Finally, if only the first-order shifts are considered, the energy splitting between

[2] All the other electrons in closed s orbitals have zero net spin ($S = 0$) and do not participate in the HF coupling. It is in contrast to the electron density change $\rho_\chi(r)$ that appears in the field-shift electronic factor in Eq. (15.1), which is of all the electrons in the atomic system; see Section 19.4 for more discussions.

nearest neighboring states F and $F-1$ among $|J-I| \leq F \leq J+I$ is given to be

$$W^{(1)}(F) - W^{(1)}(F-1) = hAF \tag{19.12}$$

which is the Landé interval rule. Furthermore, if the nuclear spin is $I = \frac{1}{2}$, then possible values of F are $J \pm \frac{1}{2} \equiv F_{\pm}$ and the shifts from the (HF-free) gross energies E_0 are given to be:

$$W^{(1)}(F) = \begin{cases} +\frac{1}{2}hAJ & = +\frac{1}{4}hA(2F_- + 1) \equiv W_+ \quad , \; F = J + \frac{1}{2} \equiv F_+ \\ -\frac{1}{2}hA(J+1) & = -\frac{1}{4}hA(2F_+ + 1) \equiv W_- \quad , \; F = J - \frac{1}{2} \equiv F_-, \end{cases} \tag{19.13}$$

as illustrated in Fig. 19-1(a), and the ratio of the shifts is $W_+^{(1)}/W_-^{(1)} = -(2F_- + 1)/(2F_+ + 1)$. Therefore, the average of the shifts weighted by the number of the Zeeman sublevels, $2F_{\pm} + 1$, in each HF state vanishes:

$$[2F_+ + 1]W_+^{(1)} + [2F_- + 1]W_-^{(1)} = 0. \tag{19.14}$$

For this reason, the HF-free energy estimated from this relation is called *center-of-mass* or *centroid* energy.

19.2 Odd-A isotopes in King plots: hyperfine splitting ratio test

For isotopes with nuclear spins, the coupling between angular momenta of electrons and nuclei further shifts (and splits) the energy level of each electronic state, in addition to the previous IS contributions that originate from non-angular couplings between electrons and the nuclear properties (e.g., nuclear charge distributions, masses, and the possible new-boson potentials from nuclei; see Sections 8.1 and 8.2). Therefore, to compare the transition frequency between isotopes with and without nuclear spin, such additional HF shifts should be eliminated, so that the comparison (i.e.,

isotope shift involving an isotope with nuclear spin) become sensitive to the nuclear properties that have been of interest in the thesis work. In other words, for the isotopes with HF structures, the energy levels of the states in the atoms before split, and thus *HF-free* frequencies of transitions have to be determined.

In this section, the problem of getting the HF-free transition frequencies is reviewed and discussed, and the resulting deviation of the points in King plots for odd-A isotopes with nuclear spins is demonstrated for Yb^+ ions and neutral Yb atoms, using the ISs measured in this work for the even-A isotopes and the measured transitions frequencies for the odd-A isotopes found in literature. The future studies of understanding and possibly using or canceling the odd-A isotopes' King-plot deviations are explored subsequently.

19.2.1 Determination of hyperfine-free frequency

As briefly mentioned at the end of Section 19.1.1, the HF-free energy of an atomic state, before the HF structures are introduced, is largely given by the center-of-mass (i.e., centroid) energy, the mean energies of two HF states weighted by the number of Zeeman sublevels in each state, for the simplest case of the HF structure: the first-order HF from spin-$\frac{1}{2}$ interaction [i.e., $\min(J, I) = \frac{1}{2}$; see Eq (19.1)]. In such a case, measuring the energy *splitting* ΔW between the two HF states with F_+ and F_- ($F_+ - F_- = 1$) is enough to determine the centroid frequency, as the *ratio* of the absolute shifts $W^{(1)}(F_\pm)$ is given. Explicitly, from Eq. (19.13),

$$\Delta W(F_+, F_-) \equiv W^{(1)}(F_+) - W^{(1)}(F_-) = hAF_+ \tag{19.15}$$

as in Eq. (19.12), and thus

$$W^{(1)}(F_\pm) = \frac{2F_\mp + 1}{4F_+}\Delta W(F_+, F_-) \tag{19.16}$$

from Eqs. (19.13) or (19.14) (note the order of $\mp$ sign in $F_\mp$), as illustrated in Fig. 19-1(b). Note that Eq. (19.15) also provides a simple way to obtain the value of the

A coefficient from a measured splitting ΔW. Developing the idea further, if the energies of the two states $E(F_\pm)$ are known, both the A coefficient and the centroid energy E_c can be obtained as below:

$$\underbrace{\begin{bmatrix} E(F_+) \\ E(F_-) \end{bmatrix}}_{\mathbf{y}} = E_c + \frac{hA}{4}\begin{bmatrix} +(2F_-+1) \\ -(2F_++1) \end{bmatrix} = \underbrace{\begin{bmatrix} 1 & +\frac{2F_-+1}{4} \\ 1 & -\frac{2F_++1}{4} \end{bmatrix}}_{X}\underbrace{\begin{bmatrix} E_c \\ hA \end{bmatrix}}_{\boldsymbol{\beta}}. \tag{19.17}$$

The values of E_c and A and their uncertainties can be obtained from the known energies $E(F_\pm)$ by *fitting* the above relation (see Section 9.2.1).

The last idea provides a straightforward generalization for the higher-spin interactions [e.g., $\min(J, I) > \frac{1}{2}$], which have additional contributions in the HF shifts from the electric or magnetic higher-pole couplings, as described in Section 19.1. For a given atomic states with J and nuclear spin I, there are contributions from the dipole (i.e., 2^1-pole) to $2^{k_{\max}}$-pole HF interactions with $k_{\max} = \min(2J, 2I)$ [see Eq. (19.2)], and there are total $k_{\max}+1$ HF states, $F_1 = |J-I|$ to $F_{k_{\max}+1} = J+I$. Then, from Eq. (19.4), the following relation can be fitted:

$$\begin{bmatrix} E(F_1) \\ \vdots \\ E(F_{k_{\max}+1}) \end{bmatrix} = \begin{bmatrix} 1 & X_1(JIF_1) & \cdots & X_{k_{\max}}(JIF_1) \\ \vdots & \vdots & & \vdots \\ 1 & X_1(JIF_{k_{\max}+1}) & \cdots & X_{k_{\max}}(JIF_{k_{\max}+1}) \end{bmatrix} \begin{bmatrix} E_c \\ hV_1 \\ \vdots \\ hV_{k_{\max}} \end{bmatrix} \tag{19.18}$$

where $X_k(JIF)$ are the angular-momentum factors for the 2^k-pole couplings, defined in Eq. (19.7), to obtain the centroid frequencies E_c and all the corresponding HF coefficients V_k [e.g., $A \equiv V_1/(JI)$, and $B \equiv 4V_2$; see Eq. (19.4)] from the experimentally determined energy $E(F_i)$ for each HF state with F_i. Here, the energy E_c from the first-order HF effects will be still called *centroid* frequency for convenience (first-order HF-free frequency would be a more precise name). An example of such a case is illustrated in Fig. 19-1(d).

There is an important observation that follows. The energies can be offset by an

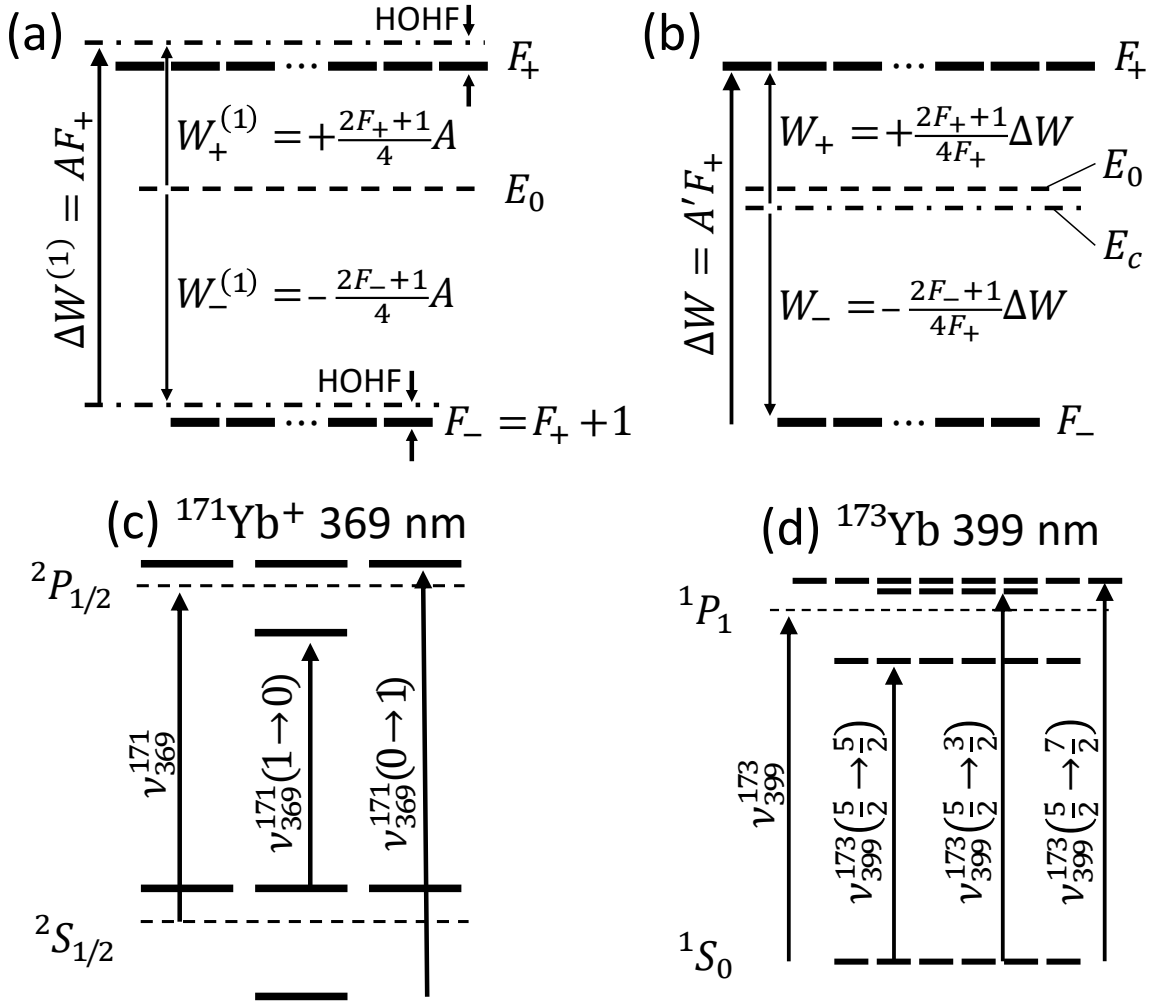

Figure 19-1: (a) Hyperfine (HF) structure of a state with two HF levels with associated A coefficient of magnetic dipole interaction (see Section 19.1.1). First-order HF shifts $W_\pm^{(1)}$ for each of $F_\pm$ levels from HF-free energy E_0 are shown [Eq. (19.13)]. Further shifts from higher-order perturbation theory (HOHF; higher-order HF shifts) are also shown. (b) Estimation of HF structure for the case in (a) (see Section 19.2.1). The values of A' and centroid energy E_c, obtained from measured HF splitting ΔW and $F_\pm$ numbers, estimate A and E_0, respectively. Difference between true HF-free energy E_0 and centroid energy E_c due to HOHF effects is highlighted. (c) HF structure of 369 nm cooling transition in ^{171}Yb$^+$ ions with $I = \frac{1}{2}$ nuclear spins as a simplest example. Transition frequencies $\nu_{369}^{171}(F^{(g)} \to F^{(e)})$ between $^2S_{1/2}$ ground and $^2P_{1/2}$ excited states' HF levels are shown. HF-free transition frequency ν_{369}^{171} between HF-free energies of the two states is estimated to add the ^{171}Yb$^+$ isotope in King plots (see Section 19.2.2). (d) HF structure of 399 nm cooling transition in neutral ^{173}Yb atoms with $I = \frac{5}{2}$ nuclear spins, with more than two HF levels in the $^1P_1$ excited state. The centroid energy E_c and A and B coefficients for magnetic dipole and electric quadrupole interactions, respectively, are estimated using Eq. (19.18).

arbitrary reference level. For instance, $E(F_1)$ can be set to zero, and then all other energies are given by the HF splittings $\Delta W(F_i, F_1)$ from the F_1 state:

$$[E(F_1), \cdots, E(F_{k_{\max}+1})]^{\intercal} = [0, \Delta W(F_2, F_1), \cdots, \Delta W(F_{k_{\max}+1}, F_1)]^{\intercal}. \qquad (19.19)$$

As there are $k_{\max}+1$ states (i.e., $k_{\max}$ splittings) when there are $k_{\max}$ HF couplings (i.e., $k_{\max}$ HF coefficients V_k), experimentally measuring all $k_{\max}$ *independent* HF splittings are always just enough to determine the values of V_k and the centroid energy relative to the energies of HF states [i.e., $E_c - E(F_i)$]. However, if the HF effects from the higher-order perturbation theory are considered as described in Section 19.1, fitting the corresponding equations becomes an underdetermined problem due to the additional HF coefficients [i.e., η and ζ in $W^{(2)}$; see Eq. (19.8)].

Returning to the consideration of the first-order HF contributions only, the *centroid frequency* $(\nu_c)^A_\chi$ of a transition χ for an isotope A with nuclear spin can be obtained by measuring, e.g., all the independent HF splittings ΔW in both the ground and excited states of the transition, and the frequency $\nu^A_\chi(F^{(g)} \to F^{(e)}) = \left[E^{(e)}(F^{(e)}) - E^{(g)}(F^{(g)})\right]/h$ of any one of the possible transitions between the HF states of the ground and excited states. If the higher-order HF effects are considered properly in the future, it would give the true HF-free frequency $(\nu_0)^A_\chi$ or simply ν^A_χ. In this view, the $(\nu_c)^A_\chi$ is a purely experimental estimate of ν^A_χ, which however ignores the higher-order perturbation theory effects as highlighted in Figs. 19-1(a,b).

Finally, if the HF-free (or centroid) frequency ν^A_χ [or $(\nu_c)^A_\chi$] is offset by the corresponding transition frequency $\nu^{A'}_\chi$ of another isotope A', the derived quantity $\nu^{AA'}_\chi$ is regarded as (centroid) *isotope shift* of the isotope pair (A, A') that involves an isotope with nuclear spin.

19.2.2 Hyperfine splittings, centroid isotope shifts, and King-plot deviations for ^{171}Yb and ^{173}Yb

For ^{A}Yb$^+$ ions and ^{A}Yb atoms with $A = 171$ and 173, which have nuclear spins $I = \frac{1}{2}$ and $\frac{5}{2}$, respectively, all the experimentally measured HF splittings ΔW and

transition frequencies $\nu_\chi^A(F^{(g)} \to F^{(e)})$ in literature are listed in Tables 19.1 and 19.2, respectively. From the data, the centroid ISs that involve the odd-A isotopes were obtained, as described in Section 19.2.1, and listed in Table 19.2 for the α: 411 nm, β: 436 nm, and γ: 467 nm transitions in Yb^+ ions (see Fig. 3-1) and δ: 578 nm and ϵ: 361 nm transitions in Yb atoms. Those new ISs were added in King plots together with the ISs between the five even-A isotopes measured in this work or in Refs. [9, 10] as shown in Fig. 19-2 (see the caption in the figure for the inverse-mass-difference factors $\mu^{AA'}$), just as the King plots in Figs. 8-1(b), 10-1, and 10-2 were obtained in Part III.

For the ^{171}Yb isotope with $I = \frac{1}{2}$, there is always at most the dipole interaction [i.e., $k_{\max} = \min(2J, 2I) \leq 1$], implying measuring only one HF splitting $\Delta W(F_+, F_-)$ is enough to determine the centroid energy E_c and A coefficient. Also, trapping, cooling $^{171}Yb^+$ ions, and performing spectroscopy of them are well-established technology (see Section 19.6.1). As a consequence, the $\Delta W(F_+, F_-)$ and $\nu_\chi^A(F^{(g)} \to F^{(e)})$ for all the relevant states and transitions of interest have been reported in literature, and thus ISs could be also obtained for those transitions.

The situation is rather different for $^{173}Yb^+$ ions. To the best of the author's knowledge, trapping $^{173}Yb^+$ ions has not been reported in the community yet, although there are some preliminary works for it [156, 225] (see Section 19.6.2). The data for HF effects are largely missing as a result.

The transition frequencies and HF splittings have been reported also for ^{171}Yb and ^{173}Yb atoms. δ: 578 nm transitions is an ideal transition for the purpose of this work, as none of the ground and excited states have an HF structure as their electronic states ($J = 0$) have no sensitivity to the nuclear spins. On the other hand, the $^1P_1$ excited state of the 399 nm cooling transition has the electric quadrupole HF coupling as well (i.e., B coefficient), yielding three HF states. The transition frequencies of and HF splittings between the states were measured with fairly high precision (sub-MHz) despite the more states and the broad linewidth (28 MHz; see Table B.1), through very careful experiments with a frequency comb and analysis of the interferences between the HF states [113]. The $^1P_1$ state is the only state of which

the B coefficient value is experimentally determined in Table 19.1, and the associated 399 nm transition paired with the δ: 578 nm transition is the only transition pair that provides the points for the ^{173}Yb isotope in the King plot [Fig. 19-2(d)].

Indeed, the odd-A-isotope-involved pairs $(171, 172)$ and $(172, 173)$ consistently show few-MHz deviations (deviations of ν_κ/ν_χ by $\lesssim 2 \times 10^{-3}$ and ν_χ of $\lesssim 3$ GHz) from straight lines determined by the even-A isotope pairs accross the King plots for different transitions pairs, which are also consistent with the reported deviations in Refs. [94, 99] for Sr and Dy, respectively.

Table 19.1: The F numbers of all the hyperfine states, hyperfine splittings ΔW between the states, and hyperfine coefficients A, B, and so on for the states in Yb^+ ions and neutral Yb atoms. All the values that are not from a reference are derived from other values in this table. The convention of the values' signs is $x^{(f)} - x^{(i)}$ for state $i \to$ state f. All the values except F numbers are shown in the unit of MHz. The values with the blue color are theoretically estimated values.

A		171	173
$^2S_{1/2}$ (Yb^+)	F	0, 1	2, 3
	Splitting	$F = 0 \to 1$: +12,642.812 118 466(2)[c]	$F = 2 \to 3$: −10,491.720 239 55(9)[h]
	HF Coeff.	A = +12,642.812 118 466(2)[a]	A = −3,497.240 079 85(3)[a] −3,482.41(18)[b]
$^2P_{1/2}$ (Yb^+)	F	0, 1	2, 3
	Splitting	$F = 0 \to 1$: +2,104.9(1.3)[d]	$F = 2 \to 3$: −1,743.6(1.2)[d]
	HF Coeff.	A = +2,104.9(1.3)[d a]	A = −581.2(4)[d a], −579.79(36)[b]
$^2D_{5/2}$ (Yb^+)	F	2, 3	0, 1, 2, 3, 4, 5
	Splitting	$F = 2 \to 3$: −190.104(3)[e]	?
	HF Coeff.	A = −63.368(1)[a]	A = +17.455(1)[b], +3.47[j] B = +1,190.4[j] C, D, E =?
$^2D_{3/2}$ (Yb^+)	F	1, 2	1, 2, 3, 4
	Splitting	$F = 1 \to 2$: +860(20)[f]	?[i]
	HF Coeff.	A = +430(10)[a]	A = −118(3)[b], −110.31[j i] B = +951.4[j i] C =?
$^2F_{7/2}$ (Yb^+)	F	3, 4	1, 2, 3, 4, 5, 6
	Splitting	$F = 3 \to 4$: +3,620.5(1)[g r]	?[m]
	HF Coeff.	A = +905.13(3)[a]	A = −249.314(15)[b m] B[k l m], C[k m], D[k m] E =?
$^3D[3/2]_{1/2}$ (Yb^+)	F	0, 1	2, 3
	Splitting	$F = 0 \to 1$: −2,209.5(1.1)[f]	$F = 2 \to 3$: +1,825.8(9)[a]
	HF Coeff.	A = −2,209.5(1.1)[a]	A = +608.6(3)[b]
$^1D[3/2]_{3/2}$ (Yb^+)	F	1, 2	1, 2, 3, 4
	Splitting	$F = 1 \to 2$: +8,880(10)[g r]	?
	HF Coeff.	A = +4,440(5)[a]	A = −1,223.0(1.4)[b] B, C =?
$^1P_1$ (Yb)	F	$\frac{1}{2}, \frac{3}{2}$	$\frac{3}{2}, \frac{5}{2}, \frac{7}{2}$
	Splitting	$F = \frac{1}{2} \to \frac{3}{2}$: −318.49(32)[o]	$F = \frac{3}{2} \to \frac{5}{2}$: −754.00(77)[o] $F = \frac{5}{2} \to \frac{7}{2}$: +840.53(47)[o]
	HF Coeff.	A = −212.33(30)[p a]	A = +59.52(20)[q a], +58.485(83)[b] B = +601.87(49)[q a]

[a] Derived assuming first-order HF only [Eq. (19.4)] [b] Eq. (19.21) and $g_I^{173}/g_I^{171} = -0.275446(14)$ (see Footnote 6) [c] Ref. [226] [d] Ref. [227] [e] Refs. [129, 153] [f] Ref. [115] [g] Ref. [225] [h] Ref. [228] [i] See experimental investigations in Ref. [225]. [j] Ref. [229] [k] Ref. [230] [l] Refs. [231, 232] [m] See theoretical investigations in Refs. [230, 231, 232]. [o] Table 19.2 [p] Ref. [113] [q] Ref. [233] [r] Uncertainty not specified; the order of least significant digit is taken as the uncertainty.

Table 19.2: Transition frequencies $\nu_\chi^A(F^{(g)} \to F^{(e)})$ between hyperfine states of transition χ's ground and excited states, and centroid isotope shift (IS) $(\nu_c)_\chi^{AA'}$ obtained in Section 19.2.1, for the transitions in Yb^+ ions and neutral Yb atoms. All the values that are not from a reference are derived from other values in this table and Table 19.1. For 399 nm, 396 nm, 935 nm, and 760 nm transitions for trapping and cooling Yb^+ ions values in this table and Table 19.1 are sufficient to trap ions of $^{171}Yb^+$ isotope, while data for 935 nm and 760 nm transitions are missing for $^{173}Yb^+$ isotope due to the complicated hyperfine structures of the $^2D_{3/2}$, $^2F_{7/2}$, and $^2D[3/2]_{3/2}$ states in the transitions (see Table 19.1, Sections 19.6.1, and 19.6.2). The transition frequencies are either shown in their absolute quantities or offset by the corresponding transition frequencies of other isotopes. The convention of the values' signs is $x^{(f)} - x^{(i)}$ for state $i \to$ state f. All the values are shown in the unit of MHz unless otherwise noted. The values with the blue color are estimated ISs from King-plot inter/extrapolations (see Section A.1).

A		171	173
369 nm $^2S_{1/2} \to {}^2P_{1/2}$ (Yb^+)	Transition	From $^{172}Yb^+$: $F = 1 \to 0$: $-3.705.1(1.3)^a$ $F = 0 \to 1$: $+11.042.63(87)^a$	From $^{172}Yb^+$: $F = 3 \to 2$: $+4818.75(99)^a$ $F = 2 \to 3$: $-7416.57(86)^a$
	IS	$\nu_{369}^{171,172} = +1{,}034.3(8)^b$	$\nu_{369}^{173,172} = -569.9(7)^b$
935 nm $^2D_{3/2} \to {}^3D[3/2]_{1/2}$ (Yb^+)	Transition	$F = 1 \to 0$: 320.569 30(7) THz[c]	
	IS		$\nu_{935}^{173,172} = +1{,}144(20)$
760 nm $^2F_{7/2} \to {}^1D[3/2]_{3/2}$ (Yb^+)	Transition	$F = 3 \to 1$: 394.424 700 THz[d] $F = 4 \to 2$: 394.429 957 THz[d]	
	IS	$\nu_{760}^{171,172} = +1{,}319.536(153)$	$\nu_{760}^{173,172} = -1{,}268(20)$
α: 411 nm $^2S_{1/2} \to {}^2D_{5/2}$ (Yb^+)	Transition	From $^{172}Yb^+$: $F = 0 \to 2$: $+10{,}912.539(153)^{e\ f}$	
	IS	$\nu_\alpha^{171,172} = +1{,}319.536(153)$	$\nu_\alpha^{173,172} = -700(10)$
β: 436 nm $^2S_{1/2} \to {}^2D_{3/2}$ (Yb^+)	Transition	$F = 0 \to 2$: 688,358,979.309 308 42(42)[g] Centroid: 688,349,174.7(7.5)	
	IS	$\nu_\beta^{171,172} = +1{,}338(10)$	$\nu_\beta^{173,172} = -712(10)$
γ: 467 nm $^2S_{1/2} \to {}^2F_{7/2}$ (Yb^+)	Transition	From $^{172}Yb^+$: $F = 0 \to 3$: $+4{,}711.821\ 757\ 3(23)^f$	
	IS	$\nu_\gamma^{171,172} = -2{,}733.756(57)$	$\nu_\gamma^{173,172} = +1{,}362(10)$
δ: 578 nm $^1S_0 \to {}^3P_0$ (Yb)	IS[h]	$\nu_\delta^{171,174} = +1{,}811.281\ 646\ 9(23)^i$	$\nu_\delta^{173,174} = +551.536\ 050(10)^l$
399 nm $^1S_0 \to {}^1P_1$ (Yb)	Transition	From ^{174}Yb: $F = \frac{1}{2} \to \frac{1}{2}$: $+1{,}153.68(25)^j$ $F = \frac{1}{2} \to \frac{3}{2}$: $+835.19(20)^j$	From ^{174}Yb: $F = \frac{5}{2} \to \frac{3}{2}$: $+503.22(70)^k$ $F = \frac{5}{2} \to \frac{5}{2}$: $-250.78(33)^j$ $F = \frac{5}{2} \to \frac{7}{2}$: $+589.51(33)^k$
	IS	$\nu_{399}^{171,174} = +941.353(157)$	$\nu_{399}^{173,174} = +290.24(24)$

[a] Via inverse process of Section 19.2.1: estimating transition frequencies $\nu_{369}^A(F^{(g)} \to F^{(e)})$ from ISs ν_{369}^A and HF splittings ΔW. [b] Ref. [227] [c] Ref. [234] [d] Ref. [125]
[e] Ref. [235] [f] Ref. [121] [g] Ref. [138] [h] This transition have no associated hyperfine structure.
[i] Ref. [10] [j] Ref. [113] [k] Ref. [233] [l] Refs. [236, 237]

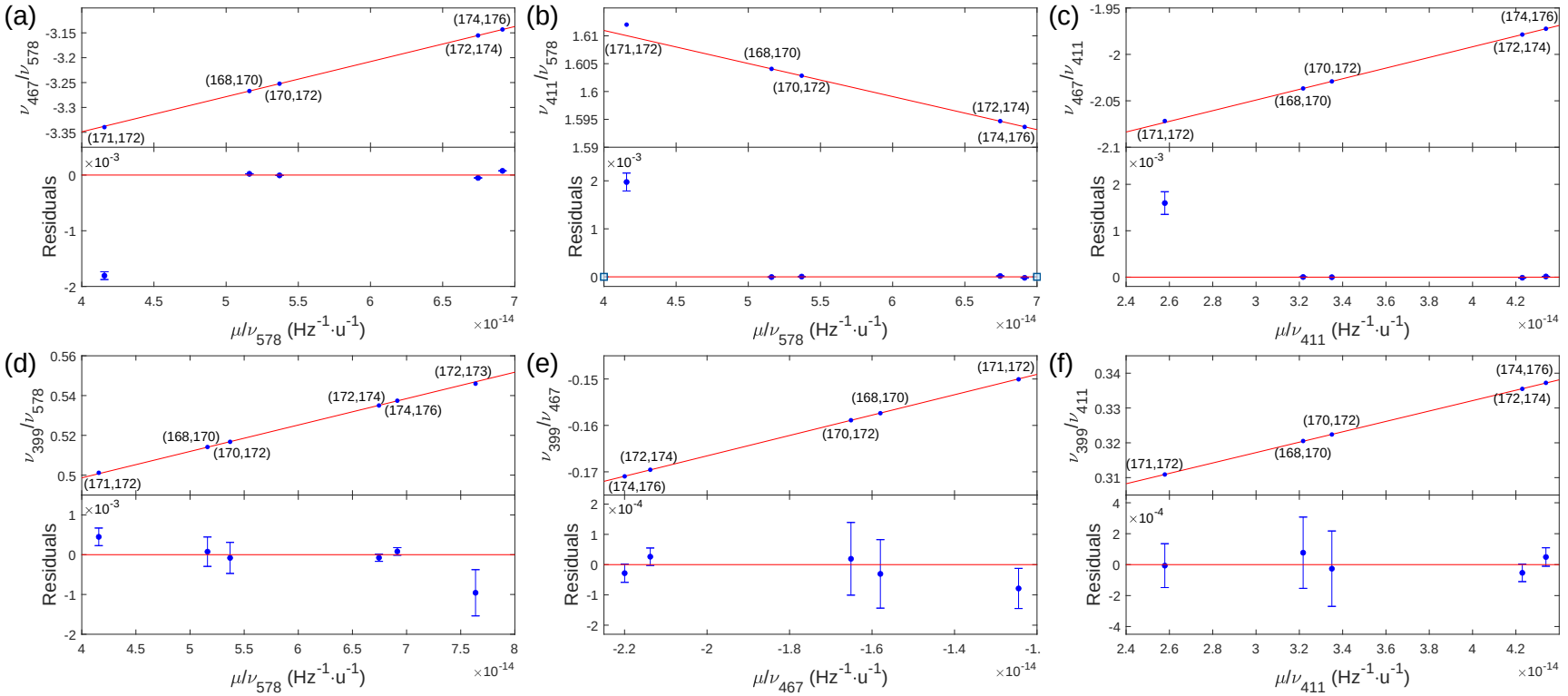

Figure 19-2: Frequency-normalized King plots [Eq. (8.11)] for transitions pairs between α: 411 nm and γ: 467 nm transitions in Yb^+ ions (see Fig. 3-1) and δ: 578 nm ($^1S_0 \rightarrow {}^3P_0$) and 399 nm ($^1S_0 \rightarrow {}^1P_1$) transitions in Yb atoms with $^{171}Yb^+$ or $^{173}Yb^+$ isotopes, listed in the order of the significance of the deviations of odd-A-isotope-involved pairs from the line formed by even-A pairs: (b) 578 nm vs 467 nm, (a) 578 nm vs 411 nm, (c) 411 nm vs 467 nm, (d) 578 nm vs 399 nm, (f) 467 nm vs 399 nm, and (e) 411 nm vs 399 nm, from centroid ISs in Table A.2 and Table 19.2. The values of $\mu^{AA'}$ for even-A can also be found in Table A.2, and $\mu^{171,172} = 34.027\,069\,78(70)\,\mathrm{u}^{-1}$ and $\mu^{172,173} = 33.692\,856\,53(65)\,\mathrm{u}^{-1}$ from m^{172} in Table A.3, $m^{171} = 170.935\,782\,944(14)\,\mathrm{u}$, and $m^{173} = 172.937\,667\,642(12)\,\mathrm{u}$ [6, 7, 20, 21, 22] (see the caption in Table A.3). The error bars indicate 1σ uncertainties.

19.2.3 Hyperfine shift ratio test and cancellation of King-plot deviation

The HF-free energy E_0 of an atomic state is not a directly measurable quantity, and so thus the absolute HF shifts $W(F)$ of each HF state from E_0. The only measurable quantities related to the HF structures are the HF splittings ΔW between the HF states, which are not enough to investigate the higher-order HF effects purely by experiments, as discussed in Section 19.2.1. For instance, for the simple spin-$\frac{1}{2}$ HF structures with two HF states, the exact *ratio* of the shifts $W(F_+)/W(F_-)$ seems not a measurable quantity, while the size of splitting ΔW is.

One way to investigate the effect of the higher-order HF effects would be to compare the measured values of the splittings ΔW to the theoretically predicted quantities. However, the test is again bound to the accuracy of atomic structure calculations described in Part IV, and furthermore, there are nuclear effects that complicate the sizes of splittings (e.g., the values of A coefficients) further as described in Section 19.3.

In this situation, the key idea of this section is that a King plot provides an accurate estimation regarding the HF-free frequencies through the nearby spinless isotopes. For two transitions χ and κ, the straight line in the King plot $(\overline{\overline{\nu}}_\chi^{AA'}, \overline{\overline{\nu}}_\kappa^{AA'}) = (\nu_\chi^{AA'}/\mu^{AA'}, \nu_\kappa^{AA'}/\mu^{AA'})$ in Eq. (8.10), determined by spinless isotopes with no HF structure, sets the ratio of the HF-free frequencies of the two transitions for odd isotopes.[3] Then, if the the centroid frequencies $(\nu_c)_{\chi,\kappa}^A$ deviate from the true HF-free frequencies $\nu_{\chi,\kappa}^A$ due to the higher-order HF effects, and furthermore, if the ratio of such deviations $(\nu_c-\nu)_\kappa^A/(\nu_c-\nu)_\chi^A$ is different from the slope $f_{\kappa\chi}$ of the King plot, then the deviations result in the King nonlinearity. It will then provide an experimentally determined relation of the overall scale and the ratio of the $(\nu_c - \nu)_{\chi,\kappa}^A$ deviations, which may be able to be studied theoretically [222, 230].

Furthermore, it might be possible to theoretically and experimentally bound the

[3]The inverse-mass-normalized King plot is used here, instead of the frequency-normalized one [Eq. (8.11)], for convenience.

ratio of the King-plot deviations of the different points:[4]

$$r_y^A = (\nu_c - \nu)_{\kappa\chi}^A \equiv (\nu_c - \nu)_\kappa^A - f_{\beta\alpha}(\nu_c - \nu)_\chi^A \tag{19.20}$$

involving different isotopes with HF structures (e.g., $^{171}\mathrm{Yb}^+$ and $^{173}\mathrm{Yb}^+$), just as the ratios of A coefficients for different isotopes are given by the ratios of nuclear g factors (see Section 19.3). In that case, if more than one such odd-A-isotope-involved point can be obtained in a King plot, those points should be able to be brought back to the King line following the given ratio, and the remaining nonlinearity might be sensitive to the nuclear effects of interest in this thesis. In other words, the well-bound ratio of HF-induced King nonlinearity can cancel the HF effects in King plots and let the points for spinful isotopes contribute to the search for new physics.

Note that, for the completeness of the discussion, the much bigger King nonlinearities observed for the odd-A isotopes might be in fact originate from possibly qualitative differences in the nuclear properties, compared to the spinless nuclei, due to the spin (e.g., possibly much bigger nuclear deformations by having a defined axis, and resultant $\langle r^4 \rangle^{AA'}$ contributions; see Section 11.1.1), rather than the higher-order HF effects.

19.3 Hyperfine anomaly

The value of an A coefficient is determined by the wavefunction of the electrons in an atom as shown in Eqs. (19.10) and (19.11). Therefore, the difference between the A coefficients for different isotopes should be only from the difference in the nuclear g factors:[5]

$$\frac{A^{A'}}{A^A} = \frac{g_I^{A'}}{g_I^A} \tag{19.21}$$

if the electronic wavefunction is the same for the two isotopes. This assumption becomes not true when the finite sizes of the nuclei are taken into account. In

[4] Just as how two-transitions electronic factors are defined; see Section 15.2

[5] The magnetic dipole HF coefficients A and the atomic mass number A (usually in superscripts) might be confusing, but the distinction should be clear from the context.

particular, for the magnetic dipole HF structure for s orbitals [Eq. (19.10)], there are two corrections in the A coefficients from their values A_{point} for point-like nuclei [238]:

$$A = A_{\text{point}}(1+\epsilon_{BW})(1+\epsilon_{BR}) \tag{19.22}$$

where the Bohr–Weisskopf (BW) correction ϵ_{BW} is due to the finite extent of nuclear magnetization [239] and the Breit–Rosenthal–Crawford–Schawlow (BR) correction ϵ_{BR} originates from the dependence of the wavefunction at the origin on the finite nuclear charge distribution [240, 241] (just like the field shifts in ISs; see Section 8.1.1). Due to the corrections, the A coefficients' ratio is also corrected as follows:

$$\begin{aligned}
\frac{A^{A'}}{A^{A}} &= \frac{g_I^{A'}}{g_I^{A}} \frac{1+\epsilon_{BW}^{A'}}{1+\epsilon_{BW}^{A}} \frac{1+\epsilon_{BR}^{A'}}{1+\epsilon_{BR}^{A}} \\
&\approx \frac{g_I^{A'}}{g_I^{A}} (1+\epsilon_{BW}^{A'}-\epsilon_{BW}^{A})(1+\epsilon_{BR}^{A'}-\epsilon_{BR}^{A}) \\
&\equiv \frac{g_I^{A'}}{g_I^{A}} (1+{}^{A'}\Delta_{BW}^{A})(1+{}^{A'}\Delta_{BR}^{A}) \\
&\approx \frac{g_I^{A'}}{g_I^{A}} (1+{}^{A'}\Delta_{BW}^{A}+{}^{A'}\Delta_{BR}^{A})
\end{aligned} \tag{19.23}$$

where ${}^{A'}\Delta_{BW}^{A} \equiv \epsilon_{BW}^{A'} - \epsilon_{BW}^{A}$ and ${}^{A'}\Delta_{BR}^{A} \equiv \epsilon_{BR}^{A'} - \epsilon_{BR}^{A}$ are defined as the differential HF anomalies of the BW and BR corrections. Then, the differential HF anomaly is *defined* as:

$${}^{A'}\Delta^{A} \equiv \frac{A^{A'}}{A^{A}} \frac{g_I^{A}}{g_I^{A'}} - 1 \tag{19.24}$$

which would be ${}^{A'}\Delta^{A} \approx {}^{A'}\Delta_{BW}^{A} + {}^{A'}\Delta_{BR}^{A}$ for s orbitals. In particular, ${}^{A'}\Delta_{BR}^{A}$ dominates over ${}^{A'}\Delta_{BW}^{A}$ when the nuclei are very similar [i.e., $a^{AA'}/A = (A-A')/A \ll 1$] [238], which would be the case for the $^{171}\text{Yb}^+$ and $^{173}\text{Yb}^+$.

For $^{171}\text{Yb}^+$ and $^{173}\text{Yb}^+$, the nuclear g-factor ratio is know with relatively high precision: $g_I^{173}/g_I^{171} = -0.275446(14)$ [227, 242],[6] and the values of the anomalies ${}^{173}\Delta^{171}$ have been reported for a couple of excited $^3P_1$ states in neutral Yb atoms [243] and the $^2S_{1/2}$ [226, 228] and $^2P_{1/2}$ states [227] in the Yb^+ ion. The future

[6] $\mu_I^{173}/\mu_I^{171} = -1.37723(7)$ [227, 242], $\mu_I^A = g_I^A \mu_N I^A$, $I^{171} = \frac{1}{2}$, and $I^{173} = \frac{5}{2}$.

HF splitting measurements for the excited states $^2D_{5/2}$ of α: 411 nm [153], $^2D_{3/2}$ of β: 436 nm, and $^2F_{7/2}$ states of γ: 467 nm transitions, by driving the microwave transitions (see Section 19.6.4), will provide accurate measurements of the $^{173}\Delta^{171}$ for those states (see Table 19.1 for the measured HF splittings for those states for $^{171}Yb^+$).

Finally, note that the HF anomaly does not contribute to the HF-induced King nonlinearities observed in Section 19.2.2. While the anomaly shifts the values of A coefficients, the ratios of the HF shifts determined by the ratios of angular-momentum factors $K(JIF)$ [see Eq. (19.4)] remain the same, and so do the centroid frequencies $(\nu_c)^A_\chi$ of transitions (see Section 19.2.1).

19.4 Complementary test for field-shift electronic factor F_χ

As shown in Eq. (15.1), the (linear) field-shift electronic factor F_χ for a transition χ is determined by the change in radial electron number density $\rho_\chi(0)$ at the origin during the transition, involving all the electrons in the atom. On the other hand, s-orbital HF splittings depend on the number density of the electrons that forms nonzero total spin $\mathbf{S}$ only (i.e., valence electrons not in closed s shells) as Eq. (19.10) shows.

Then, the values of F_χ for $\chi = \alpha$: 411 nm and β: 436 nm ($6s\,^2S_{1/2} \to 5d\,^2D_{5/2,3/2}$, respectively) transitions, derived from atomic structure calculations in Part IV (see Table C.3), can be compared with the experimental values from the HF splittings of the $6s\,^2S_{1/2}$ ground state which have been accurately measured [226, 228] (see Table 19.1). As the transition excites a valence electron from s to d orbital, the electron density change at the origin was expected to be dominated by the density of the valence $6s$ electron (d orbital has no radial density at the origin). However, the electron density of the $6s$ electron is given to be $16.02a_0^{-3}$ ($16.88a_0^{-3}$) from the measured HF splitting of the grounds state in $^{171}Yb^+$ ($^{173}Yb^+$), which would result

in the change of $-16.02a_0^{-3}$ ($-16.88a_0^{-3}$) during the transitions. While the signs are in agreement, the sizes of the densities are significantly different from the calculated values, $\sim -46a_0^{-3}$, shown in Figs. 14-2 and 14-3. One possible explanation of the significant difference is that the perturbation in the core electrons in s shells due to the change in the valence electron's state is in fact as significant as removing more than one s electron, in terms of the density at the origin. If so, this test demonstrates the significance of valence-core electron correlations, which have been taken into account in the atomic structure calculations (ASCs) performed in this work (see Section 14.3.2).

19.5 Hexadecapole hyperfine coefficients in ^{173}Yb

The electric hexadecapole HF couplings require both J and $I \geq 2$ so that $k_{\max} \geq 2$ [see Eq. (19.2)]. In particular, the limited J prohibits probing of existing nuclear hexadecapole moment for some species (c.g., ^{133}Cs with $I = \frac{9}{2}$ [230, 244]). As a consequence, the hexadecapole HF effects have been experimentally investigated only for $^{165}_{67}$Ho [245], while the magnetic dipole (A) [246], electronic quadrupole (B) [246], and magnetic octupole (C) [247][7] HF couplings have been experimentally well-studied.

Recently, ^{173}Yb$^+$ ions with $I = \frac{5}{2}$ nuclear spin and γ: $^2S_{1/2} \rightarrow {}^2F_{7/2}$ (467 nm) transition (see Fig. 3-1) was proposed as a suitable isotope and transition to probe the hexadecapole coupling [230]. While preparing the ions in the $^2F_{7/2}$ state will require an initial search for the transitions frequencies (Section 19.6.3), measuring the HF splittings with high accuracy should be straightforward by driving the microwave transitions between the HF states (see Section 19.6.4). The only and more immediate challenge would rather be trapping and cooling the ^{173}Yb$^+$ ions, which will be discussed in Section 19.6.2.

In principle, the $5d\,^2D_{5/2}$ excited state in α: 411 nm transition in Yb$^+$ ions (see

[7] A summary of nuclear magnetic octupole moments Ω and the corresponding C coefficients for nearly 20 different atomic species ranging $Z = 17$ (Cl) to 84 (Po) and their isotopes are nicely presented in Table IV in Ref. [247] (see also Table I in Ref. [230] for Ω).

Fig. 3-1) would also have the hexadecapole HF coupling. While the α transition is experimentally more preferred (finding and driving γ transition is demanding due to its extremely narrow linewidth;[8] see Table B.1), one can speculate that the $4f^{13}6s^2\,{}^2F_{7/2}$ state might be more sensitive to the hexadecapole nuclear moments due to the more complex electron configuration, compared to the $2D_{5/2}$ state, just as the γ transition is more sensitive to King-plot nonlinearity sources than the α and β: 436 nm transitions (see Section 3.1.2).

Also, both the ${}^2F_{7/2}$ and ${}^2D_{5/2}$ states should have magnetic 32-pole HF couplings (i.e., $k_{\max} = 5$) in principle, although the second-order HF effects [Eq. (19.8)] might dominate over such higher-pole HF contributions [222, 230, 247, 249].

Lastly, the octupole-moment puzzle of ^{173}Yb atoms [230], the 4-order-of-magnitude disagreement in the calculated [250] and experimentally determined [251] nuclear octupole moments Ω through ${}^3P_2$ states,[9] has been recently questioned by re-measured values of the HF splittings in the same ${}^3P_2$ state [247], which showed no significant evidence of the non-zero C coefficient. The future measurements for the HF splittings in ${}^2F_{7/2}$ or ${}^2D_{5/2}$ states will be able to add another experimental confirmation or resolution of the puzzle.

19.6 Experiments with ^{171}Yb$^+$ and ^{173}Yb$^+$

Future plans and strategies to realize the IS spectroscopy experiments with ^{171}Yb$^+$ and ^{173}Yb$^+$ ions are introduced in this section.

19.6.1 Trapping ^{171}Yb$^+$

Trapping ^{171}Yb$^+$ ions in an ion trap is a well-established technology due to the use of the ions' ground states as HF qubits [115, 125, 225, 252, 253, 254, 255, 256]. The

[8] Note, however, broadening of the linewidth by more than 2 orders of magnitude has been expected for ^{173}Yb$^+$ isotope [231, 248].

[9] The value of nuclear octupole moment calculated directly from a nuclear structure calculation [250] vs the value obtained from measured C coefficient [251] divided by the calculated electronic part $\langle (T_e)_3 \rangle_{\gamma J}$ of the C coefficient [see Eq. (19.4)] via atomic structure calculations, rigorously speaking.

experimental setup in this work has also been trapping the $^{171}Yb^{+}$ ions recently by the thesis author.

Figure 19-3 shows a level diagram for $^{171}Yb^{+}$ ions with the relevant levels and transitions. All the transition frequencies and HF splittings that are necessary to drive 369 nm for cooling, 935 nm and 760 nm for $^2D_{3/2}$ and $^2F_{7/2}$-state repumping, respectively, and 399 nm transition for photoionizing Yb atoms together with the 369 nm beam are listed in Table. 19.1 and 19.2 with sufficient precisions.

The transitions between different HF states of ground and excited states are addressed using setups described in Section 18 as follows. For the 369 nm cooling transition, a beam with frequency of $\nu_{369}^{171}(1 \to 0)$ is the main beam for cooling,[10] as the $F = 0 \to 0$ transition is highly forbidden. Another 369 nm beam from another laser, that is offset-phase-stabilized to the main cooling beam with 14.748 GHz detuning (the sum of the $^2S_{1/2}$ ground and $^2P_{1/2}$ excited states' HF splittings), drives $^2S_{1/2}\,(F = 0) \to {}^2P_{1/2}\,(F = 1)$ transitions to repump the population that occasionally falls into the $^2S_{1/2}\,(F = 0)$ HF level due to the off-resonantly driven $^2S_{1/2} \to {}^2P_{1/2}$ $(F = 1 \to 1)$ transition in every few ms or less.

A 935 nm repumping beam mainly drives $^2D_{3/2} \to {}^3D[3/2]_{1/2}$ $(F = 1 \to 0)$ transition to repump the population that decays to the $^2D_{3/2}\,(F = 1)$ state from the $^2P_{1/2}\,(F = 0)$ state which is populated by the main cooling beam. The occasionally populated $^2P_{1/2}\,(F = 1)$ state can decay to $^2D_{3/2}\,(F = 2)$ state, which is repumped through the $F = 2 \to 1$ repumping transition driven by a sideband in the 935 nm beam generated by a broadband EOM with 3.07(2) GHz modulation frequency. Interestingly, Yb^{+} ions have been able to be trapped and cooled without the sideband in practice, with the optical power as low as $\sim$1 mW and 300 µm focal waist.

The transition frequencies for the 399 nm transition in Yb atoms are also known with high precision, and driving one of the transitions would be enough as the ground-state HF states will be equally populated in the hot Yb gas from the heated oven (see Section 4.1.2),[11] unless one wants to boost up the ionization rate.

[10] See Section 19.2.1 for the notation.

[11] Note that the value of Boltzmann constant is $K_B/h = 20.84\,\mathrm{GHz/K}$.

Finally, occasionally populated ${}^2F_{7/2}\,(F = 3, 4)$ HF states (in every $>$ few hrs in the setup used here) due to atomic collisions (see Section 4.1.2) are repumped through ${}^2F_{7/2} \rightarrow {}^1D[3/2]_{3/2}$ $(F = 3 \rightarrow 1)$ and $(F = 4 \rightarrow 2)$ transitions by a 760 nm beam with a broadband EOM driven at 12.50 GHz modulation frequency.

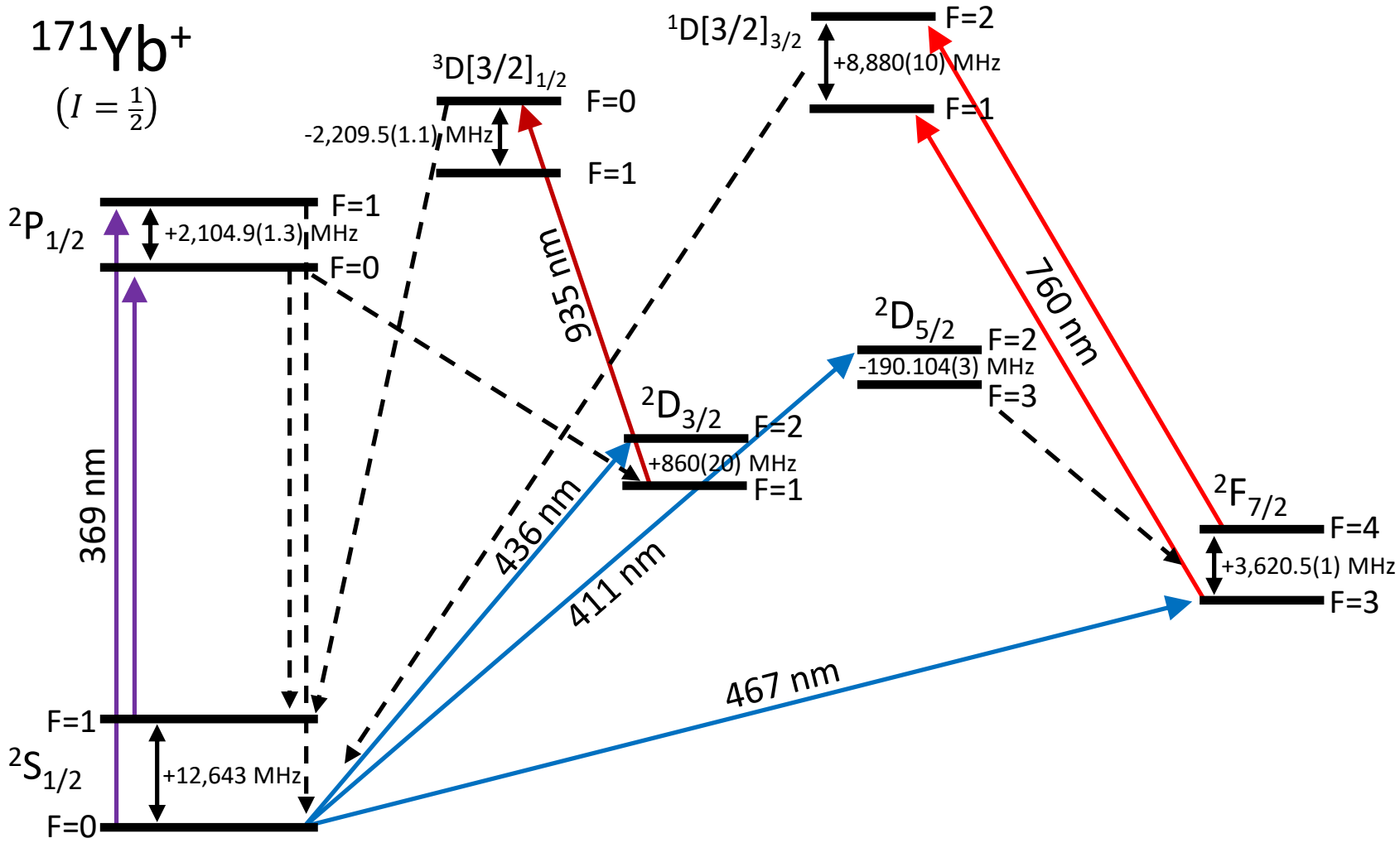

Figure 19-3: Partial level diagram for $^{171}Yb^{+}$ ions with $I = \frac{1}{2}$ nuclear spins. Solid lines show transitions between the ground and excited states' hyperfine levels, to be driven with laser beams, of which frequencies are available in Table 19.2. Dashed lines are decay channels. See Fig. 3-1 and Table B.1 for details including usages of shown transitions. Details on hyperfine structure of each state, including exact values and references for hyperfine splittings, can be found in Table 19.1.

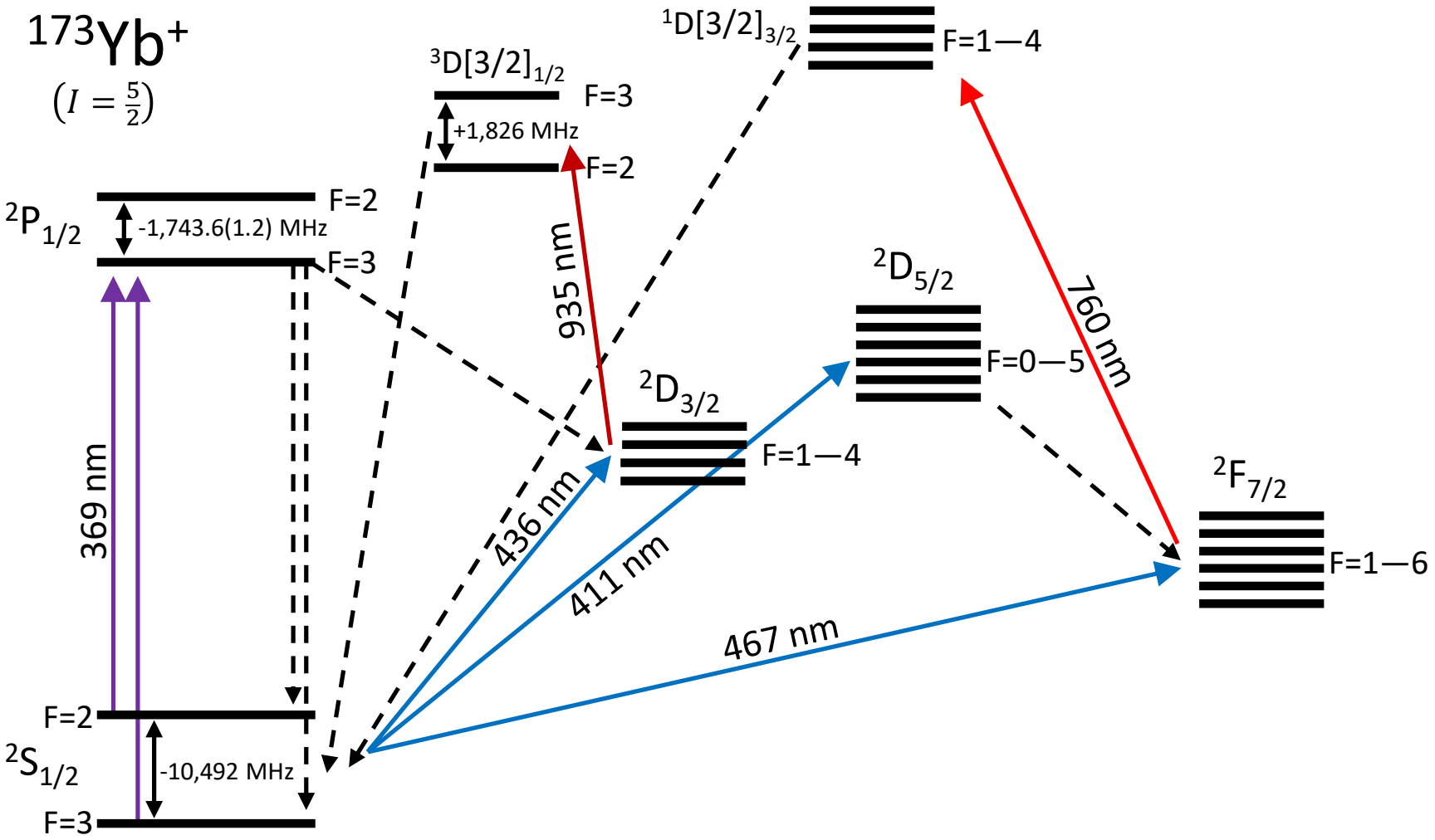

Figure 19-4: Partial level diagram for ^{173}Yb$^+$ ions with $I = \frac{5}{2}$ nuclear spins. Solid lines show transitions to be driven with laser beams. Dashed lines are decay channels. See Fig. 3-1 and Table B.1 for details including usages of shown transitions. See Tables 19.1 and 19.2 for known values of hyperfine splittings and transition frequencies, respectively. Orders of the hyperfine energy levels and splittings between them in $^2D_{5/2}$, $^2D_{3/2}$, $^2F_{7/2}$, and $^1D[3/2]_{3/2}$ states are unknown.

19.6.2 Trapping $^{173}Yb^+$

Unlike the $^{171}Yb^+$ ions, trapping $^{173}Yb^+$ ions in an ion trap has not been realized to the best of the author's knowledge, and thus data for the transition frequencies and HF splittings are largely missing as shown in Tables 19.1 and 19.2.

Figure 19-3 shows a level diagram for $^{173}Yb^+$ ions with the relevant levels and transitions. Fortunately, the data for the 369 nm cooling transition are available for the $^{173}Yb^+$ isotope. As there is no forbidden transition between the HF states of the ground and excited states,[12] the transition from both the $F = 2$ and 3 HF levels of the $^2S_{1/2}$ ground state would have to be actively driven.

The problem is in the 935 nm repumping transition. First, the $^3D[3/2]_{1/2}$ excited state is not a concern. It has only two HF states ($F = 2, 3$) with the A coefficient which can be accurately estimated from Eq. (19.21), the A value for $^{171}Yb^+$ isotope, and $g_I^{173}/g_I^{171} = -0.275446(14)$ [227, 242] (see Section 19.3). Therefore, the HF splitting can be also estimated from the Landé interval rule [Eq. (19.12)]. However, the $^2D_{3/2}$ state has 4 states with the A, B, and C coefficients. The A coefficient can be estimated as above, and the shifts from the C coefficient (i.e., magnetic octupole HF interaction) are likely small (<1 MHz [247]). Therefore, the only remaining piece of puzzle is the value of B coefficient. There are a theoretically estimated value as shown in Table 19.1, and the HF splittings between the states can be estimated using the value (together with the accurately estimated A coefficient) [Eq. (19.4)]. Finally, the HF-free ISs involving the $^{173}Yb^+$ isotope are estimated by inter/extrapolating the King plots for (578 nm,935 nm) and (399 nm,935 nm) transition pairs, as described in Section A.1.1 and listed in Table 19.2. Combining all the information obtained so far, the transition frequencies $\nu_{935}^{173}(F^{(g)} \to F^{(e)})$ between the ground and excited HF states can be estimated, and the transitions can be searched starting from the estimated frequencies. Note that Ref. [225] presents a result on the spectroscopic investigation on the 935 nm transition frequencies for $^{173}Yb^+$ ions, which might be useful.

The 399 nm transition frequencies are known for all the possible transitions in

[12] Unlike the $F = 0 \to 0$ transition in $^{171}Yb^+$ ions

$^{173}Yb^+$ ions. The 760 nm repumper is not necessary just for trapping and cooling, as the decay to the $^2F_{7/2}$ state rarely happens. The transitions can be found later once the $^{173}Yb^+$ ions are trapped in the setup.

19.6.3 Driving optical clock transitions

The optical clock transitions in $^{171}Yb^+$ and $^{173}Yb^+$ ions are ideal for the precision frequency measurements because the associated states' F values are integers, and thus the states have magnetic-field-insensitive $m_F = 0$ Zeeman sublevels.[13]

The situation for the available data to drive the clock transitions is very similar to the transitions for cooling and repumping in Sections 19.6.1 and 19.6.2. For $^{171}Yb^+$ isotope, all the transition frequencies and the HF splittings are known with sufficient precisions (see Tables 19.1 and 19.2). For $^{173}Yb^+$ isotope, the transitions should be searched starting at the frequencies derived from the accurately measured $^2S_{1/2}$ ground states' HF splitting, the accurately estimated A coefficients of the excited states and HF-free ISs, and the theoretically estimated values of the excited states' B coefficients. All the values or references that are necessary for the searches can be found in Tables 19.1 and 19.2.

19.6.4 Driving microwave transition between hyperfine states

The ion trap chip used in this work is equipped with a coplanar microwave waveguide, placed along the outer sides of DC electrodes, connected to a vacuum-compatible SMA cable and 8 GHz feedthrough [108]. Driving the 12.64 GHz microwave transition between the HF states in the $^2S_{1/2}$ ground state in an $^{171}Yb^+$ (see Table 19.1) using the on-chip waveguide has been recently demonstrated by Diana P. L. Aude Craik, a research team member, as shown in Fig. 19-5. Driving transitions between the HF states of the optical clock transitions' excited states in odd-A Yb^+'s should be straightforward, then, as the HF splittings are (expected to be) smaller than 12.64 GHz (see Table 19.1).

[13] Therefore, the switching between the symmetrically detuned Zeeman transitions is not necessary (see Section 5.3.4), which would double the data taking rates.

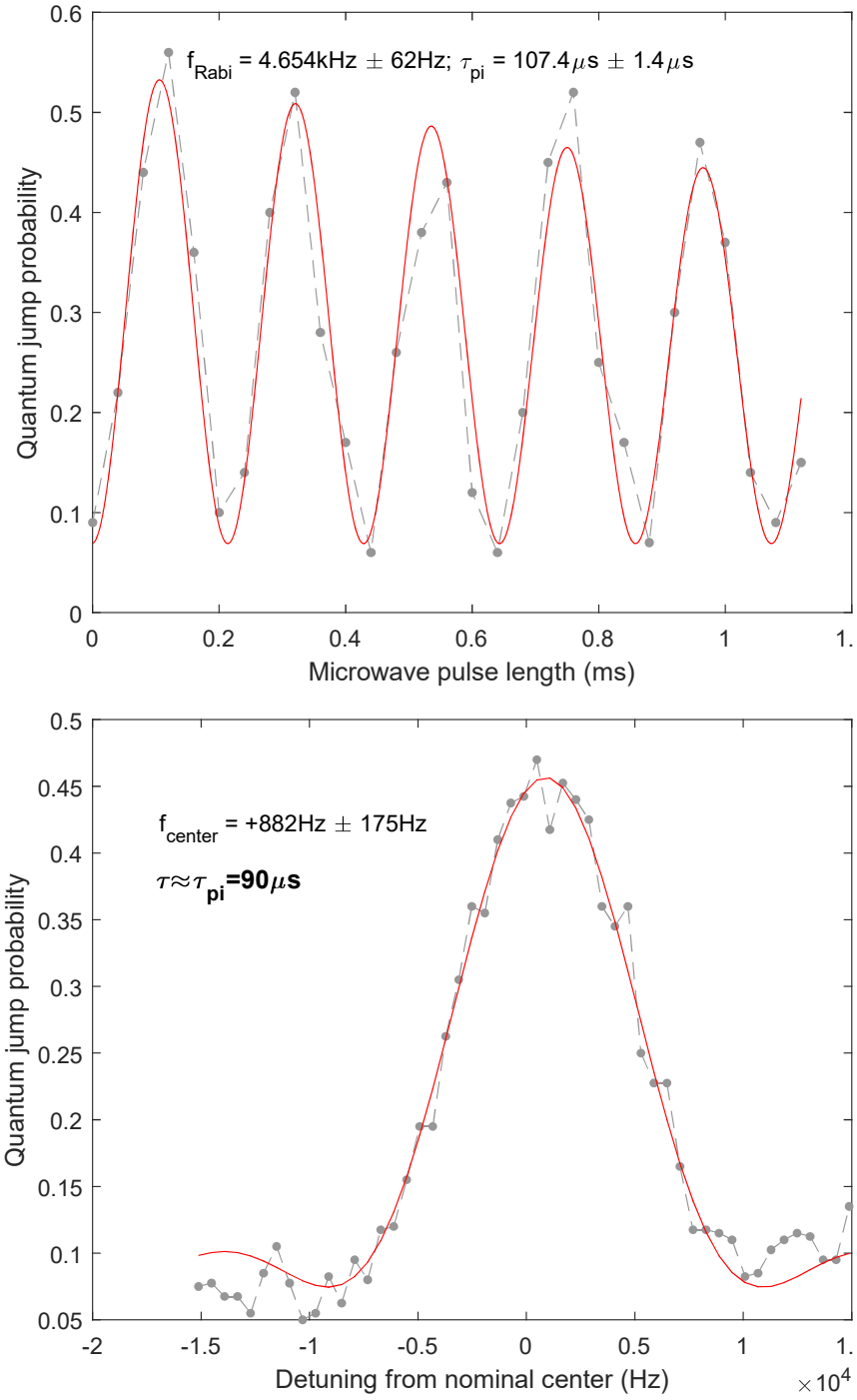

Figure 19-5: Measured excitation probability from $F = 0$ to 1 hyperfine states in the ${}^2S_{1/2}$ ground state of a trapped ${}^{171}\mathrm{Yb}^+$ ion, driven by microwave field. (Top) Rabi oscillation over different microwave pulse time. (Bottom) Rabi fringe scanned over different detunings of the microwave field from the hyperfine splitting, with a nearly-$\frac{\pi}{2}$ microwave pulse. Full credit to Diana P. L. Aude Craik for the measurements and this figure.

For $^{171}Yb^{+}$ isotope, although all the HF splittings relevant to this work have been already measured as shown in Table 19.1, some of the values do not have high precision. Driving the microwave transitions between the HF states is expected to reduce the uncertainty to possibly a few tens of Hz or lower.

Chapter 20

Unstable isotopes: more points in King plot

As discussed in Sections 8.3.4 and 8.4, ISs for more isotopes provide distinguishability of one nonlinearity source from others for more total numbers of the sources.[1] However, the typical choice of the isotopes for ion trapping is the observationally stable isotopes, or at least the isotopes with very long lifetimes which would not be a problem during a whole research cycle (e.g., $^{133}Ba^+$ with 10.5 yr half-life [96]). This is of a solid limitation on the number of available isotopes, as, e.g., Ca^+, Sr^+, Ba^+, and Yb^+ (which are the typical choices for the ion trapping) have only 5, 4, 5, and 5 such even-A stable or long-lived isotopes [and optionally 1, 1, 3, and 2 odd-A isotopes (see Section 19], respectively [25].

For Yb, there are one metastable even-A isotope: ^{166}Yb with 56.7 h half-life (see Table 20.1). The lifetime is much longer than the measurement for one isotope at a time ($\lesssim$2 hr; see Section 5.3.4), and the isotope-shift measurement for one isotope pair takes a day. Therefore, if enough amount of the isotope can be synthesized and loaded in Yb source in the vacuum chamber, it might add one more point in each King plot through the same experiments in this thesis.

[1] An intuition here is that having more isotope pairs increases the dimensions of the King nonlinearity patterns ($n-2$ dimension for n isotope pairs) and thus provides a unique decomposition of measured patterns with at most $n-2$ different predicted pattern shapes (i.e., vectors in $(n-2)$-dimensional nonlinearity map $\boldsymbol{\lambda}$).

Table 20.1: Metastable ^{A}Yb isotopes listed in the order of their half-lives $> 1\,\mathrm{s}$ in Ref. [25].

A	Half-life	
166	56.7(1)	hr
164	1.26(3)	
178	1.23(5)	
162	18.87(19)	min
160	4.8(2)	
180	2.4(5)	
158	1.49(13)	
156	26.1(7)	s
152	3.04(6)	

There is also a more promising plan: transporting synthesized unstable isotopes directly to a vacuum-connected chamber for IS spectroscopy experiments, and measuring ISs before the isotopes decay away. For Yb, for instance, there are isotopes with the half-lives of hours, minutes, and seconds as listed in Table 20.1. The fundamental limit of the IS measurement from the isotopes' lifetimes would be the linewidth of the transition spectra (e.g., Ramsey interferometry or transition-rate spectroscopy; see Section 5.2) from which the resonant frequency of the transitions are determined; the transition should be driven with probe pulses shorter than the isotopes' lifetimes, which Fourier-limit the linewidth of the beam. In practice, the decay of the nuclei might bring overheads for reloading the ions at different stages of the experiments, depending on the scale of their lifetimes: after each frequency scan of the transitions for the few-minute lifetimes (Section 5.3.6) or after each excitation probability P_e measurement for the lifetimes of seconds (Section 5.3.7). The isotopes with lifetimes of hours would not introduce significant overhead in the experiment.

A research collaborator, Dr. Ronald Fernando Garcia Ruiz at Massachusetts Institute of Technology, and his research group have built a plan for realizing the idea. They are currently developing a vacuum chamber system to purify, ionize, and decelerate Yb atoms of unstable isotopes generated at the Facility for Rare Isotope

Beams (FRIB) in Michigan, USA, and deliver them to an ion trap system for the IS spectroscopy.

As the limitation on the number of available isotopes might be lifted up in the future, distinguishing different sources of King nonlinearity will be ultimately limited by the number of available transitions (see Sections 8.3.4 and 8.4), that are narrow enough and also sensitive to new physics, and the capability of direct or indirect laser-cooling, trapping, and performing spectroscopy (e.g., sympathetic cooling and subsequent quantum logic spectroscopy of trapped ions [219]) for a given atomic system.

Chapter 21

Rydberg state: hint on new boson's mass range

As discussed in Sections 8.3.4 and 8.4, measuring ISs for more transitions may provide more numbers of King nonlinearity sources that can be distinguished. There would be, at least possibly, more available transitions in Yb^+ ions or neutral Yb atoms other than the five transitions that have been already used in this work (the α to ϵ transitions; see Table A.1, Figs. 10-1, 10-2, and 10-3).[1] Among different candidates, transitions involving Rydberg states, the atomic states with high principal quantum number n, may be particularly interesting choices as introduced in this chapter.

As discussed in Section 16.3, the heavy new bosons and nuclear effects are coupled to the electrons' wavefunctions near the origin. For the atomic species with one valence electron such as Yb^+ ions, one might expect that the wavefunction near the origin can be suppressed by exciting the valence electron to an orbital with nonzero relativistic quantum number k [e.g, not $s_{1/2}$ or $p_{1/2}$; see Eq. (14.4) for the k number and Eq. (21.1) below for the suppression].[2] However, the change in wavefunction at the origin during the transition can still be significant, because the valence electron's excitation perturbs core electrons in $s_{1/2}$ or $p_{1/2}$ orbitals as well through the valence-core correlations (see Sections 16.3 and 19.4).

[1] An example is a new proposed clock transition in Yb atoms at 1695 nm, $4f^{14}\,6s\,6p\ {}^3P_0 \rightarrow 4f^{13}\,6s^2\,6p\ (J=2)$ [35].

[2] Corresponding to $l > 0$ in the nonrelativistic case (i.e., non-s orbitals).

Such perturbation to the core $s_{1/2}$ or $p_{1/2}$ orbitals may be minimized for transitions between Rydberg states with a highly excited valence electron, of which overlap with the tightly bound core electrons would be insignificant.[3] Therefore, it is expected for the Rydberg transitions to have suppressed sensitivities to the nuclear effects and heavy-new-boson interaction.

In particular, the radial electron density of the valence electron at close distances from the origin, but outside the nucleus (i.e., $3\,\mathrm{MeV/c^2} < m_\phi < 30\,\mathrm{MeV/c^2}$), can be expressed as (see Section 16.1):

$$\rho_\Psi(r) = \frac{1}{4\pi} r^{2(\gamma-1)} \left[\zeta^{(0)} + \zeta^{(1)} r + \zeta^{(2)} r^2 + \cdots\right], \tag{21.1}$$

showing more suppression of the density $\propto r^{2(\gamma-1)} \approx r^{2(|k|-1)}$ near the origin for bigger k number. The expression gives the new-boson sensitivity D of the ISs from Eq. (15.2) as follows:

$$\begin{aligned} D_\Psi(m_\phi) &= \frac{c}{2\pi} (\lambda_c^\phi)^{2\gamma} \sum_{n=0}^{\infty} \Gamma(2\gamma+n) \zeta^{(n)} (\lambda_c^\phi)^n \\ &\approx \frac{(2|k|-1)!\hbar^{2|k|}}{2\pi c^{2|k|-1}} \frac{1}{m_\phi^{2|k|}} \left[\zeta^{(0)} + \frac{(2|k|)\zeta^{(1)}\hbar}{m_\phi c} + \frac{(2|k|)(2|k|+1)\zeta^{(2)}\hbar^2}{m_\phi^2 c^2} + \cdots\right] \end{aligned} \tag{21.2}$$

which is increasingly insensitive to the heavy boson m_ϕ for higher angular momentum $|k|$ of the electron.

Furthermore, while the effect of the heavy new boson is suppressed, the Rydberg states would be still sensitive to sufficiently light new bosons, with the Compton wavelength of the atomic scale or longer ($\lambda_c^\phi \gtrsim a_0$), through the long-range overlap of the new Yukawa-like potential to the valence electron's wavefunction [see Eq. (15.2)]. It implies that the Rydberg transitions are more selectively sensitive to lighter bosons compared to the transitions with low-lying valence electrons, of which new-boson sensitivities D are dominated by the boson's couplings to core $s_{1/2}$ and $p_{1/2}$ electrons with the suppression for heavy bosons with only $|k| = 1$ in Eq. (21.2); presumably

[3] Especially for large $|k|$ (cf. circular Rydberg states [257, 258]).

as a consequence, the relative sensitivities are largely the same across the different transitions and atomic species shown in Fig. 1-2. If the above conjectures are true and if potential new-boson signals are observed with the usual transitions but not through the Rydberg transitions, for instance, it can be suspected that the boson has a heavy mass.

Lastly, two transitions between a shared low-lying state and different Rydberg states can be used as well [e.g., $6p$ to $10d$ or $11d$], as the common state does not contribute to the King plots' sensitivity to nonlinearity sources as mentioned in Section 16.3.

In summary, transitions involving Rydberg states might be useful to suppress the nuclear effects which are not desired for probing the new boson, and also provide discrimination against bosons' masses by being more selectively sensitive to lighter bosons. This preliminary idea is planned to be investigated through the atomic structure calculations (introduced in Part IV) for Rydberg states in Yb^+ ions or Yb atoms.

Chapter 22

Outlook

Through more precise IS spectroscopy for more isotopes and transitions, the nonlinearity sources of increasing order will be distinguished experimentally. The physical origin of each source may be also identified with the aid of atomic and nuclear structure calculations, through the size and shape of the source's contribution to observed nonlinearity patterns. An optimistic future scenario is that a nonlinearity source is pinpointed, eventually, that cannot be explained by the Standard Model while it is consistent with the prediction from the new boson's (or any other new physics') effect. Such effect could be, then, crosschecked with other atomic systems, e.g., different species of atoms (see the work on the King plot for Ca^+ [87], for instance), highly charged ions [259], or maybe even molecules, through the same approach. If the seemingly new-physics effect is confirmed across the atomic systems, it would provide a strong motivation for other fields of physics to pursue focused searches on the particular candidate for new physics.

Part VI

Appendices

Appendix A

Isotope-shift spectroscopy: results

The values of isotope shifts (ISs) between stable, even-A isotopes for the α: 411 nm, β: 436 nm, and γ: 467 nm optical clock transitions in Yb^+ ions (see Fig. 3-1), measured in Part II, are listed in Table A.1. The values with reduced uncertainties from the redundant pairs of isotopes (Section 6.7) can be found in Table A.2. The absolute frequencies of the clock transitions for each isotope, obtained from the measured IS and the absolute frequencies of reference isotopes (Section 6.5), are presented in Table A.3. In particular, the estimation of the even isotopes' absolute frequencies from a measured absolute transition frequency for $^{171}Yb^+$ isotopes with the hyperfine structure using King-plot linearity is described in Section A.1, as no measured absolute frequency for an even-A isotope is available. Lastly, the measured absolute frequencies and ISs for 369 nm, 935 nm, and 760 nm transitions (Section 6.6) for cooling and repumping ions (see Section 4.1.2) are reported in Table A.4.

A.1 β: 436 nm absolute frequencies

For the β: 436 nm transition, the absolute transition frequency has not been measured for any of the stable even-A isotopes to date, to the best of the author's knowledge, while the absolute frequency of a transition between the ground and excited states' hyperfine (HF) levels $\nu_\beta^{171}(0 \to 2)$ in $^{171}Yb^+$ isotope has been measured precisely [138, 139] (see Section 19.2.1 for the notation). In this case, the absolute frequency

$\nu_\beta^{A'}$ for an even-A' isotope can be obtained if the difference in the frequency $\nu_\beta^{171}(0\to2)$ and the corresponding transition frequency $\nu_\beta^{A'}$ for the even-A' isotope, $\nu_\beta^{171}(0\to2)-\nu_\beta^{A'}$, can be determined. The absolute frequencies of other even isotopes then follow through the measured ISs in this work.

On the other hand, one of the useful applications of King-plot linearity is to estimate the unknown IS $\nu_\kappa^{A_uA'_u}$ of an isotope pair $(A_uA'_u)$ for a transition κ from the known IS $\nu_\chi^{A_uA'_u}$ of the same pair for another transition χ, once the King line is determined by the known ISs $\nu_{\chi,\kappa}^{AA'}$ for other isotope pairs (A,A'). Explicitly, in the frequency-normalized King plot $(\nu_\kappa/\nu_\chi)^{AA'}=f_{\kappa\chi}+K_{\kappa\chi}(\mu/\nu_\chi)^{AA'}$ [Eq. (8.11)], the slope $K_{\kappa\chi}$ and y-intercept $f_{\kappa\chi}$ can be fitted for the known ISs $\nu_{\chi,\kappa}^{AA'}$ and the corresponding inverse-mass differences $\mu^{AA'}$ (see Section 8.1.2). Then, if the ISs $\nu_\chi^{A_uA'_u}$ for transition χ and $\mu^{A_uA'_u}$ are known for the $(A_uA'_u)$ pair, the value of the unknown IS $\nu_\kappa^{A_uA'_u}$ can be inter/extrapolated via the *unnormalized* King plot relationship $\nu_\kappa^{A_uA'_u}=f_{\kappa\chi}\nu_\chi^{A_uA'_u}+K_{\kappa\chi}\mu^{A_uA'_u}$ [Eq. (8.9)].

The estimation becomes complicated for isotope pairs that involve isotopes with HF structures. For such isotopes, what the King plot can do is to relate the HF-free ISs $\nu_{\chi,\kappa}^{A_uA'_u}$ for transitions χ and κ as above. Then, the deviation of the frequencies $\nu_{\chi,\kappa}^{A_u}(F^{(g)}\to F^{(e)})$ from the HF-free frequencies $\nu_{\chi,\kappa}^{A_u}$ should be further estimated from measured HF splittings ΔW of the states in the χ or κ transitions, as elaborated in Section 19.2.1. Therefore, the requirements for estimating $\nu_\kappa^{A_u}(F^{(g)}\to F^{(e)})$ for a transition κ are as the following: ① The King line ($f_{\kappa\chi}$ and $K_{\kappa\chi}$) with a transition χ determined by some known ISs $\nu_{\chi,\kappa}^{AA'}$, ② known $\mu^{A_uA'_u}$, ③ a measured frequency difference $\nu_\chi^{A_u}(F^{(g)}\to F^{(e)})-\nu_\chi^{A'_u}$ (assuming isotope A'_u has no HF structure), ④ all the HF splittings ΔW in the ground and excited states of the transition χ to estimate the HF-free IS $\nu_\chi^{A_uA'_u}$ from ③, and ⑤ all the HF splittings ΔW for the transition κ to estimate the frequency difference $\nu_\kappa^{A_u}(F^{(g)}\to F^{(e)})-\nu_\kappa^{A'_u}$ from the HF-free IS $\nu_\kappa^{A_uA'_u}$ estimated via the King-plot inter/extrapolation.

For the β: 436 nm transitions, ① the experimental values of $f_{\beta\chi}$ and $K_{\beta\chi}$ are listed in Table C.4 for $\chi=\alpha$: 411 nm and γ: 467 nm transitions in Yb^+ ions (see Fig. 3-1) and δ: 578 nm and 399 nm cooling transitions in Yb atoms (see Table B.1).

For all the χ transitions, the estimated HF-free ISs $\nu_\chi^{171,172}$ are obtained through the steps ③ and ④, as listed in Table 19.2 (see Section 19.2.2). From the $\nu_\chi^{171,172}$ and ② $\mu^{171,172} = 34.027\ 069\ 78(70) \times 10^{-6}\,\mathrm{u}^{-1}$ (see the caption in Fig. 19-2), the King-plot inter/extrapolation yields $\nu_\beta^{171,172} = +1,338.683$, +1,337.721, +1,337.054, and +1,338.597 MHz for $\chi = \alpha$, γ, δ, and 399 nm Yb cooling transitions, respectively. Considering the measurement uncertainty, distribution of the values estimated from the different χ transitions, and the consistent few-MHz deviations of the odd-A-isotope-involved pairs from King lines (see Section 19.2.2), the HF-free ISs is determined to be $\nu_\beta^{171,172} = +1,338(10)$ MHz with 10 MHz upper bound on the uncertainty.

On the other hand, ⑤ the HF splittings ΔW for the β transition are also in Table 19.1, from which $\nu_\beta^{171}(0\to2) - \nu_\beta^{171} = +9,804.6(7.5)$ MHz is estimated.

Finally, by subtracting the shift $\nu_\beta^{171}(0\to2) - \nu_\beta^{171}$ estimated above and then the estimated IS $\nu_\beta^{171,172}$ from the measured absolute frequency $\nu_\beta^{171}(0\to2)$ (see Table 19.2):

$$\nu_\beta^{172} = \nu_\beta^{171}(0\to2) - \left[\nu_\beta^{171}(0\to2) - \nu_\beta^{171}\right] - \nu_\beta^{171,172}, \tag{A.1}$$

the absolute frequency for $^{172}\mathrm{Yb}^+$ isotope is estimated to be $\nu_\beta^{172} = 688.347\,837(20)$ THz with slightly more generous upper bound on the error. The estimated value agrees well to the values $\nu_\beta^{172} = 688.347\,90(10)$ THz derived from `WMFrequency` $= 344.173\,89(5)$ THz [Eq. (4.7)] that were directly measured by a Fizeau wavemeter (see Section 4.1.5.1).

The absolute transition frequencies for all other even-A isotopes are then obtained from the ISs measured in this work (see Table A.2).

A.1.1 Estimating hyperfine-free isotope shift for $^{173}\mathrm{Yb}^+$

As another application of the procedure above, the HF-free ISs for 935 nm and 760 nm repumping transitions and the α: 411 nm, β: 436 nm, and γ: 467 nm clock transitions (see Fig. 3-1) are estimated for $^{173}\mathrm{Yb}^+$ isotope, for future search for these transitions (see Sections 19.6.2 and 19.6.3).

The HF-free ISs $\nu_\chi^{173,A'}$ involving the $^{173}\mathrm{Yb}^+$ isotope are estimated for $\chi =$

δ: 578 nm and 399 nm transitions in neutral Yb atoms with high precision, as listed in Table 19.2 (see Section 19.2.2). All the ISs for the even-A isotopes to obtain the King lines ($f_{\kappa\chi}$ and $K_{\kappa\chi}$) can be found in Table A.2 and A.4 (see also Table C.4 for the fitted values of $f_{\kappa\chi}$ and $K_{\kappa\chi}$ for some of the transition pairs). $\mu^{172,173} = 33.692\ 856\ 53(65)\,\mathrm{u}^{-1}$ is obtained as described in the caption of Fig. 19-2.

Using the values above, the HF-free ISs $\chi_\kappa^{173,172}$ are estimated to be +1,145 MHz (+1,142 MHz) for the κ = 935 nm, −1,268 MHz (+1,267 MHz) for the 760 nm, −701.2 MHz (−699.6 MHz) for the α: 411 nm, −713.3 MHz (−711.6 MHz) for the β: 436 nm, and +1,364.3 MHz (+1,360.7 MHz) for the γ: 467 nm transitions, from the King plots paired with $\chi = \delta$: 578 nm (399 nm) transition. As earlier (estimating ν_β^{171} above), the two values from the different χ transitions are averaged for each κ transition, and 10 MHz upper bound on the uncertainties are assigned for the estimation, as listed in Table 19.2. The estimated ISs $\nu_{935}^{173,172}$ and $\nu_{760}^{173,172}$ for the 935 nm and 760 nm transitions have 20 MHz uncertainties, however, due to the uncertainties in the measured ISs for the even-A isotopes in Table A.4.

Table A.1: Isotope shifts $\nu_\chi^{AA'} = \nu_\chi^A - \nu_\chi^{A'}$ measured for the $\chi = \alpha : {}^2S_{1/2} \rightarrow {}^2D_{5/2}$, $\beta : {}^2S_{1/2} \rightarrow {}^2D_{3/2}$, and $\gamma : {}^2S_{1/2} \rightarrow {}^2F_{7/2}$ in Yb^+ ions (this work [5, 8]) (see Fig. 3-1); and $\delta : {}^1S_0 \rightarrow {}^3P_0$ [10] and $\epsilon : {}^1S_0 \rightarrow {}^1D_2$ [9] transitions in neutral Yb atoms for pairs (A, A') of stable even-A isotopes. Numbers in parentheses indicate 1σ statistical uncertainties.

	Isotope shift [kHz]				
(A, A')	α: 411 nm	β: 436 nm	γ: 467 nm	δ: 578 nm	ϵ: 361 nm
(168,170)	2 179 098.93(21)	2 212 391.85(37)	-4 438 160.30(50)	1 358 484.4763(23)	1 781 785.36(71)
(170,172)	2 044 854.78(34)	2 076 421.58(39)	-4 149.190.38(45)		1 672 021.51(30)
(172,174)	1 583 068.42(36)	1 609 181.47(22)	-3 132 321.60(50)	992 714 5867(23)	1 294 454.44(24)
(174,176)	1 509 055.29(28)	1 534 144.06(24)	-2 976 391.60(48)	946 921 7751(30)	1 233 942.19(31)
(168,172)			-8 587 352.00(47)		3 453 805.27(83)
(170,174)	3 627 922.95(50)	3 685 601.95(33)	-7 281 511.88(45)		
(172,176)			-6 108 712.93(44)		2 528 396.50(34)
(170,174)				2 268 486 5927(20)	

Table A.2: Improved values and uncertainties of isotope shifts $\nu^{AA'} = \nu^{A} - \nu^{A'}$ between nearest-neighboring even-A isotope pairs (A, A') (diagonal elements; in kHz) from the redundant measurements listed in Table A.1 (see Section 6.7). Correlation coefficients $\rho_{xy} = \sigma_{xy}/(\sigma_x\sigma_y)$ between $\nu^{AA'}$ for different isotope pairs are given by off-diagonal elements. Inverse-mass differences $\mu^{AA'} = 1/m^{A} - 1/m^{A'}$ calculated from the values for m^{A} in Table A.3 are also listed (see Section 9.3). Numbers in parentheses indicate 1σ statistical uncertainties.

Transition	(A, A')	(168,170)	(170,172)	(172,174)	(174,176)
α: 411 nm	(168,170)	2 179 098.93(21)			
	(170,172)		2 044 854.73(30)	-0.3286	
	(172,174)			1 583 068.35(31)	
	(174,176)				1 509 055.29(28)
β: 436 nm	(168,170)	2 212 391.85(37)			
	(170,172)		2 076 421.04(28)	-0.4235	
	(172,174)			1 609 181.29(20)	
	(174,176)				1 534 144.06(24)
γ: 467 nm	(168,170)	-4 438 160.85(38)	-0.4430	0.1879	-0.0906
	(170,172)		-4 149 190.66(32)	-0.4241	0.2045
	(172,174)			-3 132 321.38(33)	-0.4822
	(174,176)				-2 976 391.58(37)
δ: 578 nm	(168,170)	1 358 484.4763(23)			
	(170,172)		1 275 772.0060(30)	-0.7546	
	(172,174)			992 714.5867(23)	
	(174,176)				946 921.7751(30)
ϵ: 361 nm	(168,170)	1 781 784.73(55)	-0.2210		
	(170,172)		1 672 021.40(29)		
	(172,174)			1 294 454.41(21)	-0.3885
	(174,176)				1 233 942.14(25)
$\mu^{AA'}$ $[10^{-6}\,\mathrm{u}^{-1}]$	(168,170)	70.113 619 5(36)	-0.4430	0.1879	-0.0906
	(170,172)		68.506 890 49(63)	-0.4241	0.2045
	(172,174)			66.958 651 95(64)	-0.4822
	(174,176)				65.474 078 21(65)

Table A.3: Absolute frequencies ν_χ^A of the $\chi = \alpha : {}^2S_{1/2} \to {}^2D_{5/2}$, $\beta : {}^2S_{1/2} \to {}^2D_{3/2}$, and $\gamma : {}^2S_{1/2} \to {}^2F_{7/2}$ clock transitions in Yb^+ ions (see Fig. 3-1) for isotopes A, extracted from the measured ISs $\nu_\chi^{AA'}$ in this work (in Table A.2) and reference absolute frequencies $\nu_\chi^{A_0}$. For β transition, the reference frequencies were obtained from the King-plot inter/extrapolation and the wavemeter reading (see Section A.1). Masses of single ${}^A Yb^+$ ions from [6, 7, 20, 26] with the Yb ionization energy set to 6.254 160(12) eV [21, 22] are also listed. Numbers in parentheses indicate the upper bounds on the errors for β transition and 1σ statistical uncertainties for all the other values.

	Absolute frequency [THz]				
A	α: 411 nm	β: 436 nm		γ: 467 nm	m^A [u]
168	729.481 090 980 86(36)	688.352 126(20)	688.352 19(10)	642.108 197 799 37(37)	167.933 342 75(10)[d]
170	729.478 911 881 93(30)	688.349 913(20)	688.349 98(10)	642.112 635 960 21(32)	169.934 218 673(11)[e]
172	729.476 867 027 206 8(44)[a]	688.347 837(20)[b]	688.347 90(10)[c]	642.116 785 150 879 5(24)[a]	171.935 838 086(15)[e]
174	729.475 283 958 85(31)	688.346 228(20)	688.346 29(10)	642.119 917 472 25(33)	173.938 318 975(12)[e]
176	729.473 774 903 56(42)	688.344 694(20)	688.344 76(10)	642.122 893 863 83(36)	175.942 026 136(16)[e]

[a] Ref. [121] [b] From King-plot inter/extrapolation [c] From wavemeter reading [d] Ref. [26] [e] Ref. [7]

Table A.4: Measured values of absolute frequencies ν^A (upper table) and isotope shifts $\nu^{AA'} = \nu^A - \nu^{A'}$ (lower table) for the $^2S_{1/2} \rightarrow {}^2P_{1/2}$ (369 nm) cooling transition, and the $^2D_{3/2} \rightarrow {}^3D[3/2]_{1/2}$ (935 nm) and $^2F_{7/2} \rightarrow {}^1D[3/2]_{3/2}$ (760 nm) repumping transitions in Yb^+ ions (see Fig. 3-1). 100 MHz, 60 MHz, and 50 MHz uncertainties in measured absolute frequencies of the 369 nm, 760 nm, and 935 nm transitions, respectively, are specified by the manufacturer of the wavemeter (HighFinesse/Ångstrom WS/7). The differences in the transition frequencies are measured with better precision; 60 MHz, 20 MHz, and 20 MHz are given as upper bounds of the uncertainties due to the drift of the wavemeter. The frequencies for $^2F_{7/2} \rightarrow {}^1D[5/2]_{5/2}$ (638 nm) repumping transitions can be found in Ref. [4].

	Transition frequency [THz]					
	369 nm transition		935 nm transition		760 nm transition	
A	This work	Reference	This work	Reference	This work	Reference
168	811.29611(10)		320.562190(50)		394.432865(60)	
170	811.29439(10)	811.29440(13) [234]	320.565910(50)	320.56593(7) [234]	394.429590(60)	
172	811.29274(10)	811.29284(13) [234]	320.569390(50)	320.56941(7) [234]	394.426550(60)	394.4266[a] [126]
174	811.29146(10)	811.29154(13) [234]	320.572010(50)	320.57201(7) [234]	394.424145(60)	394.424[a] [127]
						394.423900[a] [125]
176	811.29025(10)	811.29031(13) [234]	320.574515(50)	320.57449(7) [234]	394.421885(60)	

	Isotope shift [MHz]			
	369 nm			
(A, A')	This work	Reference	935 nm	760 nm
(168,170)	1 720(60)		-3 720(20)	3 275(20)
(170,172)	1 650(60)	1 623.3(8) [227]	-3 480(20)	3 040(20)
(172,174)	1 280(60)	1 275.3(7) [227]	-2 620(20)	2 405(20)
(174,176)	1 210(60)	1 217.7(12) [227]	-2 505(20)	2 260(20)

[a] Uncertainty not specified.

Appendix B

Transitions in Yb^+: summary

The properties of transitions in Yb^+ ions (see Fig. 1-1) and neutral Yb atoms and beams driving the transitions in the experimental setup are summarized in Table B.1. It is assumed that all transitions have Lorentzian lineshapes while all laser beams have Gaussian transverse profiles.

List of variables

λ	Transition wavelength
f	Transition frequency
ω	Transition angular frequency
τ	The lifetime of the excited state
$\Gamma/(2\pi)$	Full width at half maximum (FWHF) linewidth of transition
b	Branching ratio
I_s	Saturation intensity of transition
P	Beam power
w	Beam waist ($1/e^2$-radius)
I	Beam intensity

Useful relations

See, e.g., Ref. [141, 145]

$$f = \frac{\omega}{2\pi} = \frac{1}{\lambda} \tag{B.1}$$

$$\Gamma = \frac{1}{\tau} \tag{B.2}$$

$$I_s = \frac{\hbar\omega^3\Gamma}{12\pi c^2 b_g} \tag{B.3}$$

$$I = \frac{2P}{\pi w^2} \tag{B.4}$$

where b_g is the branching ratio of the spontaneous decay back to the transition's ground state.[1]

B.1 Branching ratio and oscillator strength

The branching ratio b_{ik} of a spontaneous decay channel from one state in g_i-degenerate energy level i to any of g_k-degenerate states in level k is given by the ratio of the spontaneous emission rate Γ_{ik} along the channel to the total emission rate $\Gamma_i = \sum_k \Gamma_{ik}$ for all possible destination levels k. On the other hand, the absorption oscillator strength f_{ki} is related to the spontaneous emission rate Γ_{ik} in the following way [see, e.g., Eq. (17.1) in Ref. [223]]:

$$g_k f_{ki} = C\lambda_{ik}^2 g_i \Gamma_{ik} \tag{B.5}$$

where $C = (32\pi^3\alpha a_0^2 c R_\infty)^{-1} \approx 1.5 \times 10^{-14}\,\mathrm{nm}^{-2}s$ with the fine structure constant α, Bohr radius a_0, speed of light c, and Rydberg constant R_∞. Therefore, the branching ratio of a decay channel $i \to l$ is given as:

$$b_{li} = \frac{\Gamma_{il}}{\Gamma_i} = \frac{g_l f_{li}/\lambda_{ik}^2}{\sum_k g_k f_{ki}/\lambda_{ik}^2}. \tag{B.6}$$

The relation is useful to obtain branching ratios of interest when the values of

[1] Corrected for the reduced transition rate by b_g; see Eq. (B.6).

relevant oscillator strengths are known. For Yb^+ ions, a comprehensive list of the oscillator strengths of transitions below 30,000 cm^{-1} with $gf > 0.01$ is available [192].

For instance, the decay $^3D[3/2]_{1/2} \rightarrow {}^2S_{1/2}$ (297.056 nm) and $^3D[3/2]_{1/2} \rightarrow {}^2D_{3/2}$ (934.929 nm) have $gf = 0.082$ and 0.015, respectively, giving the branching ratios $b = 0.018$ and 0.982, respectively [260], for the 935 nm $^2D_{3/2}$-state repumping transition (see Fig. 3-1).

Similarly, for the 760 nm $^2F_{7/2}$-state repumping transition, $^1D[3/2]_{3/2} \rightarrow {}^2S_{1/2}$ (289.138 nm), $^1D[3/2]_{3/2} \rightarrow {}^2D_{5/2}$ (976.039 nm), $^1D[3/2]_{3/2} \rightarrow {}^2D_{3/2}$ (861.002 nm), and $^1D[3/2]_{3/2} \rightarrow {}^2F_{7/2}$ (760.074 nm) have $gf = 0.166$, 0.042, $\leq$0.01, and $\leq$0.01 (the last two transitions are not listed in Ref. [192]), giving branching ratios $b \geq 0.096$, $b = 0.022$, $b \leq 0.0066$, and $b \leq 0.0085$.

Table B.1: The properties of transitions in Yb^+ ions (see Fig. 3-1) and neutral Yb atoms and beams driving the transitions in the experimental setup. All data is for $^{172}Yb^+$ isotope unless otherwise noted. If equations are given in a table footnote, all the necessary values are from this table.

Configuration		$^1S_0 \rightarrow {}^1P_1$	$^2S_{1/2} \rightarrow {}^2P_{1/2}$	$^2D_{3/2} \rightarrow {}^3D[3/2]_{1/2}$	$^2F_{7/2} \rightarrow {}^1D[3/2]_{3/2}$	$^2F_{7/2} \rightarrow {}^1D[5/2]_{5/2}$
λ	[nm]	399[u]	369	935	760	638
f	[THz]	751.527 064 60(34)[a]	811.292 74(10)[e]	320.569 390(50)[e]	394.426 550(60)[e]	469.441 27[b]
τ	[ns]	5.7[d]	8.12(2)[c k]	37.7(5)[f i]	28.6(4)[f i]	
$\Gamma/(2\pi)$	[MHz]	28[a i]	19.6(5)[d]	4.22(6)[d]	5.56(8)[d]	
I_s	[uW/mm^2]	≈580[n b]	≈510[n b]	≈375[n o]	≈2,000[n o]	
b[t]	[%]		$^2D_{3/2}$: 0.501(15)[g k] $^2F_{7/2}$: very small[h]	$^2S_{1/2}$: 98.2[l]	$^2S_{1/2}$: ≥96[o] $^2D_{5/2}$: 4.2[o] $^2D_{3/2}$: ≤0.66[o]	$^2D_{5/2}$[m] $^2D_{3/2}$[m]
P	[mW]	5	70 µW[v], 80 µW[w]	3	7	2.5
w	[µm]		75[v], 30[w]	300	100	100
I	[mW/mm^2]		8[v], 55[w]	21	450	160
Usage		Photoionization Isotope selection	Photoionization Cooling Optical pump State readout	Repumper ($^2D_{3/2}$ state)	Repumpers ($^2F_{7/2}$ state)	

Configuration		α: $6s\ ^2S_{1/2} \rightarrow 5d\ ^2D_{5/2}$	β: $6s\ ^2S_{1/2} \rightarrow 5d\ ^2D_{3/2}$	γ: $4f^{14}6s\ ^2S_{1/2} \rightarrow 4f^{13}6s^2\ ^2F_{7/2}$
λ	[nm]	411	436	467
f	[THz]	729.476 867 027 206 8(44)[s]	688.347 837(20)[s], 688.347 90(10)[s]	642.116 785 150 879 5(24)[s]
τ		7.1(3) ms[m p]	52.7(2.4) ms[p k]	10^{+7}_{-4} yr[q], 1.58(8) yr[r j]
$\Gamma/(2\pi)$		22.3(8) Hz[m p]	3.02(14) Hz[d]	$0.50^{+0.33}_{-0.21}$ nHz[q], 3.19(16) nHz[r j]
I_s		≈410 pW/mm^2[n b]	≈48 pW/mm^2[n b]	≈6×10^{-16} W/mm^2[n b]
b[t]	[%]	$^2F_{7/2}$: 83(3)		
P	[mW]	1	0.2	160
w	[µm]	60	15	30
I	[mW/mm^2]	180	570	113,000
Usage		Optical clock transitions		

[a] Ref. [113] [b] Ref. [4] [c] Ref. [261] [d] Eq. (B.2) [e] Table A.4 [f] Ref. [130] [g] Ref. [115]
[h] Decaying once every few hours, presumable due to the collision with background gas molecules [114, 115]. [i] Unspecified isotope
[j] $^{171}Yb^+$ [k] $^{174}Yb^+$ [l] Ref. [260] (from calculation [192]) [m] Ref. [131] (unspecified branching ratios) [n] Eq. (B.3) [o] Section B.1
[p] Ref. [262] [q] Ref. [263] [r] Ref. [248] [s] Table A.3 [t] Of all known decay channels. [u] Neutral Yb [v] For Doppler cooling
[w] For ground-state zeeman level optical pump

Appendix C

Atomic structure calculation: results

The results of the atomic structure calculations (ASCs) performed in Part IV are summarized in this appendix. Table C.1 shows the calculated energy levels of the electrons' orbitals in Yb^+ ions through the Dirac-Hartree-Fock (DHF) calculations in Section 14.2 and compares the energies with reference values. Table C.2 shows the values of isotope-shift electronic factors (in Section 15) derived from the configuration-interaction (CI) calculations for the Yb^+ ions (Section 14.3) with different configurations for valence and core electrons' correlations (see Sections 14.3.1 and 14.3.2), to investigate the convergence of the results. Lastly, the calculated single, two, and three-transition electronic factors for α: $^2S_{1/2} \rightarrow {}^2D_{5/2}$ (411 nm), β: $^2S_{1/2} \rightarrow {}^2D_{3/2}$ (436 nm), and γ: $^2S_{1/2} \rightarrow {}^2F_{7/2}$ (467 nm) optical clock transitions in Yb^+ ions and δ: $^1S_0 \rightarrow {}^3P_0$ (578 nm) and ϵ: $^1S_0 \rightarrow {}^1D_2$ (361 nm) optical transitions in neutral Yb atoms (see Fig. 3-1 and Table A.1) can be found in Tables C.3, C.4, and C.5 and Figs. C-1, C-2, and C-3.

Table C.1: The results of DHF calculations for orbitals in Yb^+ ions for the core configuration $[Xe]\,4f^{14}$ (column 2), ground state $6s\ ^2S_{1/2}$ in Table 11.17 in Ref. [27] (column 3), and the orbitals up to $8spdf$ used for subsequent CI calculations (columns 4 and 5). See Section 14.2.2 for the electron configurations in $8spdf$ calculation. The energy eigenvalues E_{nk} of each orbital are shown in the unit of Hartree energy $E_h = \hbar c\alpha/a_0$ [see Eq. (14.4) for the definition of the relativistic quantum number k]. For $8spdf$ calculation, E_{nk} of the $^2S_{1/2}$ ground state and electron occupation numbers are listed. All values, except from Ref. [27], are from the final `rmcdhf.sum` files.

Subshell	Core	$^2S_{1/2}$ [27]	$8spdf$	
$n[l]_j$	E_{nk} [E_h]	E_{nk} [E_h]	E_{nk} [E_h]	Occupation
$1s_{1/2}$	-2268.17964	-2267.65237	-2267.87622	2
$2s_{1/2}$	-389.41793	-388.89269	-389.12926	2
$2p_{1/2}$	-370.58133	-370.05522	-370.29479	2
$2p_{3/2}$	-332.01338	-331.48739	-331.72693	4
$3s_{1/2}$	-90.23276	-89.70956	-89.94727	2
$3p_{1/2}$	-81.94623	-81.42221	-81.66111	2
$3p_{3/2}$	-73.61802	-73.09396	-73.33291	4
$3d_{3/2}$	-59.71622	-59.19193	-59.43105	4
$3d_{5/2}$	-57.91495	-57.3906	-57.62973	6
$4s_{1/2}$	-19.19549	-18.67246	-18.90990	2
$4p_{1/2}$	-15.79954	-15.2751	-15.51395	2
$4p_{3/2}$	-13.89841	-13.37358	-13.61237	4
$4d_{3/2}$	-8.30299	-7.77796	-8.01695	4
$4d_{5/2}$	-7.94736	-7.42207	-7.66103	6
$5s_{1/2}$	-2.95995	-2.43951	-2.67321	2
$5p_{1/2}$	-1.94173	-1.41916	-1.65888	2
$5p_{3/2}$	-1.70393	-1.18279	-1.42121	4
$4f_{5/2}$	-1.06455	-0.53899	-0.77767	6
$4f_{7/2}$	-1.00619	-0.48019	-0.71891	8
$5d_{3/2}$			-0.30797	1.25E-01
$5d_{5/2}$			-0.30563	1.88E-01
$6s_{1/2}$		-0.19652	-0.41607	6.25E-02
$6p_{1/2}$			-0.30208	6.25E-02
$6p_{3/2}$			-0.28911	1.25E-01
$5f_{5/2}$			-0.05563	1.87E-01
$5f_{7/2}$			-0.05563	2.50E-01
$6d_{3/2}$			-0.30583	1.04E-10
$6d_{5/2}$			-0.30033	1.12E-10
$7s_{1/2}$			-0.31059	7.94E-12
$7p_{1/2}$			-0.24225	5.55E-12
$7p_{3/2}$			-0.22967	1.04E-11
$8s_{1/2}$			-0.15433	8.03E-14
$6f_{5/2}$			-0.05562	1.10E-06
$6f_{7/2}$			-0.05602	1.36E-10
$7d_{3/2}$			-0.30792	1.84E-11
$7d_{5/2}$			-0.30563	1.46E-11
$7f_{5/2}$			-0.05567	8.00E-08
$7f_{7/2}$			-0.04397	6.01E-09
$8p_{1/2}$			-0.12868	4.89E-15
$8p_{3/2}$			-0.12402	2.54E-14
$8d_{3/2}$			-0.08819	1.18E-20
$8d_{5/2}$			-0.08750	1.82E-21
$8f_{5/2}$			-0.02864	2.99E-06
$8f_{7/2}$			-0.02719	2.50E-07
$E_{\rm tot}$	-14067.07238	-14067.67726	-14067.44680	

Table C.2: Electronic factors for α: 411 nm, β: 436 nm, and γ: 467 nm optical clock transitions in Yb^+ ions (see Fig. 3-1) calculated for $^{172}Yb^+$ (see Chapter 15) with different correlation layers and core orbitals allowed to be excited while generating lists of CSFs via active set approach (Section 12.2). First column (Excited core) shows the core orbitals (e.g., 4sp5sp for $4s$, $4p$, $5s$, and $5p$) from which electrons can be excited, and the number of electrons that can be excited from each core shell (e.g., SD for single or double-electron excitation) (see Section 14.3.2). Second column (Correl. layer) shows the correlation orbital layers with highest n (e.g., 8spdf for all correlation s, p, d, and f orbitals for $n \leq 8$) (see Section 14.3.1). The third column (# CSFs) shows the total number of CSFs, for all $^2S_{1/2}$, $^2D_{5/2}$, $^2D_{3/2}$, and $^2F_{7/2}$ states for α, β, and γ transitions, generated with each configuration of the core excitation and the correlation layer set. The fourth to sixth columns show the calculated transition frequencies E_χ/h for each transition χ. The remaining columns shows the one-transition electronic factors Z_χ and two-electron factors $z_{\kappa\chi} = Z_\kappa/Z_\chi$ and $Z_{\kappa\chi} = (z_{\kappa\chi} - f_{\kappa\chi})Z_\chi$ (see Sections 8.1, 8.2, and Chapter 15): field-shift (FS) factors F and f in the first table columns 7–11 (continued on the next table),

Excited core	Correl. layer	# CSFs	E_α/h	E_β/h [THz]	E_γ/h	F_α	F_β [GHz/fm^2]	F_γ	$f_{\beta\alpha}$	$f_{\gamma\alpha}$
None	6spdf	12762	751.48	731.99	1301.55	-12.3344	-12.3328	0.0518	0.99987	-0.00420
	7spdf	37425	773.37	746.48	796.84	-12.8743	-12.8615	32.1858	0.99901	-2.50000
	8spdf	75117	774.32	747.32	778.42	-12.9056	-12.8919	32.8859	0.99894	-2.54819
5spS	6spdf	34586	780.72	757.80	1328.49	-13.0054	-13.0867	11.7965	1.00625	-0.90705
	7spdf	95135	807.51	770.05	622.91	-15.4922	-15.7371	37.8189	1.01581	-2.44116
	8spdf	185782	809.29	771.30	573.01	-15.7483	-16.0107	40.1413	1.01666	-2.54893
4sp5spS	6spdf	72472	780.50	757.60	1326.72	-13.0825	-13.1645	11.8527	1.00627	-0.90600
	7spdf	195807	806.45	769.00	628.44	-15.5936	-15.8214	39.2725	1.01461	-2.51850
	8spdf	379328	808.11	770.13	580.12	-15.8519	-16.0936	41.8925	1.01525	-2.64274
5spSD	6spdf	37985	806.64	782.99	1349.40	-12.9639	-13.0300	12.0689	1.00510	-0.93096
	7spdf	104176	825.36	790.46	691.30	-15.0075	-15.2143	35.7643	1.01378	-2.38310
	8spdf	203195	826.43	791.15	646.97	-15.2238	-15.4452	38.1119	1.01454	-2.50344
Reference			729.47[a]	688.35[a]	642.12[a]				1.01141[b]	-2.22131[b]

[a] Table A.3 [b] Table C.4

Table C.2: (Continued) one-electron mass-shift (MS) factors K_χ from only normal MS (NMS; columns 1–3), specific MS (SMS; columns 4–6), and total MS as the sum of the NMS and SMS (columns 7–9) (see Section 8.1.2), and two-electron factors $k_{\kappa\chi}$ and $K_{\kappa\chi}$ from K_χ for the total MSs in the second table (continued on the next table),

Excited	Correl.	NMS			SMS			Total						
		K_α	K_β	K_γ	K_α	K_β	K_γ	K_α	K_β	K_γ	$k_{\beta\alpha} - f_{\beta\alpha}$	$k_{\gamma\alpha} - f_{\gamma\alpha}$	$K_{\beta\alpha}$	$K_{\gamma\alpha}$
			[GHz · u]			[GHz · u]			[GHz · u]				[GHz · u]	
None	6spdf	1837.38	1766.83	-75884.39	-1948.88	-1792.03	66024.46	-111.50	-25.20	-9859.93	-7.74E-1	8.84E+1	86.286	-9860.4
	7spdf	1846.90	1293.26	-57807.05	-2055.67	-1477.48	52165.79	-208.77	-184.22	-5641.26	-1.17E-1	2.95E+1	24.342	-6163.2
	8spdf	1852.15	1299.19	-56475.92	-2063.26	-1485.61	51151.49	-211.11	-186.42	-5324.43	-1.16E-1	2.78E+1	24.466	-5862.4
5spS	6spdf	927.61	956.42	-82688.78	-1763.71	-1698.96	70949.58	-836.10	-742.54	-11739.20	-1.18E-1	1.49E+1	98.787	-12497.6
	7spdf	-286.98	-659.16	-43938.53	-1343.01	-931.56	45007.32	-1629.99	-1590.72	1068.79	-3.99E-2	1.79E+0	65.037	-2910.3
	8spdf	-377.07	-758.20	-40848.61	-1308.39	-894.65	43199.68	-1685.46	-1652.85	2351.07	-3.60E-2	1.15E+0	60.693	-1945.0
4sp5spS	6spdf	903.21	931.79	-82531.87	-1740.83	-1675.83	70852.77	-837.62	-744.04	-11679.10	-1.18E-1	1.48E+1	98.830	-12438.0
	7spdf	-303.74	-663.71	-42538.79	-1321.20	-916.35	44258.72	-1624.94	-1580.06	1719.93	-4.22E-2	1.46E+0	68.618	-2372.5
	8spdf	-389.45	-755.31	-39205.86	-1288.80	-883.22	42333.42	-1678.25	-1638.53	3127.56	-3.89E-2	7.79E-1	65.309	-1307.6
5spSD	6spdf	824.69	889.96	-83456.23	-1953.74	-1929.03	71425.37	-1129.05	-1039.07	-12030.86	-8.48E-2	1.16E+1	95.737	-13082.0
	7spdf	-148.93	-472.13	-46586.52	-1558.73	-1221.68	46627.31	-1707.66	-1693.81	40.79	-2.19E-2	2.36E+0	37.381	-4028.7
	8spdf	-208.54	-539.30	-43637.36	-1530.96	-1192.58	44914.19	-1739.50	-1731.88	1276.83	-1.89E-2	1.77E+0	32.918	-3077.9
Reference													120.21[b]	5738[b]

Table C.2: (Continued) fourth-moment-FS (FFS) $G^{(4)}$ and $g^{(4)}$ (columns 1–7) and quadratic-FS (QFS) $G^{(2)}$ and $g^{(2)}$ (columns 8–14) factors in the third table (continued on the next table),

Exc	Corr	$G^{(4)}_\alpha$	$G^{(4)}_\beta$	$G^{(4)}_\gamma$	$g^{(4)}_{\beta\alpha} - f_{\beta\alpha}$	$g^{(4)}_{\gamma\alpha} - f_{\gamma\alpha}$	$G^{(4)}_{\beta\alpha}$	$G^{(4)}_{\gamma\alpha}$	$G^{(2)}_\alpha$	$G^{(2)}_\beta$	$G^{(2)}_\gamma$	$g^{(2)}_{\beta\alpha} - f_{\beta\alpha}$	$g^{(2)}_{\gamma\alpha} - f_{\gamma\alpha}$	$G^{(2)}_{\beta\alpha}$	$G^{(2)}_{\gamma\alpha}$
			[MHz/fm^4]				[kHz/fm^4]			[MHz/fm^4]				[kHz/fm^4]	
None	6spdf	9.2504	9.3261	-14.1022	8.31E-3	-1.52E+0	76.8999	-14063	33.1282	33.1243	-0.1393	5.53E-6	-6.48E-6	0.1831	-0.2146
	7spdf	10.2504	10.3261	-13.1022	8.38E-3	1.22E+0	85.8912	12524	34.5770	34.5443	-86.4408	4.68E-5	5.43E-5	1.6166	1.8776
	8spdf	11.2504	11.3261	-12.1022	7.79E-3	1.47E+0	87.6429	16566	34.6609	34.6257	-88.3209	4.89E-5	4.88E-5	1.6951	1.6931
5spS	6spdf	12.2504	12.3261	-11.1022	-7.19E-5	7.74E-4	-0.8803	9.4800	34.9284	35.1439	-31.6532	-8.02E-5	8.17E-4	-2.8004	28.5508
	7spdf	14.5905	14.8178	-35.5814	-2.29E-4	2.49E-3	-3.3460	36.3083	41.5993	42.2468	-101.4221	-2.37E-4	3.16E-3	-9.8451	131.4761
	8spdf	14.8314	15.0751	-37.7638	-2.31E-4	2.72E-3	-3.4225	40.3869	42.2861	42.9804	-107.6417	-2.49E-4	3.47E-3	-10.5236	146.9389
4sp5spS	6spdf	15.8314	16.0751	-36.7638	9.13E-3	-1.42E+0	144.47	-22421	35.1355	35.3529	-31.8024	-8.51E-5	8.64E-4	-2.9906	30.3620
	7spdf	14.6861	14.8973	-36.9455	-2.28E-4	2.82E-3	-3.3427	41.4602	41.8721	42.4739	-105.3090	-2.32E-4	3.58E-3	-9.7336	149.8846
	8spdf	14.9291	15.1532	-39.4075	-2.36E-4	3.10E-3	-3.5297	46.2766	42.5651	43.2036	-112.3254	-2.46E-4	3.96E-3	-10.4756	168.4334
5spSD	6spdf	15.9291	16.1532	-38.4075	8.97E-3	-1.48E+0	142.88	-23578	34.8172	34.9938	-32.3859	-3.28E-5	8.01E-4	-1.1432	27.8742
	7spdf	14.1345	14.3268	-33.6467	-1.75E-4	2.63E-3	-2.4703	37.1580	40.2995	40.8474	-95.9079	-1.82E-4	3.30E-3	-7.3428	133.0539
	8spdf	14.3381	14.5441	-35.8532	-1.76E-4	2.89E-3	-2.5192	41.4014	40.8799	41.4666	-102.1964	-1.97E-4	3.63E-3	-8.0653	148.1918

Table C.2: (Continued) and new-boson factor D and d for massless bosons (columns 1–7) and for $m_\phi = 17\,\mathrm{MeV/c^2}$ (columns 8–14) in consideration for the X17 boson from Be/He anomaly [28, 29, 30, 31, 32, 33] in the fourth table. The $17\,\mathrm{MeV/c^2}$ is also practically the maximum mass of a boson that can be probed with Yb ions, considering the mass $\sim$30 $\mathrm{MeV/c^2}$ that corresponds to the reduced Compton wavelength of the size of the Yb nuclei: $\sim$6 fm [19].

Exc	Corr	$m_\phi = 0$ (massless)							$m_\phi = 17\,\mathrm{MeV/c^2}$ (X17 boson [28, 29, 30, 31, 32, 33])						
		D_α	D_β [THz]	D_γ	$d_{\beta\alpha} - f_{\beta\alpha}$	$d_{\gamma\alpha} - f_{\gamma\alpha}$	$D_{\beta\alpha}$ [THz]	$D_{\gamma\alpha}$	D_α	D_β [THz]	D_γ	$d_{\beta\alpha} - f_{\beta\alpha}$	$d_{\gamma\alpha} - f_{\gamma\alpha}$	$D_{\beta\alpha}$ [GHz]	$D_{\gamma\alpha}$
None	6spdf	72661	77638	-1003428	6.86E-2	-1.38E+1	4986.53	-1003123	-13.875	-13.873	0.058	3.13E-7	4.85E-6	-0.0043	-0.0674
	7spdf	72504	74307	-925602	2.59E-2	-1.03E+1	1874.90	-744342	-14.483	-14.468	36.206	-3.44E-5	3.84E-6	0.4979	-0.0556
	8spdf	72306	74185	-913476	2.71E-2	-1.01E+1	1956.58	-729228	-14.518	-14.502	36.994	-3.74E-5	2.11E-6	0.5433	-0.0306
5spS	6spdf	59747	65885	-1182549	9.65E-2	-1.89E+1	5764.31	-1128356	-14.630	-14.722	13.279	5.70E-5	-6.29E-4	-0.8338	9.1962
	7spdf	45341	49531	-770842	7.66E-2	-1.46E+1	3473.99	-660158	-17.431	-17.709	42.590	1.66E-4	-2.23E-3	-2.8996	38.8049
	8spdf	44201	48401	-739862	7.84E-2	-1.42E+1	3464.12	-627197	-17.719	-18.017	45.208	1.86E-4	-2.45E-3	-3.3008	43.4882
4sp5spS	6spdf	59551	65689	-1181679	9.68E-2	-1.89E+1	5765.52	-1127726	-14.717	-14.810	13.343	6.37E-5	-6.65E-4	-0.9369	9.7899
	7spdf	45251	49500	-762759	7.93E-2	-1.43E+1	3588.21	-648795	-17.545	-17.804	44.230	1.67E-4	-2.48E-3	-2.9347	43.5019
	8spdf	44145	48419	-730405	8.16E-2	-1.39E+1	3601.49	-613742	-17.836	-18.111	47.184	1.76E-4	-2.74E-3	-3.1435	48.8349
5spSD	6spdf	56813	63434	-1193345	1.11E-1	-2.01E+1	6331.59	-1140454	-14.583	-14.658	13.586	3.00E-5	-6.19E-4	-0.4376	9.0336
	7spdf	44700	49059	-803034	8.37E-2	-1.56E+1	3743.43	-696511	-16.885	-17.119	40.277	1.30E-4	-2.35E-3	-2.2006	39.7110
	8spdf	44005	48361	-773352	8.45E-2	-1.51E+1	3716.52	-663188	-17.128	-17.380	42.923	1.45E-4	-2.57E-3	-2.4767	43.9984

Table C.3: Calculated values of single-transition electronic factors Z_χ ($Z \in \{F, K, G^{(4)}, G^{(2)}, D\}$) (see Sections 8.1, 8.2, and 15) for $\chi = \alpha$: $^2S_{1/2} \to {}^2D_{5/2}$ (411 nm), β: $^2S_{1/2} \to {}^2D_{3/2}$ (436 nm), and γ: $^2S_{1/2} \to {}^2F_{7/2}$ (467 nm) transitions in Yb^+ ions (see Fig. 3-1); and δ: $^1S_0 \to {}^3P_0$ (578 nm), and ϵ: $^1S_0 \to {}^1D_2$ (361 nm) transitions in neutral Yb atoms. $\omega_\chi/(2\pi)$ are transition frequencies. Calculated values for each transition are obtained from CI method using GRASP2018 [8, 24] (see Section 13) or AMBiT [8, 23]. The units of $\omega_\chi/(2\pi)$, F_χ, K_χ, $G_\chi^{(4)}$, $G_\chi^{(2)}$, and D_χ are THz, GHz/fm^2, GHz·u, MHz/fm^4, MHz/fm^4, and 10^3 THz, respectively.

	GRASP	AMBiT	Ref. [9]	Exp.
$\omega_\alpha/(2\pi)$	808.11	707.00		729.47[a] [b]
$\omega_\beta/(2\pi)$	770.13	679.86		688.35[a] [b]
$\omega_\gamma/(2\pi)$	580.12	1051.44		642.12[a] [b]
$\omega_\delta/(2\pi)$	458.36	522.78		518.30[a] [c]
$\omega_\epsilon/(2\pi)$		819.47		829.76[a] [d]
F_α	-15.852	-14.715	-17.604	
F_β	-16.094	-14.968	-18.003	
F_γ	41.892	36.218		
F_δ	-9.1508	-9.719		
F_ϵ		-13.528	-14.437	
K_α	-1678.2	-752		
K_β	-1638.5	-661		
K_γ	3127.6	12001		
K_δ				
K_ϵ				
$G_\alpha^{(4)}$	14.934		13.08	
$G_\beta^{(4)}$	15.159		13.37	
$G_\gamma^{(4)}$	-39.422			
$G_\delta^{(4)}$	8.951			
$G_\epsilon^{(4)}$			10.42	
$G_\alpha^{(2)}$	42.565	81.908	28.53	
$G_\beta^{(2)}$	43.204	83.247	28.53	
$G_\gamma^{(2)}$	-112.33	-201.12		
$G_\delta^{(2)}$		54.277		
$G_\epsilon^{(2)}$		75.322	23.34	
D_α[e]	44.145	43.158	41.235	
D_β[e]	48.419	48.634	48.795	
D_γ[e]	-730.4	-352.38		
D_δ[e]	-55.729	-42.855		
D_ϵ[e]		5.6683	4.6238	

[a] The exact value varies by the few-GHz isotope shifts; see Table A.2.
[b] Table A.3 [c] Ref. [264] [d] Ref. [21] [e] At $m_\phi = 1\,\text{eV}$. Values over different m_ϕ's are shown in Fig. C-1

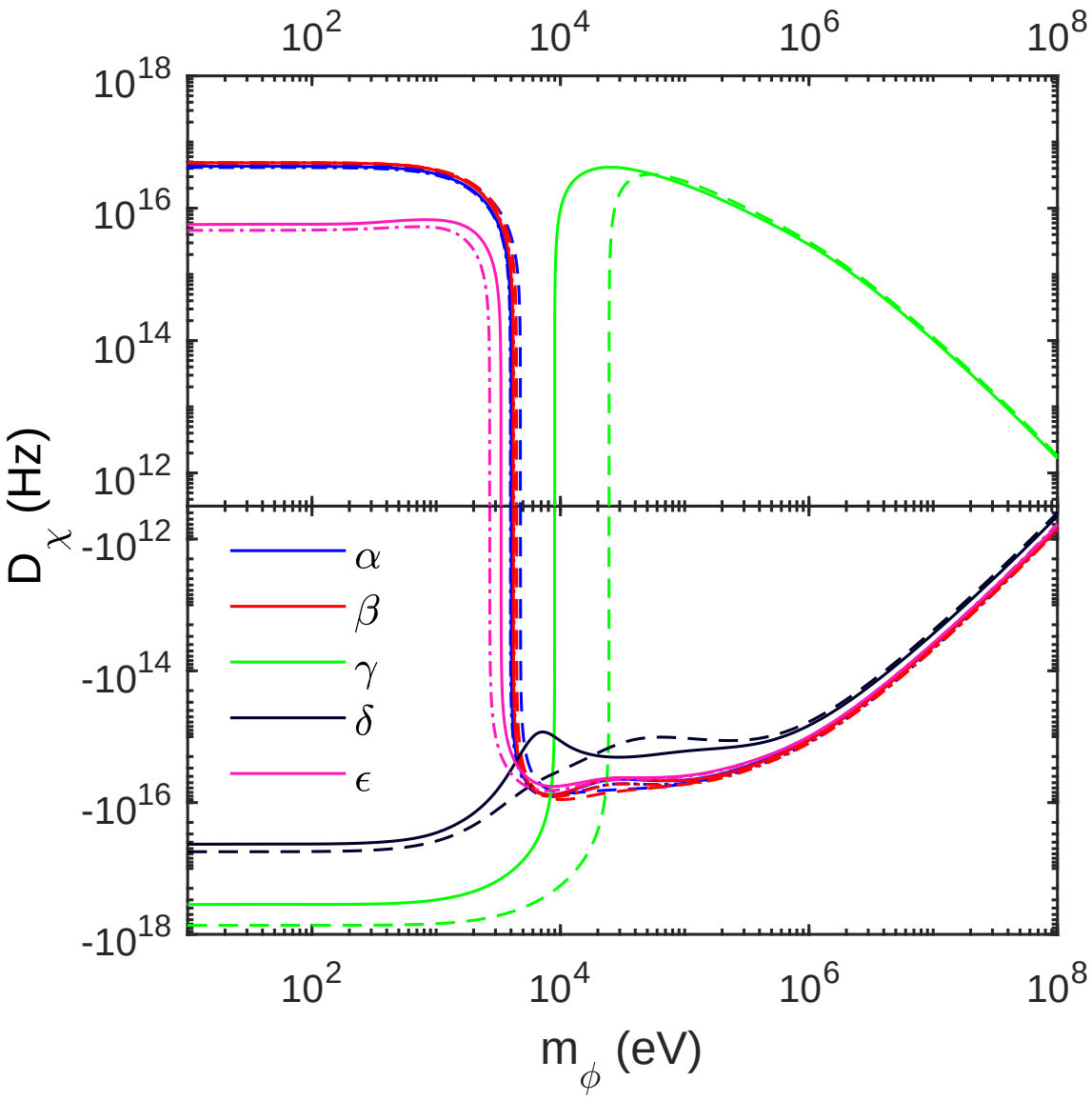

Figure C-1: Single-transition factors D_χ vs new-boson mass m_ϕ for five transitions χ coded with different colors (see legend) derived from atomic structure calculations using CI method. Solid, dashed, and dash-dotted lines are for AMBiT [8, 23], GRASP2018 [8, 24] (see Section 13), and Ref. [9], respectively.

Table C.4: Calculated and experimental values of two-transition electronic factors $f_{\kappa\chi}$ and $Z_{\kappa\chi}$ ($Z \in \{K, G^{(4)}, G^{(2)}, D\}$) (see Sections 8.1 and 8.2) for $\chi, \kappa \in \{\alpha, \beta, \gamma, \delta, \epsilon\}$. The values are calculated from the single-transition values in Table C.3. $f_{\chi\kappa}$ is dimensionless. The units of $K_{\kappa\chi}$, $G^{(4)}_{\kappa\chi}$, $G^{(2)}_{\kappa\chi}$, and $D_{\kappa\chi}$ are GHz·u, kHz/fm^4, kHz/fm^4, and 10^3 THz, respectively. The last two columns (Fit) are for data from linear fit of corresponding 2D King plots $\overline{\nu}^{AA'}_{\kappa} = f_{\kappa\chi} + K_{\kappa\chi}\overline{\mu}^{AA'}$ [Eq. (8.15)] with (X corr.) and without (No X corr.) uncertainties in and correlations between independent variables (see Sections 9.3 and 11.3). $\chi^2_{\kappa\chi}$ and $s_{\kappa\chi}$ are $\hat{\chi}^2$ and the significance of linear fit, respectively (see Sections 9.2 and 9.3).

	GRASP	AMBiT	Ref. [9]	Fit	
				X corr.	No X corr.
$f_{\beta\alpha}$	1.0152	1.0172	1.0227	1.01141025(86)	1.01141025(86)
$f_{\gamma\alpha}$	-2.6427	-2.4613		-2.2213082(14)	-2.2213084(13)
$f_{\delta\alpha}$	0.57727	0.66048		0.61172988(34)	0.61172995(35)
$f_{\epsilon\alpha}$		0.91933	0.8201	0.81761175(80)	0.81761175(80)
$f_{\gamma\beta}$	-2.603	-2.4197		-2.1962536(14)	-2.1962537(13)
$f_{\delta\beta}$	0.5686	0.64932		0.60482313(37)	0.60482322(37)
$f_{\epsilon\beta}$		0.90379	0.80192	0.80838924(76)	0.80838924(76)
$f_{\delta\gamma}$	-0.21844	-0.26835		-0.275391225(69)	-0.275391430(78)
$f_{\epsilon\gamma}$		-0.37352		-0.36807660(27)	-0.36807657(28)
$f_{\epsilon\delta}$		1.3919		1.33656619(92)	1.33656619(92)
$K_{\beta\alpha}$	65.306	103.92		120.208(23)	120.208(23)
$K_{\gamma\alpha}$	-1307.6	10150		5737.593(39)	5737.595(35)
$K_{\delta\alpha}$				363.1350(94)	363.1332(97)
$K_{\epsilon\alpha}$				1.811(21)	1.811(21)
$K_{\gamma\beta}$	-1137.6	10402		6001.679(38)	6001.683(35)
$K_{\delta\beta}$				290.5263(97)	290.5242(99)
$K_{\epsilon\beta}$				-95.402(20)	-95.402(20)
$K_{\delta\gamma}$				1943.2126(37)	1943.2019(43)
$K_{\epsilon\gamma}$				2113.679(14)	2113.681(14)
$K_{\epsilon\delta}$				-483.666(15)	-483.666(15)

Continued on the next page

Table C.4 (continued)

	GRASP	AMBiT	Ref. [9]	Fit	
				X Corr.	No X corr.
$G^{(4)}_{\beta\alpha}$	-3.5056		-6.4622		
$G^{(4)}_{\gamma\alpha}$	45.789				
$G^{(4)}_{\delta\alpha}$	329.81				
$G^{(4)}_{\epsilon\alpha}$			-306.88		
$G^{(4)}_{\gamma\beta}$	36.664				
$G^{(4)}_{\delta\beta}$	331.8				
$G^{(4)}_{\epsilon\beta}$			-301.7		
$G^{(4)}_{\delta\gamma}$	339.81				
$G^{(4)}_{\epsilon\gamma}$					
$G^{(4)}_{\epsilon\delta}$					
$G^{(2)}_{\beta\alpha}$	-10.442	-68.645	-646.64		
$G^{(2)}_{\gamma\alpha}$	162.69	471.33			
$G^{(2)}_{\delta\alpha}$		181.24			
$G^{(2)}_{\epsilon\alpha}$		22.9	-57.388		
$G^{(2)}_{\gamma\beta}$	135.51	305.24			
$G^{(2)}_{\delta\beta}$		225.81			
$G^{(2)}_{\epsilon\beta}$		84.94	461.17		
$G^{(2)}_{\delta\gamma}$		307.72			
$G^{(2)}_{\epsilon\gamma}$		198.95			
$G^{(2)}_{\epsilon\delta}$		-229.38			
$D_{\beta\alpha}{}^{\mathrm{a}}$	3.6016	4.7337	6.6257		
$D_{\gamma\alpha}{}^{\mathrm{a}}$	-613.74	-246.15			
$D_{\delta\alpha}{}^{\mathrm{a}}$	-81.212	-71.359			
$D_{\epsilon\alpha}{}^{\mathrm{a}}$		-34.008	-29.464		
$D_{\gamma\beta}{}^{\mathrm{a}}$	-604.37	-234.7			
$D_{\delta\beta}{}^{\mathrm{a}}$	-83.26	-74.433			
$D_{\epsilon\beta}{}^{\mathrm{a}}$		-38.286	-34.82		
$D_{\delta\gamma}{}^{\mathrm{a}}$	-215.28	-137.41			
$D_{\epsilon\gamma}{}^{\mathrm{a}}$		-125.95			
$D_{\epsilon\delta}{}^{\mathrm{a}}$		65.321			

Continued on the next page

Table C.4 (continued)

	GRASP	AMBiT	Ref. [9]	Fit	
				X Corr.	No X corr.
$\chi^2_{\beta\alpha}$				11.792	11.738
$\chi^2_{\gamma\alpha}$				1755.2	2057
$\chi^2_{\delta\alpha}$				10504	10010
$\chi^2_{\epsilon\alpha}$				74.581	74.575
$\chi^2_{\gamma\beta}$				2220.6	2546
$\chi^2_{\delta\beta}$				16555	15916
$\chi^2_{\epsilon\beta}$				137.48	137.91
$\chi^2_{\delta\gamma}$				57854	43986
$\chi^2_{\epsilon\gamma}$				2040.2	1920.7
$\chi^2_{\epsilon\delta}$				4511.9	4512
$s_{\beta\alpha}$				2.99σ	2.99σ
$s_{\gamma\alpha}$				41.8σ	45.3σ
$s_{\delta\alpha}$				102σ	100σ
$s_{\epsilon\alpha}$				8.36σ	8.36σ
$s_{\gamma\beta}$				47σ	50.4σ
$s_{\delta\beta}$				129σ	126σ
$s_{\epsilon\beta}$				11.5σ	11.5σ
$s_{\delta\gamma}$				241σ	210σ
$s_{\epsilon\gamma}$				45.1σ	43.7σ
$s_{\epsilon\delta}$				67.1σ	67.1σ

[a] At $m_\phi = 1\,\text{eV}$. Values over different m_ϕ's are shown in Fig. C-2

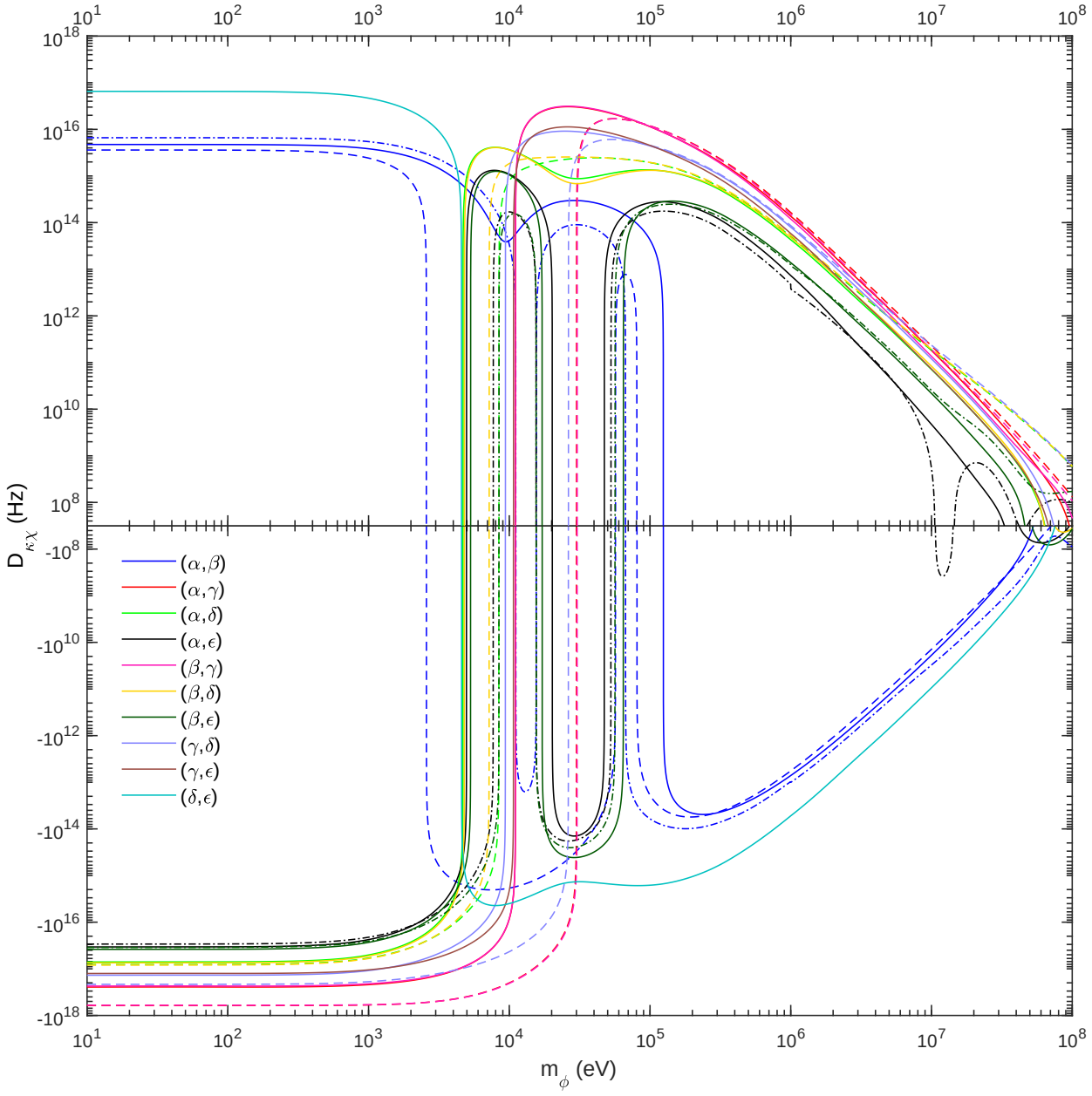

Figure C-2: Two-transition factors $D_{\kappa\chi}$ vs new-boson mass m_ϕ for variable transition pairs (χ,κ) coded with different colors (see legend) calculated using D_χ and D_κ in Fig. C-1. Solid, dashed, and dash-dotted lines are for AMBiT [8, 23], GRASP2018 [8, 24] (see Section 13), and Ref. [9], respectively (some of dashed and dash-dotted lines are missing as the corresponding $D_{\kappa\chi}$ are not available; see Table C.4).

Table C.5: Calculated and experimental values of three-transition electronic factors $f_{\eta\kappa\chi}$ and $Z_{\eta\kappa\chi}$ ($Z \in \{K, G^{(2)}, D\}$) (see Section 8.4) for $\chi, \kappa, \eta \in \{\alpha, \beta, \gamma, \delta, \epsilon\}$. The values are calculated from the two-transition values in Table C.4. $f_{\eta\kappa\chi}$ is dimensionless. The units of $K_{\eta\kappa\chi}$, $G^{(2)}_{\eta\kappa\chi}$, $D_{\eta\kappa\chi}$, and $\upsilon_{ne}D_{\chi\kappa}$ are GHz·u, kHz/fm^4, kHz/fm^4, 10^3 THz, and kHz, respectively. The last three columns (Fit) are for data from fit of corresponding 3D King plots $\overline{\overline{\nu}}^{AA'}_{\eta} = K_{\eta\kappa\chi} + f_{\eta\kappa\chi}\overline{\overline{\nu}}^{AA'}_{\chi} + f_{\eta\chi\kappa}\overline{\overline{\nu}}^{AA'}_{\kappa}$ (Linear), and $G^{(2)}_{\eta\kappa\chi}\overline{\overline{[\delta\langle r^2\rangle^2]}}^{AA'}$ (QFS) or $\upsilon_{ne}D_{\eta\kappa\chi}\overline{\overline{a}}^{AA'}$ (New boson) terms in addition to the relation (see Sections 8.4, 11.1.2, and 11.1.3). $\chi^2_{\eta\kappa\chi}$ and $s_{\eta\kappa\chi}$ are $\hat{\chi}^2$ and the significance of fit, respectively (see Sections 9.2 and 9.3).

	GRASP		AMBiT		Ref. [9]		Fit		
	Cal.	Exp.	Cal.	Exp.	Cal.	Exp.	Linear	QFS	New boson
$f_{\beta\gamma\alpha}$	0.81292						0.978(26)	0.998(27)	1.052(36)
$f_{\beta\delta\alpha}$	1.0214						1.023(13)	1.018(13)	0.993(16)
$f_{\beta\epsilon\alpha}$					1.0054		1.14(10)	1.058(99)	0.86(12)
$f_{\delta\gamma\alpha}$	19.612						1.867(41)	1.877(41)	1.965(51)
$f_{\epsilon\gamma\alpha}$							1.049(30)	1.046(33)	1.040(45)
$f_{\epsilon\delta\alpha}$							0.701(13)	0.707(14)	0.717(19)
$f_{\delta\gamma\beta}$	24.126						1.885(35)	1.880(37)	1.868(49)
$f_{\epsilon\gamma\beta}$							1.090(28)	1.047(31)	0.989(43)
$f_{\epsilon\delta\beta}$							0.673(11)	0.695(13)	0.722(19)
$f_{\epsilon\delta\gamma}$							-0.2082(32)	-0.2146(38)	-0.2223(54)
$f_{\beta\alpha\gamma}$	-0.076559						-0.015(12)	-0.006(12)	0.018(16)
$f_{\beta\alpha\delta}$	-0.010629						-0.019(21)	-0.010(21)	0.030(26)
$f_{\beta\alpha\epsilon}$					0.021058		-0.15(12)	-0.06(12)	0.18(15)
$f_{\delta\alpha\gamma}$	7.2027						0.565(18)	0.570(19)	0.609(23)
$f_{\epsilon\alpha\gamma}$							0.104(14)	0.103(15)	0.100(20)
$f_{\epsilon\alpha\delta}$							0.191(21)	0.180(23)	0.165(31)
$f_{\delta\beta\gamma}$	9.0498						0.583(16)	0.580(17)	0.575(22)
$f_{\epsilon\beta\gamma}$							0.128(13)	0.109(14)	0.082(20)
$f_{\epsilon\beta\delta}$							0.223(19)	0.187(22)	0.143(32)
$f_{\epsilon\gamma\delta}$							0.580(12)	0.557(14)	0.529(20)

Continued on the next page

Table C.5 (continued)

	GRASP		AMBiT		Ref. [9]		Fit		
	Cal.	Exp.	Cal.	Exp.	Cal.	Exp.	Linear	QFS	New boson
$K_{\beta\gamma\alpha}$	-34.804	89(21)		-80(160)			206(66)	154(69)	17(91)
$K_{\beta\delta\alpha}$							126.9(7.7)	124.2(7.8)	111.1(9.0)
$K_{\beta\epsilon\alpha}$							120.48(23)	120.53(21)	121.79(43)
$K_{\delta\gamma\alpha}$							-2880(110)	-2900(110)	-3130(130)
$K_{\epsilon\gamma\alpha}$							-596(79)	-587(85)	-570(120)
$K_{\epsilon\delta\alpha}$							-67.6(7.6)	-63.8(8.3)	-59(11)
$K_{\delta\gamma\beta}$							-3207(97)	-3190(100)	-3160(130)
$K_{\epsilon\gamma\beta}$							-865(77)	-749(86)	-590(120)
$K_{\epsilon\delta\beta}$							-160.3(5.5)	-150.1(6.4)	-138.8(8.8)
$K_{\epsilon\delta\gamma}$							986(23)	1031(27)	1083(38)
$G^{(2)}_{\beta\gamma\alpha}$	2.0139	-13.4(2.6)		-77.3(7.5)				57(18)	
$G^{(2)}_{\beta\delta\alpha}$				-74.1(4.6)				58(18)	
$G^{(2)}_{\beta\epsilon\alpha}$				-72.8(3.4)	-645.43	-636.1(8.6)		57(18)	
$G^{(2)}_{\delta\gamma\alpha}$				-106(11)				94(24)	
$G^{(2)}_{\epsilon\gamma\alpha}$				-24.4(9.6)				-6(22)	
$G^{(2)}_{\epsilon\delta\alpha}$				-6.9(5.6)				-23(19)	
$G^{(2)}_{\delta\gamma\beta}$				50.2(6.8)				-13(27)	
$G^{(2)}_{\epsilon\gamma\beta}$				59.9(6.0)				-65(22)	
$G^{(2)}_{\epsilon\delta\beta}$				52.7(7.2)				-63(20)	
$G^{(2)}_{\epsilon\delta\gamma}$				36.1(6.1)				-58(18)	
$D_{\beta\gamma\alpha}{}^{\mathrm{a}}$	-43.386	14.8(9.8)		9.2(3.9)					
$D_{\beta\delta\alpha}{}^{\mathrm{a}}$	2.7384	6.0(2.1)		6.9(1.8)					
$D_{\beta\epsilon\alpha}{}^{\mathrm{a}}$				11.0(5.1)	7.2462	12.0(4.4)			
$D_{\delta\gamma\alpha}{}^{\mathrm{a}}$	4339.4	293(14)		78.7(5.6)					
$D_{\epsilon\gamma\alpha}{}^{\mathrm{a}}$				-9.3(5.0)					
$D_{\epsilon\delta\alpha}{}^{\mathrm{a}}$				-22.3(2.2)					
$D_{\delta\gamma\beta}{}^{\mathrm{a}}$	5386.1	264(13)		60.6(5.2)					
$D_{\epsilon\gamma\beta}{}^{\mathrm{a}}$				-19.0(4.6)					
$D_{\epsilon\delta\beta}{}^{\mathrm{a}}$				-27.7(2.4)					
$D_{\epsilon\delta\gamma}{}^{\mathrm{a}}$				-53.2(2.7)					

Continued on the next page

Table C.5 (continued)

	GRASP		AMBiT		Ref. [9]		Fit		
	Cal.	Exp.	Cal.	Exp.	Cal.	Exp.	Linear	QFS	New boson
$\upsilon_{ne}D_{\beta\gamma\alpha}$									54(17)
$\upsilon_{ne}D_{\beta\delta\alpha}$									51(15)
$\upsilon_{ne}D_{\beta\epsilon\alpha}$									55(17)
$\upsilon_{ne}D_{\delta\gamma\alpha}$									88(24)
$\upsilon_{ne}D_{\epsilon\gamma\alpha}$									-5(21)
$\upsilon_{ne}D_{\epsilon\delta\alpha}$									-20(17)
$\upsilon_{ne}D_{\delta\gamma\beta}$									-12(23)
$\upsilon_{ne}D_{\epsilon\gamma\beta}$									-58(19)
$\upsilon_{ne}D_{\epsilon\delta\beta}$									-57(18)
$\upsilon_{ne}D_{\epsilon\delta\gamma}$									-52(16)
$\chi^2_{\beta\gamma\alpha}$							10.532		
$\chi^2_{\beta\delta\alpha}$							10.9		
$\chi^2_{\beta\epsilon\alpha}$							8.724		
$\chi^2_{\delta\gamma\alpha}$							15.221		
$\chi^2_{\epsilon\gamma\alpha}$							0.065554		
$\chi^2_{\epsilon\delta\alpha}$							1.4067		
$\chi^2_{\delta\gamma\beta}$							0.23876		
$\chi^2_{\epsilon\gamma\beta}$							8.3928		
$\chi^2_{\epsilon\delta\beta}$							10.248		
$\chi^2_{\epsilon\delta\gamma}$							10.481		
$s_{\beta\gamma\alpha}$							3.2454σ		
$s_{\beta\delta\alpha}$							3.3015σ		
$s_{\beta\epsilon\alpha}$							2.9536σ		
$s_{\delta\gamma\alpha}$							3.9014σ		
$s_{\epsilon\gamma\alpha}$							0.25604σ		
$s_{\epsilon\delta\alpha}$							1.1861σ		
$s_{\delta\gamma\beta}$							0.48863σ		
$s_{\epsilon\gamma\beta}$							2.897σ		
$s_{\epsilon\delta\beta}$							3.2012σ		
$s_{\epsilon\delta\gamma}$							3.2375σ		

[a] At $m_\phi = 1\,\text{eV}$. Values over different m_ϕ's are shown in Fig. C-3

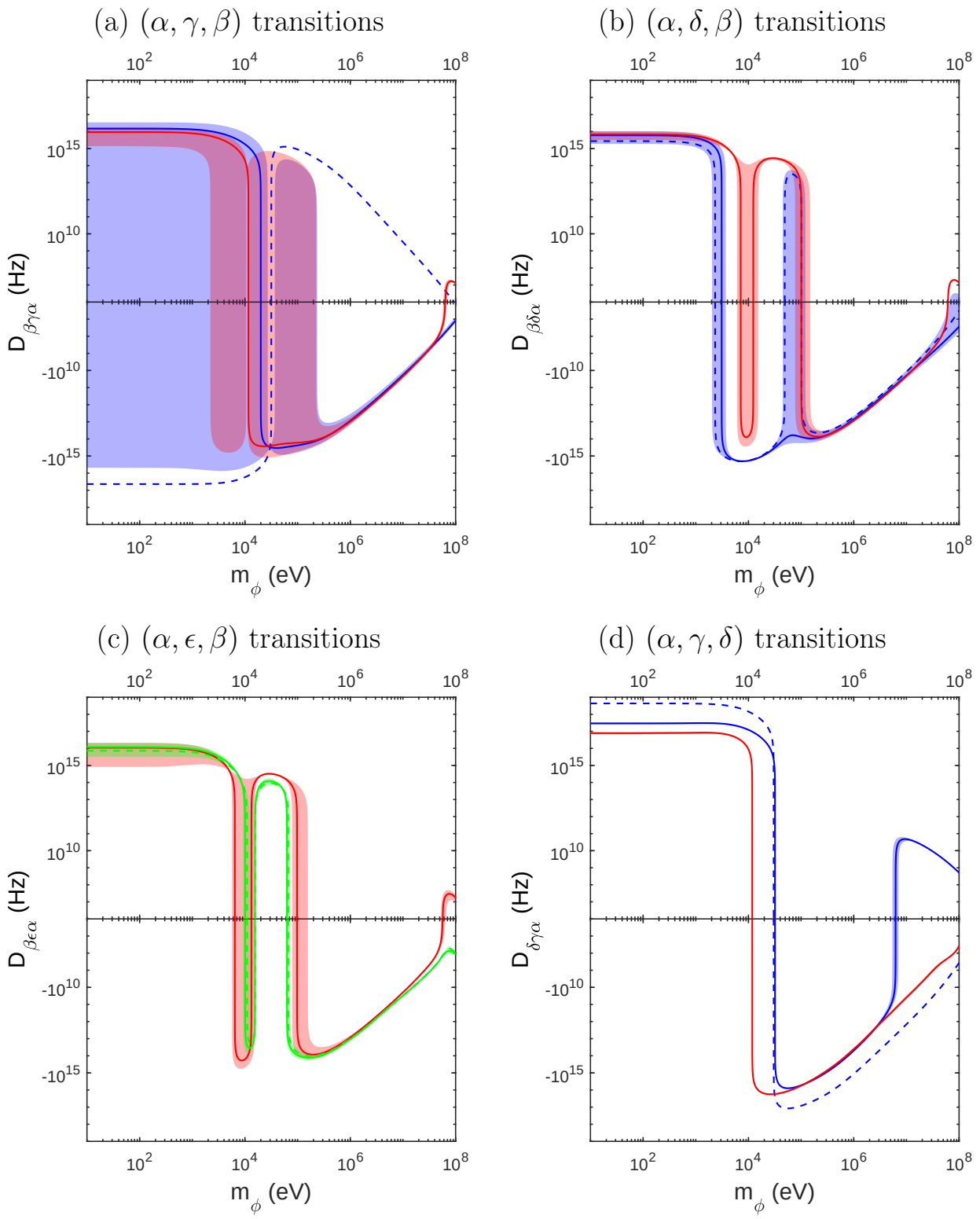

Figure C-3: Calculated $D_{\eta\kappa\chi}$ vs new-boson mass m_ϕ for all different choices of three transitions (χ, κ, η) out of five available transitions α, β, γ, δ, and ϵ, each corresponding to one of the subfigures (a – j). Solid lines correspond to the $D_{\eta\kappa\chi}$ obtained from $D_{\kappa\chi}$ and $D_{\eta\chi}$ in Fig. C-2, and $f_{\eta\chi\kappa} = G^{(4)}_{\eta\chi}/G^{(4)}_{\kappa\chi}$ ratio from the linear fit in 3D King plots (see Table C.5). (Figures and caption continue on the next page.)

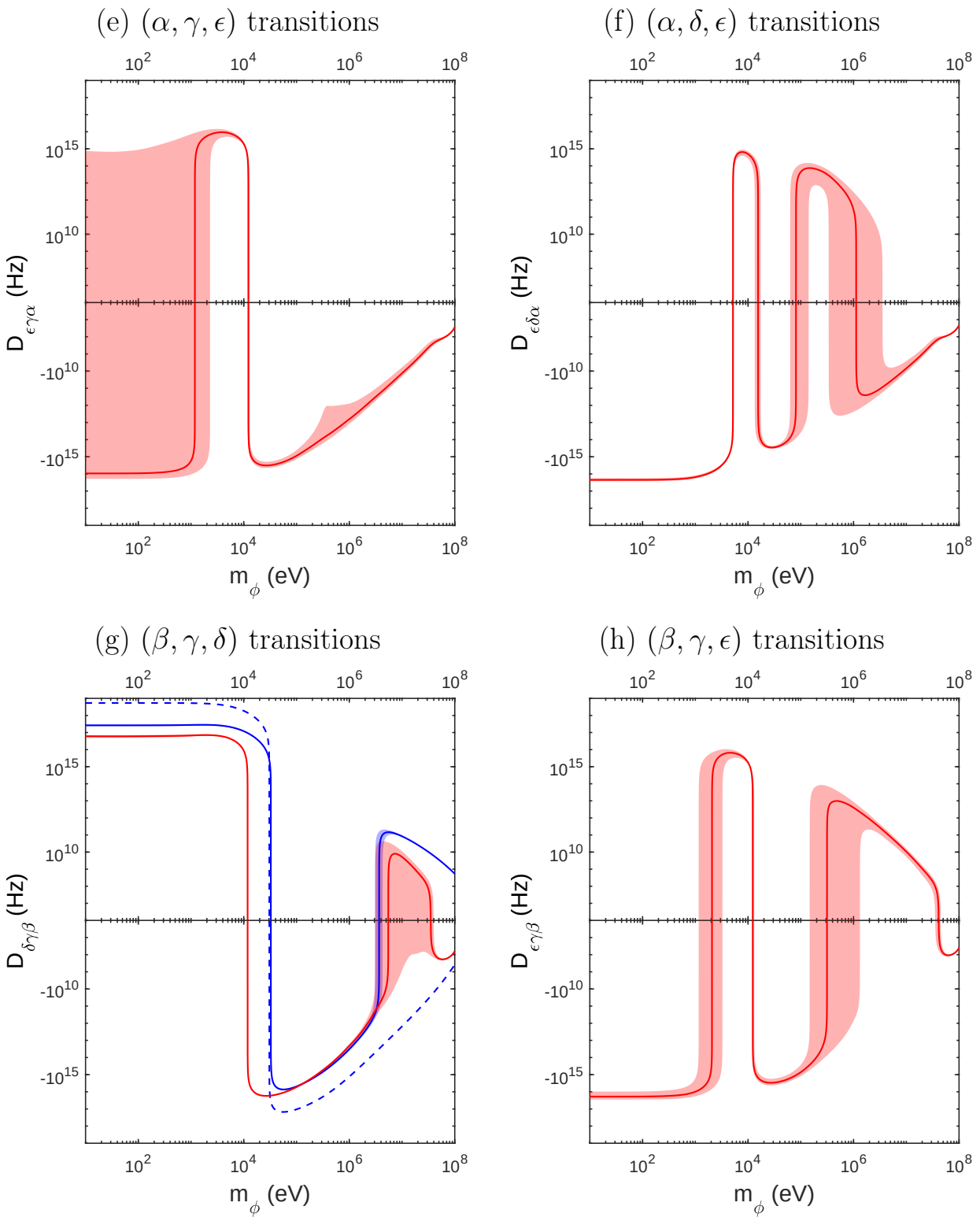

Figure C-3: (Continued) Shaded regions for $D_{\eta\kappa\chi}$ indicate 95% confidence intervals that arise from fitted $f_{\eta\chi\kappa}$'s uncertainty. Dashed lines show $D_{\eta\kappa\chi}$ calculated purely from ASCs (i.e., using calculated $f_{\eta\chi\kappa}$). Blue, red, and green colors correspond to ASCs performed using GRASP2018 [8, 24] (see Section 13), AMBiT [8, 23], and in Ref. [9], respectively. (Figures continued on the next page.)

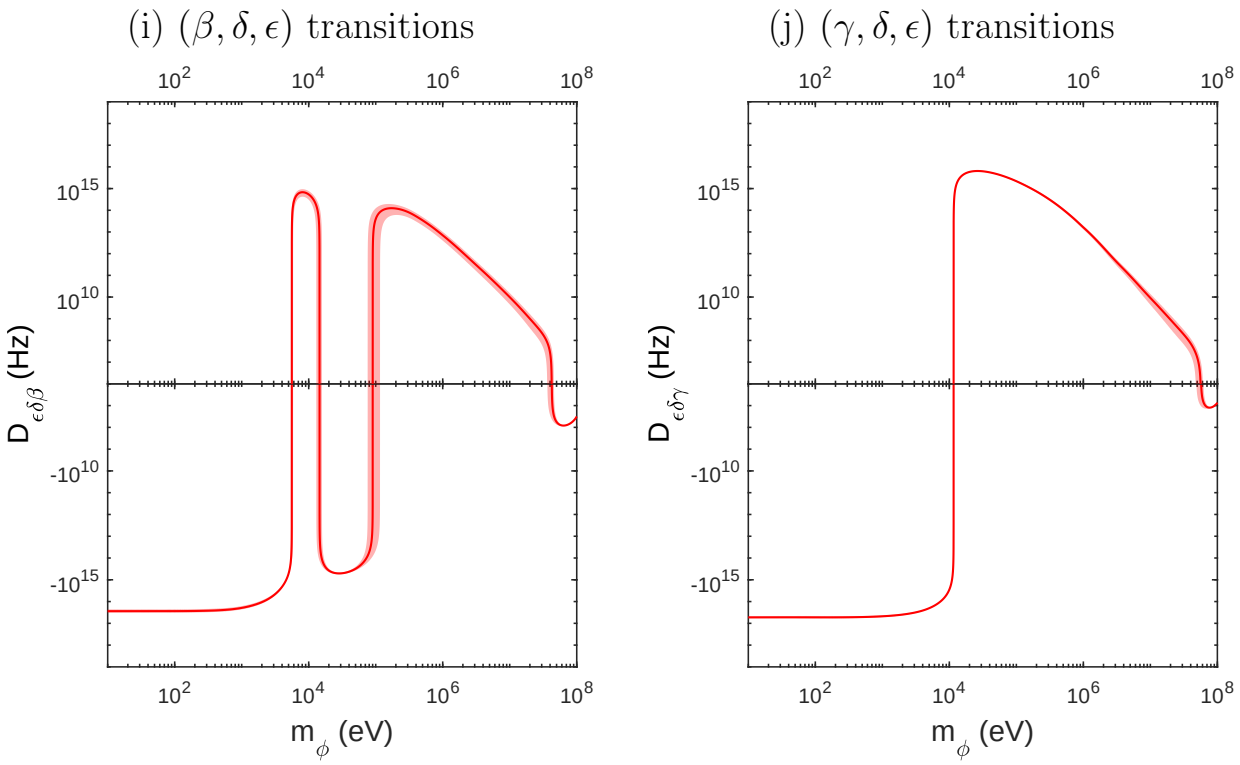

Figure C-3: (Continued)

Appendix D

Selection rules for Yb^+ clock transitions

The polarization and propagation direction of the probe beam that maximize the Rabi frequency ω_R of each Zeeman transition in the Yb^+ ions' optical clock transitions (see Fig. 3-1) are presented in this appendix.

For α: 411 nm and β: 436 nm transitions , the results are summarized in Figs. D-1 and D-2, respectively. Only the Zeeman shifts of the transitions are shown in Fig. D-3 for γ: 467 nm transitions, however; the selection rules and transition amplitudes for the γ transition can be found in Ref. [265].

A note on the theory of electric multipole transitions as well as the full derivation of the selection rules and relative transition rates of the Zeeman transitions for the α transition follow at the end of this appendix, in which some of the errors are corrected by Eugene Knyazev, a research team member (with possible further errors).

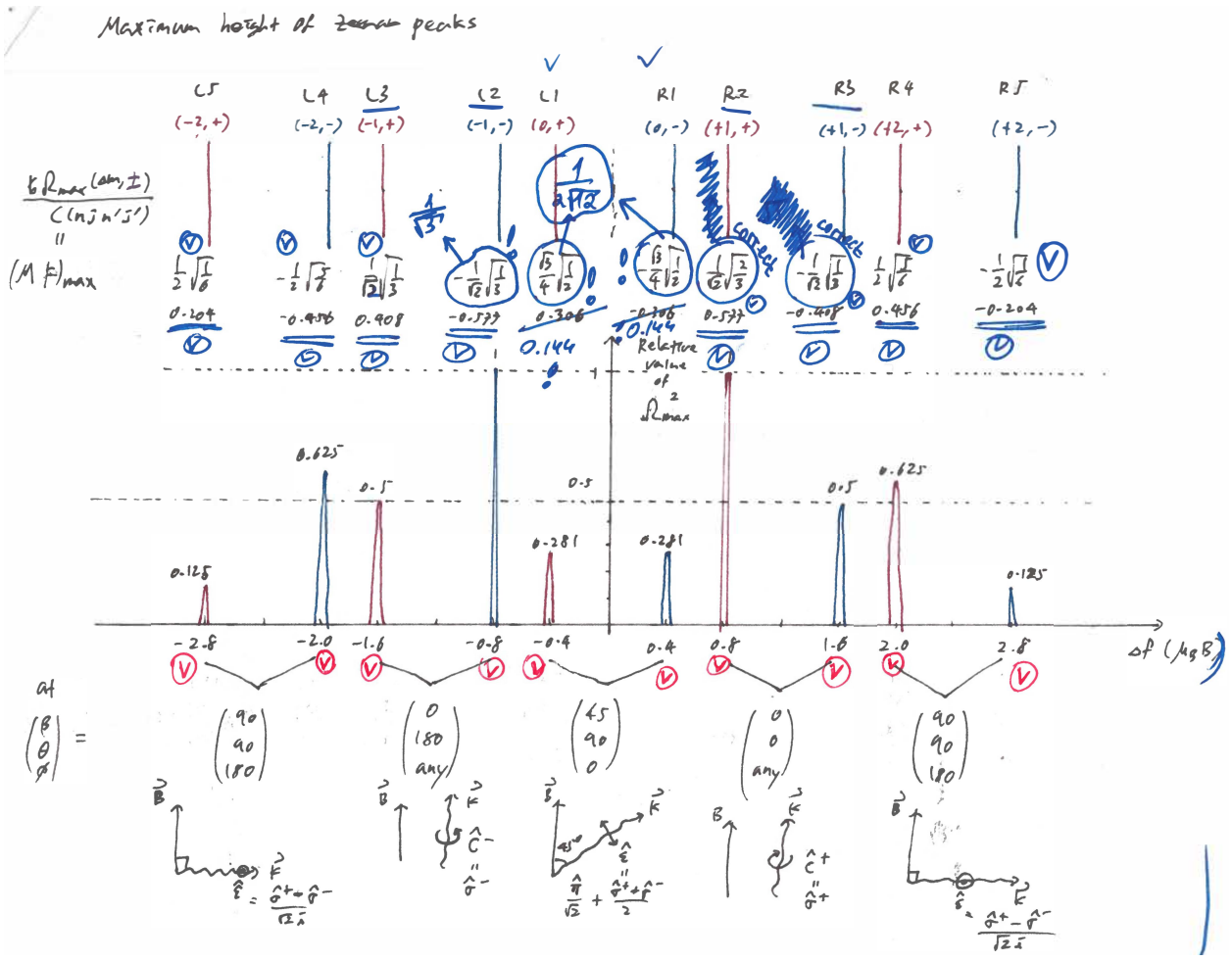

Figure D-1: The polarization $\hat{e}$ and propagation direction $\hat{k}$ of the probe beam, with respect to the quantization axis along magnetic field $\mathbf{B}$, that maximize the Rabi frequency ω_R for each Zeeman transition, and the relative magnitudes of the maximum squared Rabi frequencies ω_R^2 for α: 411 nm transition in Yb^+ ions [see also Fig. 5-2(a)]. Each peak is labeled by the change in magnetic quantum number $\Delta m = m_D - m_S$ from the $^2S_{1/2}$ ground state to $^2D_{5/2}$ excited state, and the m_S of the ground Zeeman level that the transitions starts from [e.g., $(\Delta m, \mathrm{sgn}(m_S)) = (+1, +)$ or $(-2, -)$]. The position of each peak in the x axis shows the g factor of the transition (i.e., Zeeman shift from the zero-field transition frequency in the unit of $\mu_B B$). Some errors were corrected by Eugene Knyazev.

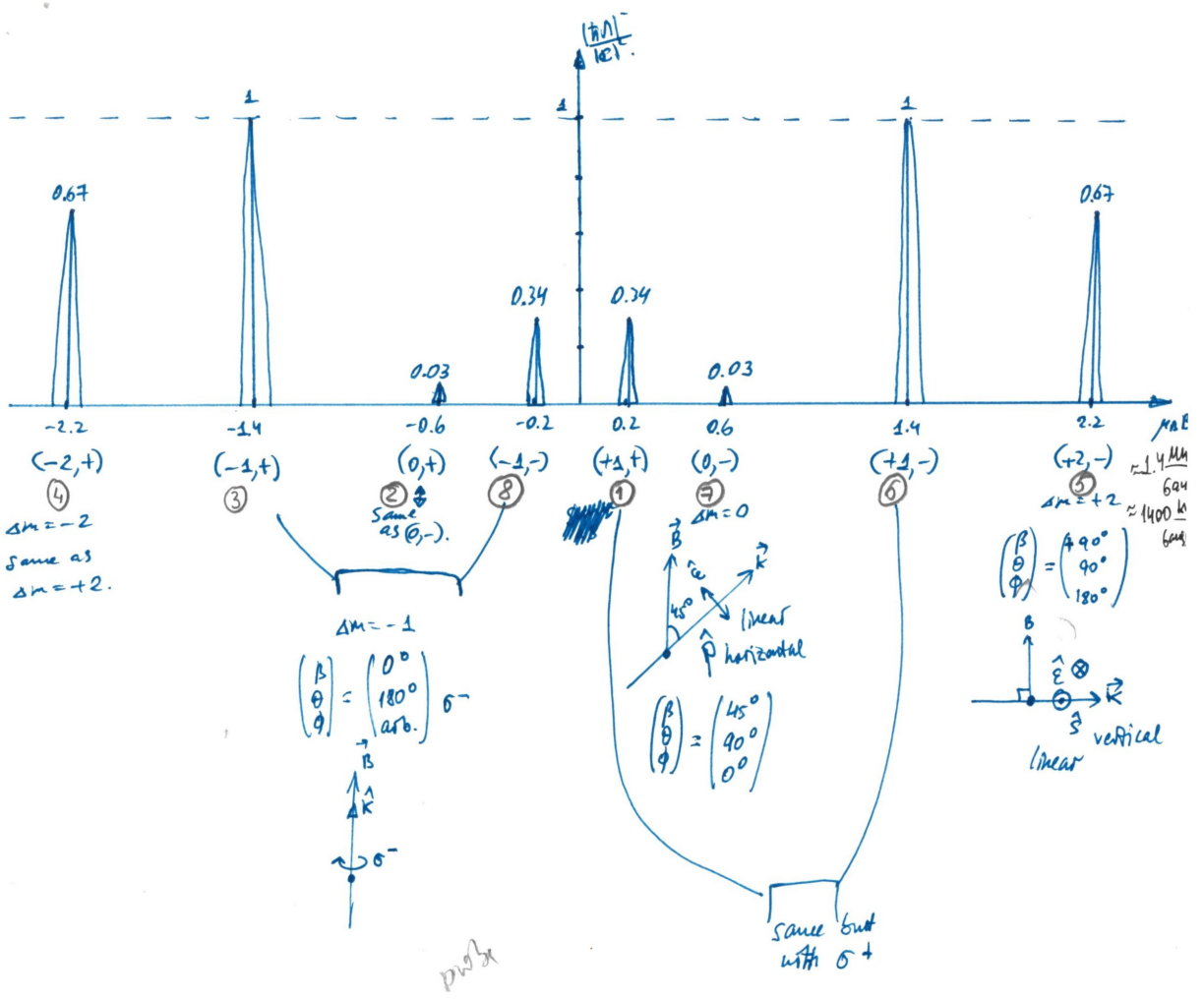

Figure D-2: The same illustration to Fig. D-1 for β: 436 nm transition in Yb^+ ions [see also Fig. 5-2(b)] derived by Eugene Knyazev.

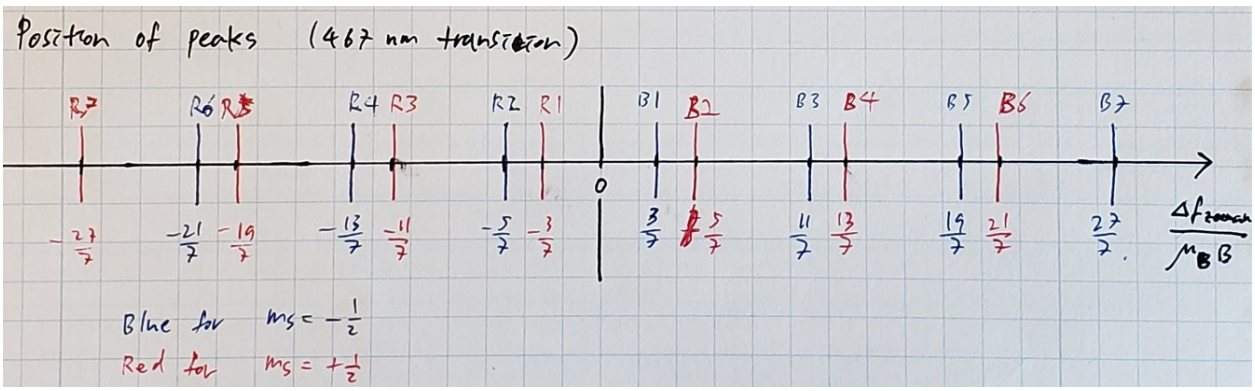

Figure D-3: The shifts of Zeeman transitions in γ: 467 nm transition in Yb^+ ions in the unit of $\mu_B B$ [see also Fig. 5-2(c)]. The Zeeman transitions shown as blue and red lines start from $m_S = -\frac{1}{2}$ and $\frac{1}{2}$ ground-state Zeeman levels, respectively.

$$H_{int} = \vec{d}\cdot\vec{E}(\vec{r}) \quad \leftarrow \text{assumes atom at origin } (\vec{R}=0)$$

$$= -e\vec{r}\cdot\hat{\varepsilon}\, E_0 e^{i\vec{k}\cdot\vec{r}} \quad \leftarrow H_{int}^{(0)},\ H_{int}^{(1)},\ H_{int}^{(2)}$$

polarization

$$e^{i\vec{k}\cdot\vec{r}} \hookrightarrow 1 + i\vec{k}\cdot\vec{r} + \frac{i^2}{2}(\vec{k}\cdot\vec{r})^2 + \cdots$$

E1, B0, E2 | B1, E3

$$Y_{l=0}^{m=0} = \sqrt{\frac{1}{4\pi}} = \text{const.}$$

$$Y_1^0 = \sqrt{\frac{3}{4\pi}}\cos\theta = \sqrt{\frac{3}{4\pi}}\frac{z}{r}$$

$$Y_1^{\pm} = \mp\sqrt{\frac{3}{4\pi}}\frac{1}{\sqrt{2}}\sin\theta\, e^{\pm i\phi} = \mp\sqrt{\frac{3}{4\pi}}\frac{x\pm iy}{\sqrt{2}r}$$

$$(x\hat{x}+y\hat{y}+z\hat{z})\cdot\hat{\varepsilon} \quad \leftarrow \hat{\pi}=\hat{z},\ \hat{\sigma}^{\pm} = \frac{\hat{x}\pm i\hat{y}}{\sqrt{2}},\ \hat{\sigma}^{\pm *} = \hat{\sigma}^{\mp},\ \hat{\pi}^{*} = \hat{\pi}$$

$$= \left(\frac{x+iy}{\sqrt{2}}\hat{\sigma}^{+*} + \frac{x-iy}{\sqrt{2}}\hat{\sigma}^{-*} + z\hat{\pi}^{*}\right)\cdot\hat{\varepsilon}$$

$$= r\sqrt{\frac{4\pi}{3}}\left(Y_1^{+1}\hat{\sigma}^{+*} + Y_1^{-1}\hat{\sigma}^{-*} + Y_1^{0}\hat{\pi}^{*}\right)\cdot\hat{\varepsilon} \quad \leftarrow \hat{\varepsilon}\cdot\hat{\varepsilon}^{*} = \delta_{\varepsilon\varepsilon'}: \text{orthogonality relation}$$

$$= r\sqrt{\frac{4\pi}{3}}\left(\underbrace{\varepsilon_{\sigma+}}_{\varepsilon_{+1}} Y_1^{+1} + \underbrace{\varepsilon_{\sigma-}}_{\varepsilon_{-1}} Y_1^{-1} + \underbrace{\varepsilon_{\pi}}_{\varepsilon_0} Y_1^{0}\right) \quad \text{for polarization } \hat{\varepsilon} = \underbrace{\varepsilon_{\sigma+}}_{\frac{\varepsilon_x - i\varepsilon_y}{\sqrt{2}}}\hat{\sigma}^{+} + \underbrace{\varepsilon_{\sigma-}}_{\frac{\varepsilon_x+i\varepsilon_y}{\sqrt{2}}}\hat{\sigma}^{-} + \underbrace{\varepsilon_{\pi}}_{\varepsilon_z}\hat{\pi}$$

$$= r\sqrt{\frac{4\pi}{3}}\sum_{\Delta m_p}\varepsilon_{\Delta m_p} Y_1^{\Delta m_p}, \quad \boxed{\Delta m_p = 0, \pm 1} \quad \leftarrow \Delta m \text{ from polarization}$$

1. $H_{int}^{(0)} = -\sqrt{\frac{4\pi}{3}}\, er \sum_{\Delta m_p}\varepsilon_{\Delta m_p} Y_1^{\Delta m_p}$

$$\hbar\Omega = \langle n'j'm'|H_{int}^{(0)}|njm\rangle$$

$$= -\sqrt{\frac{4\pi}{3}}\, e\langle n'|r|n\rangle\sum_{\Delta m_p}\varepsilon_{\Delta m_p}\langle j'm'|Y_1^{\Delta m_p}|jm\rangle$$

$$= -\sqrt{\frac{4\pi}{3}}\, e\langle n'|r|n\rangle\frac{\langle j'||Y_1||j\rangle}{\sqrt{2j'+1}}\sum_{\Delta m_p}\varepsilon_{\Delta m_p}\langle jm\,1\,\Delta m_p|j'm'\rangle$$

determined by levels ↑ depends on polarization

$\vec{J}' = \vec{J} + \vec{L}$, $l=1$ ↪ $J \to J', J\pm1, J$; 1

From $\langle jm10|jm\rangle = \frac{m}{\sqrt{j(j+1)}}$ (Wikt), $\langle J'0\,1\,0|J0\rangle = 0 \Rightarrow \Delta J = 0$ is forbidden!

$\Rightarrow \boxed{\Delta J = \pm 1}$ by triangle rule & $\boxed{\Delta m = \Delta m_p}$ as $m' = m + \Delta m_p$.

Δm goes with polarization of light.

Wigner-Eckart theorem:

$$\langle j'm'|Y_k^q|jm\rangle = \frac{(-1)^{2k}\langle j'||Y_k||j\rangle}{\sqrt{2j'+1}}\langle jmkq|j'm'\rangle \quad \text{Clebsch-Gordan coefficient.}$$

$$= (-1)^{j'-m}\langle j'||Y_k||j\rangle\begin{pmatrix} j' & k & j \\ -m' & q & m\end{pmatrix} \quad \text{Wigner 3j symb}$$

2. $H_{int}^{(1)} = -\sqrt{\frac{4\pi}{3}}\, er\sum_{\Delta m_p}\varepsilon_{\Delta m_p} Y_1^{\Delta m_p}\,(i\vec{k}\cdot\vec{r})$

$$\vec{k}\cdot\vec{r} \hookrightarrow \frac{k_x - ik_y}{\sqrt{2}}\frac{x+iy}{\sqrt{2}} + \frac{k_x+ik_y}{\sqrt{2}}\frac{x-iy}{\sqrt{2}} + k_z z$$

$$\leftarrow \vec{k} = \sum_k k\hat{k}_i\hat{e}_{\pi}, \quad k = |\vec{k}|$$

$$= r\sqrt{\frac{4\pi}{3}}k\left(\underbrace{\frac{\hat{k}_x - i\hat{k}_y}{\sqrt{2}}}_{\equiv\hat{k}_{+1}} Y_1^{+1} + \underbrace{\frac{\hat{k}_x+i\hat{k}_y}{\sqrt{2}}}_{\equiv\hat{k}_{-1}} Y_1^{-1} + \underbrace{\hat{k}_z}_{\equiv\hat{k}_0} Y_1^{0}\right)$$

$$\vec{k} = k(\hat{k}_0\hat{\pi} + \hat{k}_{+1}\hat{\sigma}^{+} + k_{-1}\hat{\sigma}^{-})$$

$$= kr\sqrt{\frac{4\pi}{3}}\sum_{\Delta m_g}\hat{k}_{\Delta m_g} Y_1^{\Delta m_g}, \quad \boxed{\Delta m_g = 0, \pm 1}: \Delta m \text{ from field gradient}$$

$$= -i\frac{4\pi}{3}\, ekr^2\sum_{\Delta m_p}\sum_{\Delta m_g}\varepsilon_{\Delta m_p}\hat{k}_{\Delta m_g} Y_1^{\Delta m_p} Y_1^{\Delta m_g}$$

$$Y_{l_1}^{m_1}\cdot Y_{l_2}^{m_2} = \sum_{l,m}\sqrt{\frac{(2l_1+1)(2l_2+1)(2l+1)}{4\pi}}\begin{pmatrix} l_1 & l_2 & l \\ m_1 & m_2 & m\end{pmatrix} Y_l^{*m}\begin{pmatrix} l_1 & l_2 & l \\ 0 & 0 & 0\end{pmatrix}$$

$$= \sum_{l,m}\sqrt{\frac{(2l_1+1)(2l_2+1)}{4\pi(2l+1)}}\langle l_1 0\, l_2 0|l0\rangle\langle l_1 m_1\, l_2 m_2|lm\rangle Y_l^m$$

$\hookrightarrow |l_1 - l_2| \le l \le l_1 + l_2$

$m = m_1 + m_2$ & $|m| \le l$

$$H^{(1)}_{int} = -i\frac{4\pi}{3} ekr^2 \sum_{\Delta m_p}\sum_{\Delta m_s} \varepsilon_{\Delta m_p} \hat{k}_{\Delta m_s} \sum_{l\Delta m} \sqrt{\frac{3\cdot 3}{4\pi(2l+1)}} \langle 1010|l0\rangle \langle 1\Delta m_p 1\Delta m_s | l\Delta m\rangle Y_l^{\Delta m}$$

$$= -i\sqrt{4\pi}\, ekr^2 \sum_{\Delta m_p}\sum_{\Delta m_s} \varepsilon_{\Delta m_p}\hat{k}_{\Delta m_s} \times \sum_{lm} \frac{1}{\sqrt{2l+1}} \langle 1010|l0\rangle \langle 1\Delta m_p|\Delta m_s (l\Delta m)\rangle Y_l^{\Delta m}$$

$\langle 1010|00\rangle = -\sqrt{\frac{1}{3}}$
$\langle 1010|10\rangle = 0 \Rightarrow l = 0, 2$
$\langle 1010|20\rangle = \sqrt{\frac{2}{3}}$

$\Delta m = 0$ if $l = 0$ (must be)
$\boxed{\Delta m = \Delta m_p + \Delta m_s}$ if $l = 2$.

$$= -i\sqrt{4\pi}\, ekr^2 \times \Big[\sum_{\Delta m_p = -\Delta m_s} \varepsilon_{\Delta m_p} \hat{k}_{\Delta m_s} \left(-\sqrt{\tfrac{1}{3}}\right) \langle 1\Delta m_p | \Delta m_s | 00\rangle Y_0^0$$

$\sqrt{\frac{1}{3}}$ for $m_1 m_2 = 1\,-1$ or $-1\,1$; $-\sqrt{\frac{1}{3}}$ for $0\,0$

$$\hookrightarrow = \left(-\sqrt{\tfrac{1}{3}}\right)\frac{1}{\sqrt{4\pi}}\left(+\sqrt{\tfrac{1}{2}}\varepsilon_{+1}\hat{k}_{-1} + \sqrt{\tfrac{1}{2}}\varepsilon_{-1}\hat{k}_{+1} - \sqrt{\tfrac{1}{2}}\varepsilon_0\hat{k}_0\right)$$

$\varepsilon_{+1}\hat{k}_{-1} + \varepsilon_{-1}\hat{k}_{+1} + \varepsilon_0\hat{k}_0 = \hat{\varepsilon}\cdot\hat{k} = 0$
$\varepsilon_0 = \varepsilon_\pi$, $\hat{k}_0 = \hat{k}_\pi$

$$= -\sqrt{\tfrac{1}{3}} \times \sqrt{\tfrac{1}{4\pi}}\left(\sqrt{\tfrac{1}{2}}\,\hat{\varepsilon}\cdot\hat{k}^{\,0} - 2\times\sqrt{\tfrac{1}{2}}\,\varepsilon_\pi\hat{k}_\pi\right)$$

$$= +\frac{2}{3}\sqrt{\frac{1}{4\pi}}\,\varepsilon_\pi\hat{k}_\pi \rightarrow H^{(1)}_{int,1} = -i\tfrac{2}{3}ekr^2\varepsilon_\pi\hat{k}_\pi$$

$$+ \sum_{\Delta m_p}\sum_{\Delta m_s} \varepsilon_{\Delta m_p}\hat{k}_{\Delta m_s}\frac{1}{\sqrt{5}} \times \sqrt{\tfrac{2}{3}}\langle 1\Delta m_p 1\Delta m_s|2\Delta m\rangle Y_2^{\Delta m}$$

$$\hookrightarrow H^{(1)}_{int,2} = -i\sqrt{\frac{8\pi}{15}}ekr^2 \sum_{\Delta m_p}\sum_{\Delta m_s} \varepsilon_{\Delta m_p}\hat{k}_{\Delta m_s}\langle 1\Delta m_p 1\Delta m_s|2\Delta m\rangle Y_2^{\Delta m}$$

$\hookrightarrow \sqrt{\frac{1}{6}\binom{2}{1+\Delta m_p}\binom{2}{1-\Delta m_p}}$

$\langle n'j'm'|H^{(1)}_{int,1}|njm\rangle$

$= -i\frac{2}{3}ek\,\varepsilon_\pi k_\pi \langle n'|r^2|n\rangle\langle j'm'|jm\rangle \Rightarrow \Delta j = 0, \Delta m = 0.$

$\langle n'j'm'|H^{(1)}_{int,2}|njm\rangle$

$$= -i\sqrt{\frac{8\pi}{15}}ek\langle n'|r^2|n\rangle \sum_{\Delta m_p}\sum_{\Delta m_s}\varepsilon_{\Delta m_p}\hat{k}_{\Delta m_s}\langle 1\Delta m_p 1\Delta m_s|2\Delta m\rangle \langle j'm'|Y_2^{\Delta m}|jm\rangle$$

$$= -i\frac{1}{5}\sqrt{\frac{8\pi}{3}}ek\, r^2_{n'n}\,(-1)^{2J-j'}\langle j'\|Y_2\|j\rangle \leftarrow \text{transition levels}$$

$$\times \sum_{\Delta m_p}\sum_{\Delta m_s}\varepsilon_{\Delta m_p}\hat{k}_{\Delta m_s}\langle 1\Delta m_p 1\Delta m_s|2\Delta m\rangle \leftarrow \text{polarization \& propagation direction}$$

$$\times \langle j(-m)j'm'|2\Delta m\rangle \leftarrow \text{CG of each transition}$$

↑ or $\langle j'm'j(-m)|2\Delta m\rangle$ with $(-1)^{-j}$ instead of $(-1)^{2J-j'}$

$$\frac{\langle J'\|Y_2\|J\rangle}{\sqrt{2J'+1}}\langle Jm\,2\Delta m|J'm'\rangle$$

$$= (-1)^{2J-J'-m'}\frac{\langle j'\|Y_2\|j\rangle}{\sqrt{5}}\langle j(-m)j'm'|2\Delta m\rangle$$

$\boxed{|\Delta j| \le 2}$ $\boxed{\Delta m \le \Delta j \le ?}$

$\boxed{m' - m = \Delta m = \Delta m_p + \Delta m_s}$

$\langle J_1 m_1 J_2 m_2|Jm\rangle = (-1)^{j_1 - m_1}\sqrt{\frac{2J+1}{2J_2+1}} \times \langle J_1 m_1 J(-m)|J_2(-m_2)\rangle$

$= (-1)^{2J_1 + J_2 - J + m_1}\sqrt{\frac{2J+1}{2J_2+1}} \times \langle J_1(-m_1)Jm|J_2 m_2\rangle$

Short story :

By expanding spatial dependent term of field one get many orders of position operator in dipole interaction Hamiltonian

$$H_{int} = \vec{d}\cdot\vec{E}(\vec{r}) \propto (\vec{d}\cdot\hat{\varepsilon})\left(1 + i\vec{k}\cdot\vec{r} + \frac{i^2}{2}(\vec{k}\cdot\vec{r})^2 + \frac{i^3}{3!}(\vec{k}\cdot\vec{r})^3 + \cdots\right)$$

While dipole term $\vec{d}\cdot\hat{\varepsilon}$ corresponds to $Y_{l=1}^{\Delta m_p}$, like angular momentum with $l=1$ and $m=\Delta m_p$ chosen by polarization $\hat{\varepsilon}$, n^{th}-order spatial term of field $\frac{i^n}{n!}(\vec{k}\cdot\vec{r})^n$ corresponds to $Y_{l_3=n}^{\Delta m_g}$, like angular momentum with magnitude $l=n$ and $m=\Delta m_g$ given by direction of beam $\hat{k}$. As it will be shown, Δm_p, Δm_g are angular momentum transfer along quantization axis from photon and field gradient, respectively.

Then n^{th} term gives product of two angular momentums which can be expanded to possible total angular momentums from two angular momentum :

$$Y_{l=1}^{\Delta m_p} \times Y_{l=n}^{\Delta m_g} = \sum_L C_L^M Y_L^M$$

which implies, from triangular rule of ang. mom. sum, $|l_1-l_2| \le L \le l_1+l_2$, possible L's are $n-1, n, n+1$, Furthermore, for a reason, $L=n$ are forbidden (i.e, $C_n^0=0$), and possible $L = n\pm1$.

On the other hand, M must be sum of those of two angular momentum, $\Delta m_p + \Delta m_g$.

For each angular momentum Y_L^M, it adds to initial angular momentum of atom (j,m) and atoms state ends up to (j',m'). That is, $|j-L| \le j' \le j+L$, $M = \Delta m_p + \Delta m_g$ or $|\Delta j| \le L = n\pm1$, $\Delta m = M = \Delta m_p + \Delta m_p$.

Now you can see two important consequence.

1) n^{th}-term makes $E(n+1)$ and $M(n)$ transitions, of which $|\Delta j| \le n+1$, $|\Delta j| \le n-1$ up to spin term $\vec{S}\cdot\vec{B}$, respectively, in leading order.

   ex) $n=0 \Rightarrow$ E1 : electric dipole transition. $S_{1/2} \to D_{5/2}$

   $n=1$: $(\vec{d}\cdot\hat{\varepsilon})\vec{k}\cdot\vec{r}$: E2 : electric quadrupole transition, M1

   $n=2$: E3 : " octopole ", M2. $\to S_{1/2} \to F_{7/2}$

   ⋮

2) Angular momentum of atom along quantization axis changes by those of photon and field gradient, given by polarization and beam direction. As maximum of ang. mom. of field gradient Δm_g is $l_g=n$, maximum Δm of transition $(j,m) \to (j',m')$ is $n+1$, i.e. $|\Delta m| \le n+1$. ex) E2 gives $|\Delta m| \le 2$

   There can be more than one combination $(\Delta m_p, \Delta m_g)$ for given Δm, and they can interfere constructively / distructively. Ex) $\Delta m = 0$ of $^2S_{1/2} \to {}^2D_{5/2}$ at $\vec{k} \perp \vec{B}$ is forbidden by distructive interference of $(\Delta m_p, \Delta m_g) = (-1,1)$ and $(1,-1)$

Ex. $^2S_{1/2} \to {}^2D_{5/2}$ (411 nm)

$J = \frac{1}{2}$ $\quad j' = \frac{5}{2}$ $\quad \Delta J = 2$

$m = \pm\frac{1}{2}$ $\quad m' = \pm\frac{1}{2}, \pm\frac{3}{2}, \pm\frac{5}{2}$

$\| \quad \| \quad \| \quad \| \quad \| \quad \|$

$m_s \quad m_p$

$\langle n'j'm' | H^{(1)}_{int} | njm \rangle$

$= -i\frac{1}{\hbar}\sqrt{\frac{\pi}{3}}\, e k \hat{r}_{nn'} (-1)^{-j} \langle j' \| Y_2 \| j \rangle$

$= C(njn'j') \cdot \sum_{\Delta m_p} \sum_{\Delta m_s} \xi_{\Delta m_p} \hat{k}_{\Delta m_s} \langle 1\, \Delta m_p\, 1\, \Delta m_s | 2\, \Delta m \rangle \langle \frac{5}{2}\, m' \frac{1}{2}\, (-m) | 2\, \Delta m \rangle$

deduced from general solution of CG coeff. →

$\delta_{\Delta m_p + \Delta m_s, \Delta m} \sqrt{\frac{1}{6}\binom{2+\Delta m}{1+\Delta m_p}\binom{2-\Delta m}{1-\Delta m_p}} \equiv G(\Delta m_p, \Delta m_s)$

$\times \delta_{\Delta m_p + \Delta m_s, \Delta m}$

$\langle J_1\, (m \mp \frac{1}{2})\, \frac{1}{2}\, (\pm\frac{1}{2}) | (J_1 \mp \frac{1}{2})\, m \rangle = \mp\sqrt{\frac{1}{2}\left(1 \mp \frac{m}{J_1 + \frac{1}{2}}\right)}$

$\langle J_1\, (m \mp \frac{1}{2})\, \frac{1}{2}\, (\pm\frac{1}{2}) | (J_1 + \frac{1}{2})\, m \rangle = \sqrt{\frac{1}{2}\left(1 \pm \frac{m}{J_1 + \frac{1}{2}}\right)}$

$\Rightarrow \langle \frac{5}{2}\, m' \frac{1}{2}\, (-(\pm\frac{1}{2})) \| 2\, \Delta m \rangle$

$\| \quad \| \quad \| \quad \| \quad \| \quad \|$

$F(\Delta m, \pm) \quad = \pm\sqrt{\frac{1}{2}\left(1 \pm \frac{\Delta m}{3}\right)}$

m_s

Depends on Δm of ground state!

Δm_p	Δm_s	Δm	
+1	+1	+2	1
+1	0	+1	$\sqrt{\frac{1}{2}}$
+1	−1	0	$\sqrt{\frac{1}{6}}$
0	0	0	$\sqrt{\frac{2}{3}}$

$G(\Delta m_p, \Delta m_s) = G(\Delta m_s, \Delta m_p) = G(-\Delta m_p, -\Delta m_s)$

← Note: symmetry factor for interchanging m's or swapping $\vec{J}_1$ and $\vec{J}_2$ in $\langle J_1 m_1 J_2 m_2 | J m \rangle$ is $(-1)^{J - J_1 - J_2}$

$\hbar\Omega(\Delta m, \pm) = C(njn'j') \, \delta_{\Delta m_p + \Delta m_s, \Delta m}$

$\times \sum_{\Delta m_p} \xi_{\Delta m_p} \sum_{\Delta m_s} \hat{k}_{\Delta m_s} G(\Delta m_p, \Delta m_s) F(\Delta m, \pm)$

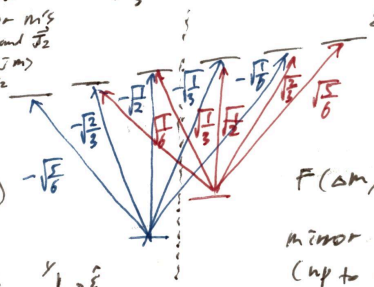

$F(\Delta m, +) = -F(-\Delta m, -)$

mirror anti-symmetry! (up to zeeman shift) as like position of zeeman levels.

Since $G(\Delta m_p, \Delta m_s)$ are the same for the same $|\Delta m|$, symmetric zeeman peaks from ground has the same GF. (that is, same peak height if component $\xi_{\Delta m_p} \hat{k}_{\Delta m_s}$ and initial population in each m_s state are the same)

Special cases:

1) $\hat{\varepsilon}$ linear $\perp \hat{\pi}$, $\hat{k} \parallel \hat{\pi}$

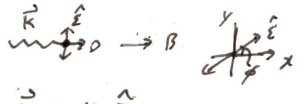

$\Rightarrow \hat{\varepsilon} = \frac{e^{-i\varphi}}{\sqrt{2}}\hat{\sigma}^+ + \frac{e^{+i\varphi}}{\sqrt{2}}\hat{\sigma}^-$, $\quad \vec{k} = k\hat{\pi}$

$\Rightarrow k_{\Delta m_s} = \delta_{0, \Delta m_s}$

$\xi_0 = 0$

$\xi_{\pm 1} = \frac{e^{\mp i\varphi}}{\sqrt{2}}$

← No ang. mom. from field gradient.

$\hbar\Omega(\Delta m, \pm) \propto \xi_{\Delta m} \hat{k}_0 G(\Delta m, 0) F(\Delta m, \pm)$ where $\Delta m = \Delta m_p \pm 1$

$= \begin{cases} \frac{e^{-i\varphi}}{\sqrt{2}} \frac{1}{\sqrt{2}} F(+1, \pm) = \pm\frac{e^{\mp i\varphi}}{2}\sqrt{\frac{2}{3}} \\ \frac{e^{+i\varphi}}{\sqrt{2}} \frac{1}{\sqrt{2}} F(-1, \mp) = \pm\frac{e^{\pm i\varphi}}{2}\sqrt{\frac{1}{3}} \end{cases}$

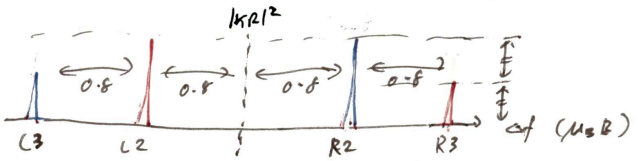

Special case 2) $\hat{\varepsilon} \parallel \hat{\pi}$, $\hat{k} \perp \hat{\pi}$

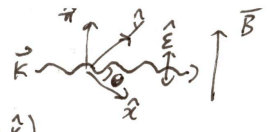

$\varepsilon_0 = 1$, $\varepsilon_{\pm 1} = 0$ $\Rightarrow$ $\Delta m_p = 0$

$\vec{k} = k(\cos\theta\,\hat{x} + \sin\theta\,\hat{y}) = k\,\frac{e^{-i\theta}\hat{\sigma}^+ + e^{+i\theta}\hat{\sigma}^-}{\sqrt{2}}$ $\Rightarrow$ $\hat{k}_0 = 0$, $\hat{k}_{\pm 1} = \frac{e^{\mp i\theta}}{\sqrt{2}}$ $\Rightarrow$ $\Delta m_g = \pm 1$

given that $G(\Delta m_p, \Delta m_g) = G(\Delta m_g, \Delta m_p)$

and F depends on Δm, as well as corresponding $\varepsilon_{\Delta m_p}$ $\hat{k}_{\Delta m_g}$ are the same, (up to phase)

spectrum should be the same to that in case 1.

3) $\hat{\varepsilon} \perp \hat{\pi}$, $\hat{k} \perp \hat{\pi}$

$\hat{k} \parallel \hat{x}$, $\hat{\varepsilon} \parallel \hat{y}$ without loss of generality.

$\Rightarrow \hat{k} = k\,\frac{\hat{\sigma}^+ + \hat{\sigma}^-}{\sqrt{2}}$ $\Rightarrow$ $\hat{k}_0 = 0$, $\hat{k}_{\pm 1} = \frac{1}{\sqrt{2}}$ $\Rightarrow \Delta m_g = \pm 1$

$\hat{\varepsilon} = \frac{\hat{\sigma}^+ - \hat{\sigma}^-}{\sqrt{2}i}$ $\Rightarrow$ $\varepsilon_0 = 0$, $\varepsilon_{\pm 1} = \mp\frac{i}{\sqrt{2}}$ $\Rightarrow \Delta m_p = \pm 1$

$\Rightarrow \Delta m = 0, \pm 2$.

$\Delta m = +2$: $\Delta m_p = \Delta m_g = +1$ $\Rightarrow$ $G(+1, +1) = 1$

$F(2, \pm) = \begin{cases} \sqrt{\frac{3}{5}} : + \\ -\sqrt{\frac{1}{5}} : - \end{cases}$

$\varepsilon_{+1}\hat{k}_{+1} = -\frac{i}{2}$

$\Rightarrow \hbar R(+2, \pm) = \begin{cases} -\frac{i}{2}\sqrt{\frac{3}{5}} : + \rightarrow R3 \\ +\frac{i}{2}\sqrt{\frac{1}{5}} : - \rightarrow R5 \end{cases}$

$\Delta m = -2$: $G(-1, -1) = G(1, 1) = 1$

$F(-2, \mp) = -F(2, \pm) = \begin{cases} -\sqrt{\frac{3}{5}} : - \\ +\sqrt{\frac{1}{5}} : + \end{cases}$

$\varepsilon_{-1}\hat{k}_{-1} = \frac{i}{2}$

$\Rightarrow \hbar R(-2, \mp) = \begin{cases} -\frac{i}{2}\sqrt{\frac{3}{5}} \rightarrow L3 \\ \frac{i}{2}\sqrt{\frac{1}{5}} \rightarrow L5 \end{cases} = \hbar R(2, \pm)$.

$\Delta m = 0$: $(\Delta m_p, \Delta m_g) = (\pm 1, \mp 1)$ $\Rightarrow$ $G(\pm 1, \mp 1) = \sqrt{\frac{1}{6}}$, $\varepsilon_{\pm 1}\hat{k}_{\mp 1} = \mp\frac{i}{2}$

$F(0, \pm) = \pm\sqrt{\frac{2}{5}}$

$\Rightarrow \hbar R(0, \pm) = \left[\varepsilon_{+1}\hat{k}_{-1}G(+1, -1) + \varepsilon_{-1}\hat{k}_{+1}G(-1, 1)\right]F(0, \pm) \rightarrow 0$

$= 0$. !

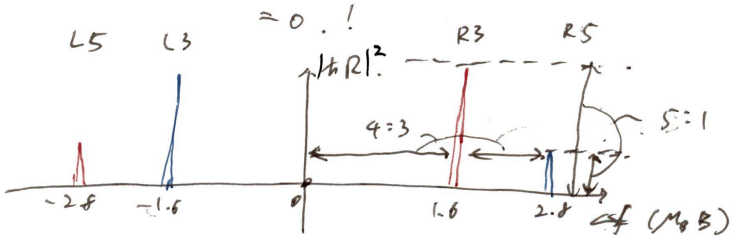

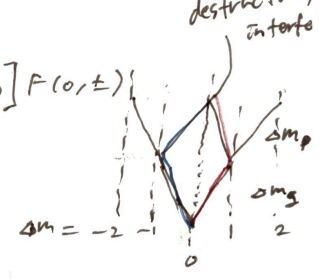

General expression of polarization and field propagation

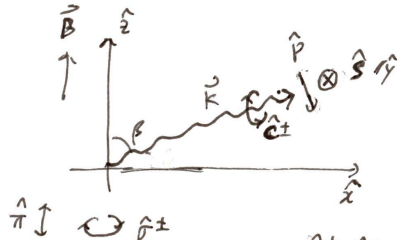

$\hat{k}_0$ $\hat{k}_{+1}$ $\hat{k}_{-1}$

$$\hat{\varepsilon} = K(\cos\beta\,\hat{z} + \sin\beta\,\hat{x}) = K\left(\cos\beta\,\hat{\pi} + \frac{\sin\beta}{\sqrt{2}}\hat{\sigma}^{+} + \frac{\sin\beta}{\sqrt{2}}\hat{\sigma}^{-}\right)$$

$$\hat{p} = -\sin\beta\,\hat{z} + \cos\beta\,\hat{x} = -\sin\beta\,\hat{\pi} + \frac{\cos\beta}{\sqrt{2}}\hat{\sigma}^{+} + \frac{\cos\beta}{\sqrt{2}}\hat{\sigma}^{-}$$

$$\hat{s} = \hat{y} = \frac{\hat{\sigma}^{+} - \hat{\sigma}^{-}}{\sqrt{2}\,i}$$

} two linear polarization

$$\hat{\varepsilon}^{\pm} = \frac{\hat{p} \pm i\hat{s}}{\sqrt{2}} = -\frac{\sin\beta\,\hat{\pi}}{\sqrt{2}} + \begin{cases} \cos^2\frac{\beta}{2}\,\hat{\sigma}^{+} - \sin^2\frac{\beta}{2}\,\hat{\sigma}^{-} & : + \\ -\sin^2\frac{\beta}{2}\,\hat{\sigma}^{+} + \cos^2\frac{\beta}{2}\,\hat{\sigma}^{-} & : - \end{cases}$$: two circular polarizations

$$= -\frac{\sin\beta}{\sqrt{2}}\,\hat{\pi} \pm \sin^2\left(\frac{\pi}{2} - \frac{\beta}{2} \pm \frac{\pi}{4}\right) \mp \sin^2\left(\frac{\pi}{2} - \frac{\beta}{2} \mp \frac{\pi}{4}\right)$$

$$\hat{p} = \frac{\hat{\varepsilon}^{+} + \hat{\varepsilon}^{-}}{\sqrt{2}}, \quad \hat{s} = \frac{\hat{\varepsilon}^{+} - \hat{\varepsilon}^{-}}{\sqrt{2}\,i}$$

$$\hat{\varepsilon} = \cos\tfrac{\beta}{2}\,e^{-i\frac{\phi}{2}}\hat{\varepsilon}^{+} + \sin\tfrac{\beta}{2}\,e^{+i\frac{\phi}{2}}\hat{\varepsilon}^{-}$$

$$= -\frac{\sin\beta}{\sqrt{2}}\left[\cos\tfrac{\theta}{2}\,e^{-i\frac{\phi}{2}} + \sin\tfrac{\theta}{2}\,e^{+i\frac{\phi}{2}}\right]\hat{\pi} \quad \rightarrow \mathcal{E}_0$$

$$+ \left(\cos^2\tfrac{\beta}{2}\cos\tfrac{\theta}{2}\,e^{-i\frac{\phi}{2}} - \sin^2\tfrac{\beta}{2}\sin\tfrac{\theta}{2}\,e^{+i\frac{\phi}{2}}\right]\hat{\sigma}^{+} \quad \rightarrow \mathcal{E}_{+1}$$

$$+ \left[-\sin^2\tfrac{\beta}{2}\cos\tfrac{\theta}{2}\,e^{-i\frac{\phi}{2}} + \cos^2\tfrac{\beta}{2}\sin\tfrac{\theta}{2}\,e^{+i\frac{\phi}{2}}\right]\hat{\sigma}^{-} \quad \rightarrow \mathcal{E}_{-1}$$

$\sqrt{2}\left[\sin\frac{\pi+\theta}{2}\cos\frac{\phi}{2} - i\sin\frac{\pi-\theta}{2}\sin\frac{\phi}{2}\right]$ ← $\mathcal{E}_{+1}$

Magnitude: $\sqrt{1+\sin\theta\cos\phi}$

Special cases of polarization

1) linear $\hat{\varepsilon} = \cos\psi\,\hat{p} + \sin\psi\,\hat{s}$

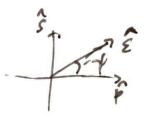

$$= \frac{e^{-i\psi}}{\sqrt{2}}\hat{\varepsilon}^{+} + \frac{e^{i\psi}}{\sqrt{2}}\hat{\varepsilon}^{-} \quad \Rightarrow \theta = \frac{\pi}{2}$$

$\phi = 2\psi$ (ϕ : angle of linear pol., θ : weight of $\hat{\sigma}^{+}, \hat{\sigma}^{-}$)

$$\Rightarrow \hat{\varepsilon} = -\sin\beta\cos\psi\,\hat{\pi} + \frac{1}{\sqrt{2}}\left(\cos^2\tfrac{\beta}{2}\,e^{-i\psi} - \sin^2\tfrac{\beta}{2}\,e^{+i\psi}\right)\hat{\sigma}^{+} + \frac{1}{\sqrt{2}}\left(-\sin^2\tfrac{\beta}{2}\,e^{-i\psi} + \cos^2\tfrac{\beta}{2}\,e^{i\psi}\right)\hat{\sigma}^{-}$$

} intensities are the same.

2) Minimize

$-\hat{\pi}$: $|\mathcal{E}_0| = -\frac{\sin\beta}{\sqrt{2}}\sqrt{1+\sin\theta\cos\phi} \Rightarrow$ zero at $\beta = 0$ or $(\theta, \phi) = (\frac{\pi}{2}, \pi)$

$\Downarrow$ $\vec{k} \parallel \vec{B}$; $\Downarrow$ $\hat{\varepsilon}$ linear & $\hat{\varepsilon} \parallel \hat{s} \perp \vec{B}$

$-\hat{\sigma}^{+}$: $|\mathcal{E}_{+1}| = 0$ if $\phi = 0$ and $\tan\frac{\theta}{2} = \cot^2\frac{\beta}{2}$

$-\hat{\sigma}^{-}$: $|\mathcal{E}_{-1}| = 0$ if $\phi = 0$ and $\tan\frac{\theta}{2} = \tan^2\frac{\beta}{2}$

↑ QWP fixed (axis vertical & horizontal) ; ↑ ratio of $\hat{\sigma}^{+}, \hat{\sigma}^{-}$ adjusted by HWP before QWP

3) $\beta = 45°$

$$\hat{\varepsilon} = -\frac{1}{2}\left[\cos\tfrac{\theta}{2}\,e^{-i\frac{\phi}{2}} + \sin\tfrac{\theta}{2}\,e^{+i\frac{\phi}{2}}\right]\hat{\pi} + \left[\frac{2+\sqrt{2}}{4}\cos\tfrac{\theta}{2}\,e^{-i\frac{\phi}{2}} - \frac{2-\sqrt{2}}{4}\sin\tfrac{\theta}{2}\,e^{+i\frac{\phi}{2}}\right]\hat{\sigma}^{+} + \left[-\frac{2-\sqrt{2}}{4}\cos\tfrac{\theta}{2}\,e^{-i\frac{\phi}{2}} + \frac{2+\sqrt{2}}{4}\sin\tfrac{\theta}{2}\,e^{+i\frac{\phi}{2}}\right]\hat{\sigma}^{-}$$

$$= -\frac{1}{2}\left[\cos\tfrac{\theta}{2}\,e^{-i\frac{\phi}{2}} + \sin\tfrac{\theta}{2}\,e^{+i\frac{\phi}{2}}\right](\hat{\pi} - \hat{x}) + \frac{i}{\sqrt{2}}\left[\cos\tfrac{\theta}{2}\,e^{-i\frac{\phi}{2}} - \sin\tfrac{\theta}{2}\,e^{+i\frac{\phi}{2}}\right]\hat{y}$$

General solution of $^2S_{1/2} \to {}^2D_{5/2}$ (4 lines)

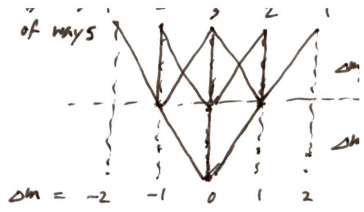

$$\text{tr}R(\Delta m,\pm) = C(nJn'J') \times \underbrace{\sum_{\Delta m_p}\xi_{\Delta m_p}\sum_{\Delta m_g}\hat{k}_{\Delta m_g}\delta_{\Delta m_p+\Delta m_g,\Delta m}\,G(\Delta m_p,\Delta m_g)}_{M(\Delta m;\hat{\xi},\vec{k})}\,P(\Delta m,\pm)$$

$M(\Delta m;\hat{\xi},\vec{k})$ /// interference of different paths for given Δm.

1) $\Delta m=-2$: $\xi_{-1}\hat{k}_{-1}\,G(-1,-1)$

$$= \left[-\sin^2\tfrac{\beta}{2}\cos\tfrac{\theta}{2}e^{-i\frac{\phi}{2}} + \cos^2\tfrac{\beta}{2}\sin\tfrac{\theta}{2}e^{i\frac{\phi}{2}}\right]\frac{\sin\beta}{\sqrt{2}} \cdot 1$$

2) $\Delta m=-1$: $(\xi_{-1}\hat{k}_0 + \xi_0\hat{k}_{-1})\,G(-1,0)$

$$= \left[-\sin^2\tfrac{\beta}{2}\cos\tfrac{\theta}{2}e^{-i\frac{\phi}{2}} + \cos^2\tfrac{\beta}{2}\sin\tfrac{\theta}{2}e^{i\frac{\phi}{2}}\right]\cos\beta - \frac{\sin\beta}{\sqrt{2}}\left[\cos\tfrac{\theta}{2}e^{-i\frac{\phi}{2}} + \sin\tfrac{\theta}{2}e^{+i\frac{\phi}{2}}\right]\cdot\frac{\sin\beta}{\sqrt{2}} \quad \times\sqrt{\tfrac{1}{2}}$$

$$\Rightarrow \frac{1}{2\sqrt{2}}\left[(\cos 2\beta-\cos\beta)\cos\tfrac{\theta}{2}e^{-i\frac{\phi}{2}} + (\cos 2\beta+\cos\beta)\sin\tfrac{\theta}{2}e^{+i\frac{\phi}{2}}\right]$$

$\hat{k}_{+1} = \hat{k}_{-1} = \frac{\sin\beta}{\sqrt{2}}$

3) $\Delta m=0$: $\xi_0\hat{k}_0\,G(0,0) + (\xi_{-1}+\xi_{+1})\hat{k}_{+1}\,G(-1,1)$

$$= -\frac{\sin\beta}{\sqrt{2}}\left[\cos\tfrac{\theta}{2}e^{-i\frac{\phi}{2}} + \sin\tfrac{\theta}{2}e^{i\frac{\phi}{2}}\right]\cos\beta\cdot\sqrt{\tfrac{2}{3}} + \cos\beta\left[\cos\tfrac{\theta}{2}e^{-i\frac{\phi}{2}} + \sin\tfrac{\theta}{2}e^{i\frac{\phi}{2}}\right]\cdot\frac{\sin\beta}{\sqrt{2}}\cdot\sqrt{\tfrac{1}{6}}$$

$$= \frac{\sqrt{3}}{4}\sin 2\beta\left[\cos\tfrac{\theta}{2}e^{-i\frac{\phi}{2}} + \sin\tfrac{\theta}{2}e^{i\frac{\phi}{2}}\right]$$

4) $\Delta m=+1$: $(\xi_0\hat{k}_{+1} + \xi_{+1}\hat{k}_0)\,G(0,1)$

$$= -\frac{\sin\beta}{\sqrt{2}}\left[\cos\tfrac{\theta}{2}e^{-i\frac{\phi}{2}} + \sin\tfrac{\theta}{2}e^{+i\frac{\phi}{2}}\right]\frac{\sin\beta}{\sqrt{2}} + \left[\cos^2\tfrac{\beta}{2}\cos\tfrac{\theta}{2}e^{-i\frac{\phi}{2}} - \sin^2\tfrac{\beta}{2}\sin\tfrac{\theta}{2}e^{+i\frac{\phi}{2}}\right]\cos\beta \quad \times\sqrt{\tfrac{1}{2}}$$

$$= \frac{1}{2\sqrt{2}}\left[(\cos 2\beta+\cos\beta)\cos\tfrac{\theta}{2}e^{-i\frac{\phi}{2}} + (\cos 2\beta-\cos\beta)\sin\tfrac{\theta}{2}e^{+i\frac{\phi}{2}}\right]$$

5) $\Delta m=+2$: $\xi_+\hat{k}_+\,G(1,1)$

$$= \left[\cos^2\tfrac{\beta}{2}\cos\tfrac{\theta}{2}e^{-i\frac{\phi}{2}} - \sin^2\tfrac{\beta}{2}\sin\tfrac{\theta}{2}e^{+i\frac{\phi}{2}}\right]\frac{\sin\beta}{\sqrt{2}} \cdot 1$$

Magnitude of $M(\Delta m;\hat{\xi},\vec{k})$

1) $\Delta m=-2$: $-\beta=0$: 0 $\quad -\beta=90°$: $\frac{1}{2\sqrt{2}}\sqrt{1-\sin\theta\cos\phi}$ $\quad -\beta=180°$: 0

Numerical analysis ⇒ Global maximum $=\frac{1}{2}$ at $(\beta,\theta,\phi)=(90°,90°,180°)$ ⟵ min 0 : horizontally linear $(\theta=90°,\phi=0)$; max $\frac{1}{2}$: vertically linear $(\theta=90°,\phi=180°)$ → $\psi=90°$

2) $\Delta m=-1$: $-\beta=0$: $\frac{1}{\sqrt{2}}\sin\frac{\theta}{2}$ ⟵ min 0 : $\hat{\sigma}^+$, max $\frac{1}{\sqrt{2}}$: $\hat{\sigma}^-$ $\quad -\beta=90°$: $-\frac{1}{2\sqrt{2}}\sqrt{1+\sin\theta\cos\phi}$ ⟵ 0 : vert. lin., $-\frac{1}{2\sqrt{2}}$: hor. lin. $\quad -\beta=180°$: $\frac{1}{\sqrt{2}}\cos\frac{\theta}{2}$ ⟵ 0 : $\hat{\sigma}^-$, $\frac{1}{\sqrt{2}}$: $\hat{\sigma}^+$

Global maximum $=\frac{1}{\sqrt{2}}$

3) $\Delta m=0$: $\frac{\sqrt{3}}{4}\sin 2\beta\sqrt{1+\sin\theta\cos\phi}$ ⇒ 0 at $\beta=0,90°$, maximum $\frac{\sqrt{3}}{4}$ at $\beta=45°$, hor. lin. polarization

4) $\Delta m=+1$: same to $\Delta m=-1$ with $\hat{\sigma}^+ \leftrightarrow \hat{\sigma}^-$

5) $\Delta m=+2$: same to $\Delta m=-2$

Maximum height of Zeeman peaks

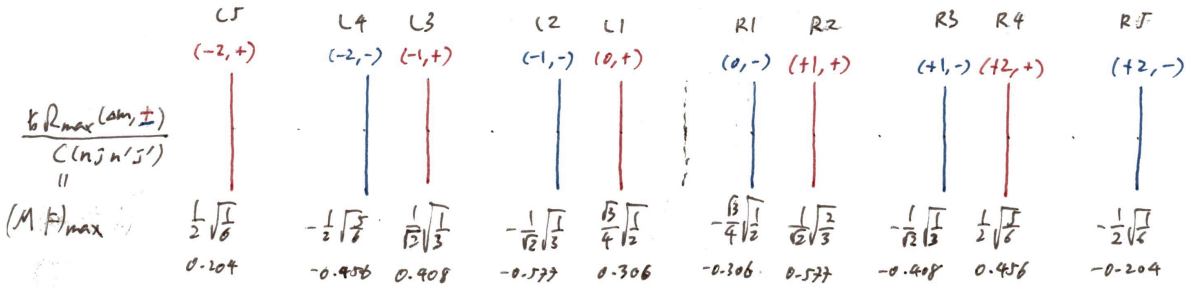

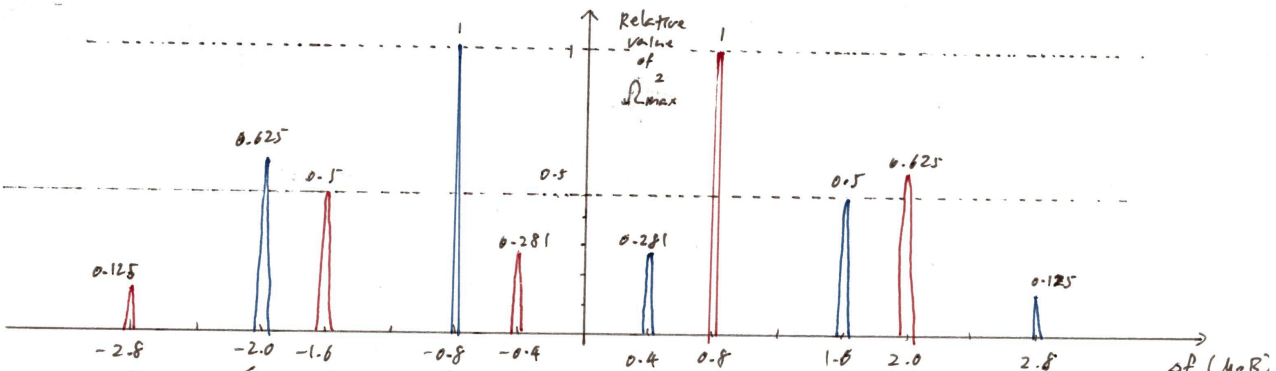

at $\begin{pmatrix}\beta\\ \theta\\ \phi\end{pmatrix}$ = $\begin{pmatrix}90\\ 90\\ 180\end{pmatrix}$ $\begin{pmatrix}0\\ 180\\ \text{any}\end{pmatrix}$ $\begin{pmatrix}45\\ 90\\ 0\end{pmatrix}$ $\begin{pmatrix}0\\ 0\\ \text{any}\end{pmatrix}$ $\begin{pmatrix}90\\ 90\\ 180\end{pmatrix}$

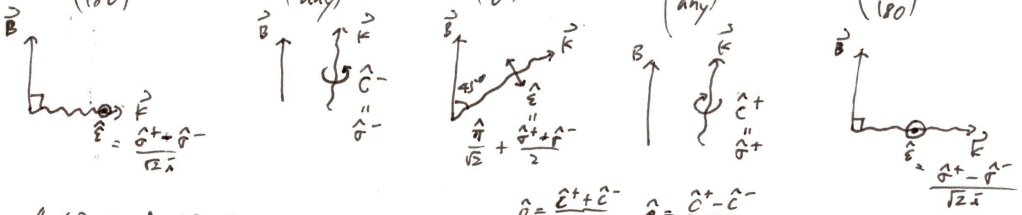

Appendix: Action of QWP

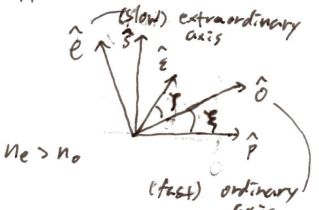

$-\frac{\pi}{2} \le \gamma \le \frac{\pi}{2}$

$-\pi \le \xi \le \pi$

$\Rightarrow \hat{o} = \frac{\hat{C}^+ + \hat{C}^-}{\sqrt{2}}$, $\hat{e} = \frac{\hat{C}^+ - \hat{C}^-}{\sqrt{2}i}$

$\hat{C}^{\pm\prime} = \frac{\hat{o} \pm i\hat{e}}{\sqrt{2}}$: Circular polarizations defined in QWP's principal plane

$= e^{\mp i\xi}\hat{C}^{\pm}$ " " " " $\hat{p}-\hat{s}$ plane.

Action of QWP : $\hat{o} \to \hat{o}$, $\hat{e} \to +i\hat{e}$

$\hat{\varepsilon} = \cos\gamma\,\hat{o} + \sin\gamma\,\hat{e} \xrightarrow{QWP} \cos\gamma\,\hat{o} + i\sin\gamma\,\hat{e}$

$= \sin\left(\frac{\pi}{4}+\gamma\right)\hat{C}^{+\prime} + \sin\left(\frac{\pi}{4}-\gamma\right)\hat{C}^{-\prime}$

$= \cos\left(\frac{\pi}{4}-\gamma\right)e^{-i\xi}\hat{C}^{+} + \sin\left(\frac{\pi}{4}-\gamma\right)e^{+i\xi}\hat{C}^{-}$

$\xrightarrow{\times e^{\mp i\xi}} \cos\left(\xi-\frac{\pi}{4}\right)e^{-i\left(\xi\pm\frac{\pi}{2}\right)}\hat{C}^{+} + \sin\left(\xi-\frac{\pi}{4}\right)e^{i\left(\xi\pm\frac{\pi}{2}\right)}\hat{C}^{-}$

$\xrightarrow{\times \pm i} \cos\left(\frac{3\pi}{4}+\gamma\right)e^{-i\left(\xi\pm\frac{\pi}{2}\right)}\hat{C}^{+} + \sin\left(\frac{3\pi}{4}+\gamma\right)e^{i\left(\xi\pm\frac{\pi}{2}\right)}\hat{C}^{-}$

$\Rightarrow \left(\frac{\theta}{2}, \frac{\phi}{2}\right) = \begin{cases}\left(\frac{\pi}{4}-\gamma,\ \xi\right), & -\frac{\pi}{4} \le \gamma \le \frac{\pi}{4} \\ \left(\frac{3\pi}{4}+\gamma,\ \xi\pm\frac{\pi}{2}\right), & \gamma \le -\frac{\pi}{4} \\ \left(\gamma-\frac{\pi}{4},\ \xi\pm\frac{\pi}{2}\right), & \frac{\pi}{4} < \gamma\end{cases}$

$\Rightarrow (\gamma, \xi) = \begin{cases}\left(\frac{\pi}{4}-\frac{\theta}{2},\ \frac{\phi}{2}\right), & 0 \le \theta \le \pi \\ \left(\frac{\theta}{2}-\frac{3\pi}{4},\ \frac{\phi}{2}\pm\frac{\pi}{2}\right), & \frac{\pi}{2} \le \theta \le \pi \\ \left(\frac{\theta}{2}+\frac{\pi}{4},\ \frac{\phi}{2}\pm\frac{\pi}{2}\right), & 0 \le \theta \le \frac{\pi}{2}\end{cases}$ ← The first condition is enough to make arbitrary (θ, ϕ) with QWP

Appendix E

Reprint of "Evidence for Nonlinear Isotope Shift in Yb^+ Search for New Boson"

This Appendix contains a reprint of Ref. [5]: I. Counts*, J. Hur*, D. P. L. Aude Craik, H. Jeon, C. Leung, J. C. Berengut, A. Geddes, A. Kawasaki, W. Jhe, and V. Vuletić, *Evidence for nonlinear isotope shift in* Yb^+ *search for new boson*, Phys. Rev. Lett. **125**, 123002 (2020) (*equal contributions).

Editors' Suggestion | Featured in Physics

Evidence for Nonlinear Isotope Shift in Yb^+ Search for New Boson

Ian Counts,[1,*] Joonseok Hur,[1,*] Diana P. L. Aude Craik,[1] Honggi Jeon,[2] Calvin Leung,[1] Julian C. Berengut,[3] Amy Geddes,[3] Akio Kawasaki,[4] Wonho Jhe,[2] and Vladan Vuletić[1,†]

[1]*Department of Physics and Research Laboratory of Electronics, Massachusetts Institute of Technology, Cambridge, Massachusetts 02139, USA*

[2]*Department of Physics and Astronomy, Seoul National University, Seoul 151-747, Korea*

[3]*School of Physics, University of New South Wales, Sydney, New South Wales 2052, Australia*

[4]*W. W. Hansen Experimental Physics Laboratory and Department of Physics, Stanford University, Stanford, California 94305, USA*

(Received 23 April 2020; accepted 27 July 2020; published 15 September 2020)

We measure isotope shifts for five Yb^+ isotopes with zero nuclear spin on two narrow optical quadrupole transitions $^2S_{1/2} \rightarrow {}^2D_{3/2}$, $^2S_{1/2} \rightarrow {}^2D_{5/2}$ with an accuracy of ~300 Hz. The corresponding King plot shows a 3×10^{-7} deviation from linearity at the 3σ uncertainty level. Such a nonlinearity can indicate physics beyond the Standard Model (SM) in the form of a new bosonic force carrier, or arise from higher-order nuclear effects within the SM. We identify the quadratic field shift as a possible nuclear contributor to the nonlinearity at the observed scale, and show how the nonlinearity pattern can be used in future, more accurate measurements to separate a new-boson signal from nuclear effects.

DOI: 10.1103/PhysRevLett.125.123002

The Standard Model (SM) of particle physics describes virtually all measurements of elementary particles exquisitely well, and yet various indirect evidence points to physics beyond the SM. This evidence includes the preponderance of dark matter of unknown composition in our Universe, astronomically observed with several different methodologies such as the rotation curves of galaxies [1], the motion of colliding galaxy clusters [2], gravitational lensing [3], and the power spectrum of the cosmic microwave background [4]. Physics beyond the SM is also being probed in various laboratory experiments, such as high-energy collisions [5], searches for weakly interacting massive particles [5], axions, and axionlike particles [6], precision measurements of the electric dipole moments of elementary particles [7], and other precision tests [8].

Dark-matter candidates can be characterized by their mass, spin, and interactions. In the intermediate mass range from ~100 eV/c^2 to ~100 MeV/c^2, a new method has been proposed to search for a dark-matter boson ϕ that couples to quarks and leptons [9,10]. The virtual exchange of ϕ between neutrons and electrons in an atom would result in a Yukawa-like potential in addition to the Coulomb potential of the nucleus (see Fig. 1). The corresponding shift in energy levels and transition frequencies is too small to be detected by directly comparing spectroscopic data to (much less accurate) atomic-structure calculations, but could potentially be detected through precision isotope-shift measurements [11–14] that allow one to sidestep electronic-structure calculations. In particular, the scaled isotope shifts on two different transitions exhibit a linear relationship (King plot [15]), and Refs. [9,10] argue that a deviation from linearity can indicate a new force mediator ϕ. Such studies are particularly timely as recent experiments analyzing nuclear decay in ^{8}Be and ^{4}He have observed a 7σ deviation from the SM [16–18] that could be potentially explained by a new boson with a mass of 17 MeV/c^2 ($X17$ boson) [19–22]. According to Ref. [10], measurements of optical transitions with a resolution of 1 Hz in select atomic systems could probe this scenario. However, higher-order effects within the SM can result in nonlinearities that limit the sensitivity to new physics [23–26].

In this Letter, we report a precision measurement of the isotope shift for five isotopes of Yb^+ ions with zero

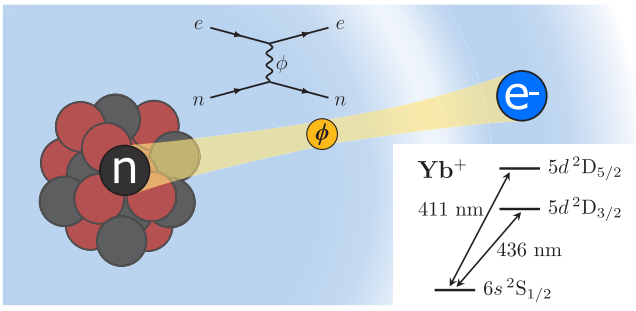

FIG. 1. New intra-atomic force between electron (e^-) and neutron (n) mediated by the virtual exchange of a hypothetical new boson ϕ. The coupling results in a Yukawa-like potential that modifies the atomic energy levels and can be probed with isotope-shift spectroscopy. We perform precision measurements of the long-lived states $^2D_{3/2}$, $^2D_{5/2}$ on individual trapped Yb^+ ions.

TABLE I. Inverse-mass differences μ_{ji} and measured isotope shifts ν_{ji} between pairs of neighboring even Yb^+ isotopes. μ_{ji} is calculated from the mass of Yb^+ ions with the ionization energy set to 6.254 eV [30–32]. The nuclear size difference $\delta\langle r^2\rangle$ is deduced from ν_{ji} using the calculated parameters $F_\alpha^{\mathrm{CI}} = -15.852$ GHz/fm^2, $F_\beta^{\mathrm{CI}} = -16.094$ GHz/fm^2, $F_\alpha^{\mathrm{MBPT}} = -16.570$ GHz/fm^2, $F_\beta^{\mathrm{MBPT}} = -16.771$ GHz/fm^2, $K_\alpha^{\mathrm{CI}} = -1678.3$ GHz · u, and $K_\beta^{\mathrm{CI}} = -1638.5$ GHz · u (see the Supplemental Material [33]). The uncertainties given here and throughout the paper for $\nu_{\alpha ji}$ and $\nu_{\beta ji}$ indicate 1σ statistical uncertainties; the estimated systematic uncertainties on these quantities are $< 20\%$ of the statistical uncertainties (see the Supplemental Material [33]). The (170,174) pair is directly measured as a cross-check [the measurements (170,174) and (170,172), (172,174) agree within 2σ] and to improve precision (see the Supplemental Material [33]). In the calculations of $\delta\langle r^2\rangle_{ji}$ from the measured isotope shifts, the average of the values for α and β is given (the difference between transitions is less than 0.2%) (see the Supplemental Material [33]), and the values of K_α and K_β from the CI calculations are used for both CI and MBPT. For the data from Ref. [64] (last column), only the statistical errors are presented in the parentheses, while the systematic errors from the calculation of the electronic factors are much larger.

Isotope pair (j,i)	μ_{ji} (10^{-6} u^{-1})	$\nu_{\alpha ji}$ (kHz) $\alpha: {}^2S_{1/2} \to {}^2D_{5/2}$	$\nu_{\beta ji}$ (kHz) $\beta: {}^2S_{1/2} \to {}^2D_{3/2}$	$\delta\langle r^2\rangle_{ji}$ (fm^2) CI	MBPT	Reference [64]
(168, 170)	70.113 698(46)	2 179 098.93(21)	2 212 391.85(37)	−0.156	−0.149	−0.1561(3)
(170, 172)	68.506 890 50(63)	2 044 854.78(34)	2 076 421.58(39)	−0.146	−0.140	−0.1479(1)
(172, 174)	66.958 651 95(64)	1 583 068.42(36)	1 609 181.47(22)	−0.115	−0.110	−0.1207(1)
(174, 176)	65.474 078 21(65)	1 509 055.29(28)	1 534 144.06(24)	−0.110	−0.105	−0.1159(1)
(170, 174)		3 627 922.95(50)	3 685 601.95(33)			

nuclear spin on two narrow optical quadrupole transitions (${}^2S_{1/2} \to {}^2D_{3/2}, {}^2D_{5/2}$) with an accuracy of ∼300 Hz. Displaying the data in a King plot [15], we observe a deviation from linearity at the 10^{-7} level, corresponding to 3 standard deviations σ. With four independent isotope-shift data points available, we further introduce a novel parametrization of the nonlinearity pattern that can be used to distinguish between nonlinearities of the same magnitude but different physical origin. At the current level of precision, the observed nonlinearity pattern is consistent with both a new boson and the quadratic field shift (QFS) [23] that we identify as the leading source of nonlinearity within the SM by means of precision electronic-structure calculations. In the future, more accurate measurements on the present and other optical transitions in Yb and Yb^+ [27–29] can discriminate between effects within and outside the SM.

Our measurements are performed with individual ${}^jYb^+$ ions ($j \in \{168, 170, 172, 174, 176\}$) trapped in a linear Paul trap and Doppler cooled on the $6s\,{}^2S_{1/2} \to 6p\,{}^2P_{1/2}$ transition to typically 500 μK [65]. We perform optical precision spectroscopy on the transitions to two long-lived excited states (with electron configurations $[\mathrm{Xe}]4f^{14}6s\,{}^2S_{1/2} \to [\mathrm{Xe}]4f^{14}5d\,{}^2D_{3/2}, {}^2D_{5/2}$) using light at the wavelengths 411 and 436 nm, respectively. The probe light is generated by a frequency-doubled Ti:Sapphire laser that is frequency stabilized to an ultralow-thermal-expansion cavity, achieving a short-term stability of ∼200 Hz. Typically, 1 mW of 411-nm light (0.2 mW of 436-nm light) is focused to a waist of $w_0 = 60$ μm ($w_0 = 15$ μm) at the location of the ion (see the Supplemental Material [33] for details).

Coherent optical Ramsey spectroscopy is carried out with two $(\pi/2)$ pulses of 411- or 436-nm light, lasting 5 μs each, separated by 10 μs. This is followed by readout of the state, performed using an electron-shelving scheme [66] (see the Supplemental Material [33]). A small magnetic field of typically ∼1.1 G is applied to separate the different Zeeman components of the $S \to D$ transition. Frequency scans are taken over the central Ramsey fringes of the two symmetric Zeeman components with the lowest magnetic-field sensitivity to find the center frequency of the transition (see the Supplemental Material [33]).

The measurement on one isotope is averaged typically for 30 minutes before we switch to a next-neighboring isotope by adjusting various loading, cooling, and repumper laser frequencies. We typically perform three interleaved measurements of each isotope to determine an isotope shift, allowing us to reach a precision on the order of ∼300 Hz (see Table I and Fig. 2), limited mainly by drifts in the frequency stabilization of the probe laser to the ultrastable cavity (see the Supplemental Material [33]).

The frequency shift $\nu_{\alpha ji}$ between isotope ${}^jYb$ and ${}^iYb$ on an optical transition α can be written as a sum of terms that factorize into a nuclear part (with subscript ji) and an electronic part (with subscript α) [9,15,24],

$$\nu_{\alpha ji} = F_\alpha \delta\langle r^2\rangle_{ji} + K_\alpha \mu_{ji} + G_\alpha [\delta\langle r^2\rangle^2]_{ji} + \upsilon_{ne} D_\alpha a_{ji}. \quad (1)$$

Here $\delta\langle r^2\rangle_{ji} \equiv \langle r^2\rangle_j - \langle r^2\rangle_i$ is the difference in squared charge radii r between isotope j and i, $\mu_{ji} \equiv 1/m_j - 1/m_i$ is the inverse-mass difference, $[\delta\langle r^2\rangle^2]_{ji} \equiv (\delta\langle r^2\rangle_{jl})^2 - (\delta\langle r^2\rangle_{il})^2$ for some fixed isotope l (the choice of l is irrelevant to the nonlinearity) (see the Supplemental Material [33]), and $a_{ji} = j - i$ is the difference in neutron number. The quantity $\upsilon_{ne} = (-1)^{s+1} y_n y_e/(4\pi\hbar c)$ is the product of the coupling factors of the new boson to the neutron y_n and electron y_e, creating a Yukawa-like potential given by $V_{ne}(r) = \hbar c \upsilon_{ne} \exp(-r/\lambda\!\!\!^{-}_c)/r$ for a boson with

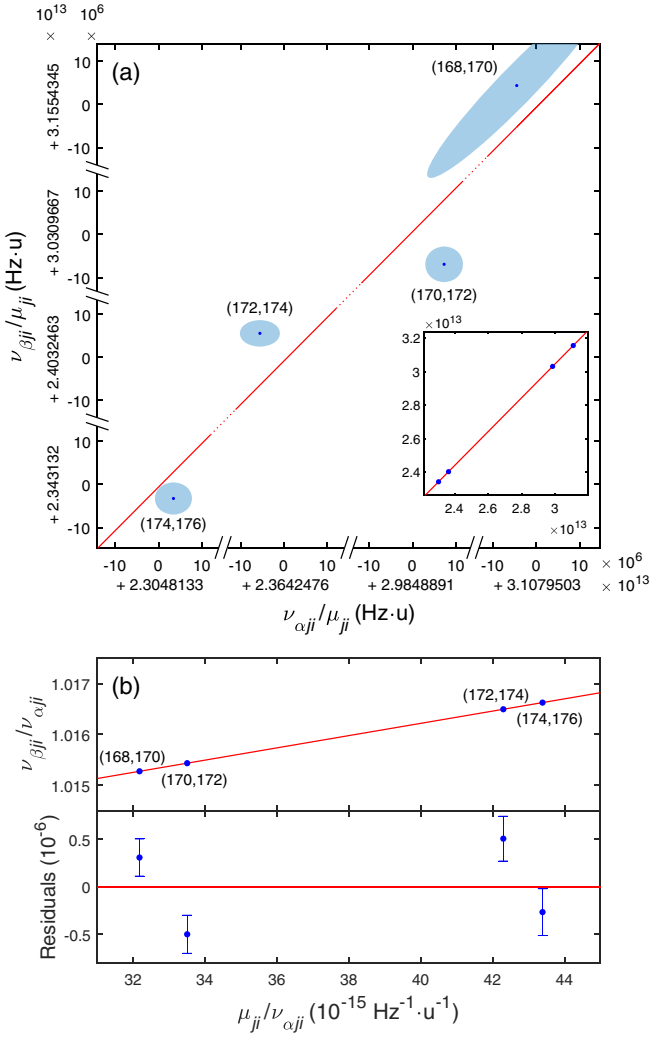

FIG. 2. (a) Standard King plot [Eq. (2)] for $\alpha = 411$ nm, ${}^2S_{1/2} \to {}^2D_{5/2}$, and $\beta = 436$ nm, ${}^2S_{1/2} \to {}^2D_{3/2}$ transitions for pairs of neighboring even Yb^+ isotopes. The inset shows the full King plot. The main figure is zoomed into the data points by a factor of 10^6. A deviation from linearity (red line) by 3 standard deviations σ is observed. The larger diagonal uncertainty for the (168,170) pair is due to the larger mass uncertainty for the $^{168}Yb^+$ isotope [30–32] (see the Supplemental Material [33]). (b) Frequency-normalized King plot [Eq. (3)] and residuals. The error bars and error ellipses indicate 1σ.

spin s, mass m_ϕ, and reduced Compton wavelength $\lambda\!\!\!^{-}_c = \hbar/(m_\phi c)$ [9,24].

For heavy elements like Yb, the first term in Eq. (1) associated with the change in nuclear size $\delta\langle r^2\rangle$ ["field shift" (FS)] dominates, while the second term is due to the electron's reduced mass and momentum correlations between electrons ("mass shift"). According to our electronic-structure calculations (see below), the third (QFS) term associated with the square of nuclear size $[\delta\langle r^2\rangle^2]_{ji}$ represents the leading-order nonlinearity [23,24] within the SM for Yb. The last term describes the isotope shift due to the Yukawa-like potential associated with the new boson ϕ. The quantities F, K, G, D are determined by the electronic wave functions of the transition [9,10,24]; see the Supplemental Material [33]. Note that the effect of the next-leading order Seltzer moment [24,67] associated with $\delta\langle r^4\rangle$ is absorbed into the QFS term; see the Supplemental Material [33].

The first two terms in Eq. (1) lead to a linear relationship between the isotope shifts (King plot [15]) when one considers two different transitions α, β,

$$\bar{\bar{\nu}}_{\beta ji} = K_{\beta\alpha} + F_{\beta\alpha}\bar{\bar{\nu}}_{\alpha ji} + G_{\beta\alpha}\overline{\overline{[\delta\langle r^2\rangle^2]}}_{ji} + \upsilon_{ne}D_{\beta\alpha}\bar{\bar{a}}_{ji}. \quad (2)$$

Here we define $F_{\beta\alpha} \equiv F_\beta/F_\alpha$, $P_{\beta\alpha} \equiv P_\beta - F_{\beta\alpha}P_\alpha$ for $P \in \{K, G, D\}$, while $\bar{\bar{z}}_{ji} \equiv z_{ji}/\mu_{ji}$ for $z \in \{\nu_\alpha, \nu_{\beta,}, [\delta\langle r^2\rangle^2], a\}$ is the inverse-mass-normalized quantity. For our purposes, where the FS dominates, the influence of mass and frequency errors is more transparent if we instead write a modified linear relationship for the frequency-normalized quantities $\bar{x}_{ji} \equiv x_{ji}/\nu_{\alpha ji}$ for $x \in \{\nu_\beta, \mu, [\delta\langle r^2\rangle^2], a\}$,

$$\bar{\nu}_{\beta ji} = F_{\beta\alpha} + K_{\beta\alpha}\bar{\mu}_{ji} + G_{\beta\alpha}\overline{[\delta\langle r^2\rangle^2]}_{ji} + \upsilon_{ne}D_{\beta\alpha}\bar{a}_{ji}. \quad (3)$$

To analyze the experimental results in this work, the transitions and isotopes are assigned as follows: $\alpha = {}^2S_{1/2} \to {}^2D_{5/2}$ (411 nm), $\beta = {}^2S_{1/2} \to {}^2D_{3/2}$ (436 nm), $j \in \{168, 170, 172, 174\}$ with $i = j + 2$, and $l = 172$.

The inset in Fig. 2(a) confirms the general linear relationship for the inverse-mass-normalized isotope shifts in a standard King plot corresponding to Eq. (2) for the two transitions α and β. However, when we zoom in by a factor of 10^6 [main Fig. 2(a)], we observe a small deviation from linearity, in the range 0.5–1 kHz in frequency units for a given data point. The frequency-normalized King plot associated with Eq. (3), as displayed in Fig. 2(b), illustrates that due to the smallness of the slope, i.e., the mass-shift electronic factor $K_{\beta\alpha}$, the mass error along the horizontal axis $\bar{\mu}_{ji}$ has a negligible effect. For all points taken together, the nonlinearity is nonzero at the level of 3σ (see the Supplemental Material [33]).

With four independent isotope pairs, we can quantify not only the magnitude of the nonlinearity, but also an associated pattern further characterizing the nonlinearity. To this end, we introduce two dimensionless nonlinearity measures

$$\zeta_\pm \equiv d_{168} - d_{170} \pm (d_{172} - d_{174}), \quad (4)$$

where $d_j \equiv \bar{\nu}_{\beta ji} - f(\bar{\mu}_{ji})$ are the vertical deviations of the four data points $\bar{\nu}_{\beta ji}$ in Fig. 2(b) from the linear fit f. ζ_+ and ζ_- characterize the two possible nonlinearities for four data points, a zigzag shape with deviation pattern $+ - + -$, and a curved nonlinearity with deviation

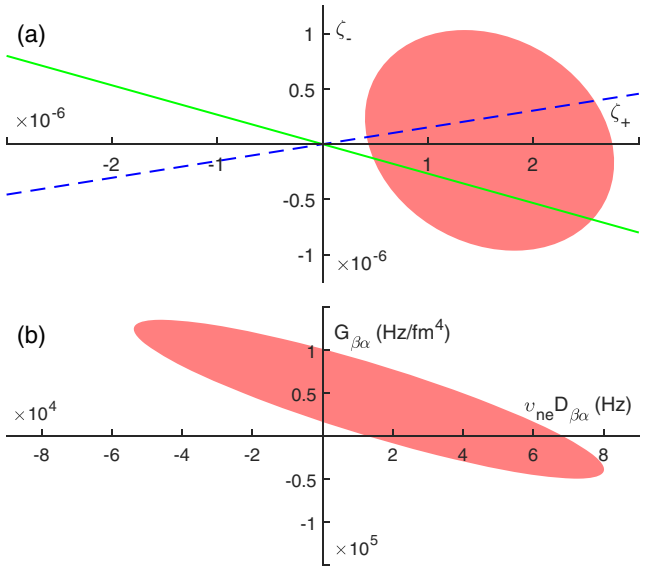

FIG. 3. (a) Nonlinearity measure (ζ_+, ζ_-) for next-neighbor isotope pairs. The red shaded region indicates the 95% confidence interval from our data. The green solid line and the blue dashed line indicate the required ratio ζ_-/ζ_+ if the nonlinearity is purely due to a new boson ϕ and the QFS, respectively. (b) Experimental nonlinearity measure along the axes of a new boson (x-axis) and the QFS (y-axis).

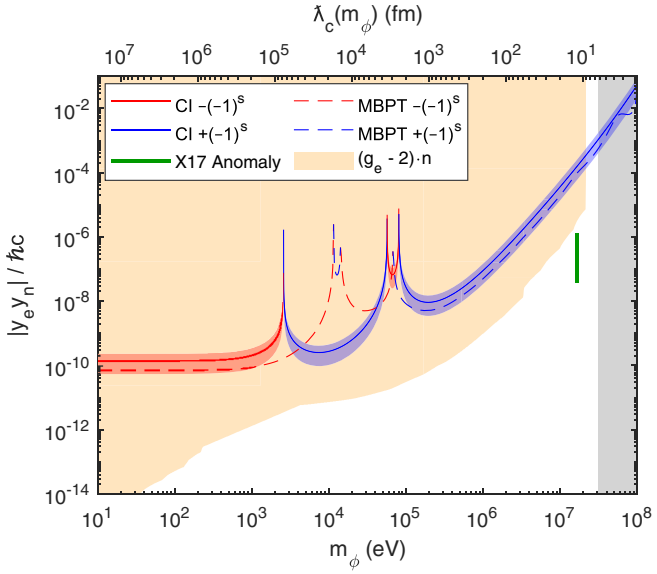

FIG. 4. Product of couplings $|y_e y_n|$ of a new boson vs boson mass m_ϕ (bottom) and reduced Compton wavelength (top), plotted under the assumption that the observed nonlinearity in Fig. 3 is dominated by the new boson. The solid line is for the CI calculation, and the dashed line is for the MBPT calculation. If the nonlinearity has a contribution from the QFS, then $|y_e y_n|$ lies below this line. The gray shade indicates the region inside the nucleus. The sign of $y_e y_n$ is color-coded: red for $-(-1)^s$ and blue for $+(-1)^s$ for a spin-s boson. The 95% confidence intervals from the statistical uncertainty in the measured isotope shift are shown as shaded areas along the solid line. The systematic uncertainty due to the wave function calculation is much larger, especially in the high-mass region. The thick green line indicates the preferred coupling range for the $X17$ boson from the Be/He anomaly [16–21]. The yellow shaded area shows the constraint from electron $g_e - 2$ measurements [77–81] combined with neutron scattering measurements [82–85] (from Ref. [10]).

pattern $+--+$, respectively. Any given nonlinearity can be represented by a point in the $\zeta_+\zeta_-$ plane [see Fig. 3(a)]. A nonlinearity that arises from the coupling of the ϕ boson to the neutron number corresponds to a fixed nonlinearity pattern and hence a given line through the origin (see the Supplemental Material [33]). The same argument holds for the QFS. Our observed nonlinearity lies close to both lines representing pure coupling to a new boson and the QFS, respectively. The experimental uncertainty region in Fig. 3(a) can be decomposed into its possible QFS and new-boson components, as shown in Fig. 3(b). It highlights the relative contributions of the two sources of nonlinearity, ranging from pure new boson to pure QFS contribution at the current level of uncertainty. With increased measurement precision, it will be possible to separate the two contributions.

In order to convert the observed nonlinearity, as represented by $\zeta_\pm$, into a physical quantity such as the coupling υ_{ne}, we need to determine the associated electronic wave functions. To cross-check our numerical simulations for systematic errors, we use two different methods, the Dirac-Hartree-Fock method [68,69] followed by the configuration interaction (CI) method [70–73], using the software package GRASP2018 [74], and many-body perturbation theory (MBPT) [75] implemented in AMBiT [76]. We calculate $F^{\mathrm{CI}}_{\beta\alpha} = 1.0153$ and $F^{\mathrm{MBPT}}_{\beta\alpha} = 1.0121$, within 0.2% and 0.07% of our experimental value $F^{\mathrm{exp}}_{\beta\alpha} = 1.01141024(86)$, respectively. For the mass shift, that is more difficult to calculate accurately; we find $K^{\mathrm{CI}}_{\beta\alpha} = 65$ GHz · u (see the Supplemental Material [33]), within a factor of 2 from the experimental value $K^{\mathrm{exp}}_{\beta\alpha} = 120.208(23)$ GHz · u. The calculated wave functions in combination with the measured frequency shift can also be used to extract the nuclear size difference $\delta\langle r^2\rangle$ (see the Supplemental Material [33]), in good agreement with other results [64]; see Table I. We also calculate $G^{\mathrm{CI}}_{\beta\alpha} = 232$ kHz/fm^4 and $G^{\mathrm{MBPT}}_{\beta\alpha} = -36$ kHz/fm^4 for the QFS, indicating a large systematic uncertainty in the calculation of this small term. The experimentally constrained range in Fig. 3(b) (24–94 kHz/fm^4) (see the Supplemental Material [33]) lies between the two calculated values.

Using the electronic-structure calculations, we can determine a boundary on the new-boson coupling from our data. Figure 4 shows the upper bound on the product of couplings $|y_e y_n|$. It is obtained by dividing the experimental value of $\upsilon_{ne} D_{\beta\alpha}$ from Fig. 3(b) (determined with the assumption that the effect of the new boson dominates the nonlinearity; i.e., $G_{\beta\alpha} = 0$), by $(-1)^{s+1} D_{\beta\alpha}(m_\phi)/(4\pi\hbar c)$ from the

TABLE II. Frequencies of the $^2S_{1/2} \rightarrow {}^2D_{5/2}$ transition.

Isotope	Absolute frequency (kHz)	Ref.
168	729 481 090 980.86(36)	This work
170	729 478 911 881.93(30)	This work
172	729 476 867 027.2068(44)	[86]
174	729 475 283 958.85(31)	This work
176	729 473 774 903.56(42)	This work

atomic-structure calculations (see the Supplemental Material [33] for the calculation of $D_{\beta\alpha}$). The calculations with the CI and the MBPT methods agree with each other to better than a factor of 2 over most of the mass range m_ϕ. The upper bound from our data on $|y_e y_n|$ is ∼200 times larger than the preferred coupling range for the $X17$ boson [19,20], and 2 orders of magnitude larger than the bound estimated in Ref. [10] from the combination of $g-2$ measurements on the electron and neutron scattering data. We note, however, that the limit on $|y_e|$ depends on additional assumptions about the new boson's spin and the symmetries of the interaction.

Finally, since the absolute optical frequency of the $^2S_{1/2} \rightarrow {}^2D_{5/2}$ transition for $^{172}Yb^+$ has recently been measured with precision at the Hz level [86], the absolute frequencies for all the other bosonic isotopes can be deduced from our isotope shift measurements. The results are summarized in Table II.

In the future, the measurement precision can be increased by several orders of magnitude by cotrapping two isotopes [12,13]. This improvement, also in combination with measurements on additional transitions, such as the $^2S_{1/2} \rightarrow {}^2F_{7/2}$ octupole transition in Yb^+ [87] or clock transitions in neutral Yb [28,29], will allow one to discriminate between nonlinearities of different origin. Characterizing the nonlinearities arising from within the SM can provide new information about the nucleus [88], especially in combination with improved electronic-structure calculations. On the other hand, if evidence for a new boson should emerge from the improved measurements, it can be independently verified by performing similar measurements on other atomic species [10], such as Ca/Ca^+ [13,89], Sr/Sr^+ [12,14], Nd^+ [90], or on highly charged ions [91–94], as well as on molecules like Sr_2 [95]. Unstable isotopes (e.g., ^{166}Yb with a half-life of ∼2.4 days) can be used to increase the number of points in the King Plot, providing strong further constraints on the origin of the nonlinearity. The generalization of nonlinearity measures $\zeta_\pm$ for more isotopes or transitions is discussed in the Supplemental Material [33].

This work was supported by the NSF and NSF CUA. This project received funding from the European Union's Horizon 2020 research and innovation programme under the Marie Sklodowska-Curie Grant No. 795121. C. L. was supported by the U. S. Department of Defense (DoD) through the National Defense Science and Engineering Graduate Fellowship (NDSEG) Program. J. C. B. is supported by the Australian Research Council (DP190100974). A. K. acknowledges the partial support of a William M. and Jane D. Fairbank Postdoctoral Fellowship of Stanford University. We thank M. Drewsen, V. V. Flambaum, P. Harris, N. Huntemann, T. Mehlstäubler, R. Milner, R. Ozeri, E. Peik, G. Perez, R. F. Garcia Ruiz, Y. Soreq, J. Thaler, and T. Zelevinsky for interesting discussions, W. Nazarewicz and P. Reinhard for providing information about the Yb nucleus, and V. Dzuba for pointing out the nuclear quadrupole deformation as a potential significant source of nonlinearity [26].

*I. C. and J. H. contributed equally to this work.
†vuletic@mit.edu

[1] V. C. Rubin, W. K. Ford, and N. Thonnard, Astrophys. J. **238**, 471 (1980).
[2] D. Clowe, M. Bradač, A. H. Gonzalez, M. Markevitch, S. W. Randall, C. Jones, and D. Zaritsky, Astrophys. J. **648**, L109 (2006).
[3] R. Massey, T. Kitching, and J. Richard, Rep. Prog. Phys. **73**, 086901 (2010).
[4] Y. Akrami *et al.* (Planck Collaboration), arXiv:1807.06205.
[5] M. Tanabashi *et al.* (Particle Data Group), Phys. Rev. D **98**, 030001 (2018).
[6] P. W. Graham, I. G. Irastorza, S. K. Lamoreaux, A. Lindner, and K. A. van Bibber, Annu. Rev. Nucl. Part. Sci. **65**, 485 (2015).
[7] T. E. Chupp, P. Fierlinger, M. J. Ramsey-Musolf, and J. T. Singh, Rev. Mod. Phys. **91**, 015001 (2019).
[8] M. S. Safronova, D. Budker, D. DeMille, Derek F. Jackson Kimball, A. Derevianko, and C. W. Clark, Rev. Mod. Phys. **90**, 025008 (2018).
[9] C. Delaunay, R. Ozeri, G. Perez, and Y. Soreq, Phys. Rev. D **96**, 093001 (2017).
[10] J. C. Berengut, D. Budker, C. Delaunay, V. V. Flambaum, C. Frugiuele, E. Fuchs, C. Grojean, R. Harnik, R. Ozeri, G. Perez *et al.*, Phys. Rev. Lett. **120**, 091801 (2018).
[11] F. Gebert, Y. Wan, F. Wolf, C. N. Angstmann, J. C. Berengut, and P. O. Schmidt, Phys. Rev. Lett. **115**, 053003 (2015).
[12] T. Manovitz, R. Shaniv, Y. Shapira, R. Ozeri, and N. Akerman, Phys. Rev. Lett. **123**, 203001 (2019).
[13] F. W. Knollmann, A. N. Patel, and S. C. Doret, Phys. Rev. A **100**, 022514 (2019).
[14] H. Miyake, N. C. Pisenti, P. K. Elgee, A. Sitaram, and G. K. Campbell, Phys. Rev. Research **1**, 033113 (2019).
[15] W. H. King, *Isotope Shifts in Atomic Spectra* (Plenum Press, New York, 1984).
[16] A. J. Krasznahorkay, M. Csatlós, L. Csige, Z. Gácsi, J. Gulyás, Á. Nagy, N. Sas, J. Timár, T. G. Tornyi, I. Vajda *et al.*, J. Phys. Conf. Ser. **1056**, 012028 (2018).
[17] A. J. Krasznahorkay, M. Csatlós, L. Csige, Z. Gácsi, J. Gulyás, M. Hunyadi, I. Kuti, B. M. Nyakó, L. Stuhl, J. Timár *et al.*, Phys. Rev. Lett. **116**, 042501 (2016).

[18] A. J. Krasznahorkay, M. Csatlos, L. Csige, J. Gulyas, M. Koszta, B. Szihalmi, J. Timar, D. S. Firak, A. Nagy, N. J. Sas *et al.*, arXiv:1910.10459.

[19] J. L. Feng, B. Fornal, I. Galon, S. Gardner, J. Smolinsky, T. M. P. Tait, and P. Tanedo, Phys. Rev. Lett. **117**, 071803 (2016).

[20] J. L. Feng, B. Fornal, I. Galon, S. Gardner, J. Smolinsky, T. M. P. Tait, and P. Tanedo, Phys. Rev. D **95**, 035017 (2017).

[21] U. D. Jentschura and I. Nándori, Phys. Rev. A **97**, 042502 (2018).

[22] D. Banerjee, V. E. Burtsev, A. G. Chumakov, D. Cooke, P. Crivelli, E. Depero, A. V. Dermenev, S. V. Donskov, R. R. Dusaev, T. Enik *et al.* (NA64 Collaboration), Phys. Rev. Lett. **120**, 231802 (2018).

[23] V. V. Flambaum, A. J. Geddes, and A. V. Viatkina, Phys. Rev. A **97**, 032510 (2018).

[24] K. Mikami, M. Tanaka, and Y. Yamamoto, Eur. Phys. J. C **77**, 896 (2017).

[25] M. Tanaka and Y. Yamamoto, arXiv:1911.05345.

[26] S. O. Allehabi, V. A. Dzuba, V. V. Flambaum, A. V. Afanasjev, and S. E. Agbemava, arXiv:2001.09422.

[27] N. Huntemann, C. Sanner, B. Lipphardt, C. Tamm, and E. Peik, Phys. Rev. Lett. **116**, 063001 (2016).

[28] Z. W. Barber, C. W. Hoyt, C. W. Oates, L. Hollberg, A. V. Taichenachev, and V. I. Yudin, Phys. Rev. Lett. **96**, 083002 (2006).

[29] M. S. Safronova, S. G. Porsev, C. Sanner, and J. Ye, Phys. Rev. Lett. **120**, 173001 (2018).

[30] W. Huang, G. Audi, M. Wang, F. G. Kondev, S. Naimi, and X. Xu, Chin. Phys. C **41**, 030002 (2017).

[31] M. Wang, G. Audi, F. G. Kondev, W. Huang, S. Naimi, and X. Xu, Chin. Phys. C **41**, 030003 (2017).

[32] R. Rana, M. Höcker, and E. G. Myers, Phys. Rev. A **86**, 050502(R) (2012).

[33] See Supplemental Material at http://link.aps.org/supplemental/10.1103/PhysRevLett.125.123002 for the details on experimental protocols, data analysis, estimation of systematic effects, and the calculation of electronic state-dependent factors, which includes Refs. [34–63].

[34] M. Cetina, Ph.D. Thesis, Massachusetts Institute of Technology, 2011.

[35] S. Olmschenk, K. C. Younge, D. L. Moehring, D. N. Matsukevich, P. Maunz, and C. Monroe, Phys. Rev. A **76**, 052314 (2007).

[36] A.-M. Mårtensson-Pendrill, D. S. Gough, and P. Hannaford, Phys. Rev. A **49**, 3351 (1994).

[37] T. Feldker, H. Fürst, N. V. Ewald, J. Joger, and R. Gerritsma, Phys. Rev. A **97**, 032511 (2018),

[38] K. Sugiyama, A. Wakita, and A. Nakata, in *Conference on Precision Electromagnetic Measurements. Conference Digest. CPEM 2000 (Cat. No. 00CH37031)* (IEEE, New York, 2000), pp. 509–510.

[39] C. Gerz, J. Roths, F. Vedel, and G. Werth, Z. Phys. D **8**, 235 (1988).

[40] B. Efron and R. Tibshirani, *An Introduction to the Bootstrap*, 1st ed. (Chapman & Hall/CRC, New York, 1993).

[41] I. Lizuain, J. G. Muga, and J. Eschner, Phys. Rev. A **76**, 033808 (2007).

[42] D. J. Berkeland, J. D. Miller, J. C. Bergquist, W. M. Itano, and D. J. Wineland, J. Appl. Phys. **83**, 5025 (1998).

[43] M. S. Safronova, M. G. Kozlov, and C. W. Clark, IEEE Trans. Ultrason. Ferroelectr. Freq. Control **59**, 439 (2012).

[44] A. Roy, S. De, B. Arora, and B. K. Sahoo, J. Phys. B **50**, 205201 (2017).

[45] D. K. Nandy and B. K. Sahoo, Phys. Rev. A **90**, 050503(R) (2014).

[46] P. Dubé, A. A. Madej, Z. Zhou, and J. E. Bernard, Phys. Rev. A **87**, 023806 (2013).

[47] C. Degenhardt, T. Nazarova, C. Lisdat, H. Stoehr, U. Sterr, and F. Riehle, IEEE Trans. Instrum. Meas. **54**, 771 (2005).

[48] C. Sanner, N. Huntemann, R. Lange, C. Tamm, and E. Peik, Phys. Rev. Lett. **120**, 053602 (2018).

[49] T. C, M. Niels, and K. Martina, *Trapped Charged Particles: A Graduate Textbook with Problems and Solutions*, Advanced Textbooks in Physics (World Scientific, Singapore, 2016).

[50] V. A. Dzuba, V. V. Flambaum, and M. G. Kozlov, Phys. Rev. A **54**, 3948 (1996).

[51] V. A. Dzuba and A. Derevianko, J. Phys. B **43**, 074011 (2010).

[52] M. S. Safronova, M. G. Kozlov, W. R. Johnson, and D. Jiang, Phys. Rev. A **80**, 012516 (2009).

[53] J. Ekman, P. Jnsson, M. Godefroid, C. Naz, G. Gaigalas, and J. Biero, Comput. Phys. Commun. **235**, 433 (2019).

[54] S. A. Blundell, P. E. G. Baird, C. W. P. Palmer, D. N. Stacey, and G. K. Woodgate, J. Phys. B **20**, 3663 (1987).

[55] M. Roberts, P. Taylor, S. V. Gateva-Kostova, R. B. M. Clarke, W. R. C. Rowley, and P. Gill, Phys. Rev. A **60**, 2867 (1999).

[56] C. Tamm, S. Weyers, B. Lipphardt, and E. Peik, Phys. Rev. A **80**, 043403 (2009).

[57] S. Webster, R. Godun, S. King, G. Huang, B. Walton, V. Tsatourian, H. Margolis, S. Lea, and P. Gill, IEEE Trans. Ultrason. Ferroelectr. Freq. Control **57**, 592 (2010).

[58] G. Fricke and K. Heilig, in *Nuclear Charge Radii*, edited by H. Schopper, Landolt-Börnstein–Group I Elementary Particles, Nuclei and Atoms Vol. 20 (Springer-Verlag, Berlin, Heidelberg, 2004), pp. 1–36.

[59] A. Papoulia, B. G. Carlsson, and J. Ekman, Phys. Rev. A **94**, 042502 (2016).

[60] M. Puchalski and K. Pachucki, Hyperfine Interact. **196**, 35 (2010).

[61] C. W. P. Palmer, J. Phys. B **20**, 5987 (1987).

[62] H. De Vries, C. De Jager, and C. De Vries, At. Data Nucl. Data Tables **36**, 495 (1987).

[63] T. Sasanuma, Ph.D. thesis, Massachusetts Institute of Technology, 1979.

[64] I. Angeli and K. Marinova, At. Data Nucl. Data Tables **99**, 69 (2013).

[65] M. Cetina, A. Bylinskii, L. Karpa, D. Gangloff, K. M. Beck, Y. Ge, M. Scholz, A. T. Grier, I. Chuang, and V. Vuletić, New J. Phys. **15**, 053001 (2013).

[66] P. Taylor, M. Roberts, S. V. Gateva-Kostova, R. B. M. Clarke, G. P. Barwood, W. R. C. Rowley, and P. Gill, Phys. Rev. A **56**, 2699 (1997).

[67] E. C. Seltzer, Phys. Rev. **188**, 1916 (1969).

[68] I. Grant, B. McKenzie, P. Norrington, D. Mayers, and N. Pyper, Comput. Phys. Commun. **21**, 207 (1980).
[69] K. Dyall, I. Grant, C. Johnson, F. Parpia, and E. Plummer, Comput. Phys. Commun. **55**, 425 (1989).
[70] P. Jönsson, A. Ynnerman, C. Froese Fischer, M. R. Godefroid, and J. Olsen, Phys. Rev. A **53**, 4021 (1996).
[71] S. G. Porsev, M. G. Kozlov, and D. Reimers, Phys. Rev. A **79**, 032519 (2009).
[72] B. Fawcett and M. Wilson, At. Data Nucl. Data Tables **47**, 241 (1991).
[73] E. Biémont, J.-F. Dutrieux, I. Martin, and P. Quinet, J. Phys. B **31**, 3321 (1998).
[74] C. Froese Fischer, G. Gaigalas, P. Jönsson, and J. Bieroń, Comput. Phys. Commun. **237**, 184 (2019).
[75] V. A. Dzuba, V. V. Flambaum, P. G. Silvestrov, and O. P. Sushkov, J. Phys. B **18**, 597 (1985).
[76] E. Kahl and J. Berengut, Comput. Phys. Commun. **238**, 232 (2019).
[77] D. Hanneke, S. Fogwell, and G. Gabrielse, Phys. Rev. Lett. **100**, 120801 (2008).
[78] D. Hanneke, S. Fogwell Hoogerheide, and G. Gabrielse, Phys. Rev. A **83**, 052122 (2011).
[79] T. Aoyama, M. Hayakawa, T. Kinoshita, and M. Nio, Phys. Rev. Lett. **109**, 111807 (2012).
[80] R. Bouchendira, P. Cladé, S. Guellati-Khélifa, F. Nez, and F. Biraben, Phys. Rev. Lett. **106**, 080801 (2011).
[81] H. Davoudiasl, H.-S. Lee, and W. J. Marciano, Phys. Rev. D **89**, 095006 (2014).
[82] R. Barbieri and T. Ericson, Phys. Lett. **57B**, 270 (1975).
[83] H. Leeb and J. Schmiedmayer, Phys. Rev. Lett. **68**, 1472 (1992).
[84] Y. N. Pokotilovski, Phys. At. Nucl. **69**, 924 (2006).
[85] V. V. Nesvizhevsky, G. Pignol, and K. V. Protasov, Phys. Rev. D **77**, 034020 (2008).
[86] H. A. Fürst, C.-H. Yeh, D. Kalincev, A. P. Kulosa, L. S. Dreissen, R. Lange, E. Benkler, N. Huntemann, E. Peik, and T. E. Mehlstäubler, arXiv:2006.14356.
[87] M. Roberts, P. Taylor, G. P. Barwood, P. Gill, H. A. Klein, and W. R. C. Rowley, Phys. Rev. Lett. **78**, 1876 (1997).
[88] P.-G. Reinhard, W. Nazarewicz, and R. F. Garcia Ruiz, Phys. Rev. C **101**, 021301(R) (2020).
[89] A. Mortensen, J. J. T. Lindballe, I. S. Jensen, P. Staanum, D. Voigt, and M. Drewsen, Phys. Rev. A **69**, 042502 (2004).
[90] N. Bhatt, K. Kato, and A. C. Vutha, arXiv:2002.08290.
[91] P. Micke, T. Leopold, S. A. King, E. Benkler, L. J. Spieß, L. Schmöger, M. Schwarz, J. R. Crespo López-Urrutia, and P. O. Schmidt, Nature (London) **578**, 60 (2020).
[92] V. A. Yerokhin, R. A. Müller, A. Surzhykov, P. Micke, and P. O. Schmidt, Phys. Rev. A **101**, 012502 (2020).
[93] R. Silwal, A. Lapierre, J. D. Gillaspy, J. M. Dreiling, S. A. Blundell, Dipti, A. Borovik, G. Gwinner, A. C. C. Villari, Y. Ralchenko *et al.*, Phys. Rev. A **98**, 052502 (2018).
[94] M. G. Kozlov, M. S. Safronova, J. R. Crespo López-Urrutia, and P. O. Schmidt, Rev. Mod. Phys. **90**, 045005 (2018).
[95] B. H. McGuyer, M. McDonald, G. Z. Iwata, M. G. Tarallo, A. T. Grier, F. Apfelbeck, and T. Zelevinsky, New J. Phys. **17**, 055004 (2015).

Appendix F

Reprint of "Evidence of Two-source King plot Nonlinearity in Spectroscopic Search for New Boson"

This Appendix contains a reprint of Ref. [8]: J. Hur*, D. P. L. A. Craik*, I. Counts*, E. Knyazev, L. Caldwell, C. Leung, S. Pandey, J. C. Berengut, A. Geddes, W. Nazarewicz, P.-G. Reinhard, A. Kawasaki, H. Jeon, W. Jhe, and V. Vuletić, *Evidence of two-source King plot nonlinearity in spectroscopic search for new boson*, Phys. Rev. Lett. **128**, 163201 (2022) (*equal contributions).

Evidence of Two-Source King Plot Nonlinearity in Spectroscopic Search for New Boson

Joonseok Hur,[1,*] Diana P. L. Aude Craik,[1,*] Ian Counts,[1,*] Eugene Knyazev,[1] Luke Caldwell,[2] Calvin Leung,[1] Swadha Pandey,[1] Julian C. Berengut,[3] Amy Geddes,[3] Witold Nazarewicz,[4] Paul-Gerhard Reinhard,[5] Akio Kawasaki,[6] Honggi Jeon,[7] Wonho Jhe,[7] and Vladan Vuletić[1,†]

[1]*Department of Physics and Research Laboratory of Electronics, Massachusetts Institute of Technology, Cambridge, Massachusetts 02139, USA*

[2]*JILA, NIST and University of Colorado, Boulder, Colorado 80309, USA*

[3]*School of Physics, University of New South Wales, Sydney, New South Wales 2052, Australia*

[4]*Facility for Rare Isotope Beams and Department of Physics and Astronomy, Michigan State University, East Lansing, Michigan 48824, USA*

[5]*Institut für Theoretische Physik, Universität Erlangen, Erlangen D-91054, Germany*

[6]*National Metrology Institute of Japan (NMIJ), National Institute of Advanced Industrial Science and Technology (AIST), 1-1-1 Umezono, Tsukuba, Ibaraki 305-8563, Japan*

[7]*Department of Physics and Astronomy, Seoul National University, Seoul 151-747, Korea*

(Received 8 January 2022; revised 19 February 2022; accepted 2 March 2022; published 22 April 2022)

Optical precision spectroscopy of isotope shifts can be used to test for new forces beyond the standard model, and to determine basic properties of atomic nuclei. We measure isotope shifts on the highly forbidden $^2S_{1/2} \rightarrow {}^2F_{7/2}$ octupole transition of trapped ^{168,170,172,174,176}Yb ions. When combined with previous measurements in Yb^+ and very recent measurements in Yb, the data reveal a King plot nonlinearity of up to 240σ. The trends exhibited by experimental data are explained by nuclear density functional theory calculations with the Fayans functional. We also find, with 4.3σ confidence, that there is a second distinct source of nonlinearity, and discuss its possible origin.

DOI: 10.1103/PhysRevLett.128.163201

Despite ample evidence for the existence of dark matter [1–4] and concerted experimental searches for candidate particles [5–8], its origin and composition remain unknown. Isotope-shift (IS) spectroscopy has been recently proposed as a tabletop method to search for dark-matter candidates in the intermediate mass range $\lesssim 100\ \mathrm{MeV}/c^2$ [9,10]. In particular, IS spectroscopy can be used to search for a hypothetical new boson, ϕ, that mediates interactions between quarks and leptons. An observable consequence is an additional isotope shift that arises from the effective interaction between neutrons and electrons. Such a shift could be detected as a deviation from linearity in a King plot [11] that compares the normalized isotope shifts for two different transitions. If at least three isotope shifts in each transition are measured, a deviation from linearity can be detected. The nonlinearity can also be caused by higher-order nuclear effects [12–18].

In our previous work, we reported evidence, at the 3σ level, for a nonlinearity in a King plot that compared two optical quadrupole transitions ($^2S_{1/2} \rightarrow {}^2D_{3/2}$, $^2D_{5/2}$) in a trapped Yb^+ ion [19]. The measurement was performed for five even isotopes, one more than required, and we also proposed a new method to assign the nonlinearity to different possible physical origins based on the observed nonlinearity pattern. At the reported measurement accuracy of ~300 Hz on two relatively similar electronic excited states, the source of the nonlinearity could not be discriminated, and was consistent both with a new boson and with standard-model (SM) nuclear shifts. IS spectroscopy in Ca^+, which has lighter nuclei and therefore lower sensitivity to both new physics and nuclear effects than Yb^+ [10], showed no King nonlinearity at the 20 Hz level [20]. At the time of completion of the present work, large King nonlinearities were also reported when comparing transitions in neutral Yb [21,22] with the quadrupole transitions in Yb^+.

In this Letter, we report IS laser spectroscopy for the highly forbidden octupole transition $^2S_{1/2} \rightarrow {}^2F_{7/2}$ in Yb^+. The electron configuration in the F state is very different from the previously measured D states [19], which increased the size of the observed King nonlinearity 20-fold (see Fig. 1). At a measurement resolution of ~500 Hz, we observe a King-plot nonlinearity with 41 standard deviations σ. Including the recent data for neutral Yb [21,22] into our analysis, the significance of the nonlinearity rises to 240σ, and analyzing the patterns [19] we show that the measurements can be consistently explained by microscopic calculations carried out within nuclear density functional theory (DFT), which provides agreement with ground-state properties of complex deformed Yb isotopes [16,23]. Combining all measured transitions in Yb^+ and Yb, we further find evidence, at the

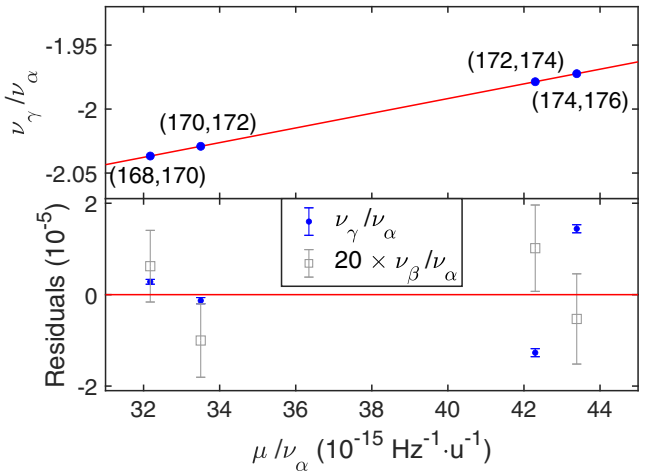

FIG. 1. Frequency-normalized King plot (top) and residuals (bottom, blue) for the γ ($^2S_{1/2} \to {}^2F_{7/2}$) transition and reference transition α ($^2S_{1/2} \to {}^2D_{5/2}$) for even-neighbor pairs ($A' = A + 2$) of Yb^+ isotopes. A deviation from linearity (red line) by 41 standard deviations σ is observed. For reference, residuals for the β ($^2S_{1/2} \to {}^2D_{3/2}$) transition [19], magnified 20-fold, are also plotted in gray. The error bars indicate 2σ uncertainties; for correlations between the errors, see Supplemental Material [24].

4.3σ level, of a second, smaller source of nonlinearity, and discuss implications for limits on a new boson. Finally, we also extract nuclear data that can be used to further fine-tune nuclear energy density functionals.

Our IS measurements are performed on individual cold trapped $^AYb^+$ ions with zero nuclear spin ($A \in \{168, 170, 172, 174, 176\}$). To make an IS measurement on the octupole transition $^2S_{1/2} \to {}^2F_{7/2}$ near 467 nm that we label γ, we first load a single ion of one isotope A into the trap, Doppler cool it to $\sim$500 μK, and measure the excitation probability when scanning the frequency of our probe laser, a frequency-doubled Ti:sapphire laser that is locked to an ultralow-thermal-expansion (ULE) cavity with linewidth $\kappa_c/(2\pi) = 30$ kHz. We measure two transitions between Zeeman sublevels that are symmetrically detuned from the zero-field transition ν_γ, and determine the center frequency ν_γ^A as the mean (see Supplemental Material [24]). A second isotope A' is then loaded into the trap and its center frequency $\nu_\gamma^{A'}$ is measured. We alternate several times between the two isotopes, achieving an accuracy of $\sim$500 Hz in our measurement of the IS $\nu_\gamma^{AA'} \equiv \nu_\gamma^A - \nu_\gamma^{A'}$, limited mainly by the long-term stability of the ULE cavity. Our measured ISs $\nu_\gamma^{AA'}$ are given in Table I. Table II lists the absolute transition frequencies derived from our measured IS in combination with the absolute transition frequency for $^{172}Yb^+$ [56].

To a very good approximation, the IS can be factored into an electronic component, which is transition dependent (labeled by a greek letter subscript) but does not depend on the isotope, and a nuclear contribution, which depends on the isotopes (labeled by AA') but not on the electronic transition [9,11,14,19]:

$$\nu_\gamma^{AA'} = F_\gamma \delta\langle r^2\rangle^{AA'} + K_\gamma \mu^{AA'} + G_\gamma^{(4)} \delta\langle r^4\rangle^{AA'} + G_\gamma^{(2)} [\delta\langle r^2\rangle^2]^{AA'} + \upsilon_{ne} D_\gamma a^{AA'} + \cdots \quad (1)$$

Here $\delta\langle r^n\rangle^{AA'} \equiv \langle r^n\rangle^A - \langle r^n\rangle^{A'}$ is the difference in the nth nuclear charge moment between isotopes A and A', $\mu^{AA'} \equiv 1/m^A - 1/m^{A'}$ is the inverse-mass difference, and $[\delta\langle r^2\rangle^2]^{AA'} \equiv (\delta\langle r^2\rangle^{AA''})^2 - (\delta\langle r^2\rangle^{A'A''})^2$, with A'' denoting a reference isotope (we use $A'' = 172$). The quantity $\upsilon_{ne} = (-1)^{s+1} y_n y_e/(4\pi\hbar c)$ is the product of the coupling constants of the new boson to the neutron y_n and electron y_e, resulting in a Yukawa-like potential given by $V_{ne}(r) = \hbar c \upsilon_{ne} \exp(-r/\lambda\!\!\!^{-}_c)/r$ for a boson with spin s, mass m_ϕ, and reduced Compton wavelength $\lambda\!\!\!^{-}_c = \hbar/(m_\phi c)$ [9,14,19]. $a^{AA'} = A - A'$ is the neutron-number difference between the two isotopes. The coefficients F, K, $G^{(4)}$, $G^{(2)}$, and D are transition-dependent quantities that quantify the field shift, the mass shift, the fourth-moment shift, the quadratic field shift (QFS), and the sensitivity to the new boson, respectively.

To eliminate the large field shift F (associated with the size change of the nucleus $\delta\langle r^2\rangle$, of order $\sim$4 GHz), and mass shift K (of order $\sim$0.2 GHz) contributions, one can use a second set of isotope shifts measured on a different

TABLE I. Isotope shifts $\nu_{\gamma,\alpha}^{AA'} = \nu_{\gamma,\alpha}^A - \nu_{\gamma,\alpha}^{A'}$ measured for the γ: $^2S_{1/2} \to {}^2F_{7/2}$ (this work) and α: $^2S_{1/2} \to {}^2D_{5/2}$ [19] transitions for pairs (A, A') of stable Yb^+ even isotopes. Inverse-mass differences $\mu^{AA'} = 1/m^A - 1/m^{A'}$ calculated from [57–60] with the Yb ionization energy set to 6.254 eV are also listed. Numbers in parentheses indicate 1σ statistical uncertainties.

(A, A')	$\nu_\gamma^{AA'}$ [MHz]	$\nu_\alpha^{AA'}$ [MHz]	$\mu^{AA'}$ [10^{-6} u^{-1}]
(168,170)	−4 438.160 30(50)	2 179.098 93(21)	70.113 619 5(36)
(170,172)	−4 149.190 38(45)	2 044.854 78(34)	68.506 890 49(63)
(172,174)	−3 132.321 60(50)	1 583.068 42(36)	66.958 651 95(64)
(174,176)	−2 976.391 60(48)	1 509.055 29(28)	65.474 078 21(65)
(168,172)	−8 587.352 00(47)		
(170,174)	−7 281.511 88(45)	3 627.922 95(50)	
(172,176)	−6 108.712 93(44)		

TABLE II. Absolute frequencies of the γ:$^2S_{1/2} \rightarrow {}^2F_{7/2}$ transition extracted from our IS measurements and the absolute frequency measurement in Refs. [56].

Isotope	Absolute frequency [THz]	Ref.
168	642.108 197 799 37(37)	[This work]
170	642.112 635 960 22(32)	[This work]
172	642.116 785 150 887 6(24)	[56]
174	642.119 917 472 26(33)	[This work]
176	642.122 893 863 84(36)	[This work]

reference transition τ to generate a King plot [11]. In its frequency-normalized version [19], the relationship studied can be written as

$$\bar{\nu}_\gamma^{AA'} = f_{\gamma\tau} + K_{\gamma\tau}\bar{\mu}^{AA'} + G_{\gamma\tau}^{(4)}\overline{\delta\langle r^4\rangle}^{AA'} + G_{\gamma\tau}^{(2)}\overline{[\delta\langle r^2\rangle^2]}^{AA'} + v_{ne}D_{\gamma\tau}\bar{a}^{AA'}, \quad (2)$$

where the notation $\bar{x}^{AA'} \equiv x^{AA'}/\nu_\tau^{AA'}$ indicates frequency-normalized terms. We define $z_{\gamma\tau} \equiv Z_\gamma/Z_\tau$ as the ratio of coefficients for transitions γ and τ, and $Z_{\gamma\tau} \equiv Z_\gamma(1 - f_{\gamma\tau}/z_{\gamma\tau})$ for $Z \in \{F, K, G^{(2)}, G^{(4)}, D\}$. The first two terms in Eq. (2) represent the linear relation between $\bar{\nu}_\gamma$ and $\bar{\mu}$ in the King plot, while the remaining terms possibly violate the linearity.

Figure 1 shows a frequency-normalized King plot using the previously measured transition α:$^2S_{1/2} \rightarrow {}^2D_{5/2}$ near 411 nm [19] as the reference transition τ. The residuals from the linear fit reveal a nonlinearity at the 10^{-5} level, corresponding to 41σ. The nonlinearity is 20 times larger than the nonlinearity we observed previously [19] comparing the two quadrupole transitions, α and β:$^2S_{1/2} \rightarrow {}^2D_{3/2}$, that have a more similar electronic structure. The recent measurements in neutral Yb [21,22], when combined with our α or β transition data, confirm a nonlinearity of a similar size (see also Fig. 2).

Having unambiguously established a King nonlinearity, we can gain information about the sources of nonlinearity by analyzing the deviation patterns [19]. With four isotope-shift data points, we can rewrite Eq. (2) in terms of four-dimensional vectors as follows:

$$\bar{\boldsymbol{\nu}}_\gamma = f_{\gamma\tau}\mathbf{1} + K_{\gamma\tau}\bar{\boldsymbol{\mu}} + (\lambda_+\boldsymbol{\Lambda}_+ + \lambda_-\boldsymbol{\Lambda}_-), \quad (3)$$

where the vector space inhabited by the vectors $z \equiv (z_1, z_2, z_3, z_4)$ with $z_k \equiv z^{A,A+2}$ ($A = 166 + 2k$ for $k = 1$, 2, 3, 4, $z \in \{\bar{\mu}, \bar{\nu}_\gamma\}$) is spanned by the basis $(\mathbf{1}, \bar{\boldsymbol{\mu}}, \boldsymbol{\Lambda}_+, \boldsymbol{\Lambda}_-)$.

The first two vectors, $\mathbf{1} \equiv (1, 1, 1, 1)$ and $\bar{\boldsymbol{\mu}}$, define a plane of King linearity (i.e., the component of $\bar{\boldsymbol{\nu}}_\gamma$ in this plane does not give rise to King nonlinearities), while the unit vectors $\boldsymbol{\Lambda}_+$ and $\boldsymbol{\Lambda}_-$, defined as $\boldsymbol{\Lambda}_+ \propto (\bar{\mu}_3 - \bar{\mu}_2, \bar{\mu}_1 - \bar{\mu}_4, \bar{\mu}_4 - \bar{\mu}_1, \bar{\mu}_2 - \bar{\mu}_3)$ and $\boldsymbol{\Lambda}_- \propto (\bar{\mu}_4 - \bar{\mu}_2, \bar{\mu}_1 - \bar{\mu}_3, \bar{\mu}_2 - \bar{\mu}_4, \bar{\mu}_3 - \bar{\mu}_1)$, span the out-of-plane space of vectors that produce a King nonlinearity (see Supplemental Material [24]). Any vector with nonzero residuals from the linear King plot fit hence has components in the space spanned by $(\boldsymbol{\Lambda}_+, \boldsymbol{\Lambda}_-)$, and can be expressed in terms of its scalar components λ_+ and λ_- along $\boldsymbol{\Lambda}_+$ and $\boldsymbol{\Lambda}_-$, respectively. ($\boldsymbol{\Lambda}_+$ and $\boldsymbol{\Lambda}_-$ correspond approximately to the zigzag $+-+-$ and curved $+--+$ patterns of residuals introduced in Ref. [19].) Both SM and new-boson effects produce nonlinearities with a defined λ_+/λ_- ratio, given by the associated nuclear factors $x^{AA'}$, and are characterized by lines along definite directions in the $\lambda_\pm$ plane (see Fig. 2).

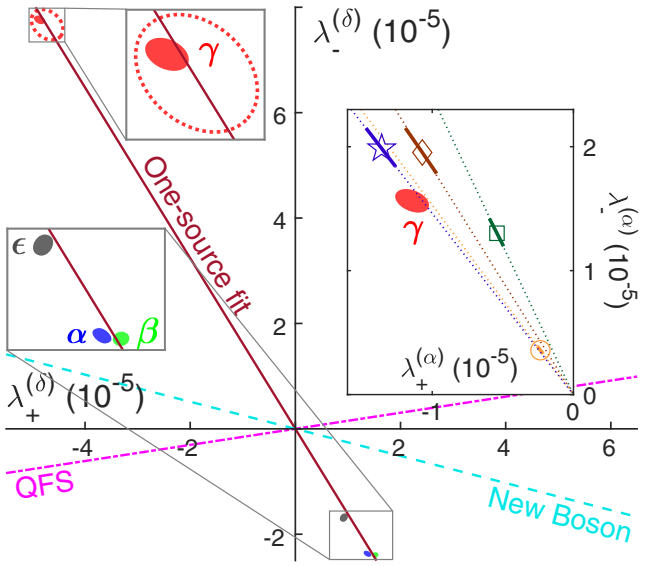

FIG. 2. Decomposition of the measured nonlinearity (solid ellipses, 95% confidence interval) onto the (λ_+, λ_-) basis for the transitions α:$^2S_{1/2} \rightarrow {}^2D_{5/2}$ in Yb^+ (blue) [19], β:$^2S_{1/2} \rightarrow {}^2D_{3/2}$ in Yb^+ (green) [19], ϵ:$^1S_0 \rightarrow {}^1D_2$ (dark gray) in Yb [22], and γ:$^2S_{1/2} \rightarrow {}^2F_{7/2}$ in Yb^+ (red, this work). The corresponding frequency-normalized King plot is generated with the reference transition δ:$^1S_0 \rightarrow {}^3P_0$ in Yb [21] ($\lambda_\pm^{(\delta)}$) that has been measured with the highest frequency accuracy. The red dotted ellipse indicates a previous preliminary measurement for the γ transition [61]. The dashed lines indicate the ratio λ_+/λ_- that would arise solely from a new boson (light blue dashed line) or the QFS (pink dash-dotted line). The brown solid line is a single-source fit to all four transitions α, β, γ, ϵ, yielding evidence for a second nonlinearity source with 4.3σ significance ($\chi^2 = 25.4$). The largest inset shows the nonlinearity in a King plot with α as the reference transition ($\lambda_\pm^{(\alpha)}$). Open symbols indicate the nonlinearity due to $\delta\langle r^4\rangle^{AA'}$ from nuclear DFT calculations with SV-min (square), RD-min (diamond), UNEDF1 (circle), and Fy(Δr) (star) energy density functionals. Short bold lines indicate the uncertainty in electronic-structure calculations (see Supplemental Material [24]).

Figure 2 displays the measured nonlinearity in the $\lambda_\pm$ plane for the γ transition, as well as for the previously measured α and β transitions in Yb^+ [19], and the recently measured ϵ:$^1S_0 \rightarrow {}^1D_2$ transition in Yb [22]. For the reference transition τ in Eq. (2), we choose in Fig. 2 the

transition δ: $^1S_0 \rightarrow {}^3P_0$ in Yb that has been very recently measured with the highest frequency accuracy [21]. All measured transitions α, β, γ, ϵ, δ are consistent with each other in that they lie nearly along the same direction in the $\lambda_\pm$ plane, indicating that the nonlinearity originates from a common dominant source for all transitions. This direction corresponds neither to a new boson $a^{AA'}$ nor to the QFS $[\delta\langle r^2\rangle^2]^{AA'}$.

To interpret the IS measurements, we performed quantified nuclear calculations of $\langle r^2\rangle$ and $\langle r^4\rangle$ using nuclear density functional theory (DFT) with realistic energy density functionals (EDFs). The nuclear charge radial moments were obtained directly from calculated charge densities as discussed in Refs. [16,23]. To explore a possible span of predictions, we consider four different EDFs: Skyrme functionals SV-min and UNEDF1, extended Skyrme functional RD-min, and the Fayans functional Fy(Δr). The calculated $\delta\langle r^4\rangle$ are multiplied by $G^{(4)}_{\gamma\alpha}$ from atomic structure calculations to predict the nonlinearity for $G^{(4)}_{\gamma\alpha}\delta\langle r^4\rangle$. For details on the calculations, see Refs. [62,63] and Supplemental Material [24].

The predicted values of $\langle r^2\rangle$ and $\langle r^4\rangle$ are impacted by several effects [16,23,64,65], including the surface thickness of nuclear density that shows a pronounced particle-number dependence due to shell effects; the relativistic corrections that contain contributions from the intrinsic nucleon form factors; and nuclear deformation and pairing effects, which also give rise to the fragmentation [23] of the single-particle spin-orbit strength that affects spin-orbit contributions to charge moments. Our DFT calculations take all these effects into account. In this respect, a King plot nonlinearity may be rooted in several nuclear structure effects impacting $\langle r^2\rangle$ and $\langle r^4\rangle$, not just one as discussed in Ref. [13]. As shown in the large inset to Fig. 2, our DFT results agree well with the observed direction in the $\lambda_\pm$ plane (see Supplemental Material [24] for details).

We can also directly compare the calculated changes in the nuclear size $\delta\langle r^2\rangle$ to the measured values. In order to be insensitive to the electronic factor F in Eq. (1), which can currently only be calculated with a typical uncertainty of $\lesssim$30%, we plot in Fig. 3(a) the ratios $\delta\langle r^2\rangle^{A,A+2}/\delta\langle r^2\rangle^{A-2,A}$ that can be determined from the experimental data with much higher accuracy. The nuclear calculations agree with the IS data to within 20%. The ratios obtained from nuclear theory show monotonically increasing trends for the three EDFs SV-min, RD-min, and UNEDF1. Only Fy(Δr) produces a trend that is consistent with data. This is yet another demonstration that the Fayans functional is better adapted to local nonmonotonic trends in charge radius data, see also Refs. [66–68]. We note that Fy(Δr) also provides a better description of nuclear quadrupole deformations as compared to other EDFs, see Supplemental Material [24] for details. This demonstrates that high-precision data on nuclear radii deliver important information for discrimination and further development of nuclear models.

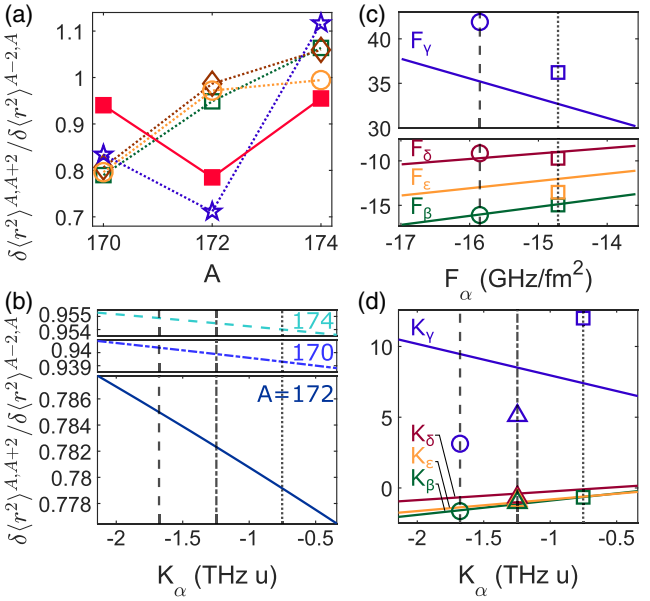

FIG. 3. (a) Comparison plot of derived values for the ratio of the mean-square nuclear radius differences between $(A, A+2)$ isotope pairs. Open symbols mark the values derived from nuclear calculations using SV-min, RD-min, UNEDF1, and Fy(Δr) energy density functionals (see Fig. 2 for symbol assignments). The red filled square symbols are values derived from measured ISs on the 411 nm transition in combination with mass shifts from configuration interaction (CI) [69–72] calculations. (b) Plot of derived values for the ratio of the mean square nuclear radius between sequential isotope pairs as a function of K_α, showing very weak dependence on K_α. (c),(d) Derived values of F_β, F_γ, F_δ, F_ϵ (K_β, K_γ, K_δ, K_ϵ) as a function of F_α (K_α), using the experimentally determined ratios $F_{\kappa\alpha}$ ($K_{\kappa\alpha}$) for $\kappa = \beta, \gamma, \delta, \epsilon$. In (b), (c), and (d), dashed (dotted) vertical lines and round (square) markers indicate values from CI calculations using GRASP2018 [73] (AMBiT [74]). Dash-dotted lines and open triangle markers correspond to CI and many-body perturbation theory (CI + MBPT) [75] calculations using AMBiT.

Our data also provide strong tests for electronic-structure calculations, as shown in Figs. 3(c) and 3(d): The field (mass) shift coefficient F_τ (K_τ) on one transition τ determines the coefficients on all other transitions κ via the experimentally determined value of $F_{\kappa\tau}$ ($K_{\kappa\tau}$) (see Supplemental Material [24] for details).

While all transitions α, β, γ, ϵ lie near a line through the origin in Fig. 2, there is a deviation from that line for all four transitions (plus the reference transition δ) with 4.3σ significance. (In contrast, the generalized King plot proposed in previous studies [14,76] provides a test only for three transitions, giving significance less than 4σ for any choices of three transitions; see Supplemental Material [24]). This second nonlinearity is too large to be explained by the QFS, which is expected to be the next largest source of nonlinearity within the SM (see

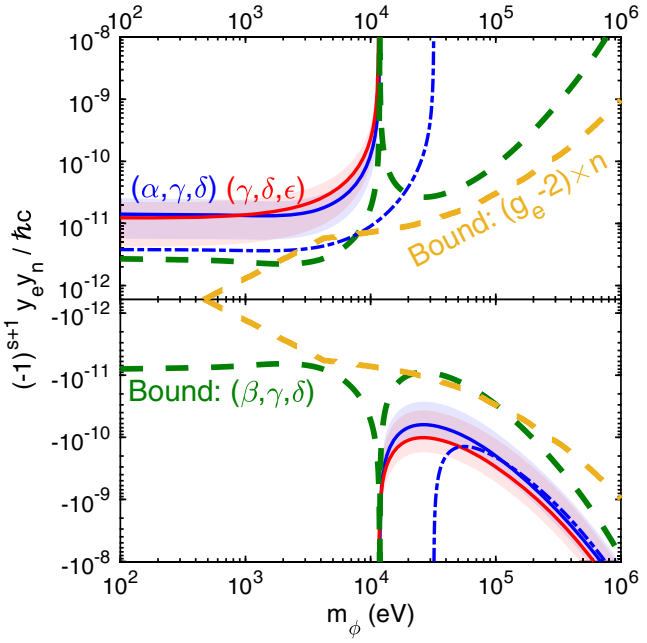

FIG. 4. Product of coupling constants $y_e y_n$ of a new boson with spin s versus boson mass m_ϕ, derived from generalized-King-plot analyses [14,76] of groups of three transitions (α, γ, δ) (blue), $(\gamma, \delta, \epsilon)$ (red), and (β, γ, δ) (green), assuming that the observed second nonlinearity is dominated by a new boson. Dashed lines indicate the lower bounds of $y_e y_n$'s excluded magnitude. Solid lines and shaded areas are center values and confidence intervals for configuration-interaction calculations using AMBiT. [we show the ≈95% confidence interval (see Supplemental Material [24]) that arises from the statistical uncertainty in the measured ISs. The systematic uncertainty due to the atomic structure calculations is larger; the dash-dotted line shows the center value of $y_e y_n$ for the (α, γ, δ) transition combination using GRASP2018 calculation results, for comparison.] The yellow line indicates the bound derived from electron $g_e - 2$ measurements [77–80] in combination with neutron scattering measurements [81–84] from Ref. [10].

Supplemental Material [24]). In Fig. 4, we show the strength of the coupling constant $y_e y_n$ for a new boson vs boson mass under the assumption that the new boson is the sole source of the second nonlinearity. Different combinations of measured transitions give similar values or bounds for the coupling strength $y_e y_n$ that is near or slightly exceeds the best other laboratory bounds given by the combination of $g - 2$ measurements on the electron and neutron scattering experiments [10,77–84].

In the future, it should be possible to reduce the experimental uncertainties by up to 4 orders of magnitude to sub-Hz levels, as has been demonstrated with simultaneously trapped Sr^+ ions [85]. In combination with improved electronic and nuclear calculations, it should then be possible to determine unambiguously if some part of the observed nonlinearity cannot be explained by physics within the SM. Besides better measurements on (more) transitions, it may also become possible to perform further measurements on unstable isotopes, which would allow the direct extraction (and elimination) of additional nuclear effects.

This work was supported by the NSF CUA and the U.S. Department of Energy, Office of Science, Office of Nuclear Physics under Grants No. DE-SC0013365 and No. DE-SC0018083 (NUCLEI SciDAC-4 collaboration). This project has received funding from the European Union's Horizon 2020 research and innovation programme under the Marie Skłodowska-Curie Grant Agreement No. 795121. J. C. B. is supported by the Australian Research Council (DP190100974). C. L. was supported by the U.S. Department of Defense (DOD) through the National Defense Science and Engineering Graduate Fellowship (NDSEG) Program.

*These authors contributed equally to this work.
†vuletic@mit.edu

[1] V. C. Rubin, W. K. Ford, and N. Thonnard, Rotational properties of 21 Sc galaxies with a large range of luminosities and radii, from NGC 4605 ($R = 4$ kpc) to UGC 2885 ($R = 122$ kpc), Astrophys. J. **238**, 471 (1980).
[2] D. Clowe, M. Bradač, A. H. Gonzalez, M. Markevitch, S. W. Randall, C. Jones, and D. Zaritsky, A direct empirical proof of the existence of dark matter, Astrophys. J. **648**, L109 (2006).
[3] R. Massey, T. Kitching, and J. Richard, The dark matter of gravitational lensing, Rep. Prog. Phys. **73**, 086901 (2010).
[4] N. Aghanim *et al.* (Planck Collaboration), Planck 2018 results–I. Overview and the cosmological legacy of Planck, Astron. Astrophys. **641**, A1 (2020).
[5] P. Zyla *et al.* (Particle Data Group), Review of particle physics, Prog. Theor. Exp. Phys. **2020**, 083C01 (2020).
[6] K. Choi, S. H. Im, and C. S. Shin, Recent progress in the physics of axions and axion-like particles, Annu. Rev. Nucl. Part. Sci. **71**, 225 (2021).
[7] T. E. Chupp, P. Fierlinger, M. J. Ramsey-Musolf, and J. T. Singh, Electric dipole moments of atoms, molecules, nuclei, and particles, Rev. Mod. Phys. **91**, 015001 (2019).
[8] M. S. Safronova, D. Budker, D. DeMille, Derek F. Jackson Kimball, A. Derevianko, and C. W. Clark, Search for new physics with atoms and molecules, Rev. Mod. Phys. **90**, 025008 (2018).
[9] C. Delaunay, R. Ozeri, G. Perez, and Y. Soreq, Probing atomic Higgs-like forces at the precision frontier, Phys. Rev. D **96**, 093001 (2017).
[10] J. C. Berengut, D. Budker, C. Delaunay, V. V. Flambaum, C. Frugiuele, E. Fuchs, C. Grojean, R. Harnik, R. Ozeri, G. Perez, and Y. Soreq, Probing New Long-Range Interactions by Isotope Shift Spectroscopy, Phys. Rev. Lett. **120**, 091801 (2018).
[11] W. H. King, *Isotope Shifts in Atomic Spectra* (Springer Science+Business Media, LLC, New York, 1984), 10.1007/978-1-4899-1786-7.
[12] V. V. Flambaum, A. J. Geddes, and A. V. Viatkina, Isotope shift, nonlinearity of King plots, and the search for new particles, Phys. Rev. A **97**, 032510 (2018).

[13] S. O. Allehabi, V. A. Dzuba, V. V. Flambaum, and A. V. Afanasjev, Nuclear deformation as a source of the non-linearity of the King plot in the Yb^+ ion, Phys. Rev. A **103**, L030801 (2021).

[14] K. Mikami, M. Tanaka, and Y. Yamamoto, Probing new intra-atomic force with isotope shifts, Eur. Phys. J. C **77**, 896 (2017).

[15] M. Tanaka and Y. Yamamoto, Relativistic effects in the search for new intra-atomic force with isotope shifts, Prog. Theor. Exp. Phys. **2020**, 103B02 (2020).

[16] P.-G. Reinhard, W. Nazarewicz, and R. F. Garcia Ruiz, Beyond the charge radius: The information content of the fourth radial moment, Phys. Rev. C **101**, 021301(R) (2020).

[17] S. O. Allehabi, V. A. Dzuba, V. V. Flambaum, A. V. Afanasjev, and S. E. Agbemava, Using isotope shift for testing nuclear theory: The case of nobelium isotopes, Phys. Rev. C **102**, 024326 (2020).

[18] R. A. Müller, V. A. Yerokhin, A. N. Artemyev, and A. Surzhykov, Nonlinearities of King's plot and their dependence on nuclear radii, Phys. Rev. A **104**, L020802 (2021).

[19] I. Counts, J. Hur, D. P. L. Aude Craik, H. Jeon, C. Leung, J. C. Berengut, A. Geddes, A. Kawasaki, W. Jhe, and V. Vuletić, Evidence for Nonlinear Isotope Shift in Yb^+ Search for New Boson, Phys. Rev. Lett. **125**, 123002 (2020).

[20] C. Solaro, S. Meyer, K. Fisher, J. C. Berengut, E. Fuchs, and M. Drewsen, Improved Isotope-Shift-Based Bounds on Bosons beyond the Standard Model through Measurements of the $^2D_{3/2} - {}^2D_{5/2}$ Interval in Ca^+, Phys. Rev. Lett. **125**, 123003 (2020).

[21] K. Ono, Y. Saito, T. Ishiyama, T. Higomoto, T. Takano, Y. Takasu, Y. Yamamoto, M. Tanaka, and Y. Takahashi, Observation of non-linearity of generalized King plot in the search for new boson, arXiv:2110.13544 [Phys. Rev. X].

[22] N. L. Figueroa, J. C. Berengut, V. A. Dzuba, V. V. Flambaum, D. Budker, and D. Antypas, Precision Determination of Isotope Shifts in Ytterbium and Implications for New Physics, Phys. Rev. Lett. **128**, 073001 (2022).

[23] P.-G. Reinhard and W. Nazarewicz, Nuclear charge densities in spherical and deformed nuclei: Toward precise calculations of charge radii, Phys. Rev. C **103**, 054310 (2021).

[24] See Supplemental Material at http://link.aps.org/supplemental/10.1103/PhysRevLett.128.163201 for the details on experimental protocols, data analysis, estimation of systematic effects, and the calculation of electronic factors and nuclear parameters, which includes Refs. [25–55].

[25] M. Aymar, A. Debarre, and O. Robaux, Highly excited levels of neutral ytterbium. II. Multichannel quantum defect analysis of odd- and even-parity spectra, J. Phys. B **13**, 1089 (1980).

[26] M. Bender, P.-H. Heenen, and P.-G. Reinhard, Self-consistent mean-field models for nuclear structure, Rev. Mod. Phys. **75**, 121 (2003).

[27] J. C. Berengut, V. A. Dzuba, and V. V. Flambaum, Isotope-shift calculations for atoms with one valence electron, Phys. Rev. A **68**, 022502 (2003).

[28] P. Bogdanovich and G. Žukauskas, Approximate allowance for superposition of configurations in atomic spectra, Sov. Phys. Collect. **23**, 13 (1983).

[29] K. Dyall, I. Grant, C. Johnson, F. Parpia, and E. Plummer, GRASP: A general-purpose relativistic atomic structure program, Comput. Phys. Commun. **55**, 425 (1989).

[30] C. L. Edmunds, T. R. Tan, A. R. Milne, A. Singh, M. J. Biercuk, and C. Hempel, Scalable hyperfine qubit state detection via electron shelving in the $^2D_{5/2}$ and $^2F_{7/2}$ manifolds in $^{171}Yb^+$, Phys. Rev. A **104**, 012606 (2021).

[31] J. Ekman, P. Jönsson, M. Godefroid, C. Nazé, G. Gaigalas, and J. Bieroń, RIS4: A program for relativistic isotope shift calculations, Comput. Phys. Commun. **235**, 433 (2019).

[32] J. Erler, P. Klüpfel, and P.-G. Reinhard, Exploration of a modified density dependence in the Skyrme functional, Phys. Rev. C **82**, 044307 (2010).

[33] I. Grant, B. McKenzie, P. Norrington, D. Mayers, and N. Pyper, An atomic multiconfigurational Dirac-Fock package, Comput. Phys. Commun. **21**, 207 (1980).

[34] N. Huntemann, M. Okhapkin, B. Lipphardt, S. Weyers, C. Tamm, and E. Peik, High-Accuracy Optical Clock Based on the Octupole Transition in $^{171}Yb^+$, Phys. Rev. Lett. **108**, 090801 (2012).

[35] Y.-Y. Jau, J. D. Hunker, and P. D. D. Schwindt, F-state quenching with CH4 for buffer-gas cooled $^{171}Yb^+$ frequency standard, AIP Adv. **5**, 117209 (2015).

[36] S. A. King, R. M. Godun, S. A. Webster, H. S. Margolis, L. A. M. Johnson, K. Szymaniec, P. E. G. Baird, and P. Gill, Absolute frequency measurement of the $^2S_{1/2}$–$^2F_{7/2}$ electric octupole transition in a single ion of $^{171}Yb^+$ with 10^{-15} fractional uncertainty, New J. Phys. **14**, 013045 (2012).

[37] M. Kortelainen, J. McDonnell, W. Nazarewicz, P.-G. Reinhard, J. Sarich, N. Schunck, M. V. Stoitsov, and S. M. Wild, Nuclear energy density optimization: Large deformations, Phys. Rev. C **85**, 024304 (2012).

[38] J. J. McLoughlin, A. H. Nizamani, J. D. Siverns, R. C. Sterling, M. D. Hughes, B. Lekitsch, B. Stein, S. Weidt, and W. K. Hensinger, Versatile ytterbium ion trap experiment for operation of scalable ion-trap chips with motional heating and transition-frequency measurements, Phys. Rev. A **83**, 013406 (2011).

[39] S. Mulholland, H. A. Klein, G. P. Barwood, S. Donnellan, P. B. R. Nisbet-Jones, G. Huang, G. Walsh, P. E. G. Baird, and P. Gill, Compact laser system for a laser-cooled ytterbium ion microwave frequency standard, Rev. Sci. Instrum. **90**, 033105 (2019).

[40] A. Kramida, Yu. Ralchenko, and J. Reader (NIST ASD Team), NIST Atomic Spectra Database (ver. 5.9), [Online]. Available: https://physics.nist.gov/asd (2021, November 2). National Institute of Standards and Technology, Gaithersburg, MD (2021).

[41] S. Olmschenk, K. C. Younge, D. L. Moehring, D. N. Matsukevich, P. Maunz, and C. Monroe, Manipulation and detection of a trapped Yb^+ hyperfine qubit, Phys. Rev. A **76**, 052314 (2007).

[42] A. Papoulia, B. G. Carlsson, and J. Ekman, Effect of realistic nuclear charge distributions on isotope shifts and progress towards the extraction of higher-order nuclear radial moments, Phys. Rev. A **94**, 042502 (2016).

[43] M. Pizzocaro, F. Bregolin, P. Barbieri, B. Rauf, F. Levi, and D. Calonico, Absolute frequency measurement of the $^1S_0$–$^3P_0$ transition of ^{171}Yb with a link to international atomic time, Metrologia **57**, 035007 (2020).

[44] B. Pritychenko, M. Birch, B. Singh, and M. Horoi, Tables of E2 transition probabilities from the first 2+ states in even-even nuclei, At. Data Nucl. Data Tables **107**, 1 (2016).

[45] M. Puchalski and K. Pachucki, Nuclear structure effects in the isotope shift with halo nuclei, Hyperfine Interact. **196**, 35 (2010).

[46] J. Hur, REDF (v1.0.0), Zenodo, 10.5281/zenodo.5818081 (2022).

[47] A. M. Ransford, Old dog, new trick: High fidelity, background-free state detection of an ytterbium ion qubit, Ph.D. thesis, The University of California, Los Angeles, 2020.

[48] P.-G. Reinhard and W. Nazarewicz, Toward a global description of nuclear charge radii: Exploring the Fayans energy density functional, Phys. Rev. C **95**, 064328 (2017).

[49] M. Roberts, P. Taylor, S. V. Gateva-Kostova, R. B. M. Clarke, W. R. C. Rowley, and P. Gill, Measurement of the $^2S_{1/2} - ^2D_{5/2}$ clock transition in a single $^{171}Yb^+$ ion, Phys. Rev. A **60**, 2867 (1999).

[50] M. S. Safronova, M. G. Kozlov, and C. W. Clark, Blackbody radiation shifts in optical atomic clocks, IEEE Trans. Ultrason. Ferroelectr. Freq. Control **59**, 439 (2012).

[51] K. Sugiyama, A. Wakita, and A. Nakata, Diode-laser-based light sources for laser cooling of trapped Yb^+ ions, in *Conference on Precision Electromagnetic Measurements. Conference Digest. CPEM 2000* (Cat. No. 00CH37031) (IEEE, Sydney, 2000), pp. 509–510, 10.1109/CPEM.2000.851105.

[52] C. Tamm, S. Weyers, B. Lipphardt, and E. Peik, Stray-field-induced quadrupole shift and absolute frequency of the 688-THz $^{171}Yb^+$ single-ion optical frequency standard, Phys. Rev. A **80**, 043403 (2009).

[53] P. Taylor, M. Roberts, S. V. Gateva-Kostova, R. B. M. Clarke, G. P. Barwood, W. R. C. Rowley, and P. Gill, Investigation of the $^2S_{1/2} - ^2D_{5/2}$ clock transition in a single ytterbium ion, Phys. Rev. A **56**, 2699 (1997).

[54] S. Webster, R. Godun, S. King, G. Huang, B. Walton, V. Tsatourian, H. Margolis, S. Lea, and P. Gill, Frequency measurement of the $^2S_{1/2} - ^2D_{3/2}$ electric quadrupole transition in a single $^{171}Yb^+$ ion, IEEE Trans. Ultrason. Ferroelectr. Freq. Control **57**, 592 (2010).

[55] W. Zhang, M. J. Martin, C. Benko, J. L. Hall, J. Ye, C. Hagemann, T. Legero, U. Sterr, F. Riehle, G. D. Cole, and M. Aspelmeyer, Reduction of residual amplitude modulation to 1×10^{-6} for frequency modulation and laser stabilization, Opt. Lett. **39**, 1980 (2014).

[56] H. A. Fürst, C.-H. Yeh, D. Kalincev, A. P. Kulosa, L. S. Dreissen, R. Lange, E. Benkler, N. Huntemann, E. Peik, and T. E. Mehlstäubler, Coherent Excitation of the Highly Forbidden Electric Octupole Transition in $^{172}Yb^+$, Phys. Rev. Lett. **125**, 163001 (2020); **128**, 149901(E) (2020).

[57] D. Nesterenko, R. de Groote, T. Eronen, Z. Ge, M. Hukkanen, A. Jokinen, and A. Kankainen, High-precision mass measurement of ^{168}Yb for verification of nonlinear isotope shift, Int. J. Mass Spectrom. **458**, 116435 (2020).

[58] W. Huang, G. Audi, M. Wang, F. G. Kondev, S. Naimi, and X. Xu, The AME2016 atomic mass evaluation (I). Evaluation of input data; and adjustment procedures, Chin. Phys. C **41**, 030002 (2017).

[59] M. Wang, G. Audi, F. G. Kondev, W. Huang, S. Naimi, and X. Xu, The AME2016 atomic mass evaluation (II). Tables, graphs and references, Chin. Phys. C **41**, 030003 (2017).

[60] R. Rana, M. Höcker, and E. G. Myers, Atomic masses of strontium and ytterbium, Phys. Rev. A **86**, 050502(R) (2012).

[61] I. Counts, Surface friction and spectroscopic probes of new physics with trapped ions, Ph.D. thesis, Massachusetts Institute of Technology, 2020.

[62] P.-G. Reinhard, B. Schuetrumpf, and J. Maruhn, The axial Hartree-Fock + BCS code SkyAx, Comput. Phys. Commun. **258**, 107603 (2021).

[63] P. Klüpfel, P.-G. Reinhard, T. J. Bürvenich, and J. A. Maruhn, Variations on a theme by Skyrme: A systematic study of adjustments of model parameters, Phys. Rev. C **79**, 034310 (2009).

[64] B. A. Brown, C. R. Bronk, and P. E. Hodgson, Systematics of nuclear RMS charge radii, J. Phys. G **10**, 1683 (1984).

[65] E. W. Otten, Nuclear radii and moments of unstable isotopes, in *Treatise on Heavy Ion Science: Volume 8: Nuclei Far From Stability*, edited by D. A. Bromley (Springer US, Boston, MA, 1989), pp. 517–638, 10.1007/978-1-4613-0713-6_7.

[66] M. Hammen *et al.*, From Calcium to Cadmium: Testing the Pairing Functional through Charge Radii Measurements of $^{100-130}Cd$, Phys. Rev. Lett. **121**, 102501 (2018).

[67] C. Gorges *et al.*, Laser Spectroscopy of Neutron-Rich Tin Isotopes: A Discontinuity in Charge Radii Across the $N = 82$ Shell Closure, Phys. Rev. Lett. **122**, 192502 (2019).

[68] A. J. Miller, K. Minamisono, A. Klose, D. Garand, C. Kujawa, J. D. Lantis, Y. Liu, B. Maaß, P. F. Mantica, W. Nazarewicz, W. Nörtershäuser, S. V. Pineda, P.-G. Reinhard, D. M. Rossi, F. Sommer, C. Sumithrarachchi, A. Teigelhöfer, and J. Watkins, Proton superfluidity and charge radii in proton-rich calcium isotopes, Nat. Phys. **15**, 432 (2019).

[69] P. Jönsson, A. Ynnerman, C. Froese Fischer, M. R. Godefroid, and J. Olsen, Large-scale multiconfiguration Hartree-Fock and configuration-interaction calculations of the transition probability and hyperfine structures in the sodium resonance transition, Phys. Rev. A **53**, 4021 (1996).

[70] S. G. Porsev, M. G. Kozlov, and D. Reimers, Transition frequency shifts with fine-structure constant variation for Fe I and isotope-shift calculations in Fe I and Fe II, Phys. Rev. A **79**, 032519 (2009).

[71] B. Fawcett and M. Wilson, Computed oscillator strengths, Landé g values, and lifetimes in Yb II, At. Data Nucl. Data Tables **47**, 241 (1991).

[72] E. Biémont, J.-F. Dutrieux, I. Martin, and P. Quinet, Lifetime calculations in Yb II, J. Phys. B **31**, 3321 (1998).

[73] C. Froese Fischer, G. Gaigalas, P. Jönsson, and J. Bieroń, GRASP2018—a Fortran 95 version of the general relativistic atomic structure package, Comput. Phys. Commun. **237**, 184 (2019).

[74] E. Kahl and J. Berengut, AMBiT: A programme for high-precision relativistic atomic structure calculations, Comput. Phys. Commun. **238**, 232 (2019).

[75] V. A. Dzuba, V. V. Flambaum, and M. G. Kozlov, Combination of the many-body perturbation theory with the configuration-interaction method, Phys. Rev. A **54**, 3948 (1996).

[76] J. C. Berengut, C. Delaunay, A. Geddes, and Y. Soreq, Generalized King linearity and new physics searches with isotope shifts, Phys. Rev. Research **2**, 043444 (2020).

[77] D. Hanneke, S. Fogwell, and G. Gabrielse, New Measurement of the Electron Magnetic Moment and the Fine Structure Constant, Phys. Rev. Lett. **100**, 120801 (2008).

[78] T. Aoyama, M. Hayakawa, T. Kinoshita, and M. Nio, Tenth-Order QED Contribution to the Electron $g-2$ and an Improved Value of the Fine Structure Constant, Phys. Rev. Lett. **109**, 111807 (2012).

[79] R. Bouchendira, P. Cladé, S. Guellati-Khélifa, F. Nez, and F. Biraben, New Determination of the Fine Structure Constant and Test of the Quantum Electrodynamics, Phys. Rev. Lett. **106**, 080801 (2011).

[80] H. Davoudiasl, H.-S. Lee, and W. J. Marciano, Muon $g-2$, rare kaon decays, and parity violation from dark bosons, Phys. Rev. D **89**, 095006 (2014).

[81] R. Barbieri and T. Ericson, Evidence against the existence of a low mass scalar boson from neutron-nucleus scattering, Phys. Lett. **57B**, 270 (1975).

[82] H. Leeb and J. Schmiedmayer, Constraint on Hypothetical Light Interacting Bosons from Low-Energy Neutron Experiments, Phys. Rev. Lett. **68**, 1472 (1992).

[83] Y. N. Pokotilovski, Constraints on new interactions from neutron scattering experiments, Phys. At. Nucl. **69**, 924 (2006).

[84] V. V. Nesvizhevsky, G. Pignol, and K. V. Protasov, Neutron scattering and extra-short-range interactions, Phys. Rev. D **77**, 034020 (2008).

[85] T. Manovitz, R. Shaniv, Y. Shapira, R. Ozeri, and N. Akerman, Precision Measurement of Atomic Isotope Shifts Using a Two-Isotope Entangled State, Phys. Rev. Lett. **123**, 203001 (2019).

Bibliography

[1] W. H. King, *Isotope Shifts in Atomic Spectra* (Springer Science+Business Media, LLC, New York, 1984).

[2] C. Delaunay, R. Ozeri, G. Perez, and Y. Soreq, Probing atomic Higgs-like forces at the precision frontier, Phys. Rev. D **96**, 093001 (2017).

[3] J. C. Berengut, D. Budker, C. Delaunay, V. V. Flambaum, C. Frugiuele, E. Fuchs, C. Grojean, R. Harnik, R. Ozeri, G. Perez, and Y. Soreq, Probing new long-range interactions by isotope shift spectroscopy, Phys. Rev. Lett. **120**, 091801 (2018).

[4] I. T. Counts, *Surface Friction and Spectroscopic Probes of New Physics with Trapped Ions*, Ph.D. thesis, Massachusetts Institute of Technology (2020).

[5] I. Counts, J. Hur, D. P. L. Aude Craik, H. Jeon, C. Leung, J. C. Berengut, A. Geddes, A. Kawasaki, W. Jhe, and V. Vuletić, Evidence for nonlinear isotope shift in Yb^+ search for new boson, Phys. Rev. Lett. **125**, 123002 (2020), Supplemental Material: `http://link.aps.org/supplemental/10.1103/PhysRevLett.125.123002`.

[6] W. Huang, G. Audi, M. Wang, F. G. Kondev, S. Naimi, and X. Xu, The AME2016 atomic mass evaluation (I). Evaluation of input data; and adjustment procedures, Chin. Phys. C **41**, 030002 (2017).

[7] M. Wang, G. Audi, F. G. Kondev, W. Huang, S. Naimi, and X. Xu, The AME2016 atomic mass evaluation (II). Tables, graphs and references, Chin. Phys. C **41**, 030003 (2017).

[8] J. Hur, D. P. L. Aude Craik, I. Counts, E. Knyazev, L. Caldwell, C. Leung, S. Pandey, J. C. Berengut, A. Geddes, W. Nazarewicz, P.-G. Reinhard, A. Kawasaki, H. Jeon, W. Jhe, and V. Vuletić, Evidence of two-source King plot nonlinearity in spectroscopic search for new boson, Phys. Rev. Lett. **128**, 163201 (2022), Supplemental Material: `http://link.aps.org/supplemental/10.1103/PhysRevLett.128.163201`.

[9] N. L. Figueroa, J. C. Berengut, V. A. Dzuba, V. V. Flambaum, D. Budker, and D. Antypas, Precision determination of isotope shifts in ytterbium and implications for new physics, Phys. Rev. Lett. **128**, 073001 (2022).

[10] K. Ono, Y. Saito, T. Ishiyama, T. Higomoto, T. Takano, Y. Takasu, Y. Yamamoto, M. Tanaka, and Y. Takahashi, Observation of nonlinearity of generalized king plot in the search for new boson, Phys. Rev. X **12**, 021033 (2022).

[11] D. Hanneke, S. Fogwell, and G. Gabrielse, New measurement of the electron magnetic moment and the fine structure constant, Phys. Rev. Lett. **100**, 120801 (2008).

[12] T. Aoyama, M. Hayakawa, T. Kinoshita, and M. Nio, Tenth-order qed contribution to the electron $g-2$ and an improved value of the fine structure constant, Phys. Rev. Lett. **109**, 111807 (2012).

[13] R. Bouchendira, P. Cladé, S. Guellati-Khélifa, F. Nez, and F. Biraben, New determination of the fine structure constant and test of the quantum electrodynamics, Phys. Rev. Lett. **106**, 080801 (2011).

[14] H. Davoudiasl, H.-S. Lee, and W. J. Marciano, Muon $g-2$, rare kaon decays, and parity violation from dark bosons, Phys. Rev. D **89**, 095006 (2014).

[15] R. Barbieri and T. Ericson, Evidence against the existence of a low mass scalar boson from neutron-nucleus scattering, Phys. Lett. **57B**, 270–272 (1975).

[16] H. Leeb and J. Schmiedmayer, Constraint on hypothetical light interacting bosons from low-energy neutron experiments, Phys. Rev. Lett. **68**, 1472–1475 (1992).

[17] Y. N. Pokotilovski, Constraints on new interactions from neutron scattering experiments, Phys. At. Nucl. **69**, 924–931 (2006).

[18] V. V. Nesvizhevsky, G. Pignol, and K. V. Protasov, Neutron scattering and extra-short-range interactions, Phys. Rev. D **77**, 034020 (2008).

[19] A. Zehnder, F. Boehm, W. Dey, R. Engfer, H. Walter, and J. Vuilleumier, Charge parameters, isotope shifts, quadrupole moments, and nuclear excitation in muonic 170–174,176yb, Nucl. Phys. A **254**, 315–340 (1975).

[20] R. Rana, M. Höcker, and E. G. Myers, Atomic masses of strontium and ytterbium, Phys. Rev. A **86**, 050502(R) (2012).

[21] A. Kramida, Y. Ralchenko, and J. Reader (NIST ASD Team), NIST Atomic Spectra Database (ver. 5.9), [Online]. Available: `https://physics.nist.gov/asd` (2021, November 2). National Institute of Standards and Technology, Gaithersburg, MD (2021).

[22] M. Aymar, A. Debarre, and O. Robaux, Highly excited levels of neutral ytterbium. II. Multichannel quantum defect analysis of odd- and even-parity spectra, J. Phys. B **13**, 1089–1109 (1980).

[23] E. Kahl and J. Berengut, AMBiT: A programme for high-precision relativistic atomic structure calculations, Comput. Phys. Commun. **238**, 232–243 (2019).

[24] C. Froese Fischer, G. Gaigalas, P. Jönsson, and J. Bieroń, GRASP2018–a Fortran 95 version of the general relativistic atomic structure package, Comput. Phys. Commun. **237**, 184–187 (2019).

[25] G. Audi, O. Bersillon, J. Blachot, and A. Wapstra, The NUBASE evaluation of nuclear and decay properties, Nucl. Phys. A **729**, 3–128 (2003).

[26] D. Nesterenko, R. de Groote, T. Eronen, Z. Ge, M. Hukkanen, A. Jokinen, and A. Kankainen, High-precision mass measurement of ^{168}Yb for verification of nonlinear isotope shift, Int. J. Mass Spectrom. **458**, 116435 (2020).

[27] I. P. Grant, *Relativistic Quantum Theory of Atoms and Molecules: Theory and Computation*, Springer Series on Atomic, Optical, and Plasma Physics, Vol. 40 (Springer Science+Business Media, LLC, New York, 2007).

[28] A. J. Krasznahorkay, M. Csatlós, L. Csige, Z. Gácsi, J. Gulyás, Á. Nagy, N. Sas, J. Timár, T. G. Tornyi, I. Vajda, and A. J. Krasznahorkay, New results on the ^{8}Be anomaly, Journal of Physics: Conference Series **1056**, 012028 (2018).

[29] A. J. Krasznahorkay, M. Csatlós, L. Csige, Z. Gácsi, J. Gulyás, M. Hunyadi, I. Kuti, B. M. Nyakó, L. Stuhl, J. Timár, T. G. Tornyi, Z. Vajta, T. J. Ketel, and A. Krasznahorkay, Observation of anomalous internal pair creation in ^{8}Be: A possible indication of a light, neutral boson, Phys. Rev. Lett. **116**, 042501 (2016).

[30] A. J. Krasznahorkay, M. Csatlos, L. Csige, J. Gulyas, M. Koszta, B. Szihalmi, J. Timar, D. S. Firak, A. Nagy, N. J. Sas, and A. Krasznahorkay, New evidence supporting the existence of the hypothetic X17 particle (2019), arXiv:1910.10459 [nucl-ex] .

[31] J. L. Feng, B. Fornal, I. Galon, S. Gardner, J. Smolinsky, T. M. P. Tait, and P. Tanedo, Protophobic fifth-force interpretation of the observed anomaly in ^{8}Be nuclear transitions, Phys. Rev. Lett. **117**, 071803 (2016).

[32] J. L. Feng, B. Fornal, I. Galon, S. Gardner, J. Smolinsky, T. M. P. Tait, and P. Tanedo, Particle physics models for the 17 MeV anomaly in beryllium nuclear decays, Phys. Rev. D **95**, 035017 (2017).

[33] U. D. Jentschura and I. Nándori, Atomic physics constraints on the X boson, Phys. Rev. A **97**, 042502 (2018).

[34] P. Zyla *et al.* (Particle Data Group), Review of particle physics, Prog. Theor. Exp. Phys. **2020**, 083C01 (2020).

[35] M. S. Safronova, S. G. Porsev, C. Sanner, and J. Ye, Two clock transitions in neutral Yb for the highest sensitivity to variations of the fine-structure constant, Phys. Rev. Lett. **120**, 173001 (2018).

[36] V. C. Rubin, W. K. Ford, and N. Thonnard, Rotational properties of 21 Sc galaxies with a large range of luminosities and radii, from NGC 4605 ($R = 4$ kpc) to UGC 2885 ($R = 122$ kpc), Astrophys. J. **238**, 471–487 (1980).

[37] D. Clowe, M. Bradač, A. H. Gonzalez, M. Markevitch, S. W. Randall, C. Jones, and D. Zaritsky, A direct empirical proof of the existence of dark matter, Astrophys. J. **648**, L109–L113 (2006).

[38] R. Massey, T. Kitching, and J. Richard, The dark matter of gravitational lensing, Rep. Prog. Phys. **73**, 086901 (2010).

[39] N. Aghanim *et al.* (Planck Collaboration), Planck 2018 results–I. Overview and the cosmological legacy of Planck, Astron. Astrophys. **641**, A1 (2020).

[40] A. M. Green and B. J. Kavanagh, Primordial black holes as a dark matter candidate, J. Phys. G **48**, 043001 (2021).

[41] J. L. Feng, S. Ritz, J. J. Beatty, J. Buckley, D. F. Cowen, P. Cushman, S. Dodelson, C. Galbiati, K. Honscheid, D. Hooper, M. Kaplinghat, A. Kusenko, K. Matchev, D. McKinsey, A. E. Nelson, A. Olinto, S. Profumo, H. Robertson, L. Rosenberg, G. Sinnis, and T. M. P. Tait, Planning the future of u.s. particle physics (snowmass 2013): Chapter 4: Cosmic frontier (2021), arXiv:1401.6085 [hep-ex] .

[42] J. L. Feng, Dark matter candidates from particle physics and methods of detection, Annual Review of Astronomy and Astrophysics **48**, 495–545 (2010).

[43] G. Aad *et al.* (ATLAS Collaboration), Observation of a new particle in the search for the Standard Model Higgs boson with the ATLAS detector at the LHC, Phys. Lett. B **716**, 1–29 (2012).

[44] B. Abi *et al.* (DUNE Collaboration), Volume i. introduction to DUNE, J. Instrum. **15** (08), T08008–T08008.

[45] S. Fukuda *et al.* (Super-Kamiokande Collaboration), The Super-Kamiokande detector, Nucl. Instrum. Methods Phys. Res. A **501**, 418–462 (2003).

[46] W. D. Arnett, J. N. Bahcall, R. P. Kirshner, and S. E. Woosley, Supernova 1987A, Annu. Rev. Astron. Astrophys. **27**, 629–700 (1989).

[47] G. Raffelt and D. Seckel, Bounds on exotic-particle interactions from SN1987A, Phys. Rev. Lett. **60**, 1793–1796 (1988).

[48] M. S. Turner, Axions from SN1987A, Phys. Rev. Lett. **60**, 1797–1800 (1988).

[49] R. Mayle, J. R. Wilson, J. Ellis, K. A. Olive, D. N. Schramm, and G. Steigman, Updated constraints on axions from SN1987A, Phys. Lett. B **219**, 515–520 (1989).

[50] M. S. Safronova, D. Budker, D. DeMille, Derek. F. Jackson. Kimball, A. Derevianko, and C. W. Clark, Search for new physics with atoms and molecules, Rev. Mod. Phys. **90**, 025008 (2018).

[51] N. Huntemann, C. Sanner, B. Lipphardt, C. Tamm, and E. Peik, Single-ion atomic clock with 3×10^{-18} systematic uncertainty, Phys. Rev. Lett. **116**, 063001 (2016).

[52] T. Bothwell, D. Kedar, E. Oelker, J. M. Robinson, S. L. Bromley, W. L. Tew, J. Ye, and C. J. Kennedy, JILA SrI optical lattice clock with uncertainty of 2.0×10^{-18}, Metrologia **56**, 065004 (2019).

[53] W. F. McGrew, X. Zhang, R. J. Fasano, S. A. Schäffer, K. Beloy, D. Nicolodi, R. C. Brown, N. Hinkley, G. Milani, M. Schioppo, T. H. Yoon, and A. D. Ludlow, Atomic clock performance enabling geodesy below the centimetre level, Nature **564**, 87–90 (2018).

[54] S. M. Brewer, J.-S. Chen, A. M. Hankin, E. R. Clements, C. W. Chou, D. J. Wineland, D. B. Hume, and D. R. Leibrandt, $^{27}Al^{+}$ quantum-logic clock with a systematic uncertainty below 10^{-18}, Phys. Rev. Lett. **123**, 033201 (2019).

[55] X. Zheng, J. Dolde, V. Lochab, B. N. Merriman, H. Li, and S. Kolkowitz, Differential clock comparisons with a multiplexed optical lattice clock, Nature **602**, 425–430 (2022).

[56] B. L. Schmittberger and D. R. Scherer, A review of contemporary atomic frequency standards (2020), arXiv:2004.09987 [physics.atom-ph] .

[57] E. G. Myers, High-precision atomic mass measurements for fundamental constants, Atoms **7**, 1 (2019).

[58] D. Budker and Derek. F. Jackson. Kimball, eds., *Optical Magnetometry* (Cambridge University Press, Cambridge, 2013).

[59] I. Fescenko, A. Jarmola, I. Savukov, P. Kehayias, J. Smits, J. Damron, N. Ristoff, N. Mosavian, and V. M. Acosta, Diamond magnetometer enhanced by ferrite flux concentrators, Phys. Rev. Research **2**, 023394 (2020).

[60] K. Bongs, M. Holynski, J. Vovrosh, P. Bouyer, G. Condon, E. Rasel, C. Schubert, W. P. Schleich, and A. Roura, Taking atom interferometric quantum sensors from the laboratory to real-world applications, Nat. Rev. Phys. **1**, 731–739 (2019).

[61] S. Ulmer, C. Smorra, A. Mooser, K. Franke, H. Nagahama, G. Schneider, T. Higuchi, S. Van Gorp, K. Blaum, Y. Matsuda, W. Quint, J. Walz, and Y. Yamazaki, High-precision comparison of the antiproton-to-proton charge-to-mass ratio, Nature **524**, 196–199 (2015).

[62] E. Widmann, C. Amsler, S. Arguedas Cuendis, H. Breuker, M. Diermaier, P. Dupré, C. Evans, M. Fleck, A. Gligorova, H. Higaki, Y. Kanai, B. Kolbinger, N. Kuroda, M. Leali, A. M. M. Leite, V. Mäckel, C. Malbrunot, V. Mascagna, O. Massiczek, Y. Matsuda, D. J. Murtagh, Y. Nagata, A. Nanda, D. Phan, C. Sauerzopf, M. C. Simon, M. Tajima, H. Spitzer, M. Strube, S. Ulmer, L. Venturelli, M. Wiesinger, Y. Yamazaki, and J. Zmeskal, Hyperfine spectroscopy of hydrogen and antihydrogen in ASACUSA, Hyperfine Interact. **240**, 5 (2019).

[63] C. Sanner, N. Huntemann, R. Lange, C. Tamm, E. Peik, M. S. Safronova, and S. G. Porsev, Optical clock comparison for lorentz symmetry testing, Nature **567**, 204–208 (2019).

[64] M. S. Safronova, The search for variation of fundamental constants with clocks, Ann. Phys. (Berl.) **531**, 1800364 (2019).

[65] T. Rosenband, D. B. Hume, P. O. Schmidt, C. W. Chou, A. Brusch, L. Lorini, W. H. Oskay, R. E. Drullinger, T. M. Fortier, J. E. Stalnaker, S. A. Diddams, W. C. Swann, N. R. Newbury, W. M. Itano, D. J. Wineland, and J. C. Bergquist, Frequency ratio of Al^+ and Hg^+ single-ion optical clocks; metrology at the 17th decimal place, Science **319**, 1808–1812 (2008).

[66] W. B. Cairncross, D. N. Gresh, M. Grau, K. C. Cossel, T. S. Roussy, Y. Ni, Y. Zhou, J. Ye, and E. A. Cornell, Precision measurement of the electron's electric dipole moment using trapped molecular ions, Phys. Rev. Lett. **119**, 153001 (2017).

[67] S. Sturm, M. Vogel, F. Köhler-Langes, W. Quint, K. Blaum, and G. Werth, High-precision measurements of the bound electron's magnetic moment, Atoms **5**, 1 (2017).

[68] H. Müntinga, H. Ahlers, M. Krutzik, A. Wenzlawski, S. Arnold, D. Becker, K. Bongs, H. Dittus, H. Duncker, N. Gaaloul, C. Gherasim, E. Giese, C. Grzeschik, T. W. Hänsch, O. Hellmig, W. Herr, S. Herrmann, E. Kajari, S. Kleinert, C. Lämmerzahl, W. Lewoczko-Adamczyk, J. Malcolm, N. Meyer, R. Nolte, A. Peters, M. Popp, J. Reichel, A. Roura, J. Rudolph, M. Schiemangk, M. Schneider, S. T. Seidel, K. Sengstock, V. Tamma, T. Valenzuela, A. Vogel, R. Walser, T. Wendrich, P. Windpassinger, W. Zeller, T. van Zoest, W. Ertmer, W. P. Schleich, and E. M. Rasel, Interferometry with bose-einstein condensates in microgravity, Phys. Rev. Lett. **110**, 093602 (2013).

[69] G. W. Biedermann, X. Wu, L. Deslauriers, S. Roy, C. Mahadeswaraswamy, and M. A. Kasevich, Testing gravity with cold-atom interferometers, Phys. Rev. A **91**, 033629 (2015).

[70] J. M. Hogan and M. A. Kasevich, Atom-interferometric gravitational-wave detection using heterodyne laser links, Phys. Rev. A **94**, 033632 (2016).

[71] P. Hamilton, M. Jaffe, P. Haslinger, Q. Simmons, H. Müller, and J. Khoury, Atom-interferometry constraints on dark energy, Science **349**, 849–851 (2015).

[72] C. Burrage and E. J. Copeland, Using atom interferometry to detect dark energy, Contemporary Physics **57**, 164–176 (2016).

[73] U. I. Safronova and M. S. Safronova, High-accuracy calculation of energies, lifetimes, hyperfine constants, multipole polarizabilities, and blackbody radiation shift in ^{39}K, Phys. Rev. A **78**, 052504 (2008).

[74] M. P. A. Jones, R. M. Potvliege, and M. Spannowsky, Probing new physics using Rydberg states of atomic hydrogen, Phys. Rev. Research **2**, 013244 (2020).

[75] N. Bezginov, T. Valdez, M. Horbatsch, A. Marsman, A. C. Vutha, and E. A. Hessels, A measurement of the atomic hydrogen Lamb shift and the proton charge radius, Science **365**, 1007–1012 (2019).

[76] R. Pohl, The Lamb shift in muonic hydrogen and the proton radius puzzle, Hyperfine Interact. **227**, 23–28 (2014).

[77] Y.-H. Lin, H.-W. Hammer, and U.-G. Meißner, New insights into the nucleon's electromagnetic structure, Phys. Rev. Lett. **128**, 052002 (2022).

[78] C. J. Baker, W. Bertsche, A. Capra, C. Carruth, C. L. Cesar, M. Charlton, A. Christensen, R. Collister, A. C. Mathad, S. Eriksson, A. Evans, N. Evetts, J. Fajans, T. Friesen, M. C. Fujiwara, D. R. Gill, P. Grandemange, P. Granum, J. S. Hangst, W. N. Hardy, M. E. Hayden, D. Hodgkinson, E. Hunter, C. A. Isaac, M. A. Johnson, J. M. Jones, S. A. Jones, S. Jonsell, A. Khramov, P. Knapp, L. Kurchaninov, N. Madsen, D. Maxwell, J. T. K. McKenna, S. Menary, J. M. Michan, T. Momose, P. S. Mullan, J. J. Munich, K. Olchanski, A. Olin, J. Peszka, A. Powell, P. Pusa, C. Ø. Rasmussen, F. Robicheaux, R. L. Sacramento, M. Sameed, E. Sarid, D. M. Silveira, D. M. Starko, C. So, G. Stutter, T. D. Tharp, A. Thibeault, R. I. Thompson, D. P. van der Werf, and J. S. Wurtele, Laser cooling of antihydrogen atoms, Nature **592**, 35–42 (2021).

[79] M. Ahmadi, B. X. R. Alves, C. J. Baker, W. Bertsche, E. Butler, A. Capra, C. Carruth, C. L. Cesar, M. Charlton, S. Cohen, R. Collister, S. Eriksson, A. Evans, N. Evetts, J. Fajans, T. Friesen, M. C. Fujiwara, D. R. Gill, A. Gutierrez, J. S. Hangst, W. N. Hardy, M. E. Hayden, C. A. Isaac, A. Ishida, M. A. Johnson, S. A. Jones, S. Jonsell, L. Kurchaninov, N. Madsen, M. Mathers, D. Maxwell, J. T. K. McKenna, S. Menary, J. M. Michan, T. Momose, J. J. Munich, P. Nolan, K. Olchanski, A. Olin, P. Pusa, C. Ø. Rasmussen, F. Robicheaux, R. L. Sacramento, M. Sameed, E. Sarid, D. M. Silveira, S. Stracka, G. Stutter, C. So, T. D. Tharp, J. E. Thompson, R. I. Thompson, D. P. van der

Werf, and J. S. Wurtele, Observation of the 1S–2S transition in trapped antihydrogen, Nature **541**, 506–510 (2017).

[80] S. V. Nguyen, S. C. Doret, C. B. Connolly, R. A. Michniak, W. Ketterle, and J. M. Doyle, Evaporative cooling of metastable helium in the multi-partial-wave regime, Phys. Rev. A **72**, 060703 (2005).

[81] V. V. Flambaum, A. J. Geddes, and A. V. Viatkina, Isotope shift, nonlinearity of King plots, and the search for new particles, Phys. Rev. A **97**, 032510 (2018).

[82] K. Mikami, M. Tanaka, and Y. Yamamoto, Probing new intra-atomic force with isotope shifts, Eur. Phys. J. C **77**, 896 (2017).

[83] M. Tanaka and Y. Yamamoto, Relativistic effects in the search for new intra-atomic force with isotope shifts, Prog. Theor. Exp. Phys. **2020**, 103B02 (2020).

[84] S. O. Allehabi, V. A. Dzuba, V. V. Flambaum, A. V. Afanasjev, and S. E. Agbemava, Using isotope shift for testing nuclear theory: The case of nobelium isotopes, Phys. Rev. C **102**, 024326 (2020).

[85] V. A. Yerokhin, R. A. Müller, A. Surzhykov, P. Micke, and P. O. Schmidt, Nonlinear isotope-shift effects in Be-like, B-like, and C-like argon, Phys. Rev. A **101**, 012502 (2020).

[86] R. A. Müller, V. A. Yerokhin, A. N. Artemyev, and A. Surzhykov, Nonlinearities of King's plot and their dependence on nuclear radii, Phys. Rev. A **104**, L020802 (2021).

[87] C. Solaro, S. Meyer, K. Fisher, J. C. Berengut, E. Fuchs, and M. Drewsen, Improved isotope-shift-based bounds on bosons beyond the standard model through measurements of the $^2\mathrm{D}_{3/2} - {}^2\mathrm{D}_{5/2}$ interval in Ca^+, Phys. Rev. Lett. **125**, 123003 (2020).

[88] V. A. Dzuba and A. Derevianko, Dynamic polarizabilities and related properties of clock states of the ytterbium atom, J. Phys. B **43**, 074011 (2010).

[89] S. G. Porsev, A. Derevianko, and E. N. Fortson, Possibility of an optical clock using the $6\,{}^1S_0 \to 6\,{}^3P_0^o$ transition in ^{171,173}Yb atoms held in an optical lattice, Phys. Rev. A **69**, 021403 (2004).

[90] Z. W. Barber, J. E. Stalnaker, N. D. Lemke, N. Poli, C. W. Oates, T. M. Fortier, S. A. Diddams, L. Hollberg, C. W. Hoyt, A. V. Taichenachev, and V. I. Yudin, Optical lattice induced light shifts in an yb atomic clock, Phys. Rev. Lett. **100**, 103002 (2008).

[91] F. Gebert, Y. Wan, F. Wolf, C. N. Angstmann, J. C. Berengut, and P. O. Schmidt, Precision isotope shift measurements in calcium ions using quantum logic detection schemes, Phys. Rev. Lett. **115**, 053003 (2015).

[92] F. W. Knollmann, A. N. Patel, and S. C. Doret, Part-per-billion measurement of the $4\,^2S_{1/2} \rightarrow 3\,^2D_{5/2}$ electric-quadrupole-transition isotope shifts between $^{42,44,48}Ca^+$ and $^{44}Ca^+$, Phys. Rev. A **100**, 022514 (2019).

[93] T. Manovitz, R. Shaniv, Y. Shapira, R. Ozeri, and N. Akerman, Precision measurement of atomic isotope shifts using a two-isotope entangled state, Phys. Rev. Lett. **123**, 203001 (2019).

[94] H. Miyake, N. C. Pisenti, P. K. Elgee, A. Sitaram, and G. K. Campbell, Isotope-shift spectroscopy of the $^1S_0 \rightarrow {}^3P_1$ and $^1S_0 \rightarrow {}^3P_0$ transitions in strontium, Phys. Rev. Research **1**, 033113 (2019).

[95] M. Hammen, W. Nörtershäuser, D. L. Balabanski, M. L. Bissell, K. Blaum, I. Budinčević, B. Cheal, K. T. Flanagan, N. Frömmgen, G. Georgiev, C. Geppert, M. Kowalska, K. Kreim, A. Krieger, W. Nazarewicz, R. Neugart, G. Neyens, J. Papuga, P.-G. Reinhard, M. M. Rajabali, S. Schmidt, and D. T. Yordanov, From calcium to cadmium: Testing the pairing functional through charge radii measurements of $^{100\text{–}130}Cd$, Phys. Rev. Lett. **121**, 102501 (2018).

[96] D. Hucul, J. E. Christensen, E. R. Hudson, and W. C. Campbell, Spectroscopy of a synthetic trapped ion qubit, Phys. Rev. Lett. **119**, 100501 (2017).

[97] U. Dammalapati, S. De, K. Jungmann, and L. Willmann, Isotope shifts of $6s5d\,^3\mathrm{D}$–$6s6p\,^1\mathrm{P}_1$ transitions in neutral barium, Eur. Phys. J. D **53**, 1–8 (2009).

[98] N. Bhatt, K. Kato, and A. C. Vutha, Nd^+ isotope shift measurements in a cryogenically cooled neutral plasma, Phys. Rev. A **101**, 052505 (2020).

[99] M. Lu, S. H. Youn, and B. L. Lev, Spectroscopy of a narrow-line laser-cooling transition in atomic dysprosium, Phys. Rev. A **83**, 012510 (2011).

[100] J. A. R. Griffith, G. R. Isaak, R. New, and M. P. Ralls, Anomalies in the optical isotope shifts of samarium, J. Phys. B **14**, 2769–2780 (1981).

[101] C. W. P. Palmer and D. N. Stacey, Theory of anomalous isotope shifts in samarium, J. Phys. B **15**, 997–1005 (1982).

[102] F. Riehle, P. Gill, F. Arias, and L. Robertsson, The CIPM list of recommended frequency standard values: guidelines and procedures, Metrologia **55**, 188–200 (2018).

[103] R. H. Dicke, The effect of collisions upon the doppler width of spectral lines, Phys. Rev. **89**, 472–473 (1953).

[104] L. Karpa, A. Bylinskii, D. Gangloff, M. Cetina, and V. Vuletić, Suppression of ion transport due to long-lived subwavelength localization by an optical lattice, Phys. Rev. Lett. **111**, 163002 (2013).

[105] M. Cetina, A. Bylinskii, L. Karpa, D. Gangloff, K. M. Beck, Y. Ge, M. Scholz, A. T. Grier, I. Chuang, and V. Vuletić, One-dimensional array of ion chains coupled to an optical cavity, New J. Phys. **15**, 053001 (2013).

[106] A. Bylinskii, D. Gangloff, and V. Vuletić, Tuning friction atom-by-atom in an ion-crystal simulator, Science **348**, 1115–1118 (2015).

[107] D. Gangloff, A. Bylinskii, I. Counts, W. Jhe, and V. Vuletić, Velocity tuning of friction with two trapped atoms, Nat. Phys. **11**, 915–919 (2015).

[108] M. Cetina, *Hybrid Approaches to Quantum Information Using Ions, Atoms and Photons*, Ph.D. thesis, Massachusetts Institute of Technology (2011).

[109] A. Bylinskii, *Friction under microscope with trapped ions in optical lattices*, Ph.D. thesis, Massachusetts Institute of Technology (2016).

[110] D. A. Gangloff, *Nanocontacts controlled atom-by-atom in an ion-crystal friction emulator*, Ph.D. thesis, Massachusetts Institute of Technology (2016).

[111] M. Berglund and M. E. Wieser, Isotopic compositions of the elements 2009 (IUPAC Technical Report), Pure Appl. Chem. **83**, 397–410 (2011).

[112] D. J. Berkeland, J. D. Miller, J. C. Bergquist, W. M. Itano, and D. J. Wineland, Minimization of ion micromotion in a paul trap, Journal of Applied Physics **83**, 5025–5033 (1998).

[113] M. Kleinert, M. E. Gold Dahl, and S. Bergeson, Measurement of the yb i ${}^1S_0$–${}^1P_1$ transition frequency at 399 nm using an optical frequency comb, Phys. Rev. A **94**, 052511 (2016).

[114] M. M. Schauer, J. R. Danielson, A.-T. Nguyen, L.-B. Wang, X. Zhao, and J. R. Torgerson, Collisional population transfer in trapped Yb^+ ions, Phys. Rev. A **79**, 062705 (2009).

[115] S. Olmschenk, K. C. Younge, D. L. Moehring, D. N. Matsukevich, P. Maunz, and C. Monroe, Manipulation and detection of a trapped Yb^+ hyperfine qubit, Phys. Rev. A **76**, 052314 (2007).

[116] R. W. P. Drever, J. L. Hall, F. V. Kowalski, J. Hough, G. M. Ford, A. J. Munley, and H. Ward, Laser phase and frequency stabilization using an optical resonator, Appl. Phys. B **31**, 97–105 (1983).

[117] E. D. Black, An introduction to Pound–Drever–Hall laser frequency stabilization, American Journal of Physics **69**, 79–87 (2001).

[118] N. C. Wong and J. L. Hall, Servo control of amplitude modulation in frequency-modulation spectroscopy: demonstration of shot-noise-limited detection, J. Opt. Soc. Am. B **2**, 1527–1533 (1985).

[119] L. Li, F. Liu, C. Wang, and L. Chen, Measurement and control of residual amplitude modulation in optical phase modulation, Rev. Sci. Instrum. **83**, 043111 (2012).

[120] W. Zhang, M. J. Martin, C. Benko, J. L. Hall, J. Ye, C. Hagemann, T. Legero, U. Sterr, F. Riehle, G. D. Cole, and M. Aspelmeyer, Reduction of residual amplitude modulation to 1×10^{-6} for frequency modulation and laser stabilization, Opt. Lett. **39**, 1980–1983 (2014).

[121] H. A. Fürst, C.-H. Yeh, D. Kalincev, A. P. Kulosa, L. S. Dreissen, R. Lange, E. Benkler, N. Huntemann, E. Peik, and T. E. Mehlstäubler, Coherent excitation of the highly forbidden electric octupole transition in $^{172}Yb^{+}$, Phys. Rev. Lett. **125**, 163001 (2020), Erratum: Phys. Rev. Lett. **128**, 149901(E) (2022).

[122] N. Huntemann, M. Okhapkin, B. Lipphardt, S. Weyers, C. Tamm, and E. Peik, High-accuracy optical clock based on the octupole transition in $^{171}Yb^{+}$, Phys. Rev. Lett. **108**, 090801 (2012).

[123] K. Hosaka, S. A. Webster, A. Stannard, B. R. Walton, H. S. Margolis, and P. Gill, Frequency measurement of the $^2S_{1/2}-{}^2F_{7/2}$ electric octupole transition in a single $^{171}Yb^{+}$ ion, Phys. Rev. A **79**, 033403 (2009).

[124] G. H. Zhang, B. Braverman, A. Kawasaki, and V. Vuletić, Note: Fast compact laser shutter using a direct current motor and three-dimensional printing, Rev. Sci. Instrum. **86**, 126105 (2015).

[125] A. M. Ransford, *Old Dog, New Trick: High Fidelity, Background-free State Detection of an Ytterbium Ion Qubit*, Ph.D. thesis, University of California, Los Angeles (2020).

[126] Y.-Y. Jau, J. D. Hunker, and P. D. D. Schwindt, F-state quenching with CH4 for buffer-gas cooled $^{171}Yb^{+}$ frequency standard, AIP Adv. **5**, 117209 (2015).

[127] K. Sugiyama, A. Wakita, and A. Nakata, Diode-laser-based light sources for laser cooling of trapped Yb^{+} ions, in *Conference on Precision Electromagnetic Measurements. Conference Digest. CPEM 2000 (Cat. No.00CH37031)* (IEEE, Sydney, NSW, Australia, 2000) pp. 509–510.

[128] S. Mulholland, H. A. Klein, G. P. Barwood, S. Donnellan, P. B. R. Nisbet-Jones, G. Huang, G. Walsh, P. E. G. Baird, and P. Gill, Compact laser system for a laser-cooled ytterbium ion microwave frequency standard, Rev. Sci. Instrum. **90**, 033105 (2019).

[129] C. L. Edmunds, T. R. Tan, A. R. Milne, A. Singh, M. J. Biercuk, and C. Hempel, Scalable hyperfine qubit state detection via electron shelving in the $^2D_{5/2}$ and $^2F_{7/2}$ manifolds in $^{171}Yb^{+}$, Phys. Rev. A **104**, 012606 (2021).

[130] R. W. Berends, E. H. Pinnington, B. Guo, and Q. Ji, Beam-laser lifetime measurements for four resonance levels of Yb II, J. Phys. B **26**, L701–L704 (1993).

[131] P. Taylor, M. Roberts, S. V. Gateva-Kostova, R. B. M. Clarke, G. P. Barwood, W. R. C. Rowley, and P. Gill, Investigation of the $^2S_{1/2}-^2D_{5/2}$ clock transition in a single ytterbium ion, Phys. Rev. A **56**, 2699–2704 (1997).

[132] N. F. Ramsey, A molecular beam resonance method with separated oscillating fields, Phys. Rev. **78**, 695–699 (1950).

[133] N. F. Ramsey, V. Molecular-beam magnetic resonance methods, in *Molecular Beams*, International series of monographs on physics (Oxford University Press, Oxford, 1956) pp. 115–144.

[134] I. I. Rabi, Space quantization in a gyrating magnetic field, Phys. Rev. **51**, 652–654 (1937).

[135] M. Bishof, X. Zhang, M. J. Martin, and J. Ye, Optical spectrum analyzer with quantum-limited noise floor, Phys. Rev. Lett. **111**, 093604 (2013).

[136] K. Hosaka, S. Webster, P. Blythe, A. Stannard, D. Beaton, H. Margolis, S. Lea, and P. Gill, An optical frequency standard based on the electric octupole transition in Yb^+, IEEE Trans. Instrum. Meas. **54**, 759–762 (2005).

[137] B. Efron and R. Tibshirani, *An Introduction to the Bootstrap*, 1st ed. (Chapman & Hall/CRC, New York, 1993).

[138] R. M. Godun, P. B. R. Nisbet-Jones, J. M. Jones, S. A. King, L. A. M. Johnson, H. S. Margolis, K. Szymaniec, S. N. Lea, K. Bongs, and P. Gill, Frequency ratio of two optical clock transitions in $^{171}Yb^+$ and constraints on the time variation of fundamental constants, Phys. Rev. Lett. **113**, 210801 (2014).

[139] C. Tamm, S. Weyers, B. Lipphardt, and E. Peik, Stray-field-induced quadrupole shift and absolute frequency of the 688-THz $^{171}Yb^+$ single-ion optical frequency standard, Phys. Rev. A **80**, 043403 (2009).

[140] S. M. Barnett, On the recoil and doppler shifts, J. Mod. Opt. **57**, 1445–1447 (2010).

[141] C. Cohen-Tannoudji and D. Guery-Odelin, *Advances in Atomic Physics: An Overview* (World Scientific, Singapore, 2011).

[142] G. M. Stéphan, T. T. Tam, S. Blin, P. Besnard, and M. Têtu, Laser line shape and spectral density of frequency noise, Phys. Rev. A **71**, 043809 (2005).

[143] G. Di Domenico, S. Schilt, and P. Thomann, Simple approach to the relation between laser frequency noise and laser line shape, Appl. Opt. **49**, 4801–4807 (2010).

[144] I. Lizuain, J. G. Muga, and J. Eschner, Motional frequency shifts of trapped ions in the Lamb-Dicke regime, Phys. Rev. A **76**, 033808 (2007).

[145] C. J. Foot, *Atomic Physics*, Oxford Master Series in Physics (Oxford University Press, Oxford, 2005).

[146] M. S. Safronova, M. G. Kozlov, and C. W. Clark, Blackbody radiation shifts in optical atomic clocks, IEEE Trans. Ultrason. Ferroelectr. Freq. Control **59**, 439–447 (2012).

[147] S. G. Porsev and A. Derevianko, Multipolar theory of blackbody radiation shift of atomic energy levels and its implications for optical lattice clocks, Phys. Rev. A **74**, 020502 (2006).

[148] S. G. Porsev and A. Derevianko, Erratum: Multipolar theory of blackbody radiation shift of atomic energy levels and its implications for optical lattice clocks [Phys. Rev. A 74, 020502(R) (2006)], Phys. Rev. A **86**, 029904 (2012).

[149] A. Roy, S. De, B. Arora, and B. K. Sahoo, Accurate determination of blackbody radiation shift, magic and tune-out wavelengths for the $6S_{1/2} \rightarrow 5D_{3/2}$ clock transition in Yb^+, Journal of Physics B: Atomic, Molecular and Optical Physics **50**, 205201 (2017).

[150] T. Schneider, E. Peik, and C. Tamm, Sub-Hertz optical frequency comparisons between two trapped $^{171}Yb^+$ ions, Phys. Rev. Lett. **94**, 230801 (2005).

[151] S. N. Lea, S. A. Webster, and G. P. Barwood, Polarisabilities and blackbody shifts in Sr^+ and Yb^+, in *Proceedings of the 20th European Frequency and Time Forum* (IEEE, Braunschweig, Germany, 2006) pp. 302–307.

[152] P. Dubé, A. A. Madej, Z. Zhou, and J. E. Bernard, Evaluation of systematic shifts of the $^{88}Sr^+$ single-ion optical frequency standard at the 10^{-17} level, Phys. Rev. A **87**, 023806 (2013).

[153] T. R. Tan, C. L. Edmunds, A. R. Milne, M. J. Biercuk, and C. Hempel, Precision characterization of the $^2D_{5/2}$ state and the quadratic zeeman coefficient in $^{171}Yb^+$, Phys. Rev. A **104**, L010802 (2021).

[154] A. A. Madej, J. E. Bernard, P. Dubé, L. Marmet, and R. S. Windeler, Absolute frequency of the $^{88}Sr^+$ $5s\,^2S_{1/2}$–$4d\,^2D_{5/2}$ reference transition at 445 THz and evaluation of systematic shifts, Phys. Rev. A **70**, 012507 (2004).

[155] K. Matsubara, K. Hayasaka, Y. Li, H. Ito, S. Nagano, M. Kajita, and M. Hosokawa, Frequency measurement of the optical clock transition of $^{40}Ca^+$ ions with an uncertainty of 10^{-14} level, Appl. Phys. Express **1**, 067011 (2008).

[156] W. M. Itano, External-field shifts of the $^{199}Hg^+$ optical frequency standard, J. Res. Natl. Inst. Stand. Technol. **105**, 829–837 (2000).

[157] J. R. P. Angel, P. G. H. Sandars, and G. K. Woodgate, Direct measurement of an atomic quadrupole moment, J. Chem. Phys. **47**, 1552–1553 (1967).

[158] D. K. Nandy and B. K. Sahoo, Quadrupole shifts for the $^{171}Yb^{+}$ ion clocks: Experiments versus theories, Phys. Rev. A **90**, 050503 (2014).

[159] G. P. Barwood, H. S. Margolis, G. Huang, P. Gill, and H. A. Klein, Measurement of the electric quadrupole moment of the $4d\,^2D_{5/2}$ level in $^{88}Sr^{+}$, Phys. Rev. Lett. **93**, 133001 (2004).

[160] T. Schneider, *Optical Frequency Standard with a Single* $^{171}Yb^{+}$ *Ion*, Ph.D. thesis, Universität Hannover (2005).

[161] T. Bothwell, C. J. Kennedy, A. Aeppli, D. Kedar, J. M. Robinson, E. Oelker, A. Staron, and J. Ye, Resolving the gravitational redshift across a millimetre-scale atomic sample, Nature **602**, 420–424 (2022).

[162] M. Bacelar Valente, Einstein's redshift derivations: its history from 1907 to 1921, Circumscribere **22**, 1–16 (2018).

[163] C. Degenhardt, T. Nazarova, C. Lisdat, S. H., U. Sterr, and F. Riehle, Influence of chirped excitation pulses in an optical clock with ultracold calcium atoms, IEEE Trans. Instrum. Meas. **54**, 771–775 (2005).

[164] C. Sanner, N. Huntemann, R. Lange, C. Tamm, and E. Peik, Autobalanced ramsey spectroscopy, Phys. Rev. Lett. **120**, 053602 (2018).

[165] D. S. Hughes and C. Eckart, The effect of the motion of the nucleus on the spectra of Li I and Li II, Phys. Rev. **36**, 694–698 (1930).

[166] A. Harvey and F. A. Jenkins, Alternating intensities and isotope effect in the blue-green absorption bands of Li_2, Phys. Rev. **35**, 789–801 (1930).

[167] J. P. Vinti, Isotope shift in magnesium, Phys. Rev. **56**, 1120–1132 (1939).

[168] E. C. Seltzer, *K* X-ray isotope shifts, Phys. Rev. **188**, 1916–1919 (1969).

[169] S. A. Blundell, P. E. G. Baird, C. W. P. Palmer, D. N. Stacey, and G. K. Woodgate, A reformulation of the theory of field isotope shift in atoms, J. Phys. B **20**, 3663–3681 (1987).

[170] H. Schopper, ed., *Nuclear Charge Radii* (SpringerMaterials, Heidelberg, 2004).

[171] I. Angeli and K. Marinova, Table of experimental nuclear ground state charge radii: An update, At. Data Nucl. Data Tables **99**, 69–95 (2013).

[172] W. H. King, Comments on the article "Peculiarities of the isotope shift in the samarium spectrum", J. Opt. Soc. Am. **53**, 638–639 (1963).

[173] J. Ekman, P. Jönsson, M. Godefroid, C. Nazé, G. Gaigalas, and J. Bieroń, RIS4: A program for relativistic isotope shift calculations, Comput. Phys. Commun. **235**, 433–446 (2019).

[174] C. W. P. Palmer, Reformulation of the theory of the mass shift, J. Phys. B **20**, 5987–5996 (1987).

[175] D. M. Rossi, P. Adrich, F. Aksouh, H. Alvarez-Pol, T. Aumann, J. Benlliure, M. Böhmer, K. Boretzky, E. Casarejos, M. Chartier, A. Chatillon, D. Cortina-Gil, U. Datta Pramanik, H. Emling, O. Ershova, B. Fernandez-Dominguez, H. Geissel, M. Gorska, M. Heil, H. T. Johansson, A. Junghans, A. Kelic-Heil, O. Kiselev, A. Klimkiewicz, J. V. Kratz, R. Krücken, N. Kurz, M. Labiche, T. Le Bleis, R. Lemmon, Y. A. Litvinov, K. Mahata, P. Maierbeck, A. Movsesyan, T. Nilsson, C. Nociforo, R. Palit, S. Paschalis, R. Plag, R. Reifarth, D. Savran, H. Scheit, H. Simon, K. Sümmerer, A. Wagner, W. Waluś, H. Weick, and M. Winkler, Measurement of the dipole polarizability of the unstable neutron-rich nucleus ^{68}Ni, Phys. Rev. Lett. **111**, 242503 (2013).

[176] J. C. Berengut, C. Delaunay, A. Geddes, and Y. Soreq, Generalized King linearity and new physics searches with isotope shifts, Phys. Rev. Research **2**, 043444 (2020).

[177] C. F. Van Loan, The ubiquitous Kronecker product, J. Comput. Appl. Math. **123**, 85–100 (2000).

[178] H. V. Henderson and S. R. Searle, The vec-permutation matrix, the vec operator and Kronecker products: a review, Linear Multilinear Algebra **9**, 271–288 (1981).

[179] S. O. Allehabi, V. A. Dzuba, V. V. Flambaum, and A. V. Afanasjev, Nuclear deformation as a source of the nonlinearity of the King plot in the Yb^+ ion, Phys. Rev. A **103**, L030801 (2021).

[180] P.-G. Reinhard, W. Nazarewicz, and R. F. Garcia Ruiz, Beyond the charge radius: The information content of the fourth radial moment, Phys. Rev. C **101**, 021301(R) (2020).

[181] P.-G. Reinhard and W. Nazarewicz, Nuclear charge densities in spherical and deformed nuclei: Toward precise calculations of charge radii, Phys. Rev. C **103**, 054310 (2021).

[182] B. Pritychenko, M. Birch, B. Singh, and M. Horoi, Tables of E2 transition probabilities from the first 2+ states in even–even nuclei, At. Data Nucl. Data Tables **107**, 1–139 (2016).

[183] B. A. Brown, C. R. Bronk, and P. E. Hodgson, Systematics of nuclear RMS charge radii, J. Phys. G **10**, 1683–1701 (1984).

[184] E. W. Otten, Nuclear radii and moments of unstable isotopes, in *Treatise on Heavy Ion Science: Volume 8: Nuclei Far From Stability*, edited by D. A. Bromley (Springer US, Boston, MA, 1989) pp. 517–638.

[185] A. Papoulia, B. G. Carlsson, and J. Ekman, Effect of realistic nuclear charge distributions on isotope shifts and progress towards the extraction of higher-order nuclear radial moments, Phys. Rev. A **94**, 042502 (2016).

[186] M. Puchalski and K. Pachucki, Nuclear structure effects in the isotope shift with halo nuclei, Hyperfine Interact. **196**, 35–42 (2010).

[187] R. J. Bartlett, Adventures in DFT by a wavefunction theorist, J. Chem. Phys **151**, 160901 (2019).

[188] M. Y. Amusia, A. Z. Msezane, and V. R. Shaginyan, Density functional theory versus the Hartree-Fock method: Comparative assessment, Phys. Scr. **68**, C133–C140 (2003).

[189] C. Froese Fischer, T. Brace, and P. Jönsson, *Computational Atomic Structure: An MCHF Approach* (IOP Publishing, Philadelphia, USA, 1997).

[190] B. Fawcett and M. Wilson, Computed oscillator strengths, Landé g values, and lifetimes in Yb II, At. Data Nucl. Data Tables **47**, 241–317 (1991).

[191] P. Jönsson, A. Ynnerman, C. Froese Fischer, M. R. Godefroid, and J. Olsen, Large-scale multiconfiguration Hartree-Fock and configuration-interaction calculations of the transition probability and hyperfine structures in the sodium resonance transition, Phys. Rev. A **53**, 4021–4030 (1996).

[192] E. Biémont, J.-F. Dutrieux, I. Martin, and P. Quinet, Lifetime calculations in Yb II, J. Phys. B **31**, 3321–3333 (1998).

[193] S. G. Porsev, M. G. Kozlov, and D. Reimers, Transition frequency shifts with fine-structure constant variation for Fe I and isotope-shift calculations in Fe I and Fe II, Phys. Rev. A **79**, 032519 (2009).

[194] V. A. Dzuba, V. V. Flambaum, and M. G. Kozlov, Combination of the many-body perturbation theory with the configuration-interaction method, Phys. Rev. A **54**, 3948–3959 (1996).

[195] M. S. Safronova, M. G. Kozlov, W. R. Johnson, and D. Jiang, Development of a configuration-interaction plus all-order method for atomic calculations, Phys. Rev. A **80**, 012516 (2009).

[196] I. Grant, B. McKenzie, P. Norrington, D. Mayers, and N. Pyper, An atomic multiconfigurational Dirac-Fock package, Comput. Phys. Commun. **21**, 207–231 (1980).

[197] K. Dyall, I. Grant, C. Johnson, F. Parpia, and E. Plummer, GRASP: A general-purpose relativistic atomic structure program, Comput. Phys. Commun. **55**, 425–456 (1989).

[198] F. Parpia, C. Froese Fischer, and I. Grant, GRASP92: A package for large-scale relativistic atomic structure calculations, Comput. Phys. Commun. **94**, 249–271 (1996).

[199] P. Jönsson, X. He, C. Froese Fischer, and I. Grant, The grasp2K relativistic atomic structure package, Comput. Phys. Commun. **177**, 597–622 (2007).

[200] P. Jönsson, G. Gaigalas, J. Bieroń, C. Froese Fischer, and I. Grant, New version: Grasp2K relativistic atomic structure package, Comput. Phys. Commun. **184**, 2197–2203 (2013).

[201] C. Froese Fischer, G. Gaigalas, P. Jönsson, and J. Bieroń, GRASP2018–a Fortran 95 version of the general relativistic atomic structure package, Mendeley Data (2019).

[202] General Relativistic Atomic Structure Package, GitHub repository, accessed: 2022-03-10.

[203] J. Bieroń, C. Froese Fischer, G. Gaigalas, I. Grant, and P. Jönsson, *A practical guide to GRASP2018–A collection of Fortran 95 programs with parallel computing using MPI* (2018).

[204] The official website for Ubuntu Desktop, accessed: 2022-03-10.

[205] J. Hur, REDF (v1.0.0), Zenodo, 10.5281/zenodo.5818081 (2022).

[206] G. Gaigalas, Z. Rudzikas, and C. Froese Fischer, An efficient approach for spin–angular integrations in atomic structure calculations, J. Phys. B **30**, 3747–3771 (1997).

[207] G. Gaigalas, An efficient approach for spin–angular integrations in atomic structure calculations, Lith. J. Phys. **39**, 79–105 (1999).

[208] C. Nazé, E. Gaidamauskas, G. Gaigalas, M. Godefroid, and P. Jönsson, RIS3: A program for relativistic isotope shift calculations, Comput. Phys. Commun. **184**, 2187–2196 (2013).

[209] MIT Satori user documentation, accessed: 2022-04-30.

[210] IBM POWER9 processor chip, accessed: 2022-04-30.

[211] Red Hat Enterprise Linux 8, accessed: 2022-04-30.

[212] Open MPI: Open Source High Performance Computing, accessed: 2022-04-30.

[213] J. B. Mann and W. R. Johnson, Breit interaction in multielectron atoms, Phys. Rev. A **4**, 41–51 (1971).

[214] S. Fritzsche, Level structure and properties of open f-shell elements, Atoms **10**, 1–16 (2022).

[215] M. R. Kalita, J. A. Behr, A. Gorelov, M. R. Pearson, A. C. DeHart, G. Gwinner, M. J. Kossin, L. A. Orozco, S. Aubin, E. Gomez, M. S. Safronova, V. A. Dzuba, and V. V. Flambaum, Isotope shifts in the $7s \to 8s$ transition of francium: Measurements and comparison to *ab initio* theory, Phys. Rev. A **97**, 042507 (2018).

[216] G. Fricke and K. Heilig, Introduction, in *Nuclear Charge Radii*, Landolt-Börnstein - Group I Elementary Particles, Nuclei and Atoms, Vol. 20, edited by H. Schopper (Springer-Verlag, Berlin/Heidelberg, 2004) pp. 1–36.

[217] E. A. Donley, T. P. Heavner, F. Levi, M. O. Tataw, and S. R. Jefferts, Double-pass acousto-optic modulator system, Rev. Sci. Instrum. **76**, 063112 (2005).

[218] L.-S. Ma, P. Jungner, J. Ye, and J. L. Hall, Delivering the same optical frequency at two places: accurate cancellation of phase noise introduced by an optical fiber or other time-varying path, Opt. Lett. **19**, 1777–1779 (1994).

[219] P. O. Schmidt, T. Rosenband, C. Langer, W. M. Itano, J. C. Bergquist, and D. J. Wineland, Spectroscopy using quantum logic, Science **309**, 749–752 (2005).

[220] C. A. Sackett, D. Kielpinski, B. E. King, C. Langer, V. Meyer, C. J. Myatt, M. Rowe, Q. Turchette, W. M. Itano, D. J. Wineland, *et al.*, Experimental entanglement of four particles, Nature **404**, 256–259 (2000).

[221] J. J. . Bollinger, W. M. Itano, D. J. Wineland, and D. J. Heinzen, Optimal frequency measurements with maximally correlated states, Phys. Rev. A **54**, R4649–R4652 (1996).

[222] K. Beloy, A. Derevianko, and W. R. Johnson, Hyperfine structure of the metastable $^3P_2$ state of alkaline-earth-metal atoms as an accurate probe of nuclear magnetic octupole moments, Phys. Rev. A **77**, 012512 (2008).

[223] G. W. F. Drake, ed., *Springer Handbook of Atomic, Molecular, and Optical Physics*, Springer Handbooks (Springer, New York, 2006).

[224] G. K. Woodgate, *Elementary Atomic Structure*, 2nd ed. (Oxford University Press Inc., New York, 1980).

[225] C. Roman, *Expanding the* $^{171}\mathrm{Yb}^+$ *toolbox: the* $^2\mathrm{F}^o_{7/2}$ *state as resource for quantum information science*, Ph.D. thesis, University of California, Los Angeles (2021).

[226] P. Fisk, M. Sellars, M. Lawn, and G. Coles, Accurate measurement of the 12.6 GHz "clock" transition in trapped $^{171}Yb^+$ ions, IEEE Trans. Ultrason. Ferroelectr. Freq. Control **44**, 344–354 (1997).

[227] A.-M. Mårtensson-Pendrill, D. S. Gough, and P. Hannaford, Isotope shifts and hyperfine structure in the 369.4-nm $6s$-$6p_{1/2}$ resonance line of singly ionized ytterbium, Phys. Rev. A **49**, 3351–3365 (1994).

[228] A. Münch, M. Berkler, C. Gerz, D. Wilsdorf, and G. Werth, Precise ground-state hyperfine splitting in ^{173}Yb II, Phys. Rev. A **35**, 4147–4150 (1987).

[229] W. M. Itano, Quadrupole moments and hyperfine constants of metastable states of Ca^+, Sr^+, Ba^+, Yb^+, Hg^+, and Au, Phys. Rev. A **73**, 022510 (2006).

[230] D. Xiao, J. Li, W. C. Campbell, T. Dellaert, P. McMillin, A. Ransford, C. Roman, and A. Derevianko, Hyperfine structure of $^{173}Yb^+$: Toward resolving the ^{173}Yb nuclear-octupole-moment puzzle, Phys. Rev. A **102**, 022810 (2020).

[231] V. A. Dzuba and V. V. Flambaum, Hyperfine-induced electric dipole contributions to the electric octupole and magnetic quadrupole atomic clock transitions, Phys. Rev. A **93**, 052517 (2016).

[232] M. J. Petrasiunas, E. W. Streed, T. J. Weinhold, B. G. Norton, and D. Kielpinski, Optogalvanic spectroscopy of metastable states in Yb^+, Appl. Phys. B **107**, 1053–1059 (2012).

[233] Q. McKnight, A. Dodson, T. Sprenkle, T. Bennett, and S. Bergeson, Comment on "laser cooling of ^{173}Yb for isotope separation and precision hyperfine spectroscopy", Phys. Rev. A **97**, 016501 (2018).

[234] J. J. McLoughlin, A. H. Nizamani, J. D. Siverns, R. C. Sterling, M. D. Hughes, B. Lekitsch, B. Stein, S. Weidt, and W. K. Hensinger, Versatile ytterbium ion trap experiment for operation of scalable ion-trap chips with motional heating and transition-frequency measurements, Phys. Rev. A **83**, 013406 (2011).

[235] M. Roberts, P. Taylor, S. V. Gateva-Kostova, R. B. M. Clarke, W. R. C. Rowley, and P. Gill, Measurement of the $^2S_{1/2}$–$^2D_{5/2}$ clock transition in a single $^{171}Yb^+$ ion, Phys. Rev. A **60**, 2867–2872 (1999).

[236] C. Clivati, G. Cappellini, L. F. Livi, F. Poggiali, M. S. de Cumis, M. Mancini, G. Pagano, M. Frittelli, A. Mura, G. A. Costanzo, F. Levi, D. Calonico, L. Fallani, J. Catani, and M. Inguscio, Measuring absolute frequencies beyond the GPS limit via long-haul optical frequency dissemination, Opt. Express **24**, 11865–11875 (2016).

[237] N. Poli, Z. W. Barber, N. D. Lemke, C. W. Oates, L. S. Ma, J. E. Stalnaker, T. M. Fortier, S. A. Diddams, L. Hollberg, J. C. Bergquist, A. Brusch, S. Jefferts, T. Heavner, and T. Parker, Frequency evaluation of the doubly forbidden $^1S_0 \rightarrow^3 P_0$ transition in bosonic ^{174}Yb, Phys. Rev. A **77**, 050501 (2008).

[238] J. R. Persson, Table of hyperfine anomaly in atomic systems, At. Data Nucl. Data Tables **99**, 62–68 (2013).

[239] A. Bohr and V. F. Weisskopf, The influence of nuclear structure on the hyperfine structure of heavy elements, Phys. Rev. **77**, 94–98 (1950).

[240] J. E. Rosenthal and G. Breit, The isotope shift in hyperfine structure, Phys. Rev. **41**, 459–470 (1932).

[241] M. F. Crawford and A. L. Schawlow, Electron-nuclear potential fields from hyperfine structure, Phys. Rev. **76**, 1310–1317 (1949).

[242] L. Olschewski, Determination of the nuclear magnetic moments on free ^{43}Ca-, ^{87}Sr-, ^{135}Ba-, ^{137}Ba-, ^{171}Yb-, and ^{173}Yb-atoms by means of optical pumping (in German), Z. Physik **249**, 205–227 (1972).

[243] B. Budick and J. Snir, Hyperfine-structure anomalies of stable ytterbium isotopes, Phys. Rev. A **1**, 545–551 (1970).

[244] V. Gerginov, A. Derevianko, and C. E. Tanner, Observation of the nuclear magnetic octupole moment of ^{133}Cs, Phys. Rev. Lett. **91**, 072501 (2003).

[245] W. Dankwort, J. Ferch, and H. Gebauer, Hexadecapole interaction in the atomic ground state of ^{165}Ho, Z. Phys. **267**, 229–237 (1974).

[246] N. Stone, Table of nuclear magnetic dipole and electric quadrupole moments, Atomic Data and Nuclear Data Tables **90**, 75–176 (2005).

[247] R. P. de Groote, S. Kujanpää, A. Koszorús, J. G. Li, and I. D. Moore, Magnetic octupole moment of ^{173}Yb using collinear laser spectroscopy, Phys. Rev. A **103**, 032826 (2021).

[248] R. Lange, A. A. Peshkov, N. Huntemann, C. Tamm, A. Surzhykov, and E. Peik, Lifetime of the $^2F_{7/2}$ level in Yb^+ for spontaneous emission of electric octupole radiation, Phys. Rev. Lett. **127**, 213001 (2021).

[249] K. Beloy, A. Derevianko, V. A. Dzuba, G. T. Howell, B. B. Blinov, and E. N. Fortson, Nuclear magnetic octupole moment and the hyperfine structure of the $5D_{3/2,5/2}$ states of the Ba^+ ion, Phys. Rev. A **77**, 052503 (2008).

[250] S. A. Williams, Magnetic octupole moments of axially symmetric deformed nuclei, Phys. Rev. **125**, 340–346 (1962).

[251] A. K. Singh, D. Angom, and V. Natarajan, Observation of the nuclear magnetic octupole moment of ^{173}yb from precise measurements of the hyperfine structure in the $^3P_2$ state, Phys. Rev. A **87**, 012512 (2013).

[252] K. A. Landsman, C. Figgatt, T. Schuster, N. M. Linke, B. Yoshida, N. Y. Yao, and C. Monroe, Verified quantum information scrambling, Nature **567**, 61–65 (2019).

[253] C. Figgatt, A. Ostrander, N. M. Linke, K. A. Landsman, D. Zhu, D. Maslov, and C. Monroe, Parallel entangling operations on a universal ion-trap quantum computer, Nature **572**, 368–372 (2019).

[254] K. Wright, K. M. Beck, S. Debnath, J. M. Amini, Y. Nam, N. Grzesiak, J.-S. Chen, N. C. Pisenti, M. Chmielewski, C. Collins, K. M. Hudek, J. Mizrahi, J. D. Wong-Campos, S. Allen, J. Apisdorf, P. Solomon, M. Williams, A. M. Ducore, A. Blinov, S. M. Kreikemeier, V. Chaplin, M. Keesan, C. Monroe, and J. Kim, Benchmarking an 11-qubit quantum computer, Nature communications **10**, 1–6 (2019).

[255] R. J. Niffenegger, J. Stuart, C. Sorace-Agaskar, D. Kharas, S. Bramhavar, C. D. Bruzewicz, W. Loh, R. T. Maxson, R. McConnell, D. Reens, G. N. West, J. M. Sage, and J. Chiaverini, Integrated multi-wavelength control of an ion qubit, Nature **586**, 538–542 (2020).

[256] D. Hucul, *A Modular Quantum System of Trapped Atomic Ions*, Ph.D. thesis, University of Maryland, College Park (2015).

[257] R. C. Teixeira, A. Larrouy, A. Muni, L. Lachaud, J.-M. Raimond, S. Gleyzes, and M. Brune, Preparation of long-lived, non-autoionizing circular Rydberg states of strontium, Phys. Rev. Lett. **125**, 263001 (2020).

[258] F. Roussel, M. Cheret, L. Chen, T. Bolzinger, G. Spiess, J. Hare, and M. Gross, Observation of circular-metastable doubly excited states of barium, Phys. Rev. Lett. **65**, 3112–3115 (1990).

[259] M. G. Kozlov, M. S. Safronova, J. R. Crespo López-Urrutia, and P. O. Schmidt, Highly charged ions: Optical clocks and applications in fundamental physics, Rev. Mod. Phys. **90**, 045005 (2018).

[260] H. M. Meyer, M. Steiner, L. Ratschbacher, C. Zipkes, and M. Köhl, Laser spectroscopy and cooling of Yb^+ ions on a deep-UV transition, Phys. Rev. A **85**, 012502 (2012).

[261] S. Olmschenk, D. Hayes, D. N. Matsukevich, P. Maunz, D. L. Moehring, K. C. Younge, and C. Monroe, Measurement of the lifetime of the $6p\ ^2P^o_{1/2}$ level of Yb^+, Phys. Rev. A **80**, 022502 (2009).

[262] N. Yu and L. Maleki, Lifetime measurements of the $4f^{14}5d$ metastable states in single ytterbium ions, Phys. Rev. A **61**, 022507 (2000).

[263] M. Roberts, P. Taylor, G. P. Barwood, P. Gill, H. A. Klein, and W. R. C. Rowley, Observation of an electric octupole transition in a single ion, Phys. Rev. Lett. **78**, 1876–1879 (1997).

[264] M. Pizzocaro, F. Bregolin, P. Barbieri, B. Rauf, F. Levi, and D. Calonico, Absolute frequency measurement of the $^1S_0$–$^3P_0$ transition of ^{171}Yb with a link to international atomic time, Metrologia **57**, 035007 (2020).

[265] S. A.-L. Schulz, A. A. Peshkov, R. A. Müller, R. Lange, N. Huntemann, C. Tamm, E. Peik, and A. Surzhykov, Generalized excitation of atomic multipole transitions by twisted light modes, Phys. Rev. A **102**, 012812 (2020).